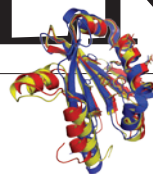


# THIS WEEK

## EDITORIALS

**WORLD VIEW** China's new 'forests' not as green as they may seem **p.371**

**HIGH SCORES** Online gamers untangle protein structures **p.373**



**TRENDS** The world falls short on infant-mortality goals **p.375**

## The wrong message on vaccines

*Unfounded fears about vaccines are already reaching worrisome proportions. No public figure should stoke them — as US presidential hopeful Michele Bachmann has done.*

In 2009 and 2010, fewer than half of all US states reported that the proportion of children aged five to six who were properly vaccinated against measles before they entered school had reached the desired 95%. In parts of the country, the rate of refusal of mandatory childhood vaccinations for non-medical reasons stands at 25%. And as-yet-unpublished data show that this rate is continuing to increase.

The results of vaccine refusal are already evident in Europe. France reported 4,937 cases of measles in the first three months of this year — nearly as many as in all of 2010. In total, 30 countries in the World Health Organization's European region reported a marked increase in measles cases early this year. At some point, the herd immunity that protects the unvaccinated and the immunosuppressed could be lost.

Against this backdrop, it is vital that public debates on vaccination stick to the facts — and that politicians who make science-supported decisions be applauded. Unfortunately, it was Michele Bachmann who received the applause at the Republican presidential candidates' debate earlier this month. The Minnesota congresswoman had attacked rival candidate Rick Perry for his failed attempt in 2007, as Texas governor, to mandate vaccination against human papilloma virus (HPV) for 11- and 12-year-old schoolgirls, as recommended by the US Centers for Disease Control and Prevention (CDC) in Atlanta, Georgia.

Perhaps Perry did the right thing for the wrong reasons: he has close

ties to pharmaceutical company Merck, a generous donor to his campaigns and the only maker of an HPV vaccine at the time of his attempt. But his goal was laudable: HPV is the most common sexually transmitted infection in the country and the major cause of cervical cancer, which kills 4,000 US women each year. The Food and Drug Administration has also approved the HPV jab for the prevention of vulvar and vaginal cancers, and of anal cancer in both males and females.

That did not stop Bachmann from making the astonishingly irresponsible claim, on national television, that the vaccine is a "potentially dangerous drug". She later suggested that it is linked to "mental retardation". Yet the CDC says that the vaccine is safe. Some 35 million doses have been delivered in the United States since its approval, but just 0.05% of recipients have reported side effects, mostly minor. Nor is there scientific support for the belief that presumably drives Bachmann's misstatements — that vaccinating prepubescent girls will somehow encourage them to become sexually active.

If Bachmann wants to do right by the millions of girls she claims to care about, she ought to retract her words and urge HPV vaccination. That might do more than anything else to combat an increasingly common parental mindset that takes for granted the past century of gains against infectious disease, and in so doing threatens to reverse them. ■

## Beyond the bomb

*Twenty years after the end of the cold war scientists and the military still need each other.*

With a science and technology budget that currently stands at about US\$12 billion per year, the US defence complex is the world's largest investor in military research. Much of the money has gone into developing weapons of unprecedented lethality, but a large fraction supports 'dual-use' research, whose products — from the Internet to the Global Positioning System — have enriched society as a whole. And the trove of military data has proved surprisingly useful to scientists studying environmental change (see page 388).

Military efforts are also helping to improve public health. Studies of traumatic brain injuries inflicted by bomb blasts (see page 390) could aid in the diagnosis and treatment of brain injuries in civilians. And the need to keep troops healthy has resulted in advances ranging from a partially effective vaccine against HIV to a mobile-phone-based reporting system for disease cases (see page 395).

Such programmes have been strengthened by JASON, an independent panel of high-level scientists whose advice is often brutally frank

(see page 397). But the Pentagon can and should do much more to support dual-use science — by, for example, minimizing the bureaucracy and secrecy that still make it far too difficult for outsiders to gain access to military data.

Defence officials should also insist that their public-health research be meticulously transparent about goals and methods — this is crucial to overcoming mistrust in the developing world. At home, the Pentagon could enhance its credibility among academics by funding discussions on the ethical, legal and social implications of its research — for example, the development of robotic warfare (see page 399).

Most fundamentally, Congress and the Pentagon should continue their strong support for military science. This is not as axiomatic as it was when the United States was in a decades-long, high-stakes technological race with the Soviet Union. Much of today's military research, in the United States and elsewhere, consists of shorter-term problem-solving, such as how to deal with low-tech roadside explosives, or the development of virtual worlds for training troops or aiding their post-injury recovery (see page 406). As the mission becomes more diffuse, high-level support for military science may wane, especially as the Pentagon's overall funding comes under scrutiny (see page 386). Yet cutting and narrowing military research would be short-sighted, especially when the concept of national security is itself expanding, to include not just military strength, but public health, economic vigour, dealing with climate change, and all the other factors that make for a strong society. ■



## China's new forests aren't as green as they seem

*Impressive reports of increased forest cover mask a focus on non-native tree crops that could damage the ecosystem, says Jianchu Xu.*

In the United Nations' 2011 International Year of Forests, China is heralded as a superstar. Almost single-handedly, the country has halted long-term forest loss across Asia, and even turned it into a net gain. Since the 1990s, China has planted more than 4 million hectares of new forest each year.

Earlier this month, President Hu Jintao pledged that China would do even more. He told a meeting of the Asia-Pacific Economic Cooperation Forum in Beijing that the nation would increase its total area of forest by 40 million hectares over the next decade. China, he said, is ready to make new contributions to green, sustainable growth.

It sounds impressive, but we risk failing to see the wood for the trees. In China, 'forest' includes uncut primary forest, regenerating natural forest and monoculture plantations of non-native trees. The last of these accounts for most of the 'improvement' in forest cover.

The State Forestry Administration has claimed that total forest cover in China reached 20.36% in 2008. Most of this results from the increase in tree crops such as fruit trees, rubber and eucalyptus, not recovery of natural forest, yet Chinese data do not record this shift. The change threatens ecosystem services, particularly watershed protection and biodiversity conservation.

Exotic tree species are being planted in arid and semi-arid conditions, where perennial grasses with their extensive root systems would be better protectors of topsoil. Plantation monocultures harbour little diversity; they provide almost no habitat for the country's many threatened forest species. Plantations generate less leaf litter and other organic inputs than native forests, so soil fauna and flora decrease, and groundwater depletion can be exacerbated by deep-rooted non-native trees that use more water than native species. Afforestation in water-stressed regions might provide wind-breaks, and tree plantations offer some carbon storage. But these benefits come at a high cost to other ecological functions.

Why the intense focus on forest cover? China has long promoted the planting of tree crops. Since 1999, the Grain for Green programme has resulted in some 22 million hectares of new trees on sloping farmland. The programme began after the 1998 Yangtze River floods, which the government blamed on loss of tree cover, although reductions in riparian buffers and soil infiltration capacity probably also had a major role.

Since 2008, forest tenure reform has encouraged the privatization of former collective forests, with more than 100 million hectares affected. Privatization can benefit local economies. But in the absence of any management framework, it has also promoted conversion of natural forests

into plantations: smallholders often fell natural forests for immediate income, then plant monoculture tree crops for long-term investment.

Although the Chinese government has shown that it understands environmental fragility, its scientific and policy guidelines do not adequately address the country's diversity of landscapes and ecosystems. I have seen massive tree plantations on the Tibetan Plateau, in areas where forests never grew before. Local governments face the need to respond to the national imperative for increased forest cover by planting fast-growing species, while also generating the biggest local economic benefits possible. This explains why unsuitable species such as aspens are planted in north China, whereas eucalyptus and rubber trees proliferate in the south.

Perhaps the International Year of Forests can help decision-makers to focus on the various meanings of 'forest', and the trade-offs each type entails. Natural recovery is still the best way to restore damaged forests, but restoration requires targeted involvement using the best science.

Afforestation can restore ecosystem function only if the right species are planted in the right place. Further studies are needed on how the mix of species affects ecosystem functions. Sloping lands, for example, benefit from perennial root systems and associated soil microfauna, but trees are not the only, or necessarily the best, way to establish these root systems.

China's forestry mandate should focus on enhancing environmental services, but policy-makers cannot ignore rural livelihoods. Technical know-how should be provided to local foresters and farmers. Doing away with narrow, one-size-fits-all management targets would also help. The

country, with its state-managed market economy, can afford direct payments for forest ecosystem services, but they should only be offered for natural or regenerated forests with proven biological or ecological value.

As an ecologist and agroforestry practitioner, I would like to see China establish parallel forest-management programmes for recovery and restoration of natural forests, and for incorporating working trees into farmlands. Each should include best practices from ecosystem science; a clear definition of tree crop plantations for timber or non-timber products would clarify the separate systems. A dual strategy would require increased collaboration throughout China's land-management ministries, well supported by interdisciplinary research. But it could ensure that China's massive investment in forests provides maximum benefits, to both local livelihood and the environment. ■

**Jianchu Xu** is a senior scientist at the World Agroforestry Centre and a professor at the Kunming Institute of Botany, Chinese Academy of Sciences. e-mail: J.C.Xu@cgiar.org

**I HAVE SEEN  
MASSIVE TREE  
PLANTATIONS  
ON THE TIBETAN  
PLATEAU, IN AREAS  
WHERE  
FORESTS  
NEVER GREW.**

➔ **NATURE.COM**  
Discuss this article  
online at:  
[go.nature.com/yvjiso](http://go.nature.com/yvjiso)



# SEVEN DAYS

The news in brief

## POLICY

### Deepwater report

The full catalogue of failures that led to the destruction of the Deepwater Horizon drilling rig and the subsequent oil spill in the Gulf of Mexico last year have been laid out in the final US government report, released on 14 September. Investigators from the Bureau of Ocean Energy Management, Regulation and Enforcement and the US Coast Guard conclude that rig-owners Transocean, contracting company Halliburton and “designated operator” BP all violated a number of federal regulations. See [go.nature.com/gxp9i4](http://go.nature.com/gxp9i4) for more.

### TB in Europe

The World Health Organization (WHO) has launched a programme to slash soaring rates of drug-resistant tuberculosis (TB) in Europe. Just one-third of an estimated 80,000 drug-resistant TB infections are reported to the European Centre for Disease Prevention and Control and the WHO in Europe each year. The WHO programme aims to raise this to 85% by 2015, and to treat three-quarters of those cases. The US\$5 billion needed will come from industry, non-profit organizations and the 53 member states in the WHO European region. See [go.nature.com/rczftm](http://go.nature.com/rczftm) for more.

### Israel joins CERN

Israel has become the first non-European country to join CERN, Europe's high-energy physics research centre near Geneva, Switzerland. The country, which is the centre's 21st member, will get voting rights on CERN's council and will have to contribute to the centre's budget. Its membership was officially



## Hope for space telescope

A US Senate subcommittee voted on 14 September to continue funding the James Webb Space Telescope (pictured), the successor to the Hubble Space Telescope. Its climbing price tag, now estimated at US\$8.7 billion, is devouring NASA's astrophysics budget, and a subcommittee in the House of Representatives had voted to cancel the project. The Senate subcommittee, led by Barbara Mikulski (Democrat, Maryland), wants the telescope to get \$530 million in 2012 — much more than the \$374 million in the president's budget request. See [go.nature.com/ei3ije](http://go.nature.com/ei3ije) for more.

confirmed on 16 September, after Israel's cabinet voted to join the lab in April (see *Nature* 472, 265; 2011).

### Stem-cell lawsuit

Two researchers seeking to block US government funding of research using human embryonic stem cells are still battling to continue their lawsuit. On 19 September, James Sherley and Theresa Deisher appealed against a 27 July decision in which a federal judge ruled against

their case (*Nature* 476, 14–15; 2011). See [go.nature.com/dkrlwj](http://go.nature.com/dkrlwj) for more.

### Biofuels error

Countries that encourage increased use of energy from biomass may be overestimating the savings in greenhouse-gas emissions. In an Opinion report published on 15 September, the 19-strong scientific committee of the European Environment Agency has criticized what it calls a “serious accounting

error” if policies incorrectly assume that the combustion of biomass is carbon-neutral. That is not always the case: the biomass may replace forest that would otherwise store carbon, or replace food crops that must then be planted and harvested on other land that was once forest. Emissions resulting from such changes in land use are not correctly accounted for in, for example, the European Union's Renewable Energy Directive, the committee said.

### Global Fund review

The Global Fund to Fight AIDS, Tuberculosis and Malaria needs a major overhaul, according to a report released on 19 September. The fund, based in Geneva, Switzerland, had commissioned the review after it discovered corruption and fraud affecting some US\$39 million of its grants (see *Nature* 470, 6; 2011). The report says that the fund should shift its focus away from getting money out as quickly as possible: the group needs better auditing and management of grants, and should measure its success in terms of its impact on health, not how much it spends. The fund welcomed the report. See [go.nature.com/w87mnc](http://go.nature.com/w87mnc) for more.

## RESEARCH

### NASA's mega-rocket

NASA revealed its latest designs for a heavy-launch vehicle on 14 September. The Space Launch System is set to be more than 10 metres taller than the Saturn V launcher, and would be the most powerful rocket ever to lift people into space, with configurations for both 70 and 130 tonnes of thrust. NASA officials say that they're aiming for a late-2017 crewless test flight, in advance of a 2021 manned test.

C. GUNN/NASA

The programme would cost US\$3 billion a year to get to the test launch — less than the agency spent annually on the shuttle programme. See [go.nature.com/3393u5](http://go.nature.com/3393u5) for more.

## Body on a chip

Even though US politicians have not yet authorized its creation, a proposed new translational-medicine centre at the National Institutes of Health (NIH) is already getting busy. On 16 September, the NIH and the US military together proposed a US\$140-million five-year effort to develop a chip inlaid with human cells for testing new drugs. The NIH's share of this effort would be administered through the proposed new National Center for Advancing Translational Sciences. The centre is also advertising for a director. See [go.nature.com/9ahvkb](http://go.nature.com/9ahvkb) for more.

## Radio-array rivals

Australia and South Africa submitted their final bids to host the Square Kilometre Array of radio telescopes on 15 September. Australia is proposing to build the array in the mostly empty interior of Western Australia, with outstations as far away as New Zealand. South Africa would build its version in the Karoo Desert, with parts extending into eight neighbouring

countries, including islands in the Indian Ocean. A group of external experts will scrutinize the bids, with a decision by the project's board of directors expected early next year. Construction of the €1.5-billion (US\$2.1-billion) array is set to begin in 2016.

### EVENTS



## Mountain quake

A 6.9-magnitude earthquake struck the sparsely populated Himalayan state of Sikkim, northeastern India, on 18 September. As *Nature* went to press, the quake had killed 81 people, including some in nearby West Bengal, Bihar, Nepal and Tibet, and rain and mudslides were hampering rescue efforts (**pictured**).

### BUSINESS

## Nuclear exit

German engineering firm Siemens is pulling out of nuclear power for good. In an interview with *Der Spiegel* on 18 September, chief executive

Peter Löscher announced that the Munich-based company would no longer build or finance nuclear power plants in Germany or elsewhere. Löscher said that the decision was largely due to the nuclear accident at Fukushima Daiichi in Japan and the German government's decision to shut down its existing nuclear plants by 2022. See [go.nature.com/zay8ra](http://go.nature.com/zay8ra) for more.

### PEOPLE

## Innovation boss

Alexander von Gabain took over as head of the European Union's European Institute of Innovation and Technology (EIT) on 15 September, replacing founding chairman Martin Schuurmans. Von Gabain, a microbiologist at the Max Perutz Laboratories in Vienna and a co-founder of the Austrian biotechnology company Intercell, plans to get the EIT more involved in biomedical science.

## Schön loses PhD

The University of Konstanz in Germany was correct to withdraw the doctoral degree of disgraced physicist Jan Hendrik Schön, a court in the state of Baden-Württemberg has ruled. Schön, formerly a staff physicist at Bell Laboratories in Murray Hill, New Jersey — the development arm of Lucent Technologies

## COMING UP

### 26–30 SEPTEMBER

The World Conference on Marine Biodiversity takes place in Aberdeen, UK, discussing research priorities. [www.marine-biodiversity.org](http://www.marine-biodiversity.org)

### 27–30 SEPTEMBER

The International Council for Science holds its triennial general assembly in Rome. The agenda includes reshaping global programmes for environmental research. [go.nature.com/egukv6](http://go.nature.com/egukv6)

### 30 SEPTEMBER

The Tevatron, Fermilab's particle accelerator in Batavia, Illinois, shuts down. See page 379 for more.

— is notorious for a string of high-profile fabrications in the fields of organic and molecular electronics. Last year, Schön successfully sued his alma mater for its 2004 decision to revoke his 1997 PhD thesis (for which there is no suspicion of data fabrication). But in a 14 September judgement, the state court agreed with Konstanz that later misconduct also showed 'unworthiness' to hold the doctorate. The court added that the judgement could not be appealed.

## Global-health head

Trevor Mundel, currently head of development at Swiss drug firm Novartis, will be the new president of the Global Health Programme at the Bill & Melinda Gates Foundation in Seattle, Washington, the foundation announced on 13 September. Mundel, taking over from 1 December, replaces Tachi Yamada, who retired in June after five years as president.

➔ [NATURE.COM](http://NATURE.COM)

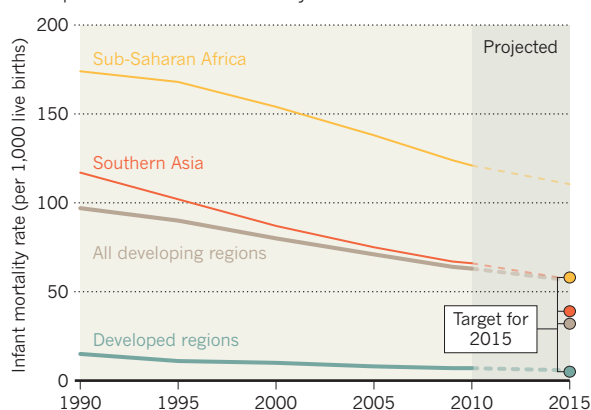
For daily news updates see: [www.nature.com/news](http://www.nature.com/news)

## TREND WATCH

Insufficient progress is being made to drive down global infant mortality, a report from the United Nations concludes. Developed regions are rated as 'on track' to meet their 2015 target of 5 deaths in under-fives per 1,000 live births. But although death rates have dropped rapidly in developing nations, the fall is not enough to achieve a 32 per 1,000 target by the same date, warns the UN's child mortality estimation group. In 2010, developing nations had an average of 63 deaths per 1,000, with sub-Saharan Africa on 121.

## SLOW PROGRESS ON INFANT DEATHS

The developing world is likely to miss its 2015 Millennium Development Goal on infant mortality.



# NEWS IN FOCUS

**PHYSICS** Researchers bid a fond farewell to the top US particle collider **p.379**

**EXOPLANETS** Rash of results see astronomers close in on exo-Earths **p.383**

**MISCONDUCT** Disgraced Austrian doctor gets job back **p.384**

**SPECIAL SECTION** A look inside the military-science complex **p.386**



L. SOLT/DALLAS MORNING NEWS/CORBIS



Alzheimer's disease and diabetes.

But no treatment that involves anything more than “minimal manipulation” of adult stem cells outside the body has been approved by the FDA. Although bone-marrow transplants, for example, involve extraction and reinjection of haematopoietic stem cells, those cells are not cultured or significantly processed.

“Any procedure involving removing cells from the body and manipulating them — even if it’s something as simple as centrifuging them or putting them in a plastic tube — and then putting them elsewhere in the body poses risks,” says Paul Knoepfler, a stem-cell specialist at the Institute for Regenerative Cures at the University of California, Davis. No clinical trials have shown any evidence of efficacy, he says. “Patient testimonials cited by the people selling the treatments have little if any meaning.”

Depending on exactly how the cells are processed and administered, many of these procedures are illegal in the United States. But that didn’t stop Perry from being injected with a concoction of his own stem cells in July to treat a back complaint. Perry’s procedure was carried out by Stanley Jones, a surgeon based in Houston, Texas, who specializes in cosmetic procedures and who is a friend of the governor.

The previous month, Perry had supported legislation that authorized Texas’s health commission to create a stem-cell bank in which patients would be able to deposit their adult stem cells for future use.

## PUBLIC INTEREST

Texas has poured millions of dollars into studying and commercializing adult stem-cell treatments through its Emerging Technology Fund, an initiative created at Perry’s behest. Perry sees the treatments as both a potential boon to the Texan economy and an alternative to treatments that use embryonic stem cells, which he opposes. In a 25 July letter, he asked the Texas Medical Board (TMB), which regulates the state’s physicians and is currently reviewing its policy on stem-cell treatments, to take a lenient view on the procedures. “It is my hope that Texas will become the world’s leader in the research and use of adult stem cells,” he wrote. “With the right policies in place, we can lead the nation in advancing adult-stem-cell research that will treat diseases, cure cancers and, ultimately, save lives.” ▶

Texas governor Rick Perry has received a stem-cell treatment deemed illegal in the United States.

## REGENERATIVE MEDICINE

# Texas prepares to fight for stem cells

*Enthusiasm for unapproved treatments worries regulators.*

BY DAVID CYRANOSKI

There’s a showdown brewing in the state of Texas — and it could get ugly. On one side stands the US Food and Drug Administration (FDA), which is clamping down on the proliferation of unapproved stem-cell treatments being offered to Americans. On the other is state governor Rick Perry, who is riding high in the polls as the Republican

party’s favoured candidate for the 2012 presidential elections — and a staunch advocate of the stem-cell treatments.

At least a dozen companies in the United States offer the treatments, which involve extracting adult stem cells from a patient’s tissue, culturing them, then reinjecting the cells. The theory is that the cells will flourish and replace diseased or damaged tissue in a range of conditions from spinal-cord injury to



► Although scientists and physicians in Texas are excited about the funding to develop stem-cell science, many are concerned that treatments will reach the clinic before safety and efficacy are properly established. “I do believe governor Perry is pushing research to the clinic too quickly,” says Kirstin Matthews, who researches science and technology policy at Rice University in Houston, and who is a member of the TMB’s stakeholder group, which is helping to draft the board’s stem-cell policy.

“People should know what they are doing,” adds Mari Robinson, executive director of the TMB. “Otherwise they’ll try to use it for everything from getting rid of wrinkles to curing cancer.”

The TMB’s draft stem-cell policy is open for public consultation, and will be finalized in November. In a series of written submissions, scientists have pushed for more patient protection. “As a biomedical researcher, I feel the extremes of regulatory burden every day, but I also feel that we must protect patients from risky treatments advanced by overzealous, even greedy, entrepreneurs,” wrote Bettie Sue Masters, a biochemist at the University of Texas Health Science Center in San Antonio.



**“I feel that we must protect patients from risky treatments advanced by overzealous, even greedy, entrepreneurs.”**

Bettie Sue Masters

#### APPROPRIATE OVERSIGHT

Mary Ellen Weber, vice-president in charge of government affairs and policy at the University of Texas Southwestern Medical Center in Dallas, hopes that patients will be properly informed that any benefits that they experience may not be attributable to the stem-cell treatment, and may not be long-lived. By contrast, she warned in a letter to the TMB, the “risks conferred by stem-cell therapy may be delayed and permanent”. Consequently, any adult stem-cell procedures should be looked at by an institutional review board, she wrote.

But state representative Rick Hardcastle, who introduced the legislation to authorize the Texas stem-cell bank, has questioned the need for institutional-review-board consideration of procedures that use adult stem cells. “It was not, and is not, my intent to create onerous and unnecessary regulations to impede the practice and research of physicians in regards to the use of investigational agents,” he wrote to the TMB on 23 August.

Although the TMB’s forthcoming policy is meant to provide clearer guidance on the use

of adult stem cells in the state, physicians and companies are still subject to FDA regulations. And there are growing signs that Perry’s ambition is on a collision course with recent efforts by the FDA to flex its regulatory muscle.

For many years, stem-cell clinics have been able to flourish by skirting the FDA regulations. Some clinics recruit patients in the United States and then send them overseas for treatment: the Stem Cell Treatment Institute in San Diego, for example, treats its patients in Mexico. Others invoke a ‘compassionate use’ exemption to FDA regulations, which allows them to charge patients for experimental therapies if no other treatment options are available. Some argue that the FDA has no jurisdiction over their activities, claiming that adult stem cells are not drugs — merely the patient’s own tissue — and therefore not subject to FDA oversight.

“The growth in the number of clinics and companies marketing stem-cell products without approval is explosive,” says Doug Sipp, who studies global stem-cell regulation at the RIKEN Center for Developmental Biology in Kobe, Japan. “The United States is becoming one of the most rapidly expanding markets for unregulated stem-cell applications.”

The FDA has long pursued a policy of trying to get companies to comply with the regulations, rather than prosecuting them. Recently, however, it has taken stronger steps to crack down. On 15 August, for example, the agency sent a warning letter to Chuck Naparalla, chief executive of TCA Cellular Therapy in Covington, Louisiana, saying that the company had failed to meet safety standards in some of its five FDA-approved clinical trials of its stem-cell therapies. The FDA also accused it of selling treatments to patients “outside of clinical protocols”. TCA Cellular Therapy has not responded to *Nature*’s repeated requests for information on its efforts to comply with the FDA’s demands.

On 18 August, after an investigation by the FDA and the FBI, Fredda Branyon, former owner of Global Laboratories in Scottsdale, Arizona, was convicted by the US Attorney’s office in the Southern District of Texas court of selling unauthorized stem-cell products across state lines.

And in a court case that began last year, the FDA is demanding that Regenerative Sciences of Colorado stop selling its adult stem-cell product Regenxx (see *Nature* 466, 909; 2010). Christopher Centeno, medical director of Regenerative Sciences, claims that “the Regenxx procedure is the practice of medicine, something Congress and the courts have expressly prohibited the FDA from regulating”. The FDA argues that Regenxx falls under its jurisdiction because it is classed as a biological drug under the Code of Federal Regulations 21 on human cells and tissues. That regulation allows the reinjection of a patient’s adult stem cells if they have been

“minimally manipulated”, but the FDA says that the culturing involved in Regenxx is not minimal because “the cells are grown, processed and mixed with drug products outside the body”.

While the FDA is busy in court, Texas’s enthusiasm for stem-cell treatment is growing fast.

The cells used to treat Perry were cultivated at a recently opened laboratory in Houston that is jointly run by RNL Bio, a stem-cell company headquartered in Seoul, and Celltex Therapeutics, a company established and run by Jones and David Eller, former chairman of the board of Texas A&M University and now a supporter and adviser to Perry. Neither Perry nor Jones responded to *Nature*’s interview requests.

RNL Bio’s affiliated clinics in the United States take fat samples from patients and send the cells to Seoul for processing. The manipulated cells are not approved for reinjection in the United States or South Korea, so patients typically travel to China or Japan for the procedure. RNL Bio is now being investigated by the Korean government after two people who underwent this procedure in Japan died (see *Nature* 468, 485; 2010). Jones himself travelled to Japan last year

to receive an injection of cells, prepared by RNL Bio, to treat his arthritis — successfully, he claims.

Perry’s procedure was reportedly carried out in the United States, at Jones’s clinic. The FDA declined to discuss any ongoing or future investigations into stem-cell clinics, but a former reviewer at the FDA’s Center for Biologics Evaluation and Research, which regulates the clinical use of stem cells, says: “If



**“I do believe governor Perry is pushing research to the clinic too quickly.”**

Kirstin Matthews

Perry was treated in the United States, it was clearly in violation” of FDA regulations.

Jones has said that Perry may be prepared to stand up to the FDA over the issue. In a letter to the TMB, Jones wrote: “Please don’t make this difficult, as Governor Perry has really gone all out personally to make stem cells available to people in need of them in Texas.”

“He is incidentally not against a challenge from any government agency that wants to impede us in Texas,” Jones added.

Jones is now set to treat Hardcastle, who has multiple sclerosis. The former FDA reviewer, however, says that after the publicity over Perry’s procedure, it would be standard practice for the agency to warn Jones against carrying out further injections. “If you do it a second time, you could be in hot water.”

The showdown could be about to begin. ■

## PHYSICS

# Fermilab faces life after the Tevatron

*As collider shuts down, US particle physicists shift focus.*

BY EUGENIE SAMUEL REICH

**L**ike an old and celebrated race track, the giant particle accelerator known as the Tevatron is down to its final laps.

Shortly after 2 p.m. on 30 September, with reporters watching by video link from a nearby auditorium, an operator at the Fermi National Accelerator Laboratory (Fermilab) in Batavia, Illinois, will divert the final bunches of protons and antiprotons speeding around the Tevatron's 6.3-kilometre ring, sending them barreling into a solid metal block. The experiment that ruled high-energy physics for more than 25 years will then be over, its funding expired.

The shutdown will provide an occasion to dwell on the Tevatron's past successes (see 'Smashing success'), but it also marks Fermilab's transition to smaller and lower-profile experiments that explore different kinds of physics. Champagne corks are not expected to pop following the closure. "We're not that happy," says Roger Dixon, head of the lab's accelerator division. "It's a solemn occasion."

The closure is a consequence of tight US physics funding and the advent of the Large Hadron Collider (LHC) at CERN, Europe's high-energy physics lab near Geneva, Switzerland. The LHC broke the Tevatron's record for collision energy in 2009 and has been running steadily since 2010. In 2008, a US Department of Energy advisory panel recommended that the country switch its focus in accelerator physics from the 'energy frontier' that would be dominated by the LHC to the 'intensity frontier', in which researchers aim to increase the number of particles produced per second. Instead of creating previously unknown particles by pushing collisions to higher energies, the new strategy will be to investigate rare

interactions involving known particles. The lab is already running three experiments to create and study neutrinos — nearly massless particles that interact only weakly with ordinary matter — using protons from accelerators that also feed the Tevatron. By modifying storage rings and accelerators that will become available when the Tevatron closes, Fermilab should be able to bring two more neutrino experiments online by 2014, followed by two experiments on muons, heavier cousins of the electron. The lab is also working on a proposal for an experiment called Project X, which would increase the intensity of the accelerator beams from 750 kilowatts to more than 2 megawatts, and would allow detailed comparisons of the properties of matter and antimatter. The project has yet to receive approval from the Department of Energy.

For US-based particle physicists, the change is likely to mean smaller research groups — perhaps 100 or 200 per experiment, rather than 600 for each of the Tevatron's two detector collaborations. "It's a big shift," says Regina Rameika, project manager of one of the neutrino experiments now under construction.

As for the Tevatron, its detectors and magnets are ultimately destined for the waste dump, but immediate plans are to run tours of the soon-to-be-accessible beam cavities and detectors for some of the roughly 15,000 school children who visit Fermilab each year. Meanwhile, scientists working at the Tevatron will continue to analyse the data that it has produced — looking for signals of the Higgs particle that is thought to endow all others with mass, or for evidence that will narrow the probable range of its mass. "We expect we will be adding to our legacy," says Dmitri Denisov, spokesman for the Tevatron's DZero collaboration. ■

## SMASHING SUCCESS

Discoveries at the Tevatron particle collider (**pictured, below**) confirmed the standard model of physics and set the course for new investigations beyond it.



R. HAHN/FERMI LAB

### 3 JULY 1983

Protons accelerated to a record 512 gigaelectronvolts.

### 13 OCTOBER 1985

Proton-antiproton collisions seen for the first time, at 1.6 teraelectronvolts.

### 3 MARCH 1995

The top quark discovered, the last fundamental constituent of matter. Its energy signatures are **pictured, bottom**.

### 18 NOVEMBER 1996

Observation of antihydrogen, the first antimatter atoms.

### 5 MARCH 1998

The  $B_c$  meson, the last undiscovered quark-antiquark pair, is spotted.

### 1 MARCH 2001

Higher-energy phase of operation begins.

### 25 SEPTEMBER 2006

Discovery that  $B_s$  mesons transform into their own antiparticles spontaneously.

### 23 OCTOBER 2006

Discovery of the  $\Sigma_b^\pm$  baryons, which include a bottom quark.

### 1 JUNE 2007

Discovery of the  $\Xi_b^0$  baryon, which includes a bottom and a strange quark.

### 4 AUGUST 2008

Experimental evidence restricts the possible mass range of the Higgs boson.

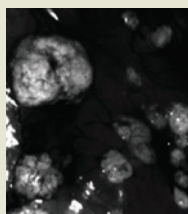


KERR/COM MULTIMEDIA/FERMI LAB



**MORE  
ONLINE**

#### TOP STORY



Glowing cells help cancer surgeons to target tumours  
[go.nature.com/oowaey](http://go.nature.com/oowaey)

#### MORE NEWS

- The PhD Movie makes stars out of real-life scientists  
[go.nature.com/yxlb9q](http://go.nature.com/yxlb9q)
- The Netherlands pushes for innovation  
[go.nature.com/liuxi8](http://go.nature.com/liuxi8)
- Clues emerge to explain first successful HIV vaccine trial  
[go.nature.com/6c3src](http://go.nature.com/6c3src)





Soldiers are yet to see any effective new countermeasures against bioterror agents.

#### BIODEFENCE

# Pentagon rethinks bioterror effort

*Critics say US\$1.5-billion initiative has not delivered results.*

BY ERIKA CHECK HAYDEN

In the film *Contagion*, it takes just a few months for scientists to make a vaccine against a deadly virus. Yet a real US military programme that aimed to do just that is being dismantled after five years of trying.

The Transformational Medical Technologies (TMT) initiative, born in the US Department of Defense in 2006, was originally conceived as a five-year, US\$1.5-billion project that would substantially accelerate the development of countermeasures to protect soldiers against biological attacks. Made into a permanent programme in 2009, it set out to sequence the genomes of potential bioterror agents, explore new drug technologies and develop 'broad-spectrum' therapies that would work against multiple bacterial and viral pathogens — especially haemorrhagic fever viruses such as Ebola and Marburg. Supporters of the programme point out that three candidate drugs developed under the programme, for pathogens including Ebola virus, are now in clinical trials.

The TMT programme, however, has ceased to exist as a stand-alone effort. Alan Rudolph, director of Chemical and Biological Technologies for the TMT's parent office, the Defense Threat Reduction Agency, is folding some TMT projects into other Pentagon efforts and reordering their priorities. Critics say that it has failed in its underlying objective to provide a faster, game-changing approach to biodefence. No antibiotics developed by the TMT have entered clinical trials. The drug candidates it has developed are designed for single pathogens, not multiple threats. And although the programme is set to award a major clinical-trial contract later this year, the drug being tested would treat not exotic, untreatable pathogens but ordinary influenza, a disease already heavily researched outside the Pentagon.

Michael Osterholm of the University of Minnesota's Center for Infectious Disease Research



**BEYOND THE BOMB**  
Science and the military  
[nature.com/military](http://nature.com/military)

and Policy thinks that the programme was overambitious and ill-conceived. "They're wasting tonnes of money," he says.

The programme's architects have vigorously defended its record. "There is a success there that we need to build on," says Jean Reed, who, as deputy assistant to the secretary of defence for chemical and biological defence and chemical demilitarization, laid the plans for the TMT. Now a consultant to the National Defense University in Washington DC, Reed adds that the programme has become the archetype within the defence department for the "development of treatments for biologically engineered and naturally occurring disease threats".

"The TMT from its inception was a high-risk, high-payoff or high-failure effort," says David Hough, who became TMT programme manager in January 2007. He says that the effort has paid off: "If we get an engineered threat or something that we haven't seen before that is causing a lot of deaths, we think we can respond to that." He says that the programme's track record is better than that of the Pentagon's traditional chemical and biological defence research effort over the past decade.

Although the TMT aimed to transform biodefence, it encountered many of the roadblocks that have hindered the nation's biodefence effort as a whole, which has spent \$60 billion since 2001 with only modest returns (see *Nature* 477, 150–152; 2011). Developing broad-spectrum drugs for the battlefield has proved difficult because regulators are more accustomed to evaluating drugs that target one specific disease, and drug companies prefer to focus on diseases that affect many people rather than on obscure pathogens that could serve as bioweapons.

These considerations helped to lead the TMT into focusing on influenza in 2009. That year, US government officials were faced with the double threat of H1N1 swine flu, which threatened to explode into a devastating pandemic, and the more deadly H5N1 bird flu virus, which was continuing to infect small numbers of people.

Government officials were "practically paralysed by the fear that they were dealing with two strains at a time; they didn't know what they were going to do", says Darrell Galloway, Rudolph's predecessor at the Defense Threat Reduction Agency, who was a driving force for the TMT from its inception until he retired in January 2010. Galloway saw influenza as an opening to prove the programme's worth. In May 2009, he awarded a contract to AVI BioPharma of Bothell, Washington, to make a flu drug against the H1N1 virus, using its genetic sequence as a basis. Within months, the company had made a drug and tested it in ferrets.

Yet the move angered some within the Pentagon and perplexed observers, because

K. KULISH/CORBIS



influenza is the focus of considerable research funded by the US Department of Health and Human Services. "I'm having a really hard time making a connection between the investments we're making and the benefit to soldiers," said one staff member at the Defense Threat Reduction Agency.

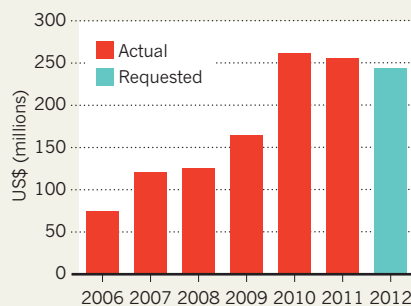
The TMT also stumbled because companies attracted to biodefence tend to be small and inexperienced. Larger, established companies prefer to pursue more profitable markets, fearing that the federal government will commit to stockpiling only limited amounts of drugs developed for defence purposes.

The company behind all three TMT drugs now in clinical trials, AVI BioPharma, has never had a drug approved by the US Food and Drug Administration. The company's technology uses antisense, in which short pieces of genetic material bind to a pathogen's genes and block their production. The technology has led to few approved drugs owing to safety problems and a lack of efficacy. Still, the TMT and the Army awarded the company a \$291-million, six-year contract last year to fund two clinical trials, for its drugs against Ebola and Marburg viruses. Now AVI BioPharma has set its sights on a contract for clinical trials of its antisense drug for H1N1.

AVI BioPharma's chief executive, Chris Garabedian, says that the company's technology

## THE COST OF COUNTERMEASURES

The budget for the Transformational Medical Technologies programme has more than trebled since 2006.



is safer than that tested by other drug firms, and thus can be used in higher doses that are more likely to be effective than other antisense drugs that have failed in the past.

But critics say that it was a mistake for the TMT to invest so much in a technology that does not have a proven track record in infectious disease. "Everybody in that field thinks antisense is a failure, except the [defence department] programme manager," says one biodefence analyst, who did not want to be named.

Rudolph, who succeeded Galloway last

September, controls the chemical and biological defence research budget, which includes standard drug- and vaccine-research programmes as well as the TMT. Rudolph is combining the TMT research money (see 'The cost of countermeasures') with that for traditional projects, and refocusing on four priorities: surveillance and diagnostics, sensors, countermeasures and decontamination technologies.

Rudolph has retained some TMT projects, such as the pathogen-sequencing studies led by Ian Lipkin of Columbia University in New York, who was a technical adviser on *Contagion*. But he has cut others, such as a five-year, \$24.7-million contract awarded in 2008 to Peregrine Pharmaceuticals of Tustin, California, to find antibodies against haemorrhagic fevers. The TMT funding for AVI BioPharma's two clinical trials will continue, however, as the trials are managed separately by Hough.

Whether the dismantling of the TMT will improve the Pentagon's biodefence success rate remains to be seen, says Tom Inglesby at the Center for Biosecurity of the University of Pittsburgh Medical Center in Baltimore, Maryland. "In the end, the question will be, 'Did Rudolph make progress in the time he was there with the money that he had?' Ultimately, he will be held accountable." ■

## ASTRONOMY

# Hints of exo-Earths spark desire for a closer look

*Of the latest clutch reported, one is among the most Earth-like yet, another orbits two suns.*

BY ERIC HAND

Geoffrey Marcy finds it strange to turn people away from a conference about planets beyond our Solar System. “This is a field that had three of us in 1995,” marvels Marcy, a pioneering exoplanet hunter at the University of California, Berkeley.

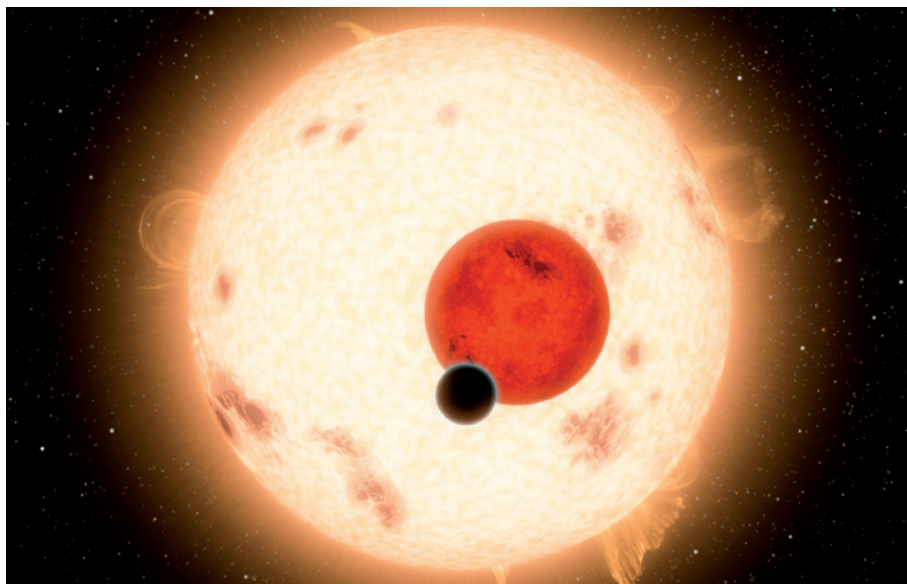
But as an organizer of last week’s Extreme Solar Systems II conference, he had to decline applicants by the dozen. The Jackson Lake Lodge auditorium in Wyoming’s Grand Teton National Park was packed to its 330-person capacity as speakers announced a flood of new detections, and the air was alive with talk of a ‘golden age’ of exoplanet astronomy.

Along with the discoveries came some sobering news. Rocky, Earth-like planets may be less common than many hoped, and unexpectedly ‘noisy’ stars are slowing the hunt. Moreover, astronomers cannot learn much beyond the basics — mass or size and orbit — of the planets they do find. “What we need is a telescope in space that can image and take spectra of truly Earth-like planets,” Marcy says. “We still need that desperately.”

For now, however, indirect methods are keeping astronomers busy. One trove of discoveries came from a European team that watches stars for the slight wobble that signals the gravitational pull of an unseen planet. Their instrument, the High Accuracy Radial velocity Planet Searcher (HARPS), which is attached to a 3.6-metre telescope at the European Southern Observatory in La Silla, Chile, yielded 41 new planets, including one of the most Earth-like yet. At 3.6 times the mass of Earth, it sits in the ‘habitable zone’ around its star, the Goldilocks range of distances at which a planet’s surface would be neither too hot nor too cold for water to be liquid.

There was also news from astronomers working with Kepler, a NASA space telescope that stares fixedly at a field of about 155,000 stars in search of transits: the very slight dip in the brightness of a star as a planet crosses in front. The Kepler team announced that they have now detected 1,781 candidate planets, including 123 that are Earth-sized (see ‘Sizing up the sample’). Among the objects was a novelty: a circumbinary, or a planet orbiting a pair of stars.

Both groups are now confident enough to start making pronouncements about the



The Saturn-sized planet Kepler-16b (black) orbits two dwarf stars. It is not thought to be habitable.

statistics of planets in orbit close to a star — the kind that both Kepler and HARPS are most sensitive to. The HARPS team, for instance, estimates that about half of Sun-like stars have at least one planet with an orbital period of 100 days or fewer, and that many of these systems boast several such planets. Greg Laughlin, an astronomer at the University of California, Santa Cruz, points out that the Solar System — in which only Mercury has such a short period (88 days) — might end up looking like the oddball. “The big news is that there’s this staggering population of planets that you’d never suspect from looking at our own Solar System,” he says.

Extrapolating from Kepler data, Wesley Traub, chief scientist of NASA’s exoplanet exploration programme, took a stab at a more fundamental question: what fraction of Sun-like stars have rocky, Earth-sized planets farther from the star, in a habitable zone? His optimistic answer: 34%.

But many observers dismiss these calculations as premature. Marcy points out that the Kepler statistics suggest a drop off

in the frequency of planets smaller than ‘super-Earths’ — exoplanets with a radius 1.25–2 times that of Earth. “Is Kepler having

trouble detecting truly Earth-sized planets?” asks Marcy. “Or are they rare? We don’t know.”

The stars themselves are making the hunt difficult. Instruments such as HARPS detect the tug of a planet from tiny shifts in the frequency of a star’s spectral lines. Many researchers hoped that a new tool for calibrating the position of those lines, called a laser frequency comb, would enable HARPS to detect the minuscule signal from a planet as small as Earth. But it seems that all but the most quiescent stars have enough surface turbulence to drown out so small a signal. Similarly, the Kepler team has said that because of stellar noise, the mission will now need 8 years, rather than the originally planned 3.5 years, to detect all of the Earth-like planets around its target stars (see *Nature* 477, 142–143; 2011).

Even after true Earth analogues have been detected, neither HARPS nor Kepler will be able to determine whether they have an Earth-like atmosphere containing, for instance, oxygen or carbon dioxide. For a few giant planets that pass in front of their stars, instruments such as the Spitzer Space Telescope have been able to analyse the spectrum of starlight shining through the planet’s thick atmosphere, gleaned clues about its composition. But Marcy says that doing transmission spectroscopy on the thin ring of atmosphere ▶

➔ **NATURE.COM**  
For more on the  
problem of stellar  
noise, see:  
[go.nature.com/joxl6f](http://go.nature.com/joxl6f)

NASA/JPL-CALTECH

► surrounding an Earth-sized planet is beyond the reach of even the 6.5-metre James Webb Space Telescope, the orbital observatory that NASA hopes to launch by 2018 if it does not fall victim to cost overruns. “James Webb, yea or nay, is not the answer to our prayers,” Marcy says.

As a result, researchers such as Marcy and Traub stress the need to go beyond the indirect techniques of HARPS and Kepler, and gather the faint light from the planet itself, which is normally invisible in the glare of the parent star. For that, astronomers need either a giant space telescope equipped with a device for blocking starlight, or an interferometer, consisting of several telescopes flying in formation. NASA did develop a proposal for such a space telescope, called Terrestrial Planet Finder, and the European Space Agency hoped to fly a similar mission called Darwin. But budgetary constraints have left both missions in limbo, unlikely to advance to the front of either agency's queue until well into the next decade. At the conference, Traub raised the issue. “People are not thinking deeply about the distant future. People are wrapped up with what they're doing right now,” he says. “Clearly, I'm concerned.”

But Laughlin isn't as worried. He says that the enthusiasm and momentum in planet-hunting may lead to an unexpected solution. “People have a history of being inventive when they need to be,” he says. He points to French philosopher Auguste Comte, who in 1835 wrote that astronomers might be able to learn about the shapes, sizes and motions of stars, but that stellar densities, temperatures and chemical compositions would be “forever denied to us”.

Within three decades, astronomical spectroscopy was starting to answer all of those questions. ■

## MISCONDUCT

# Austria reinstates disgraced doctor

*Physician at heart of retracted clinical trial can return to work.*

BY ALISON ABBOTT

He carried out clinical trials without ethical approval. He failed to provide raw data for his high-profile publications. He falsified legal documents. But despite this record, an employment commission has ordered that Austrian urologist Hannes Strasser be readmitted to his teaching post at the Medical University of Innsbruck.

Now the university is trying to find a way out of the embarrassing situation — one that highlights the weakness and tardiness of Austria's system for dealing with research misconduct. “We are being forced by a legal decision to let him back when we think he has no place here,” says the university's rector, Herbert Lochs.

The university suspended Strasser three years ago after serious concerns were first raised about his trial of a novel stem-cell therapy for urinary incontinence. The therapy relied on injecting stem cells and fibroblasts derived from the patients' own tissue into the urinary sphincter; it had been developed by Innovacell Biotechnologie in Innsbruck, a company co-founded by Strasser, and with which he is no longer involved. But many patients reported no improvement after the therapy, and others claim that it caused their bladders to seal over.

A subsequent investigation by the Austrian government's Agency for Health and Food Safety (AGES) found a series of ethical and legal misdemeanours, which led them to conclude that the trial was illegal and invalid (see *Nature* **454**, 922–923; 2008). *The Lancet* withdrew Strasser's paper reporting the trial's results (S. Kleinert and R. Horton *Lancet* **372**, 789–790; 2008).

But on 8 September the Vienna-based National Disciplinary Committee — which adjudicates on employment issues relating to civil servants (including university professors) — revoked Strasser's suspension. The committee based its decision on the outcome of a case brought to an Innsbruck court in which the university hospital sued Strasser and his department head Georg Bartsch for €1.2 million (US\$1.6 million) — its estimated cost for giving Strasser's treatment to 400 patients not involved in clinical trials. The court refused the claim on 3 August, stating that there was no proof that Strasser had intended financial deception. Bartsch was too ill to stand trial.

However, the court also stated that Strasser had provided false testimony during a 2008 civil damages case brought by a patient who had received the treatment, and that he had falsified evidence in the AGES investigation, which considered legal issues surrounding the clinical trials. It fined him €4,500.

The university plans to appeal against Strasser's reinstatement. In the meantime, the university has asked Strasser only to prepare unscheduled lectures: “We don't want him to get into clinical work,” says Lochs.

In separate legal cases, several patients who say the treatment harmed them are now trying to bring charges of grievous bodily harm against Strasser, according to the Innsbruck-based lawyer Thomas Juen, who has previously represented trial patients seeking damages.

Earlier this year, the Medical University of Innsbruck completed its own investigation into the scientific aspects of the case, finding that Bartsch and Strasser had engaged in what Lochs views as “massive scientific misconduct”.

The university's slowness in carrying out the investigation has been widely criticized. One academic, who asked to remain anonymous, said he believed that a timely, formal statement that Strasser had perpetrated serious scientific misconduct might have helped avert the disciplinary committee's revocation of his dismissal. Juen adds that he is surprised that the disciplinary committee revoked Strasser's suspension so quickly, “given that appeals are ongoing, and that looming cases of grievous bodily harm on the part of patients have not yet come to court”.

Strasser did not respond to *Nature's* request for an interview, and Bartsch was unavailable for comment as a result of his illness. Strasser, however, was quoted in a local newspaper as saying that he wants to return to clinical practice and that the hospital administration may not be able to stop him. ■

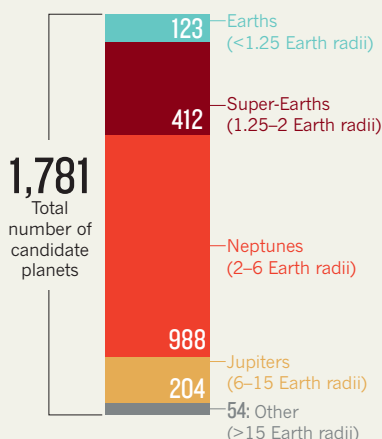
## CORRECTION

The News story ‘Canadian ozone network faces axe’ (*Nature* **477**, 257–258; 2011) stated that Environment Canada planned to cut 776 jobs. Although 776 employees will be affected by workforce changes, only about 300 posts are being eliminated.

SOURCE: NASA KEPLER TEAM

## SIZING UP THE SAMPLE

Since February, the Kepler team has increased its catalogue of candidate planets by 45%. In that time, the number of Earth-sized candidates has nearly doubled, from 68 to 123.





► surrounding an Earth-sized planet is beyond the reach of even the 6.5-metre James Webb Space Telescope, the orbital observatory that NASA hopes to launch by 2018 if it does not fall victim to cost overruns. “James Webb, yea or nay, is not the answer to our prayers,” Marcy says.

As a result, researchers such as Marcy and Traub stress the need to go beyond the indirect techniques of HARPS and Kepler, and gather the faint light from the planet itself, which is normally invisible in the glare of the parent star. For that, astronomers need either a giant space telescope equipped with a device for blocking starlight, or an interferometer, consisting of several telescopes flying in formation. NASA did develop a proposal for such a space telescope, called Terrestrial Planet Finder, and the European Space Agency hoped to fly a similar mission called Darwin. But budgetary constraints have left both missions in limbo, unlikely to advance to the front of either agency's queue until well into the next decade. At the conference, Traub raised the issue. “People are not thinking deeply about the distant future. People are wrapped up with what they're doing right now,” he says. “Clearly, I'm concerned.”

But Laughlin isn't as worried. He says that the enthusiasm and momentum in planet-hunting may lead to an unexpected solution. “People have a history of being inventive when they need to be,” he says. He points to French philosopher Auguste Comte, who in 1835 wrote that astronomers might be able to learn about the shapes, sizes and motions of stars, but that stellar densities, temperatures and chemical compositions would be “forever denied to us”.

Within three decades, astronomical spectroscopy was starting to answer all of those questions. ■

## MISCONDUCT

# Austria reinstates disgraced doctor

*Physician at heart of retracted clinical trial can return to work.*

BY ALISON ABBOTT

He carried out clinical trials without ethical approval. He failed to provide raw data for his high-profile publications. He falsified legal documents. But despite this record, an employment commission has ordered that Austrian urologist Hannes Strasser be readmitted to his teaching post at the Medical University of Innsbruck.

Now the university is trying to find a way out of the embarrassing situation — one that highlights the weakness and tardiness of Austria's system for dealing with research misconduct. “We are being forced by a legal decision to let him back when we think he has no place here,” says the university's rector, Herbert Lochs.

The university suspended Strasser three years ago after serious concerns were first raised about his trial of a novel stem-cell therapy for urinary incontinence. The therapy relied on injecting stem cells and fibroblasts derived from the patients' own tissue into the urinary sphincter; it had been developed by Innovacell Biotechnologie in Innsbruck, a company co-founded by Strasser, and with which he is no longer involved. But many patients reported no improvement after the therapy, and others claim that it caused their bladders to seal over.

A subsequent investigation by the Austrian government's Agency for Health and Food Safety (AGES) found a series of ethical and legal misdemeanours, which led them to conclude that the trial was illegal and invalid (see *Nature* **454**, 922–923; 2008). *The Lancet* withdrew Strasser's paper reporting the trial's results (S. Kleinert and R. Horton *Lancet* **372**, 789–790; 2008).

But on 8 September the Vienna-based National Disciplinary Committee — which adjudicates on employment issues relating to civil servants (including university professors) — revoked Strasser's suspension. The committee based its decision on the outcome of a case brought to an Innsbruck court in which the university hospital sued Strasser and his department head Georg Bartsch for €1.2 million (US\$1.6 million) — its estimated cost for giving Strasser's treatment to 400 patients not involved in clinical trials. The court refused the claim on 3 August, stating that there was no proof that Strasser had intended financial deception. Bartsch was too ill to stand trial.

However, the court also stated that Strasser had provided false testimony during a 2008 civil damages case brought by a patient who had received the treatment, and that he had falsified evidence in the AGES investigation, which considered legal issues surrounding the clinical trials. It fined him €4,500.

The university plans to appeal against Strasser's reinstatement. In the meantime, the university has asked Strasser only to prepare unscheduled lectures: “We don't want him to get into clinical work,” says Lochs.

In separate legal cases, several patients who say the treatment harmed them are now trying to bring charges of grievous bodily harm against Strasser, according to the Innsbruck-based lawyer Thomas Juen, who has previously represented trial patients seeking damages.

Earlier this year, the Medical University of Innsbruck completed its own investigation into the scientific aspects of the case, finding that Bartsch and Strasser had engaged in what Lochs views as “massive scientific misconduct”.

The university's slowness in carrying out the investigation has been widely criticized. One academic, who asked to remain anonymous, said he believed that a timely, formal statement that Strasser had perpetrated serious scientific misconduct might have helped avert the disciplinary committee's revocation of his dismissal. Juen adds that he is surprised that the disciplinary committee revoked Strasser's suspension so quickly, “given that appeals are ongoing, and that looming cases of grievous bodily harm on the part of patients have not yet come to court”.

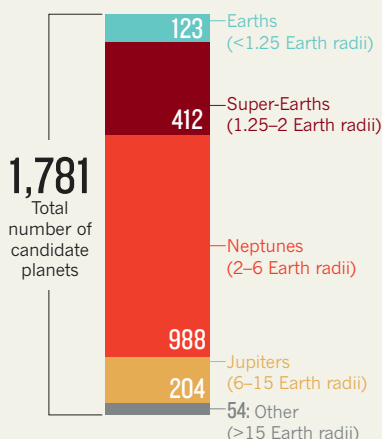
Strasser did not respond to *Nature's* request for an interview, and Bartsch was unavailable for comment as a result of his illness. Strasser, however, was quoted in a local newspaper as saying that he wants to return to clinical practice and that the hospital administration may not be able to stop him. ■

## CORRECTION

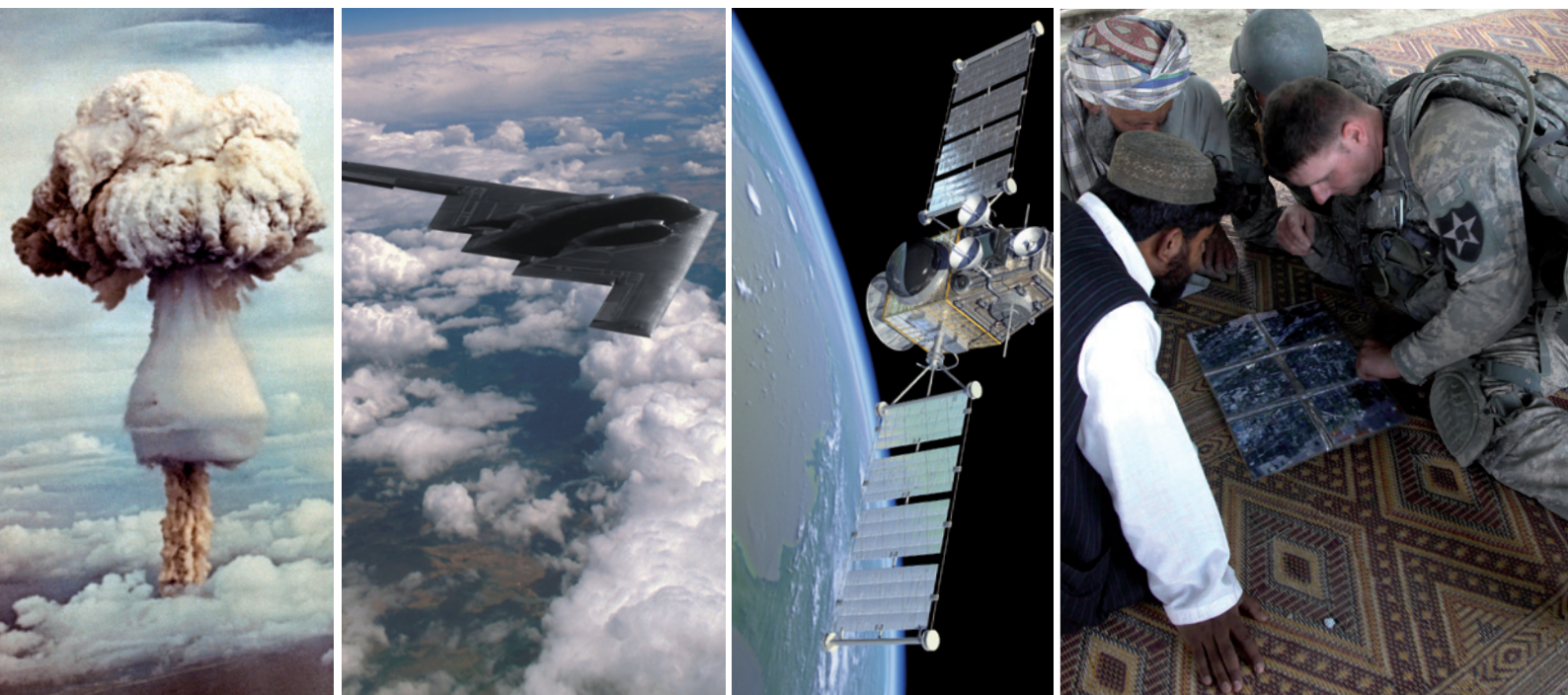
The News story ‘Canadian ozone network faces axe’ (*Nature* **477**, 257–258; 2011) stated that Environment Canada planned to cut 776 jobs. Although 776 employees will be affected by workforce changes, only about 300 posts are being eliminated.

## SIZING UP THE SAMPLE

Since February, the Kepler team has increased its catalogue of candidate planets by 45%. In that time, the number of Earth-sized candidates has nearly doubled, from 68 to 123.



SOURCE: NASA KEPLER TEAM



# THE CHANGING FACE OF MILITARY SCIENCE

Basic research funded by the Pentagon is facing an uncertain future.

BY SHARON WEINBERGER

In 2005, as roadside bomb attacks were claiming ever more lives in Iraq, senior Pentagon officials called on the academic community to join a 'Manhattan Project' to counter these improvised explosive devices. By invoking the Second World War race to build the atomic bomb, military leaders seemed to be pushing for a massive investment in science that could, like the first nuclear weapon, turn the tide of war.

Academics responded with a collective shrug. The Pentagon's grand rhetoric wasn't matched with any great influx of funding for science, and it wasn't clear how any one technology could help fight a loosely organized, deliberately low-tech enemy. Besides, says Julia Erdley, deputy science adviser to the Pentagon's Joint Improvised Explosive Device Defeat Organization, "we are looking for near-term solutions".

Six years later, the Department of Defense (DOD) has spent more than US\$17 billion on countering improvised explosive devices, but, as Erdley suggests, the vast majority of that money has gone on implementing known solutions such as stronger armour for vehicles and personnel, not advanced research. Roadside bombs remain the single biggest killer of US and allied troops in Iraq and Afghanistan. Pentagon officials now admit that there is no technological 'silver bullet' for preventing, detecting and disarming roadside bombs, and their Manhattan project rhetoric has long since been replaced with more sober talk of disrupting highly

distributed terrorist networks (see *Nature* 471, 566–568; 2011).

The failure to mobilize the scientific community for the war on terror stands in stark contrast to what happened in the cold war, when Pentagon-supported science boomed, and was viewed as a crucial asset to counter Soviet technological prowess. Today's military has to operate in much more ambiguous and complex environments, in which 'soft' skills such as trust-building, intelligence-gathering and cultural insight may prove as decisive as any technological advantage. Given this new military reality, it is becoming less clear what science and technology research has to offer.

## BROKEN PROGRAMMES

That uncertainty may help to explain what some now see as a lack of sustained Pentagon support for blue-sky basic science and a preference for applied research with a short-term pay-off. "We believe that important aspects of the DoD basic research programs are 'broken' to an extent that neither throwing more money at these problems nor simple changes in procedures and definitions will fix them," wrote the JASONS, a defence advisory

**As the key to winning wars shifts from atomic bombs, stealth bombers and satellites to community work, the value of science to the military is diminishing.**



**BEYOND THE BOMB**  
Science and the military  
[nature.com/military](http://nature.com/military)

US DOE/SPL; E. SIMONSEN/GETTY IMAGES; R. HARRIS/SPL; J. JACOBSON/AP



group made up of independent scientists, in the most recent publicly available assessment of Pentagon science and technology. (Completed in 2009, the JASON report was released to the public in May 2010.)

On the surface, the Pentagon's science base looks healthy enough, and it supports a vast array of research (see page 369). The science and technology budget, which consists of basic research, applied research and advanced technology development — budget categories 6.1, 6.2 and 6.3 in Pentagon parlance — has fallen from its post-11 September 2001 peak in 2005, when it reached some \$14.7 billion per year (see 'Rise and fall'). But most of that decline came in the advanced-technology category, not basic research. And the total still stands at about \$12 billion a year, nearly twice the \$6.8 billion budget of the US National Science Foundation, and much higher than defence science expenditures in Europe, where countries have traditionally spent only a fraction of what the United States spends on the military. In 2009, the most recent year for which figures are available, the members of European Defence Agency — every country in the European Union except Denmark — spent an aggregate of only €2.26 billion (US\$3.1 billion) in the 'research and technology' category, the vast majority of which goes to the development of advanced aircraft and other weaponry, not science.

Pentagon research also had a champion in former US defence secretary Robert Gates, a one-time CIA director who had been president of Texas A&M University in College Station before he came to the DOD in 2006.

For example, Gates was well aware that in many academic fields, notably the social sciences, relations with the military have been fraught and often hostile since the Vietnam War (1955–75). In 2008, hoping to rebuild those ties, Gates proposed Minerva: a basic-science programme that would specifically focus on the social sciences. Gates saw Minerva as emblematic of military science's changing mission. "The challenges facing the world require a much broader conception and application of national power than just military prowess," he said in announcing the programme. "The government and the Department of Defense need to engage additional intellectual disciplines — such as history, anthropology, sociology and evolutionary psychology."

## MAGNIFICENT SEVEN

Beginning with the president's fiscal year 2012 budget request this past February, Gates set a target of 2% annual growth in the basic-science budget over the coming years, and pledged to hold the applied- and advanced-technology accounts steady. That was particularly heartening news for those disciplines to which defence funding is crucial. About one-third of all the funding for oceanography research and computer science in the United States comes from the Pentagon, for example, as does a majority of the funding for mechanical engineering (see *Nature* **466**, 656–657; 2010). "Physics research is no longer tied so exclusively to military funding," says David Kaiser, a historian of science at the Massachusetts Institute of Technology in Cambridge, "although it still has a large role." And the defence department is also now the largest single source of funding for research into traumatic brain injury (see page 390).

Shortly before stepping down on 30 June this year, Gates signed off a new science and technology plan for the Pentagon. The policy includes a list of priorities — which Pentagon insiders immediately dubbed the 'magnificent seven' — to be used for budget planning over the next five years.

And yet, Gates's efforts also illustrate some of the many strains in the Pentagon's science and technology programme. Minerva, in particular, has met with decidedly mixed reactions, as academics question whether

the Pentagon has any business setting the course of social-science research (see *Nature* **455**, 583–585; 2008). And the magnificent-seven list, which includes topics such as research to counter weapons of mass destruction, and engineering resilient systems, arguably hasn't done much to inspire the scientific community. "It would be hard to categorize it as bold or prescient," says Mark Lewis, an aerospace engineer at the University of Maryland in College Park and a former chief scientist of the US Air Force. It is essentially a compendium of the individual military services' wish

lists. A Pentagon spokesperson also says that there are no funding goals tied to the magnificent seven.

A more fundamental issue is what many observers see as a lack of high-level vision and coordination for Pentagon research. In earlier decades, that coordination was carried out by the director for defence research and engineering (DDR&E), a position established in 1958 after the Soviet launch of the Sputnik satellite. Located in the Pentagon's power centre — the Office of the Secretary of Defense — this director oversaw all of the department's science and technology programmes.

But in the late 1970s, the position ceded much of its authority over budget and policy to the under secretary for acquisition — the chief weapons buyer. The DDR&E, recently renamed the assistant secretary of defence for research and engineering, was left with a limited staff, overseeing a vast portfolio of science accounts at the individual services and the Pentagon-wide Defense Advanced Research Projects Agency. In recent years, the office has become marginalized, with its staff fending off spending cuts in the science budget, rather than being a driving force in military science policy.

And even when the office succeeds in defending basic research, according to the 2009 JASON report, the research inexorably gets pushed towards immediate applications. In a sample of 258 basic-research projects funded by the Air Force Office of Scientific Research in 2007, and a similar sample funded by the Army Research Office, the group found that as many as 81% "are not, even by a generous stretch, 6.1 research".

The JASONs urged the defence department to elevate and strengthen the DDR&E office, and make it independent of weapons acquisition. But the defence-department bureaucracy has given no sign that any such change is in the offing.

In the meantime, the Pentagon faces a more urgent threat. "We're starting to see a downward trend in R&D funding," says Todd Harrison, a fellow at the Center for Strategic and Budgetary Assessments in Washington DC. The Obama administration has already asked the Pentagon to cut \$400 billion from its budgets over the next 12 years — the current budget is about \$700 billion per year — and there's no guarantee that those cuts won't be expanded as Congress struggles to trim the US federal deficit, or that the money won't come from the science and technology budget.

Lewis sees Gates's commitment to increasing basic-science spending as one of the most important changes in the Pentagon's science policy over the past few years. The question now, however, is whether Gates's successor, former CIA director Leon Panetta, will uphold that commitment. Lewis points to the new defence secretary's confirmation hearings on Capitol Hill, when he was specifically asked that question. Panetta replied that he valued basic research — but that "all defence appropriations must be considered during this time of budget constraints".

In other words, everything is on the table for cuts, including science. "That would be a profound change," says Lewis. ■ [SEE EDITORIAL P.369](#)

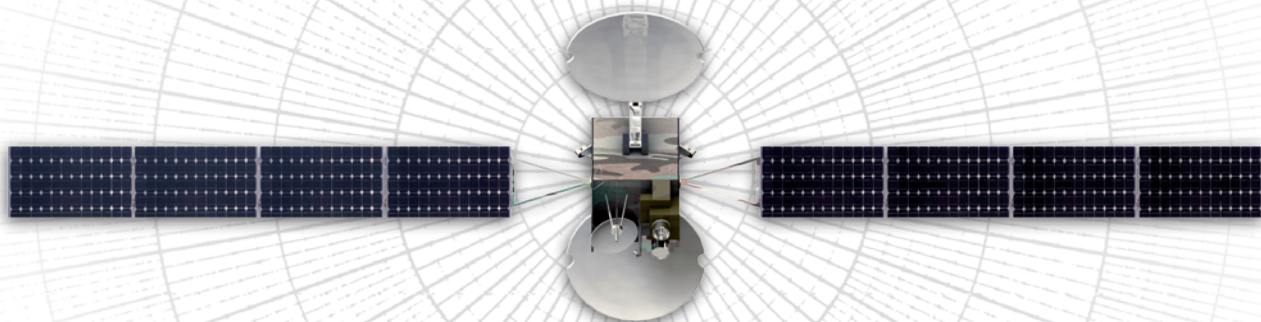
**Sharon Weinberger** is a Carnegie fellow at Northwestern University's Medill School of Journalism.

## RISE AND FALL

Pentagon spending on science and technology fell after the end of the cold war, then surged again during the war on terrorism. But the current drop could go deeper and last longer.







# SHARED INTELLIGENCE

The military has a vast array of scientifically valuable data — some more accessible than you think.

BY GEOFF BRUMFIEL

No one monitors our planet more closely than the military. Thirty-six thousand kilometres above Earth, US Air Force satellites watch for the heat plume of a ballistic missile. An array of other surveillance satellites patrol lower altitudes. Some can see a rifle from space; others penetrate cloud cover with radar, seeking military hardware or installations. Still closer in, aircraft and drones fly over conflict zones collecting intelligence, and seismometers listen for shudders from an underground nuclear test. Even the deepest oceans are prowled by military submarines, watching their foreign adversaries.

Through most of their history, the data collected by this vast blanket of military sensors have been highly classified. But on occasions when scientists are lucky enough to see the data, their view is considerably different from that of the generals. Satellites designed to track missiles can also spot the flaming trails of meteors; aerial photographs of Iraq have allowed archaeologists to trace ancient canals. Even the military's most banal weather satellites collect data on ocean precipitation that are valuable for understanding Earth's energy cycles.

After the cold war, some of these data did start trickling out to scientists, mainly in the United States, which has vast military resources and a vibrant scientific community. The flow ebbed after 2000 — but there are hints that it is resuming, and that more fruitful data collaborations are to come. A group of security-cleared scientists called MEDEA has recently rekindled ties with the US intelligence community to discuss the use of military environmental data for the study of climate change. And an agreement set to be finalized in October between NASA and the US Air Force will give astronomers unprecedented access to data on meteors entering the atmosphere. Some details of those data must be obfuscated to preserve state secrets, but researchers say that the trove nonetheless has enormous scientific potential. "I think it's become more useful now than it ever has been before," says John Orcutt, an oceanographer at

the University of California, San Diego, and a member of MEDEA.

In the United States, the start of the Manhattan Project in 1942 set the tone for collaboration between the modern military and civilian scientists. The greatest physicists of the era, conscripted to build the atomic bomb, spent years working closely with the US Army. The Pentagon has used outside scientists to help shape its capabilities ever since. It maintains a handful of quasi-academic labs near university campuses, and a truculent panel of independent scientists — known as the JASONs — advises it on technical topics such as submarine detection and nuclear weapons (see page 397).

At the same time, opportunistic collaborations have sprung up between civilian scientists and the defence establishment. With the advent of nuclear submarine warfare in the 1950s, the US Navy devoted enormous resources to mapping and understanding the sea floor — including mid-ocean ridges, where Navy mapping yielded clues to the theory of plate tectonics, according to Raymond Jeanloz, an Earth scientist at the University of California, Berkeley, and a long-time member of the JASONs. Seismic networks used to monitor nuclear tests have also mapped earthquakes. Jeffrey Richelson, a historian at the National Security Archive in Washington DC, says that since the 1970s, the US defence department has occasionally shared satellite imagery with civilian agencies in response to natural disasters such as flooding and forest fires.

But the military's most sensitive data remained off-limits to academics. In 1967, for example, early-warning radar in Alaska spotted pulsars — rotating stars that emit a pulsing radio signal — months before any civilian astronomers did. The staff sergeant who made the observations kept quiet about his discovery for 40 years, until the sightings were declassified in 2007 (ref. 1).

After the end of the cold war, restrictions began to loosen. In the mid-1990s, astronomers struck up an ad hoc arrangement with Air Force Space Command in which they could ask for data on



**BEYOND THE BOMB**  
Science and the military  
[nature.com/military](http://nature.com/military)

A CRISANTE/SHUTTERSTOCK

specific meteors that had been collected by missile-warning satellites. At around the same time, Al Gore, then a Democratic senator from Tennessee, began to ask what the intelligence community could offer climate scientists. Gore was interested in environmental issues and had also served on intelligence and military committees in Congress. He wrote to Robert Gates, then the director of the Central Intelligence Agency, prompting Gates to invite a group of scientists to gain security clearance and take a look at what the military had to offer. After Gore took office as Bill Clinton's vice-president in 1993, the group solidified under the name MEDEA — Measurements of Earth Data for Environmental Analysis.

"With the proper justification, I could ask for almost anything," says William Schlesinger, a MEDEA member and president of the Cary Institute of Ecosystem Studies in Millbrook, New York. Schlesinger used reconnaissance imagery going back to the Second World War to search for climate change's influence on desertification of the Sahara (he didn't find any)<sup>2</sup>.

### TRADE SECRETS

MEDEA did succeed in getting intelligence satellites to systematically photograph locations of environmental interest in the Arctic, Antarctic and the continental United States. In 1995, the group also successfully lobbied for the release of images from early photo-reconnaissance satellites Corona, Argon and Lanyard, which took more than 860,000 photographs of Earth between 1960 and 1972, recorded on rolls of film. Since then, an entire cottage industry has sprung up involving archaeologists who search for roads and other ancient features in the photos, many of which show tracts of land that have since been consumed by urban sprawl. Jason Ur, an archaeologist at Harvard University in Cambridge, Massachusetts, for example, has used them to map massive canals dug by ancient Assyrian kings<sup>3</sup> (see 'Spying on an ancient city').

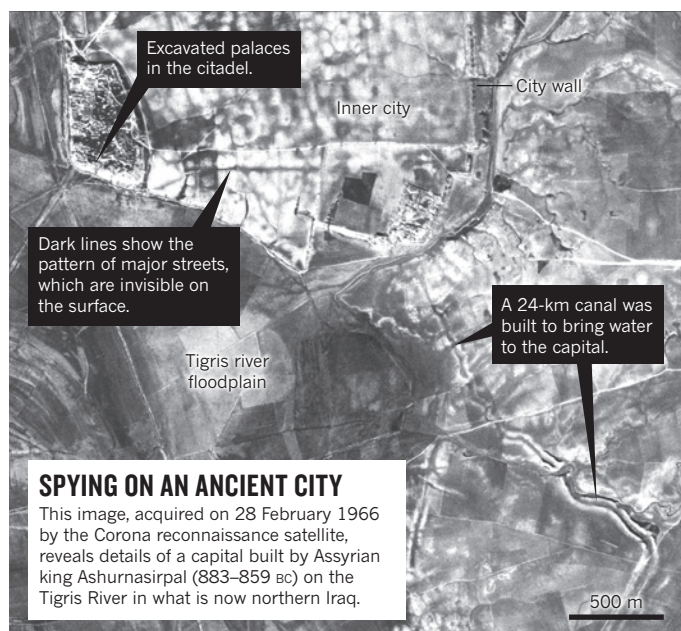
In the late 1990s, work by Gore and MEDEA led the United States and Russia to declassify Arctic-sea-ice data recorded between the 1970s and 1990s by satellites, submarines and other sources. Scientists have since been able to use those data to reconstruct the gradual thinning of Arctic ice in the decades before civilian monitoring began. "Without the early classified data, people wouldn't have a clue," says Ralph Cicerone, the president of the US National Academy of Sciences.

Then, around 2000, MEDEA abruptly halted its work and, in 2009, the informal meteor data from the Air Force stopped flowing too. No one really knows why. But such twists and turns are the price of working with the intelligence community. As Schlesinger puts it, researchers aren't privy to the "darkened world where a bunch of people make a decision".

## "WITH THE PROPER JUSTIFICATION, I COULD ASK FOR ALMOST ANYTHING."

Sharing will never be a priority for those charged with defending the United States, says Steven Aftergood, who heads the Project on Government Secrecy at the Federation of American Scientists in Washington DC and has spent decades tracking the US intelligence agencies. Even if information is unclassified, agencies may not want to dole it out freely — or devote resources to converting it into formats that scientists can use. "No organization spontaneously discloses and shares its information; that's just a bureaucratic law of physics," Aftergood says. Political pressure, such as that applied by Gore, is key to persuading intelligence agencies to share data, he says.

These days, new collaborations are emerging. In 2008, congressional committees concerned about climate change quietly reconvened MEDEA to examine whether military- and intelligence-community assets could supply environmental data. The answer was yes, according to Cicerone, who has served as informal chair of MEDEA since 2008. Although intelligence satellites aren't as useful as custom-built instruments, the panel concluded that they could fill some gaps in climate data



gathered by civilian satellites, particularly given recent budget shortfalls and launch failures such as the loss of the NASA Orbiting Carbon Observatory in February 2009 (ref. 4).

Also in 2009, MEDEA persuaded intelligence officials to publicly share images of areas of environmental interest that had, by that time, been photographed regularly for more than a decade. The images are now archived as the Global Fiduials Library, available through the US Geological Survey (USGS). Orcutt says they are "relatively priceless at this point" because they are gathered roughly once every few weeks — more frequently and continuously than those from civilian research satellites.

Lindley Johnson, who oversees NASA's Near-Earth Object Observation programme, believes that the space policy unveiled in 2010 by US President Barack Obama, which explicitly endorses data sharing, may have smoothed his efforts to secure data from the US Air Force. Johnson says the new arrangement, which will give astronomers access to data from missile-warning satellites on all meteors — not just the ones researchers knew about already — will allow scientists to gain a better understanding of the range of near-Earth objects in orbit.

How much science will emerge from these burgeoning relationships remains to be seen. So far, the newly available image libraries of the Arctic and Antarctic have seen only modest use from scientists. "One of our biggest challenges is to educate the science community about the existence of our programme," says Bruce Molnia, executive director of the Civil Applications Committee at the USGS in Reston, Virginia, which oversees civilian use of classified image data. And the members of MEDEA, who have access to the full array of classified data, are, for now at least, using it to address policy questions raised by government agencies — such as what national security risks are posed by climate change — rather than conducting fundamental research of their own choosing.

Yet Cicerone is hopeful that even more of the intelligence data being collected can eventually be shared. It is now feasible to save almost everything that the military's eyes and ears are recording about Earth. "As scientists, we don't want observations to be thrown away," he says. "With the Earth, as time passes, you just get one shot at it." ■ SEE EDITORIAL P.369

**Geoff Brumfiel** is a senior reporter for Nature in London.

1. Brumfiel, G. *Nature* **448**, 974–975 (2007).
2. Schlesinger, W. H. & Gramenopoulos, N. *Global Change Biol.* **2**, 137–141 (1996).
3. Ur, J. A. *Iraq* **67**, 317–345 (2005).
4. Brumfiel, G. *Nature* **457**, 1067 (2009).





The high-pressure shock waves generated by the detonation of roadside bombs can cause invisible damage to the brain.

Wartime explosions may be creating an epidemic of brain damage — and a major challenge for scientists.

BY SHARON WEINBERGER

# THE BRAIN WAR



To Burt, the blasts he experienced in Afghanistan eventually became a kind of music. The detonation of C4 and other such military-grade explosives felt like extremely high notes — painful, yet over quickly. But blasts from bombs made out of fertilizer — a favourite of Afghan insurgents — were like standing next to a speaker at a rock concert: the dull bass thuds didn't necessarily hurt, but they would reverberate through his body like a wave, and stay with him for a long time afterwards.

They're with him still. Burt, who asks that his real name not be used, spent four months as a tactical adviser to a US military bomb-disposal unit in Afghanistan, during which he was within 50 metres of a detonating improvised explosive device (IED) more than 18 times. His sleeping problems began even before he left. So did the headaches, the ringing in his ears and the nausea. He started to forget things — a problem that got even worse after he returned home. Burt would find himself in a room in his house and wonder why he was there. One time, he told his wife they should try a new restaurant in town. She replied that they had eaten there with friends just a few days before.

As recently as two years ago, this constellation of symptoms might have been diagnosed as a classic case of post-traumatic stress disorder (PTSD), a psychological condition that can be caused by the constant stress of being in combat. But Burt, now on medical leave, blames those low notes. He is convinced that the body-shaking blasts did something to his brain. And many doctors, medical researchers and military officials have come to believe he is right.

The visible toll of insurgent-made IEDs has been awful enough. In the ten years since military operations began in Afghanistan and then Iraq, IEDs have killed more than 3,000 US and allied troops, and wounded roughly ten times that number. But many more troops have been

exposed to multiple blasts and not suffered any visible physical injuries. Like Burt, they often report an array of symptoms, ranging from sleep disturbance to problems concentrating. And an increasing body of evidence suggests that the repeated concussions have left them with an invisible, subcellular-level form of traumatic brain injury (TBI) that not only impairs their day-to-day functioning, but also increases their long-term risk of developing neurodegenerative diseases.

"We've got a lot of guys out there that might be 30 years old that have

symptoms, could take years: some 20 compounds and interventions have been tested in more than 50 trials in the past 30 years. "People just look at this field and turn around and run," Koroshetz says.

#### PLAYING CATCH-UP

The good news is that the Pentagon has finally begun to put a high priority on understanding, diagnosing and treating these injuries. But, as officials there now admit, it is playing catch-up after too many years of ignoring the problem.

"The system of care was really in denial for the longest time," says

## "PEOPLE JUST LOOK AT THIS FIELD AND TURN AND RUN."

been blown up a dozen times," says Kevin Kit Parker, a biomedical engineer at Harvard University in Cambridge, Massachusetts, who is conducting research on TBI. "And the risk that these guys are going to get a disease like Alzheimer's or Parkinson's is soaring."

The number of troops affected by this kind of silent TBI has already topped 200,000, according to the Defense and Veterans Brain Injury Center in Washington DC. A survey done by the Rand Corporation, a not-for-profit research firm in Santa Monica, California, suggests it could be as high as 320,000. The Pentagon and the US Department of Veterans Affairs, which are responsible for the health care of current and former troops, respectively, are getting worried about a potential epidemic of disability and dementia. The disorder also presents a major challenge for researchers.

No one fully understands what the blast waves are doing to the brain, explains Walter Koroshetz, deputy director of the US National Institute of Neurological Disorders and Stroke in Bethesda, Maryland. Thanks to mounting evidence from professional sports, he says, "it's been known for a long time that repetitive head injuries lead to chronic degenerative disease. But no one has really got a hold on how that happens."

Worse, he says, coming up with an effective treatment, and not just alleviating

Colonel Christian Macedonia, a physician with the US Army who serves as medical-sciences adviser to Admiral Michael Mullen, chairman of the Joint Chiefs of Staff. Partly this was just the culture of the military, says Macedonia: because most soldiers dazed by a blast wave seemed to recover very quickly — on the surface — the attitude was, "Hey, shake it off".

When the symptoms did begin to show, he says, troops with TBI were often misdiagnosed as having PTSD, which has similar symptoms. And veterans of Iraq and Afghanistan have all too often been exposed to physical and psychological traumas that could easily cause both.

But most of all, Macedonia thinks that the reluctance to recognize silent TBI was "the ghost of the Gulf War" — the ongoing scientific controversy around the diffuse symptoms described by many troops who served in the 1991 conflict. Study after study has failed to identify a root cause for Gulf War syndrome, he says, so when people started coming forward with TBI — yet another constellation of complaints that could not be linked to a single cause — the frustrated military-medicine hierarchy just didn't want to hear about it.

That attitude didn't begin to shift until senior military leaders began to sense a dissonance between the official reports they were being given and what they saw when visiting injured troops.

One crucial moment came in 2009 when Marine Corps commandant General James Amos toured Walter Reed Hospital in Bethesda, Maryland, and was introduced to a patient who said, with considerable effort, "General, I know who you are. I have a picture of you and I together in Iraq."

It turned out that Amos had a copy of the picture, too. It had been taken just two years earlier, when he had posed with a group of marines who had just survived an IED that had detonated directly under their vehicle. Thanks to the vehicle's advanced armour, all of them seemed unscathed. But this young man, a bomb-disposal expert, went straight back to work and was quickly exposed to several more blasts. His physical condition deteriorated rapidly, his life began to unravel and — after some difficulty getting the military medical establishment to recognize his TBI — he had been admitted to Walter Reed with severe neurological problems.

Amos describes the meeting as a seminal moment for him. "This TBI business is real, and we've got to get past the point of ignoring it," he recalls of his reaction. "We need to do something about it."

Mullen was coming to much the same conclusion. Concerned that he wasn't getting a full picture of the brain-injury problem, he asked Macedonia to help organize a 'Gray Team' of researchers and medical professionals with combat experience to look at the realities of TBI on the battlefield.

The Gray Team (named after the brain's grey matter) made its first visit to Afghanistan in 2009, says Macedonia, and quickly concluded that Mullen's suspicions were well founded. Official reports had claimed that more than 90% of troops with concussion were being assessed with the 13-point Military Acute Concussion Evaluation (MACE). But when the Gray Team travelled to Afghanistan, the group found that the vast majority of medical professionals — in both large military hospitals and remote outposts — didn't even know what a MACE was. "Doctors couldn't tell you the first thing about it, even though they had all the training materials," says Macedonia. No one was enforcing the screening.



**BEYOND THE BOMB**  
Science and the military  
[nature.com/military](http://nature.com/military)

In parallel with the efforts of the Gray Team, the Defense Advanced Research Projects Agency (DARPA) and the Office of Naval Research were sponsoring a study that for the first time sought to understand how the brain is affected by blast waves, which may cause different injuries from the blunt-force trauma seen in sports injuries. The study focused on breachers: marines who specialize in using explosives to enter buildings. The first paper is only now going through review, but researchers say that they have found evidence of neurological impairment in the instructors, who have had long-term, repeated exposure to low-level blasts.

On 21 June 2010, guided in part by the breacher study, the Pentagon announced its first policies for identifying and treating people who may have TBI. Included were the first military-wide mandatory triggers for screening troops, including a rule that anyone within 50 metres of a blast had to be evaluated for signs of brain injury.

#### THE RESEARCH SCRAMBLE

The Pentagon has also started to make up for its long neglect of brain-injury research. The Department of Defense's Congressionally

Directed Medical Research Programs, one of the major conduits for medical-research funding, provided no money specifically for TBI or PTSD between 1999 and 2005. In fiscal year 2006, a small amount, US\$3.7 million, went to PTSD, but TBI was not even listed as a research topic. In 2007, how-

**"THIS TBI BUSINESS IS REAL, AND WE'VE GOT TO GET PAST THE POINT OF IGNORING IT."**

ever, mounting reports of battle-field brain injuries persuaded Congress to allocate \$150 million for TBI research, with another \$150 million for PTSD research.

That influx of money was enough to open the door to people such as Parker, one of the few medical researchers working on TBI who has combat experience. His research focus had been on cardiac cell mechanics. But in 2002, he served the first of his two tours of duty as an infantry officer in Afghanistan and began to see the effects of TBI on his fellow soldiers. The bombs then were still relatively small and unsophisticated — artillery shells hooked up to garage-door openers, for instance. But

by the time of his second tour in 2009, troops were encountering 200-kilogram fertilizer bombs that could blow unarmoured vehicles to smithereens. As he puts it, only half jokingly, once people started trying to kill him with IEDs, "I figured I had better turn into some kind of neuroscientist".

In fact, Parker's first formal involvement with brain-injury research began when he attended a DARPA workshop on the subject in 2005. There he learned that one of the challenges was to understand the effects of an explosive blast on the brain. With his background in cell mechanics, Parker immediately began to wonder about integrins, receptors that mediate the cell's attachment to surrounding tissue. Could a blast wave damage them enough to disrupt the proteins' functioning?

The idea got a cool reception at first, says Parker, who is now a member of the Gray Team. "The community that does neuroscience and understands cell

mechanics is non-existent," he says. "It's like if you're used to reading English and I hand you a paper in Mandarin Chinese: it's going to be kind of difficult." But a grant from DARPA allowed Parker and his group to develop an *in vitro* model to test his idea. And in July, his team published a paper showing that the idea is essentially correct: blast-induced brain injury sets off a cellular chain reaction that disrupts integrin signalling, impairing connections among the brain's neurons (M. A. Hemphill *et al.* *PLoS ONE* 6, e22899; 2011).

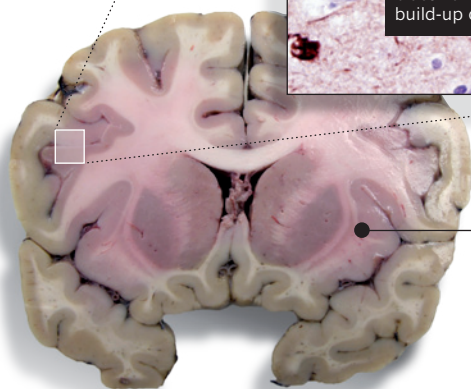
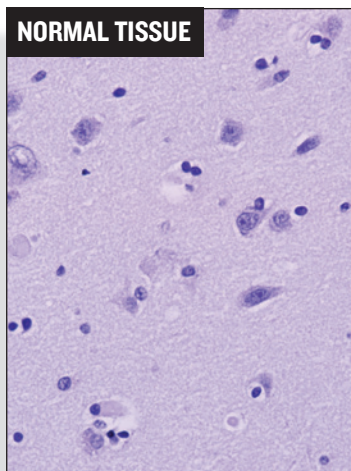
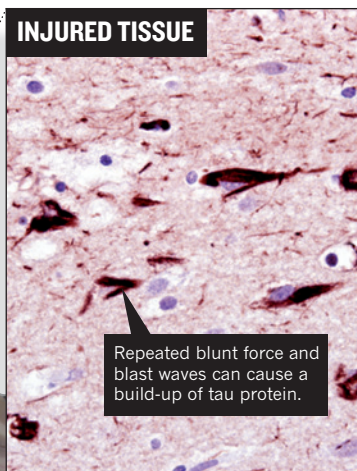
The increased funding has also led to progress towards a blood test for diagnosing silent TBI. Currently, clinicians can only infer the presence of such brain damage by cognitive-impairment tests. This means that, because the symptoms overlap with those of other disorders, brain-injury researchers can't always be sure about what they're measuring — and patients might not be receiving the most appropriate care. Now, after looking at a variety of proteins that seem to become elevated in the bloodstream after a brain injury, army-funded researchers tested two that seemed especially promising in small-scale, phase II clinical trials. Known as ubiquitin C-terminal hydrolase (UCH-L1) and glial fibrillary acidic protein (GFAP), they will soon be tested in large-scale, phase III trials.

Working independently of the Pentagon, Bennet Omalu, a forensic pathologist at the University of California, Davis, and the chief medical examiner for San Joaquin County in California, has started to look at veterans' brains for chronic traumatic encephalopathy. First identified in professional athletes involved in contact sports, this neurodegenerative disorder is believed to be caused by multiple concussions. In November, Omalu expects to publish what may be the first case study demonstrating chronic traumatic encephalopathy in a military veteran with silent TBI.

The young man had been exposed to multiple blasts during two deployments to Iraq, explains Omalu, who in 2005 published the first evidence of chronic traumatic encephalopathy, which he

## TRAUMA IN THE BRAIN

Brains affected by blunt force and blast waves can show few outward signs of injury. But a microscope reveals neurological abnormalities similar to those found in Alzheimer's disease.







The US military is experimenting with the use of electroencephalography during the baseline pre-deployment testing of its troops.

had identified from autopsy samples from an American football player (B. I. Omalu *et al. Neurosurgery* 57, 128–134; 2005). After returning home, the man began to experience memory problems, mood disorders and self-control problems. Then, aged 27, he committed suicide. With the permission of his relatives, says Omalu, “I got his brain, examined it, and lo and behold, he had CTE changes” — abnormal accumulations of the tau protein associated with Alzheimer’s disease and other dementias (see ‘Trauma in the brain’).

#### LIMITED ACCESS

Few medical researchers working on brain injuries have an easy way to collaborate with the Pentagon. Its unique combination of bureaucracy and national-security considerations prevents access to many data and brain-tissue samples that could be useful for medical researchers. For example, access to the Pentagon’s Joint Theater Trauma Registry — a compilation of all military trauma-related data — is highly restricted, lest enemies use the information to improve their ability to injure US soldiers. “Giving

the NIH access is not impossible, but it is very, very difficult,” says Major General James Gilman, who heads the US Army Medical Research and Materiel Command at Fort Detrick, Maryland.

There have been some signs of change. A joint programme by the US National Institutes of Health (NIH) and the Uniformed Services University of the Health Sciences, both in Bethesda, recently hired a neuropathologist specifically to look at brain tissue of deceased troops, although access to the tissue is not yet guaranteed. Also, the Pentagon and the NIH agreed in August to develop a database for TBI that is similar to the ones created for Alzheimer’s disease, autism and cancer research. The idea is to standardize data collection across studies so that researchers can compare results more easily.

Among other things, such comparisons should help investigators to get a clearer picture of how well TBI therapies work. They need as much help as they can get, says Koroshetz: for all the progress in understanding the causes and progression of silent TBI, treatments remain elusive. Dozens of clinical trials have been done over the past

two decades, looking at everything from antioxidants to hyperbaric oxygen. “No one has been able to figure out how to make a difference,” says Koroshetz. “In terms of outcomes in patients, there is very little, if any, evidence that any single thing works.”

The Pentagon has come a long way from just three years ago, when TBI was mostly ignored. In January, it became mandatory for the military to track all concussive injuries, and troops now receive pre-deployment cognitive testing that can be used as a baseline in case they are later affected by concussion. Experiments with brain-wave measurements are also under way. And with the new reporting requirements, the military is creating what is likely to be the single largest repository of data on TBI.

The question is how to keep the momentum going. That may prove difficult, given the United States’ mounting budget woes. After the initial boost in 2007, funding levels for TBI research dropped dramatically. In fiscal year 2011, the congressional appropriation specifically for the Pentagon’s brain-injury research is expected to be just \$45 million. “Where’s

the interest, where’s the support, where’s the national effort?” asks Colonel Dallas Hack, director of the army’s Combat Casualty Care Research Program at Fort Detrick.

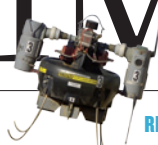
Brigadier General Robert Thomas, the army’s assistant surgeon-general, hopes that the military’s involvement is now doing for research and treatment of brain injuries what it has done in the past for yellow fever, trauma care and medical evacuation. For better or worse, he says, “combat is the greatest catalyst to medical innovation”.

But in the meantime, Burt and the hundreds of thousands of other people with brain injuries can only hope that progress comes in time to help them. Once an ambitious multi-tasker, Burt says he now has problems with basic tasks. These days, he can get around the house, and even manage trips to the store — as long as he makes lists or uses some other form of reminder. “But I will never be what I was,” he says. ■ **SEE EDITORIAL P.369**

**Sharon Weinberger** is a Carnegie fellow at Northwestern University’s Medill School of Journalism.



# COMMENT



**SECURITY** The self-appointed experts who solve US defence problems **p.397**

**POLICY** Robot soldiers raise regulatory and ethical challenges **p.399**

**RISK** Why nuclear plants and complex systems are prone to fail **p.404**

**METRICS** Rewards should follow impact factors in China **p.407**

J. PEARSON/US AIR FORCE



Global security: US officers collaborating with Kenyan community health workers in 2011.

## Joining forces

Civilians and the military must cooperate on global disease control, say **David Blazes** and **Kevin Russell**.

“Vulnerability is universal,” wrote Margaret Chan, director-general of the World Health Organization (WHO), in *The World Health Report 2007*. The words ring even truer today. Heightened concern about the 2009 influenza pandemic, the rapid global spread of antimicrobial-resistant organisms and even the popularity of *Contagion*, a film featuring a lethal airborne virus, capture this sentiment.

Global public health has become a national-security and foreign-policy issue. Rapid transportation of people, diseases and information has increased public-health threats — from emerging influenza strains to bioterrorism — that cannot be managed solely through conventional practices such as isolation and quarantine. Effective global disease surveillance, timely detection of

outbreaks and appropriate responses that help to control epidemics are the essential tools of public-health security.

Here, civilian organizations have much to gain by working with the military. While many public-health agencies struggle for funds, the militaries of various nations are investing in public-health security. Military scientific efforts towards characterization, prevention and vaccine development for emerging infectious diseases, for example, improve the lives of civilians as well as soldiers, in peace and war.

But tensions can arise from the different

priorities of civilian and military groups. Our experience leading US military disease surveillance activities leaves us convinced that such vital collaborations can succeed if there is transparency and trust on all sides.

### FROM SOLDIERS TO CITIZENS

Armies have long worked to prevent their personnel from contracting or spreading diseases, in the process making seminal contributions to public-health security that also benefit civilians. Ronald Ross, a British officer in the Indian Medical Service in the late nineteenth century, was the first to work out that *Anopheles* mosquitoes transmit malaria to humans. During the building of the Panama Canal at the start of the twentieth century, US Army researcher Walter Reed made discoveries about yellow fever that helped to control the disease and allow the completion of the construction, which opened new trade routes. US Army scientists developed vaccines for hepatitis A in the 1990s and hepatitis E in the 2000s<sup>1</sup>. And in 2009, working with local Thai officials and others, US Army scientists developed the first vaccine to partially protect against HIV<sup>2</sup>.

Indeed, the US Department of Defense (DOD) dedicates hundreds of millions of dollars every year to understanding infectious diseases and pathogens worldwide. Since 1997, the DOD Global Emerging Infections Surveillance and Response System (GEIS) has spent about US\$54 million a year on emerging infectious diseases. It coordinates a network of institutes that includes research laboratories in Egypt, Cambodia, Peru, Thailand and Kenya. Scientists in these labs have made breakthroughs including isolation of new pathogens, the first description of *Plasmodium falciparum* that are resistant to artemisinin antimalarials and contributions to annual flu vaccines (including the seed strain for the 2009 H1N1 influenza A virus)<sup>3</sup>.

The scope of DOD investment is broad. In addition to disease surveillance, it includes: enhancing global biosafety and securing existing high-risk biological agents; HIV prevention and treatment; and the development of diagnostics and vaccines for vector-borne infections and diarrhoeal disease. Several DOD laboratories collaborate with the WHO as reference laboratories, and with developing countries on topics including occupational health, human subject



**BEYOND THE BOMB**  
Science and the military  
[nature.com/military](http://nature.com/military)

► research protection, electronic disease surveillance and outbreak response.

These successes have not come easily. Some people are concerned that military engagement in public health shifts priorities away from health to security topics, even though security has been part of the WHO's remit since its inception — its constitution states that the "health of all peoples is fundamental to the attainment of peace and security". Local officials and scientists sometimes hesitate to trust military public-health personnel, believing that the military's agenda is to protect its staff, citizens and allies ahead of others, or believing misinformation about the military's engagement with biological weapons.

Sometimes, open, mutually beneficial relationships are not possible. For example, in regions with active conflict, such as Iraq, US military officials conduct disease surveillance among its forces, but it is often difficult to focus on local health issues. But more commonly, the military's aim is to maintain security for civilians and soldiers alike. A healthy society is more stable than an unhealthy one.

## THE WAY FORWARD

The military can do much to build trust. When military scientists work with local scientists, by sharing projects and data and by jointly reporting results, they prove their commitment to transparency. By focusing on local diseases, they build relationships. It is in the military's interest to do so, because cosmopolitan diseases are more likely than exotic pandemic strains to affect populations, and widespread illness could compromise a region's security.

Local officials who engage with the military can harness a wealth of resources and expertise. Small pilot projects can help to build confidence among those on the ground.

Transparency is a tenet of the International Health Regulations. The regulations — agreed to by 194 countries in 2005, entering into force in 2007 — set standards for the

detection, diagnosis, reporting and control of a public-health emergency of international concern. The framework also encourages developed countries to assist other states in building these core capabilities, which the GEIS programme has endeavoured to provide through its efforts in developing countries.

The US military's commitment to transparency was demonstrated in the 2009 H1N1 influenza pandemic. The first cases were discovered by the Naval Health Research Center in San Diego, California, (a hub of the GEIS network) and were reported to the WHO through the US Centers for Disease Control and Prevention (CDC). Researchers across

**"Local officials and scientists sometimes hesitate to trust military public-health personnel."**

the GEIS network (see 'A global network') assisted 14 other nations in making their first diagnoses<sup>3</sup>.

The GEIS network also promotes sharing genetic data on potential pathogens freely through GenBank submissions. In the past year, the GEIS network has deposited genetic sequences for more than 1,000 strains of influenza A from around the world, to increase worldwide representation in the WHO's Global Influenza Surveillance and Response System. This open approach contrasts with the 'viral sovereignty' attitude adopted by some countries, which in the past have not shared influenza samples because of inequitable access to diagnostics, vaccines or treatments derived from viruses originating in their country. In response, this spring, the WHO created a Pandemic Influenza Preparedness framework for virus sharing, benefits sharing and standard material transfer agreements.

A model lab for scientific transparency, institutional trust and effective public-health security is the Naval Medical Research Unit 3 (NAMRU-3) in Cairo. It was established in the 1940s to work with

the Egyptian Ministry of Health on the fight against typhus, at the time a cause of epidemics in Egypt and worldwide<sup>4</sup>. The lab has since become integral in studying a variety of infectious diseases such as food-borne and respiratory illness that affect locals and military personnel. The relationship was so valued that the lab was the only official US government presence to remain in Egypt during the Six-Day War in 1967.

Work on H5N1 Avian influenza and other infectious diseases continues at NAMRU-3, where 250 Egyptian scientists and technicians work alongside 21 US military colleagues<sup>4</sup>. Just after the H1N1 influenza pandemic was declared in May 2009, NAMRU-3 trained 73 scientists from 32 countries within 3 weeks on molecular diagnosis of this new strain with CDC assistance, regardless of country of origin and focused only on underlying need of public-health assistance<sup>3</sup>.

The development of an open-source software system for electronic disease surveillance is another military effort that has benefitted international and local disease-monitoring programmes. A partnership between GEIS and the Johns Hopkins Applied Physics Lab in Laurel, Maryland, created the Suite for Automated Global Electronic bioSurveillance, which can use mobile phones to report cases of disease, by voice or text message, and then collate the data to inform public-health leadership<sup>5</sup>. This system has been piloted in Peru, the Philippines and Cambodia. It is being offered to all free of charge and with no requirement to share data, although sharing aggregate information with the WHO can be facilitated by the system and is encouraged.

In this time of increasing global complexity and fiscal constraints, all components of society, including the military, should work together to secure global public health through transparent actions. The struggle between life and death plays out both on the battlefield and in the hospital. It is time we fought for global public-health security together. ■ SEE EDITORIAL P.369

**David L. Blazes and Kevin L. Russell** are at the Armed Forces Health Surveillance Center, Silver Spring, Maryland 20904, USA. e-mail: david.blazes@us.army.mil

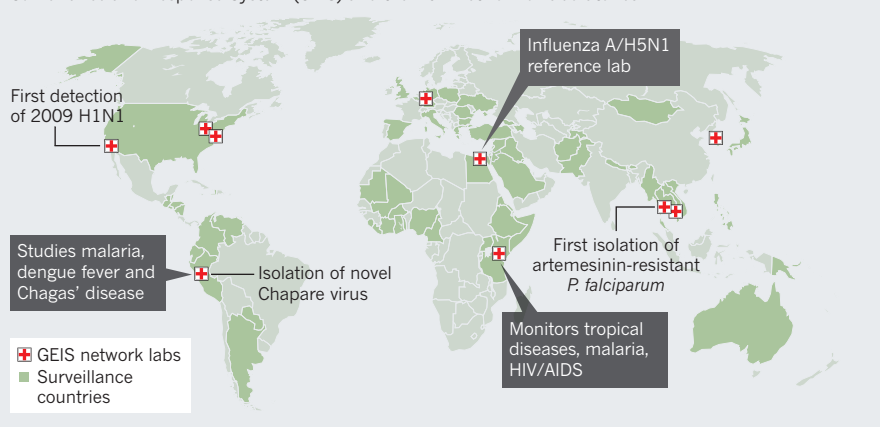
1. Grabenstein, J. D., Pittman, P. R., Greenwood, J. T., Engler, R. J. *Epidemiol. Rev.* **28**, 3–26 (2006).
2. Rerks-Ngarm, S. et al. *N. Engl. J. Med.* **361**, 2209–2220 (2009).
3. Russell, K. L. et al. *BMC Public Health* **11**(Suppl. 2) S2 (2011).
4. Peake, J. B., Morrison, J. S., Ledgerwood, M. M., Gannon, S. E. *The Defense Department's Enduring Contributions to Global Health* (Center for Strategic and International Studies, 2011); available at: <http://go.nature.com/yxfnp5>
5. Lewis, S. H. et al. *PLoS ONE* **6**, e19750 (2011).

**Disclaimer:** the views expressed are those of the authors and do not represent the official position of the US Army, Navy or Department of Defense.

SOURCE: GEIS

## A GLOBAL NETWORK

The US military supports public-health initiatives in many countries through its Global Emerging Infections Surveillance and Response System (GEIS) and the DOD network of laboratories.







# The world's most independent defence science advisers

**Ann Finkbeiner** explains JASON, the autonomous group of academics that has been reporting to the US government on military matters for more than 50 years.

Ten years ago, for a short time, a 40-year-long relationship between the US Department of Defense and JASON, a small, secret group of elite science advisers, came apart. The Defense Advanced Research Projects Agency, or DARPA, directed JASON to add three specific people as members. JASON replied that it selected its own members according to exacting criteria, which the three did not meet. DARPA pointed out that it was the channel through which JASON subcontracted with others, plus the source of nearly half its budget, so JASON should accept the three, or else no channel and no money. JASON chose the latter. The relationship with DARPA was over and remains so.

JASON would have been out of business, but for the flurry of phone calls and e-mails that then went up and down the defence hierarchy. The office at the top, that of the Secretary of Defense, sent a polite note to the office of the Assistant Secretary of Defense for Research and Engineering (ASDR&E), which sits just above DARPA: "Please look into this JASON issue and see if it makes sense to retain

them." The ASDR&E thought it did and provided JASON with a new channel and new money. As a result, JASON's position as a freelance government adviser now seems secure.

Here's the point: if you're a government and you want defence science advice that has no possible self-interest and that you can trust to be as close to the truth as nature allows, then you want an adviser that is independent enough to divorce you.

JASON is autonomous and it isn't obliged to please; its reports are technical and famously neutral. It has managed to stay in business for 50 years by maintaining a moving balance between usefulness and independence. To meet the government's evolving national-security problems, JASON adjusted its scientific expertise. And to keep the JASONs in JASON — even as members changed from theorists with summers off to scientists with labs to run — JASON remained its own boss.



**BEYOND THE BOMB**  
Science and the military  
[nature.com/military](http://nature.com/military)

JASON comprises 30–40 scientists, mostly stellar academics, usually with broad interests, all with top-secret clearances. The scientists meet for six weeks every summer in La Jolla, California, in what they say are grubby little offices, to answer questions from five to ten sponsors, all government agencies. Questions must be well defined, specific, answerable and useful. So, as the JASONs say, no "standing around admiring the problem". And answers must be technical, that is, based on equations and arguments from scientific first principles. JASON occasionally does experiments but declines to provide examples. It doesn't touch policy.

About 40% of the questions it tackles come from a changing stable of sponsors — including the Department of Homeland Security, for which JASON has done studies on the detection of radiological material on cargo ships. The other 60% is split between the Department of Energy (on the nuclear stockpile, which JASON has so far judged to be disease-free); the ASDR&E (on the unpredictability of rare events such as terrorist attacks, given a surprising lack of good

ILLUSTRATIONS BY DAVID PARKINSON

► data sets); and the intelligence community (we're unlikely ever to know). Half to three-quarters of JASON's studies are classified. JASON currently has more requests for studies than it can accept.

Governments have many ways of getting advice from scientists, but JASON is unique. The other scientists advising the defence department are chosen by the department and often come from the defence industry. The National Academy of Sciences is self-selected and highly respected, but it prefers to work on unclassified studies, doesn't do its own research and its reports can take years. Organizations such as MITRE are science advisory corporations who work only for the government. The closest analogues to JASON in size and speed are a handful of elite groups of academics — the US Information Science and Technology group and the UK Blackett Group, for instance — that advise specific government sponsors, such as DARPA or the UK Ministry of Defence. But these sponsors created the groups, help to choose their members and the members typically rotate out after a few years.

JASON created itself: in January 1960, around 20 atomic physicists, mostly theorists, got together to advise a post-Sputnik government on nuclear matters. Researchers have always been invited to join only by JASON's self-appointed management. They stay on as active members or as senior advisers as long as they like, unless asked to quit by management. And (because everyone asks) JASON is not an acronym. It is a name given to the group by Mildred Goldberger, wife of founding member Murph Goldberger, after the Greek myth, because she thought of the advisers as golden heroes.

JASON's autonomy raises the question of how the group manages to stay in business. One reason is its members' longevity: JASON can provide its sponsors with a kind of corporate memory. Incoming head Gerald Joyce, a biochemist at the Scripps Research Institute in La Jolla, has been a member for 14 years and hasn't hit the median yet. It takes that long, he says, to "know who's on the chess board and how things are done". Otherwise, like any freelancer with a cadre of repeat customers, JASON ensures that its expertise and its customers' questions are, as JASONS say, impedance-matched — an electronics term for complementary cables that allow the fullest flow of current.

### NUCLEAR TO NUCLEUS

In its first decade, JASON's studies were for DARPA and were largely related to cold-war problems of nuclear test bans and missile defence. They addressed questions such as 'could the right satellite detect the infrared signature of an enemy missile's launch?' By the early 1970s, DARPA had branched out beyond physics to materials and computer

sciences. After some acrimony, JASON began adding non-physicists.

At the same time, it also began to work for other sponsors — including the Central Intelligence Agency, NASA and the new Department of Energy. For these it studied, for instance, pollution from supersonic jetliners and primitive models of climate change. Through the 1970s and early 1980s, another new sponsor, the US Navy, asked for studies on the internal ocean waves left by submarines; on the use of extremely long radio waves to communicate with submarines at great depths; and on a technique that became ocean acoustic tomography. Accordingly, by the end of the 1980s, members included computer scientists, astronomers, geoscientists, mathematicians, materials scientists, engineers and oceanographers.

Current studies include cybersecurity, defences against improvised explosive devices and pharmaceutical intervention in cognition. Notably, several projects have been on defending against biological weapons. JASON now has what current head, Roy Schwitters, a physicist at the University of Texas at Austin, calls "a crackerjack biology crowd". In fact, in the 1990s, when JASON began to add biologists, it had to run cross-cultural training sessions, even teaching physicists to sequence DNA. Since then its studies have included: ways to counter bioweapons designers who might use genetic engineering to produce deadly microbes; possible links between the Navy's sonar exercises and mini-epidemics of beached whales; and, most recently, the potential benefits of analysing genetic

information from all military personnel. Today, only half of the JASONS are physicists.

JASON's impact is difficult to gauge. It does not formally track its studies' outcomes; most reports disappear into classified programmes or are lost in the niceties of the governmental decision-making process. The JASONS feel that their niche is advising on classified science, which cannot be sent out for peer review, is done in small, isolated communities of government scientists and, as a result, risks straying out of the realm of reality. The JASONS speculate that they've saved the government billions of dollars in non-working technologies.

Government sponsors would rather not talk about JASON's influence except in generalities. They say that the JASONS are often arrogant and naive but also scientifically smart, reliably objective and not subject to political expedience. They say they don't ask JASON unless they really want the answer, and will offer only hypothetical examples. Say the director of an agency wants to develop a technology, but it turns out not to work. He asks his agency's science advisory board for help. The board hesitates to nix the technology, so it recommends further research. The director suspects the board is being polite. He asks JASON because, as one sponsor put it, giving an unworkable technology to JASON is like throwing raw meat to a lion.

Here's a real case: on JASON's advice, the ASDR&E killed a programme to develop a rail gun for the army. JASON had found that a gun powered by an electric current could shoot projectiles along a pair of metal rails farther and faster than conventional artillery, but making it small enough to put on a tank would require too many miracles.

### A VISIBLE IMPACT

The exception to the general opacity about JASON's impact is a series of studies the group has been doing since its birth on the technologies underlying nuclear test bans. The first JASONS — who were, or were trained by, scientists involved in the Manhattan Project — inherited a need to control nuclear weapons. Early on, JASON worked on various ways to verify whether a country was cheating on a nuclear treaty by testing weapons. For instance, could you tell the difference between the seismic signature of a nuclear test and that of an earthquake? Would a test in an underground cave muffle the explosion's seismic signature? Later, JASON worked on ways to find out whether the nuclear stockpile had become old and ineffectual, and therefore an unreliable deterrent. In 1995, a JASON study ruled that nuclear weapons could be judged reliable without being tested, allowing the administration of President Bill Clinton to sign the Comprehensive Test Ban Treaty.

Current studies, done for the Department of Energy, continue to focus on the nuclear





stockpile. JASON now sees a healthy stockpile as obviating the need for designing new weapons and as an alternative to resuming underground testing. One such study helped to doom the push, by the administration of former president George W. Bush, to develop a new bomb: the Reliable Replacement Warhead. Over the years, JASON's studies have vetted the national laboratories' nuclear stockpile programmes enough times that Congress occasionally mandates that a programme can't be re-funded until JASON reviews it.

The JASONs feel strongly about this work. Scientists' role in maintaining public confidence in the nuclear deterrent, says Schwitters, is "incredibly important". Joyce agrees: "We feel responsible to the heritage."

Today, the group's biggest challenge is keeping the JASONs attending regularly — they call it the 'sticking coefficient'. The JASONs are paid a large amount — US\$850 per day in 2004 — although they could make ten times more consulting for industry. They also admire each other and take pleasure in working together on topics new to all of them; they say it is like being in graduate school again. And their interest in the country's security is intense.

But working for six weeks of an academic's precious summer, summer after summer, carries costs to his (just 10% of the JASONs are women) research, career and family life. So some JASONs come to La Jolla for just four days a week, or come one summer and not the next, or show up only for certain studies. Nobody likes that: too much of JASON's value to both its sponsors and its members depends on long, argumentative interactions. "It can't be done casually," says one member.

When Joyce becomes head in the autumn, he will survey JASON's expertises — which he thinks of as finding keywords for each member — and ask regular sponsors which keywords they need most. He will tell the sponsors that the JASONs don't think they can usefully do social-science studies (occasionally requested for understanding insurgents and terrorists) and remind them that JASON doesn't advise on policy.

"We work with the sponsor to find the right study," he says. "We operate on billable hours, and our budget is the sum of what we're doing. We're sort of a collective independent contractor. There are others out there, but this model is very powerful." ■

**Ann Finkbeiner** is the author of *The Jasons: The Secret History of Science's Postwar Elite* and was a columnist for *Defense Technology International*. e-mail: anniekf@gmail.com



An RQ-4 Global Hawk unmanned aerial vehicle before a mission in southwest Asia in November 2010.

A. KIN/US AIR FORCE

## A world of killer apps

Leaders are ill-prepared for the ethical complications of new 'killer applications', says **P. W. Singer**.

A president arguing that his nation isn't at war because his forces are using only robotic weapons. An arms-control meeting forlornly trying to ban the development of armed autonomous robots. Criminals using tiny robotic helicopters in a jewellery heist. These are not tales from an Isaac Asimov novel; they are real events that happened within the past year.

From gunpowder to the atomic bomb to robots, history is full of weapons technologies so disruptive that they change the rules. These deadly applications, or 'killer apps', often begin in the military sector but have ripple effects beyond their intended uses. The Manhattan Project to develop the first atomic bomb was at its core a military-funded experiment to bundle the greatest explosive power into the smallest delivery package possible.

But that research opened up entirely new areas of physics, revolutionized the energy

industry and transformed world politics.

What is different today is the speed with which our technology can outpace our ethical and policy responses to it. Astounding advances grab the headlines so frequently that the public has become numb to their significance — whether it is robotic planes, directed-energy weapons such as high-energy lasers, or 'electric skin', tiny sensors that are applied to the body like tattoos.

We are "giants" when it comes to technology, but "ethical infants" when it comes to understanding its consequences, as US Army general Omar Bradley remarked in 1948. Bradley was referring to nuclear research, but as the pace of technologic change takes off, that gulf — between our sophisticated inventions and our crude grasp of the consequences — continues to widen. We need to start bridging it.

### I, ROBOT

Robotics is an excellent case study of this gulf. Over the past ten years, the United States and 45 other nations have gone from looking at robots as mere science fiction to using them in their military forces. For ►



stockpile. JASON now sees a healthy stockpile as obviating the need for designing new weapons and as an alternative to resuming underground testing. One such study helped to doom the push, by the administration of former president George W. Bush, to develop a new bomb: the Reliable Replacement Warhead. Over the years, JASON's studies have vetted the national laboratories' nuclear stockpile programmes enough times that Congress occasionally mandates that a programme can't be re-funded until JASON reviews it.

The JASONs feel strongly about this work. Scientists' role in maintaining public confidence in the nuclear deterrent, says Schwitters, is "incredibly important". Joyce agrees: "We feel responsible to the heritage."

Today, the group's biggest challenge is keeping the JASONs attending regularly — they call it the 'sticking coefficient'. The JASONs are paid a large amount — US\$850 per day in 2004 — although they could make ten times more consulting for industry. They also admire each other and take pleasure in working together on topics new to all of them; they say it is like being in graduate school again. And their interest in the country's security is intense.

But working for six weeks of an academic's precious summer, summer after summer, carries costs to his (just 10% of the JASONs are women) research, career and family life. So some JASONs come to La Jolla for just four days a week, or come one summer and not the next, or show up only for certain studies. Nobody likes that: too much of JASON's value to both its sponsors and its members depends on long, argumentative interactions. "It can't be done casually," says one member.

When Joyce becomes head in the autumn, he will survey JASON's expertises — which he thinks of as finding keywords for each member — and ask regular sponsors which keywords they need most. He will tell the sponsors that the JASONs don't think they can usefully do social-science studies (occasionally requested for understanding insurgents and terrorists) and remind them that JASON doesn't advise on policy.

"We work with the sponsor to find the right study," he says. "We operate on billable hours, and our budget is the sum of what we're doing. We're sort of a collective independent contractor. There are others out there, but this model is very powerful." ■

**Ann Finkbeiner** is the author of *The Jasons: The Secret History of Science's Postwar Elite* and was a columnist for Defense Technology International. e-mail: anniekf@gmail.com



An RQ-4 Global Hawk unmanned aerial vehicle before a mission in southwest Asia in November 2010.

## A world of killer apps

Leaders are ill-prepared for the ethical complications of new 'killer applications', says **P. W. Singer**.

A president arguing that his nation isn't at war because his forces are using only robotic weapons. An arms-control meeting forlornly trying to ban the development of armed autonomous robots. Criminals using tiny robotic helicopters in a jewellery heist. These are not tales from an Isaac Asimov novel; they are real events that happened within the past year.

From gunpowder to the atomic bomb to robots, history is full of weapons technologies so disruptive that they change the rules. These deadly applications, or 'killer apps', often begin in the military sector but have ripple effects beyond their intended uses. The Manhattan Project to develop the first atomic bomb was at its core a military-funded experiment to bundle the greatest explosive power into the smallest delivery package possible.

But that research opened up entirely new areas of physics, revolutionized the energy

industry and transformed world politics.

What is different today is the speed with which our technology can outpace our ethical and policy responses to it. Astounding advances grab the headlines so frequently that the public has become numb to their significance — whether it is robotic planes, directed-energy weapons such as high-energy lasers, or 'electric skin' tiny sensors that are applied to the body like tattoos.

We are "giants" when it comes to technology, but "ethical infants" when it comes to understanding its consequences, as US Army general Omar Bradley remarked in 1948. Bradley was referring to nuclear research, but as the pace of technologic change takes off, that gulf — between our sophisticated inventions and our crude grasp of the consequences — continues to widen. We need to start bridging it.

### I, ROBOT

Robotics is an excellent case study of this gulf. Over the past ten years, the United States and 45 other nations have gone from looking at robots as mere science fiction to using them in their military forces. For ►



**BEYOND THE BOMB**  
Science and the military  
[nature.com/military](http://nature.com/military)





Left, new legs and eyes: a mock up of the New BigDog, intended to carry equipment for ground troops; right, a US soldier prepares an RQ-11 Raven in Iraq, 2006.

▶ example, the US military used only a handful of unmanned aerial systems in the 2003 invasion of Iraq, but now has more than 7,000 unmanned aerial systems and 12,000 unmanned ground systems in its inventory. As a sign of things to come, the US Air Force now trains more unmanned-systems operators than fighter and bomber pilots combined.

The effect of this shift goes beyond pilots' lives saved. US President Barack Obama recently argued that he did not need congressional approval for military operations in Libya because they were carried out by unmanned aerial systems such as the MQ-1 Predator and the MQ-9 Reaper. In Pakistan, US unmanned systems have made more than 250 strikes against suspected terrorists since 2004. Notably, these strikes are carried out by CIA drones rather than military ones, meaning even less oversight. The number of US drone strikes last year alone was several times larger than it was in the opening round of the Kosovo war, but — unlike that war — there has been no congressional authorization and little public debate.

The growth in non-military uses of robotics, especially those developed originally for the military, also raises ethical issues. Police departments in cities such as Miami, Florida, and Ogden, Utah, have sought special licences to operate unmanned aerial surveillance systems. This past spring, Congress legislated that US civilian airspace should be opened to allow more widespread use of such systems by 2015. This will mean a

boom for the robotics industry, but it will also raise new challenges to legal concepts such as privacy or probable cause for search or arrest. Police once needed warrants if they wanted to peek over citizens' fences; now they have the technology to do it from above, over an entire city. As one federal district court judge told me, this is "a Supreme Court case waiting to happen".

History shows us that neglecting to address these issues of law and ethics can have immense consequences. Using a submarine to attack shipping, for example, was once science fiction. When it became reality, the dispute over 'fair use' of such technology drew the United States into the First World War, ultimately leading to the nation's rise as a superpower.

#### CODE OF ETHICS

Today, the US Air Force has argued that its unmanned spy planes, if targeted by radar, have the same right to defend themselves with ammunition as its pilots have. This conferral on unmanned systems of the right to pre-emptive 'self'-defence makes sense from one perspective, but could also be a legal-dispute-turned-international-crisis in the making, as well as a huge (and probably unintentional) first step for the cause of robots' rights.

The importance and urgency of such complex challenges demands cross-disciplinary discussion — among technology researchers and manufacturers, customers and users, regulators and policy-makers, social

scientists and philosophers. But traversing the boundaries between those sectors still feels like crossing between foreign lands.

A major reason for this is insularity. Academic journals of each field focus inward, professional conferences are attended only by the like-minded, and those who attempt to straddle disciplines or engage the public are viewed as 'less serious'. In robotics, a striking example of this disconnect comes from a survey of the 25 stakeholders who most shape the field, conducted by the field's professional trade group, the Association for Unmanned Vehicles Systems International based in Arlington, Virginia. Asked whether they foresaw that the continued development of unmanned systems might bring 'any social, ethical, or moral problems', 60% of these leaders answered with a simple 'No'. I experienced this head-in-the-sand attitude when a professor sent me an angry e-mail after a talk I gave at a leading engineering school. He chastised me for "troubling" his students "by asking them to think about the ethics of their work".

In turn, our policy leaders are ill-prepared for the questions and debates that inevitably follow technological developments. Those responsible for funding and deployment decisions often fail to understand even the basics of the technology they're considering. I witnessed this when a senior adviser to the US defence secretary expressed surprise to me that the United States was using "so many" robotic systems (even though

BOSTON DYNAMICS/WHENN.COM/NEWSOM (LEFT); C. SCHULZE/DEUTSCH PRESSE AGENTUR/NEWSOM





Clockwise from left: a device that fits in a backpack; an MQ-1 Predator; information gathering in Iraq; TALON robots can be used for bomb disarming or combat.

US ARMY: J. LOCK/410TH AIR EXPEDITIONARY WING/NEWSCOM; J. HOWE/WPN/UPPA/PHOTOSHOT; M. CONTRERAS/US NAVY

he drove the budget that paid for them), and then told me how he thought a three-dimensional version of the Internet might be possible “one day”. He spoke about virtual worlds as if they were an exotic concept like time travel, apparently unaware that they already exist.

Similarly, when I gave a talk last year to the strategy office at the US Pentagon on some of the military, policy, legal and ethical ramifications of the growing use of robotics, one senior officer asked me: “Who is thinking about all this stuff?” I replied: “Everyone thinks it’s you!”

### BRAVE NEW WORLD

It doesn’t have to be this way. Our academic training still follows the specialized model. Top researchers in artificial intelligence may go through their entire university educations without taking a single class on ethics, history or law.

In turn, there are public-policy undergraduates, international-law professors and philosophy doctoral students writing essays, articles and dissertations on military drones without having seen one, learned how it works or even interviewed anyone who has.

No future scientist or policy-maker should graduate so ill-equipped. We can and must start training students to engage with complex multidisciplinary problems, by requiring those in the sciences to take courses in the humanities and vice versa.

At a public policy level, we need a new approach to handling major programmes of

technology research, which always includes an exploration of each one’s broader ramifications outside the lab. If environmental impact surveys are mandatory to begin construction of new laboratory buildings, why are no similar ‘ethical, legal, and social implications’ (ELSI) studies required of the research that goes on in them once built? A better model is the one used by the Human Genome Project, which set aside up to 5% of its annual budget for ELSI discussions.

**“The US Air Force now trains more unmanned-systems operators than fighter pilots.”**

We have to be realistic about what such studies can achieve. They don’t solve all the tough problems, but they can provoke debates that will help us identify the true issues. Today, for example, scientists recognize that their work in genetic testing has implications in areas such as health care or privacy, and policy-makers are aware that the field is potentially powerful. But no one is wasting time on unrealistic arguments about, for example, cloning Super Soldiers. The debates on the implications of genetic testing are not always resolved, but the tenor and content of the discussion — in both the lab and the policy spheres — are much improved. Yet genetics is the exception to the rule.

By comparison, those working on killer apps in robotics and other cutting-edge research fields should be asking themselves

questions such as: from whom is it ethical to accept research and development money? What attributes, such as weaponization, autonomy or intelligence, should I design into my technology? Which organizations and individuals should be allowed to buy and use my technology? Who should own or be able to access information gathered by my technology? If someone is harmed in association with the technology, who is responsible, and how is this determined?

Yet, unlike future medical professionals, researchers seeking answers to these questions received little training on ethics in graduate school and have no professional code or support structure to turn to. Policy-makers and legislators should also be better prepared to deal with the issues posed by taking a killer app beyond the lab.

We must get cracking. More killer apps are coming, and they’ll bring a host of grand possibilities and perils with them. Mathematician-turned-satirist Tom Lehrer once wrote: “Once the rockets are up, who cares where they come down? That’s not my department”; says Wernher von Braun.”

Until we start learning how to wrestle with the implications of our technologies, the joke will be on the rest of us. ■ [SEE EDITORIAL P.369](#)

**P. W. Singer** is director of the 21st Century Defense Initiative at the Brookings Institution, Washington DC 20036, USA, and author of *Wired for War: The Robotics Revolution and Conflict in the 21st Century*. He can be contacted through [www.pwsinger.com](http://www.pwsinger.com).





Oil supplies have remained steady for 40 years despite disruptions such as the Kuwaiti well fires in 1991.

## ENERGY

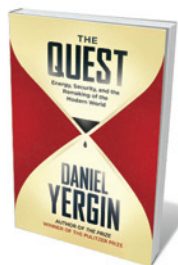
# Burning desires

An obsession with oil distorts an account of the security of energy supplies, argues **Vaclav Smil**.

An incessant flow of energy is the basis of modern civilization, so a secure energy supply — particularly the availability of oil — is inevitably the focus of much public and media interest. Energy expert Daniel Yergin duly focuses on the past, present and future supply of crude oil and on concerns about the security of the fuel's supply. But with his narrow focus on oil, he passes up the opportunity to delve more deeply into our energy challenge.

In *The Quest*, Yergin, chairman of the US consultancy IHS Cambridge Energy Research Associates, ranges over the history of modern oil and gas production and electricity generation, the security of petroleum supplies and the evolution of concerns about global warming. He deals with key episodes of modern oil development, such as increasing Russian production, rising Chinese demand, supply disruptions, the controversy over peak oil production and unconventional resources such as oil shale. Yergin then turns to global warming and alternative energy, with an emphasis on photovoltaics and wind.

➔ **NATURE.COM**  
For Nature's energy special, see:  
[go.nature.com/jyfb2i](http://go.nature.com/jyfb2i)



**The Quest: Energy, Security, and the Remaking of the Modern World**  
DANIEL YERGIN  
Allen Lane/Penguin Books: 2011. 704 pp.  
£30.00/\$37.95

The book, which is sliced into more than 400 short sections, covers policy and economics more than science and technology. Its analysis of energy sources is uneven. Coal, for example, warrants a single page. Yet during the twentieth century, coal supplied the world with more energy than did oil. In 2010, coal combustion accounted for 30% of all global commercial energy (compared with nearly 34% for oil) and 40% of electricity generation.

Yergin is no catastrophist. He presents ample evidence to counter the notion that we are running out of oil: new discoveries, exploitation of additional reserves in existing fields and unconventional oil resources will maintain the flow for the foreseeable future, he says. Globally, the market has remained well supplied despite the comings and

goings of dictators and ayatollahs, and major disruptions in output.

Since the early 1970s, there have been many such disruptions, starting with the embargo by the Organization of the Petroleum Exporting Countries (OPEC) in 1973–74, and the decline of extraction in the United States, which was the world's

**“Particularly in rich countries, energy security depends more on using fuel and electricity rationally.”**

largest producer until 1975. These were followed by the Iranian revolution in 1979; Iraq's takeover of Kuwait in 1990; the demise of the Soviet Union in 1991; the rise

of oil imports by China, which was a net exporter of oil until 1994; the US invasion of Iraq in 2003; and, most recently, the Libyan civil war.

Through all of this, global oil extraction rose by two-thirds, from 2.3 billion tonnes in 1970 to 3.9 billion tonnes in 2010. Adjusted for inflation, crude oil is cheaper than it was 30 years ago, and in many countries, governments take a larger chunk of the price of petrol in tax than goes to the demonized OPEC or multinational oil companies.

Nevertheless, Yergin is sufficiently worried about maintaining an undisrupted oil supply that he feels energy security should be integral to foreign policy, given the high costs and long lead times of energy development. But I would argue that, particularly in rich countries, energy security depends more on using fuel and electricity rationally.

More important than OPEC's manoeuvrings is our continuing reliance on hundreds of millions of inexcusably inefficient vehicles, our preference for poorly insulated houses, our often mindless mobility and our consumption of energy-intensive junk. And as for the rapidly modernizing countries, is China's only choice to copy the US model of mass car ownership?

Yergin makes no comparisons of what nations actually do with energy — for instance, how much they need to secure a decent quality of life. Poor people in developing countries obviously need more energy, but how much more? As much as is already consumed, per capita, by their urban compatriots? Or, eventually, as much as in the United States, where the usage per head is twice as high as that in the richest European countries?

The book is silent on these matters. Instead, Yergin concludes that “this quest for energy goes without end”. But it cannot — and should not. ■

**Vaclav Smil** is an energy scientist and professor in the Faculty of Environment, University of Manitoba, Winnipeg, Canada. e-mail: [vsml@cc.umanitoba.ca](mailto:vsml@cc.umanitoba.ca)

# IN RETROSPECT

## Normal Accidents

As Japan strives to overcome the Fukushima nuclear disaster, **Nick Pidgeon** reflects on Charles Perrow's classic book about why complex technologies fail.

In publishing, much hinges on timing. So it was with Charles Perrow's influential book *Normal Accidents*. Its publication in 1984 was followed by a string of major technological disasters — including the Bhopal industrial chemical leak in India in December 1984, the explosion of the US space shuttle *Challenger* in January 1986, and the Chernobyl nuclear accident in Russia in April that year. Each cried out for the sort of detailed analysis that Perrow supplied. Now, more than a year after the Deepwater Horizon oil-rig blowout in the Gulf of Mexico, and in the aftermath of the nuclear disaster at Fukushima Daiichi in Japan in March, the book's message seems again prescient.

*Normal Accidents* contributed key concepts to a set of intellectual developments in the 1980s that revolutionized how we think about safety and risk. It made the case for examining technological failures as the product of complex interacting systems, and highlighted organizational and management factors as the main causes of failures. Technological disasters could no longer be ascribed to isolated equipment malfunction, operator error or random acts of God.

As one of the foremost US authorities on the sociology of large organizations, Perrow admits that he came to the topic of risk and technology almost by mistake. He was invited to provide a background paper for the President's Commission On The Accident At Three Mile Island, which enquired into the 1979 nuclear incident near Harrisburg, Pennsylvania. A very small leak of water into an instrumentation system had triggered an escalating chain of events at the Three Mile Island plant, involving both component malfunctions and operator errors. The result was a major loss of coolant to the reactor, not unlike the recent tragic events in Japan.

There was no single cause of the Three



Radiation monitoring at Three Mile Island in 1979.

Mile Island accident, nor of the Fukushima disaster. Numerous, seemingly inconsequential difficulties that had not been predicted by the plant designers combined to defeat multiple safety systems. Perrow concluded that the failure at Three Mile Island was a consequence of the system's immense complexity. Such modern high-risk systems, he realized, were prone to failures however well they were managed. It was inevitable that they would eventually suffer what he termed a 'normal accident'.

Therefore, he suggested, we might do better to contemplate a radical redesign or, if that was not possible, to abandon such technologies entirely. Foreseeing one of the problems at Fukushima, Perrow wrote in 1984 that "nuclear plants could be made marginally less complex if the spent storage pool were removed from the premises". Because such pools typically require constant cooling and attention, a reactor accident forcing an evacuation of the building, or a complete loss of power to the fuel cooling system, would then risk a serious fuel fire and significant release of radiation from the storage ponds.

*Normal Accidents* introduced two

concepts: 'interactive complexity', meaning the number and degree of system inter-relationships; and 'tight coupling', or the degree to which initial failures can concatenate rapidly to bring down other parts of the system. Universities, for example, are interactively complex but only loosely coupled — decisions are often influenced by unanticipated factors but effects are felt slowly. By contrast, modern production lines are often tightly coupled, with close and rapid transformations between one stage and the next, but have simple relationships between those stages. Neither tends to suffer systemic accidents.

When systems exhibit both high complexity and tight coupling, as at Three Mile Island, the risk of failure becomes high. Worse still, according to Perrow, the addition of more safety devices — the stock response to a previous failure — might further reduce the safety margins if it adds complexity. For example, when a British European Airways Trident jet crashed with the loss of all lives near London Heathrow Airport in 1972 after it stalled during take-off, the pilots were unable to diagnose the fault amid at least nine other cockpit warnings and alarms that went off as a result.

### A HISTORY OF FAILURE

Six years before *Normal Accidents*, British sociologist Barry Turner published his analysis of 80 major UK system failures in the lesser-known but similarly influential book *Man-Made Disasters* (Wykeham Science Press, 1978; I contributed to the posthumous 1997 second edition). Turner, too, emphasized the ways in which system complexity can defeat attempts to anticipate risks. But his theory differed crucially from Perrow's — it gave a more acute description of the organizational, management and communication failings that occur before an accident.

Major accidents do not spring into life on the day of the visible failure; they have a social and cultural context and a history. The problems at Three Mile Island, as we now know, were foreshadowed by similar near-miss events in other US pressurized-water plants — notably at the Davis-Besse nuclear plant near Oak Harbor, Ohio, in 1977. This raises the question of why safety information



**Normal Accidents: Living with High-Risk Technologies**  
CHARLES PERROW  
First published by Basic Books, 1984.  
Reprinted Princeton University Press: 1999.  
386 pp. \$35



and learning were not shared among operators. Disaster analysis of man-made incidents — in contrast to normal accidents — implied that if the background conditions incubated over time, there was some possibility of prior detection even when systems were complex.

Tensions are evident in the comparison of Turner's and Perrow's accounts — between the possibilities for foresight and fatalism. These resurfaced several years later in debates among US scholars over 'normal accidents' versus 'high-reliability organizations'. Similar discussions were seen in related work in Europe on safety culture and organizational accidents. The fundamental question, posed by influential political scientist Scott Sagan in his book *The Limits of Safety* (Princeton University Press, 1993), was: are normal accidents inevitable or can the combination of interactive complexity and tight coupling be safely managed?

The high-reliability researchers believed that it could. They studied cases such as the flight operations on aircraft carriers, where the conditions for normal accidents exist but the systems operate safely each day. They identified cultural factors, such as collective decision-making and organizational learning, as key reasons why an otherwise toxic combination of complexity and risk can be managed. By contrast, critics such as Sagan pointed out that even these systems had serious near-misses from time to time, and that normal accidents could always occur as a result.

That debate is still unresolved. Nevertheless, the analyses of Perrow and Turner were ahead of their time and their legacy remains profound. Many subsequent accident inquiries drew on their insights — most notably the space shuttle *Columbia* Accident Investigation Board report in 2003. Enquiries into the Fukushima disaster will benefit too, but we need a wider appreciation of how future normal accidents might gestate, and a better understanding of the actions of organizations and people, both intended and unintended, that generate major risks.

The world still faces many systemic risk challenges, including those of runaway climate change, financial-market failure and information security. Although many advances in safety technology, engineering practice and risk management have been made over the past 30 years, organizational and technical complexity remain integral to the many systems that drive such risks. *Normal Accidents* is a testament to the value of rigorous thinking when applied to a critical problem. ■

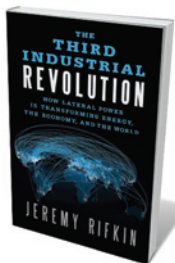
**Nick Pidgeon** is professor of applied psychology at Cardiff University, Wales, CF10 3AT, UK.  
e-mail: pidgeonn@cardiff.ac.uk

## Books in brief



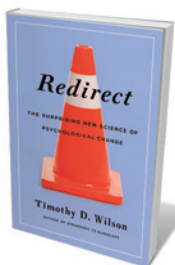
**Lifeblood: How To Change The World, One Dead Mosquito at a Time**  
Alex Perry C. HURST 208 pp. £16.99 (2011)

Journalist Alex Perry chronicles two years of US philanthropist Ray Chambers's crusade against malaria. A mix of science, history and research, this is a fascinating take on a disease that kills a million people a year. Chambers's story is just as intriguing. Pragmatism, business sense and bullheadedness gave him an advantage over the formulaic and often cost-ineffective approaches of many aid agencies. His Wall Street clout helped him to bring world leaders on board. And his focus on solutions such as bed nets and poverty eradication has, says Perry, enabled him to save millions of lives.



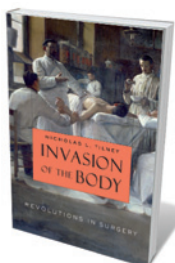
**The Third Industrial Revolution: How Lateral Power Is Transforming Energy, the Economy, and the World**  
Jeremy Rifkin PALGRAVE MACMILLAN 304 pp. £16.99 (2011)

Green energy and the Internet will revolutionize society and environment. So argues economist Jeremy Rifkin in this blueprint for global change. The five pillars of his vision for a post-fossil economy are a shift to renewables; a miniature power plant in every building; hydrogen storage for intermittent energy; an 'intergrid' for sharing energy that harnesses Internet technology; and eco-transport that runs on plug-in electricity and fuel cells. With the European Union already on board, this is a big idea with backbone.



**Redirect: The Surprising New Science of Psychological Change**  
Timothy D. Wilson LITTLE, BROWN 288 pp. \$25.99 (2011)

The stories we tell ourselves shape our lives, says social psychologist Timothy D. Wilson. Editing them can help us to redirect our thoughts and actions. He trawls through multitudinous 'happiness formulae' in popular-psychology books to show what doesn't work — from critical incident stress debriefing for trauma victims to the Healthy Families America initiative to prevent child abuse. What does work, he says, is simpler, subtler and backed by sound research: writing exercises, 'rewind' therapy, helping children to develop healthy narratives of their own and practising tolerance.



**Invasion of the Body: Revolutions in Surgery**  
Nicholas L. Tilney HARVARD UNIVERSITY PRESS 384 pp. \$29.95 (2011)

Tumours removed, joints replaced, organs transplanted: every weekday, 85,000 non-emergency operations take place in the United States alone. Distinguished US surgeon Nicholas L. Tilney intersperses moments from his own career with a rousing history of the evolution of surgery, breakthrough by breakthrough — from near-butcher to today's fine-tuned procedures. Wading through the gore with aplomb, he covers anaesthesia, pharmaceuticals, sepsis, health-care reform, surgery in war and in peace, facial transplants and more.



**About Time: Cosmology and Culture at the Twilight of the Big Bang**  
Adam Frank FREE PRESS 432 pp. \$26 (2011)

In this eloquent book, physicist and astronomer Adam Frank explores the interweaving of social and cosmological time. His trek through the history of humanity takes a parallel look at how we have gained a deeper grasp of the Universe during our time on Earth. Starting at the dawn of consciousness, he brings us through millennia of revolutions — from the development of agriculture, industry and the rise of cities to the emergence of string theory and ideas about eternal inflation and the multiverse.

and learning were not shared among operators. Disaster analysis of man-made incidents — in contrast to normal accidents — implied that if the background conditions incubated over time, there was some possibility of prior detection even when systems were complex.

Tensions are evident in the comparison of Turner's and Perrow's accounts — between the possibilities for foresight and fatalism. These resurfaced several years later in debates among US scholars over 'normal accidents' versus 'high-reliability organizations'. Similar discussions were seen in related work in Europe on safety culture and organizational accidents. The fundamental question, posed by influential political scientist Scott Sagan in his book *The Limits of Safety* (Princeton University Press, 1993), was: are normal accidents inevitable or can the combination of interactive complexity and tight coupling be safely managed?

The high-reliability researchers believed that it could. They studied cases such as the flight operations on aircraft carriers, where the conditions for normal accidents exist but the systems operate safely each day. They identified cultural factors, such as collective decision-making and organizational learning, as key reasons why an otherwise toxic combination of complexity and risk can be managed. By contrast, critics such as Sagan pointed out that even these systems had serious near-misses from time to time, and that normal accidents could always occur as a result.

That debate is still unresolved. Nevertheless, the analyses of Perrow and Turner were ahead of their time and their legacy remains profound. Many subsequent accident inquiries drew on their insights — most notably the space shuttle *Columbia* Accident Investigation Board report in 2003. Enquiries into the Fukushima disaster will benefit too, but we need a wider appreciation of how future normal accidents might gestate, and a better understanding of the actions of organizations and people, both intended and unintended, that generate major risks.

The world still faces many systemic risk challenges, including those of runaway climate change, financial-market failure and information security. Although many advances in safety technology, engineering practice and risk management have been made over the past 30 years, organizational and technical complexity remain integral to the many systems that drive such risks. *Normal Accidents* is a testament to the value of rigorous thinking when applied to a critical problem. ■

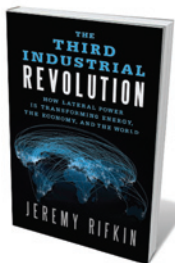
**Nick Pidgeon** is professor of applied psychology at Cardiff University, Wales, CF10 3AT, UK.  
e-mail: pidgeonn@cardiff.ac.uk

## Books in brief



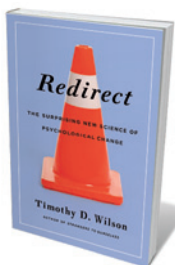
**Lifeblood: How To Change The World, One Dead Mosquito at a Time**  
Alex Perry C. HURST 208 pp. £16.99 (2011)

Journalist Alex Perry chronicles two years of US philanthropist Ray Chambers's crusade against malaria. A mix of science, history and research, this is a fascinating take on a disease that kills a million people a year. Chambers's story is just as intriguing. Pragmatism, business sense and bullheadedness gave him an advantage over the formulaic and often cost-ineffective approaches of many aid agencies. His Wall Street clout helped him to bring world leaders on board. And his focus on solutions such as bed nets and poverty eradication has, says Perry, enabled him to save millions of lives.



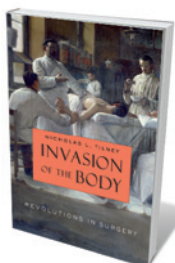
**The Third Industrial Revolution: How Lateral Power Is Transforming Energy, the Economy, and the World**  
Jeremy Rifkin PALGRAVE MACMILLAN 304 pp. £16.99 (2011)

Green energy and the Internet will revolutionize society and environment. So argues economist Jeremy Rifkin in this blueprint for global change. The five pillars of his vision for a post-fossil economy are a shift to renewables; a miniature power plant in every building; hydrogen storage for intermittent energy; an 'intergrid' for sharing energy that harnesses Internet technology; and eco-transport that runs on plug-in electricity and fuel cells. With the European Union already on board, this is a big idea with backbone.



**Redirect: The Surprising New Science of Psychological Change**  
Timothy D. Wilson LITTLE, BROWN 288 pp. \$25.99 (2011)

The stories we tell ourselves shape our lives, says social psychologist Timothy D. Wilson. Editing them can help us to redirect our thoughts and actions. He trawls through multitudinous 'happiness formulae' in popular-psychology books to show what doesn't work — from critical incident stress debriefing for trauma victims to the Healthy Families America initiative to prevent child abuse. What does work, he says, is simpler, subtler and backed by sound research: writing exercises, 'rewind' therapy, helping children to develop healthy narratives of their own and practising tolerance.



**Invasion of the Body: Revolutions in Surgery**  
Nicholas L. Tilney HARVARD UNIVERSITY PRESS 384 pp. \$29.95 (2011)

Tumours removed, joints replaced, organs transplanted: every weekday, 85,000 non-emergency operations take place in the United States alone. Distinguished US surgeon Nicholas L. Tilney intersperses moments from his own career with a rousing history of the evolution of surgery, breakthrough by breakthrough — from near-butcher to today's fine-tuned procedures. Wading through the gore with aplomb, he covers anaesthesia, pharmaceuticals, sepsis, health-care reform, surgery in war and in peace, facial transplants and more.



**About Time: Cosmology and Culture at the Twilight of the Big Bang**  
Adam Frank FREE PRESS 432 pp. \$26 (2011)

In this eloquent book, physicist and astronomer Adam Frank explores the interweaving of social and cosmological time. His trek through the history of humanity takes a parallel look at how we have gained a deeper grasp of the Universe during our time on Earth. Starting at the dawn of consciousness, he brings us through millennia of revolutions — from the development of agriculture, industry and the rise of cities to the emergence of string theory and ideas about eternal inflation and the multiverse.





The SubSafe software creates a virtual submarine to train personnel to find safety equipment.

## Q&A Robert Stone

# The virtual trainer

Robert Stone, director of the Human Interface Technologies Team at the University of Birmingham, UK, develops 'serious games' for training soldiers and sailors. He explains how immersion in virtual worlds can prepare military personnel for their experiences on the battlefield — and help them to heal after they return.

### How useful are virtual environments in military training?

Even with today's technology, we can't fully replace the experience of live combat or military activities. But where current training practices fall short, virtual environments or serious gaming can fill the gap.

### What sort of environments do you model?

We train a range of military recruits — from new submariners to those who will patrol areas to locate improvised explosive devices in Afghanistan and the United Kingdom. One project involves a virtual British town. We program it for different scenarios — say, a suspect package left at a railway station. Army instructors work with trainees to pick and place objects, such as the command vehicle, cordons or robot disposal vehicles; they then discuss appropriate questions to ask the police or witnesses, to build up a strong picture of the developing incident.

### Is virtual training proven to work?

Yes. For example, *SubSafe* is a three-dimensional recreation of a nuclear submarine, built using game-technology software. Naval instructors use it to train submariners, particularly in locating

safety equipment — fire extinguishers, breathing apparatus and thermal imagers. When we evaluated the software with trainees at the naval base in Devonport, UK, over 18 months, we found that there was a significant improvement in the real-world performance of the guys who got the software, compared with those who did not. That's important because in the future, the United Kingdom will have fewer submarines, which means less time for trainees on real vessels.



Robert Stone and his training program *SubSafe*.



### BEYOND THE BOMB

Science and the military  
[nature.com/military](http://nature.com/military)

### Can your work help soldiers who return from combat?

We plan to use the technology to provide restorative environments for returnees who have had serious surgery, such as amputations. Display screens at the ends of their hospital beds would show a view of sea- and landscapes in real time: evidence suggests that exposure to blue-green environments — such as seascapes and meadows — improves recovery and reduces the need for analgesics. Virtual environments will be used as part of therapeutic 'guided imagery' and relaxation techniques. We also aim to help amputees to prepare their remaining muscles for prosthetic devices, using motion-sensing devices in tandem with virtual environments — so that they can virtually walk along a beach, scuba-dive, skim stones or throw a frisbee.

### What are the challenges for an academic working with the military?

It is a difficult area to break into. These projects are not something you can perform in splendid academic isolation; you have to go into the field and understand the jobs that these guys do. I've flown on helicopters, been to sea in submarines and fired small Gatling guns off the side of Royal Navy ships. There are risks — I once experienced a helicopter gearbox failure, and have been marooned on the bottom of a Scottish loch in a damaged three-person submersible.

### Does it help that most recruits are familiar with computer games?

Yes; the games culture is helping us to manage the expectations and engagement of future military-simulation users. Many young recruits have been put in front of simulators using older technologies, and have said: "We can do better than this at home." That way, you lose hearts and minds instantly. But if you show them something that looks the part, such as the *Call of Duty* series of action games, you instantly have their attention.

### Are some people still sceptical?

That never goes away. It's not just the older members of the armed forces; we get it from younger officers as well. Fortunately, when they have seen the results, most of them come around very quickly. It is all part of the challenge. ■

INTERVIEW BY DANIEL CRESSEY

# Correspondence

## US pathology centre units will live on

We wish to point out that several elements of the US Armed Forces Institute of Pathology (AFIP) have survived its closure and have been relocated within the Department of Defense (*Nature* **476**, 270–272; 2011).

These units include the Depleted Uranium and Imbedded Fragment Laboratory, the Molecular Laboratory, Telepathology, the Automated Central Tumor Registry, the Veterinary Pathology Program (including residency training), the Armed Forces Medical Examiner function, the Histotechnology Training Program, and the congressionally funded Combat Wound Initiative. The Department of Veterans' Affairs has assumed responsibility for the capabilities of the Biophysical Research Laboratory.

The Department of Defense is working to make the vast collection of the former AFIP Tissue Repository (now part of the Joint Pathology Center) broadly available for research. At our request, the Institute of Medicine has convened a panel of national experts in biorepository management, medical informatics, medical ethics and pathology. The panel's task is to recommend the optimal and sustainable use of repository material; who should have access to it; technologies needed to utilize the repository; and ethical considerations over the use in research of material originally collected for clinical purposes.

Several institutes are collaborating in pathology translational research and in supporting key clinical-research initiatives and education efforts. These include the Uniformed Services University of the Health Sciences, the Joint Task Force National Capital Region Medical (and its subordinate units, the Joint Pathology Center and Walter Reed National Military Medical Center), other

organizations in the Department of Defense, and Veterans' Affairs.

These collaborations will be part of a new era of intergovernmental and public–private partnerships that will create vital research and clinical interactions. The celebrated history of AFIP and its importance to the broader research, clinical and academic communities provide the perfect foundation.

**Thomas P. Baker** *Joint Pathology Center, Silver Spring, Maryland, USA. thomas.p.baker@us.army.mil*  
**John M. Mateczun** *Joint Task Force National Capital Region Medical, Bethesda, Maryland, USA.*

**Charles L. Rice** *Uniformed Services University of the Health Sciences, Bethesda, Maryland, USA.*

## China's academic autocracy must go

Many scientists in China share Nai-Xing Wang's dissatisfaction with the dominant role of journal impact factors in the country's scientific evaluation system (*Nature* **476**, 253; 2011). But I contend that even an imperfect law is better than no law.

Replacing this rigid evaluation system with a more flexible one could send Chinese academia into chaos. Leaders of universities and research institutions could then establish their own evaluation systems, designing them to favour their particular interests. For example, a professor who is connected to a scientific journal might be tempted to rank papers published in that journal more highly when evaluating the performance of his or her university.

Chinese researchers should benefit from the strict implementation of impact-factor evaluation criteria. But the rewards for meeting these targets aren't always forthcoming. A good relationship with the few leading executives who

control China's academia is also important, as it is for gaining access to the best scientific projects and for promotions.

The key task is therefore to eradicate this autocratic control. Researchers would then be able to concentrate solely on their work.

**Nai-Zhuo Zhao** *Northeast Normal University, Changchun, China.*

*naizhuo.zhao@gmail.com*

## Review boards: vital to protect subjects

On behalf of the Consortium of Independent Review Boards, a non-profit US organization for ethical review of clinical research and protection of participants, I object to your suggestion that a US government proposal to overhaul institutional review board (IRB) regulations would increase the use of commercial IRBs that have an “unsettling incentive to approve trials” (*Nature* **476**, 125; 2011).

You imply that independent IRBs put research subjects at risk. However, all review boards are subject to a high level of federal regulation and inspection. Inspections by the US Food and Drug Administration involve thorough site visits and assessment of policies, procedures and records.

Independent IRBs protect research participants by reviewing studies conducted by private clinics and community and academic hospitals. Without such IRBs, patient access to promising experimental treatments would be curtailed and research would be unduly protracted.

Consortium members commit to a code of ethics requiring them to protect the IRB from economic influences when reviewing research, minimize ‘IRB shopping’ and promote ethical marketing. The consortium also requires members to be accredited by independent bodies such as the Association for the Accreditation

of Human Research Protection Programs (see *Nature* **477**, 280; 2011).

The consortium believes that the proposed overhaul of the regulations warrants careful review, and urges the research community to focus on identifying substantive measures that support the highest standards for protecting human subjects in clinical research.

**Cami Gearhart** *Consortium of Independent Review Boards, Washington DC, USA.*  
*www.consortiumofirb.org*

## Make integrity key to recruitment

Far from being a vague ideal, the complex and sensitive issue of maintaining integrity in science is a critical imperative. In my view, it would help to demand and monitor integrity in scientists and managers from the outset (*Nature* **476**, 251, 262; 2011).

Most researchers know from their training that honesty is fundamental to scientific integrity. But some managers and agency officials can find themselves in difficult situations. A manager must cope with the competing pressures of supporting and protecting the scientists working on a project, ensuring the survival of the scientific institution and pleasing unforgiving political masters — possibly all under public scrutiny. Even an honest manager might fear being undermined by a rival colleague or, worse, by a scientist who is cavalier about professional ethics.

The only way to achieve scientific integrity across the board is to ensure that personal and professional values (as well as knowledge and skills) are primary criteria for the employment of both scientists and managers. These values must be demonstrated and constantly monitored, not just presumed.

**Alfred P. Zarb** *Leura, New South Wales, Australia.*  
*zarbap@ozemail.com.au*



## FORUM Ageing

# Longevity hits a roadblock

Increased expression of sirtuin proteins has been shown to enhance lifespan in several organisms. New data indicate that some of the reported effects may have been due to confounding factors in experimental design. Here, experts discuss the significance of these data for research into ageing. **SEE LETTER P.482**

### THE PAPER IN BRIEF

- Previous work<sup>1–4</sup> had shown that increased expression of the yeast protein Sir2 and of related sirtuin proteins in the nematode *Caenorhabditis elegans* and the fruitfly *Drosophila melanogaster* extends lifespan.
- Burnett *et al.*<sup>5</sup> believed that the organisms' genetic backgrounds, because they had not been controlled, might have affected those results, and so they repeated the experiments after standardizing the backgrounds.
- By means of genetic backcrossing (Fig. 1), the authors show that sirtuin overexpression and longevity in *C. elegans* are separable.

- Two *Drosophila* strains that had been reported to be long-lived as a result of sirtuin overexpression were not long-lived when compared with a genetically appropriate control strain.
- The study refutes yet another previous observation — that the increase in fly lifespan that occurs with dietary restriction depends on sirtuins.
- In an accompanying Brief Communication Arising, Viswanathan and Guarente<sup>6</sup> show that sirtuin overexpression leads to a smaller increase in *C. elegans* lifespan than previously reported.

## A valuable background check

DAVID B. LOMBARD & SCOTT D. PLETCHER

Burnett and colleagues' in-depth study<sup>5</sup> of the influence of Sir2 overexpression on lifespan in *C. elegans* and *Drosophila*, as well as on diet-modulated longevity in the fly, shows that the protein has no effect, challenging previous publications<sup>1,2,4</sup>. But since when does *Nature* publish negative results?

Well, sirtuins are exceptional. Anything that can influence ageing captures the public's imagination, and — since the reports that sirtuins are involved in increasing lifespan in invertebrates — research into these proteins has exploded. Moreover, the seven mammalian sirtuins have been implicated in the suppression of numerous age-associated diseases, including neurodegenerative disorders, cardiac dysfunction, hearing loss and neoplasia<sup>7</sup>.

Meanwhile, heated controversies have arisen regarding aspects of sirtuin biology. These involve the proteins' roles in the response to dietary restriction; the mechanism of action of reported sirtuin activators; and whether the role of Sir2 in promoting longevity — first identified in yeast — is evolutionarily conserved in other organisms. The disagreements

fostered complaints of publication bias and disproportionate scientific and commercial emphasis on the role of sirtuins in longevity. So, here we are.

Burnett *et al.*<sup>5</sup> were thorough. They generated an impressive collection of lifespan experiments, and these were replicated and the results contributed by several laboratories. The data were supported by backcrossing and by genetic and biochemical analyses. But an accompanying report from Viswanathan and Guarente<sup>6</sup>, although confirming some of Bur-

**Challenging published results is an essential, self-correcting aspect of science.**

nett and co-workers' findings, shows that worms overexpressing Sir2 retain modestly increased (10–13%) lifespan after backcrossing — consistent with data reported elsewhere<sup>8</sup>.

At best, therefore, these papers indicate that Sir2 overexpression is just one of more than 100 genetic manipulations currently known to increase worm and/or fly lifespan to some degree, with many others having larger effects.

Given the demonstrated importance of sirtuins in mammals, why rehash the precise role of Sir2 in worm and fly ageing? First, challenging published results is an essential, self-correcting aspect of

science. Second, invertebrate models continue to contribute to the understanding of sirtuin biology in mammals, and so future studies must be interpreted in the context of these new data. Third, the new reports<sup>5,6</sup> reinforce the importance of rigorous genetic background control when interpreting the effects of single gene mutations. Studies in *Drosophila* suggest that 8–10 generations of backcrossing are required before the genetic background can be considered reasonably well controlled; this needs to be the standard in worms too (Fig. 1). For genetically engineered mutant mice, where this approach may be impractical, analysis of independent transgenic animal lines and/or reversal of traits upon re-expression of the gene of interest should be undertaken to ensure that that gene is indeed responsible for the effect under investigation.

Perhaps the most interesting issue is the apparent disconnect between these new results and the powerful effects of sirtuins on age-associated disease in mammals. Maybe sirtuins have their strongest effects on specific aspects of physiological homeostasis and stress responses, rather than in modulating ageing per se. For example, consistent with published data<sup>9</sup>, Burnett *et al.*<sup>5</sup> show that Sir2 overexpression makes worms resistant to toxic protein aggregates. Also, increased expression of the related SIRT1 protein in mice suppresses metabolic dysfunction and the development of certain types of cancer, without increasing overall lifespan<sup>10</sup>. Although roles for other mammalian sirtuins in promoting longevity have not been explored, such studies are under way in several laboratories. So the latest reports<sup>5,6</sup> are unlikely to be the final word on sirtuins and ageing.

David B. Lombard is in the Department of Pathology and Institute of Gerontology, and Scott D. Pletcher is in the Department of Molecular and Integrative Physiology and Institute of Gerontology, University of Michigan, Ann Arbor, Michigan 48109, USA.  
e-mails: davidlom@umich.edu; spletch@umich.edu

# Don't write sirtuins off

CARLES CANTÓ & JOHAN AUWERX

The role of Sir2 and its mammalian counterpart SIRT1 as lifespan regulators, proposed on the basis of work done exclusively in simple organisms, has been grounds for intensive discussion. Studies on yeast lifespan were the first to cast doubt on the role of sirtuins in longevity<sup>11</sup>. And Burnett and colleagues' elegant work<sup>5</sup> puts a final nail in the coffin. Let's not forget, however, that an overwhelming body of evidence indicates that sirtuins have crucial roles in metabolic homeostasis.

The new paper, indeed, dampens the longevity claims assigned to Sir2. But one caveat of most of the genetic work in simple organisms is that it is rarely accompanied by biochemical studies that reveal the extent to which the manipulations of a gene or protein are translated into altered activity. Sirtuins are protein deacetylase enzymes, and so in this case it remains unclear how manipulation of the gene encoding Sir2 changes the acetylation state of its main target proteins. Such information would establish beyond doubt that the absence of the Sir2 gene is not compensated for by increased activity of another member of the sirtuin family.

As for the relevance of these data<sup>5,6</sup> to the role of sirtuins in mammals, it was previously shown that mice overexpressing SIRT1 do not live longer<sup>12</sup>. Initially, this lack of effect on lifespan was attributed either to insufficient expression of the SIRT1 transgene or to possible confounding functional compensation of protein deacetylation by other Sir2-related proteins. However, if Burnett and colleagues' results can be extended to mice, then the earlier mouse data<sup>12</sup> are not so astonishing after all. The main role of SIRT1 in mammals might not be directly related to lifespan regulation.

If not to control lifespan, what is the main function of SIRT1? The answer may lie in the observation that the activity of SIRT1 depends strictly on the levels of the coenzyme NAD<sup>+</sup>, which acts as a co-substrate for the deacetylation reaction that SIRT1 catalyses. Changes in NAD<sup>+</sup> levels, which reflect the metabolic activity of the cell, hence modulate SIRT1 activity according to the cellular energy status. This NAD<sup>+</sup> dependence makes SIRT1 an attractive integrative node for metabolic sensing and for transcriptional regulation, as SIRT1 influences post-translational modification of transcription factors and histone proteins<sup>3</sup>.

In contrast to the observations on lifespan, the effects of SIRT1-related proteins favouring metabolic flexibility are based on a wealth of genetic, physiological and pharmacological evidence, and are conserved from yeast to mammals. In mammals, SIRT1 mediates

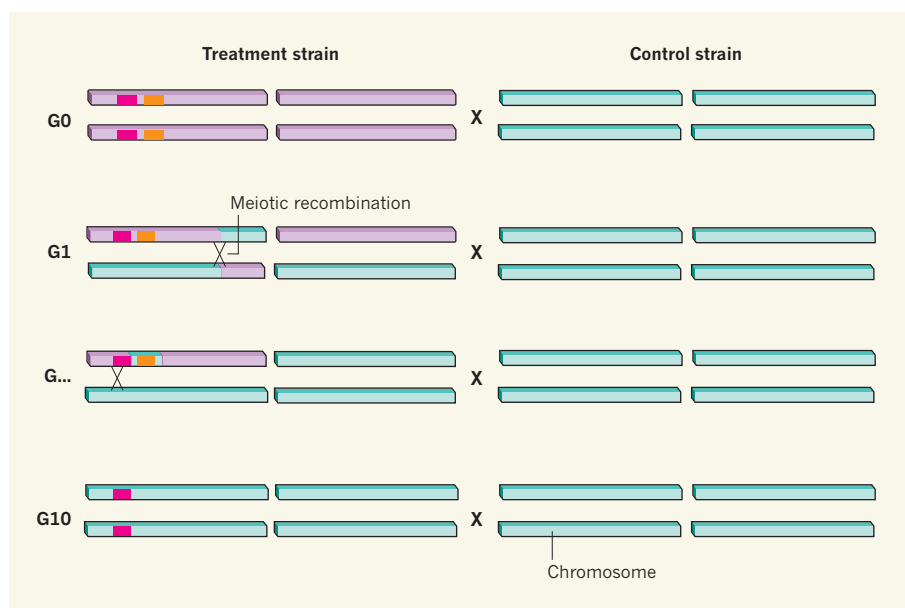


**Figure 1 | Eliminating effects of confounding genetic sequences.** Burnett *et al.*<sup>5</sup> show that genetic backcrossing is essential to ensure that comparisons between treatment and control strains of an organism are not confounded by differences unrelated to the gene of interest (pink). Confounding effects may be due to a large effect of a nearby gene (orange) or small effects of many genes throughout the genome (occurring within the purple elements). At generation 0 (G0, no backcrossing), these influences predominate. With backcrossing, processes such as independent chromosome segregation and meiotic recombination introduce variants from the control strain (blue elements) into the treatment strain, reducing the possibility of confounding effects. Although most differences between the two strains are rapidly lost (at a rate of roughly 50% per generation), closely linked differences often persist for many generations. It is only after recombination occurs sufficiently closely to the gene of interest (at G10 or so) that genetic backgrounds can be considered properly controlled and that differences can be attributed to the gene of interest.

metabolic and transcriptional adaptations to situations of energy stress and nutrient deprivation by enhancing respiration by the mitochondria, the cell's energy producers. Mice overexpressing SIRT1 are therefore protected from the metabolic damage caused by a high-fat diet<sup>10</sup>.

**One caveat of most of the genetic work in simple organisms is that it is rarely accompanied by biochemical studies.**

effect on lifespan in mice fed regular chow<sup>15</sup>. Conversely, outbred mice lacking SIRT1 show deficiencies in metabolism and cannot respond properly to the lifespan-increasing effects of calorie restriction<sup>12</sup>. This highlights how the metabolic adaptations that SIRT1 induces might indirectly influence mammalian lifespan.

Indeed, although in light of Burnett and colleagues' findings<sup>5</sup> the appeal of sirtuins as a *sensu stricto* lifespan determinant might be gone, SIRT1 activation remains a promising approach to delaying general age-related physiological decline and to treating numerous

inherited and acquired diseases characterized by defective mitochondrial function. The astonishing ability of SIRT1 to enhance 'healthspan' by promoting metabolic fitness will also guarantee it a long life as a subject for further exciting research. ■

Carles Cantó is at the Nestlé Institute of Health Sciences, CH-1015 Lausanne, Switzerland. Johan Auwerx is in the École Polytechnique Fédérale de Lausanne, CH-1015 Lausanne, Switzerland. e-mail: johan.auwerx@epfl.ch

1. Tissenbaum, H. A. & Guarente, L. *Nature* **410**, 227–230 (2001).
2. Rogina, B. & Helfand, S. L. *Proc. Natl Acad. Sci. USA* **101**, 15998–16003 (2004).
3. Cantó, C. & Auwerx, J. *Trends Endocrinol. Metab.* **20**, 325–331 (2009).
4. Bauer, J. H. *et al.* *Aging* **1**, 38–48 (2009).
5. Burnett, C. *et al.* *Nature* **477**, 482–485 (2011).
6. Viswanathan, M. & Guarente, L. *Nature* <http://dx.doi.org/10.1038/nature10440> (2011).
7. Guarente, L. *N. Engl. J. Med.* **364**, 2235–2244 (2011).
8. Rizki, G. *et al.* *PLoS Genet.* **7**, e1002235 (2011).
9. Parker, J. A. *et al.* *Nature Genet.* **37**, 349–350 (2005).
10. Herranz, D. *et al.* *Nature Commun.* **1**, 3 (2010).
11. Kaeblerlein, M. & Powers, R. W. III *Ageing Res. Rev.* **6**, 128–140 (2007).
12. Herranz, D. & Serrano, M. *Nature Rev. Cancer* **10**, 819–823 (2010).
13. Lagouge, M. *et al.* *Cell* **127**, 1109–1122 (2006).
14. Baur, J. A. *et al.* *Nature* **444**, 337–342 (2006).
15. Pearson, K. J. *et al.* *Cell Metab.* **8**, 157–168 (2008).



# Slippery when wetted

The slick interior of the pitcher plant has inspired a slippery material possessing self-lubricating, self-cleaning and self-healing properties. The secret is to infuse a porous material with a liquid that repels oils and water. [SEE LETTER P.443](#)

MICHAEL NOSONOVSKY

The legendary water repellence of lotus leaves has inspired a field of research aimed at making similarly 'superhydrophobic' surfaces. But it's much more difficult to make omniphobic materials, which repel oils as well as water. On page 443 of this issue, Wong *et al.*<sup>1</sup> report a radical new approach to making omniphobic surfaces that was inspired by another member of the plant family: the insect-eating pitcher plant.

An ancient Indian poem, the *Bhagavad Gita*, has this to say about a seeker of truth: "Having abandoned attachment, he acts untainted by evil, just as a lotus leaf is not wetted." Here, as in many cultures, the lotus is used as a symbol of purity because of its ability to emerge clean from muddy water. Examination of lotus leaves in the 1990s using scanning probe microscopy<sup>2</sup> revealed that this ability is a result of the leaves' surface microstructure: each leaf is covered with tiny bumps called papillae. When the surface is wetted by water, a so-called composite solid-air-liquid interface forms in which water sits atop pockets of air trapped between the papillae (Fig. 1a). This drastically reduces the solid-water contact area, so that water droplets form an almost perfect sphere and easily roll on the surface, washing away dust in the process. This superhydrophobic behaviour is often referred to as the lotus effect.

Different models that connect surface roughness with water wetting have been proposed, including the Cassie-Baxter model<sup>3</sup> (which describes a three-phase solid-air-liquid composite interface; Fig. 1a), and the Wenzel model<sup>4</sup> (which invokes a simpler two-phase system in which no air pockets are trapped between the solid and the water; Fig. 1b). The Cassie-Baxter model explains superhydrophobicity, and has helped in the development of techniques for structuring the surfaces of different materials to mimic the lotus effect. These materials find applications in the field of tribology — the study of friction, wear and lubrication — and in other areas of engineering.

Making superhydrophobic surfaces is a challenge, but it is far more difficult to produce oleophobic surfaces that repel organic liquids such as oils. This is because oil molecules are nonpolar, and have a much lower surface energy than polar water molecules; it is therefore not energetically favourable for oil droplets to form as spheres on a solid surface. Omniphobic surfaces that are both oleophobic and hydrophobic are highly desirable for many applications — they could, for example, be used to prevent dirt from collecting on optical devices or to prevent moving parts in micrometre-scale devices from sticking to each other. Previous approaches for making oleophobic and omniphobic surfaces have involved

the design of complicated surface geometries to prevent oil from penetrating into valleys between bumps<sup>5</sup>.

Wong *et al.*<sup>1</sup> suggest a new approach, inspired by the surface of the insect-eating pitcher plant *Nepenthes*. The plant captures prey using a slippery, water-lubricated surface — insects that step on the surface at the rim of the pitcher slide down into digestive juices at the bottom<sup>6</sup>. The surface is slippery because the lubricant forms a continuous film that repels oils on the insects' feet. Although the surface has microstructures, these are irregular (unlike those of lotus-inspired surfaces), and serve only to hold the lubricant in place.

The authors mimicked pitcher-plant surfaces by making a sponge-like material and filling it with a lubricating liquid to create slippery liquid-infused porous surfaces (SLIPS). When a droplet of another liquid is placed on the material, a composite solid-lubricant-liquid interface is formed (Fig. 1c). The lubricant has a similar function to the air pockets in the lotus effect, but it also forms a continuous film, similar to that on the surfaces of pitcher plants. Unlike lotus-mimicking materials, SLIPS can be oleophobic, and the presence of a lubricant means that friction at the surfaces is very low. In fact, by choosing lubricants that are immiscible with both water and oils, the authors prepared SLIPS that have highly promising omniphobic properties. What's more, the SLIPS could withstand high pressures, were wear-resistant, and even healed themselves in the case of minor damage — all of which are advantages over lotus-mimicking materials.

The development of SLIPS typifies two themes that are likely to dominate the field of biomimetic and functional surfaces in coming years. The first is the integration of self-healing, self-lubricating and self-cleaning capabilities into surfaces. Friction and wear are usually viewed as causes of energy dissipation and material deterioration, but under certain circumstances they can lead to increased order at interfaces<sup>7</sup>. This can form the basis of the capabilities mentioned above. Indeed, this is what happens with the SLIPS — when the porous material in SLIPS is damaged by wear or impact, a combination of effects (chemical potential, concentration and pressure gradients) facilitates the lubricant's transport to the surface, restoring the materials' self-lubricating and self-cleaning properties.

The second theme is the idea that the wetting of rough surfaces can be more complex than is predicted by either the two-phase Wenzel model or the three-phase Cassie-Baxter model. Indeed, multi-phase interfaces involving a variety of components — solids, oils, water, lubricants, air and so on — have been identified, and show great promise for new applications such as underwater oleophobicity.

Not only are Wong and colleagues' SLIPS of fundamental interest, but they will probably also lead to the development of new materials

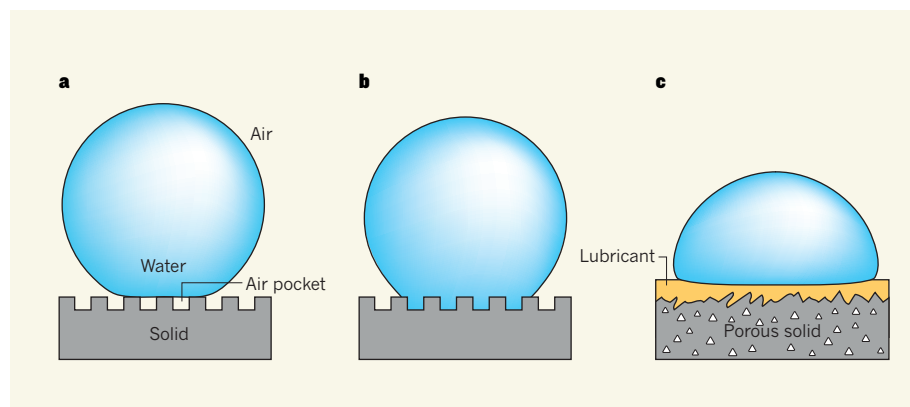


**Figure 1 | Forms of surface wetting.** a, The Cassie-Baxter model of surface wetting proposes that water droplets sitting on rough surfaces form a solid-air-liquid interface. Air pockets trapped beneath the droplet reduce the contact between the water and the surface. If the surface features are of the right size and are regular, then the surface becomes water repellent. b, In the Wenzel model, no air pockets form, and so the surface is completely wetted by the droplet. c, Wong *et al.*<sup>1</sup> have made porous materials that are infused with, and wetted by, a liquid lubricant that repels water and oils. The surface features do not themselves generate water repellence, but serve to hold the lubricant in place.

for many applications — in biomedical devices, for example, or as coatings to prevent the icing or fouling of surfaces. Currently, the main weakness of SLIPS is their durability, which is limited by how long the lubricant stays in the pores without evaporating or leaking. Another problem is that there are strict limitations on the chemical properties of the lubricants: they must be immiscible with both water and oil, but they should also penetrate into the pores of the underlying material. The authors' preliminary studies into these issues are encouraging, but additional research is needed before applications will emerge. ■

Michael Nosonovsky is in the Department

of Mechanical Engineering, College of Engineering & Applied Science, University of Wisconsin–Milwaukee, Milwaukee, Wisconsin 53211, USA.

e-mail: nosonovs@uwm.edu

1. Wong, T.-S. *et al.* *Nature* **477**, 443–447 (2011).
2. Barthlott, W. & Neinhuis, C. *Planta* **202**, 1–8 (1997).
3. Cassie, A. B. D. & Baxter, S. *Trans. Faraday Soc.* **40**, 546–551 (1944).
4. Wenzel, R. N. *Ind. Eng. Chem.* **28**, 988–994 (1936).
5. Tuteja, A., Choi, W., Mabry, J. M., McKinley, G. H. & Cohen, R. E. *Proc. Natl Acad. Sci. USA* **105**, 18200–18205 (2008).
6. Bohn, H. F. & Federle, W. *Proc. Natl Acad. Sci. USA* **101**, 14138–14143 (2004).
7. Nosonovsky, M. & Rohatgi, P. K. *Biomimetics in Materials Science: Self-healing, Self-lubricating, and Self-cleaning Materials* (Springer, in the press).

## SYNTHETIC BIOLOGY

# A yeast for all reasons

Scientists have begun to overhaul a yeast's genome to make it more stable, engineerable and evolvable. Remarkably, the part-natural, part-synthetic yeast cells function and reproduce without obvious ill effects. [SEE LETTER P.471](#)

PETER J. ENYEART & ANDREW D. ELLINGTON

The baker's yeast *Saccharomyces cerevisiae* is a model organism, and therefore one of the best-understood biological systems on the planet. Nevertheless, the Byzantine complexity of its inner workings still keeps bioengineers up at night, and continues to provide fodder for experimentation. If scientists could 'refactor' model organisms — that is, recode their genomes to be simpler and more amenable to human understanding and tinkering — then science and biotechnology based on those organisms could proceed at an accelerated pace. On page 471 of this issue, Dymond *et al.*<sup>1</sup> present a major advance towards this end: the construction of a functional, partly synthetic version of the *S. cerevisiae* genome.

Rewriting genomes to meet the specifications of humans has been a stated goal of synthetic biology for some time<sup>2</sup>. But the labour and expense involved in actually making such radical changes to genomes, coupled with uncertainties about the chances of improving on what nature spent billions of years perfecting, have meant that only a few serious tilts at genome re-engineering have been made. Previous noteworthy examples include the refactoring of 12,000 base pairs (about 30%) of a virus genome<sup>3</sup> and the removal of 'amber' stop codons — nucleotide sequences that signal the termination of translation — from the bacterium *Escherichia coli*<sup>4</sup>, a feat that should allow researchers to rewrite portions of the bacterium's genetic code at will. And, of course, the genome of a *Mycoplasma* bacterium has been synthesized *de novo* by

workers at the J. Craig Venter Institute in Rockville, Maryland, and used to infuse a working cell<sup>5</sup>.

Dymond *et al.*<sup>1</sup> have now raised the bar by starting work on eukaryotes (organisms such as fungi, plants and animals), which have much larger and more complex genomes than bacteria. More specifically, the authors have replaced sections of two chromosomes of *S. cerevisiae* — 90,000 bases at the end of chromosome IX, and 30,000 bases at the end of chromosome VI — with synthetic DNA. Their eventual goal is presumably to replace the entire genome of 12 million base pairs with a human-designed sequence.

To make their synthetic DNA, Dymond *et al.* entirely removed 20 regions from the naturally occurring yeast chromosomes. Most of these regions were repetitive sequences (which can cause DNA segments to be deleted or even cause chromosomes to mis-segregate), or sequences that were non-functional or redundant. The authors also recoded all genes longer than 500 bases to contain 'watermarks' — sequences that allow the synthetic DNA to

be easily differentiated from natural sequences using standard laboratory methods, but that do not change the sequences of proteins encoded by genes. As in the previously reported work<sup>4</sup> in *E. coli*, Dymond and colleagues<sup>1</sup> modified amber stop codons in the DNA of *S. cerevisiae* so that they could be recoded in the future, for example to encode unnatural amino acids for insertion into yeast proteins.

Astoundingly, the authors found that yeast cells containing the modified genome suffered no growth defects and displayed minimal differences in gene expression in comparison with the wild-type strain. The entire sequence of the artificially added DNA was faithfully reproduced by living cells, which is either a testament to the robustness of human engineering or a sign that God's fingerprints are fainter than creationists would have you believe.

In addition to the changes mentioned earlier, Dymond and co-workers introduced sequence elements known as loxP sites after every non-essential gene in their synthetic DNA, and at several other positions. In the presence of an enzyme called Cre recombinase, these loxP sites stochastically recombined with each other, either deleting or inverting the intervening sequence of DNA. The authors were thus able to generate a vast library of yeast genomes, containing all manner of random architectures, at will. Such libraries could be screened or evolved to find new yeast strains that are better suited to living in a given environment. Moreover, because yeast is used to produce alcohol, proteins and high-value organic compounds, new strains generated in this way might prove to be useful for industry, in the same way that a simplified *E. coli* strain has proved to be an excellent platform for producing large quantities of proteins<sup>6</sup>.

The obvious extension of Dymond and colleagues' work is to rebuild the entire yeast genome. However, given that the currently completed synthetic sequences represent only about 1% of the whole genome, rebuilding the remainder is a daunting task. One issue is that, even though the aggregated cost of the materials, apparatus and consumables used in DNA synthesis has been steadily decreasing, the construction of entire genomes remains inordinately expensive<sup>7</sup>.

Even more problematic is the cost of labour. A comparison of recent endeavours in genome synthesis and modification (Table 1) reveals

TABLE 1 | LABOUR REQUIRED FOR GENOME SYNTHESIS

Organism (year)	DNA bases synthesized (% of genome)	DNA bases per year of labour*
T7 bacteriophage (2005) <sup>2</sup>	12,000 (30)	1,300
<i>Mycoplasma mycoides</i> (2010) <sup>5</sup>	1,080,000 (100)	15,000
<i>Escherichia coli</i> (2011) <sup>4</sup>	4,600,000 (100) or 28,000 (0.6) <sup>†</sup>	96,000 or 600 <sup>†</sup>
<i>Saccharomyces cerevisiae</i> (2011) <sup>1</sup>	120,000 (1)	2,700

\*Estimated as follows: total bases synthesized/[number of authors × 3], assuming that 3 years is the average time spent by a person on genome-synthesis projects.

<sup>†</sup>Depending on whether the entire genome or only synthetic oligonucleotides are counted.



for many applications — in biomedical devices, for example, or as coatings to prevent the icing or fouling of surfaces. Currently, the main weakness of SLIPS is their durability, which is limited by how long the lubricant stays in the pores without evaporating or leaking. Another problem is that there are strict limitations on the chemical properties of the lubricants: they must be immiscible with both water and oil, but they should also penetrate into the pores of the underlying material. The authors' preliminary studies into these issues are encouraging, but additional research is needed before applications will emerge. ■

Michael Nosonovsky is in the Department

of Mechanical Engineering, College of Engineering & Applied Science, University of Wisconsin–Milwaukee, Milwaukee, Wisconsin 53211, USA.

e-mail: nosonovs@uwm.edu

1. Wong, T.-S. *et al.* *Nature* **477**, 443–447 (2011).
2. Barthlott, W. & Neinhuis, C. *Planta* **202**, 1–8 (1997).
3. Cassie, A. B. D. & Baxter, S. *Trans. Faraday Soc.* **40**, 546–551 (1944).
4. Wenzel, R. N. *Ind. Eng. Chem.* **28**, 988–994 (1936).
5. Tuteja, A., Choi, W., Mabry, J. M., McKinley, G. H. & Cohen, R. E. *Proc. Natl Acad. Sci. USA* **105**, 18200–18205 (2008).
6. Bohn, H. F. & Federle, W. *Proc. Natl Acad. Sci. USA* **101**, 14138–14143 (2004).
7. Nosonovsky, M. & Rohatgi, P. K. *Biomimetics in Materials Science: Self-healing, Self-lubricating, and Self-cleaning Materials* (Springer, in the press).

## SYNTHETIC BIOLOGY

# A yeast for all reasons

Scientists have begun to overhaul a yeast's genome to make it more stable, engineerable and evolvable. Remarkably, the part-natural, part-synthetic yeast cells function and reproduce without obvious ill effects. [SEE LETTER P.471](#)

PETER J. ENYEART & ANDREW D. ELLINGTON

The baker's yeast *Saccharomyces cerevisiae* is a model organism, and therefore one of the best-understood biological systems on the planet. Nevertheless, the Byzantine complexity of its inner workings still keeps bioengineers up at night, and continues to provide fodder for experimentation. If scientists could 'refactor' model organisms — that is, recode their genomes to be simpler and more amenable to human understanding and tinkering — then science and biotechnology based on those organisms could proceed at an accelerated pace. On page 471 of this issue, Dymond *et al.*<sup>1</sup> present a major advance towards this end: the construction of a functional, partly synthetic version of the *S. cerevisiae* genome.

Rewriting genomes to meet the specifications of humans has been a stated goal of synthetic biology for some time<sup>2</sup>. But the labour and expense involved in actually making such radical changes to genomes, coupled with uncertainties about the chances of improving on what nature spent billions of years perfecting, have meant that only a few serious tilts at genome re-engineering have been made. Previous noteworthy examples include the refactoring of 12,000 base pairs (about 30%) of a virus genome<sup>3</sup> and the removal of 'amber' stop codons — nucleotide sequences that signal the termination of translation — from the bacterium *Escherichia coli*<sup>4</sup>, a feat that should allow researchers to rewrite portions of the bacterium's genetic code at will. And, of course, the genome of a *Mycoplasma* bacterium has been synthesized *de novo* by

workers at the J. Craig Venter Institute in Rockville, Maryland, and used to infuse a working cell<sup>5</sup>.

Dymond *et al.*<sup>1</sup> have now raised the bar by starting work on eukaryotes (organisms such as fungi, plants and animals), which have much larger and more complex genomes than bacteria. More specifically, the authors have replaced sections of two chromosomes of *S. cerevisiae* — 90,000 bases at the end of chromosome IX, and 30,000 bases at the end of chromosome VI — with synthetic DNA. Their eventual goal is presumably to replace the entire genome of 12 million base pairs with a human-designed sequence.

To make their synthetic DNA, Dymond *et al.* entirely removed 20 regions from the naturally occurring yeast chromosomes. Most of these regions were repetitive sequences (which can cause DNA segments to be deleted or even cause chromosomes to mis-segregate), or sequences that were non-functional or redundant. The authors also recoded all genes longer than 500 bases to contain 'watermarks' — sequences that allow the synthetic DNA to

be easily differentiated from natural sequences using standard laboratory methods, but that do not change the sequences of proteins encoded by genes. As in the previously reported work<sup>4</sup> in *E. coli*, Dymond and colleagues<sup>1</sup> modified amber stop codons in the DNA of *S. cerevisiae* so that they could be recoded in the future, for example to encode unnatural amino acids for insertion into yeast proteins.

Astoundingly, the authors found that yeast cells containing the modified genome suffered no growth defects and displayed minimal differences in gene expression in comparison with the wild-type strain. The entire sequence of the artificially added DNA was faithfully reproduced by living cells, which is either a testament to the robustness of human engineering or a sign that God's fingerprints are fainter than creationists would have you believe.

In addition to the changes mentioned earlier, Dymond and co-workers introduced sequence elements known as loxP sites after every non-essential gene in their synthetic DNA, and at several other positions. In the presence of an enzyme called Cre recombinase, these loxP sites stochastically recombined with each other, either deleting or inverting the intervening sequence of DNA. The authors were thus able to generate a vast library of yeast genomes, containing all manner of random architectures, at will. Such libraries could be screened or evolved to find new yeast strains that are better suited to living in a given environment. Moreover, because yeast is used to produce alcohol, proteins and high-value organic compounds, new strains generated in this way might prove to be useful for industry, in the same way that a simplified *E. coli* strain has proved to be an excellent platform for producing large quantities of proteins<sup>6</sup>.

The obvious extension of Dymond and colleagues' work is to rebuild the entire yeast genome. However, given that the currently completed synthetic sequences represent only about 1% of the whole genome, rebuilding the remainder is a daunting task. One issue is that, even though the aggregated cost of the materials, apparatus and consumables used in DNA synthesis has been steadily decreasing, the construction of entire genomes remains inordinately expensive<sup>7</sup>.

Even more problematic is the cost of labour. A comparison of recent endeavours in genome synthesis and modification (Table 1) reveals

TABLE 1 | LABOUR REQUIRED FOR GENOME SYNTHESIS

Organism (year)	DNA bases synthesized (% of genome)	DNA bases per year of labour*
T7 bacteriophage (2005) <sup>2</sup>	12,000 (30)	1,300
<i>Mycoplasma mycoides</i> (2010) <sup>5</sup>	1,080,000 (100)	15,000
<i>Escherichia coli</i> (2011) <sup>4</sup>	4,600,000 (100) or 28,000 (0.6) <sup>†</sup>	96,000 or 600 <sup>†</sup>
<i>Saccharomyces cerevisiae</i> (2011) <sup>1</sup>	120,000 (1)	2,700

\*Estimated as follows: total bases synthesized/[number of authors × 3], assuming that 3 years is the average time spent by a person on genome-synthesis projects.

<sup>†</sup>Depending on whether the entire genome or only synthetic oligonucleotides are counted.

that DNA synthesis at the scale of the yeast genome will require either armies of scientists — such as the wonderful group of undergraduate students currently working on similar projects<sup>8</sup> with Dymond and co-workers — or new methodologies. The authors' landmark work<sup>1</sup> confirms that automated DNA synthesis and assembly techniques are becoming necessary, and that the total synthesis of genomes is likely to supersede piecemeal approaches to genome modification. Given a little push here and there from technological advances, the age of designer genomes is nigh. ■

Peter J. Enyeart is at the Institute for Cell and Molecular Biology, University of

Texas at Austin, and Andrew D. Ellington is in the Department of Chemistry and Biochemistry, University of Texas at Austin, Austin, Texas 78712, USA.  
e-mails: peter.eneart@mail.utexas.edu; andy.ellington@mail.utexas.edu

1. Dymond, J. S. *et al.* *Nature* **477**, 471–476 (2011).
2. Endy, D. *Nature* **438**, 449–453 (2005).
3. Chan, L. Y., Kosuri, S. & Endy, D. *Mol. Syst. Biol.* **1**, 2005.0018 (2005).
4. Isaacs, F. J. *et al.* *Science* **333**, 348–353 (2011).
5. Gibson, D. G. *et al.* *Science* **329**, 52–56 (2010).
6. Sharma, S. S., Blattner, F. R. & Harcum, S. W. *Metab. Eng.* **9**, 133–141 (2007).
7. Carr, P. A. & Church, G. M. *Nature Biotechnol.* **27**, 1151–1162 (2009).
8. Dymond, J. S. *et al.* *Genetics* **181**, 13–21 (2009).

and, subsequently, to transfer it to a receiving dot through an empty channel, in which the electron 'surfs' on the acoustic wave.

Hermelin *et al.* and McNeil *et al.* demonstrated successful single-electron transfer between the dots by detecting coincident emission and capture at both dots. These were detected with devices that are routinely used for charge detection in quantum dots<sup>3</sup>: sensitive electrometers that are placed closed to the dots. The efficiency of the authors' approach<sup>1,2</sup> was such that it allowed, for example, McNeil *et al.*<sup>2</sup> to reliably transfer single electrons back and forth between the dots over a cumulative distance of about 0.25 millimetres — nearly a macroscopic distance. Hermelin *et al.* went on to show that, after initially loading a dot with two electrons, it is possible to split them apart: one stays in the dot and the other is captured by a receiving dot.

These experiments<sup>1,2</sup> are particularly relevant with a view to using single-electron buses for retrieving and distributing quantum information stored in quantum dots that are embedded in complex networks. It has been shown<sup>3,5</sup> that electronic spin can be manipulated quantum mechanically with ever-increasing fidelity. It is therefore possible to imagine manipulating an information-encoding single spin in one quantum dot, then transporting it to another distant dot in the network. What's more, by using a double quantum dot, one could foresee the creation of an arbitrary two-electron superposition spin state<sup>5</sup> and its transfer between distant quantum dots. This would pave the way for studying quantum entanglement of two electrons in a solid-state environment.

All of these exciting possibilities offered by the set-ups of Hermelin *et al.* and McNeil *et al.* require that single-electron transfers do not degrade quantum information, an aspect that is not addressed in their work. Because new electron-manipulation techniques always come with unexpected dissipation mechanisms, it is not clear whether the electrons can retain their spin state, and so the encoded information, during their travels in the channel. However, recent advances in spin manipulation and control<sup>5,6</sup> call for optimism. We should therefore be confident that the demonstrated single-electron bus will go quantum in the not-so-distant future. ■

Takis Kontos is at the Laboratoire Pierre Aigrain, École Normale Supérieure, 75231 Paris Cedex 05, France.  
e-mail: kontos@lpa.ens.fr

1. Hermelin, S. *et al.* *Nature* **477**, 435–438 (2011).
2. McNeil, R. P. G. *et al.* *Nature* **477**, 439–442 (2011).
3. Hanson, R., Kouwenhoven, L. P., Petta, J. R., Tarucha, S. & Vandersypen, L. M. K. *Rev. Mod. Phys.* **79**, 1217–1265 (2007).
4. Fève, G. *et al.* *Science* **316**, 1169–1172 (2007).
5. Fioletti, S., Bluhm, H., Mahalu, D., Umansky, V. & Yacoby, A. *Nature Phys.* **5**, 903–908 (2009).
6. Bluhm, H. *et al.* *Nature Phys.* **7**, 109–113 (2011).

## QUANTUM PHYSICS

# Single electrons take the bus

Single-electron circuitry is a promising route for quantum information processing. The demonstration of single-electron transfer between two distant quantum dots brings this technology a step closer. [SEE LETTERS P.435 & P.439](#)

TAKIS KONTOS

The realization of electronic machines that exploit the laws of quantum mechanics is a dream for many physicists. Among the different architectures proposed so far for meeting this goal, one very promising option is based on quantum dots: nanometre-sized electron boxes, or conducting islands, that can comprise as little as one electron. As with classical electronic devices, the construction of such a quantum machine requires 'wires' to connect up the elements of the machine's internal electronic circuitry. But in the quantum world, making such wires is not a trivial matter.

Two papers in this issue, one by Hermelin *et al.*<sup>1</sup> (page 435) and the other by McNeil *et al.*<sup>2</sup> (page 439), demonstrate wires, or 'buses', that can carry only a single electron and interconnect two distant quantum dots. These findings provide a building block for the implementation of large-scale networks of quantum dots, which will be necessary to scale-up techniques for local quantum manipulation that are currently performed only at the single-quantum-dot level<sup>3</sup>.

In quantum dots, confinement can be such that the characteristic charging energy of the dot — the energy it takes to add an extra electron to it — exceeds thermal fluctuations at cryogenic temperatures. In such a situation, known as a Coulomb blockade, electrons passing through the quantum dot have to do so one

by one. This fact, combined with the discreteness of the quantum dot's energy spectrum, makes the dots ideal sources of single electrons<sup>4</sup>.

The usual way to extract a single electron from a quantum dot is to raise the last occupied energy level of the dot to well above the characteristic energy (the Fermi level) of the electronic reservoir to which the dot is coupled. This can be done with the help of an electrostatic 'gate' electrode. In this manner, the electron 'sitting' on the last occupied energy level is forced energetically to 'fall off' into the electronic reservoir; conversely, an electron can be absorbed from the electronic reservoir by lowering a previously unoccupied energy level below the Fermi level. Because an electron emitted in such a way rapidly mixes with other electrons in the electronic reservoir, knowledge of that electron's initial electronic state will be deficient, and any quantum information stored in the electron will be lost. This explains why extracting an electron from a dot and capturing it in another one is far from trivial.

To isolate a single electron and implement a single-electron bus, Hermelin *et al.*<sup>1</sup> and McNeil *et al.*<sup>2</sup> took an alternative approach that involves moving a quantum dot rather than acting directly on its energy levels. The basic idea is to distort the electrostatic potential that traps the dot's electron, using an acoustic wave that propagates across the surface of the device hosting the dot. The acoustic wave, which is induced by a microwave pulse, allowed the authors to expel a single electron from the dot



that DNA synthesis at the scale of the yeast genome will require either armies of scientists — such as the wonderful group of undergraduate students currently working on similar projects<sup>8</sup> with Dymond and co-workers — or new methodologies. The authors' landmark work<sup>1</sup> confirms that automated DNA synthesis and assembly techniques are becoming necessary, and that the total synthesis of genomes is likely to supersede piecemeal approaches to genome modification. Given a little push here and there from technological advances, the age of designer genomes is nigh. ■

Peter J. Enyeart is at the Institute for Cell and Molecular Biology, University of

Texas at Austin, and Andrew D. Ellington is in the Department of Chemistry and Biochemistry, University of Texas at Austin, Austin, Texas 78712, USA.  
e-mails: peter.eneart@mail.utexas.edu; andy.ellington@mail.utexas.edu

1. Dymond, J. S. *et al.* *Nature* **477**, 471–476 (2011).
2. Endy, D. *Nature* **438**, 449–453 (2005).
3. Chan, L. Y., Kosuri, S. & Endy, D. *Mol. Syst. Biol.* **1**, 2005.0018 (2005).
4. Isaacs, F. J. *et al.* *Science* **333**, 348–353 (2011).
5. Gibson, D. G. *et al.* *Science* **329**, 52–56 (2010).
6. Sharma, S. S., Blattner, F. R. & Harcum, S. W. *Metab. Eng.* **9**, 133–141 (2007).
7. Carr, P. A. & Church, G. M. *Nature Biotechnol.* **27**, 1151–1162 (2009).
8. Dymond, J. S. *et al.* *Genetics* **181**, 13–21 (2009).

and, subsequently, to transfer it to a receiving dot through an empty channel, in which the electron 'surfs' on the acoustic wave.

Hermelin *et al.* and McNeil *et al.* demonstrated successful single-electron transfer between the dots by detecting coincident emission and capture at both dots. These were detected with devices that are routinely used for charge detection in quantum dots<sup>3</sup>: sensitive electrometers that are placed closed to the dots. The efficiency of the authors' approach<sup>1,2</sup> was such that it allowed, for example, McNeil *et al.*<sup>2</sup> to reliably transfer single electrons back and forth between the dots over a cumulative distance of about 0.25 millimetres — nearly a macroscopic distance. Hermelin *et al.* went on to show that, after initially loading a dot with two electrons, it is possible to split them apart: one stays in the dot and the other is captured by a receiving dot.

These experiments<sup>1,2</sup> are particularly relevant with a view to using single-electron buses for retrieving and distributing quantum information stored in quantum dots that are embedded in complex networks. It has been shown<sup>3,5</sup> that electronic spin can be manipulated quantum mechanically with ever-increasing fidelity. It is therefore possible to imagine manipulating an information-encoding single spin in one quantum dot, then transporting it to another distant dot in the network. What's more, by using a double quantum dot, one could foresee the creation of an arbitrary two-electron superposition spin state<sup>5</sup> and its transfer between distant quantum dots. This would pave the way for studying quantum entanglement of two electrons in a solid-state environment.

All of these exciting possibilities offered by the set-ups of Hermelin *et al.* and McNeil *et al.* require that single-electron transfers do not degrade quantum information, an aspect that is not addressed in their work. Because new electron-manipulation techniques always come with unexpected dissipation mechanisms, it is not clear whether the electrons can retain their spin state, and so the encoded information, during their travels in the channel. However, recent advances in spin manipulation and control<sup>5,6</sup> call for optimism. We should therefore be confident that the demonstrated single-electron bus will go quantum in the not-so-distant future. ■

Takis Kontos is at the Laboratoire Pierre Aigrain, École Normale Supérieure, 75231 Paris Cedex 05, France.  
e-mail: kontos@lpa.ens.fr

1. Hermelin, S. *et al.* *Nature* **477**, 435–438 (2011).
2. McNeil, R. P. G. *et al.* *Nature* **477**, 439–442 (2011).
3. Hanson, R., Kouwenhoven, L. P., Petta, J. R., Tarucha, S. & Vandersypen, L. M. K. *Rev. Mod. Phys.* **79**, 1217–1265 (2007).
4. Fève, G. *et al.* *Science* **316**, 1169–1172 (2007).
5. Fioletti, S., Bluhm, H., Mahalu, D., Umansky, V. & Yacoby, A. *Nature Phys.* **5**, 903–908 (2009).
6. Bluhm, H. *et al.* *Nature Phys.* **7**, 109–113 (2011).

## QUANTUM PHYSICS

# Single electrons take the bus

Single-electron circuitry is a promising route for quantum information processing. The demonstration of single-electron transfer between two distant quantum dots brings this technology a step closer. [SEE LETTERS P.435 & P.439](#)

TAKIS KONTOS

The realization of electronic machines that exploit the laws of quantum mechanics is a dream for many physicists. Among the different architectures proposed so far for meeting this goal, one very promising option is based on quantum dots: nanometre-sized electron boxes, or conducting islands, that can comprise as little as one electron. As with classical electronic devices, the construction of such a quantum machine requires 'wires' to connect up the elements of the machine's internal electronic circuitry. But in the quantum world, making such wires is not a trivial matter.

Two papers in this issue, one by Hermelin *et al.*<sup>1</sup> (page 435) and the other by McNeil *et al.*<sup>2</sup> (page 439), demonstrate wires, or 'buses', that can carry only a single electron and interconnect two distant quantum dots. These findings provide a building block for the implementation of large-scale networks of quantum dots, which will be necessary to scale-up techniques for local quantum manipulation that are currently performed only at the single-quantum-dot level<sup>3</sup>.

In quantum dots, confinement can be such that the characteristic charging energy of the dot — the energy it takes to add an extra electron to it — exceeds thermal fluctuations at cryogenic temperatures. In such a situation, known as a Coulomb blockade, electrons passing through the quantum dot have to do so one

by one. This fact, combined with the discreteness of the quantum dot's energy spectrum, makes the dots ideal sources of single electrons<sup>4</sup>.

The usual way to extract a single electron from a quantum dot is to raise the last occupied energy level of the dot to well above the characteristic energy (the Fermi level) of the electronic reservoir to which the dot is coupled. This can be done with the help of an electrostatic 'gate' electrode. In this manner, the electron 'sitting' on the last occupied energy level is forced energetically to 'fall off' into the electronic reservoir; conversely, an electron can be absorbed from the electronic reservoir by lowering a previously unoccupied energy level below the Fermi level. Because an electron emitted in such a way rapidly mixes with other electrons in the electronic reservoir, knowledge of that electron's initial electronic state will be deficient, and any quantum information stored in the electron will be lost. This explains why extracting an electron from a dot and capturing it in another one is far from trivial.

To isolate a single electron and implement a single-electron bus, Hermelin *et al.*<sup>1</sup> and McNeil *et al.*<sup>2</sup> took an alternative approach that involves moving a quantum dot rather than acting directly on its energy levels. The basic idea is to distort the electrostatic potential that traps the dot's electron, using an acoustic wave that propagates across the surface of the device hosting the dot. The acoustic wave, which is induced by a microwave pulse, allowed the authors to expel a single electron from the dot

## GENOMICS

# Endless variation most beautiful

The genetic basis of traits can be understood by comparing the DNA of varieties of the same species. The genomes of many varieties of a model plant organism have now been sequenced, and the results are revelatory. [SEE ARTICLE P.419](#)

MICHAEL BEVAN

Charles Darwin wrote<sup>1</sup> of the “endless forms most beautiful” of species that have arisen from natural selection. But his words also apply to the genetic variation within species such as the highly adaptable plant *Arabidopsis thaliana* (Fig. 1). The first analyses of the sequences of multiple genomes of *A. thaliana*<sup>2–4</sup>, including one on page 419 of this issue by Gan *et al.*<sup>4</sup>, have now been published. These studies provide a foundation for identifying the factors that shape genome change, and for mapping genome-sequence variation among a wide range of *A. thaliana* varieties that represents the plant's diversity. They should also facilitate the association of phenotypes (the observable characteristics of an organism) with genotypes (inherited genetic information) — most importantly in crop plants.

The genome sequences of most organisms are represented by examples taken from a single individual of each species, the choice of which has often been haphazardly forced on researchers by technological and financial limitations. New sequencing technologies, such as the Illumina methods<sup>5</sup> used in the latest studies<sup>2–4</sup>, have removed the need for such arbitrary choices and provided exciting opportunities to explore sequence diversity within species. There is a huge range of organisms that can be studied, but it can be argued that two classes of genome deserve high priority for diversity studies: human genomes, because of the enduring interest in our origins and diseases; and plant genomes, because of humans' complete dependence on them for food.

*Arabidopsis* has an evanescent and opportunistic life cycle, much to the chagrin of gardeners. The plant colonized extensive regions of Eurasia and North Africa after the most recent ice age, spreading from refuges in the Iberian Peninsula and central Asia<sup>6</sup>. Subsequent European colonization then allowed it to spread worldwide. *Arabidopsis* is a widely used experimental plant because it is compact and easily grown, has a rapid life cycle and self-pollinates. Its compact genetic code was the first plant genome to be sequenced<sup>7</sup>, providing an accurate foundation for the current studies<sup>2–4</sup>.



**Figure 1 | Small but successful.** The unassuming plant *Arabidopsis thaliana* has colonized the world. The genome sequences<sup>2–4</sup> of many varieties of *A. thaliana* should reveal the genetic basis of its adaptive traits.

Preliminary analyses<sup>8</sup> of *Arabidopsis* genomes showed that plants from different geographical locations exhibit many commonly held genetic variations, consistent with the comparatively recent spread of the plant from a few locations and with frequent mixing of populations. The preliminary work also revealed that genome-wide association studies (GWAS) hold exceptional promise for identifying sequence variations that affect a wide range of plant phenotypes, many of which could be useful in agricultural crops.

As they report in *Nature Genetics*, Cao *et al.*<sup>2</sup> have now sequenced the genomes of 80 strains of *Arabidopsis* that represent the genetic diversity of the plant across its extensive geographical range. By sequencing short pieces (or reads) of DNA and mapping them to a reference *Arabidopsis* genome, the authors identified single nucleotide polymorphisms (SNPs) — sequence variations between strains that involve single nucleotides. DNA sections that couldn't be mapped to the reference genome in this way were assembled *de novo* and then checked to see whether they could be anchored to the reference through the alignment of base pairs. This allowed more-extensive sequence variation to be identified.

In a related study published in the

*Proceedings of the National Academy of Sciences*, Schneeberger *et al.*<sup>3</sup> sequenced four varieties of *Arabidopsis* using a ‘sub-assembly’ approach. This involved clustering short reads into groups that correspond to certain regions of a reference genome<sup>7</sup>, assembling the reads into continuous sections (blocks), and then assembling the blocks into larger and larger sections until the whole genome was constructed. Gan *et al.*<sup>4</sup> also used a sub-assembly approach to sequence 18 *Arabidopsis* varieties.

The advantage of sub-assembly approaches is that, as far as possible, different genomes are assembled independently. This changes the focus of comparative genomics: instead of comparing one or many genomes with a single reference, many genomes are compared with each other. Sub-assembly approaches also capture a spectrum of sequence variation broader than changes involving just a few nucleotides, thereby allowing a fundamental re-evaluation of sequence variation within a species. Indeed, this is one goal of the ambitious 1001 Genomes Project<sup>9</sup>, of which the three latest papers<sup>2–4</sup> are part. The project has already sequenced 471 *Arabidopsis* varieties, and has a further 706 in its pipeline.

The new studies<sup>2–4</sup> identified extensive genome-sequence changes between varieties. For example, SNPs and copy-number variants (differences in the number of duplications of one or more sections in a genome) are frequent. Another finding is that a significant proportion of *Arabidopsis* variation involves chemical changes to methylated cytosine bases. Cytosines are often methylated during epigenetic modifications to DNA, which alter gene expression without affecting DNA sequence, and the latest data<sup>2–4</sup> suggest that such epigenetic changes have the potential to cause mutations. Furthermore, large numbers of genes in different *Arabidopsis* varieties contain premature stop codons (short sequences that signal the termination of translation), which would probably adversely affect the functions of proteins encoded by those genes. Interestingly, many of these genes also contain compensatory changes that would be expected to restore protein function. The most dramatic sequence variations were detected mainly in the studies that used sub-assembly approaches<sup>3,4</sup>, indicating that these approaches should be adopted in the future to maximize detection of a wide range of genomic variation in *Arabidopsis* and in crop plants.

The greatest variability within *Arabidopsis* was found in genes involved in defence and responses to the environment<sup>2–4</sup>; the same is true of sequence variation between species and between taxonomic families. Gan *et al.*<sup>4</sup> assessed differences in gene expression between 18 naturally occurring varieties, and found that extensive genetic variation was concentrated within a short section (100 base pairs) that controls the expression of an adjacent gene. This accounted for much

BLICKWINKEL/ALAMY



of the variation in expression between strains. The differences in expression affected other genes, mainly those involved in responses to pathogens and those encoding a family of transcription factors that control flowering.

The broad spectrum of genomic change identified in the three landmark studies<sup>2–4</sup> can be used to associate phenotypes — including ‘quantitative’ phenotypes that underlie complex traits — with sequence variation. With this in mind, Gan *et al.*<sup>4</sup> sequenced the 18 diverse varieties of *Arabidopsis* that have been intercrossed to create a structured population<sup>10</sup> used for mapping complex traits to DNA sequence variation. By contrast, Cao and co-workers’ genomic data<sup>2</sup>, along with other data from the *Arabidopsis* 1001 Genomes Project, can be used to relate phenotypic variation to the underlying genotypic variation observed in GWAS.

Comparative genome studies have already provided many useful results. A pioneering study<sup>8</sup> that examined 107 phenotypes of *Arabidopsis* in 96 diverse, genotyped lines found associations between several adaptive phenotypes and sequence variations. Similar approaches have been used in a study of 517 local varieties of rice to identify genetic variation associated with 14 useful agronomic traits<sup>11</sup>. Another genome-wide study has shown that adaptation of certain strains of *Arabidopsis* to high salt conditions is associated with sequence variation in a gene that encodes a sodium-transporter protein<sup>12</sup>. GWAS in general are also showing exceptional promise for identifying causal sequence variation in complex emergent traits in plants, such as crop yield and quality<sup>13</sup>.

The application of high-throughput DNA sequencing and genome-capture technology will inevitably lead to the large-scale re-sequencing of the genomes of crop species, in much the same way that the tiny, relatively simple *Arabidopsis* genome has been re-sequenced in the three new studies<sup>2–4</sup>. These technologies will revolutionize plant breeding by enabling a wide variety of phenotypic variations to be mined for their associated sequence variations, which can then be used to select breeding lines<sup>13</sup>. This will substantially reduce the time taken to create varieties of crop plants that are adapted to cope with changes in growing conditions or new pathogens, and/or to improve crop yield. ■

**Michael Bevan** is in the Cell and Developmental Biology Department, John Innes Centre, Norwich NR4 7UH, UK. e-mail: michael.bevan@jic.ac.uk

1. Darwin, C. *On the Origin of Species by Means of Natural Selection* (Murray, 1859).
2. Cao, J. *et al.* *Nature Genet.* <http://dx.doi.org/10.1038/ng.911> (2011).
3. Schneeberger, K. *et al.* *Proc. Natl Acad. Sci. USA* **108**, 10249–10254 (2011).
4. Gan, X. *et al.* *Nature* **477**, 419–423 (2011).
5. Bentley, D. R. *et al.* *Nature* **456**, 53–59 (2008).
6. Sharbel, T. F., Haubold, B. & Mitchell-Olds, T.

- Mol. Ecol.* **9**, 2109–2118 (2000).
7. The Arabidopsis Genome Initiative *Nature* **408**, 796–815 (2000).
8. Atwell, S. *et al.* *Nature* **465**, 627–631 (2010).
9. www.1001genomes.org

10. Kover, P. X. *et al.* *PLoS Genet.* **5**, e1000551 (2009).
11. Huang, X. *et al.* *Nature Genet.* **42**, 961–967 (2010).
12. Baxter, I. *et al.* *PLoS Genet.* **5**, e10011193 (2010).
13. Hamblin, M. T., Buckler, E. S. & Jannick, J.-L. *Trends Genet.* **27**, 98–106 (2011).

## VACCINOLOGY

# Precisely tuned antibodies nab HIV

**Newly discovered neutralizing antibodies that target sites on the envelope proteins of HIV-1 provide a window on how some of the most powerful of these antibodies acquire their potency and breadth of activity. SEE LETTER P.466**

PAUL R. CLAPHAM & SHAN LU

The huge variation among HIV-1 viruses presents a formidable challenge for the development of an effective vaccine: a successful vaccine would probably need to elicit the production of broadly acting neutralizing antibodies. The challenge is even more daunting when one considers that HIV-1 has evolved many ways to evade the neutralizing antibodies of infected subjects<sup>1</sup>. Nevertheless, a few HIV-infected individuals (dubbed ‘elite neutralizers’) do develop antibodies that potently nullify diverse HIV-1 strains. The discovery and characterization of these powerful antibodies is gaining momentum — as evidenced by three exciting new studies<sup>2–4</sup>, including one by Walker *et al.*<sup>2</sup> on page 466 of this issue.

Until 2009, it was difficult to isolate broadly neutralizing antibodies against HIV-1, and only a few had been described (Table 1). Such antibodies are generally derived as monoclonal

antibodies, obtained from individual B cells — the immune cells that function as factories for antibody production. Two such antibodies (2F5 and 4E10) target the transmembrane glycoprotein gp41 of HIV-1, which anchors the viral envelope to the underlying virus particle<sup>5,6</sup> (Fig. 1). Two other antibodies (b12 and 2G12) target the outer envelope protein gp120. Of these, b12 blocks the binding site to CD4 (ref. 7), the main receptor for HIV on the surface of immune cells called T cells, whereas 2G12 binds to glycans<sup>6</sup>, sugar components on the HIV-1 envelope. Over the past two years, a succession of studies has identified further monoclonal antibodies that target gp120. Antibodies that bind to newly discovered sites overlapping the CD4 binding site — HJ16 and particularly VRC01 — show greatly improved breadth of action and potency over those already known<sup>8,9</sup>, and the antibodies PG9, PG16 and CH01 to CH04 target a previously unknown quaternary structure on gp120 that

**TABLE 1 | A HISTORY OF HIV-1 NEUTRALIZING ANTIBODIES**

Monoclonal antibody	Year of discovery	Specificity		Glycan involvement	Ref.
		Envelope glycoprotein	Target site		
2F5	1993	gp41	MPER	No	5
4E10	1994	gp41	MPER	No	6
b12	1994	gp120	CD4bs	No	7
2G12	1994	gp120	Glycan structure	Yes	6
PG9	2009	gp120	V2/V3 loops	Yes	10
PG16	2010 2011	gp120	CD4bs	No	9
CH01–04				No	4
PGT141				No	3
VRC01	2010	gp120	CD4bs	No	8
VRC-PG04	2011	gp120	CD4bs	No	8
3BNC60	2011	gp120	CD4bs	No	8
HJ16	2010	gp120	CD4bs	No	8
PGT121	2011	gp120	V3 loop	Yes	2
PGT125					
PGT135					

Each of the listed antibodies originated from a single HIV-1-positive elite neutralizer. MPER, membrane-proximal region of gp41; CD4bs, CD4-binding site.

of the variation in expression between strains. The differences in expression affected other genes, mainly those involved in responses to pathogens and those encoding a family of transcription factors that control flowering.

The broad spectrum of genomic change identified in the three landmark studies<sup>2–4</sup> can be used to associate phenotypes — including ‘quantitative’ phenotypes that underlie complex traits — with sequence variation. With this in mind, Gan *et al.*<sup>4</sup> sequenced the 18 diverse varieties of *Arabidopsis* that have been intercrossed to create a structured population<sup>10</sup> used for mapping complex traits to DNA sequence variation. By contrast, Cao and co-workers’ genomic data<sup>2</sup>, along with other data from the *Arabidopsis* 1001 Genomes Project, can be used to relate phenotypic variation to the underlying genotypic variation observed in GWAS.

Comparative genome studies have already provided many useful results. A pioneering study<sup>8</sup> that examined 107 phenotypes of *Arabidopsis* in 96 diverse, genotyped lines found associations between several adaptive phenotypes and sequence variations. Similar approaches have been used in a study of 517 local varieties of rice to identify genetic variation associated with 14 useful agronomic traits<sup>11</sup>. Another genome-wide study has shown that adaptation of certain strains of *Arabidopsis* to high salt conditions is associated with sequence variation in a gene that encodes a sodium-transporter protein<sup>12</sup>. GWAS in general are also showing exceptional promise for identifying causal sequence variation in complex emergent traits in plants, such as crop yield and quality<sup>13</sup>.

The application of high-throughput DNA sequencing and genome-capture technology will inevitably lead to the large-scale re-sequencing of the genomes of crop species, in much the same way that the tiny, relatively simple *Arabidopsis* genome has been re-sequenced in the three new studies<sup>2–4</sup>. These technologies will revolutionize plant breeding by enabling a wide variety of phenotypic variations to be mined for their associated sequence variations, which can then be used to select breeding lines<sup>13</sup>. This will substantially reduce the time taken to create varieties of crop plants that are adapted to cope with changes in growing conditions or new pathogens, and/or to improve crop yield. ■

**Michael Bevan** is in the Cell and Developmental Biology Department, John Innes Centre, Norwich NR4 7UH, UK. e-mail: michael.bevan@jic.ac.uk

1. Darwin, C. *On the Origin of Species by Means of Natural Selection* (Murray, 1859).
2. Cao, J. *et al.* *Nature Genet.* <http://dx.doi.org/10.1038/ng.911> (2011).
3. Schneeberger, K. *et al.* *Proc. Natl Acad. Sci. USA* **108**, 10249–10254 (2011).
4. Gan, X. *et al.* *Nature* **477**, 419–423 (2011).
5. Bentley, D. R. *et al.* *Nature* **456**, 53–59 (2008).
6. Sharbel, T. F., Haubold, B. & Mitchell-Olds, T.

- Mol. Ecol.* **9**, 2109–2118 (2000).
7. The Arabidopsis Genome Initiative *Nature* **408**, 796–815 (2000).
8. Atwell, S. *et al.* *Nature* **465**, 627–631 (2010).
9. www.1001genomes.org

10. Kover, P. X. *et al.* *PLoS Genet.* **5**, e1000551 (2009).
11. Huang, X. *et al.* *Nature Genet.* **42**, 961–967 (2010).
12. Baxter, I. *et al.* *PLoS Genet.* **5**, e10011193 (2010).
13. Hamblin, M. T., Buckler, E. S. & Jannick, J.-L. *Trends Genet.* **27**, 98–106 (2011).

## VACCINOLOGY

# Precisely tuned antibodies nab HIV

**Newly discovered neutralizing antibodies that target sites on the envelope proteins of HIV-1 provide a window on how some of the most powerful of these antibodies acquire their potency and breadth of activity. SEE LETTER P.466**

PAUL R. CLAPHAM & SHAN LU

**T**he huge variation among HIV-1 viruses presents a formidable challenge for the development of an effective vaccine: a successful vaccine would probably need to elicit the production of broadly acting neutralizing antibodies. The challenge is even more daunting when one considers that HIV-1 has evolved many ways to evade the neutralizing antibodies of infected subjects<sup>1</sup>. Nevertheless, a few HIV-infected individuals (dubbed ‘elite neutralizers’) do develop antibodies that potently nullify diverse HIV-1 strains. The discovery and characterization of these powerful antibodies is gaining momentum — as evidenced by three exciting new studies<sup>2–4</sup>, including one by Walker *et al.*<sup>2</sup> on page 466 of this issue.

Until 2009, it was difficult to isolate broadly neutralizing antibodies against HIV-1, and only a few had been described (Table 1). Such antibodies are generally derived as monoclonal

antibodies, obtained from individual B cells — the immune cells that function as factories for antibody production. Two such antibodies (2F5 and 4E10) target the transmembrane glycoprotein gp41 of HIV-1, which anchors the viral envelope to the underlying virus particle<sup>5,6</sup> (Fig. 1). Two other antibodies (b12 and 2G12) target the outer envelope protein gp120. Of these, b12 blocks the binding site to CD4 (ref. 7), the main receptor for HIV on the surface of immune cells called T cells, whereas 2G12 binds to glycans<sup>6</sup>, sugar components on the HIV-1 envelope. Over the past two years, a succession of studies has identified further monoclonal antibodies that target gp120. Antibodies that bind to newly discovered sites overlapping the CD4 binding site — HJ16 and particularly VRC01 — show greatly improved breadth of action and potency over those already known<sup>8,9</sup>, and the antibodies PG9, PG16 and CH01 to CH04 target a previously unknown quaternary structure on gp120 that

**TABLE 1 | A HISTORY OF HIV-1 NEUTRALIZING ANTIBODIES**

Monoclonal antibody	Year of discovery	Specificity		Glycan involvement	Ref.
		Envelope glycoprotein	Target site		
2F5	1993	gp41	MPER	No	5
4E10	1994	gp41	MPER	No	6
b12	1994	gp120	CD4bs	No	7
2G12	1994	gp120	Glycan structure	Yes	6
PG9	2009	gp120	V2/V3 loops	Yes	10
PG16	2010–2011	gp120	CD4bs	No	11
CH01–04				No	2
PGT141				No	3
VRC01	2010	gp120	CD4bs	No	9
VRC-PG04	2011	gp120	CD4bs	No	4
3BNC60	2011			No	3
HJ16	2010	gp120	CD4bs	No	8
PGT121	2011	gp120	V3 loop	Yes	2
PGT125					
PGT135					

Each of the listed antibodies originated from a single HIV-1-positive elite neutralizer. MPER, membrane-proximal region of gp41; CD4bs, CD4-binding site.



includes binding sites in its V2 and V3 loops<sup>10,11</sup>.

Walker *et al.*<sup>2</sup> describe a diverse set of monoclonal antibodies that bind to a newly identified site at the base of the V3 variable loop. For antibodies from at least one of the HIV-infected subjects, this site includes glycans, which, ironically, usually assemble on the envelope to prevent antibody binding. These new antibodies are tenfold more potent than previously described broadly acting monoclonal antibodies, but maintain activity against diverse HIV-1 viruses even at relatively low doses.

In the two other reports, Scheid *et al.*<sup>3</sup> and Wu *et al.*<sup>4</sup> investigate large numbers of newly identified monoclonal antibodies that they amplified from samples obtained from several elite neutralizers; many of these antibodies have similar specificity and breadth of activity to VRC01 — until now the most potent and broadly acting antibody. Scheid and colleagues use a new approach that increases the recovery of antibody genes from B cells and, notably, they confirm that such antibodies were circulating in the serum of an elite neutralizer. Both reports are a reassuring indication that VRC01-like antibodies are not extremely rare but are repeatedly generated, at least by elite neutralizers.

The antibodies present in adult human blood recognize hundreds of millions of different foreign proteins. Yet the human genome has only a limited number of genes that encode antibodies. Antibody diversity is partly achieved by a process called affinity maturation, which generates mutations in the antibody genes in B cells. If single B cells carrying mutated antibodies on their surface bind efficiently to a target protein antigen, this stimulates the cells to multiply and to produce larger amounts of the antibodies. To date, all of the broad and potent neutralizing antibodies that target the HIV envelope (particularly VRC01-like antibodies) have been shown to contain many mutations and seem to have gone through repeated rounds of mutagenesis and selection of antibody variants.

Wu *et al.*<sup>4</sup> combine in-depth sequencing and crystal-structure analyses to examine the diversity of VRC01-like antibody sequences in HIV-infected patients. Their data provide a fascinating insight into the families of VRC01-like antibody variants in individual subjects: there is an increasing divergence from the original antibody gene, the breadth and potency increasing with the number of mutations or amino-acid substitutions in the antibody sequence. Remarkably, the most broadly acting and potent antibodies from the infected individuals had converged on structures similar to VRC01 that optimized interactions with the site on the envelope that makes the first contact with CD4. The related experiments of Scheid *et al.* support these observations.

Studies over the past few years, culminating in the reports summarized here<sup>2–4</sup>, have shown beyond doubt that HIV-1-positive subjects can elicit potent and broadly active neutralizing

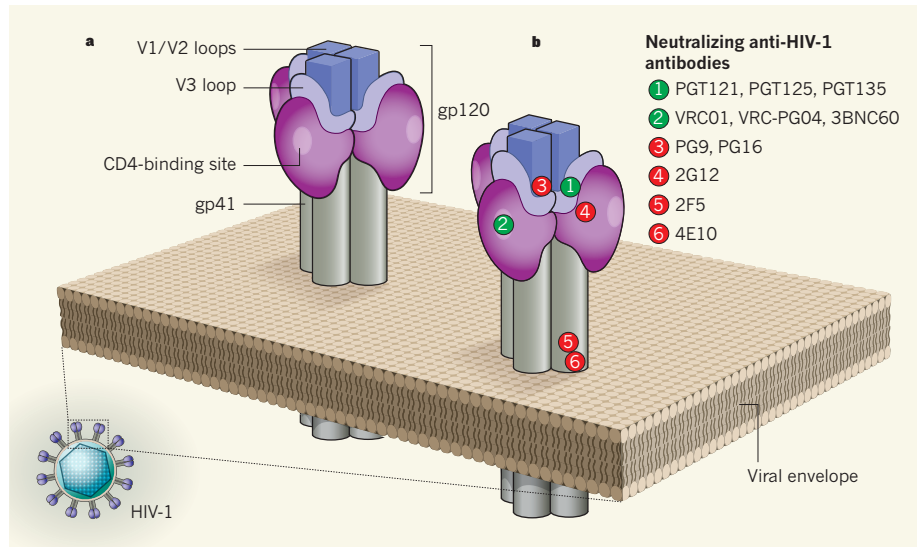


**Figure 1 | Spike-studded HIV-1.** The envelope of HIV-1 carries spikes. **a**, Each spike is made of three molecules of the surface glycoprotein gp120 and three molecules of the transmembrane glycoprotein gp41. Glycoprotein gp120 contains variable V1/V2 and V3 loops, as well as the binding site for CD4. **b**, The binding sites of broadly acting and potent HIV-1-specific neutralizing antibodies are shown as coloured circles. The target sites investigated by the new studies — a site at the base of the V3 loop<sup>2</sup> and the CD4-binding site<sup>3,4</sup> — are marked by green circles.

antibodies and that there are several exposed and relatively invariant sites on the viral envelope that are vulnerable to such antibodies.

These observations have obvious implications for the development of HIV vaccines. However, the optimism they bring needs to be tempered with caution, at least for now. This is because it is unclear how immunogenic molecules that will elicit such antibodies could be designed and administered. The current studies investigate the neutralizing antibodies themselves and the structure of envelope target molecules to which they bind, but do not address the design of immunogens or immunization strategies that could induce similar antibodies.

Nevertheless, the studies highlight two major problems. First, several target molecules of the broad, potent antibodies — including the glycans identified by Walker *et al.*<sup>2</sup> — are notoriously inefficient as immunogens, and it is not clear how the dramatic improvements required to make them effective could be achieved. Second, as discussed, the most potent and broadly acting antibodies have undergone substantial affinity maturation over a long period. It is not known whether the same features can be achieved with limited vaccinations in a much shorter process. Wu and colleagues<sup>4</sup> argue that knowing the structures and sequences of antibodies that are intermediates or precursors to the most effective versions will help in designing and identifying envelope immunogens that can steer developing antibodies towards breadth and potency.

Key questions remain. Why do so few HIV-infected individuals develop broad and potent neutralizing antibodies? And are there further, as yet unknown, envelope targets for neutralizing

antibodies? One final piece of information in Walker and co-workers' report is derived from a concept in traditional vaccinology. Using theoretical modelling, they argue that a combination of antibodies possessing different target specificities will increase the breadth and potency of neutralization, as described in a previous study<sup>12</sup>. Taking into account the increasing number of potential targets for broadly neutralizing antibodies on the HIV-1 envelope, it is possible that a vaccine able to elicit a combination of antibodies targeting different sites will confer breadth, potency and protection, even if individual antibody components don't reach maximal neutralizing concentrations. ■

**Paul R. Clapham** is in the Program in Molecular Medicine and Department of Microbiology and Physiological Systems, and **Shan Lu** is in the Department of Medicine, University of Massachusetts Medical School, Worcester, Massachusetts 01605, USA. S.L. is also at the China-US Vaccine Research Center, Nanjing Medical University. e-mails: paul.clapham@umassmed.edu; shan.lu@umassmed.edu

1. Pantophlet, R. & Burton, D. R. *Annu. Rev. Immunol.* **24**, 739–769 (2006).
2. Walker, L. M. *et al. Nature* **477**, 466–470 (2011).
3. Scheid, J. F. *et al. Science* **333**, 1633–1637 (2011).
4. Wu, X. *et al. Science* **333**, 1593–1602 (2011).
5. Muster, T. *et al. J. Virol.* **67**, 6642–6647 (1993).
6. Buchacher, A. *et al. AIDS Res. Hum. Retroviruses* **10**, 359–369 (1994).
7. Barbas, C. F. III *et al. Proc. Natl Acad. Sci. USA* **91**, 3809–3813 (1994).
8. Corti, D. *et al. PLoS ONE* **5**, e8805 (2010).
9. Wu, X. *et al. Science* **329**, 856–861 (2010).
10. Walker, L. M. *et al. Science* **326**, 285–289 (2009).
11. Bonsignori, M. *et al. J. Virol.* **85**, 9998–10009; <http://dx.doi.org/10.1128/JVI.05045-11> (2011).
12. Scheid, J. F. *et al. Nature* **458**, 636–640 (2009).

# Multiple reference genomes and transcriptomes for *Arabidopsis thaliana*

Xiangchao Gan<sup>1\*</sup>, Oliver Stegle<sup>2\*</sup>, Jonas Behr<sup>3\*</sup>, Joshua G. Steffen<sup>4\*</sup>, Philipp Drewe<sup>3\*</sup>, Katie L. Hildebrand<sup>5</sup>, Rune Lyngsoe<sup>6</sup>, Sebastian J. Schultheiss<sup>3</sup>, Edward J. Osborne<sup>4</sup>, Vipin T. Sreedharan<sup>3</sup>, André Kahles<sup>3</sup>, Regina Bohnert<sup>3</sup>, Géraldine Jean<sup>3</sup>, Paul Derwent<sup>7</sup>, Paul Kersey<sup>7</sup>, Eric J. Belfield<sup>8</sup>, Nicholas P. Harber<sup>8</sup>, Eric Kemen<sup>9</sup>, Christopher Toomajian<sup>5</sup>, Paula X. Kover<sup>10</sup>, Richard M. Clark<sup>4</sup>, Gunnar Ratsch<sup>3</sup> & Richard Mott<sup>1</sup>

Genetic differences between *Arabidopsis thaliana* accessions underlie the plant's extensive phenotypic variation, and until now these have been interpreted largely in the context of the annotated reference accession Col-0. Here we report the sequencing, assembly and annotation of the genomes of 18 natural *A. thaliana* accessions, and their transcriptomes. When assessed on the basis of the reference annotation, one-third of protein-coding genes are predicted to be disrupted in at least one accession. However, re-annotation of each genome revealed that alternative gene models often restore coding potential. Gene expression in seedlings differed for nearly half of expressed genes and was frequently associated with *cis* variants within 5 kilobases, as were intron retention alternative splicing events. Sequence and expression variation is most pronounced in genes that respond to the biotic environment. Our data further promote evolutionary and functional studies in *A. thaliana*, especially the MAGIC genetic reference population descended from these accessions.

Interpreting the consequences of genetic variation has typically relied on a reference sequence, relative to which genes and variants are annotated. However, this may cause bias, because genes may be inactive in the reference but expressed in the population<sup>1</sup>, suggesting that sequencing and re-annotating individual genomes is necessary. Advances in sequencing<sup>2</sup> make this tractable for *Arabidopsis thaliana*<sup>3–5</sup>, whose natural accessions (strains) are typically homozygous. Relative to the 119-megabase (Mb) high-quality reference sequence from Col-0 (ref. 6), diverse accessions harbour a single nucleotide polymorphism (SNP) about every 200 base pairs (bp) (ref. 3), and indel variation is pervasive<sup>3,7,8</sup>. Characterizing this variation is crucial for dissecting the genetic architecture of traits by quantitative trait locus mapping in recombinant inbred lines (see, for example, ref. 9) or genome-wide association in natural accessions<sup>10</sup>.

Here we have sequenced and accurately assembled the single-copy genomes of 18 accessions that, with Col-0, are the parents of more than 700 Multiparent Advanced Generation Inter-Cross (MAGIC) lines<sup>9</sup>, similar to the maize Nested Association Mapping (NAM)<sup>11</sup> population and the murine Collaborative Cross<sup>12</sup>. These accessions comprise a geographically and phenotypically diverse sample across the species<sup>9</sup>. Using the genomes, seedling transcriptomes and computational gene predictions we have characterized the ancestry, polymorphism, gene content and expression profile of the accessions. We show that the functional consequences of polymorphisms are often difficult to interpret in the absence of gene re-annotation and full sequence data. The assembled genomes also contribute to the *A. thaliana* 1001 Genomes Project<sup>3–5,13</sup>.

## Genome sequencing, assembly and variants

We assembled the 18 genomes so that single-copy loci would be contiguous, with less than one assembly error per gene, and therefore

suitable for annotation. Accessions were sequenced with Illumina paired-end reads<sup>2</sup> (Supplementary Table 1), generally with two libraries with 200-bp and 400-bp inserts and reads of 36 and 51 bp, respectively, to between 27-fold and 60-fold coverage. Each genome was assembled by using five cycles of iterative read mapping<sup>14</sup> combined with *de novo* assembly<sup>15</sup> (Supplementary Information sections 2 and 3, and Supplementary Tables 1 and 2). We aligned reads to the final assemblies to detect polymorphic regions<sup>8</sup> lacking read coverage (2.1–3.7 Mb per accession; Supplementary Table 3 and Supplementary Fig. 2). At unique loci, polymorphic regions probably reflect complex polymorphisms<sup>3,8</sup>. The average N50 length (the contig size such that 50% of the entire assembly is contained in contigs equal to or longer than this value) of contiguous read coverage between polymorphic regions was 80.8 kb (Supplementary Table 4).

To report complex alleles consistently, we defined all variants against the multiple alignment consensus of Col-0 and the assembled genomes. For each accession there were 497,668–789,187 single-base differences from Col-0, and about 45,000 ambiguous nucleotides (Supplementary Table 5). The latter may reflect heterozygosity (particularly in Po-0; Supplementary Figs 5–7) or copy-number variants, and they were largely in transposable elements and repeats covering 21.9% of the genome (Supplementary Information section 5.1, and Supplementary Figs 8 and 9). Of 3.07 million SNPs, 45.2% were private to single accessions.

We identified 1.20 million indels, and 104,090 imbalanced substitutions, in which a sequence in Col-0 was replaced by a different sequence (Supplementary Tables 3 and 7). Although 57.5% of indels or imbalanced substitutions were shorter than 6 bp, 1.9% were longer than 100 bp, and overall 14.9 Mb of Col-0 sequence was absent in one or more accessions (Fig. 1a and Supplementary Fig. 8). The assemblies were about 1.6% and about 4.3% shorter than the reference (including

<sup>1</sup>Wellcome Trust Centre for Human Genetics, University of Oxford, Oxford OX3 7BN, UK. <sup>2</sup>Max Planck Institute for Intelligent Systems and Max Planck Institute for Developmental Biology, Spemannstraße 38, 72076 Tübingen, Germany. <sup>3</sup>Friedrich Miescher Laboratory, Max Planck Society, Spemannstraße 39, 72076 Tübingen, Germany. <sup>4</sup>Department of Biology, University of Utah, Salt Lake City, Utah 84112-5330, USA. <sup>5</sup>Department of Plant Pathology, Kansas State University, Manhattan, Kansas 66506-5502, USA. <sup>6</sup>Department of Statistics, University of Oxford, South Parks Road, Oxford OX1 3TG, UK. <sup>7</sup>European Bioinformatics Institute, Wellcome Trust Genome Campus, Hinxton, Cambridge CB10 1SD, UK. <sup>8</sup>Department of Plant Sciences, University of Oxford, South Parks Road, Oxford OX1 3RB, UK. <sup>9</sup>The Sainsbury Laboratory, Norwich NR4 7UH, UK. <sup>10</sup>Department of Biology and Biochemistry, University of Bath, Bath BA2 7AY, UK.

\*These authors contributed equally to this work.



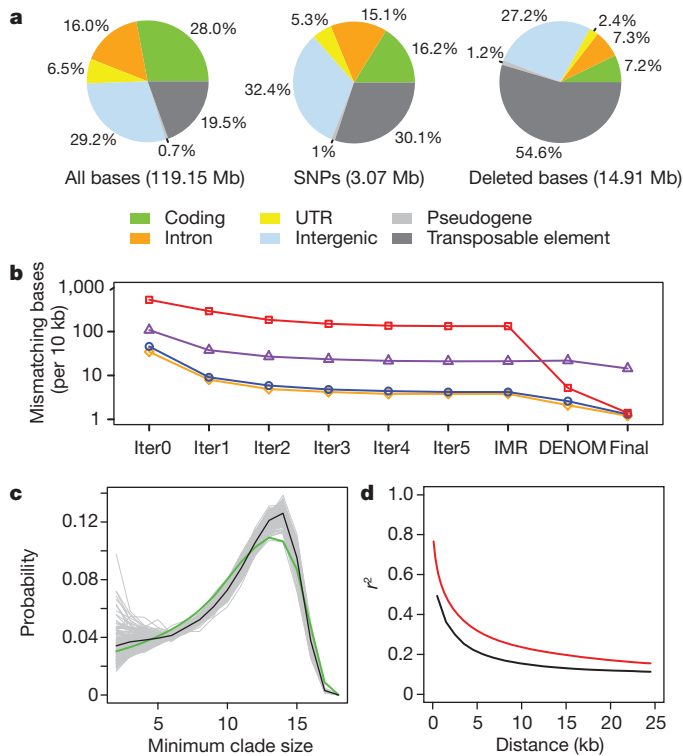


**Figure 1 | Assembly and variation of 18 genomes of *A. thaliana*.**

**a**, Classification of sequence, SNPs and indels based on the Col-0 genome. **b**, Assembly accuracy (y-axis; base substitution errors per 10 kb) measured relative to four validation data sets at each of eight stages in the IMR/DENOM assembly pipeline (x-axis). Bur-0 survey (blue line): 1,442 survey sequences (about 417 bp each) in predominantly genic regions<sup>19</sup>; Bur-0 divergent (red line): 188 sequences (each about 254 bp) highly divergent from Col-0 (ref. 3); Ler-0 nonrepetitive (orange line): a predominantly single-copy 175-kb Ler-0 sequence on chromosome 5; Ler-0 repetitive (purple line): a highly repetitive 339-kb Ler-0 locus on chromosome 3 (ref. 18; Supplementary Information section 4). Iter, iteration. **c**, Genome-wide distribution of the minimum clade size for all pairs of accessions (excluding Po-0). Each pair is represented by a grey line, the mean over all pairs by the black line and the random distribution by the green line. **d**, Decay in linkage disequilibrium with distance (Po-0 excluded). The black line shows  $r^2$  between SNPs; the red line shows phylogenetic  $r^2$  (Supplementary Information section 6).

and excluding polymorphic regions, respectively), probably reflecting limitations in detecting long insertions. Although sequence differences were enriched in transposable-element and intergenic regions, about 17% of bases deleted in one or more accessions were annotated as genic in Col-0 (Fig. 1a and Supplementary Fig. 8). The density of sequence differences is greater than between classical inbred strains of mice<sup>16</sup>, but less than between lines of maize<sup>17</sup>.

Both iterative and *de novo* assembly improved accuracy, with the latter being most effective at divergent loci (Fig. 1b, Supplementary Table 2 and Supplementary Fig. 10). As assessed with about 1.2 Mb of genomic dideoxy data<sup>3,18,19</sup> (Supplementary Information section 4), the substitution error rate was about 1 per 10 kb in single-copy regions, and about tenfold higher in transposable-element-rich regions. Further, RNA-seq reads covered about 100,000 SNPs per accession with 99.72% concordance (Supplementary Table 5), and junction sequences for 66 of 68 (97%) long indels and imbalanced substitutions were confirmed by PCR and dideoxy sequencing (Supplementary Table 8). The substitution error rate for our assemblies was comparable to that reported for four other *A. thaliana* genome assemblies<sup>4</sup>.

## Genome-wide patterns of ancestry

The ancestral relationships of the accessions vary genome-wide. We computed phylogenies<sup>20</sup> across 1.25 million biallelic, non-private SNPs

(Supplementary Information section 6). The ancestry of each pair of accessions within a phylogeny was quantified by using the genome-wide distribution of the minimum clade size of the subphylogeny containing the pair (Fig. 1c). Despite their wide geographical origins, with the exception of Po-0 and Oy-0, all pairs have distributions similar to that of an unstructured sample. The probability of recent co-ancestry is slightly higher than expected for a few pairs of accessions, with extended haplotype sharing at a minority of loci (Supplementary Figs 11–15), perhaps reflecting selective sweeps<sup>7</sup>. Both linkage disequilibrium and correlation between neighbouring phylogenies decrease by 50% within 5 kb (Fig. 1d and Supplementary Fig. 16). Variation among the 18 accessions is similar to a diverse global *A. thaliana* sample<sup>7,8</sup> in nucleotide diversity (Supplementary Figs 11–15), correlation with genomic features (Supplementary Tables 9–12) and structural variants (Supplementary Fig. 17).

## Gene annotation and transcript diversity

A naive projection of the coordinates of the 27,206 nuclear protein-coding genes from Col-0 (TAIR10 annotation) onto the 18 genomes predicted that 93.4% of proteins were changed in at least one accession, with 32% of the total being affected by genic deletions, premature termination codons, or other disruptions (Supplementary Table 13). This large tally of disrupted genes implies that reference annotations cannot be transferred reliably; in fact, re-annotation reveals compensating changes, ensuring that many genes encode apparently functional proteins (Fig. 2a). Thus, in 96.2% of the 8,757 genes affected, the naive annotations were replaced by an alternative gene model in at least one accession (Fig. 2b and Supplementary Fig. 18). We predicted new splice sites in 64% of the 2,572 genes with splice site disruptions (in 696 cases the new sites were within 30 bp of the original ones; see, for example, Fig. 2a). Finally, there was evidence of alternative splicing in 2,106 genes (Supplementary Information sections 10.10–10.13).

For genome annotation and expression analyses (for example Figs 2–4), we generated 78-bp RNA-seq reads from two biological replicates of seedling mRNA (about 9.5 million mapped reads per accession, including Col-0; Supplementary Information section 9, and Supplementary Table 14). We integrated read alignments<sup>21</sup> with sequence-based gene predictions<sup>22</sup> by using mGene.ngs (Supplementary Information sections 9–10.3, and Supplementary Fig. 19). On average, 24,681 coding genes were predicted for each accession. Comparison of Col-0 *de novo* predictions with TAIR10 annotations (Supplementary Table 16) showed that these predictions are more accurate (transcript *F*-score 65.2%) than using the genome sequence (mGene<sup>22</sup>, 59.6%) or RNA-seq alignments alone (Cufflinks<sup>23</sup>, 37.5%; Supplementary Table 17). Finally, we consolidated the *de novo* annotations by incorporating TAIR10 annotations where applicable (Supplementary Information section 10.4, and Supplementary Fig. 20); novel transcript structures for a known TAIR10 gene were only accepted if each newly predicted intron was confirmed by RNA-seq alignments, or if the reference gene model was severely disrupted.

We found, on average, 42,338 transcripts per accession (excluding Col-0), of which 5.5% (2,316) were novel (Table 1 and Supplementary Table 18). In each accession there were, on average, 319 novel genes (or gene fragments) supported by RNA-seq (Table 1); 717 novel genes were found in total, 496 whose sequence was present in Col-0 but not annotated, and 221 absent from the Col-0 genome but present in the *de novo* assemblies of the accessions. We found protein or expressed sequence tag matches for 74.9% of the new genes, primarily from *A. thaliana*, *A. lyrata* or other Brassicaceae species (Supplementary Information sections 10.8 and 10.9).

For accession Can-0, we generated additional independent higher coverage RNA-seq data from seedling, root and floral bud, which we used to confirm 83.3% of re-annotated introns (read alignment over splice junction) and 59.9% of transcripts (confirmation of every intron, or read coverage of 50% of the transcript for single exon

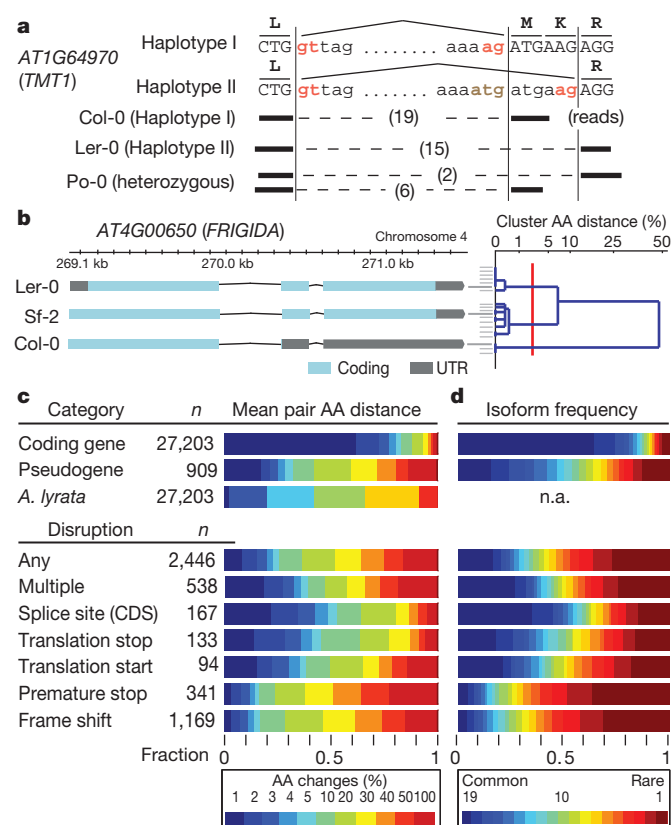


**Figure 2 | Transcript and protein variation.** **a**, Example of a splice site change between two haplotypes for the gene *AT1G64970*. Haplotype I (Col-0) is spliced with an intron 6 bp (two amino acids) shorter than haplotype II (Ler-0); Po-0 (heterozygous) shows allele-specific expression of both. **b**, Re-annotation of the *FRIGIDA* locus showing annotations for accessions Sf-2 (functional), and Col-0 (truncated by a premature stop) and Ler-0 (non-functional) (Supplementary Figs 18 and 42). Right: the 19 accessions are shown clustered on the basis of the AA distance between their *FRIGIDA* amino-acid sequences. Common isoform clusters (at distance 2% or less; red line) are shown, leading to three clusters with three, seven and nine accessions. **c**, Proteome diversity for coding genes, pseudogenes and *A. lyrata* genes (top) and for genes with disruptions (bottom). Reported is the fraction of genes with relative AA distance to other accessions (average over pairs) in the given colour-coded interval (Supplementary Information section 10.7). **d**, Frequency of isoforms of coding genes and pseudogenes (top), and those associated with different disruptions (bottom).

transcripts; Table 1). We also obtained additional RNA-seq data for Col-0 and found similar confirmation rates for the reference annotation (Supplementary Table 19). Moreover, for Can-0 we confirmed 72.1% and 84.2% of novel introns and transcripts. Many novel introns stemmed from splice disruptions that tended to be weakly expressed so RNA-seq evidence was scarcer (Supplementary Fig. 22). Finally, more than 75% of novel alternative splicing events were supported by RNA-seq (Supplementary Information section 10.5).

## Proteome diversity

To understand the effect of genetic diversity on proteins, it is insufficient to study isolated DNA polymorphisms in the context of the reference annotation. We therefore defined the distance between two amino-acid (AA) sequences by the fraction of amino-acid residues that did not align identically in their global alignment. For example, for *FRIGIDA*, between Col-0 and Sf-2, a premature stop codon leads to an AA distance of 49% (Fig. 2b). In 77% of proteins, the mean AA distance between all accessions was less than 3% (Fig. 2c). However, on average, 747 proteins per accession had a distance larger than 50% to any TAIR10 protein, with markedly greater variation for pseudogenes. As expected, variation between *A. thaliana* and its congener *A. lyrata*<sup>24</sup> exceeds that observed among *A. thaliana* accessions (Fig. 2c and

Supplementary Fig. 23). Disruptions to splice sites and translation start and stop codons typically caused less severe effects than premature stop codons or frame shifts (Fig. 2c) when compensating splice sites created alternative in-frame splicing (for example Fig. 2a and Supplementary Fig. 24).

Next, we identified protein isoforms across accessions (Fig. 2b, right; distinct isoforms differ by at least roughly 2% AA distance; Supplementary Information section 10.7). For 80% of protein coding genes the most frequent isoform was very common (frequency at least 15 out of 19), whereas isoforms for pseudogenes usually occurred at lower frequency. Moreover, isoforms for large disruptions were rare (frequency 3 or less) for 37% of affected genes (Fig. 2d). This was most pronounced for premature stops and frameshifts, where purifying selection is expected to be strongest.

As expected<sup>3,7</sup>, disease resistance genes of the coiled-coil and Toll interleukin 1 receptor subfamilies of the Nucleotide-Binding Leucine Rich Repeat (NB-LRR) gene family were predicted to encode the most variable proteins (Fig. 4a and Supplementary Fig. 26). F-box and defensin-like genes implicated in diverse processes including defence<sup>25,26</sup> were also highly variable. In contrast, housekeeping genes showed little variation.

## Variation in seedling gene expression

Median expression heritability of protein-coding genes was 39%, similar to that of novel genes (36%) and pseudogenes (38%), and more than for non-coding RNAs (30%) (Supplementary Fig. 27). In total, 75% (20,550) of protein-coding genes (and 21% of non-coding RNAs and 21% of pseudogenes) were expressed in at least one accession (false discovery rate (FDR) 5%), and 46% (9,360) of expressed protein-coding genes were differentially expressed between at least one pair of accessions<sup>27</sup> (Fig. 3a; FDR 5%, Supplementary Information section 11). Of these, 19% (1,750) had more than tenfold expression changes, and 1.5% (142) more than 100-fold (Fig. 3b). For about 60% of genes, at least five accessions contributed to expression variation (Fig. 4d; Supplementary Information section 11.8).

Although the small sample size (19) precludes genome-wide association scans to identify *trans* expression quantitative trait loci (eQTLs), we identified potential *cis*-acting nucleotide variants, copy-number variants and gene structural variants (for example large indels and gene structure changes) associated with expression for 9% (836) of differentially expressed genes (FDR 5%; Supplementary Information section 12.2; we assessed gene-copy-number variation as in Supplementary Information section 12.4). Much of this variation was highly heritable (Fig. 3a). Consistent with identifying likely causal variants, 85% and 93% of associated SNPs and single-nucleotide indels for *cis*-eQTLs were within 5 and 10 kb of the gene, respectively, and were strikingly concentrated in the 100-bp promoter region and 5' genic sequences (Fig. 3c, d). This was also true for heritable intron retention events, in which most *cis* associations were within the intron or less than 1 kb distant (Supplementary Fig. 32). Our results corroborate the general findings<sup>28–31</sup> of extensive *cis* regulation of gene expression in *A. thaliana*. Neither environmental variation nor population structure markedly affected expression variation (Supplementary Information section 13). Copy-number and structural variants were associated with expression in 3% (240) of differentially expressed genes, including 45% (64 out of 142) of genes with more than 100-fold differences (Fig. 3b), consistent with array studies<sup>29</sup>.

Differential gene expression varied by gene ontology (GO) and gene family (Fig. 4b–d, Supplementary Table 24 and Supplementary Figs 39–41). Seventeen of the 18 GO classifications that were enriched for differential expression ( $P < 10^{-3}$ ) concerned response to the biotic environment, including pathogen defence and the production of glucosinolates<sup>32</sup> to deter herbivores (Supplementary Table 24). These include NB-LRR genes (echoing protein variation), of which 74% were differentially expressed at up to 400-fold change, and for which many accessions typically contributed to differential expression



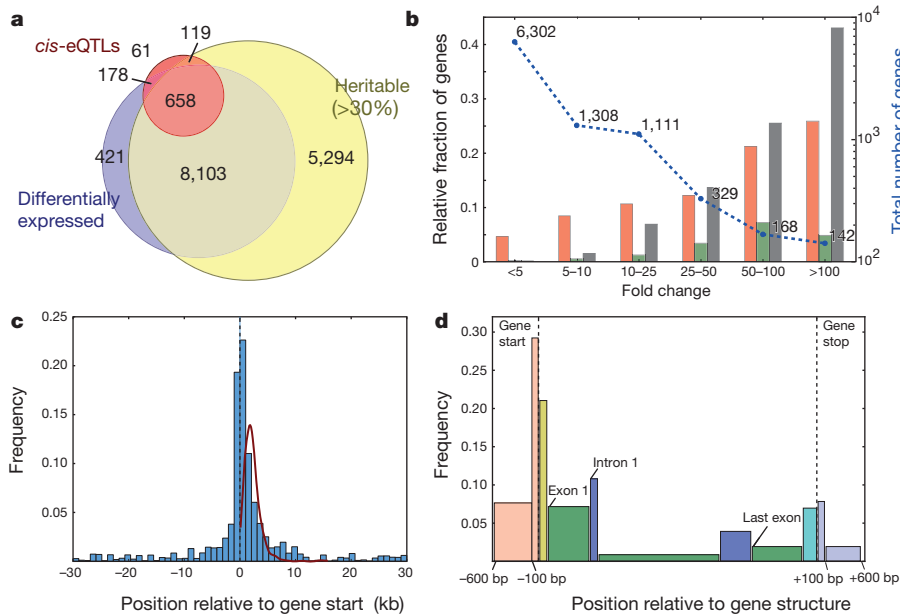


**Figure 3 | Quantitative variation of coding gene expression.** **a**, The overlap between heritable (more than 30%) and differentially expressed (FDR 5%) genes, and genes with a *cis*-eQTL (FDR 5%). **b**, Differentially expressed genes and genes with *cis*-eQTLs (FDR 5%) categorized by fold change. Nucleotide variants (orange bars; 647 *cis*-eQTLs) are SNPs and single-base indels; copy-number variants (green bars; 42 *cis*-eQTLs) are regions with elevated coverage in aligned genomic reads in at least one accession; gene structural variants (black bars; 227 *cis*-eQTLs) are accession-specific deletions, insertions or changes to the gene model. **c**, The spatial distribution of nucleotide-variant eQTLs relative to the start of protein-coding genes (FDR 5%, overlapping genes removed;  $n = 647$ ). The line shows density of gene length. **d**, Frequencies of nucleotide-variant eQTLs in protein-coding genes, classified by component (bar widths are proportional to the components' average physical lengths): red bars, upstream; yellow bars, 5' untranslated region; green bars, coding sequence exons; blue bars, introns; cyan bars, 3' untranslated region; grey bars, downstream.

(Fig. 4b–d). Patterns for housekeeping genes (such as ribosomal proteins, eukaryotic initiation factors or kinesins) were markedly different: although many were differentially expressed, fold changes were generally small, with variation more often being limited to a few accessions (Fig. 4b–d). Differentially expressed genes generally had much higher nucleotide diversity at synonymous sites relative to other expressed genes, a pattern also observed but less extreme at non-synonymous sites (Supplementary Table 25). This suggests that differences in expression level were not due solely to reduced selective constraint.

The type II MADS box transcription factor family<sup>33</sup> showed striking expression polymorphisms (Fig. 4b–d), including for the *FLOWERING LOCUS C* (*FLC*)<sup>34</sup> and *MADS AFFECTING FLOWERING* (*MAF*) genes<sup>35</sup>. *FLC*, a floral inhibitor expressed highly in accessions that require prolonged cold (vernalization) to flower<sup>36</sup>, varied more than 400-fold (Supplementary Fig. 42). F-box and defensin-like genes were exceptional in that expression was restricted in a minority of genes (41% and 12%, respectively; Fig. 4b), perhaps reflecting tissue-specific or environment-specific expression<sup>25,37</sup>.

Our data suggest that high turnover for some F-box families in the *A. thaliana* lineage<sup>7</sup> extends to gene expression as well.

## Conclusion

Our study goes beyond cataloguing polymorphisms<sup>7,17</sup> to provide genome sequences for a moderately sized population sample (see also refs 4, 16). In doing so, we were able to annotate each genome largely independently of the Col-0 reference. We found that disruptive polymorphisms were frequently compensated for, thereby conserving coding potential and highlighting the limitation of inferring consequences of polymorphisms in the absence of complete sequence data.

Our assemblies are accurate and largely complete in single-copy regions, although additional work will be needed to assemble the roughly 20% of the genome comprising repeats and transposable elements. Disentangling copy variation, long insertions and other genomic rearrangements remains a challenge. The methods we developed are of immediate relevance to the broader *A. thaliana* 1001 Genomes Project<sup>5</sup> and to other organisms, and highlight the importance of RNA-seq data for annotation.

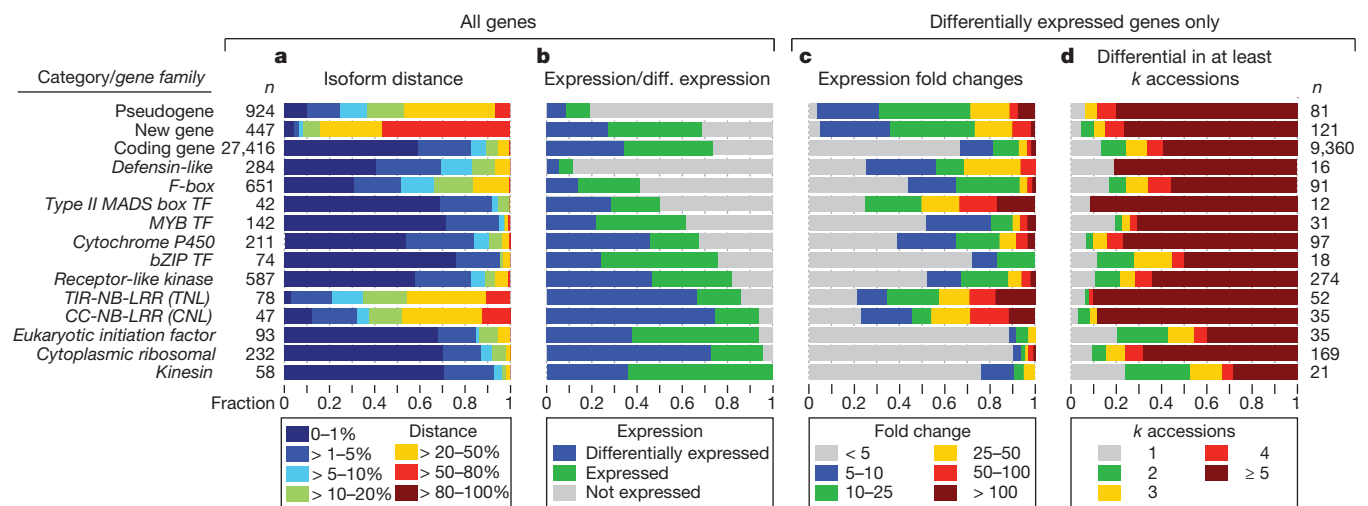


**Figure 4 | Protein diversity and gene expression vary by gene category or family.** The numbers next to each row are gene counts. The gene families were selected from Supplementary Figs 26 and 39–41 to represent the breadth of observed variation. **a**, Distribution of average AA distances to other accessions (compare with Fig. 2c). **b**, Fraction of unexpressed, expressed and differentially

expressed genes (expressed is a superset of differentially expressed). **c**, Distribution of genes categorized by fold change (between lowest and highest across 19 accessions). **d**, Distribution of the numbers of accessions contributing to differential expression. TF, transcription factor; CC, coiled-coil; TIR, Toll interleukin-1 receptor; NB-LRR, nucleotide-binding leucine-rich repeat.

**Table 1 | Summary of gene predictions**

Type	Total		Novel	
	Per accession	RNA-seq confirmed (%)	Per accession	RNA-seq confirmed (%)
Genes	33,197	62.7	319	88.4
Transcripts	42,338	59.9	2,316	84.2
Introns	127,640	83.3	1,345	72.1
Start codons	33,264	n.a.	503	n.a.
Stop codons	33,720	n.a.	528	n.a.
Intron retentions	1,192	78.1	873	76.5
Exon skips	80	80.5	38	76.7

'Total' and 'novel' are average counts over all 19 accessions. 'RNA-seq confirmed' gives the percentage fully confirmed using independent RNA-seq data (three tissues) for Can-0, the most divergent accession.

Finally, despite using only 19 accessions, we fine-mapped *cis*-eQTLs to small genomic regions (less than 10 kb), suggesting that analogous genome-wide scans in the more than 700 derived MAGIC lines could have single-gene mapping resolution for some loci. Our findings indicate that the MAGIC lines, for which population structure is largely mitigated<sup>9</sup>, will be an important and complementary resource to genome-wide association studies in *A. thaliana* populations<sup>10</sup>.

## METHODS SUMMARY

We used the same seed stocks for Col-0 and the 18 accessions Bur-0, Can-0, Ct-1, Edi-0, Hi-0, Kn-0, Ler-0, Mt-0, No-0, Po-0, Oy-0, Rsch-4, Sf-2, Tsu-0, Wil-2, Ws-0, Wu-0 and Zu-0 that originated the MAGIC lines. DNA and RNA sequencing was performed with standard (DNA) or modified (RNA-seq) Illumina protocols. All methods are described fully in Supplementary Methods; software is available from the authors on request.

Received 9 June; accepted 5 August 2011.

Published online 28 August 2011.

- Johanson, U. *et al.* Molecular analysis of *FRIGIDA*, a major determinant of natural variation in *Arabidopsis* flowering time. *Science* **290**, 344–347 (2000).
- Bentley, D. R. *et al.* Accurate whole human genome sequencing using reversible terminator chemistry. *Nature* **456**, 53–59 (2008).
- Ossowski, S. *et al.* Sequencing of natural strains of *Arabidopsis thaliana* with short reads. *Genome Res.* **18**, 2024–2033 (2008).
- Schneeberger, K. *et al.* Reference-guided assembly of four diverse *Arabidopsis thaliana* genomes. *Proc. Natl Acad. Sci. USA* **108**, 10249–10254 (2011).
- Weigel, D. & Mott, R. The 1001 genomes project for *Arabidopsis thaliana*. *Genome Biol.* **10**, 107, doi:10.1186/gb-2009-10-5-107 (2009).
- The Arabidopsis Genome Initiative. Analysis of the genome sequence of the flowering plant *Arabidopsis thaliana*. *Nature* **408**, 796–815 (2000).
- Clark, R. M. *et al.* Common sequence polymorphisms shaping genetic diversity in *Arabidopsis thaliana*. *Science* **317**, 338–342 (2007).
- Zeller, G. *et al.* Detecting polymorphic regions in *Arabidopsis thaliana* with resequencing microarrays. *Genome Res.* **18**, 918–929 (2008).
- Kover, P. X. *et al.* A multiparent advanced generation inter-cross to fine-map quantitative traits in *Arabidopsis thaliana*. *PLoS Genet.* **5**, e1000551 (2009).
- Atwell, S. *et al.* Genome-wide association study of 107 phenotypes in *Arabidopsis thaliana* inbred lines. *Nature* **465**, 627–631 (2010).
- McMullen, M. D. *et al.* Genetic properties of the maize nested association mapping population. *Science* **325**, 737–740 (2009).
- Durrant, C. *et al.* Collaborative cross mice and their power to map host susceptibility to *Aspergillus fumigatus* infection. *Genome Res.* **21**, 1239–1248 (2011).
- Cao, J. *et al.* Whole-genome sequencing of multiple *Arabidopsis thaliana* populations. *Nature Genet.* doi:10.1038/ng.911 (28 August 2011).
- Lunter, G. & Goodson, M. Stampy: a statistical algorithm for sensitive and fast mapping of Illumina sequence reads. *Genome Res.* **21**, 936–939 (2011).
- Li, R. *et al.* De novo assembly of human genomes with massively parallel short read sequencing. *Genome Res.* **20**, 265–272 (2010).
- Keane, T. M. *et al.* Mouse genomic variation and its effect on phenotypes and gene regulation. *Nature* doi:10.1038/nature10413 (in the press).
- Gore, M. A. *et al.* A first-generation haplotype map of maize. *Science* **326**, 1115–1117 (2009).
- Lai, A. G., Denton-Giles, M., Mueller-Roeber, B., Schippers, J. H. & Dijkwel, P. P. Positional information resolves structural variations and uncovers an evolutionarily divergent genetic locus in accessions of *Arabidopsis thaliana*. *Genome Biol. Evol.* advance online publication, doi:10.1093/gbe/evr038 (27 May 2011).
- Nordborg, M. *et al.* The pattern of polymorphism in *Arabidopsis thaliana*. *PLoS Biol.* **3**, e196, doi:10.1371/journal.pbio.0030196 (2005).
- Song, Y. S. & Hein, J. Constructing minimal ancestral recombination graphs. *J. Comput. Biol.* **12**, 147–169 (2005).
- Jean, G., Kahles, A., Sreedharan, V. T., De Bona, F. & Ratsch, G. in *Current Protocols in Bioinformatics* Ch. 11, Unit 11.6 (Wiley, 2010).
- Schweikert, G. *et al.* mGene: accurate SVM-based gene finding with an application to nematode genomes. *Genome Res.* **19**, 2133–2143 (2009).
- Trapnell, C. *et al.* Transcript assembly and quantification by RNA-Seq reveals unannotated transcripts and isoform switching during cell differentiation. *Nature Biotechnol.* **28**, 511–515 (2010).
- Hu, T. T. *et al.* The *Arabidopsis lyrata* genome sequence and the basis of rapid genome size change. *Nature Genet.* **43**, 476–481 (2011).
- Silverstein, K. A., Graham, M. A., Paape, T. D. & VandenBosch, K. A. Genome organization of more than 300 defensin-like genes in *Arabidopsis*. *Plant Physiol.* **138**, 600–610 (2005).
- Gagne, J. M., Downes, B. P., Shiu, S. H., Durski, A. M. & Vierstra, R. D. The F-box subunit of the SCF E3 complex is encoded by a diverse superfamily of genes in *Arabidopsis*. *Proc. Natl Acad. Sci. USA* **99**, 11519–11524 (2002).
- Anders, S. & Huber, W. Differential expression analysis for sequence count data. *Genome Biol.* **11**, R106, doi:10.1186/gb-2010-11-10-r106 (2010).
- Keurentjes, J. J. *et al.* Regulatory network construction in *Arabidopsis* by using genome-wide gene expression quantitative trait loci. *Proc. Natl Acad. Sci. USA* **104**, 1708–1713 (2007).
- Plantegenet, S. *et al.* Comprehensive analysis of *Arabidopsis* expression level polymorphisms with simple inheritance. *Mol. Syst. Biol.* **5**, 242, doi:10.1038/msb.2008.79 (2009).
- West, M. A. *et al.* Global eQTL mapping reveals the complex genetic architecture of transcript-level variation in *Arabidopsis*. *Genetics* **175**, 1441–1450 (2007).
- Zhang, X., Cal, A. J. & Borevitz, J. O. Genetic architecture of regulatory variation in *Arabidopsis thaliana*. *Genome Res.* **21**, 725–733 (2011).
- Howe, G. A. & Jander, G. Plant immunity to insect herbivores. *Annu. Rev. Plant Biol.* **59**, 41–66 (2008).
- Kaufmann, K., Melzer, R. & Theissen, G. MIK-type MADS-domain proteins: structural modularity, protein interactions and network evolution in land plants. *Gene* **347**, 183–198 (2005).
- Sheldom, C. C. *et al.* The LFL MADS box gene: a repressor of flowering in *Arabidopsis* regulated by vernalization and methylation. *Plant Cell* **11**, 445–458 (1999).
- Ratcliffe, O. J., Kumimoto, R. W., Wong, B. J. & Riechmann, J. L. Analysis of the *Arabidopsis* MADS AFFECTING FLOWERING gene family: *MAF2* prevents vernalization by short periods of cold. *Plant Cell* **15**, 1159–1169 (2003).
- Lempe, J. *et al.* Diversity of flowering responses in wild *Arabidopsis thaliana* strains. *PLoS Genet.* **1**, 109–118 (2005).
- Schmid, M. *et al.* A gene expression map of *Arabidopsis thaliana* development. *Nature Genet.* **37**, 501–506 (2005).

**Supplementary Information** is linked to the online version of the paper at [www.nature.com/nature](http://www.nature.com/nature).

**Acknowledgements** We thank C. Jiang and C. Brown for technical help; P. Dijkwel, K. Schneeberger and D. Weigel for providing sequence data in advance of publication; and J. Flint, M. Tsiantis, E. Feil, L. Hurst, A. Wachter and D. Weigel for comments on the manuscript. Funding was provided by the Biotechnology and Biological Sciences Research Council (BBSRC) BB/F022697/1 (to R.M. and P.X.K.), BB/D016029/2 (to P.X.K. and R.M.), BB/F020759/1 (to N.P.H.) and BB/F019793/1 to P.K. (P.E. Birney), by core funding of the Max Planck Society (to G.R.), the German Research Foundation RA1894/1-1 and RA1894/2-1 (to G.R.), Volkswagen Stiftung (to O.S.), the National Science Foundation (NSF) 0929262 (to R.C. and C.T.) and 0820985 (to R.C.), Principal Investigator L. Sieburth), and award no. KUK-11-002-03 (to N.P.H.), made by King Abdullah University of Science and Technology (KAUST). D. Buck, I. Ragoussis and colleagues in the Wellcome Trust Centre for Human Genetics Genomics Core performed most of the genomic sequencing, supported by the Wellcome Trust Core grant 090532/Z/09/Z. Contribution no. 11-388-J from the Kansas Agricultural Experiment Station.

**Author Contributions** R.M., R.C., G.R., P.X.K. and C.T. conceived and led the project. R.M. and X.G. developed and performed genome assembly and analysis. R.C. J.S. and E.O. sequenced the transcriptomes and performed analyses. R.L. performed the ancestral recombination graph analysis. C.T. and K.L.H. performed population genetics analyses. S.J.S., G.J., G.R. and A.K. developed and applied RNA-seq alignment. J.B., G.R., S.J.S., A.K. and R.B. annotated the genomes and analysed their proteins. P.D., G.R. and O.S. performed differential expression analyses. O.S. and P.D. performed genetic association analysis of expression traits. V.T.S. processed data for display in Gbrowse. N.P.H., E.B. and X.G. performed experimental confirmations. P.K. and P.D. constructed the Ensembl version of the variation data. E.K. performed genomic sequencing. R.M., R.C., G.R., P.X.K., C.T., X.G. and O.S. wrote the paper with input from all authors.

**Author Information** DNA sequencing data are deposited in the European Nucleotide Archive ([www.ebi.ac.uk/ena/](http://www.ebi.ac.uk/ena/)) under accession number ERP000565. RNA sequencing data are deposited in the Gene Expression Omnibus ([www.ncbi.nlm.nih.gov/geo/](http://www.ncbi.nlm.nih.gov/geo/)) under accession number GSE30814. Data are also available at <http://mus.well.ox.ac.uk/19genomes>. Genome annotations are viewable at <http://fml.mpg.de/gbrowse-19g>. Reprints and permissions information is available at [www.nature.com/reprints](http://www.nature.com/reprints). The authors declare no competing financial interests. Readers are welcome to comment on the online version of this article at [www.nature.com/nature](http://www.nature.com/nature). This paper is distributed under the terms of the Creative Commons Attribution-Non-Commercial-Share Alike licence, and is freely available to all readers at [www.nature.com/nature](http://www.nature.com/nature). Correspondence and requests for materials should be addressed to R.M. ([richard.mott@well.ox.ac.uk](mailto:richard.mott@well.ox.ac.uk)), G.R. ([Gunnar.Raetsch@tuebingen.mpg.de](mailto:Gunnar.Raetsch@tuebingen.mpg.de)), R.C. ([clark@biology.utah.edu](mailto:clark@biology.utah.edu)), P.X.K. ([p.x.kover@bath.ac.uk](mailto:p.x.kover@bath.ac.uk)) or C.T. ([toomajia@ksu.edu](mailto:toomajia@ksu.edu)).



# CTCF-binding elements mediate control of V(D)J recombination

Chunguang Guo<sup>1\*</sup>, Hye Suk Yoon<sup>1\*</sup>, Andrew Franklin<sup>1\*</sup>, Suvi Jain<sup>1</sup>, Anja Ebert<sup>2</sup>, Hwei-Ling Cheng<sup>1</sup>, Erica Hansen<sup>1</sup>, Orion Despo<sup>1</sup>, Claudia Bossen<sup>3</sup>, Christian Vettermann<sup>4</sup>, Jamie G. Bates<sup>4</sup>, Nicholas Richards<sup>1</sup>, Darienne Myers<sup>1</sup>, Harin Patel<sup>1</sup>, Michael Gallagher<sup>1</sup>, Mark S. Schlissel<sup>4</sup>, Cornelis Murre<sup>3</sup>, Meinrad Busslinger<sup>2</sup>, Cosmas C. Giallourakis<sup>1,5</sup> & Frederick W. Alt<sup>1</sup>

**Immunoglobulin heavy chain (IgH) variable region exons are assembled from V<sub>H</sub>, D and J<sub>H</sub> gene segments in developing B lymphocytes. Within the 2.7-megabase mouse *Igh* locus, V(D)J recombination is regulated to ensure specific and diverse antibody repertoires. Here we report in mice a key *Igh* V(D)J recombination regulatory region, termed intergenic control region 1 (ICR1), which lies between the V<sub>H</sub> and D clusters. Functionally, ICR1 uses CTCF looping/insulator factor-binding elements and, correspondingly, mediates *Igh* loops containing distant enhancers. ICR1 promotes normal B-cell development and balances antibody repertoires by inhibiting transcription and rearrangement of D<sub>H</sub>-proximal V<sub>H</sub> gene segments and promoting rearrangement of distal V<sub>H</sub> segments. ICR1 maintains ordered and lineage-specific V<sub>H</sub>(D)J<sub>H</sub> recombination by suppressing V<sub>H</sub> joining to D segments not joined to J<sub>H</sub> segments, and V<sub>H</sub> to DJ<sub>H</sub> joins in thymocytes, respectively. ICR1 is also required for feedback regulation and allelic exclusion of proximal V<sub>H</sub>-to-DJ<sub>H</sub> recombination. Our studies elucidate a long-sought *Igh* V(D)J recombination control region and indicate a new role for the generally expressed CTCF protein.**

The variable region exons of IgH, Ig light (IgL) and T-cell receptor genes are assembled during B- or T-cell development from variable (V), diversity (D) and joining (J) gene segments<sup>1</sup>. The V(D)J recombination reaction is initiated by RAG endonuclease<sup>1</sup>. RAG cleaves only paired gene segments flanked, respectively, by complementary recombination signals (RSs) referred to as 12RSs and 23RSs, a restriction referred to as the 12/23 rule<sup>1</sup>. The cleaved segments are then fused via classical non-homologous end-joining (C-NHEJ)<sup>2</sup>. The mouse *Igh* locus contains hundreds of V<sub>H</sub> gene segments within a several-megabase (Mb) region, followed downstream by a 100 kilobase (kb) 'intergenic' region separating the most downstream V<sub>H</sub> (generally referred to as V<sub>H81X</sub>, but formally denoted V<sub>H7183.a2.3</sub>; NCBI accession number AJ851868)<sup>3</sup> from D<sub>FL16.1</sub>, the first of 13 clustered D<sub>H</sub> segments. The most downstream D (D<sub>Q52</sub>) lies upstream of 4 J<sub>H</sub> segments (J<sub>H1</sub>–J<sub>H4</sub>)<sup>4</sup>. V<sub>H</sub> and J<sub>H</sub> gene segments are flanked by 23RSs and D segments are flanked on both sides by 12RSs, ensuring that V<sub>H</sub>(D)J<sub>H</sub> assembly involves joining V<sub>H</sub> and J<sub>H</sub> segments to the upstream and downstream sides of a D<sub>H</sub> segment, respectively<sup>4</sup>. The *Igh* constant region (C<sub>H</sub>) exons lie in the 200-kb region downstream of the J<sub>H</sub> segments; RNA splicing fuses productively assembled V<sub>H</sub>(D)J<sub>H</sub> and C<sub>H</sub> exons during *Igh* messenger RNA formation.

*Igh* V(D)J recombination in developing B cells is regulated to be highly ordered and stage specific; thus, D<sub>H</sub>-to-J<sub>H</sub> joining developmentally occurs first on both alleles in pre-progenitor (pro)-B cells followed by appendage of a V<sub>H</sub> to a DJ<sub>H</sub> complex in pro-B cells<sup>4–6</sup>. Direct joining of a V<sub>H</sub> to an un-rearranged D<sub>H</sub> does not occur, even though theoretically permitted by the 12/23 rule<sup>3,7</sup>. The V<sub>H</sub>-to-DJ<sub>H</sub> joining step is also regulated to achieve lineage specificity; thus, although developing T cells generate DJ<sub>H</sub> joins, they do not form complete V<sub>H</sub> (D)J<sub>H</sub> exons<sup>7,8</sup>. At the pro-B stage, V(D)J recombination is regulated in the context of allelic exclusion, with a signal from a productive (that is,  $\mu$  IgH protein-encoding) V<sub>H</sub>(D)J<sub>H</sub> rearrangement

inhibiting V<sub>H</sub>-to-DJ<sub>H</sub> joining on the other *Igh* allele, if it is in the DJ<sub>H</sub> configuration<sup>5</sup>. Expression of the  $\mu$  chain also signals development to the precursor (pre)-B cell stage and *Igl* V(D)J recombination<sup>9</sup>. To generate such signals in pro-B cells,  $\mu$  IgH chains must pair with surrogate IgL chains<sup>10</sup>. Subsequently,  $\mu$  chains must pair with IgL chains in pre-B cells to mediate the pre-B-to-IgM<sup>+</sup> B-cell transition. Lastly, *Igh* V(D)J recombination is regulated to ensure utilization of V<sub>H</sub> segments across the large V<sub>H</sub> locus. However, proximal V<sub>H</sub> segments, particularly V<sub>H81X</sub>, are rearranged more frequently than distal V<sub>H</sub> segments, leading to over-representation in primary V<sub>H</sub>(D)J<sub>H</sub> repertoires<sup>3</sup>. Repertoire normalization for distal V<sub>H</sub> segments in mature B cells relies on cellular selection<sup>3,11</sup>, promoted, in part, by the inability of certain proximal V<sub>H</sub> segments, including V<sub>H81X</sub>, to pair with surrogate IgL chains and IgL chains<sup>12,13</sup>.

V(D)J recombination at all antigen receptor loci is effected by the common V(D)J recombinase comprised of RAG and C-NHEJ components. Regulation of *Igh* V(D)J recombination in the context of order/stage, lineage and allelic exclusion is achieved via modulation of substrate V, D and J accessibility<sup>14,15</sup>. Correlates of such accessibility include transcription of un-rearranged gene segments and certain DNA and histone modifications<sup>4,14–21</sup>. *Igh* locus contraction and looping may also mediate higher-order regulation of V(D)J recombination, for example by bringing distant V<sub>H</sub> segments into proximity with the DJ<sub>H</sub><sup>8,22–24</sup>. Until now, *cis* elements that control order, lineage-specificity, allelic exclusion and/or differential V<sub>H</sub> utilization have been elusive<sup>16,19</sup>. The only known long-range *Igh* regulatory elements are a transcriptional enhancer (termed iE $\mu$ ) in the intron between the J<sub>H</sub> and C<sub>H</sub> segments and a set of long-range enhancers (termed the 3' *Igh* regulatory region) downstream of the C<sub>H</sub> segments<sup>18,25</sup>. The iE $\mu$  transcriptional enhancer is required for efficient *Igh* V(D)J recombination, particularly V<sub>H</sub>-to-DJ<sub>H</sub> joining<sup>26–28</sup>, although the mechanisms by which it influences this process are unknown<sup>18</sup>. Thus far, the 3' *Igh*

<sup>1</sup>Howard Hughes Medical Institute, The Children's Hospital, The Immune Disease Institute; Department of Genetics, Harvard Medical School, 300 Longwood Avenue, Boston, Massachusetts 02115, USA.

<sup>2</sup>Research Institute of Molecular Pathology, Dr. Bohr-Gasse 7, A-1030 Vienna, Austria. <sup>3</sup>Division of Biological Sciences, 0377, University of California, San Diego, La Jolla, California 92093, USA. <sup>4</sup>Department of Molecular & Cell Biology, University of California, Berkeley, California 94720, USA. <sup>5</sup>Gastrointestinal Unit, Massachusetts General Hospital, 55 Fruit Street, Boston, Massachusetts 02114, USA.

\*These authors contributed equally to this work.

regulatory region has not been implicated in V(D)J recombination<sup>25</sup>. As most critical aspects of *Igh* V(D)J recombination are regulated at the V<sub>H</sub>-to-D<sub>H</sub> step<sup>7,8</sup>, relevant regulatory elements may reside in the 100 kb intergenic region separating the V<sub>H</sub> and D<sub>H</sub> segments (see Supplementary Discussion)<sup>7,16,17,19,29,30</sup>.

### Role in normal B-cell development

The region several kilobases upstream of D<sub>FL16.1</sub> harbours chromatin modifications<sup>29,31,32</sup> and two CTCF-binding elements (CBEs)<sup>29,31–33</sup> suggestive of a potential regulatory region (Supplementary Fig. 1). CTCF is an 11-zinc-finger nuclear protein implicated in transcriptional insulation, chromatin boundary formation, transcriptional activation/repression and chromosome looping<sup>34–36</sup>. There are several other potential *cis*-elements closely linked to these CBEs including potential PU.1<sup>31</sup> and YY1-binding sites (using the JASPAR database). We refer to this cluster of factor-binding sites as IGCR1 (Fig. 1). To test for a role in *Igh* V(D)J recombination, we generated an IGCR1-deleted 129SV allele in which the 4.1-kb DNA fragment that contains

both the CBEs and other binding sites was deleted in the mouse germ line (Fig. 1a and Supplementary Fig. 2). To test for specific roles of the CBEs, we generated mice in which both were replaced with scrambled sequences that do not bind CTCF (Supplementary Figs 1 and 3). Mice heterozygous or homozygous for the IGCR1 deletion are referred to, respectively, as IGCR1<sup>+/-</sup> and IGCR1<sup>-/-</sup>, and mice heterozygous or homozygous for the dual CBE mutation are referred to, respectively, as IGCR1/CBE<sup>+/-</sup> or IGCR1/CBE<sup>-/-</sup>. Because generation of mutant alleles involved *loxP* insertion, we generated control lines heterozygous or homozygous for the *loxP* insertion referred to, respectively, as *loxP*<sup>+/-</sup> or *loxP*<sup>+/+</sup> (Fig. 1a). As wild-type, *loxP*<sup>+/-</sup> and *loxP*<sup>+/+</sup> mice gave essentially identical results, we refer to them collectively as 'controls'. As a further control, we deleted an approximately 2-kb DNA fragment downstream of the D<sub>H</sub>-proximal end of IGCR1 and found no obvious phenotype (Supplementary Fig. 10).

IGCR1/CBE<sup>+/-</sup> or IGCR1/CBE<sup>-/-</sup> mice had similar splenic IgM<sup>+</sup> B-cell numbers as controls (Fig. 1b and Supplementary Fig. 5a). However, IGCR1/CBE<sup>+/-</sup> and, more so, IGCR1/CBE<sup>-/-</sup> mice had

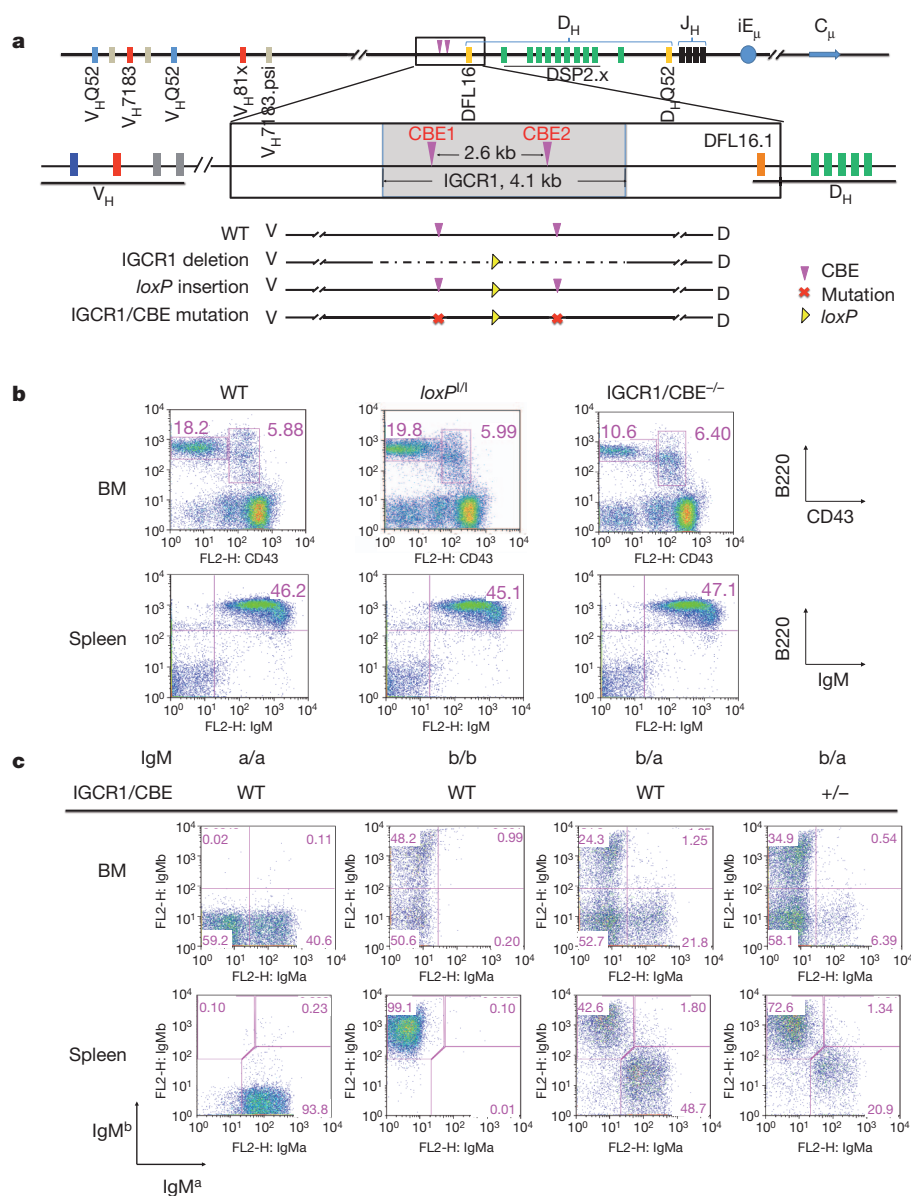


**Figure 1 | Mutation of IGCR1 CBEs impairs B-cell development.** **a**, Murine 129SV *Igh* locus (NCBI accession number: AJ851868) schematic showing the 4.1-kb IGCR1 region in wild type (WT) compared to IGCR1-deleted, *loxP*-inserted, or CBE-mutated configuration. **b**, Flow cytometry analysis of IgM<sup>+</sup> bone marrow (BM) and IgM<sup>+</sup> splenic B-cell populations in wild-type, *loxP*<sup>+/+</sup>

and IGCR1/CBE<sup>-/-</sup> mice. In bone marrow the B220<sup>int</sup>CD43<sup>+</sup> pro-B and B220<sup>int</sup>CD43<sup>-</sup> pre-B cell populations are indicated. **c**, Expression of IgM<sup>a</sup> and IgM<sup>b</sup> allotypic markers in bone marrow and spleen from wild-type IgM<sup>a</sup>/IgM<sup>a</sup> (pure 129SV), wild-type IgM<sup>b</sup>/IgM<sup>b</sup> (pure C57BL/6), wild-type F1 (IgM<sup>a</sup>/IgM<sup>b</sup>) and heterozygous mutant IGCR1/CBE<sup>-/-</sup> IgM<sup>a</sup>/wild-type IgM<sup>b</sup> mice.



a substantial diminution in bone marrow pre-B cell numbers (Fig. 1b and Supplementary Fig. 5b). As the pro-B-to-pre-B transition is signalled by a productive  $V_H(D)J_H$  in pro-B cells, this developmental defect suggests an *Igh* V(D)J recombination defect. As a more sensitive test for the roles of IGCR1 in B-cell development, we bred 129SV IGCR1/CBE<sup>+/-</sup> mice with C57BL/6 wild-type mice to generate F1 mice with a wild-type *Igm*<sup>b</sup> allele and a CBE-mutated *Igm*<sup>a</sup> allele and assayed B cells for surface IgM<sup>a</sup> and IgM<sup>b</sup> expression. Remarkably, whereas normal F1 mice, as expected, have roughly equal numbers of IgM<sup>a</sup>- and IgM<sup>b</sup>-expressing B cells (but not both due to *Igh* allelic exclusion), most IgM<sup>+</sup> bone marrow and splenic B cells in F1 mice carrying the IGCR1 CBE-mutant *Igm*<sup>a</sup> allele express IgM<sup>b</sup> (Fig. 1c). Thus, mutation of the IGCR1 CBEs renders an *Igh* allele ineffective in supporting B-cell development when competing against a wild-type *Igh* allele. We found identical B-cell developmental defects in IGCR1<sup>+/-</sup> and IGCR1<sup>-/-</sup> mice (Supplementary Figs 4b, c and 5c, d).

### Mediation of diverse *Igh* repertoires

We used a polymerase chain reaction (PCR) approach (Supplementary Fig. 6a) to assay for DJ<sub>H</sub> and V<sub>H</sub>(D)J<sub>H</sub> rearrangements in purified control, IGCR1/CBE<sup>+/-</sup>, IGCR1/CBE<sup>-/-</sup>, IGCR1<sup>+/-</sup> and IGCR1<sup>-/-</sup> bone marrow pro-B and pre-B cells, and in splenic B cells. We assayed for rearrangements of the two most D<sub>H</sub>-proximal V<sub>H</sub> families (V<sub>H</sub>7183 and V<sub>H</sub>Q52) and the most distal V<sub>H</sub> family (V<sub>H</sub>J558). *Igl* Vκ-to-Jκ joins were assayed as a stage-specific control and the mouse *Dlg5* gene as a loading control. Levels of DJ<sub>H</sub> and VκJκ rearrangements did not vary markedly among different populations or genotypes; thus, V(D)J recombination in general was not affected by the mutations (Fig. 2a and Supplementary Fig. 6). However, relative levels of proximal V<sub>H</sub>7183DJ<sub>H</sub> rearrangements were markedly increased and those of distal V<sub>H</sub>J558DJ<sub>H</sub> rearrangements markedly reduced in IGCR1/CBE<sup>-/-</sup> and IGCR1<sup>-/-</sup> pro-B cells, with both being intermediate in IGCR1/CBE<sup>+/-</sup> and IGCR1<sup>+/-</sup> pro-B cells (Fig. 2a and Supplementary Fig. 6).

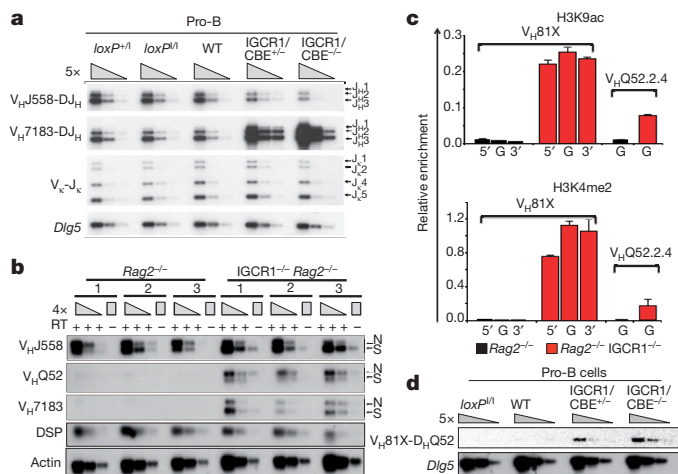


**Figure 2 | IGCR1 mutations alter V<sub>H</sub> usage, germline transcription and rearrangement order.** **a**, PCR analyses of indicated V<sub>H</sub> family rearrangements in pro-B cells from indicated mice compared to a *Dlg5* loading control. Results are typical of four experiments. Bands corresponding to rearrangements to various J<sub>H</sub> segments are indicated on right. **b**, RT-PCR analysis of indicated germline V<sub>H</sub> transcripts in three independent wild-type and IGCR1<sup>-/-</sup> A-MuLV-virus-transformed *Rag2*<sup>-/-</sup> pro-B-cell lines. N, nonspliced sense/antisense; S, spliced sense. **c**, ChIP-qPCR analyses of H3K4me2 and H3K9ac histone modifications at indicated V<sub>H</sub> segments in 129SV *Rag2*<sup>-/-</sup> (black) and *Rag2*<sup>-/-</sup> IGCR1<sup>-/-</sup> (red) A-MuLV-transformed pro-B lines. The 5' region (5'), gene body (G) and 3' region (3') of V<sub>H</sub>81X and gene body (G) of V<sub>H</sub>Q52.2.4 were analysed. Average values and standard deviations of three experiments with one line shown are representative of results from both. **d**, Semi-quantitative PCR analyses of direct V<sub>H</sub>-to-D rearrangements in sorted pro-B cells from indicated mice. The PCR assays used for panels **a**, **b** and **d** are diagrammed in Supplementary Figs 6a, 7a and 8a.

Within the two proximal V<sub>H</sub> families, V<sub>H</sub> usage was even more skewed towards the most D-proximal members in IGCR1<sup>-/-</sup> pro-B cells (Supplementary Fig. 6c). Together, these findings are consistent with IGCR1 mutations resulting in *cis*-acting increases and *cis*-acting decreases, respectively, in proximal and distal V<sub>H</sub> rearrangement. Given that the proximal V<sub>H</sub> segments contribute to a substantial fraction of V<sub>H</sub>(D)J<sub>H</sub> rearrangements (about 40%) in normal pro-B cells<sup>3,11</sup>, increased V<sub>H</sub>7183 joins in IGCR1/CBE<sup>+/-</sup> and IGCR1<sup>+/-</sup> pro-B cells indicates that the absolute level of V<sub>H</sub>-to-DJ<sub>H</sub> rearrangements on mutant alleles, although even more biased towards proximal V<sub>H</sub> segments than normal, is not decreased. In the various IGCR1 mutant pre-B cells and splenic IgM<sup>+</sup> B cells repertoire bias remained; although the extent was progressively moderated (Supplementary Fig. 6), probably due to cellular selection for V<sub>H</sub> repertoire normalization.

### Regulation of germline V<sub>H</sub> transcription

To measure germline V<sub>H</sub> transcripts, we generated *Rag2*-deficient Abelson murine leukaemia virus (A-MuLV)-transformed wild-type, IGCR1<sup>+/-</sup> and IGCR1<sup>-/-</sup> pro-B lines. *Rag2*-deficient lines have unrearranged *Igh* alleles; thus, any detected V<sub>H</sub> transcripts are germline. RNA was assayed via reverse transcriptase PCR (RT-PCR) for V<sub>H</sub> expression, using one primer from the V<sub>H</sub> leader sequence and another from downstream of the RS (Supplementary Fig. 7a). On the basis of size, the PCR assay detects both unspliced germline V<sub>H</sub> transcripts (sense or antisense) and slightly smaller, spliced sense germline V<sub>H</sub> transcripts (Fig. 2b). *Rag2*<sup>-/-</sup> pro-B lines had robust D<sub>H</sub> transcripts and spliced and un-spliced V<sub>H</sub>J558 transcripts, but lacked readily detectable V<sub>H</sub>Q52 or V<sub>H</sub>7183 transcripts (Fig. 2b). However, *Rag2*<sup>-/-</sup> IGCR1<sup>+/-</sup> and, more so, *Rag2*<sup>-/-</sup> IGCR1<sup>-/-</sup> pro-B lines showed marked upregulation of spliced and unspliced V<sub>H</sub>Q52 and V<sub>H</sub>7183 transcripts with normal levels of V<sub>H</sub>J558 and D<sub>H</sub> transcripts (Fig. 2b and Supplementary Fig. 7d). We even detected by northern blotting a ~3.5-kb V<sub>H</sub>81X-hybridizing transcript in RNA from *Rag2*<sup>-/-</sup> IGCR1<sup>-/-</sup> lines, but not in wild-type *Rag2*<sup>-/-</sup> lines (Supplementary Fig. 7f). Primary *Rag2*<sup>-/-</sup> IGCR1<sup>-/-</sup> pro-B cells also strongly upregulated germline V<sub>H</sub>7183 transcripts (Supplementary Fig. 7e). Lastly, chromatin immunoprecipitation-sequencing (ChIP-seq) and chromatin immunoprecipitation-quantitative PCR (ChIP-qPCR) analyses revealed that deletion of IGCR1 led to a marked increase in active histone marks over V<sub>H</sub>81X (V<sub>H</sub>7183.a2.3) and the adjacent V<sub>H</sub>Q52.a2.4 germline gene segments (Fig. 2c and Supplementary Fig. 7b, c). Thus, IGCR1 suppresses activation of germline V<sub>H</sub> segments over distances of at least 100 kb.

### Role in order and lineage specificity

We assayed for V<sub>H</sub>81X-to-germline-DQ52 joins via PCR with a forward V<sub>H</sub>81X-specific primer and a reverse primer from sequences between DQ52 and J<sub>H</sub>1 (Supplementary Fig. 8). Whereas we did not detect direct V<sub>H</sub>81X-to-DQ52 joins in control pro-B cells, we readily detected them in IGCR1/CBE<sup>+/-</sup>, IGCR1/CBE<sup>-/-</sup>, IGCR1<sup>+/-</sup> and IGCR1<sup>-/-</sup> pro-B cells (Fig. 2d and Supplementary Fig. 8). Sequences of 133 independent direct V<sub>H</sub>7183DQ52 joins revealed that 120 involved V<sub>H</sub>81X, 12 involved the downstream pseudo-V<sub>H</sub>7183, and one involved the next V<sub>H</sub>7183 upstream of V<sub>H</sub>81X (Supplementary Table 2). Therefore, integrity of the IGCR1 CBEs is required for ordered *Igh* V(D)J recombination in pro-B cells, at least for proximal V<sub>H</sub> segments.

To examine potential IGCR1 roles in lineage-specific *Igh* V(D)J recombination, we assayed for D-to-J<sub>H</sub>, V<sub>H</sub>-to-DJ<sub>H</sub> and Vκ-to-Jκ rearrangements in DNA from CD4<sup>+</sup>CD8<sup>+</sup> (double-positive) thymocytes from control and IGCR1/CBE<sup>+/-</sup>, IGCR1/CBE<sup>-/-</sup>, IGCR1<sup>+/-</sup> and IGCR1<sup>-/-</sup> mice (Fig. 3a and Supplementary Fig. 9). We detected DQ52J<sub>H</sub> rearrangements in all mice (Fig. 3a and Supplementary Fig. 9). However, whereas there were no V<sub>H</sub>(D)J<sub>H</sub> rearrangements in controls, we readily detected V<sub>H</sub>(D)J<sub>H</sub> rearrangements of proximal V<sub>H</sub>7183 and V<sub>H</sub>Q52 segments, but not distal V<sub>H</sub>J558 segments, in mutant double-positive thymocytes (Fig. 3a and Supplementary Fig. 9). Lack of VκJκ

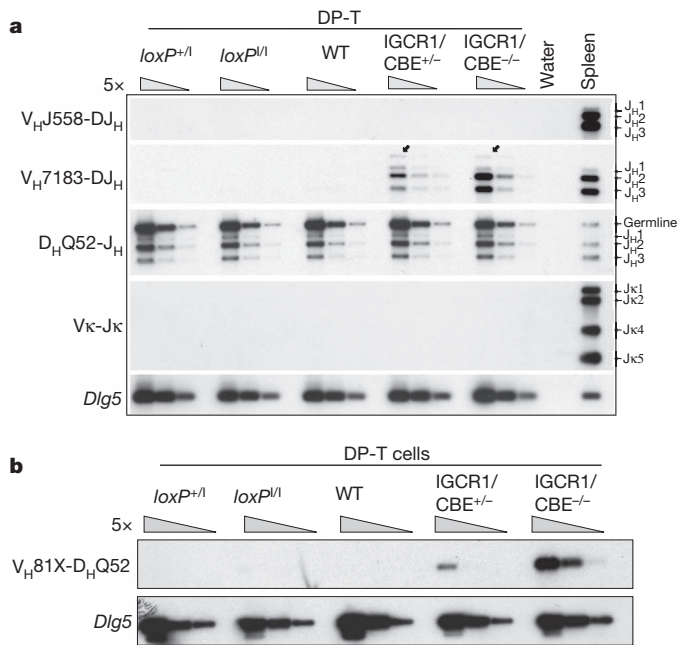


**Figure 3 | IGCR1/CBE mutations lead to  $V_H(D)J_H$  and  $V_HD$  rearrangements in thymocytes.** **a**, PCR analyses of  $V_H$  family rearrangements in sorted double-positive thymocytes (DP-T) and total splenic B cells from indicated mice with *Dlg5* as a loading control. Bands corresponding to rearrangements to various  $J_H$  segments are indicated on right. *Igk* rearrangement ( $V_kJ_k$ ) served as a control for B-cell contamination. **b**, Semi-quantitative PCR analyses of direct  $V_H$ -to- $D$  rearrangements in sorted double-positive T cells (DP-T cells) from indicated mice. Assays are diagrammed in Supplementary Figs 6a and 8a.

rearrangements confirmed absence of B-cell contamination. Cloning and sequencing of  $V_{H7183}$ - and  $V_{H52}$ -to- $DJ_H$  rearrangements from  $IGCR1^{-/-}$  double-positive thymocytes revealed predominant utilization of the most proximal  $V_H$  segments ( $V_{H81X}$  and  $V_{H52.a2.4}$ ; Supplementary Tables 3 and 4). We also assayed for direct  $V_{H81X}$ -to-germline  $D_{Q52}$  joins in double-positive thymocytes (Fig. 3b and Supplementary Fig. 8). As expected, controls lacked detectable direct  $V_H$ -to- $D$  joins; but such joins were readily apparent in mutant thymocytes (Fig. 3b and Supplementary Fig. 8). Nucleotide sequencing of 32  $V_HD$  joins revealed 29 used  $V_{H81X}$  and the rest used the downstream pseudo- $V_{H7183}$  (Supplementary Table 2). Thus,  $IGCR1$  CBEs are required for lineage-specific *Igh*  $V_H$ -to- $DJ_H$  recombination.

### Role in proximal $V_H$ feedback regulation

Surface staining of splenic B cells heterozygous for the  $IGCR1$ -deleted *Igm<sup>a</sup>* allele and a wild-type *Igm<sup>b</sup>* allele did not reveal allelic inclusion (Supplementary Fig. 4c). Likewise, no *Igm<sup>a</sup>/Igm<sup>b</sup>* double expressers were found in nearly 900 individual  $IGCR1^{+/-}$  F1 splenic B cells by

cytoplasmic staining (Supplementary Fig. 11a). Hybridoma analyses showed that about 60% of wild-type B cells had a productive  $V_H(D)J_H$  on one allele and a  $DJ_H$  on the other (that is,  $V_H(D)J_H^+/DJ_H^-$  configuration) and about 40% had  $V_H(D)J_H$  rearrangements on both alleles (that is,  $V_H(D)J_H^+/V_H(D)J_H^-$  configuration) (Fig. 4a). This 60/40 ratio reflects feedback regulation of  $V_H$ -to- $DJ_H$  joining from productive rearrangements<sup>5,6</sup>. In  $IGCR1^{+/-}$  B cells, this ratio inverted to 30/70, demonstrating that heterozygous  $IGCR1$  deletion markedly increases B cells with  $V_H(D)J_H$  joins on both alleles, despite allelic exclusion at the protein level. Analyses of 39  $V_H(D)J_H/V_H(D)J_H$   $IGCR1^{+/-}$  B-cell hybridomas revealed that most had a  $V_H(D)J_H^+$  that used a distal  $V_H$  and a  $V_H(D)J_H^-$  that used  $V_{H81X}$  or a nearby proximal  $V_H$  (Supplementary Table 6). The skewed  $V_H(D)J_H^+/V_H(D)J_H^-$  ratio in  $IGCR1^{+/-}$  B cells can be explained by frequent early formation of  $V_{H81X}DJ_H$  rearrangements on the mutant allele. Thus,  $V_{H81X}DJ_H^+$  rearrangements would exclude rearrangement of the wild-type allele but would be lost developmentally; leading to most peripheral B cells deriving from progenitors that formed productive  $V_H(D)J_H$  rearrangements on the wild-type allele subsequent to  $V_{H81X}(D)J_H^-$  rearrangements on the mutant allele (Supplementary Fig. 11d).

The extremely high representation of proximal  $V_H$  segments (for example,  $V_{H81X}$ ) rearranged on the  $IGCR1$ -deleted allele might mask allelic inclusion because productive  $V_{H81X}$  rearrangements are selected against cellularly<sup>10,12,13</sup>. Therefore, to examine further potential effects of  $IGCR1$ -deletion on allelic exclusion, we assayed the  $V_H(D)J_H^+/DJ_H^-$  versus  $V_H(D)J_H^+/V_H(D)J_H^-$  ratio of  $IGCR1^{-/-}$  hybridomas. Because both *Igh* alleles would be similarly biased for proximal  $V_H$  rearrangements in  $IGCR1^{-/-}$  B cells, one still would expect the 60/40 ratio if  $V_H$ -to- $DJ_H$  recombination was feedback regulated (Supplementary Fig. 11e). However, we found an inverted ratio of 20/80 in  $IGCR1^{-/-}$  hybridomas (Fig. 4a), strongly suggesting that  $IGCR1$ -deleted alleles escape feedback regulation, at least for proximal  $V_H$  segments (Supplementary Fig. 11e). Because of the ambiguities of cellular selection against  $V_{H81X}$  and the lack of allotypically marked  $IGCR1$ -deleted alleles, we tested for escape from feedback inhibition by assaying for endogenous rearrangements in peripheral B cells from mice with a productive  $V_H(D)J_H$  knock-in *Igh* allele (VB1-8 knock-in) that was  $IGCR1^+$  and a second allele that was  $IGCR1^+$  or  $IGCR1^-$ . Notably,  $IGCR1^{+/-}$  VB1-8 knock-in B cells had a more than 20-fold increased level of  $V_{H7183}$  rearrangements compared to  $IGCR1^{+/+}$  VB1-8 knock-in B cells, but little if any change in the very low level rearrangement of distal  $V_H$  segments (Fig. 4b). Moreover, most rearrangements in  $IGCR1^{+/-}$  VB1-8 knock-in B cells were non-productive  $V_{H81X}$  rearrangements (Supplementary Fig. 11f), consistent with a lack of substantial allelic inclusion at the protein level in  $IGCR1^{+/-}$  F1 splenic B cells resulting from selection against  $V_{H81X}$  expression (Supplementary Figs 4c and 11a). We conclude that  $IGCR1$  is required to allow feedback regulation of the most proximal  $V_H$  segments.

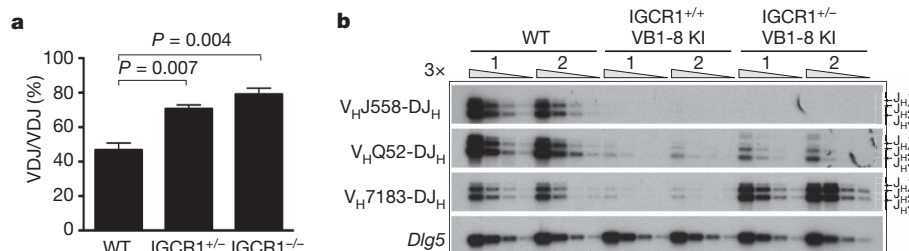


**Figure 4 |  $IGCR1$  is required to allow feedback regulation of proximal  $V_H$ -to- $DJ_H$  recombination.** **a**, Mean percentage of splenic B cells with  $V_H(D)J_H$  rearrangements on both *Igh* alleles as determined by analyses of hybridomas from three independent sets of wild-type,  $IGCR1^{+/-}$  and  $IGCR1^{-/-}$  mice (Supplementary Table 5). Error bars represent standard deviation. *P* values

were calculated by Student's *t*-test. **b**, *Igh*  $V_H(D)J_H$  rearrangements in splenic B cells from two independent wild-type and VB1-8 knock-in (KI) mice carrying either a wild-type ( $IGCR1^{+/+}$  VB1-8 KI) or an  $IGCR1$ -deleted ( $IGCR1^{+/-}$  VB1-8 KI) second allele. Bands corresponding to rearrangements to various  $J_H$  segments are indicated on right. *Dlg5* is the loading control.



## IGCR1 mediates chromosomal *Igh* loops

We considered that IGCR1 might mediate *Igh* loops that would include iE $\mu$  and thereby modulate V(D)J recombination. The next CBEs downstream of IGCR1 are a set of 10, about 5 kb downstream of the 3' *Igh* regulatory region (3' *Igh* CBEs). To test for interactions between the IGCR1 and 3' *Igh* CBEs, we performed quantitative chromosome conformation capture (3C) assays on 129SV *Rag2*<sup>-/-</sup>IGCR1<sup>+/+</sup> and *Rag2*<sup>-/-</sup>IGCR1<sup>-/-</sup> A-MuLV-transformed pro-B lines. These analyses revealed interaction between the IGCR1 and 3' *Igh* CBE locales in *Rag2*<sup>-/-</sup>IGCR1<sup>+/+</sup> pro-B lines (Fig. 5a and Supplementary Fig. 12a), as found in another study<sup>37</sup>. We also found this interaction in double-positive thymocytes (Supplementary Fig. 13). Notably, this interaction was eliminated in *Rag2*<sup>-/-</sup>IGCR1<sup>-/-</sup> pro-B lines (Fig. 5a and Supplementary Fig. 12a). We also found interactions between the iE $\mu$  locale and the IGCR1 and 3' *Igh* CBE locales in

*Rag2*<sup>-/-</sup>IGCR1<sup>+/+</sup> A-MuLV-transformed pro-B cells that were diminished in *Rag2*<sup>-/-</sup>IGCR1<sup>-/-</sup> pro-B lines (Fig. 5b and Supplementary Fig. 12b). Lastly, we found strong interactions between the iE $\mu$  and 3' *Igh* regulatory region, as reported for mature B cells<sup>38</sup>, but these were not diminished by IGCR1 deletion (Fig. 5b). These studies demonstrate that IGCR1 mediates formation of 300-kb iE $\mu$ -containing *Igh* loops to the 3' *Igh* CBE locale in pro-B lines, with iE $\mu$  also being directly juxtaposed to the IGCR1 locale in an IGCR1-dependent manner, probably within the larger loop. As iE $\mu$  lacks CBEs, its interactions with the IGCR1 locale are probably mediated, at least in part, by factors other than CTCF.

## Discussion

IGCR1, through its CBEs, mediates ordered and lineage-specific V<sub>H</sub>-to-DJ<sub>H</sub> recombination and balances proximal versus distal V<sub>H</sub>

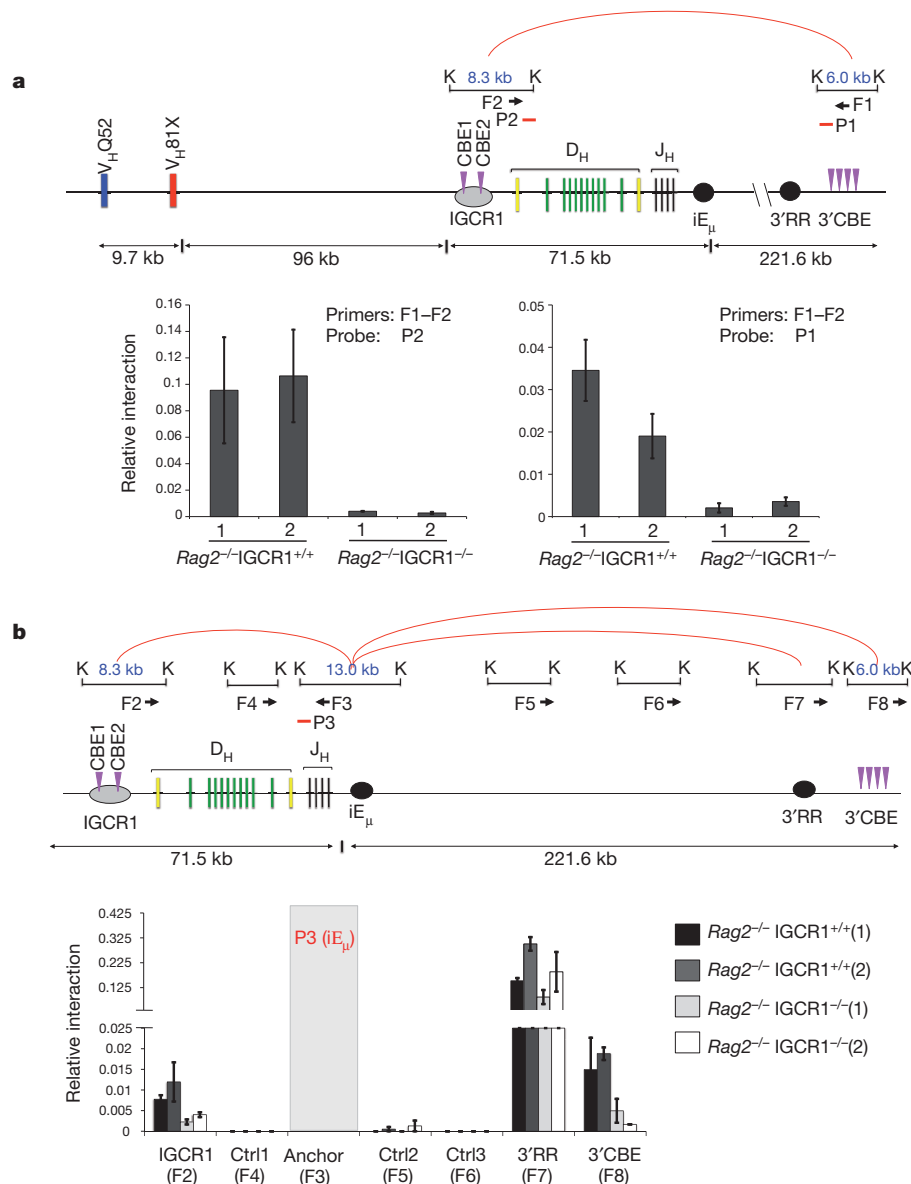


**Figure 5 | IGCR1 mediates long-distance *Igh* chromosomal loops.**

**a**, Schematic of chromosome interactions between IGCR1-containing and 3' *Igh* CBE-containing KpnI restriction fragments in 3C assays. Interactions between IGCR1 and 3' *Igh* CBE locales in 129SV *Rag2*<sup>-/-</sup> and *Rag2*<sup>-/-</sup>IGCR1<sup>-/-</sup> A-MuLV-transformed pro-B cells were quantified by real-time PCR (Taqman) using probe P2 (left) and probe P1 (right). **b**, Schematic of chromosome interactions between iE $\mu$ -containing KpnI restriction fragment and indicated KpnI restriction fragments in other *Igh* locales. Interactions

between iE $\mu$  and IGCR1, iE $\mu$  and 3' *Igh* regulatory region (RR) locales, iE $\mu$  and 3' *Igh* CBE locales in *Rag2*<sup>-/-</sup> and *Rag2*<sup>-/-</sup>IGCR1<sup>-/-</sup> A-MuLV-transformed pro-B cells were quantified by real-time PCR using a probe (P3) from the iE $\mu$  locale. F1-F8 indicate primers used for PCR. K indicates KpnI sites. Red arcs indicate interactions detected in *Rag2*<sup>-/-</sup> cells. The average association frequency of three independent 3C experiments with two independent A-MuLV-transformed lines from each genotype is shown with standard deviation indicated.

rearrangement. Indeed, IGCR1 functions are required for an *Igh* allele to efficiently generate peripheral B cells. Notably, IGCR1 and its CBEs are not required for overall  $V_H$ -to-DJ<sub>H</sub> recombination levels, but rather to decrease relative recombination of proximal  $V_H$  segments, particularly  $V_{H81X}$ . Inability of the dominant  $V_{H81X}$  to promote B-cell development probably leads to developmental defects associated with IGCR1 mutations. Yet, the enigmatic  $V_{H81X}$  is strongly conserved across mouse strains<sup>39</sup> and, correspondingly, has been suggested to have important roles in early antibody repertoires<sup>40</sup>. Now, we find that IGCR1 has a key role in regulating  $V_{H81X}$  rearrangement. IGCR1 also is required to allow feedback regulation of proximal  $V_H$ -to-DJ<sub>H</sub> rearrangements, implicating IGCR1 as a critical element for the allelic exclusion of  $V_{H81X}$  and other very proximal  $V_H$  segments. Our findings indicate that IGCR1 allows feedback by suppressing early, unordered proximal  $V_H$  rearrangement, providing the first evidence, to our knowledge, in support of a long-standing hypothesis that ordered  $V_H$ -to-DJ<sub>H</sub> joining provides a means of mediating allelic exclusion<sup>5,6</sup>. However, we found no evidence for loss of feedback regulation of distal  $V_H$  segments, in accordance with the proposal that locus contraction mediates their allelic exclusion<sup>24</sup>.

Our findings show that IGCR1-mediated promotion of the utilization of  $V_H$  segments up to several megabases distant does not involve alterations in distal  $V_H$  transcription. In pro-B cells, *Igh* contraction promotes distal  $V_H$  usage<sup>23,24</sup>. In the absence of certain transcription (for example, Pax-5 or YY1) or chromatin-modifying (for example, Ezh2) factors, distal  $V_H$  transcription is unimpaired but *Igh* contraction does not occur, diminishing distal  $V_H$  rearrangement. In such factor-deficient pro-B cells, transcription and rearrangement of proximal  $V_H$  segments does not increase<sup>8,41–43</sup>, in contrast to the marked increases in IGCR1<sup>−/−</sup> pro-B cells. This phenotypic difference is consistent with IGCR1 normalizing  $V_H$  repertoires via mechanisms other than *Igh* contraction. We suggest that IGCR1 promotes distal  $V_H$  usage indirectly by preventing premature proximal  $V_H$  rearrangement via insulating functions before contraction, thereby preserving DJ<sub>H</sub> substrates for distal  $V_H$  rearrangement. The location of CBEs throughout the  $V_H$  portion of *Igh* led to the notion that recruitment of  $V_H$  segments into DJ<sub>H</sub> recombination centres<sup>44</sup> subsequent to contraction is promoted via interaction of  $V_H$  and IGCR1 CBEs<sup>45</sup>. Owing to the dominance of proximal  $V_H$  rearrangements on IGCR1-mutant alleles, assays for such putative IGCR1 functions require additional model systems.

IGCR1 CBEs suppress inappropriate transcription and rearrangement of proximal  $V_H$  segments 100 kb or more upstream. These suppressive functions are consistent with enhancer insulating functions of CBEs *in vitro*<sup>29,35</sup>, which may relate to loop formation<sup>35</sup>. We propose that IGCR1 CBEs mediate loops with downstream 3' *Igh* CBEs that segregate the DJ<sub>H</sub> and  $V_H$  portions of *Igh* into separate regulatory domains during the D-to-J<sub>H</sub> rearrangement stage of B-cell development, blocking activity of iEμ or other elements beyond IGCR1 (refs 17, 19; Supplementary Fig. 14a). Thus, inactivation of the IGCR1 CBEs allows transcriptional enhancing activity to extend to the proximal  $V_H$  segments promoting their premature rearrangement (Supplementary Fig. 14b). Notably, such activity does not appear to extend beyond the most proximal  $V_H$  segments, which may result from formation of new CBE-mediated loops to upstream  $V_H$  CBEs in the absence of IGCR1. In DJ<sub>H</sub>-containing pro-B cells, IGCR1-insulating functions that prevent  $V_H$ -to-D<sub>H</sub> rearrangements must be neutralized to allow  $V_H$ -to-DJ<sub>H</sub> joining (Supplementary Fig. 14c). As CTCF binding to *Igh* CBEs does not vary with B-cell stage<sup>32,33</sup>, other factors must modulate activity of bound CTCF within IGCR1 to allow for *Igh*-specific functions. Such factors might include CTCF modifications, interacting proteins such as cohesin<sup>32,33</sup>, or CBE sequence context<sup>35</sup> and orientation<sup>46,47</sup>. In addition, other putative binding elements within IGCR1 may recruit proteins, such as YY1, that have been implicated in modulating CTCF function<sup>35</sup>.

## METHODS SUMMARY

**Mice.** The targeting strategy and analysis of IGCR1-deleted and CBE-mutated embryonic stem (ES) cells is diagrammed in Supplementary Figs 2a and 3a (see Methods for details). The Institutional Animal Care and Use Committee of The Children's Hospital (Boston, Massachusetts) approved all animal work.

**V(D)J rearrangement assays.** PCR assays for D-to-J<sub>H</sub> or  $V_H$ -to-DJ<sub>H</sub> rearrangements were performed as described<sup>30</sup> (see Supplementary Table 1 for primers). Generation of B-cell hybridomas and V(D)J recombination analyses was performed as described<sup>48</sup>.

**RT-PCR and northern blot.** RT-PCR and northern blotting assays for germline transcripts of *Igh* gene segments were performed as described<sup>30</sup> (primers for RT-PCR and northern blot probes are in Supplementary Table 1).

**3C.** 3C assays were performed as described<sup>49</sup>.

**ChIP-seq/ChIP-qPCR assays.** Assays were done as described<sup>32</sup>.

**Full Methods** and any associated references are available in the online version of the paper at [www.nature.com/nature](http://www.nature.com/nature).

**Received 30 November 2010; accepted 18 July 2011.**

**Published online 11 September 2011.**

- Schatz, D. G. Antigen receptor genes and the evolution of a recombinase. *Semin. Immunol.* **16**, 245–256 (2004).
- Zhang, Y. *et al.* The role of mechanistic factors in promoting chromosomal translocations found in lymphoid and other cancers. *Adv. Immunol.* **106**, 93–133 (2010).
- Yancopoulos, G. D. *et al.* Preferential utilization of the most J<sub>H</sub>-proximal  $V_H$  gene segments in pre-B-cell lines. *Nature* **311**, 727–733 (1984).
- Perlot, T. & Alt, F. W. Cis-regulatory elements and epigenetic changes control genomic rearrangements of the IgH locus. *Adv. Immunol.* **99**, 1–32 (2008).
- Alt, F. W. *et al.* Ordered rearrangement of immunoglobulin heavy chain variable region segments. *EMBO J.* **3**, 1209–1219 (1984).
- Jung, D., Giallourakis, C., Mostoslavsky, R. & Alt, F. W. Mechanism and control of V(D)J recombination at the immunoglobulin heavy chain locus. *Annu. Rev. Immunol.* **24**, 541–570 (2006).
- Bates, J. G., Cado, D., Nolla, H. & Schlissel, M. S. Chromosomal position of a  $V_H$  gene segment determines its activation and inactivation as a substrate for V(D)J recombination. *J. Exp. Med.* **204**, 3247–3256 (2007).
- Fuxa, M. *et al.* Pax5 induces V-to-DJ rearrangements and locus contraction of the immunoglobulin heavy-chain gene. *Genes Dev.* **18**, 411–422 (2004).
- Reth, M. G., Ammirati, P., Jackson, S. & Alt, F. W. Regulated progression of a cultured pre-B-cell line to the B-cell stage. *Nature* **317**, 353–355 (1985).
- Melchers, F. *et al.* Repertoire selection by pre-B-cell receptors and B-cell receptors, and genetic control of B-cell development from immature to mature B cells. *Immunol. Rev.* **175**, 33–46 (2000).
- Malynn, B. A., Yancopoulos, G. D., Barth, J. E., Bona, C. A. & Alt, F. W. Biased expression of JH-proximal VH genes occurs in the newly generated repertoire of neonatal and adult mice. *J. Exp. Med.* **171**, 843–859 (1990).
- Decker, D. J., Boyle, N. E. & Klinman, N. R. Predominance of nonproductive rearrangements of VH81X gene segments evidences a dependence of B cell clonal maturation on the structure of nascent H chains. *J. Immunol.* **147**, 1406–1411 (1991).
- ten Boekel, E., Melchers, F. & Rolink, A. G. Changes in the  $V_H$  gene repertoire of developing precursor B lymphocytes in mouse bone marrow mediated by the pre-B cell receptor. *Immunity* **7**, 357–368 (1997).
- Yancopoulos, G. D. & Alt, F. W. Developmentally controlled and tissue-specific expression of unrearranged  $V_H$  gene segments. *Cell* **40**, 271–281 (1985).
- Yancopoulos, G. D., Blackwell, T. K., Suh, H., Hood, L. & Alt, F. W. Introduced T cell receptor variable region gene segments recombine in pre-B cells: evidence that B and T cells use a common recombinase. *Cell* **44**, 251–259 (1986).
- Corcoran, A. E. The epigenetic role of non-coding RNA transcription and nuclear organization in immunoglobulin repertoire generation. *Semin. Immunol.* **22**, 353–361 (2010).
- Feeney, A. Epigenetic regulation of V(D)J recombination. *Semin. Immunol.* **22**, 311–312 (2010).
- Subrahmanyam, R. & Sen, R. RAGs' eye view of the immunoglobulin heavy chain gene locus. *Semin. Immunol.* **22**, 337–345 (2010).
- Jhunjhunwala, S., van Zelm, M. C., Peak, M. M. & Murre, C. Chromatin architecture and the generation of antigen receptor diversity. *Cell* **138**, 435–448 (2009).
- Abarrategui, I. & Krangel, M. S. Germline transcription: a key regulator of accessibility and recombination. *Adv. Exp. Med. Biol.* **650**, 93–102 (2009).
- Bergman, Y. & Cedar, H. Epigenetic control of recombination in the immune system. *Semin. Immunol.* **22**, 323–329 (2010).
- Sayegh, C. E., Jhunjhunwala, S., Riblet, R. & Murre, C. Visualization of looping involving the immunoglobulin heavy-chain locus in developing B cells. *Genes Dev.* **19**, 322–327 (2005).
- Jhunjhunwala, S. *et al.* The 3D structure of the immunoglobulin heavy-chain locus: implications for long-range genomic interactions. *Cell* **133**, 265–279 (2008).
- Roldán, E. *et al.* Locus 'decontraction' and centromeric recruitment contribute to allelic exclusion of the immunoglobulin heavy-chain gene. *Nature Immunol.* **6**, 31–41 (2004).
- Pinaud, E. *et al.* The IgH locus 3' regulatory region: pulling the strings from behind. *Adv. Immunol.* **110**, 27–70 (2011).



26. Sakai, E., Bottaro, A., Davidson, L., Sleckman, B. P. & Alt, F. W. Recombination and transcription of the endogenous Ig heavy chain locus is effected by the Ig heavy chain intronic enhancer core region in the absence of the matrix attachment regions. *Proc. Natl Acad. Sci. USA* **96**, 1526–1531 (1999).
27. Perlot, T., Alt, F. W., Bassing, C. H., Suh, H. & Pinaud, E. Elucidation of IgH intronic enhancer functions via germ-line deletion. *Proc. Natl Acad. Sci. USA* **102**, 14362–14367 (2005).
28. Afshar, R., Pierce, S., Bolland, D. J., Corcoran, A. & Oltz, E. M. Regulation of IgH gene assembly: role of the intronic enhancer and 5'DQ52 region in targeting DHJH recombination. *J. Immunol.* **176**, 2439–2447 (2006).
29. Featherstone, K., Wood, A. L., Bowen, A. J. & Corcoran, A. E. The mouse immunoglobulin heavy chain V-D intergenic sequence contains insulators that may regulate ordered V(D)J recombination. *J. Biol. Chem.* **285**, 9327–9338 (2010).
30. Giallourakis, C. C. *et al.* Elements between the IgH variable (V) and diversity (D) clusters influence antisense transcription and lineage-specific V(D)J recombination. *Proc. Natl Acad. Sci. USA* **107**, 22207–22212 (2010).
31. Lin, Y. C. *et al.* A global network of transcription factors, involving E2A, EBF1 and Foxo1, that orchestrates B cell fate. *Nature Immunol.* **11**, 635–643 (2010).
32. Ebert, A. *et al.* The distal V<sub>H</sub> gene cluster of the *Igh* locus contains distinct regulatory elements with pax5 transcription factor-dependent activity in pro-B cells. *Immunity* **34**, 175–187 (2011).
33. Degner, S. C., Wong, T. P., Jankevicius, G. & Feeney, A. J. Cutting edge: developmental stage-specific recruitment of cohesin to CTCF sites throughout immunoglobulin loci during B lymphocyte development. *J. Immunol.* **182**, 44–48 (2009).
34. Williams, A. & Flavell, R. A. The role of CTCF in regulating nuclear organization. *J. Exp. Med.* **205**, 747–750 (2008).
35. Phillips, J. E. & Corces, V. G. CTCF: master weaver of the genome. *Cell* **137**, 1194–1211 (2009).
36. Bulger, M. & Groudine, M. Enhancers: the abundance and function of regulatory sequences beyond promoters. *Dev. Biol.* **339**, 250–257 (2010).
37. Degner, S. C. *et al.* CCCTC-binding factor (CTCF) and cohesin influence the genomic architecture of the *Igh* locus and antisense transcription in pro-B cells. *Proc. Natl Acad. Sci. USA* **108**, 9566–9571 (2011).
38. Wuerffel, R. *et al.* S-S synapsis during class switch recombination is promoted by distantly located transcriptional elements and activation-induced deaminase. *Immunity* **27**, 711–722 (2007).
39. Hirano, S. L. *et al.* Identity of IGHV-7183.1 (V81x) coding and recombination signal sequences among wild-derived mice. *Immunogenetics* **53**, 54–58 (2001).
40. Hardy, R. R. & Hayakawa, K. B cell development pathways. *Annu. Rev. Immunol.* **19**, 595–621 (2001).
41. Hesslein, D. G. *et al.* Pax5 is required for recombination of transcribed, acetylated, 5' IgH V gene segments. *Genes Dev.* **17**, 37–42 (2003).
42. Su, I. H. *et al.* Ezh2 controls B cell development through histone H3 methylation and *Igh* rearrangement. *Nature Immunol.* **4**, 124–131 (2003).
43. Liu, H. *et al.* Yin Yang 1 is a critical regulator of B-cell development. *Genes Dev.* **21**, 1179–1189 (2007).
44. Ji, Y. *et al.* The *in vivo* pattern of binding of RAG1 and RAG2 to antigen receptor loci. *Cell* **141**, 419–431 (2010).
45. Degner-Leisso, S. C. & Feeney, A. J. Epigenetic and 3-dimensional regulation of V(D)J rearrangement of immunoglobulin genes. *Semin. Immunol.* **22**, 346–352 (2010).
46. MacPherson, M. J. & Sadowski, P. D. The CTCF insulator protein forms an unusual DNA structure. *BMC Mol. Biol.* **11**, 101 (2010).
47. Kyrchanova, O., Chetverina, D., Maksimenko, O., Kuliyev, A. & Georgiev, P. Orientation-dependent interaction between *Drosophila* insulators is a property of this class of regulatory elements. *Nucleic Acids Res.* **36**, 7019–7028 (2008).
48. Dudley, D. D. *et al.* Impaired V(D)J recombination and lymphocyte development in core RAG1-expressing mice. *J. Exp. Med.* **198**, 1439–1450 (2003).
49. Hagege, H. *et al.* Quantitative analysis of chromosome conformation capture assays (3C-qPCR). *Nature Protocols* **2**, 1722–1733 (2007).

**Supplementary Information** is linked to the online version of the paper at [www.nature.com/nature](http://www.nature.com/nature).

**Acknowledgements** We thank Y. Fujiwara and P.-Y. Huang for generating chimaeric mice. This work was supported by NIH grants RO1 AI20047 (to F.W.A.), RO1 HL48702 and AI40227 (to M.S.S.), CA054198-20 (to C.M.) and K08 AI070839 (to C.C.G.). M.B. was supported by the Austrian GEN-AU initiative and Boehringer Ingelheim. C.G. is supported by an Irvington Institute Postdoctoral Fellowship from the Cancer Research Institute. C.V. is supported by a Marie Curie Fellowship. C.B. is supported by an EMBO fellowship. F.W.A. is an Investigator of the Howard Hughes Medical Institute.

**Author Contributions** C.G., H.S.Y., A.F., C.C.G. and F.W.A. conceived, designed and/or performed most experiments, interpreted most results, and wrote the manuscript. With respect to other authors, S.J. performed experiments for Figs 2, 3, 4 and Supplementary Fig. 11 and contributed to interpretation of the data; A.E. and M.B. contributed the work in Fig. 2c and Supplementary 7a–c. C.V., J.G.B. and M.S.S. contributed the work in Supplementary Fig. 10; and C.B. and C.M. performed FISH experiments on IGC1<sup>−/−</sup> cells that helped frame aspects of the discussion and models; all of these authors contributed to polishing the manuscript. All other authors provided technical assistance with various experiments or data analysis.

**Author Information** Reprints and permissions information is available at [www.nature.com/reprints](http://www.nature.com/reprints). The authors declare no competing financial interests. Readers are welcome to comment on the online version of this article at [www.nature.com/nature](http://www.nature.com/nature). Correspondence and requests for materials should be addressed to F.W.A. ([alt@enders.tch.harvard.edu](mailto:alt@enders.tch.harvard.edu)) or C.C.G. ([cgiallourakis@partners.org](mailto:cgiallourakis@partners.org)).

## METHODS

**Generation of IGCR1-deleted mice.** A targeting construct was designed to replace IGCR1 (4.1 kb) with a NeoR gene cassette oriented in the direction from the D clusters to V clusters (Supplementary Fig. 2a). A 4.3-kb arm upstream of IGCR1 and a 2.9-kb arm downstream of IGCR1 were PCR amplified (see Supplementary Table 1 for primers) from TC1 embryonic stem (ES) cell DNA (129 strain) and cloned into the pLNTK targeting vector in the desired orientation. The targeting construct was then electroporated into TC1 ES cells, and successful targeting assessed by Southern blot analyses using StuI- or SpeI-digested genomic DNA and upstream or downstream genomic probes as outlined in detail in Supplementary Fig. 2a. Three independently targeted ES clones were subjected to adenovirus-mediated Cre deletion to remove the NeoR gene and injected for *Rag2*-deficient blastocyst complementation (RDBC)<sup>50</sup> or for germline transmission.

**Generation of IGCR1 CBE-mutated mice.** Two 4.2-kb DNA fragments consecutively located over the IGCR1 region were PCR amplified (see Supplementary Table 1 for primers) and cloned into a pGEM-T easy (Promega) vector (Supplementary Fig. 3a). One fragment included CBE1 and the other included CBE2. PCR site-directed mutagenesis was used to introduce scrambled mutations of the 20-bp CBE1 and 19-bp CBE2 sites in each arm, respectively (see Supplementary Table 1 for primers). Restriction endonuclease recognition sites were incorporated into the mutated CBE sequences (NheI for upstream and SpeI for downstream arms). Then, these two DNA fragments were cloned into a targeting vector pLNTK as upstream and downstream arms. The targeting construct was electroporated into TC1 ES cells, and successfully targeted clones, including no mutations (*loxP* insertion control) and the CBE1 and 2 double mutation were assessed by Southern blot analyses using StuI-, SpeI- or HindIII/NheI-digested genomic DNA with appropriate probes (Supplementary Fig. 3b). Two independently targeted clones were subjected to adenovirus-mediated Cre deletion to remove the NeoR gene and injected for RDBC or for germline transmission. For RDBC, sorted double-positive T cells from chimaeras were genotyped by PCR and restriction enzyme digestion (see Supplementary Fig. 3c). Wild-type 129SV and C57BL/6 mice were purchased from Jackson Laboratory. *Rag2*-deficient mice on a 129 background were purchased from Taconic.

**Electrophoretic mobility shift assay.** Probes were prepared by annealing complementary oligonucleotides (Supplementary Table 1). Annealed oligonucleotides were purified on 4% agarose gels and end-labelled with <sup>32</sup>P-γ-ATP. Nuclear extracts were prepared from *Rag2*-deficient A-MuLV-transformed pro-B cell lines. Electrophoretic mobility shift assay (EMSA) reactions were conducted in a mixture of 5% glycerol, 150 mM KCL, 20 mM HEPES, pH 7.9, 5 mM MgCl<sub>2</sub>, 1 mM dithiothreitol (DTT), 0.5% Triton X-100, 400 ng poly(dG-dC). 2 μg of nuclear extract was incubated with anti-CTCF or anti-IgG antibodies at 4 °C for 20 min and labelled probes and/or competitor un-labelled probes were added to the reactions. The reactions were electrophoresed with 0.5× TBE buffer (89 mM Tris Base, 89 mM boric acid, 2 mM EDTA, pH 8.0) at 30 V, and visualized by autoradiography.

**V(D)J recombination assays.** Genomic DNA was purified from sorted bone marrow pro-B (IgM<sup>+</sup>B220<sup>+</sup>CD43<sup>+</sup>), pre-B (IgM<sup>+</sup>B220<sup>+</sup>CD43<sup>+</sup>) cells, and splenic mature B (IgM<sup>+</sup>B220<sup>+</sup>CD43<sup>+</sup>) cells, and double-positive T (B220<sup>+</sup>CD4<sup>+</sup>CD8<sup>+</sup>) cells. Fivefold serial dilutions of genomic DNA (200 ng, 40 ng, 8 ng) was used to perform PCR to analyse V(D)J rearrangements. Primers used in this assay are listed in Supplementary Table 1. Primers flanking exon 6 of the *Dlg5* gene were used as a loading control under the same conditions. Vκ-to-Jκ rearrangement PCRs were performed to confirm specificity of sorted B-cell populations, and to exclude potential B-cell contamination during double-positive T-cell analysis. PCR products were gel electrophoresed and transferred to determine V(D)J recombination by Southern blotting using radiolabelled oligonucleotide probes (see Supplementary Table 1 for sequences) and visualized by autoradiography.

**RNA isolation and RT-PCR.** Total RNA was isolated using Trizol (Invitrogen). One microgram of RNA was used to generate cDNA with reverse transcriptase Superscript III (Invitrogen) with random hexamers according to manufacturer's protocols. Approximately, 1/40 of the reverse-transcription-generated cDNA was analysed by PCR. Primers that were used for PCR are provided in Supplementary Table 1.

**Intracytoplasmic staining.** Intracytoplasmic staining was performed as described previously<sup>51</sup>. Briefly, splenic B cells from F1 mice with a wild-type *IgM*<sup>b</sup> allele and an IGCR1-deleted *IgM*<sup>a</sup> allele were purified by MACS paramagnetic beads

following the manufacturer's protocol and stimulated for 4 days with LPS. Cells were fixed, permeabilized and then stained with FITC-labelled anti-mouse IgM<sup>a</sup> and biotin-labelled anti-mouse IgM<sup>b</sup> revealed by streptavidin-conjugated Texas Red. Cells were examined using a fluorescent microscope for IgM<sup>a</sup> and IgM<sup>b</sup> allotypic expressers.

**Hybridoma assay and Southern blot.** Splenic B cells were isolated from wild-type, IGCR1<sup>+/-</sup> and IGCR1<sup>-/-</sup> mice, and fused with NS1 cells after stimulation with 25 ng ml<sup>-1</sup> IL-4 and 500 ng ml<sup>-1</sup> anti-CD40 antibody for 4 days in culture. Hybridoma cells were plated and selected in HAT medium as previously described<sup>48</sup>. Genomic DNA from hybridomas was isolated and digested with StuI to determine V(D)J rearrangement configurations by Southern blot (Supplementary Fig. 11). DNA from the clones that showed V<sub>H</sub>(D)<sub>H</sub> rearrangement on both alleles was subjected to PCR using an upstream V<sub>H</sub> primer (specific to V<sub>HJ558</sub>, V<sub>HJ52</sub> or V<sub>HJ183</sub> V<sub>H</sub> gene families) and a downstream J<sub>H4</sub> primer, and the amplified junctions were cloned and sequenced to identify productive and non-productive V<sub>H</sub>(D)<sub>H</sub> rearrangements.

**Transgenic mice.** IGCR1<sup>+/-</sup> mice were bred with the mutant mice harbouring a pre-assembled *Igh* VB1-8DJ<sub>H4</sub> allele<sup>52</sup>. B cells were purified by MACS paramagnetic beads from VB1-8DJ<sub>H4</sub> knock-in mice with either wild-type IGCR1 (IGCR1<sup>+/+</sup> VB1-8 knock-in) or IGCR1 deletion (IGCR1<sup>-/-</sup> VB1-8 knock-in) on the other *Igh* allele. Genomic DNA was isolated and V(D)J rearrangement of V<sub>HJ183</sub>, V<sub>HJ52</sub>, and V<sub>HJ558</sub> segments were amplified as described in Supplementary Fig. 6a.

**ChIP.** Rabbit polyclonal antibodies recognizing the following histone tail modifications were used: H3K9ac (Millipore; 07-352), H3K4me2 (Millipore; 07-030) and H3K4me3 (Diagenode; pAB-003-050). ChIP analysis and ChIP sequencing of A-MuLV-transformed pro-B cells was performed as described<sup>32</sup>. The sequence reads obtained by paired-end Solexa sequencing with a read length of 76 nucleotides were mapped to the 129SV mouse reference genome. The ChIP-qPCR analysis was performed by quantifying the precipitated DNA on a MyiQ instrument (Bio-Rad) as described<sup>32</sup>. The amount of precipitated DNA was determined as percentage relative to input DNA to obtain relative enrichment compared to the precipitated DNA of the control *Bcar3* enhancer<sup>53</sup>. Tenfold dilutions of input material were used to generate a standard curve, and ChIP samples were quantified relative to input using the iQ5 software. The oligonucleotides used for real-time PCR analysis are shown in Supplementary Table 1.

**3C.** The 3C assays were performed essentially as previously described<sup>49</sup>. Briefly, 2 × 10<sup>7</sup> cells were cross-linked with 1% formaldehyde for 10 min. The reaction was quenched with glycine (0.125 M). Cells were lysed in 10 mM Tris pH.8, 10 mM NaCl and 0.2% NP-40 followed by 15 strokes using a dounce homogenizer. The resulting nuclei were washed in restriction enzyme buffer, resuspended with the same buffer containing 0.3% SDS, and incubated for 1 h at 37 °C. To sequester SDS, 2% Triton X-100 was added, and incubated for 1 h at 37 °C. 400 U KpnI was added and incubated overnight at 37 °C. KpnI was inactivated with 1.6% SDS and incubated for 25 min at 68 °C. The samples were ligated in ligation buffer (50 mM Tris, 10 mM MgCl<sub>2</sub>, 1% Triton X-100, 100 mM DTT and 0.1 M ATP) with T4 DNA ligase overnight at 16 °C. The crosslinks within 3C library products were reversed and the DNA purified by overnight treatment with proteinase K at 65 °C as per assay protocol. Quantitative real-time PCR using a standard curve was conducted to measure the frequency of the 3C products within each sample. Standard curves for 3C assays were generated using BACs containing the IGCR1, iEμ and 3' *Igh* CBE locales within the *Igh* locus (RP23-38K22, RP23-334P5 and RP24-275024) that were KpnI-digested and then religated to generate all possible 3C products within the locus. Taqman applied real-time PCR was used to determine a 3C frequency by averaging the amount of 3C products produced for a given amplicon and dividing that value by the amount of loading control determined by loading control amplicon (see Supplementary Table 1).

50. Chen, J. *et al.* Mutations of the intronic IgH enhancer and its flanking sequences differentially affect accessibility of the JH locus. *EMBO J.* **12**, 4635–4645 (1993).
51. Barreto, V. & Cumano, A. Frequency and characterization of phenotypic Ig heavy chain allelically included IgM-expressing B cells in mice. *J. Immunol.* **164**, 893–899 (2000).
52. Sonoda, E. *et al.* B cell development under the condition of allelic inclusion. *Immunity* **6**, 225–233 (1997).
53. McManus, S. *et al.* The transcription factor Pax5 regulates its target genes by recruiting chromatin-modifying proteins in committed B cells. *EMBO J.* **30**, 2388–2404 (2011).



# Electrons surfing on a sound wave as a platform for quantum optics with flying electrons

Sylvain Hermelin<sup>1</sup>, Shintaro Takada<sup>2</sup>, Michihisa Yamamoto<sup>2,3</sup>, Seigo Tarucha<sup>2,4</sup>, Andreas D. Wieck<sup>5</sup>, Laurent Saminadayer<sup>1,6</sup>, Christopher Bäuerle<sup>1</sup> & Tristan Meunier<sup>1</sup>

Electrons in a metal are indistinguishable particles that interact strongly with other electrons and their environment. Isolating and detecting a single flying electron after propagation, in a similar manner to quantum optics experiments with single photons<sup>1,2</sup>, is therefore a challenging task. So far only a few experiments have been performed in a high-mobility two-dimensional electron gas in which the electron propagates almost ballistically<sup>3–5</sup>. In these previous works, flying electrons were detected by means of the current generated by an ensemble of electrons, and electron correlations were encrypted in the current noise. Here we demonstrate the experimental realization of high-efficiency single-electron source and detector for a single electron propagating isolated from the other electrons through a one-dimensional channel. The moving potential is excited by a surface acoustic wave, which carries the single electron along the one-dimensional channel at a speed of  $3 \mu\text{m ns}^{-1}$ . When this quantum channel is placed between two quantum dots several micrometres apart, a single electron can be transported from one quantum dot to the other with quantum efficiencies of emission and detection of 96% and 92%, respectively. Furthermore, the transfer of the electron can be triggered on a timescale shorter than the coherence time  $T_2^*$  of GaAs spin qubits<sup>6</sup>. Our work opens new avenues with which to study the teleportation of a single electron spin and the distant interaction between spatially separated qubits in a condensed-matter system.

Quantum electron optics is a field aiming at the realization of photon experiments with flying electrons in nanostructures at the single-electron level. Important tools with which to infer complex photon correlations inaccessible from ensemble measurements are single-photon sources and single-photon detectors. In contrast with photons, electrons are strongly interacting particles and they usually propagate in a Fermi sea filled with other electrons. Each electron therefore inevitably mixes with the others of the Fermi sea, which implies that the quantum information stored within the charge or the spin of the single electron will be lost over short lengths. To perform quantum electron-optical experiments at the single-electron level, one therefore needs a source of single electrons, a controlled propagating medium and a single-electron detector. It has been proposed that edge states in the quantum Hall effect can serve as a one-dimensional (1D) propagating channel for flying electrons. As a result of Coulomb blockade, quantum dots have been demonstrated to be a good source of single electrons<sup>7,8</sup> and can also serve as a single-electron detector. Indeed, once an electron has been stored in a quantum dot, its presence can be inferred routinely by charge detection<sup>9</sup>. Nevertheless, re-trapping the electron in another quantum dot after propagation in an edge state turns out to be extremely difficult, and currently all the information extracted from such experiments is coming from ensemble measurements<sup>10,11</sup>. Here we show that a single flying electron—an electron surfing on a sound wave—can be sent on demand from a quantum dot by means of a 1D quantum channel and re-trapped in a second

quantum dot after propagation. The 1D quantum channel consists of a depleted region several micrometres long in a two-dimensional electron gas (2DEG). The electron is dragged along by exciting a surface acoustic wave (SAW) and propagates isolated from the other electrons inside the 1D channel<sup>12</sup>. The processes of loading and unloading of the flying electron from the quantum channel into a quantum dot turn out to be highly efficient. Moreover, we show that the transfer of the electron can be triggered with a timescale smaller than the coherence time  $T_2^*$  of GaAs spin qubits<sup>6</sup>. Because both electron spin directions are treated on the same foot in the SAW quantum channel, one expects that the spin coherence during the transport is conserved. Naturally, new possibilities will emerge to address the question of scalability in spin qubit systems<sup>6,13,14</sup>.

To transport a single electron from one quantum dot to the other separated by a 3- $\mu\text{m}$  1D channel (see Fig. 1 and Methods), the following procedure is applied. First, the region between the two electrodes, which define the 1D channel, is fully depleted. As a consequence, direct linear electron transport from one end of the channel to the other is blocked because the Fermi energy lies below the potential induced by the gates. Second, by applying microwave excitation to the interdigitated transducer (IDT), SAW-induced moving quantum dots are generated<sup>12</sup> as a result of the piezoelectric properties of GaAs (see also Supplementary Information). By adding a quantum dot to each side of the 1D channel and tuning both quantum dots into the single electron regime, it is then possible to transport a single electron from one quantum dot across the 1D channel and catch it inside the second quantum dot. Stability diagrams for both quantum dots as a function

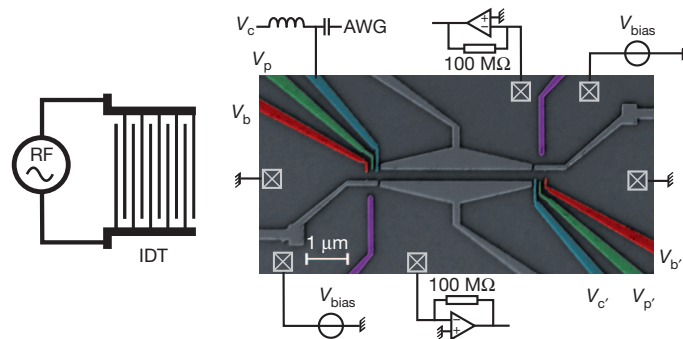


**Figure 1 | Experimental device and measurement setup.** Scanning electron microscope image of the single-electron transfer device, and diagram of the experimental setup. Two quantum dots, which can be brought into the single-electron regime, are separated by a 1D channel 3  $\mu\text{m}$  long, as shown. Each quantum dot is capacitively coupled to a QPC close by that is used as an electrometer<sup>9</sup>. By applying a microwave burst 65 ns long on the IDT (see Methods for details), a train of about 150 moving quantum dots is created in the 1D channel. Gate  $V_c$  is connected to a home-made bias tee to allow nanosecond manipulation of the dot potential. RF, radio frequency.

<sup>1</sup>Institut Néel, CNRS, and Université Joseph Fourier, 38042 Grenoble, France. <sup>2</sup>Department of Applied Physics, University of Tokyo, Tokyo, 113-8656, Japan. <sup>3</sup>ERATO-JST, Kawaguchi-shi, Saitama 331-0012, Japan. <sup>4</sup>ICORP (International Cooperative Research Project) Quantum Spin Information Project, Atsugi-shi, Kanagawa, 243-0198, Japan. <sup>5</sup>Lehrstuhl für Angewandte Festkörperphysik, Ruhr-Universität Bochum, Universitätsstrasse 150, 44780 Bochum, Germany. <sup>6</sup>Institut Universitaire de France, 103 boulevard Saint-Michel, 75005 Paris, France.

of the applied voltage on the two gates controlling the two barriers of the quantum dot are shown in Fig. 2a, b. They demonstrate that the system can be tuned into a regime consisting of few electrons<sup>15</sup>. As expected, the charge degeneracy lines disappear when the barrier height between each dot and the reservoir is increased (corresponding to increasingly negative voltages  $V_b$  and  $V_{b'}$ ). This also changes the position of the quantum-dot minimum and brings the electron closer to the 1D channel, to a position where a better transfer to SAW quantum dots is expected.

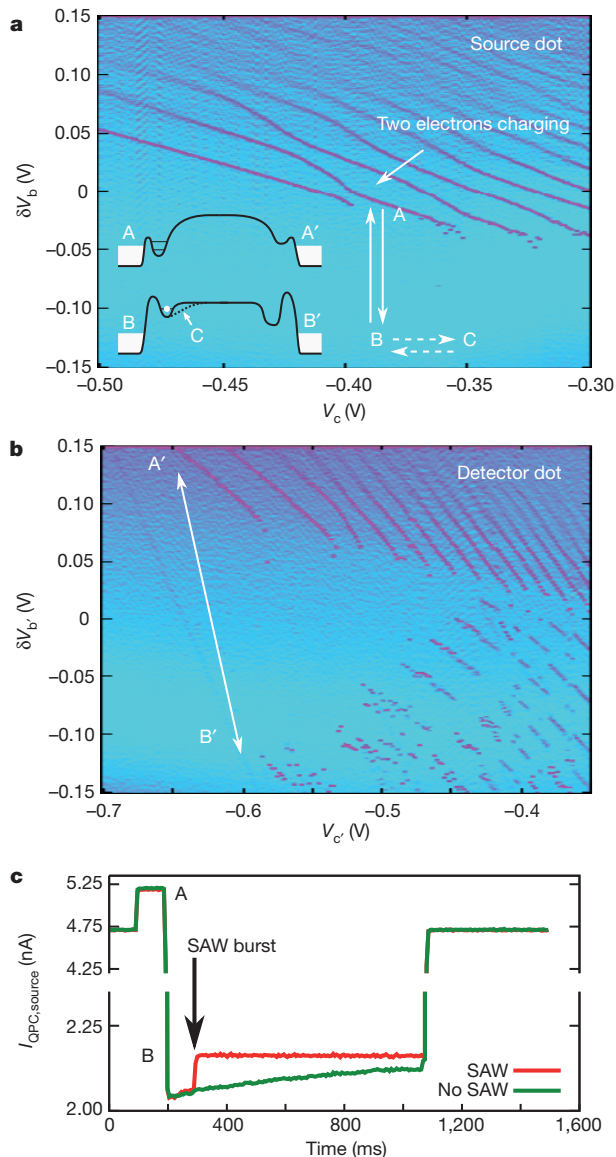


**Figure 2 | Stability diagrams of the two quantum dots and charge detection.** **a, b**, Stability diagram of the left (a) and right (b) dot obtained via charge detection by varying respectively gate voltages ( $V_b$  or  $V_c$ ) and ( $V_{b'}$  or  $V_{c'}$ ) (see Fig. 1). Sweeps in  $V_b$  and  $V_{b'}$  are fast and are performed within 1 s from +0.15 V to −0.15 V (3 ms per point). When the barrier height is made higher ( $V_b$  or  $V_{b'}$  more negative), metastable charge states with timescales longer than the  $V_b$  or  $V_{b'}$  sweep time are observed. In the very negative  $V_{b'}$  part of the diagram for the right dot, the electrons will finally tunnel out. When the sweep direction of  $V_{b'}$  is reversed, these charge detection steps are absent. Inset to **a**: schematic diagram of the dots and channel electrostatic potential applied by the gates to the electron at different points in the stability diagram (see the text). **c**, Average QPC time trace along the voltage sequence of the single-electron source. Without the microwave burst applied on the IDT, we observe a lifetime for the metastable one-electron charge state of 700 ms. Applying a microwave burst, the electron in the metastable state is forced to quit the quantum dot with very high probability.

The protocol of the single-electron source for a SAW quantum channel is a sequence made of three dot-gate voltage steps (see Fig. 2a). At working point A on Fig. 2a, the left quantum dot (the single-electron source) is loaded with one electron on a timescale close to microseconds and unresolved with the setup detection bandwidth. It is then brought rapidly to working point B, where the chemical potential of the single electron state lies above the Fermi energy and the coupling to the 1D channel is expected to be large. The actual position of B is not crucial as long as the electron is sufficiently protected from tunnelling out of the dot and the dot potential is high enough to facilitate the charging of the electron into the moving SAW dot (see inset to Fig. 2a). For each sequence, the quantum point contact (QPC) conductance time-trace is recorded to observe single-shot loading and unloading of the dot. This sequence is repeated 1,000 times to obtain measurement statistics; the resulting averaged time-traces are shown in Fig. 2c. An exponential decay of the presence of the electron in the dot as a function of the time spent at working point B is observed in the experimental data, corresponding to a tunnelling time close to 1 s as indicated by the green line. This gate pulsing sequence is then repeated by adding a burst of microwaves to the IDT with a pulse length of several tens of nanoseconds, applied 100 ms after the system is brought into position B. The microwave burst creates a moving quantum dot, which lifts the electron, initially trapped in the left quantum dot, above the tunnel barrier and drags it out of the quantum dot. This results in a jump in the QPC current, as shown by the red line.

To demonstrate that the electron has been loaded into a moving quantum dot and not expelled into the reservoir, it is essential to detect the coincidence between events when the electron leaves the single-electron source (left dot) and when it is trapped in the single-electron detector (right dot). This is realized by a second voltage pulse sequence on the right dot: when the single-electron source is brought in position B, the detector dot is armed by pulsing its gates to working point B', where the steady state is the zero-electron state and the coupling to the channel is large. At this working point both QPC traces are recorded simultaneously. No charge variation is observed during the first 50 ms where the system is kept in position B. A microwave pulse is sent with a time lag of 50 ms. After the recording, the detector is reinitialized to zero electron at working point A', where the captured electron can tunnel efficiently into the reservoir. Typical single-shot readout curves are presented in Fig. 3a–d. Coincidences are observed between events when an electron leaves the source quantum dot and an electron is detected in the receiver quantum dot within the same time slot (Fig. 3a). These events correspond to the situation in which one electron has been loaded in the electron source (left dot), is then transferred in the quantum channel (the moving quantum dots) and is received in the detector (right dot). In contrast with photon detectors, here the electron still exists after detection. A set of experiments described in Fig. 3 allows the full characterization of the high quantum efficiency of both the single-electron source and the single-electron detector observed in the experiment: 96% for the single-electron source and 92% for the single-electron detector (see Fig. 3e).

In quantum dots it is possible to load not just one but two electrons. By waiting long enough<sup>16</sup>, the two electrons will be in a singlet state at zero magnetic field and are hence entangled in the spin degree of freedom. The ability to separate the two electrons and to bring only one of them to the second quantum dot is of potential interest for the transfer of quantum information and is the essence of the quantum teleportation protocol<sup>2,17–19</sup>. By analogy with photons, this is the equivalence of a two-photon entangled source<sup>20</sup>. Moreover, in contrast with a photon detector, the electron detector can discriminate easily whether one, two or more electrons have left the single-electron source and are captured in the single-electron detector (see Fig. 2a). The protocol consists of loading the left dot with exactly two electrons by moving gate voltages  $V_b$  and  $V_c$  into the two-electron regime of the stability diagram. The quantum dot is then tuned towards the working point where loading of the moving quantum dots is possible (point B).



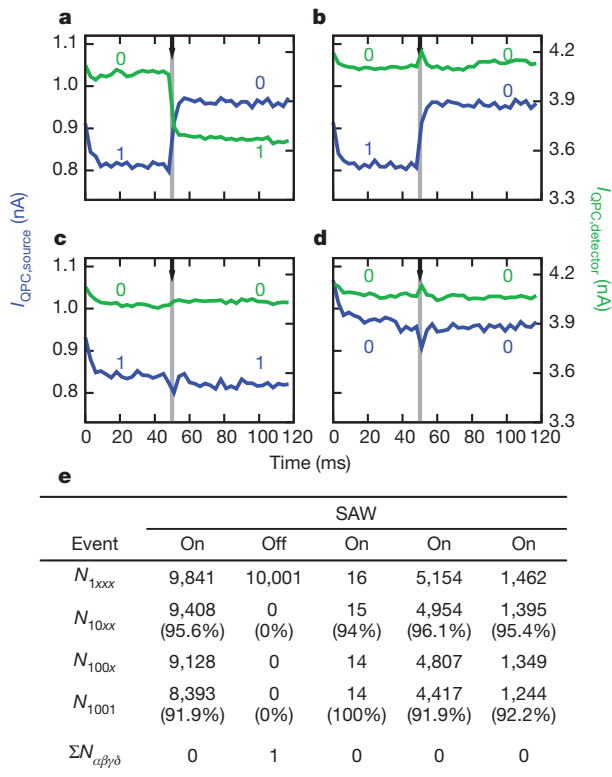


**Figure 3 | Coincidence between emission and detection of a single electron.** **a–d**, Coincidence between the two single-shot QPC time traces at voltage working points B and B' corresponding to the different events  $N_{1001}$  (**a**),  $N_{1000}$  (**b**),  $N_{1100}$  (**c**) and  $N_{0000}$  (**d**). The position in time of the RF burst is indicated by the black arrow. At this specific time, the small peak or dip observed on time traces is the result of the SAW-induced enhancement or reduction, respectively, of the QPC current. The notation  $N_{\alpha\beta\gamma\delta}$  corresponds to the number of events with  $\alpha$  or  $\beta$  electrons in the source dot before or after the microwave burst, respectively, and to  $\gamma$  or  $\delta$  electrons in the receiver dot before or after the microwave burst, respectively. When one index is replaced by  $x$ , the corresponding output result is disregarded. Event  $N_{1000}$  corresponds to the situation in which the electron has been transferred from the source to the detector and is immediately kicked out of the detector dot by the same RF burst and is therefore not detected. Events for which  $\beta + \delta > \alpha + \gamma$  are called 'bad' events. **e**, Summary table for the different events over 10,001 traces for different source dot loading probabilities ( $N_{1xxx}$ ) with or without the RF burst. The loading probability can be tuned on demand by changing the voltage gate position A in the stability diagram around the charge degeneracy point. The summation at the bottom table is for  $(\beta + \alpha) > \delta + \gamma$ .

Different possibilities for the emission of electrons into the quantum channel are observed. Indeed, when starting with exactly two electrons in the source dot, one can achieve the outcome that either exactly one or both electrons are emitted from the source and received in the detector dot, as shown by the single-shot traces for QPC detection of the two dots (see Fig. 4a–d). The probability of each event varies with the working voltage at point B. For very negative gate voltage  $V_c$ , about half of the time the two electrons are separated, meaning that only one electron is transferred, and the other half of the time both electrons are transported (see Fig. 4e). For the events in which both electrons leave the dot, the electrons are most probably loaded into two different moving quantum dots. More interestingly, when pulsing gate voltage  $V_c$  more positively, a situation can be realized in which only one of the two electrons of the left dot is efficiently emitted and consequently captured by the right dot (see Fig. 4e). In this case, the probability of sending the two electrons is markedly reduced, to less than 3%, and the probability of effectively separating the two electrons approaches 90%.

To use single-electron transfer in quantum operations using spin qubits, one has to show that coherence of the electron spin after electron transfer is preserved. Measurement and coherent manipulations

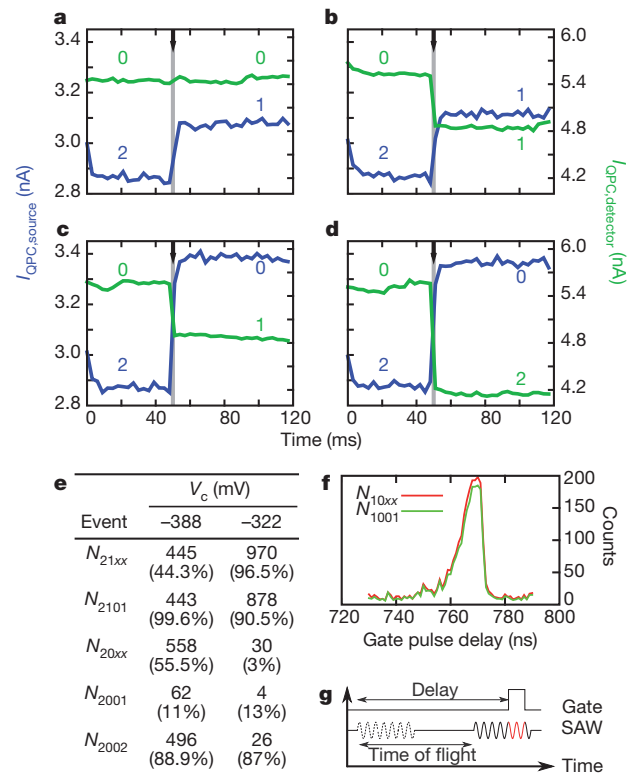


**Figure 4 | Coincidence between emission and detection of two electrons and triggered nanosecond electron transfer.** **a–d**, Coincidence between the two single-shot QPC time traces at voltage working points B and B' corresponding to the different events  $N_{2100}$  (**a**),  $N_{2101}$  (**b**),  $N_{2001}$  (**c**) and  $N_{2002}$  (**d**). **e**, Summary table of the different events over 1,005 traces for dot configurations  $V_c = -0.388$  V and  $V_c = -0.322$  V. **f**, Evolution of the number of  $N_{1001}$  and  $N_{10xx}$  events as a function of the delay between the 1-ns gate pulse and the 65-ns microwave burst when a single electron is loaded into the single-electron source. **g**, Schematic diagram of the timing sequence between the 1-ns gate pulse and the microwave burst applied to the IDT.

of electron spins can be straightforwardly implemented in our setup, and the spin coherence time  $T_2^*$  of an ensemble of electrons stored in SAW-assisted moving quantum dots has been shown to be as long as 25 ns (ref. 21). A necessary condition for investigating coherent transport of a single electron spin is to be able to trigger the electron transfer within a timescale that is short compared with  $T_2^*$ . Indeed, a microwave pulse 250 ns in duration corresponds to about 700 moving quantum dots, and the experiments described above demonstrate the ability to load the electron into one of the moving quantum dots produced by each SAW microwave burst. We now show that the number of minima of the microwave burst in which the electron is loaded can be reduced to two. For this purpose, the single-electron source voltage sequence is slightly modified. After charging of the quantum dot, the system is brought to position B (see Fig. 2a) slightly on the more negative side with respect to  $V_c$ , and the duration of the microwave pulse is shortened to a minimum of 65 ns. At this voltage position, the barrier height to the quantum channel is increased and the transfer probability of an electron into the quantum channel is as low as 5% when excited with the SAW microwave burst. To trigger single-electron transfer, a 1-ns voltage pulse on  $V_c$  with a positive value (voltage position C in Fig. 2a) is added to this sequence. In Fig. 4f the evolution of the number of events in which one electron leaves the single-electron source and one electron is detected in the single-electron detector ( $N_{1001}$ ) is plotted as a function of the delay between the 1-ns gate pulse and the 65-ns microwave burst. High transfer probabilities reaching 90% are observed only for time delays of roughly 765 ns, corresponding to the propagation time of the surface acoustic wave from the IDT to the dot region. Taking into account the pulse

length of the gate and the distance between two minima of the SAW, only two moving quantum dots can then be the hosts of the transported electron during the gate pulse, as indicated schematically in Fig. 4g. This demonstrates the ability to load on demand and in a very reproducible manner one of the two minima of the train of moving quantum dots with a single electron during the 1-ns gate pulse. The use of a faster arbitrary waveform generator should allow the electron to be loaded on demand into the same moving quantum dot.

These experiments represent the first milestone on the road to a new experimental platform for realizing quantum optics with flying electrons implemented in gated 2DEG heterostructures and transported by surface acoustic waves. High quantum efficiency of both the single-electron detector and the single-electron source are shown and potentially enable the measurement of all moments of the electron correlations<sup>22</sup>. In comparison with other implementations in similar systems, the propagating electron is physically isolated from the other conduction electrons of the heterostructure. In bringing together two propagating quantum buses separated by a tunnel barrier, a beam splitter for flying electrons can be implemented<sup>23,24</sup> and Hanbury Brown and Twiss-type experiments in which there are stronger Coulomb interactions between electrons could be realized. Future experiments should allow coherent spin transfer and provide new insight into the feasibility of quantum teleportation protocols and on the potential scalability of spin qubits.

## METHODS SUMMARY

The device is defined by Schottky gates in an n-AlGaAs/GaAs 2DEG-based heterostructure (the properties of the 2DEG are as follows:  $\mu \approx 10^6 \text{ cm}^2 \text{ V}^{-1} \text{ s}^{-1}$ ,  $n_s \approx 1.4 \times 10^{11} \text{ cm}^{-2}$ , depth 90 nm) with standard split-gate techniques. The charge configuration of both dots is measured by means of the conductance of both QPCs by biasing it with a direct-current voltage of 300  $\mu\text{V}$ ; the current is measured with a current-to-voltage converter with a bandwidth of 1.4 kHz. The voltage on each gate can be varied on a timescale down to microseconds. In addition, the gate biased with voltage  $V_G$ , controlling the coupling between the left dot and the 1D channel, is connected to a homemade bias tee to allow nanosecond manipulation of the dot potential by means of an arbitrary function generator (Tektronix AWG 5014). The IDT, which is placed about 2 mm to the left of the sample, is made of 70 pairs of lines 70  $\mu\text{m}$  in length and 250 nm in width with a 1- $\mu\text{m}$  spacing. The IDT is orientated perpendicular to the direction of the 1D channel defined along the crystal axis [110] of the GaAs wafer; it has a frequency bandwidth of about 20 MHz.

Received 26 April; accepted 4 August 2011.

- Aspect, A., Grangier, P. & Roger, G. Experimental tests of realistic local theories via Bell's theorem. *Phys. Rev. Lett.* **47**, 460–463 (1981).
- Bouwmeester, D. *et al.* Experimental quantum teleportation. *Nature* **390**, 575–579 (1997).
- Neder, I. *et al.* Interference between two indistinguishable electrons from independent sources. *Nature* **448**, 333–337 (2007).
- Henny, M. *et al.* The fermionic Hanbury Brown and Twiss experiment. *Science* **284**, 296–298 (1999).
- Liu, R. C., Odom, B., Yamamoto, Y. & Tarucha, S. Quantum interference in electron collision. *Nature* **391**, 263–265 (1998).
- Petta, J. R. *et al.* Coherent manipulation of coupled electron spins in semiconductor quantum dots. *Science* **309**, 2180–2184 (2005).
- Splettstoesser, J., Ol'khovskaya, S., Moskalets, M. & Büttiker, M. Electron counting with a two-particle emitter. *Phys. Rev. B* **78**, 205110 (2008).

- Fève, G. *et al.* An on-demand coherent single-electron source. *Science* **316**, 1169–1172 (2007).
- Field, M. *et al.* Measurements of Coulomb blockade with a noninvasive voltage probe. *Phys. Rev. Lett.* **70**, 1311–1314 (1993).
- Ji, Y. *et al.* An electronic Mach–Zehnder interferometer. *Nature* **422**, 415–418 (2003).
- Roulleau, P. *et al.* Direct measurement of the coherence length of edge states in the integer quantum Hall regime. *Phys. Rev. Lett.* **100**, 126802 (2008).
- Talyanskii, V. I. *et al.* Single-electron transport in a one-dimensional channel by high-frequency surface acoustic waves. *Phys. Rev. B* **56**, 15180–15184 (1997).
- Koppens, F. H. L. *et al.* Driven coherent oscillations of a single electron spin in a quantum dot. *Nature* **442**, 766–771 (2006).
- Bluhm, H. *et al.* Dephasing time of GaAs electron-spin qubits coupled to a nuclear bath exceeding 200  $\mu\text{s}$ . *Nature Phys.* **7**, 109–111 (2011).
- Buks, E., Schuster, R., Heiblum, M., Mahalu, D. & Umansky, V. Dephasing in electron interference by a 'which-path' detector. *Nature* **391**, 871–874 (1998).
- Meunier, T. *et al.* Experimental signature of phonon-mediated spin relaxation in a two-electron quantum dot. *Phys. Rev. Lett.* **98**, 126601 (2007).
- Barrett, M. D. *et al.* Deterministic quantum teleportation of atomic qubits. *Nature* **429**, 737–739 (2004).
- Riebe, M. *et al.* Deterministic quantum teleportation with atoms. *Nature* **429**, 734–737 (2004).
- Nielsen, M. A. & Chuang, I. L. *Quantum Computation and Quantum Information* (Cambridge Univ. Press, 2000).
- Stevenson, R. M. *et al.* A semiconductor source of triggered entangled photon pairs. *Nature* **439**, 179–182 (2006).
- Stötz, J. A. H., Hey, R., Santos, P. V. & Ploog, K. H. Coherent spin transport through dynamic quantum dots. *Nature Mater.* **4**, 585–588 (2005).
- Gustavsson, S. *et al.* Counting statistics of single-electron transport in a quantum dot. *Phys. Rev. Lett.* **96**, 076605 (2006).
- del Alamo, J. & Eugster, C. C. Quantum field-effect directional coupler. *Appl. Phys. Lett.* **56**, 78–80 (1990).
- Tsukada, N., Wieck, A. D. & Ploog, K. Proposal of novel electron wave coupled devices. *Appl. Phys. Lett.* **56**, 2527–2529 (1990).

**Supplementary Information** is linked to the online version of the paper at [www.nature.com/nature](http://www.nature.com/nature).

**Acknowledgements** We thank Y. Launay and P. Perrier for technical support. We acknowledge technical support from the 'Pôles Électroniques' of the 'Département Nano et MCBT' from the Institut Néel. M.Y. acknowledges financial support by Grant-in-Aid for Young Scientists A (no. 20684011) and ERATO-JST (080300000477). S.T. acknowledges financial support from Special Coordination Funds for Promoting Science and Technology (NanoQuine), Japan Science and Technology Agency Strategic International Cooperative Program, Japanese Ministry of Education, Culture, Sports, Science, and Technology KAKENHI 'Quantum Cybernetics', and Intelligence Advanced Research Projects Activity project 'Multi-Qubit Coherent Operations' through Harvard University. A.D.W. acknowledges expert help from D. Reuter and support of the Deutsche Forschungsgemeinschaft (SPP1285) and the Bundesministerium für Bildung und Forschung (QuaHLRep 01BQ1035). C.B. acknowledges financial support from Centre National de la Recherche Scientifique (DREI) – Japan Society for the Promotion of Science (nos PRC 424 and L08519). T.M. acknowledges financial support from Marie-Curie European Reintegration Grant 224786. We are grateful to the Nanoscience Foundation of Grenoble for partial financial support of this work.

**Author Contributions** S.H. and T.M. conceived and performed the experiments and analysed the data. Sh.T., M.Y. and S.T. were in charge of the sample fabrication and early stages of the experiment. A.D.W. performed the molecular beam epitaxy growth of the high-mobility GaAs/AlGaAs heterostructure. C.B. and T.M. wrote the manuscript. All authors contributed to the manuscript and discussed the results extensively.

**Author Information** Reprints and permissions information is available at [www.nature.com/reprints](http://www.nature.com/reprints). The authors declare no competing financial interests. Readers are welcome to comment on the online version of this article at [www.nature.com/nature](http://www.nature.com/nature). Correspondence and requests for materials should be addressed to C.B. ([bauerle@grenoble.cnrs.fr](mailto:bauerle@grenoble.cnrs.fr)) or T.M. ([tristan.meunier@grenoble.cnrs.fr](mailto:tristan.meunier@grenoble.cnrs.fr)).



# On-demand single-electron transfer between distant quantum dots

R. P. G. McNeil<sup>1</sup>, M. Kataoka<sup>1,2</sup>, C. J. B. Ford<sup>1</sup>, C. H. W. Barnes<sup>1</sup>, D. Anderson<sup>1</sup>, G. A. C. Jones<sup>1</sup>, I. Farrer<sup>1</sup> & D. A. Ritchie<sup>1</sup>

Single-electron circuits of the future, consisting of a network of quantum dots, will require a mechanism to transport electrons from one functional part of the circuit to another. For example, in a quantum computer<sup>1</sup> decoherence and circuit complexity can be reduced by separating quantum bit (qubit) manipulation from measurement and by providing a means of transporting electrons between the corresponding parts of the circuit<sup>2</sup>. Highly controlled tunnelling between neighbouring dots has been demonstrated<sup>3,4</sup>, and our ability to manipulate electrons in single- and double-dot systems is improving rapidly<sup>5–8</sup>. For distances greater than a few hundred nanometres, neither free propagation nor tunnelling is viable while maintaining confinement of single electrons. Here we show how a single electron may be captured in a surface acoustic wave minimum and transferred from one quantum dot to a second, unoccupied, dot along a long, empty channel. The transfer direction may be reversed and the same electron moved back and forth more than sixty times—a cumulative distance of 0.25 mm—without error. Such on-chip transfer extends communication between quantum dots to a range that may allow the integration of discrete quantum information processing components and devices.

Our device consists of two quantum dots connected by a long channel (Fig. 1A). Negative voltages applied to patterned metal surface gates deplete a two-dimensional electron gas that lies 90 nm below the

surface. The voltages are chosen such that the potential of the system is above the Fermi energy, and in thermal equilibrium the dots and channel contain no electrons.

The quantum dots are adjusted by the two plunger and barrier gates. Each plunger raises and lowers the corresponding dot and each barrier controls the degree of isolation between that dot and the neighbouring reservoir. Charge in each quantum dot is detected by its effect on the conductance of high-resistance constrictions<sup>9</sup> on the other side of a narrow ‘separation’ gate. A single electron can be initialized in one quantum dot (Fig. 1B, d) and then transferred at will to the other dot using a short burst of surface acoustic waves (SAWs). In a piezoelectric material (such as GaAs), SAWs create a moving potential modulation that can trap and transport electrons. The transferred electron can be returned using a second SAW pulse travelling in the opposite direction, giving two-way transfer.

Initialization of the dots is shown schematically in Fig. 1B. To set up an occupied left-hand quantum dot (LQD), the left-hand barrier gate (LBG) and left-hand plunger gate (LPG) are lowered to populate the LQD (Fig. 1B, a); the LBG is raised, isolating the LQD from the reservoir (Fig. 1B, b); and the LPG is raised to depopulate the dot selectively, leaving one electron (Fig. 1B, c) or more if desired (Supplementary Fig. 1). The LBG and LPG can then be stepped to their final voltages (Fig. 1B, d). The dot now contains a chosen number of electrons held close to, but below, the channel potential. An empty dot is initialized in

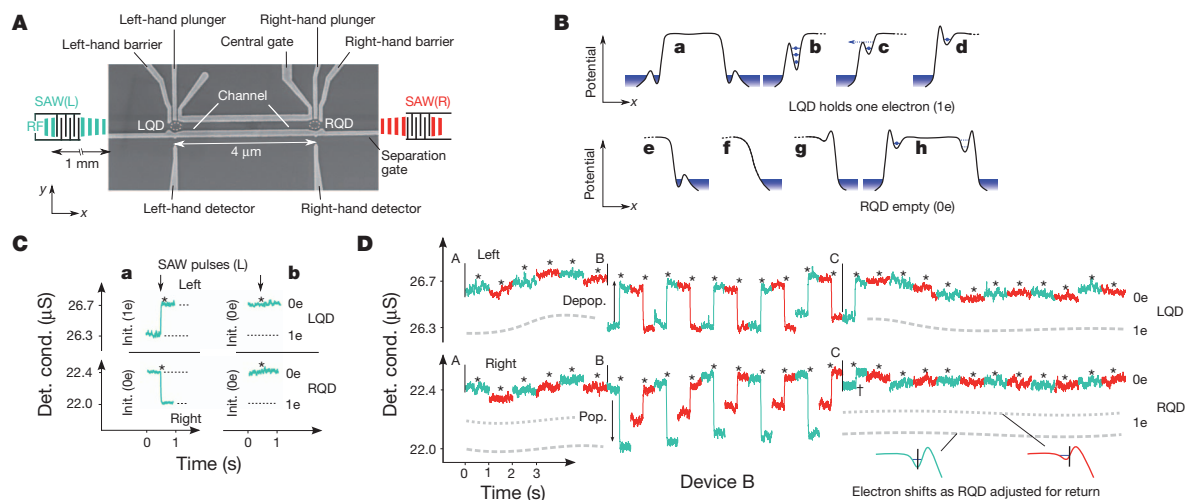


**Figure 1 | Device, initialization and single-electron transfer.** **A**, Scanning electron micrograph of device. Voltages applied to gates (light grey) create quantum dots (dashed circles) connected by a 4-μm channel. Applying a microwave (RF) pulse to the left- and right-hand transducers (placed 1 mm from the device) generates SAW pulses that trap and transport electrons. **B**, Schematic of the potential between the LQD and the RQD during initialization of the LQD with one electron (1e) (a–d) and then the RQD with no electrons (0e) (e–h). **C**, Change in detector conductance when SAW pulse (\*) is applied to the system set up as in **B**, h. The empty RQD is populated when

the electron leaves the LQD. The second pair of traces shows a control case in which the LQD starts empty (0e) (traces are 1 s long). **D**, Single-electron rally: the quantum dots and the channel are initialized to be empty before time A. Between time A and time B, a series of control pulses is used to verify that system is empty. At time B an electron is loaded into LQD. Between time B and time C, there is two-way transfer of a single electron between the quantum dots. At time C, the electron is removed from the system using a clearing pulse. The SAW pulse duration is 300 ns. The small step marked '+' is a random switching event and is not SAW driven. The time between traces is not plotted.

<sup>1</sup>Cavendish Laboratory, University of Cambridge, J. J. Thomson Avenue, Cambridge CB3 0HE, UK. <sup>2</sup>National Physical Laboratory, Hampton Road, Teddington TW11 0LW, UK.

a similar way but with the plunger gate being raised first (Fig. 1B, e–h). The final voltages for both the empty and occupied quantum dots (Fig. 1B, d and h) are the same and, thus, detector conductance indicates the number of electrons in each dot (Supplementary Information).

On-demand depopulation of an initialized quantum dot is achieved by a brief SAW pulse. Applying a microwave signal to the left-hand transducer generates a SAW. The accompanying potential modulation, moving at  $2,870 \text{ m s}^{-1}$ , captures the electron from the LQD and transfers it in 1.4 ns to the right-hand quantum dot (RQD). Part a of Fig. 1C shows the conductance of the left- and right-hand detectors for an occupied LQD (1e) and an unoccupied RQD (0e) when a SAW pulse (300 ns long) is sent from the left (SAW(L)). The transfer of charge is shown by simultaneous step changes in the detector conductance.

We know that the quantum dots are not simply exchanging electrons with their neighbouring reservoirs (in the direction opposite to that of SAW propagation) during the SAW pulse sequences, because in the control case, with an empty starting dot, no change in detector conductance is seen (Fig. 1C, b)). It is possible that electrons are instead being transferred by means of a ‘Newton’s cradle’ arrangement, whereby an electron from one dot moves into the channel, causing a series of electrons in traps along the channel to ‘shuffle up’, ejecting the last electron into the second dot. However, the SAW amplitude is 2.5 times greater than that at which electrons are caught in the channel, so there are no electrons to be shuffled along. Thus, in part a of Fig. 1C a single electron is being transferred between the dots.

The two transducers allow for bidirectional transfer between the quantum dots, and single electrons (or pairs) can be sent backwards and forwards in bursts (as in a game of ‘ping-pong’) with ‘rallies’ comprising tens to hundreds of SAW pulses. Figure 1D is an example of such a single-electron rally. Both quantum dots are emptied before time A, and six control pulses (three SAW(L)–SAW(R) pairs) show the system to be empty. At time B, an electron is loaded into the LQD. The electron is then sent back and forth by ten alternating SAW pulses (five pairs) until at time C the RQD barrier is partly lowered and a ‘clearing’ pulse removes the electron from the channel—in this case to the right-hand reservoir but potentially into the next section of a quantum dot circuit. The small step in the right detector signal ( $\dagger$ ) is a random switching event near the detector. It is not coincident with the SAW pulse but occurs 50 ms later. No further electron movement is seen in the subsequent ten pulses.

In this device, rallies of over 60 pulses were possible with a single electron going back and forth between the quantum dots. A run of 35 transfers is shown in Fig. 2a, and the statistics of the full data set are shown in Fig. 2b. Rallies are broken when the transfer fails, which can occur in one of two ways. Occasionally, depopulation of the starting dot fails (marked F in Fig. 2b), in which case no electron arrives in the second dot. The chances of this can be reduced by increasing the potential of the starting dot, towards that of the channel, or by increasing the SAW amplitude, although larger SAWs can pose problems, for example by lifting the transferred electron over the barrier of the second dot. Given successful depopulation, transfer may still fail if the electron becomes trapped in the channel (marked T). This type of failure was more common in pulses from the weaker, right-hand, transducer and examples can be seen in Fig. 2a (also marked T). Here a SAW(R) pulse fails to transfer the electron all the way to the LQD, leaving it trapped in the channel. However, the next pulse from the other transducer recovers this electron, returning it to the RQD. The probability of recovery (marked R) is lower than the probability of transfer (marked S), indicating that electrons trapped in the channel may relax deeper into impurity traps than electrons that are carried through in SAW minima. This second type of error can also occur in another way (X, not shown), described later, but this can be eliminated by lowering the potential in the second dot.

A third error mechanism (marked E in Fig. 2b) is the arrival of an additional electron, which is then transferred with the initial electron. Electrons are seen to enter the system during pulses from the right-hand

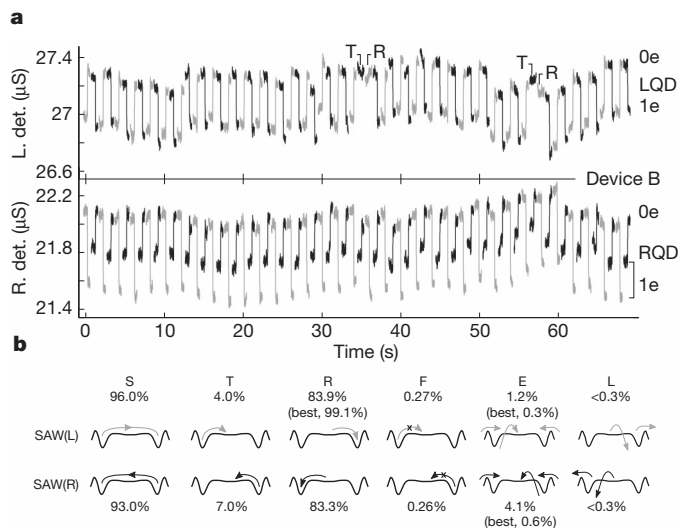


**Figure 2 | Single-electron transfer reliability.** a, Example of bidirectional electron transfer. An electron is transferred between the quantum dots 35 times before getting trapped in the channel (T). The next SAW(L) pulse recovers the electron (R). The SAW pulse duration is 300 ns, and the time between traces is not plotted. b, Transfer statistics for full data set (excerpt seen in a), showing probabilities of various events for SAW(L) and SAW(R): ideal transfer (S), depopulation to channel trap (T), recovery from channel (R), failure to depopulate (F), arrival of additional electron (E), loss of electron from system (L). Values in parentheses are for different voltages.

transducer that may have been caused or exacerbated by adjusting the RQD before the SAW(R) pulses started. No electrons appeared in the system during SAW(L) pulses. Increasing the isolation of the quantum dots and the channel from the surrounding reservoirs will reduce this. In none of the traces is the electron seen to leave the system (marked L).

The ability of SAWs to transport electrons depends on the SAW amplitude relative to the potential<sup>10,11</sup>. Removing an electron from the starting dot requires a SAW of sufficient amplitude to overcome the sloping potential and lift the electron into the channel. If the SAW amplitude is too large, it will carry the electron over the far barrier and out of the second dot. Thus, there is a practical limit to the SAW amplitude for a given barrier–plunger combination, and for small-amplitude SAWs the dot needs to be raised towards the channel potential. Figure 3a shows the mean initial population of the LQD and Fig. 3b shows how depopulation changes with SAW power and plunger voltage ( $V_{\text{LPG}}$ ). The potential gradient between the LQD and the channel decreases as  $V_{\text{LPG}}$  increases, allowing smaller-amplitude SAWs with a shallower gradient to lift electrons from the dot. Thus, the onset of depopulation occurs along a diagonal line, between the dashed lines in Fig. 3b, and depopulation of the deeper dots requires larger-amplitude SAWs.

The pulse width of the SAWs may be varied instead of the power. It has previously been shown<sup>12</sup> that a SAW can be used to modulate the barriers to an isolated dot, causing population and depopulation of the dot in a probabilistic process that requires many cycles to ensure a depopulation probability of >50%. Figure 3c shows how SAW pulse width, that is, the number of attempts or SAW minima, affects depopulation of the LQD.

Applied pulses are not reproduced exactly in the SAW pulses owing to bandwidth limitations of the transducers; pulses longer than 14 ns should vary only in duration and not in peak amplitude. At a pulse width of 10.0 ns (27.7 cycles), the reduction in pulse amplitude due to transducer bandwidth is visible at the lower plunger voltages, where electrons cannot be depopulated. At 12.6 ns (34.9 cycles), just ~7 cycles more, depopulation is seen across almost the full range, and, as expected, at 14.5 ns the SAW is able to remove electrons over the same range as pulses of much longer width. From the rapid onset as the



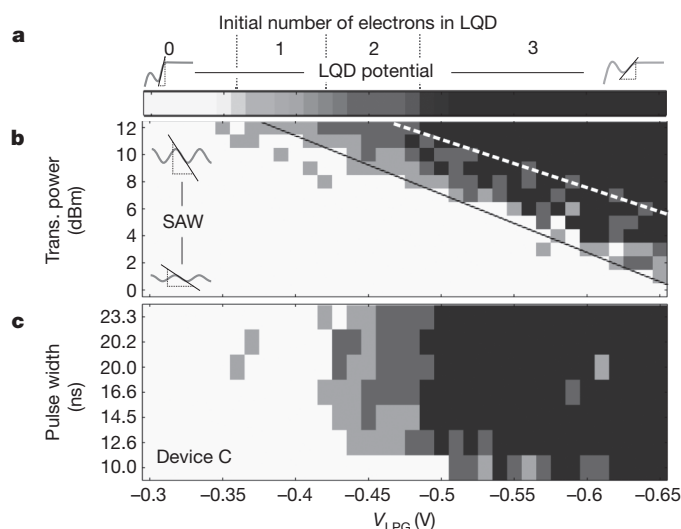


**Figure 3 | Dependence of LQD depopulation on SAW power and pulse width.** **a**, Initial population of LQD as a function of plunger voltage ( $V_{LPG}$ ). The same greyscale key is used in **b** and **c** to indicate the number of electrons removed by the pulse. **b**, Depopulation of the LQD at different SAW(L) transducer powers; pulse width, 100 ns. The relative slope of the SAW (maximum slope as indicated) and the potential determine whether depopulation occurs. **c**, Depopulation of the LQD at different pulse widths for a SAW(L) power of 11 dBm. Pulse widths shorter than 14.5 ns do not achieve full amplitude, so depopulation fails at smaller values of  $V_{LPG}$ . By comparison with **b**, the peak SAW powers at pulse widths of 10 and 12.6 ns can be estimated as 7 and 10 dBm, respectively. Pulse widths are measured values of the microwave source and not linearly spaced.

pulse width increases, with depopulation going from approximately zero to complete in just 12.5 cycles, we can say that once a sufficient SAW amplitude is reached, depopulation occurs during the first few ( $\sim 7$ ) cycles of the pulse. Pulses applied to a transducer with a wider bandwidth (fewer fingers) would have shorter rise times, allowing this to be probed further.

This system also provides a method of investigating energy loss mechanisms for electrons above the Fermi energy. As a SAW minimum transfers an electron, it lifts it over 'bumps' in the potential, raising and lowering its potential energy as necessary. However, when the potential gradient exceeds the maximum SAW gradient, confinement is lost and a 'hot' electron escapes backwards towards the channel (Fig. 4a). The energy at which this occurs depends on the underlying potential. Figure 4b shows how varying the right-hand barrier voltage ( $V_{RBG}$ ) affects the escape probability and the initial energy of escaping electrons. An electron starts in the RQD and a long (300-ns) SAW pulse is sent from the left. Electrons escaping the SAW potential at a low energy will remain in the dot (Z in Fig. 4a), at higher energies they will escape to the channel (Y), and at energies above the channel maximum they will reach the LQD (X). During a pulse, an X or Y electron may be returned to the RQD and 'recycled', with its ultimate position (LQD, trapped in channel, RQD) being determined during the last part of the SAW pulse as the amplitude drops. For  $V_{RBG} > -1.2$  V, transfer to the LQD is unlikely, no electrons are transferred to the LQD and the probability of staying in the RQD (Z) is  $>90\%$ . For  $V_{RBG} < -1.3$  V, the probability of leaving the RQD (X or Y) increases to  $>50\%$  and the probability of escaping to the LQD (X) reaches 25%. In Fig. 4b, open symbols are for a less negative plunger voltage and show a reduced probability of transfer from the RQD because this dot is correspondingly deeper.

Electrons with a large excess of energy rapidly lose energy by emitting an optical phonon (of energy 36 meV) in about 1 ps (ref. 13), comparable to the time taken by an electron to cross one quantum dot. Electrons with energies less than 36 meV can emit acoustic phonons only with typical energies  $\leq 0.1$  meV, and emit these phonons more slowly. In the low-energy limit, this is on a 100-ns timescale<sup>14</sup>. The addition of a gate across the centre of the channel, capable of being

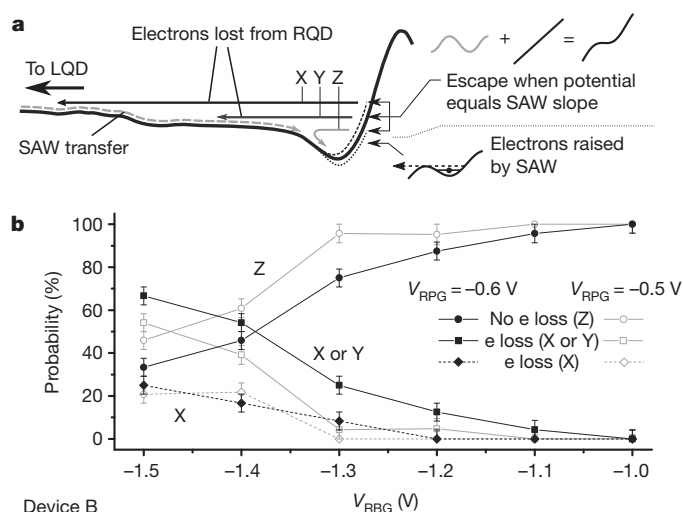


**Figure 4 | Backscattering of electrons in the RQD due to SAW(L).** **a**, An electron in the RQD will be lifted up the right-hand barrier by SAW(L) until it either leaves the system or the underlying potential becomes too steep for the SAW minimum to retain the electron. Electrons remain in the dot (Z), escape to traps in the channel (Y) or escape to the LQD (X). **b**, Probabilities of events X, Y, Z as functions of barrier voltage. (Open symbols are for a slightly deeper RQD potential ( $V_{RPG}$ )). A threshold is evident at around  $-1.3$  V: for  $V_{RBG} < -1.3$  V, escape to the LQD is possible, whereas for  $V_{RBG} > -1.3$  V, escape to the LQD is prevented by the channel potential. Error bars, 1 s.d.

pulsed at high frequencies, would provide a method of investigating emission of acoustic phonons by high-energy electrons.

This source of high-energy electrons may be of use in p-n junction devices as a way to controllably introduce single electrons into a region of holes as a single-photon source<sup>15</sup>, without requiring negatively charged gates in close proximity to the holes.

To be useful in a quantum information circuit, the transfer of an electron must not cause its spin state to decohere. Coherent transfer of a collection of spins has been demonstrated over a distance of 70  $\mu\text{m}$  (for a particular wafer orientation), with the potential to extend this much further<sup>16</sup>; and coherent oscillations of charge have been shown over a submicrometre distance<sup>17</sup>. Fluctuations in the magnetic field created by nuclear spins ( $B_{\text{Nuc}}$ ) are the main cause of dephasing in static quantum dots; however, an electron trapped in a moving SAW quantum dot samples many different local  $B_{\text{Nuc}}$  fields, spending only a brief time in each. The average  $B_{\text{Nuc}}$ , and hence, dephasing, is reduced by three orders of magnitude owing to the motion of the SAW (more details of dephasing mechanisms are given in Supplementary Information). It is therefore likely that coherent transfer of spins is achievable and that dephasing will actually be suppressed during transfer.

In an ideal quantum dot network, with a perfectly smooth potential, an electron could simply be allowed to 'roll' from an elevated starting dot down to the second dot. In practice, the potential is far from perfect and irregularities in the background potential would make this method of transfer highly unreliable. A pulse of SAWs, however, can be used to modulate the channel temporarily, assisting the transfer in a peristaltic-like movement, the amplitude of which can be tuned to the minimum required to overcome desired obstacles, allowing on-demand removal and delivery of single electrons between distant quantum dots in a manner that should be compatible with many of the quantum computing proposals based on electronic spin states in semiconductors.

## METHODS SUMMARY

The two-dimensional electron gas was formed at the interface of a GaAs/AlGaAs heterostructure. Before depletion, the carrier density was  $1.6 \times 10^{11} \text{ cm}^{-2}$  and the carrier mobility was  $1.8 \times 10^6 \text{ cm}^2 \text{ V}^{-1} \text{ s}^{-1}$ . We made several devices; results for devices B and C are reported here. Devices and transducers were patterned by electron-beam lithography. All measurements were made at 300 mK. Radio-frequency signals were applied to transducers using an Agilent 8648D source

(external modulation option). To prevent Bragg reflections, transducers were of double-element design<sup>18</sup>, with 30 pairs of fingers. The detector circuits shared a common source with a  $\sim 1$ -mV d.c. bias. In device B, the position of the RQD was adjusted between the capture and transfer positions to aid depopulation by the weaker, right-hand, transducer. This adjustment shifted the dot minimum relative to the right-hand detector, making the return steps smaller. The gate set-up time between traces was 2–8 s. The applied radio-frequency power in Fig. 1d was 10 dBm for SAW(L) and 18 dBm for SAW(R), and the attenuation from the source to the transducers was 10 dB for SAW(L) and 20–30 dB for SAW(R).

Received 5 May; accepted 12 August 2011.

1. Loss, D. & DiVincenzo, D. P. Quantum computation with quantum dots. *Phys. Rev. A* **57**, 120–126 (1998).
2. Barnes, C. H. W., Shilton, J. M. & Robinson, A. M. Quantum computation using electrons trapped by surface acoustic waves. *Phys. Rev. B* **62**, 8410–8419 (2000).
3. Petta, J. R. *et al.* Coherent manipulation of coupled electron spins in semiconductor quantum dots. *Science* **309**, 2180–2184 (2005).
4. Pioro-Ladrière, M. *et al.* Electrically driven single-electron spin resonance in a slanting Zeeman field. *Nature Phys.* **4**, 776–779 (2008).
5. Elzerman, J. M. *et al.* Single-shot read-out of an individual electron spin in a quantum dot. *Nature* **430**, 431–435 (2004).
6. Hanson, R. *et al.* Single-shot readout of electron spin states in a quantum dot using spin-dependent tunnel rates. *Phys. Rev. Lett.* **94**, 196802 (2005).
7. Morello, A. *et al.* Single-shot readout of an electron spin in silicon. *Nature* **467**, 687–691 (2010).
8. Hanson, R., Kouwenhoven, L. P., Petta, J. R., Tarucha, S. & Vandersypen, L. M. K. Spins in few-electron quantum dots. *Rev. Mod. Phys.* **79**, 1217–1265 (2007).
9. Field, M. *et al.* Measurements of Coulomb blockade with a noninvasive voltage probe. *Phys. Rev. Lett.* **70**, 1311–1314 (1993).
10. Kataoka, M., Barnes, C. H. W., Beere, H. E., Ritchie, D. A. & Pepper, M. Experimental investigation of the surface acoustic wave electron capture mechanism. *Phys. Rev. B* **74**, 085302 (2006).
11. Rahman, S., Kataoka, M., Barnes, C. H. W. & Langtangen, H. P. Numerical investigation of a piezoelectric surface acoustic wave interaction with a one-dimensional channel. *Phys. Rev. B* **74**, 035308 (2006).
12. Kataoka, M. *et al.* Single-electron population and depopulation of an isolated quantum dot using a surface-acoustic-wave pulse. *Phys. Rev. Lett.* **98**, 046801 (2007).
13. Taubert, D. *et al.* Relaxation of hot electrons in a degenerate two-dimensional electron system: transition to one-dimensional scattering. *Phys. Rev. B* **83**, 235404 (2011).
14. Fujisawa, T. *et al.* Spontaneous emission spectrum in double quantum dot devices. *Science* **282**, 932–935 (1998).
15. Gell, J. R. *et al.* Surface-acoustic-wave-driven luminescence from a lateral p–n junction. *Appl. Phys. Lett.* **89**, 243505 (2006).
16. Stotz, J. A. H., Hey, R., Santos, P. V. & Ploog, K. H. Coherent spin transport through dynamic quantum dots. *Nature Mater.* **4**, 585–588 (2005).
17. Kataoka, M. *et al.* Coherent time evolution of a single-electron wave function. *Phys. Rev. Lett.* **102**, 156801 (2009).
18. Morgan, D. *Surface Acoustic Wave Design* 9–18 (Academic, 2007).

**Supplementary Information** is linked to the online version of the paper at [www.nature.com/nature](http://www.nature.com/nature).

**Acknowledgements** The authors acknowledge funding from the UK EPSRC, Toshiba Research Europe Limited and QIPIRC.

**Author Contributions** R.P.G.M., M.K., C.J.B.F. and C.H.W.B. designed the experiment; I.F. and D.A.R. provided wafers; D.A. and G.A.C.J. performed electron-beam lithography; R.P.G.M. processed samples and analysed data; R.P.G.M. and M.K. performed experiments; R.P.G.M., C.J.B.F. and M.K. wrote the paper.

**Author Information** Reprints and permissions information is available at [www.nature.com/reprints](http://www.nature.com/reprints). The authors declare no competing financial interests. Readers are welcome to comment on the online version of this article at [www.nature.com/nature](http://www.nature.com/nature). Correspondence and requests for materials should be addressed to C.J.B.F. ([cjbf@cam.ac.uk](mailto:cjbf@cam.ac.uk)).



# Bioinspired self-repairing slippery surfaces with pressure-stable omniphobicity

Tak-Sing Wong<sup>1</sup>, Sung Hoon Kang<sup>1</sup>, Sindy K. Y. Tang<sup>1</sup>, Elizabeth J. Smythe<sup>2</sup>, Benjamin D. Hatton<sup>1</sup>, Alison Grinthal<sup>1</sup> & Joanna Aizenberg<sup>1</sup>

Creating a robust synthetic surface that repels various liquids would have broad technological implications for areas ranging from biomedical devices and fuel transport to architecture but has proved extremely challenging<sup>1</sup>. Inspirations from natural non-wetting structures<sup>2–6</sup>, particularly the leaves of the lotus, have led to the development of liquid-repellent microtextured surfaces that rely on the formation of a stable air–liquid interface<sup>7–9</sup>. Despite over a decade of intense research, these surfaces are, however, still plagued with problems that restrict their practical applications: limited oleophobicity with high contact angle hysteresis<sup>9</sup>, failure under pressure<sup>10–12</sup> and upon physical damage<sup>1,7,11</sup>, inability to self-heal and high production cost<sup>1,11</sup>. To address these challenges, here we report a strategy to create self-healing, slippery liquid-infused porous surface(s) (SLIPS) with exceptional liquid- and ice-repellency, pressure stability and enhanced optical transparency. Our approach—inspired by *Nepenthes* pitcher plants<sup>13</sup>—is conceptually different from the lotus effect, because we use nano/microstructured substrates to lock in place the infused lubricating fluid. We define the requirements for which the lubricant forms a stable, defect-free and inert ‘slippery’ interface. This surface outperforms its natural counterparts<sup>2–6</sup> and state-of-the-art synthetic liquid-repellent surfaces<sup>8,9,14–16</sup> in its capability to repel various simple and complex liquids (water, hydrocarbons, crude oil and blood), maintain low contact angle hysteresis ( $<2.5^\circ$ ), quickly restore liquid-repellency after physical damage (within 0.1–1 s), resist ice adhesion, and function at high pressures (up to about 680 atm). We show that these properties are insensitive to the precise geometry of the underlying substrate, making our approach applicable to various inexpensive, low-surface-energy structured materials (such as porous Teflon membrane). We envision that these slippery surfaces will be useful in fluid handling and transportation, optical sensing, medicine, and as self-cleaning and anti-fouling materials operating in extreme environments.

The cutting edge in development of synthetic liquid-repellent surfaces is currently inspired by the lotus effect<sup>2</sup>: water droplets are supported by surface textures on a composite solid–air interface that enables them to roll off easily<sup>17,18</sup>. However, this approach, while promising, suffers from inherent limitations that severely restrict its applicability. First, trapped air is a largely ineffective cushion against organic liquids or complex mixtures that, unlike water, have low surface tension, which strongly destabilizes suspended droplets<sup>19</sup>. Moreover, the air trapped within the texture cannot stand up to pressure, so that liquids, particularly those with low surface tension, can easily penetrate the texture under even slightly increased pressures or upon impact<sup>10</sup>, conditions commonly encountered with driving rain or in underground transport pipes. Furthermore, synthetic textured solids are prone to irreversible defects arising from mechanical damage and fabrication imperfections<sup>1,11</sup>: because each defect enhances the likelihood of the droplet pinning and sticking in place, textured surfaces are not only difficult to optimize for liquid mobility but inevitably stop working over time as

irreparable damage accumulates. Recent progress in pushing these limits with increasingly complex structures and chemistries remains outweighed by substantial trade-offs in physical stability, optical properties, large-scale feasibility, and/or difficulty and expense of fabrication<sup>8,9,14,15</sup>.

Nature, however, offers a remarkably simple alternative idea that has nothing to do with the lotus effect yet again capitalizes on micro-textures: instead of using the structures to repel impinging liquids directly, systems such as the *Nepenthes* pitcher plant use them to lock-in an intermediary liquid that then acts by itself as the repellent surface<sup>13</sup>. Well-matched solid and liquid surface energies, combined with the microtextural roughness, create a highly stable state in which the liquid fills the spaces within the texture and forms a continuous overlying film<sup>20</sup>. In pitcher plants, this film is aqueous and effective enough to cause insects that step on it to slide from the rim into the digestive juices at the bottom by repelling the oils on their feet<sup>21</sup>.

Inspired by this idea, we report synthetic liquid-repellent surfaces—which we name ‘slippery liquid-infused porous surface(s)’ (SLIPS)—that each consist of a film of lubricating liquid locked in place by a micro/nanoporous substrate (Fig. 1a). The premise for our design is that a liquid surface is intrinsically smooth and defect-free down to the molecular scale; provides immediate self-repair by wicking into damaged sites in the underlying substrate; is largely incompressible; and can be chosen to repel immiscible liquids of virtually any surface tension. We show that our SLIPS creates a smooth, stable interface that nearly eliminates pinning of the liquid contact line for both high- and low-surface-tension liquids, minimizes pressure-induced impalement into the porous structures, self-heals and retains its function following mechanical damage, and can be made optically transparent.

We designed the SLIPS based on three criteria: (1) the lubricating liquid must wick into, wet and stably adhere within the substrate, (2) the solid must be preferentially wetted by the lubricating liquid rather than by the liquid one wants to repel, and (3) the lubricating and impinging test liquids must be immiscible. The first requirement is satisfied by using micro/nanotextured, rough substrates whose large surface area, combined with chemical affinity for the liquid, facilitates complete wetting by, and adhesion of, the lubricating fluid (Supplementary Fig. 1)<sup>22,23</sup>. To satisfy the second criterion—the formation of a stable lubricating film that is not displaced by the test liquid (Fig. 1b)—we determine the chemical and physical properties required for working combinations of substrates and lubricants. We compare the total interfacial energies of textured solids that are completely wetted by either an arbitrary immiscible liquid ( $E_A$ ), or a lubricating fluid with ( $E_1$ ) or without ( $E_2$ ) a fully wetted immiscible test liquid floating on top of it. To ensure the solid is wetted preferentially by the lubricating fluid one should have  $\Delta E_1 = E_A - E_1 > 0$  and  $\Delta E_2 = E_A - E_2 > 0$ . The equations can be expressed as (see Supplementary Discussion)<sup>24</sup>:

$$\Delta E_1 = R(\gamma_B \cos \theta_B - \gamma_A \cos \theta_A) - \gamma_{AB} > 0 \quad (1)$$

<sup>1</sup>School of Engineering and Applied Sciences, Wyss Institute for Biologically Inspired Engineering and Kavli Institute for Bionano Science and Technology, Harvard University, Cambridge, Massachusetts 02138, USA. <sup>2</sup>Schlumberger-Doll Research Center, Schlumberger, Cambridge, Massachusetts 02139, USA.

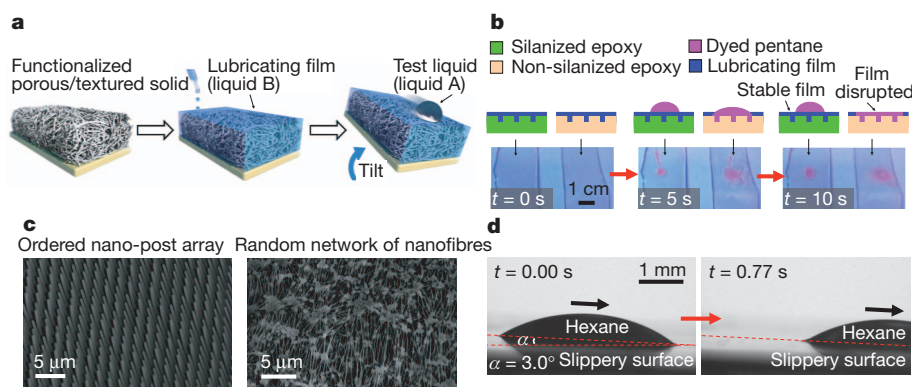


**Figure 1 | Design of SLIPS.** **a**, Schematics showing the fabrication of a SLIPS by infiltrating a functionalized porous/textured solid with a low-surface-energy, chemically inert liquid to form a physically smooth and chemically homogeneous lubricating film on the surface of the substrate (see Methods Summary). **b**, Comparison of the stability and displacement of lubricating films on silanized and non-silanized textured epoxy substrates. Top panels show schematic side views; bottom panels show time-lapse optical images of

top views. Dyed pentane was used to enhance visibility. **c**, Scanning electron micrographs showing the morphologies of porous/textured substrate materials: an epoxy-resin-based nanofabricated post array (left) and a Teflon-based porous nanofibre network (right). **d**, Optical micrographs demonstrating the mobility of a low-surface-tension liquid hydrocarbon—hexane ( $\gamma_A = 18.6 \pm 0.5 \text{ mN m}^{-1}$ , volume  $\sim 3.6 \mu\text{l}$ )—sliding on a SLIPS at a low angle ( $\alpha = 3.0^\circ$ ).

$$\Delta E_2 = R(\gamma_B \cos \theta_B - \gamma_A \cos \theta_A) + \gamma_A - \gamma_B > 0 \quad (2)$$

where  $\gamma_A$  and  $\gamma_B$  are the surface tensions for the test liquid to be repelled and the lubricating fluid,  $\gamma_{AB}$  is the interfacial tension at the liquid–liquid interface,  $\theta_A$  and  $\theta_B$  are the equilibrium contact angles of the immiscible test liquid and the lubricating fluid on a flat solid surface, and  $R$  is the roughness factor (the ratio between the actual and projected surface areas of the textured solids<sup>23</sup>).

From these principles, we fabricated a set of SLIPS designed to repel liquids spanning a broad range of surface tensions. To generate roughness, we tested two types of porous solids, periodically ordered and random: arrays of nanoposts functionalized with a low-surface-energy polyfluoroalkyl silane<sup>25</sup>, and a random network of Teflon nanofibres distributed throughout the bulk substrate, respectively (Fig. 1c). For the lubricating film, we chose low-surface-tension perfluorinated liquids (for example, 3M Fluorinert FC-70,  $\gamma_B = 17.1 \text{ mN m}^{-1}$ ; or DuPont Krytox oils) that are non-volatile and are immiscible with both aqueous and hydrocarbon phases and therefore able to form a stable, slippery interface with our solid substrates (that is,  $\Delta E_1 > 0$  and  $\Delta E_2 > 0$ ) for a variety of polar and non-polar liquids including water, acids and bases, alkanes, alcohols and ketones (Figs 1d and 2a, b). The SLIPS were generated through liquid imbibition into the porous materials<sup>23</sup>, resulting in a homogeneous and nearly molecularly smooth surface with a roughness of about 1 nm (Supplementary Fig. 2).

Each of these SLIPS exhibits extreme liquid repellency as signified by very low contact angle hysteresis ( $\Delta\theta < 2.5^\circ$ , Fig. 2b) and by very low sliding angles ( $\alpha \leq 5^\circ$  for droplet volume  $\geq 2 \mu\text{l}$ ; Supplementary Fig. 3) against liquids of surface tension ranging from  $\sim 17.2 \pm 0.5 \text{ mN m}^{-1}$  (*n*-pentane) to  $72.4 \pm 0.1 \text{ mN m}^{-1}$  (water). Contact angle hysteresis (that is, the difference between the advancing and receding contact angles of a moving droplet), and sliding angle (that is, the surface tilt required for droplet motion) directly characterize resistance to mobility<sup>26</sup>; the low values therefore confirm a lack of pinning, consistent with a nearly defect-free surface<sup>27</sup>. Based on the measured contact angle hysteresis and droplet volume ( $\sim 4.5 \mu\text{l}$ ), the estimated liquid retention force<sup>28</sup> on each of the SLIPS is  $0.83 \pm 0.22 \mu\text{N}$  for  $n = 6$ . This performance is nearly an order of magnitude better than the state-of-the-art lotus-leaf-inspired omniphobic surfaces, whose liquid retention forces are of the order of 5  $\mu\text{N}$  for low-surface-tension liquids (that is,  $\gamma_A < 25 \text{ mN m}^{-1}$ ) at similar liquid volumes<sup>9</sup>. Moreover, the liquid-repellency of SLIPS is insensitive to texture geometry (Fig. 2b), provided that the lubricating layer covers the textures (Supplementary Fig. 4). This further confirms that liquid repellency is primarily conferred by the lubricating film, with the porous solid having the

secondary, but critically important, role of immobilizing the film. Additionally, unlike lotus-leaf-inspired omniphobic surfaces where contact angle hysteresis depends on liquid surface tension and increases dramatically upon decrease of surface tension (Fig. 2b), such a dependence is absent for SLIPS owing to the chemical homogeneity and physical smoothness of the liquid–liquid interface.

Experiments performed in a pressurized nitrogen environment show that SLIPS are capable of repelling water and liquid hydrocarbons both at and while transitioning to a pressure of  $\sim 676 \text{ atm}$  (the highest available pressure in our setup). This is equivalent to the hydrostatic pressure at a depth of  $\sim 7 \text{ km}$  (Fig. 2c, Supplementary Movie 1). To our knowledge, the highest recorded pressure stability of a superhydrophobic surface for water is  $\sim 7 \text{ atm}$  (ref. 16). However, it is important to note that pressure stability for structured surfaces decreases drastically for liquids with low surface tension. For example, recent pressure stability studies of omniphobic surfaces based on impacting hexadecane droplets and evaporating octane droplets demonstrated stability up to only 400 to 1,400 Pa ( $4 \times 10^{-3}$  to  $1.4 \times 10^{-2} \text{ atm}$ )<sup>9,10</sup>. Whereas the reported omniphobic surfaces fail upon dynamic impact of low-surface-tension liquids<sup>10</sup>, SLIPS repel impacting droplets for a wide assortment of liquid hydrocarbons (Supplementary Fig. 5).

The lubricating film also serves as a self-healing coating to rapidly restore the liquid-repellent function following damage of the porous material by abrasion or impact. The fluidic nature of the lubricating layer means that the liquid simply flows towards the damaged area by surface-energy-driven capillary action<sup>29</sup>, and spontaneously refills the physical voids. As observed by high-speed camera imaging, the measured self-recovery time for a  $\sim 50\text{-}\mu\text{m}$  fluid displacement of the FC-70 lubricating layer on an epoxy-resin-based SLIPS is  $\sim 150 \text{ ms}$  (Fig. 3a)<sup>15</sup>. Even more impressively, SLIPS can repeatedly restore their liquid-repellent function upon recurring, large-area physical damage (Fig. 3b, Supplementary Fig. 6 and Supplementary Movie 2).

We further demonstrate that, by choosing substrate and lubricant materials with matching refractive indices, SLIPS can be engineered for enhanced optical transparency in visible and/or near-infrared wavelengths (Fig. 3c–e). Optical transparency is challenging to achieve through superhydrophobic surfaces, because they require nanostructures with dimensions under the sub-diffraction limit ( $< \sim 100 \text{ nm}$ )<sup>30</sup>; the large difference in refractive index at the solid–air interface of these structured surfaces results in significant light scattering that reduces light transmission (Fig. 3c–e).

In addition to repelling liquids in their pure forms, SLIPS effectively repel complex fluids, such as crude oil (Fig. 4a, Supplementary



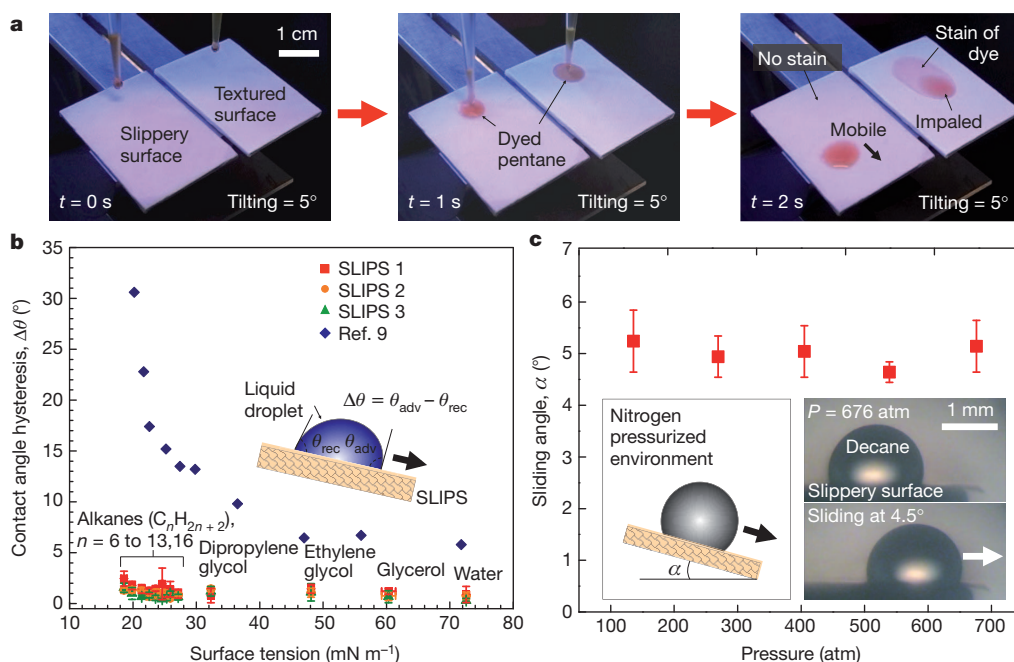


**Figure 2 | Omniphobicity and high-pressure stability of SLIPS.** **a**, Time-sequence images comparing mobility of pentane droplets ( $\gamma_A = 17.2 \pm 0.5 \text{ mN m}^{-1}$ , volume  $\sim 30 \mu\text{l}$ ) on a SLIPS and a superhydrophobic, air-containing Teflon porous surface. Pentane is repelled on the SLIPS, but it wets and stains the traditional superhydrophobic surface. **b**, Comparison of contact angle hysteresis as a function of surface tension of test liquids (indicated) on SLIPS and on an omniphobic surface reported in ref. 9. In the inset, the advancing and receding contact angles of a liquid droplet are denoted as  $\theta_{\text{adv}}$  and  $\theta_{\text{rec}}$ , respectively. SLIPS 1, 2 and 3 refer to the surfaces made of Teflon porous membrane (SLIPS 1), an array of epoxy posts of

geometry 1 (pitch  $\sim 2 \mu\text{m}$ , height  $\sim 5 \mu\text{m}$ , post diameter  $\sim 300 \text{ nm}$ ) (SLIPS 2) and an array of epoxy posts of geometry 2 (pitch  $\sim 900 \text{ nm}$ , height  $\sim 500 \text{ nm}$ , post diameter  $\sim 300 \text{ nm}$ ) (SLIPS 3). Error bars indicate standard deviations from three independent measurements. **c**, A plot showing the high pressure stability of SLIPS, as evident from the low sliding angle of a decane droplet ( $\gamma_A = 23.6 \pm 0.1 \text{ mN m}^{-1}$ , volume  $\sim 3 \mu\text{l}$ ) subjected to pressurized nitrogen gas in a pressure chamber (Supplementary Methods, Supplementary Movie 1). Error bars indicate standard deviations from at least seven independent measurements.

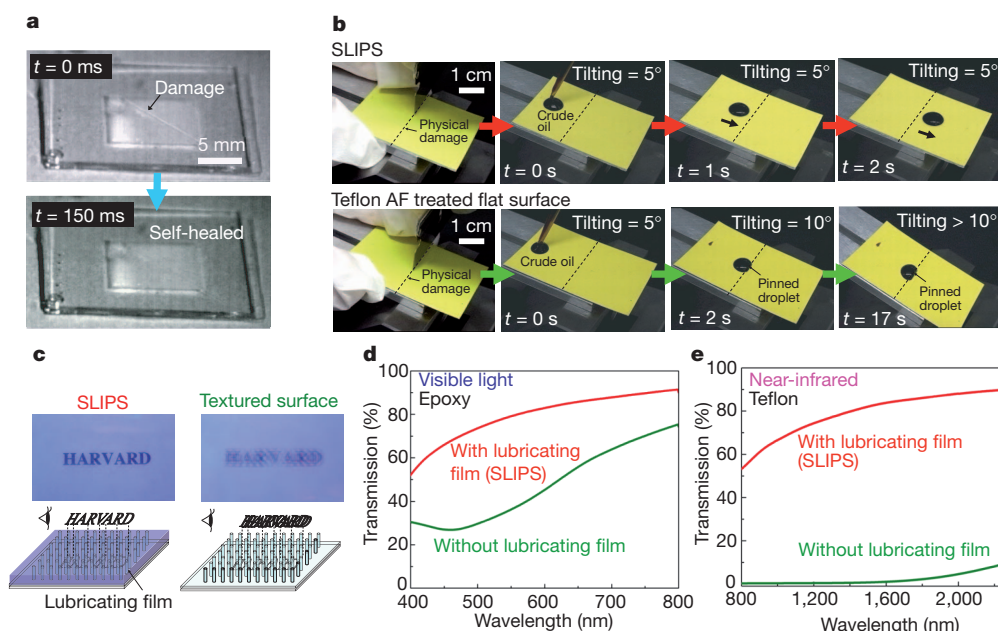


**Figure 3 | Self-healing and optical transparency of SLIPS.** **a**, Time-lapse images showing the capability of a SLIPS to self-heal from physical damage  $\sim 50 \mu\text{m}$  wide on a timescale of the order of 100 ms. **b**, Time-lapse images showing the restoration of liquid repellency of a SLIPS after physical damage, as compared to a typical hydrophobic flat surface (coated with DuPont Teflon AF amorphous fluoropolymers) on which oil remains pinned at the damage site (Supplementary Movie 2). **c**, Optical images showing enhanced optical

transparency of an epoxy-resin-based SLIPS (left) as compared to significant scattering in the non-infused superhydrophobic nanostructured surface (right) in the visible light range. Top panels show top views; bottom panels show schematic side views. **d**, Optical transmission measurements for an epoxy-resin-based SLIPS in the visible light range (400–750 nm). **e**, Optical transmission measurements for a Teflon-based SLIPS in the near-infrared range (800–2,300 nm).

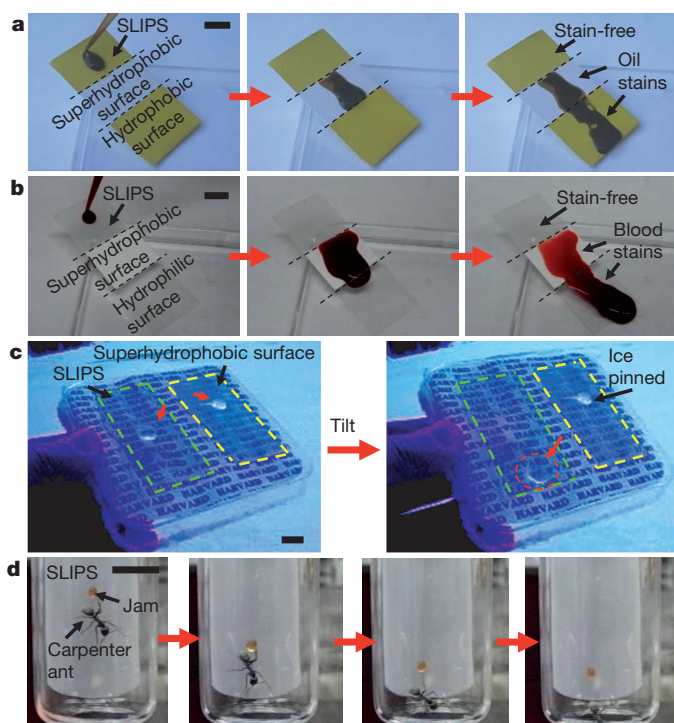


**Figure 4 | Repellency of complex fluids, ice and insects by SLIPS.**

**a**, Movement of light crude oil on a substrate composed of a SLIPS, a superhydrophobic Teflon porous membrane, and a flat hydrophobic surface. Note the slow movement on and staining of the latter two regions (Supplementary Movie 3). **b**, Comparison of the ability to repel blood by a SLIPS, a superhydrophobic Teflon porous membrane, and a flat hydrophilic glass surface. Note the slow movement on and staining of the latter two regions (Supplementary Movie 4). **c**, Ice mobility on a SLIPS (highlighted in green) compared to strong adhesion to an epoxy-resin-based nanostructured superhydrophobic surface (highlighted in yellow, see also Supplementary Movie 5). The experiments were performed outdoors (note the snow in the background) when temperature and relative humidity were  $-4^{\circ}\text{C}$  and  $\sim 45\%$ , respectively. Note also the reduced frosting and the resulting transparency of the SLIPS. **d**, Demonstration of the inability of a carpenter ant to hold on to SLIPS. The ant (and a drop of fruit jam it is attracted to) slide along the SLIPS when the surface is tilted (Supplementary Movie 6). Note that the ant can stably attach to normal flat hydrophobic surfaces, such as Teflon. All scale bars represent 10 mm.

Movie 3) and blood (Fig. 4b, Supplementary Movie 4), that rapidly wet and stain most existing surfaces. SLIPS also repel ice (Fig. 4c, Supplementary Movie 5) and can serve as anti-sticking, slippery surfaces for insects (Fig. 4d, Supplementary Movie 6)—a direct mimicry of pitcher plants. The omniphobic nature of our SLIPS also helps to protect the surface from a wide range of particulate contaminants by allowing self-cleaning by a broad assortment of fluids that collect and remove the particles from the surface (Supplementary Fig. 7 and Supplementary Movie 7). Any of these capabilities could be compromised over time if the lubricant evaporates or is lost owing to shearing under high flow conditions, so choosing a lubricant with a minimal evaporation rate or an enhanced viscosity, or integrating the SLIPS with a fluid reservoir that enables continual self-replenishing (Supplementary Fig. 8), enables prolonged operation.

No synthetic surface reported until now possesses all the unique characteristics of SLIPS: negligible contact angle hysteresis for low-surface-tension liquids and their complex mixtures, low sliding angles, instantaneous and repeatable self-healing, extreme pressure stability and optical transparency. Our bioinspired SLIPS, which are prepared simply by infiltrating low-surface-energy porous solids with lubricating liquids, provide a straightforward and versatile solution for liquid repellency and resistance to fouling. Because low-surface-energy porous solids are abundant and commercially available, and the structural details are irrelevant to the resulting performance, one can turn any

of these solids into highly omniphobic surfaces without the need to access expensive fabrication facilities. Any liquid film is inherently smooth, self-healing and pressure resistant, so the lubricant can be chosen to be either biocompatible, index-matched with the substrate, optimized for extreme temperatures, or otherwise suitable for specific applications. With a broad variety of commercially available lubricants that possess a range of physical and chemical properties, we are currently exploring the limits of the performance of SLIPS for long-term operation and under extreme conditions, such as high flow, turbulence, and high- or low-temperature environments. It is anticipated that SLIPS can be developed to serve as omniphobic materials capable of meeting emerging needs in biomedical fluid handling, fuel transport, anti-fouling, anti-icing, self-cleaning windows and optical devices, and many more areas that are beyond the reach of current technologies.

## METHODS SUMMARY

The lubricating fluids used for the experiments were perfluorinated fluids (such as 3 M Fluorinert FC-70, DuPont Krytox 100 and 103). Two types of porous solids were used in the experiments, periodically ordered epoxy-resin-based nanostructured surfaces and a random network of Teflon nanofibrous membranes. Specifically, Teflon membranes with average pore size of  $\geq 200$  nm and thickness of  $\sim 60$ – $80$   $\mu\text{m}$  were purchased from the Sterlitech Corporation. These membranes were used as received without further modification (SLIPS 1 sample). The epoxy-resin-based nanostructured surfaces were made from silicon masters through the replica moulding method<sup>25</sup>. The resulting dimensions of the nanostructures in the epoxy replica were: diameter  $\sim 300$  nm, height  $\sim 5$   $\mu\text{m}$ , pitch  $\sim 2$   $\mu\text{m}$  for the SLIPS 2 sample, and diameter  $\sim 300$  nm, height  $\sim 500$  nm– $2$   $\mu\text{m}$ , pitch  $\sim 900$  nm for the SLIPS 3 sample. The epoxy replicas were further rendered hydrophobic by putting the samples in a vacuum desiccator overnight with a glass vial containing 0.2 ml heptadecafluoro-1,1,2,2-tetrahydrodecyltrichlorosilane (available from Gelest Inc.). To prepare the SLIPS, lubricating fluid was added onto the porous solids to form an over-coated layer. With matching surface chemistry and roughness, the fluid will spread spontaneously onto the whole substrate through capillary wicking. The thickness of the over-coated layer can be controlled by the fluid volume given a known surface area of the sample. Further details of the methods are available in the Supplementary Information.

Received 8 June; accepted 11 August 2011.

1. Quéré, D. Wetting and roughness. *Annu. Rev. Mater. Res.* **38**, 71–99 (2008).
2. Barthlott, W. & Neinhuis, C. Purity of the sacred lotus, or escape from contamination in biological surfaces. *Planta* **202**, 1–8 (1997).
3. Gao, X. F. & Jiang, L. Water-repellent legs of water striders. *Nature* **432**, 36 (2004).
4. Hansen, W. R. & Autumn, K. Evidence for self-cleaning in gecko setae. *Proc. Natl Acad. Sci. USA* **102**, 385–389 (2005).
5. Gao, X. F. *et al.* The dry-style antifogging properties of mosquito compound eyes and artificial analogues prepared by soft lithography. *Adv. Mater.* **19**, 2213–2217 (2007).
6. Epstein, A. K., Pokroy, B., Seminara, A. & Aizenberg, J. Bacterial biofilm shows persistent resistance to liquid wetting and gas penetration. *Proc. Natl Acad. Sci. USA* **108**, 995–1000 (2011).
7. Quéré, D. Non-sticking drops. *Rep. Prog. Phys.* **68**, 2495–2532 (2005).
8. Tuteja, A. *et al.* Designing superoleophobic surfaces. *Science* **318**, 1618–1622 (2007).
9. Tuteja, A., Choi, W., Mabry, J. M., McKinley, G. H. & Cohen, R. E. Robust omniphobic surfaces. *Proc. Natl Acad. Sci. USA* **105**, 18200–18205 (2008).
10. Nguyen, T. P. N., Brunet, P., Coffinier, Y. & Boukherroub, R. Quantitative testing of robustness on superomniphobic surfaces by drop impact. *Langmuir* **26**, 18369–18373 (2010).
11. Bocquet, L. & Lauga, E. A smooth future? *Nature Mater.* **10**, 334–337 (2011).
12. Poetes, R., Holtzmann, K., Franze, K. & Steiner, U. Metastable underwater superhydrophobicity. *Phys. Rev. Lett.* **105**, 166104 (2010).
13. Bohn, H. F. & Federle, W. Insect aquaplaning: *Nepenthes* pitcher plants capture prey with the peristome, a fully wettable water-lubricated anisotropic surface. *Proc. Natl Acad. Sci. USA* **101**, 14138–14143 (2004).
14. Ahuja, A. *et al.* Nanonails: a simple geometrical approach to electrically tunable superoleophobic surfaces. *Langmuir* **24**, 9–14 (2008).
15. Li, Y., Li, L. & Sun, J. G. Bioinspired self-healing superhydrophobic coatings. *Angew. Chem. Int. Ed. Engl.* **49**, 6129–6133 (2010).
16. Lee, C. & Kim, C. J. Underwater restoration and retention of gases on superhydrophobic surfaces for drag reduction. *Phys. Rev. Lett.* **106**, 014502 (2011).
17. Cassie, A. B. D. & Baxter, S. Wettability of porous surfaces. *Trans. Faraday Soc.* **40**, 0546–0550 (1944).
18. Cassie, A. B. D. & Baxter, S. Large contact angles of plant and animal surfaces. *Nature* **155**, 21–22 (1945).
19. Shafirin, E. G. & Zisman, W. A. Constitutive relations in the wetting of low energy surfaces and the theory of the retraction method of preparing monolayers. *J. Phys. Chem.* **64**, 519–524 (1960).



20. Bauer, U. & Federle, W. The insect-trapping rim of *Nepenthes* pitchers: surface structure and function. *Plant Signal. Behav.* **4**, 1019–1023 (2009).
21. Federle, W., Riehle, M., Curtis, A. S. G. & Full, R. J. An integrative study of insect adhesion: mechanics and wet adhesion of pretarsal pads in ants. *Integr. Comp. Biol.* **42**, 1100–1106 (2002).
22. Wenzel, R. N. Resistance of solid surfaces to wetting by water. *Ind. Eng. Chem.* **28**, 988–994 (1936).
23. Courbin, L. *et al.* Imbibition by polygonal spreading on microdecorated surfaces. *Nature Mater.* **6**, 661–664 (2007).
24. de Gennes, P.-G., Brochard-Wyart, F. & Quéré, D. *Capillarity and Wetting Phenomena: Drops, Bubbles, Pearls, Waves* 15–18 (Springer, 2003).
25. Pokroy, B., Epstein, A. K., Persson-Gulda, M. C. M. & Aizenberg, J. Fabrication of bioinspired actuated nanostructures with arbitrary geometry and stiffness. *Adv. Mater.* **21**, 463–469 (2009).
26. Chen, W. *et al.* Ultrahydrophobic and ultralyophobic surfaces: some comments and examples. *Langmuir* **15**, 3395–3399 (1999).
27. Delmas, M., Monthieux, M. & Ondarcuhu, T. Contact angle hysteresis at the nanometer scale. *Phys. Rev. Lett.* **106**, 136102 (2011).
28. Furrmidge, C. G. Studies at phase interfaces. 1. Sliding of liquid drops on solid surfaces and a theory for spray retention. *J. Colloid Sci.* **17**, 309–324 (1962).
29. Ishino, C., Reyssat, M., Reyssat, E., Okumura, K. & Quéré, D. Wicking within forests of micropillars. *Europhys. Lett.* **79**, 56005 (2007).
30. Nakajima, A., Fujishima, A., Hashimoto, K. & Watanabe, T. Preparation of transparent superhydrophobic boehmite and silica films by sublimation of aluminum acetylacetonate. *Adv. Mater.* **11**, 1365–1368 (1999).

**Supplementary Information** is linked to the online version of the paper at [www.nature.com/nature](http://www.nature.com/nature).

**Acknowledgements** T.-S.W. acknowledges funding support from the Croucher Foundation Postdoctoral Fellowship. We thank K. E. Martin for help with the drop impact test. We also thank J. C. Weaver and P. Allen for help in manuscript preparation. The work was supported partially by the AFOSR MURI award FA9550-09-1-0669-DOD35CAP (optical properties), and ARO MURI award W911NF-09-1-0476 (robustness and self-repair). We acknowledge the use of the facilities at the Harvard Center for Nanoscale Systems supported by the NSF under award ECS-0335765.

**Author Contributions** T.-S.W. and J.A. conceived the research. J.A. supervised the research. T.-S.W., S.H.K. and S.K.Y.T. designed the experiments. T.-S.W. carried out surface wettability characterizations. S.H.K. prepared samples and conducted data analysis. T.-S.W., S.H.K. and S.K.Y.T. carried out surface morphology characterizations. T.-S.W. and S.H.K. carried out drop impact tests and ice experiments. E.J.S. and T.-S.W. carried out the high pressure and optical transmission measurements. B.D.H. and T.-S.W. carried out blood compatibility tests. T.-S.W., S.H.K., A.G. and J.A. wrote the manuscript.

**Author Information** Reprints and permissions information is available at [www.nature.com/reprints](http://www.nature.com/reprints). The authors declare no competing financial interests. Readers are welcome to comment on the online version of this article at [www.nature.com/nature](http://www.nature.com/nature). Correspondence and requests for materials should be addressed to J.A. ([jaiz@seas.harvard.edu](mailto:jaiz@seas.harvard.edu)).

# Widespread iron-rich conditions in the mid-Proterozoic ocean

Noah J. Planavsky<sup>1</sup>, Peter McGoldrick<sup>2</sup>, Clinton T. Scott<sup>1</sup>, Chao Li<sup>1,3</sup>, Christopher T. Reinhard<sup>1</sup>, Amy E. Kelly<sup>1</sup>, Xuelei Chu<sup>4</sup>, Andrey Bekker<sup>5</sup>, Gordon D. Love<sup>1</sup> & Timothy W. Lyons<sup>1</sup>

**The chemical composition of the ocean changed markedly with the oxidation of the Earth's surface<sup>1</sup>, and this process has profoundly influenced the evolutionary and ecological history of life<sup>2,3</sup>. The early Earth was characterized by a reducing ocean–atmosphere system, whereas the Phanerozoic eon (less than 542 million years ago) is known for a stable and oxygenated biosphere conducive to the radiation of animals. The redox characteristics of surface environments during Earth's middle age (1.8–1 billion years ago) are less well known, but it is generally assumed that the mid-Proterozoic was home to a globally sulphidic (euxinic) deep ocean<sup>2,3</sup>. Here we present iron data from a suite of mid-Proterozoic marine mudstones. Contrary to the popular model, our results indicate that ferruginous (anoxic and Fe<sup>2+</sup>-rich) conditions were both spatially and temporally extensive across diverse palaeogeographic settings in the mid-Proterozoic ocean, inviting new models for the temporal distribution of iron formations and the availability of bioessential trace elements during a critical window for eukaryotic evolution.**

It is well established that Earth evolved from having an early anoxic ocean devoid of eukaryotes to one that is fully oxygenated and teeming with complex life. However, the timing and mechanisms of Earth's redox evolution are still debated. Foremost, marine redox conditions and atmospheric oxygen levels remain poorly constrained during the period between the Earth's oxygen-deficient early history (more than ~2.4 billion years (Gyr) ago) and the dominantly oxygenated realm of the Phanerozoic (the last ~0.542 Gyr). Traditional arguments held that ocean oxygenation was responsible for the disappearance of large iron formations at 1.8 Gyr ago (ref. 1). More recently, the majority opinion among Precambrian workers has instead favoured a deep mid-Proterozoic ocean with a vast or perhaps even global reservoir of hydrogen sulphide<sup>4–6</sup>, and H<sub>2</sub>S, much like oxygen, would have titrated the dissolved iron needed for the deposition of iron formations. It is further proposed that these euxinic (anoxic and sulphidic) conditions would have hindered the expansion and diversification of eukaryotes, because of the insolubility of bioessential trace elements, such as molybdenum, in sulphidic waters<sup>7</sup>. Consistent with a shift to euxinia, well-preserved sedimentary rocks from the Animikie basin on the Superior craton were suggested to capture the transition to a global sulphidic ocean<sup>6</sup> at ~1.8 Gyr ago. It is now apparent, however, that large iron formations were deposited tens of millions of years after the deposition of this sedimentary succession<sup>8,9</sup> and that iron-rich conditions persisted in deep waters in the Animikie basin even after the deposition of the largest Animikie iron formations<sup>8,10</sup>, demanding that we rethink the spatiotemporal details of Proterozoic ocean redox and specifically the character of the mid-Proterozoic ocean (1.8–1.0 Gyr ago)<sup>10</sup>.

In contrast with endmember euxinic or oxic Proterozoic deep-ocean models, a third possibility has recently been proposed: that anoxic and iron-rich deepwater conditions may have been common throughout the Precambrian, including the mid-Proterozoic<sup>3,8,10,11</sup>. This surprising

view of ocean evolution finds its origins in part with recent evidence that the ocean was ferruginous in the terminal Proterozoic<sup>12–14</sup>, suggesting continuity with the iron-formation-favouring conditions present before 1.8 Gyr ago. Alternatively, researchers have also asserted that the Neoproterozoic was instead a special case—marked by a return to the iron-rich state of the early Precambrian as a consequence of supercontinent break-up<sup>13</sup>, extensive glaciations<sup>15</sup>, and drawdown of marine sulphate caused by a billion years of deepwater euxinia and pyrite burial<sup>12</sup>. Although tantalizing, the ferruginous mid-Proterozoic model is currently hindered by a billion-year gap in direct evidence from the geological record for this marine redox state. Our study fills that data gap with results from four diverse mid-Proterozoic depositional settings that all point to iron-rich marine waters. Included are samples from the McArthur basin in north-central Australia—the only basin so far that has yielded direct evidence for mid-Proterozoic euxinia<sup>16,17</sup>.

To evaluate ancient redox chemistry, we have applied a well-established sequential iron extraction scheme to fine-grained sedimentary rocks<sup>18</sup>. The accumulation of biogeochemically reactive iron, termed 'highly reactive iron' (Fe<sub>HR</sub>), is linked to the redox conditions in the water column overlying the site of sedimentary deposition. In modern oxic marine sediments, Fe<sub>HR</sub> comprises less than 38% of the total sedimentary iron pool (that is, Fe<sub>HR</sub>/Fe<sub>T</sub> < 0.38), reflecting the detrital sediment flux in the absence of dissolved iron in the O<sub>2</sub>-containing water column. Enrichments beyond this limit (Fe<sub>HR</sub>/Fe<sub>T</sub> > 0.38) are a clear signature of transport, scavenging and deposition of additional iron from an anoxic water column<sup>3,12</sup>. Because mineralogical changes associated with even moderate burial alteration (such as iron uptake into secondary silicate minerals) can decrease the pool of Fe<sub>HR</sub>, the upper limit is possibly lower than 0.38 in older rocks<sup>19</sup>, suggesting that essentially all of our samples could have formed under anoxic conditions (Fig. 1). Where anoxia is indicated, we can further distinguish between ferruginous (Fe<sup>2+</sup> > H<sub>2</sub>S) and euxinic (H<sub>2</sub>S > Fe<sup>2+</sup>) environments by measuring the extent to which Fe<sub>HR</sub> has reacted with H<sub>2</sub>S to form pyrite (Fe<sub>Py</sub>/Fe<sub>HR</sub>). Accordingly, anoxic shales with Fe<sub>Py</sub>/Fe<sub>HR</sub> > 0.8 are considered to have been deposited under euxinic conditions<sup>11,12</sup>.

Because the McArthur basin has had a defining role in previous arguments for mid-Proterozoic euxinia<sup>16,17,20,21</sup>, we began our search for ferruginous conditions with an additional analysis of fresh drill cores of shale from deep-water settings in this region. We specifically investigated the iron chemistry of the ~1.64-Gyr-old Barney Creek and Lady Loretta formations in the McArthur and Mount Isa basins, respectively. Our samples are from geographically widespread marine sequences that extend over more than 2,000 km across northern Australia. We included locations with palaeogeographic positions closer to the open ocean compared with past studies in the region that also focused on marine palaeoredox. In addition, we targeted the deepest-water facies as delineated in previous detailed basin analysis (see, for example, ref. 22).

<sup>1</sup>Department of Earth Sciences, University of California, Riverside, California 92521, USA. <sup>2</sup>CODES ARC Centre of Excellence in Ore Deposits, University of Tasmania, Tasmania 7001, Australia. <sup>3</sup>State Key Laboratory of Biogeology and Environmental Geology, China University of Geosciences, Wuhan 430074, China. <sup>4</sup>Institute of Geology and Geophysics, Chinese Academy of Sciences, Beijing 100029, China. <sup>5</sup>Department of Geological Sciences, University of Manitoba, Winnipeg, Manitoba R3T 2N2, Canada.

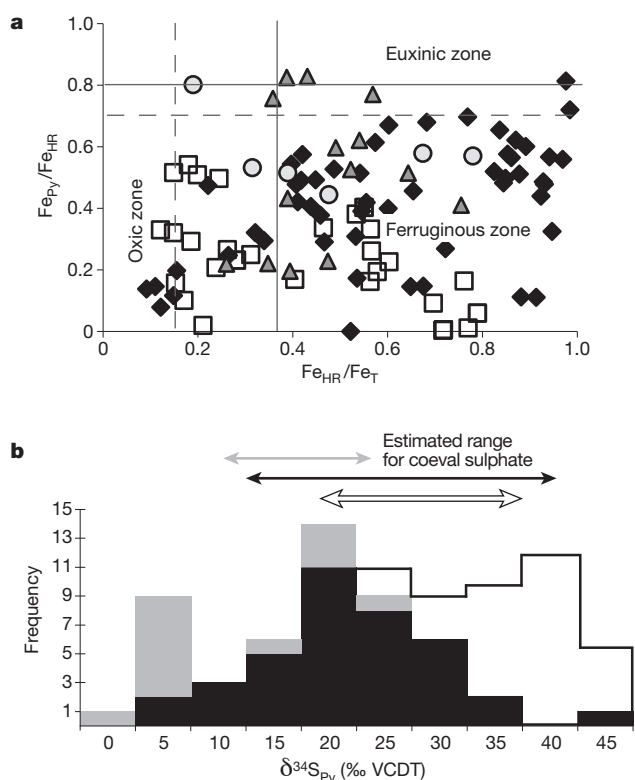


**Figure 1 | Iron speciation and sulphur isotope data for mid-Proterozoic shales.** Data from the 1.64-Gyr-old Mt Isa Superbasin (black diamonds and bars), the 1.7-Gyr-old Chuanlinggou Formation (white squares and bars), the 1.45-Gyr-old Newland Formation (grey triangles and bars) and the 1.2-Gyr-old Borden basin (grey circles). **a**, The vast majority of our samples have ratios of highly reactive to total iron ( $\text{Fe}_{\text{HR}}/\text{Fe}_{\text{T}}$ ) and of pyrite to highly reactive iron ( $\text{Fe}_{\text{Py}}/\text{Fe}_{\text{HR}}$ ) falling above 0.15–0.38 and below 0.7–0.8, respectively, which is diagnostic of sediment accumulation beneath an anoxic and iron-rich (non-sulphidic) water column. **b**, Pyrite  $\delta^{34}\text{S}$  isotope values ( $\delta^{34}\text{S}_{\text{Py}}$ ) relative to Vienna Canyon Diablo Troilite (VCDT). Estimates for sulphate  $\delta^{34}\text{S}$  values are from refs 32, 33.

$\text{Fe}_{\text{HR}}/\text{Fe}_{\text{T}}$  values in both the Barney Creek and Lady Loretta formations are generally above 0.38, conservatively indicating deposition under anoxic conditions (Fig. 1a). The vast majority of these samples have  $\text{Fe}_{\text{Py}}/\text{Fe}_{\text{HR}}$  ratios well below 0.8, which is consistent with a persistently sulphide-free water column. Together, these ratios point to widespread ferruginous conditions over thick (hundreds of metres) stratigraphic intervals, indicating prolonged periods of ferruginous deep waters, with the likelihood of laterally contemporaneous occurrences of euxinia<sup>16,17</sup> in certain small or isolated sub-basins and/or on the shallower margins. Previous regional studies have argued for a relatively strong marine connection during deposition at our specific sample locations (see Supplementary Information), suggesting that deep ocean waters enriched in dissolved  $\text{Fe}^{2+}$  may have exchanged with the McArthur and Mt Isa basins.

Given these exciting results, we were obliged to look beyond this region for records of mid-Proterozoic ferruginous waters. With this goal, we analysed additional suites of carbonaceous shales from other, widely distributed mid-Proterozoic basins, emphasizing well-preserved (sub-greenschist) shales from diverse palaeogeographic settings spanning the mid-Proterozoic. Each of these additional units yielded abundant samples with  $\text{Fe}_{\text{HR}}/\text{Fe}_{\text{T}} > 0.38$  and  $\text{Fe}_{\text{Py}}/\text{Fe}_{\text{HR}} < 0.8$  (Fig. 1a), signifying widespread ferruginous depositional conditions. Our data include samples from the 1.7-Gyr-old Chuanlinggou Formation in northern China, the 1.45-Gyr-old Belt Supergroup in the north-central USA and the 1.2-Gyr-old Borden basin in Arctic Canada. The Chuanlinggou Formation is interpreted as being a passive-margin sequence, suggesting a strong connection to the open ocean, and the Borden basin was a

passive margin that evolved into a foredeep setting. In contrast, the Belt basin probably represents an extensional marine setting with transiently more restricted depositional conditions (see Supplementary Information).

A small subset of samples from the Mt Isa superbasin, the Belt Supergroup and the Borden basin have significant iron enrichments and  $\text{Fe}_{\text{Py}}/\text{Fe}_{\text{HR}}$  near 0.8 (Fig. 1a), suggesting that sulphidic conditions may have developed episodically in the water column. The lack of persistently euxinic conditions in the Belt Supergroup is surprising. As a semi-isolated, probably marginal marine system with evidence for high rates of primary productivity<sup>23</sup>, the Belt basin would seem ideally suited to developing euxinia—as we see in the modern, restricted Black Sea. Clear fingerprints of ferruginous conditions in the Chuanlinggou Formation are also revealing: as a passive-margin sequence lacking indications of appreciable basin restriction, this setting provides one of our best windows on conditions in the open Proterozoic ocean.

Our finding of iron-rich conditions in several mid-Proterozoic marine settings contrasts with the widely accepted view of globally persistent and pervasive deep euxinia. However, this discovery is entirely consistent with an emerging view of Precambrian ocean chemistry brought to light by the most recent trace-metal and iron speciation studies from younger and older portions of the Precambrian ocean. Specifically, there is evidence for coexisting iron-rich and  $\text{H}_2\text{S}$ -rich conditions in several Neoproterozoic<sup>24–27</sup>, early and middle Palaeoproterozoic<sup>10,28</sup> and early and late Neoproterozoic settings<sup>13,14</sup> (Fig. 2). Ferruginous conditions were apparently widespread in the deeper portions of the ocean, whereas sulphide was probably limited to highly productive regions along the continental margins<sup>10,13,25,26</sup>, which is analogous to the more reducing conditions in modern oxygen minimum zones. Our data fill a billion-year gap in the evidence for this marine redox state, indicating a hitherto undocumented continuity of iron-rich conditions throughout the Precambrian.

Our finding of extensive ferruginous conditions is also consistent with a recent study of marine molybdenum inventories<sup>27</sup>, which argued that the extent of euxinic depositional environments during the mid-Proterozoic could have been severalfold that of the modern ocean ( $\ll 1\%$ ) but far from whole-ocean euxinia. Similarly, mid-Proterozoic Mo isotope data are easily explained through greatly expanded (relative to today) but still largely local euxinia, with deep

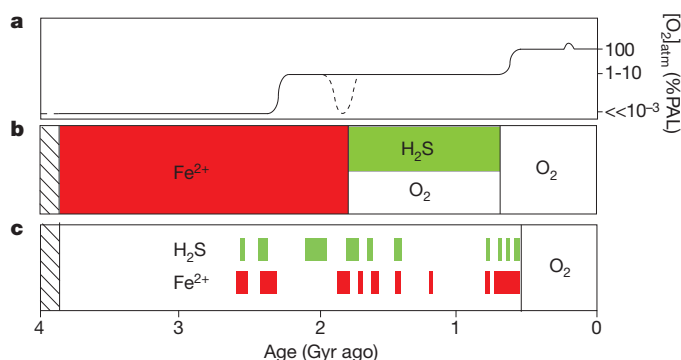


**Figure 2 | Summary of marine chemical conditions in the Precambrian.**

**a**, Estimates of atmospheric oxygen compared with present atmospheric level (PAL). **b**, Classical models of the chemical composition of the deep ocean. **c**, Distribution of Precambrian euxinic and ferruginous deep waters, based on the shale record. Our study provides evidence for extensively developed and likely persistent ferruginous conditions in the deep ocean during the mid-Proterozoic, which was previously thought to have been characterized by either oxygenated or sulphide-rich conditions. The emerging view based on redox studies of marine shales is that during the mid-Proterozoic, when there were relatively low levels of atmospheric oxygen, both euxinic and ferruginous waters were common, and often stratified, below the oxygenated surface-mixing zone. In the Phanerozoic, with higher levels of atmospheric oxygen, the deep oceans were anoxic for only short periods (see the text for details).



waters that were dominantly ferruginous and thus less efficient at burying Mo (see, for example, ref. 20).

We argue that the flux of organic matter was central to controlling the redox landscape of the mid-Proterozoic ocean, as has been suggested for other—both older and younger—instances of Precambrian euxinia<sup>10,13,25</sup>. Estimates for dissolved sulphate levels in the mid-Proterozoic ocean range from 500 to 3,000  $\mu\text{M}$  (see Supplementary Information). Even the lower estimate for sulphate is well above the upper limit for dissolved iron, which is fixed at roughly 100  $\mu\text{M}$  by the solubilities of iron carbonates and silicates<sup>2</sup>. Therefore, ferruginous marine conditions must instead mirror limited sulphide production<sup>13</sup>. Sulphide is produced anaerobically by bacteria at the expense of organic matter. It follows that spatial gradients in the organic flux and, ultimately, organic productivity may have limited the extent of euxinia.

Consistent with an organic matter delivery control on the distribution of sulphidic marine conditions, the analysed samples contain substantially less organic carbon than do typical euxinic Precambrian and Phanerozoic shales. Samples in our study contain on average less than 1% organic carbon, which is severalfold lower than concentrations common in euxinic shales (see, for example, ref. 27). Low levels of organic matter in ferruginous shales suggest relatively low productivity in the overlying water column. In addition, there is a sulphur isotope signal consistent with bacterial sulphate reduction occurring predominantly in the porewaters. Pyrite in our samples has  $\delta^{34}\text{S}$  values that are slightly lower than or equivalent to coeval sulphate (Fig. 1b). A simple explanation for these results is that bacterial sulphate reduction is occurring largely in sediments where potentially high isotopic fractionations are muted by limited sulphate availability. Sulphate supplies in the sediments would be controlled by rates of diffusional replenishment, and associated deficiencies would be exacerbated by the comparatively small amount of sulphate in mid-Proterozoic seawater. In other words, limited availability of organic matter probably caused the onset of appreciable bacterial sulphate reduction to be restricted to the sediments. However, these sulphur isotope results do not completely exclude water column sulphur cycling.

For ferruginous conditions to have been extensive in the mid-Proterozoic ocean, dissolved oxygen acquired in surface waters through photosynthesis and gas exchange with the overlying atmosphere must have been consumed as deep water masses aged. Oxygen will be consumed through the degradation of sinking organic matter and, if oxygen remains available at depth, by hydrothermally sourced reductants (see, for example, ref. 29). Our results indicate that the flux of  $\text{Fe}^{2+}$  into deep waters typically exceeded rates of sulphide generation in all but nearshore or restricted regions with relatively high rates of primary productivity that fuelled localized sulphate reduction in the water column.

Our results also call for a reconsideration of the factors controlling the temporal distribution of large iron formations. In contrast with the canonical view, in which iron formations disappeared as the deep ocean evolved from iron to oxygen or sulphide domination<sup>1,4</sup>, the long persistence of ferruginous conditions in our model argues that iron formations are anomalous sedimentary deposits linked in most cases to an enhanced iron supply by means of strong hydrothermal inputs<sup>8</sup>. Consistent with our ocean model, the amount of hydrothermal iron released to the oceans has varied greatly with marine sulphate concentrations<sup>30</sup> and mantle plume activity as reflected by dyke swarms and large igneous provinces<sup>8</sup>.

Our findings cast a new perspective on mid-Proterozoic environmental conditions, ecology and evolution. For example, evidence for extensive ferruginous conditions throughout the Proterozoic ocean provides a simple answer to the apparent conundrum of increasing enzymatic use of iron, molybdenum and cobalt during the mid-Proterozoic as inferred by a recent study of the evolution of almost 4,000 gene families<sup>31</sup>. It is possible for these bioessential metals to have been readily available in an ocean with pervasively ferruginous deep

waters, in contrast with the certainty of biolimitation if deep waters were globally sulphidic<sup>7</sup>. Free sulphide in the water column greatly decreases the solubility of these elements. It remains to be tested, however, whether broad, but far from global, extents of euxinia in a stratified ocean were still able to pull down trace metal inventories at least locally to biologically critical levels, as suggested in previous work<sup>27</sup>. More generally, our data now provide the foundation for a unified model for the chemical evolution of the Precambrian ocean consistent with diverse redox tracers and bridging past work bracketing the mid-Proterozoic. Recognizing the spatial and temporal heterogeneity expected in a dynamic early ocean, we propose the almost continuous coexistence of sulphide-rich and iron-rich conditions for billions of years beneath oxic surface waters as the backdrop for Precambrian biological evolution, and specifically the protracted radiation of eukaryotes and the ultimate rise of animals.

## METHODS SUMMARY

Iron speciations were performed at the University of California, Riverside (UCR), using a well-calibrated sequential extraction protocol designed to quantify the different pools of  $\text{Fe}_{\text{HR}}$  (ref. 18). A small portion of sample powder (~100 mg) was used for the extractions, and iron concentrations were determined with an Agilent 7500ce inductively coupled plasma mass spectrometry (ICP-MS) at UCR.  $\text{Fe}_{\text{py}}$  was calculated on the basis of the weight percentage of sulphur extracted during a 2-h hot chromous chloride distillation followed by iodometric titration. Total iron concentrations were determined by one of two methods: X-ray fluorescence at the CODES Research Centre at the University of Tasmania, or a three-acid digest and ICP-MS analysis at UCR. Sulphur isotope measurements were made at UCR with a ThermoFinnigan Delta V continuous-flow stable-isotope-ratio mass spectrometer after a chromous chloride distillation, where the pyrite-S was reprecipitated as  $\text{Ag}_2\text{S}$ .

**Full Methods** and any associated references are available in the online version of the paper at [www.nature.com/nature](http://www.nature.com/nature).

Received 25 January; accepted 23 June 2011.

Published online 7 September 2011.

- Holland, H. D. Sedimentary mineral deposits and the evolution of Earth's near-surface environments. *Econ. Geol.* **100**, 1489–1509 (2005).
- Canfield, D. E. The early history of atmospheric oxygen: homage to Robert A. Garrels. *Annu. Rev. Earth Planet. Sci.* **33**, 1–36 (2005).
- Lyons, T. W., Anbar, A., Severmann, S., Scott, C. & Gill, B. Tracking euxinia in the ancient ocean: a multiproxy perspective and Proterozoic case study. *Annu. Rev. Earth Planet. Sci.* **37**, 507–534 (2009).
- Canfield, D. E. A new model for Proterozoic ocean chemistry. *Nature* **396**, 450–453 (1998).
- Lyons, T. W., Reinhard, C. T. & Scott, C. Redox redux. *Geobiology* **7**, 489–494 (2009).
- Poulton, S. W., Fralick, P. W. & Canfield, D. E. The transition to a sulphidic ocean similar to 1.84 billion years ago. *Nature* **431**, 173–177 (2004).
- Anbar, A. D. & Knoll, A. H. Proterozoic ocean chemistry and evolution: a bioinorganic bridge. *Science* **297**, 1137–1142 (2002).
- Bekker, A. *et al.* Iron formation: the sedimentary product of a complex interplay among mantle, tectonic, oceanic, and biospheric processes. *Econ. Geol.* **105**, 467–508 (2010).
- Wilson, J. P. *et al.* Geobiology of the late Paleoproterozoic Duck Creek Formation, Western Australia. *Precamb. Res.* **179**, 135–149 (2010).
- Poulton, S. W., Fralick, P. W. & Canfield, D. E. Spatial variability in oceanic redox structure 1.8 billion years ago. *Nature Geosci.* **3**, 486–490 (2010).
- Poulton, S. W. & Canfield, D. E. Ferruginous conditions: a dominant feature of the ocean through Earth's history. *Elements* **7**, 107–112 (2011).
- Canfield, D. E. *et al.* Ferruginous conditions dominated later Neoproterozoic deep-water chemistry. *Science* **321**, 949–952 (2008).
- Johnston, D. T. *et al.* An emerging picture of Neoproterozoic ocean chemistry: insights from the Chuar Group, Grand Canyon, USA. *Earth Planet. Sci. Lett.* **290**, 64–73 (2010).
- Li, C. *et al.* A stratified redox model for the Ediacaran Ocean. *Science* **328**, 80–83 (2010).
- Swanson-Hysell, N. L. *et al.* Cryogenian glaciation and the onset of carbon-isotope decoupling. *Science* **328**, 608–611 (2010).
- Brocks, J. J. *et al.* Biomarker evidence for green and purple sulphur bacteria in a stratified Palaeoproterozoic sea. *Nature* **437**, 866–870 (2005).
- Johnston, D. T. *et al.* Sulfur isotope biogeochemistry of the Proterozoic McArthur Basin. *Geochim. Cosmochim. Acta* **72**, 4278–4290 (2008).
- Poulton, S. W. & Canfield, D. E. Development of a sequential extraction procedure for iron: implications for iron partitioning in continentally derived particulates. *Chem. Geol.* **214**, 209–221 (2005).
- Raiswell, R. Turbidite depositional influences on the diagenesis of Beecher's Trilobite Bed and the Hunsrück Slate; sites of soft tissue pyritization. *Am. J. Sci.* **305**, 105–129 (2008).

20. Kendall, B., Creaser, R. A., Gordon, G. W. & Anbar, A. D. Re–Os and Mo isotope systematics of black shales from the Middle Proterozoic Velkerri and Wollongorang Formations, McArthur Basin, northern Australia. *Geochim. Cosmochim. Acta* **73**, 2534–2558 (2009).
21. Shen, Y., Knoll, A. H. & Walter, M. R. Evidence for low sulphate and anoxia in a mid-Proterozoic marine basin. *Nature* **423**, 632–635 (2003).
22. McGoldrick, P., Winefield, P., Bull, S., Selley, D. & Scott, R. Sequences, synsedimentary structures, and sub-basins: the where and when of SEDEX zinc systems in the southern McArthur Basin, Australia. *Soc. Econ. Geol. Spec. Publ.* **15**, 1–23 (2010).
23. Lyons, T. W., Luepke, J. J., Schreiber, M. E. & Zieg, G. A. Sulfur geochemical constraints on Mesoproterozoic restricted marine deposition: lower Belt Supergroup, northwestern United States. *Geochim. Cosmochim. Acta* **64**, 427–437 (2000).
24. Kendall, B. *et al.* Pervasive oxygenation along late Archaean ocean margins. *Nature Geosci.* **3**, 647–652 (2010).
25. Reinhard, C. T., Raiswell, R., Scott, C., Anbar, A. D. & Lyons, T. W. A Late Archaean sulfidic sea stimulated by early oxidative weathering of the continents. *Science* **326**, 713–716 (2009).
26. Scott, C. *et al.* Late Archaean euxinic conditions before the rise of atmospheric. *Geology* **39**, 119–122 (2011).
27. Scott, C. *et al.* Tracing the stepwise oxygenation of the Proterozoic ocean. *Nature* **452**, 457–460 (2008).
28. Bekker, A. *et al.* Fractionation between inorganic and organic carbon during the Lomagundi (2.22–2.1 Ga) carbon isotope excursion. *Earth Planet. Sci. Lett.* **271**, 278–291 (2008).
29. Slack, J. F., Grenne, T., Bekker, A., Rouxel, O. J. & Lindberg, P. A. Suboxic deep seawater in the late Paleoproterozoic: evidence from hematitic chert and iron formation related to seafloor-hydrothermal sulfide deposits, central Arizona, USA. *Earth Planet. Sci. Lett.* **255**, 243–256 (2007).
30. Kump, L. R. & Seyfried, W. E. Hydrothermal Fe fluxes during the Precambrian: effect of low oceanic sulfate concentrations and low hydrostatic pressure on the composition of black smokers. *Earth Planet. Sci. Lett.* **235**, 654–662 (2005).
31. David, L. A. & Alm, E. J. Rapid evolutionary innovation during an Archaean genetic expansion. *Nature* **469**, 93–96 (2011).
32. Chu, X., Zhang, T., Zhang, Q. & Lyons, T. W. Sulfur and carbon isotope records from 1700 to 800 Ma carbonates of the Jixian section, northern China: Implications for secular isotope variations in Proterozoic seawater and relationships to global supercontinental events. *Geochim. Cosmochim. Acta* **71**, 4668–4692 (2007).
33. Gellatly, A. M. & Lyons, T. W. Trace sulfate in mid-Proterozoic carbonates and the sulfur isotope record of biospheric evolution. *Geochim. Cosmochim. Acta* **69**, 3813–3829 (2005).

**Supplementary Information** is linked to the online version of the paper at [www.nature.com/nature](http://www.nature.com/nature).

**Acknowledgements** We thank P. Emsbo, S. Bull and D. Winston for formative discussions, P. Fralick for constructive comments, and S. Bates and J. Owens for assistance with the analyses. This work was supported by funding from the National Science Foundation (NSF) Graduate Research Fellowship programme, Geological Society of America and American Philosophical Society, to N.J.P.; from the NSF Division of Earth Sciences, the NASA Exobiology Program and Astrobiology Institute and the UTAS Visiting Fellows programme to T.W.L.; from the Agouron Institute to T.W.L. and G.D.L.; and from Natural Sciences and Engineering Research Council of Canada to A.B. P.McG. was supported through the Australian Research Council's Centre of Excellence programme.

**Author Contributions** P.McG., A.B., T.W.L., X.C., C.L. and N.J.P. collected samples, and P.McG., N.J.P., C.T.S. and C.L. analysed them. All authors were involved in the writing and the design and interpretations of this study.

**Author Information** Reprints and permissions information is available at [www.nature.com/reprints](http://www.nature.com/reprints). The authors declare no competing financial interests. Readers are welcome to comment on the online version of this article at [www.nature.com/nature](http://www.nature.com/nature). Correspondence and requests for materials should be addressed to T.W.L. ([timothy.lyons@ucr.edu](mailto:timothy.lyons@ucr.edu)).

## METHODS

The extraction method used in this study to speciate between the reactive iron pools in fine-grained siliciclastic rocks and sediments has been described in detail elsewhere, and we therefore provide only an overview here. In short, our iron speciations were performed at UCR, using a well-calibrated sequential extraction protocol designed to quantify the different pools of  $\text{Fe}_{\text{HR}}$  (refs 6, 18).  $\text{Fe}_{\text{HR}}$  is subdivided into three subpools, each with the potential to react with hydrogen sulphide on diagenetic timescales: carbonate-associated iron extracted with a sodium acetate solution ( $\text{Fe}_{\text{carb}}$ ), ferric oxides extracted with a dithionite solution ( $\text{Fe}_{\text{ox}}$ ), and mixed-valence iron oxides, principally magnetite, extracted with ammonium oxalate ( $\text{Fe}_{\text{mag}}$ ). We used  $\sim 100$  mg of sample powder, and the sequential extracts were analysed with an Agilent 7500ce ICP-MS. Pyrite ( $\text{Fe}_{\text{py}}$ ) is also included in the  $\text{Fe}_{\text{HR}}$  pool.  $\text{Fe}_{\text{py}}$  was calculated (assuming a stoichiometry of  $\text{FeS}_2$ ) on the basis of the weight percentage of sulphur extracted during a 2-h hot chromous chloride distillation followed by iodometric titration. The assumption of a  $\text{FeS}_2$  stoichiometry in the sulphide pool was tested through extensive extractions for acid-volatile sulphide with hot  $\text{SnCl}_2$ -HCl (15%  $\text{SnCl}_2$ , 6 M HCl) for 1 h.

The samples included here all contain less than 0.1% sulphur extractable by HCl. Total iron concentrations were determined by one of two methods: X-ray fluorescence at the CODES Research Centre at the University of Tasmania, or a three-acid digestion followed by ICP-MS analysis at UCR. On the basis of duplicate analyses and Geostandard monitoring, reproducibility of iron measurements was better than 5%. However, samples with less than 0.1% iron were found to be reproducible to two decimal places, but the error can exceed 5%. At such low levels of iron, these errors have no impact on our conclusions.

We determined concentrations of total organic carbon by taking the difference between carbonate carbon liberated by 4 M HCl and total carbon released by combustion at 1,450 °C, both of which were measured with an ELTRA C/S determinator at UCR. Last, also at UCR, pyrite-S was extracted for isotope measurements by using the same chromous chloride distillation but, in this case, reprecipitating the pyrite-S as  $\text{Ag}_2\text{S}$ . Sulphur isotope measurements were made with a ThermoFinnigan Delta V continuous-flow stable-isotope-ratio mass spectrometer. Reproducibility was better than 0.2‰ on the basis of single-run and long-term standard monitoring.



# Phylogenomics reveals deep molluscan relationships

Kevin M. Kocot<sup>1</sup>, Johanna T. Cannon<sup>1</sup>, Christiane Todt<sup>2</sup>, Mathew R. Citarella<sup>3</sup>, Andrea B. Kohn<sup>3</sup>, Achim Meyer<sup>4</sup>, Scott R. Santos<sup>1</sup>, Christoffer Schander<sup>2</sup>, Leonid L. Moroz<sup>3,5</sup>, Bernhard Lieb<sup>4</sup> & Kenneth M. Halanych<sup>1</sup>

Evolutionary relationships among the eight major lineages of Mollusca have remained unresolved despite their diversity and importance. Previous investigations of molluscan phylogeny, based primarily on nuclear ribosomal gene sequences<sup>1–3</sup> or morphological data<sup>4</sup>, have been unsuccessful at elucidating these relationships. Recently, phylogenomic studies using dozens to hundreds of genes have greatly improved our understanding of deep animal relationships<sup>5</sup>. However, limited genomic resources spanning molluscan diversity has prevented use of a phylogenomic approach. Here we use transcriptome and genome data from all major lineages (except Monoplacophora) and recover a well-supported topology for Mollusca. Our results strongly support the Aculifera hypothesis placing Polyplacophora (chitons) in a clade with a monophyletic Aplacophora (worm-like molluscs). Additionally, within Conchifera, a sister-taxon relationship between Gastropoda and Bivalvia is supported. This grouping has received little consideration and contains most (>95%) molluscan species. Thus we propose the node-based name Pleistomollusca. In light of these results, we examined the evolution of morphological characters and found support for advanced cephalization and shells as possibly having multiple origins within Mollusca.

With over 100,000 described extant species in eight major lineages, Mollusca is the second most speciose animal phylum<sup>6</sup>. Many molluscs are economically important as food and producers of pearls and shells whereas others cause economic damage as pests, biofoulers and invasive species. Molluscs are also biomedically important as models for the study of brain organization, learning and memory as well as vectors of parasites. Although shelled molluscs have one of the best fossil records of any animal group, evolutionary relationships among major molluscan lineages have been elusive.

Morphological disparity among the major lineages of Mollusca has prompted numerous conflicting phylogenetic hypotheses (Fig. 1). The vermiform Chaetodermomorpha (also known as Caudofoveata) and Neomeniomorpha (also known as Solenogastres) traditionally have been considered to represent the plesiomorphic state of Mollusca because of their 'simple' internal morphology and lack of shells<sup>7</sup>. Whether these two lineages constitute a monophyletic group, Aplacophora<sup>8</sup>, or a

paraphyletic grade<sup>4,9</sup> has been widely debated. Some workers have considered the presence of sclerites a synapomorphy for a clade Aculifera, uniting Polyplacophora (chitons; which have both sclerites and shells) and Aplacophora. In contrast, Polyplacophora has alternatively been placed with Conchifera (Bivalvia, Cephalopoda, Gastropoda, Monoplacophora and Scaphopoda) in a clade called Testaria uniting the shelled molluscs<sup>4</sup>. Morphology has been interpreted to divide Conchifera into a gastropod/cephalopod clade (Cyrtosoma) and a bivalve/scaphopod clade (Diasoma)<sup>6</sup>. Unfortunately, because of varying interpretations of features as derived or plesiomorphic, a lack of clear synapomorphies, and often unclear character homology, the ability of morphology to resolve such deep phylogenetic events is limited.

Molecular investigations of molluscan phylogeny have relied primarily on nuclear ribosomal gene sequences (18S and 28S)<sup>1–3,10</sup>, and have also offered little resolution. Maximum likelihood (ML) analyses of 18S, 28S or both<sup>1</sup> recovered most major lineages monophyletic, but support at deeper nodes was generally weak. Subsequent analyses of a combined data set (18S, 28S, 16S, cytochrome *c* oxidase I and histone H3)<sup>2</sup> yielded similar results, namely that bivalves were not monophyletic and support values at most deep nodes were low. Expanding on this study, further work supported a sister-taxon relationship between chitons and monoplacophorans (Serialia) but support at other deep nodes was generally low<sup>3</sup>. Moreover, Mollusca was not recovered monophyletic (a result significantly supported by Approximately Unbiased, AU, tests; Supplementary Table 1) possibly due to contaminated neomenioid sequences<sup>10</sup>.

Morphological and traditional molecular phylogenetic approaches have failed to robustly reconstruct mollusc phylogeny. Notably, several recent phylogenomic studies (for example, refs 5 and 11) have significantly advanced our understanding of metazoan evolution by using sequences derived from genome and transcriptome data. With this approach, numerous orthologous protein-coding genes can be identified and employed in phylogeny reconstruction. Many of these genes are constitutively expressed and can be easily recovered from even limited expressed sequence tag (EST) surveys. Additionally, these genes are usually informative for inferring higher-level phylogeny because of their conserved nature due to their functional importance.

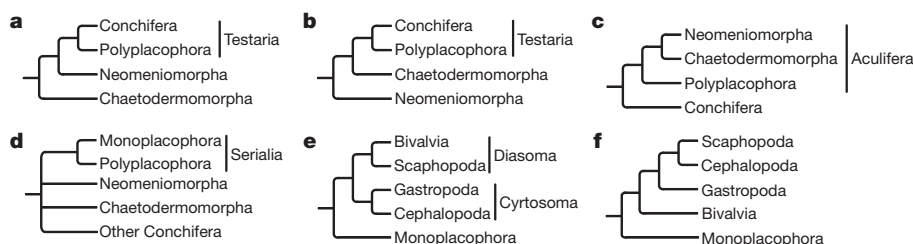


**Figure 1 | Leading hypotheses of molluscan phylogeny.** **a**, Adenopoda hypothesis placing Chaetodermomorpha basal. **b**, Hepagastralia hypothesis placing Neomeniomorpha basal. **c**, Aculifera hypothesis placing Aplacophora sister to Polyplacophora. **d**, Serialia hypothesis allying Polyplacophora and

Monoplacophora. **e**, Diasoma and Cyrtosoma hypotheses allying bivalves to scaphopods and gastropods to cephalopods, respectively. **f**, Unnamed hypothesis, allying scaphopods and cephalopods.

<sup>1</sup>Department of Biological Sciences, Auburn University, 101 Rouse Life Sciences, Auburn, Alabama 36849, USA. <sup>2</sup>Department of Biology and Centre for Geobiology, University of Bergen, P.O. Box 7800, NO-5020 Bergen, Norway. <sup>3</sup>The Whitney Laboratory for Marine Bioscience, University of Florida, 9505 Ocean Shore Blvd., St. Augustine, Florida 32080, USA. <sup>4</sup>Institute of Zoology, Johannes Gutenberg University, Müllerweg 6, D-55099 Mainz, Germany. <sup>5</sup>Department of Neuroscience, University of Florida, Gainesville, Florida 32611, USA.

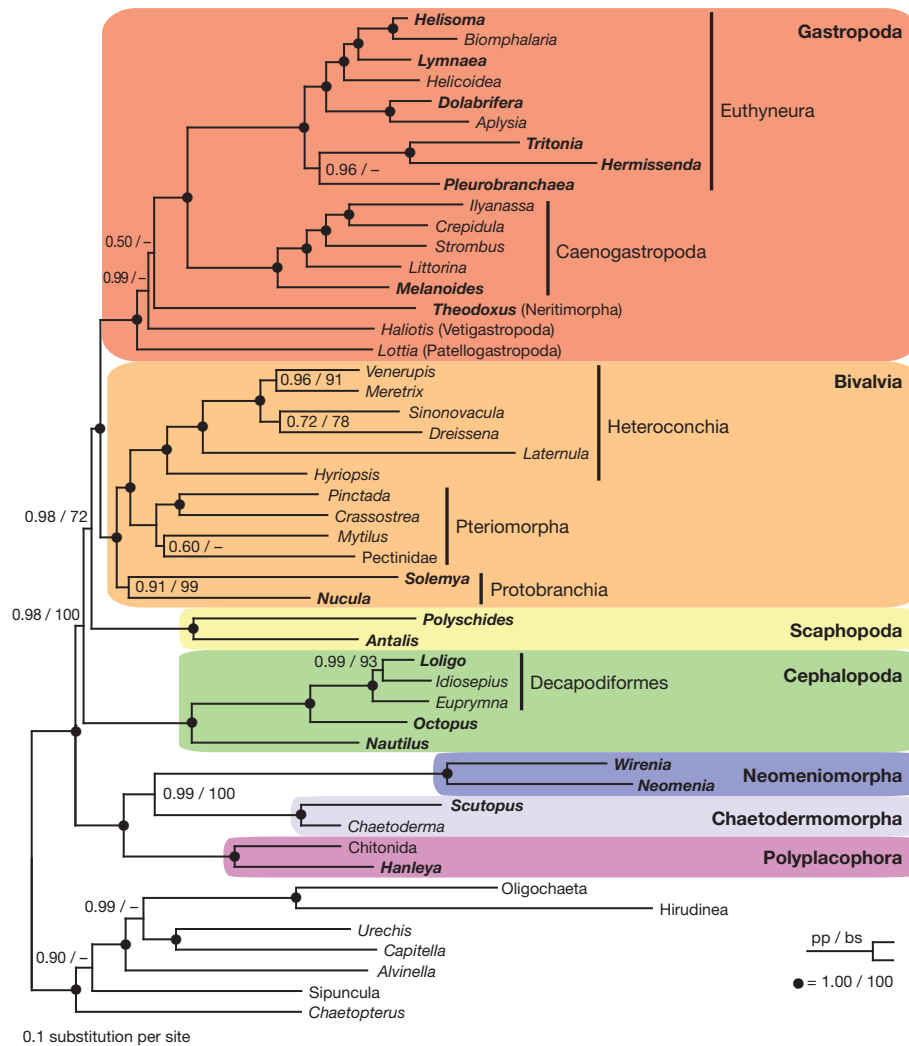


**Figure 2 | Relationships among major lineages of Mollusca based on 308 genes.** Bayesian inference topology shown with ML bootstrap support values (bs) >50 and posterior probabilities (pp) >0.50 are listed at each node. Filled

circles represent nodes with bs = 100 and pp = 1.00. Taxa from which new data were collected are shown in bold.

Here, we used such a phylogenomic approach to investigate evolutionary relationships among the major lineages of Mollusca. High-throughput transcriptome data were collected from 18 operational taxonomic units (OTUs; Supplementary Table 2), and augmented with publicly available ESTs and genomes (Supplementary Table 3). To increase data set completeness, data from closely related species were combined in eleven cases, resulting in a total of 42 mollusc OTUs. Every major lineage of Mollusca was represented in the data set by at least two distantly related species, except for monoplacophorans that live in deep marine habitats and could not be procured in adequate condition for transcriptome analyses. For sequence processing and orthology determination, a bioinformatic pipeline was developed that builds upon previous studies (see Methods and Supplementary Fig. 2). This pipeline identified 308 orthologous genes suitable for concatenation and phylogenetic analyses (Supplementary Table 4), totalling 84,614 amino acid positions.

To determine the appropriate outgroup to Mollusca, preliminary analyses including a broad range of lophotrochozoans and the cnidarian *Nematostella* were conducted. *Nematostella* was included to verify that neomeniid data did not contain cnidarian contamination (see Methods). Maximum likelihood (ML) analyses using the best-fitting model for each gene strongly supported Annelida as the sister taxon of Mollusca (bootstrap support, bs = 100, Supplementary Fig. 3), whereas Bayesian inference (BI) placed Entoprocta + Cyclophora sister to

Mollusca with poor support (posterior probability, pp = 0.62, Supplementary Fig. 4). Relationships among major lineages of Mollusca were consistent between analyses with multiple outgroups (Supplementary Figs 3–4) or with only Annelida as outgroup (Fig. 2 and Supplementary Fig. 5; additional information on outgroup selection in Supplementary Results). On the basis of these results, Annelida was selected as outgroup for all other analyses to reduce computational complexity and potential homoplasy from distant or fast-evolving outgroups. This final data matrix including all 308 genes (Fig. 3) had an average percentage of genes sampled per taxon of 41% and an overall matrix completeness of 25.6%, comparable to other major phylogenomic data sets (for example, ref 11). ML and BI analyses of this matrix

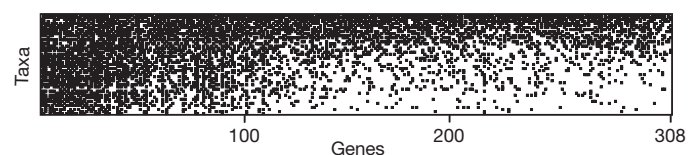


**Figure 3 | Data matrix coverage.** Genes are ordered along the x-axis from left to right from best sampled to worst sampled. Taxa are ordered along the y-axis from top to bottom from most genes sampled to fewest genes sampled. Black squares represent a sampled gene fragment and white squares represent a missing gene fragment.

yielded nearly identical topologies within Mollusca, except for relationships among basal gastropods and placements of the sea slug *Pleurobranchaea* and the bivalve *Mytilus* (Fig. 2 and Supplementary Fig. 5). High leaf stability scores for all OTUs (Supplementary Table 3) and strong support for most nodes suggest all OTUs were represented by sufficient data to be reliably placed. Remarkably, branch lengths were relatively uniform; cephalopods did not show long branches as previously reported in analyses of 18S and 28S<sup>1–3,10</sup>.

All major lineages of Mollusca were monophyletic with strong support (bs = 100%, pp = 1.00). Importantly, there was strong support at all deep nodes, although the node placing Scaphopoda received moderate support in ML (bs = 72%) but strong support in BI (pp = 0.98). A clade including Aplacophora and Polyplacophora was unequivocally supported (bs = 100%, pp = 1.00) and placed sister to Conchifera, consistent with the Aculifera hypothesis. Moreover, we found strong support (bs = 100%, pp = 0.99) for a sister relationship between Neomeniomorpha and Chaetodermomorpha, supporting the Aplacophora hypothesis but contrary to previous molecular<sup>1–3,10</sup> and morphological<sup>4</sup> studies. To evaluate alternatives to the Aculifera and Aplacophora hypotheses, we used AU tests (Supplementary Table 5). These tests rejected the Testaria hypothesis, which allies chitons with the other shelled molluscs ( $P < 0.02$ ) and placement of either aplacophoran taxon as sister to all other molluscs (both  $P < 0.01$ ). Aculiferan monophyly supports interpretation of the Palaeozoic taxon '*Helminthochiton*' *thraivensis* as possessing features intermediate between chitons and aplacophorans<sup>12</sup>, and interpretation of dorsal, serially arranged calcareous structures as a possible aculiferan synapomorphy<sup>13</sup>. Specifically, the chaetoderm *Chaetoderma*<sup>14</sup> and some, but not all, neomenioids<sup>15</sup> possess dorsal, serially repeated sclerite-secreting regions during development. Notably, chiton valves are not thought to be homologous to aculiferan sclerites<sup>16</sup>, although certain genes involved in patterning these structures may be. Our results highlight a need for developmental gene expression studies of aculiferans to address this issue.

Within a monophyletic Conchifera (bs = 100%, pp = 0.98), Gastropoda and Bivalvia were supported as derived sister taxa (bs = 100%, pp = 1.0). Traditionally, a sister relationship between gastropods and bivalves, which relates the two most speciose lineages of molluscs, has received little consideration. However, this relationship has been recovered in molecular studies with relatively limited taxon sampling across Mollusca<sup>5,17</sup>. Similarities between the veliger larvae of gastropods and lamellibranch bivalves have been long recognized. Most notably, both possess larval retractor muscles and a velum muscle ring<sup>18</sup>. Another potential synapomorphy is loss of the anterior ciliary rootlet in locomotory cilia of gastropods and bivalves<sup>19</sup>. Because of strong support for a gastropod/bivalve clade in most analyses and the implications of this hypothesis for understanding molluscan evolution, we propose the node-based name Pleistomollusca, which includes the last common ancestor of Gastropoda and Bivalvia and all descendents (Fig. 4). Etymology of this name (*pleistos* from Greek for 'most') recognizes the incredible species diversity of this clade of molluscs which we conservatively estimate to contain >95% of described mollusc species.

Sister to Pleistomollusca is Scaphopoda (albeit with moderate support in ML; bs = 72%, pp = 0.98) and Cephalopoda represents the sister taxon of all other conchiferan lineages sampled. Despite strong support values for a gastropod/bivalve clade, AU tests failed to reject Scaphopoda as sister to any other conchiferan lineage ( $P > 0.5$ ). Given the limited sampling for Scaphopoda, additional data may help solidify its position. Nonetheless, all results presented here clearly refute the traditional view of a sister relationship between gastropods and cephalopods (Cyrtosoma;  $P < 0.01$ ). Features thought to be diagnostic of this clade include a well-developed, free head with cerebrally innervated eyes and a nervous system with visceral loop inwards of the dorsoventral musculature<sup>6</sup>. However, these characters must be reinterpreted as either symplesiomorphies lost in scaphopods and bivalves, or convergences. Notably,

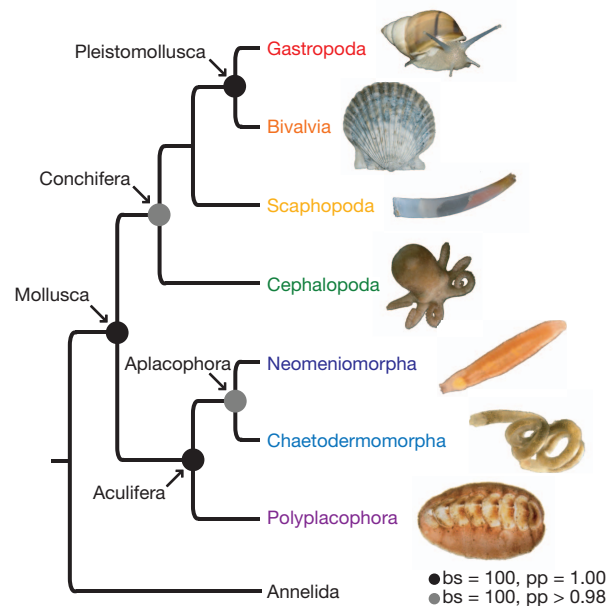


**Figure 4 | Deep molluscan phylogeny as inferred in the present study.** Black circles represent nodes with bs = 100 and pp = 1.00. Gray circles represent nodes with bs = 100 and pp  $\geq 0.98$ . The actual specimens of *Polyschides* and *Hanleya* used in this study are shown. Photos are not to scale. A full-page version of this figure is presented in Supplementary Fig. 1.

the high degree of cephalization in gastropods and cephalopods has recently been suggested to have evolved independently<sup>20</sup>.

The phylogenomic approach used here also holds promise for resolving relationships within major lineages. For example, although their phylogeny has been widely debated, our broadly sampled caenogastropod subtree was strongly supported throughout (bs = 100, pp = 1.0) and consistent with previous morphological analysis<sup>21</sup>. We also recovered opisthobranchs paraphyletic with respect to Pulmonata, agreeing with recent morphological and molecular studies<sup>22</sup>. Additionally, our analyses confirm bivalve monophyly with deposit-feeding protobranchs sister to filter-feeding lamellibranchs.

To assess robustness of the reconstructed topology further, we examined the influences of matrix completeness, gene inclusion and substitution models on phylogenetic reconstruction (Supplementary Table 6). Analyses of the 200 and 100 best-sampled genes (Supplementary Figs 6 and 7) recovered the same branching order and relative level of support among major lineages as the full data set. For gene inclusion, matrices of only non-ribosomal (Supplementary Fig. 8) and only ribosomal protein genes (Supplementary Fig. 9) were analysed to address issues of different gene classes (for example, ribosomal proteins) biasing phylogenetic signal<sup>5</sup>. Support values for deep nodes inferred from non-ribosomal protein genes were generally weak and Aplacophora, Polyplacophora and Bivalvia were not recovered monophyletic. In contrast, analysis of only ribosomal protein genes recovered all major lineages monophyletic with strong support in BI but moderate support for most deep nodes in ML (see also ref. 17). Although ribosomal protein and non-ribosomal protein genes seem to be contributing different amounts of phylogenetic signal, support for most nodes was greater when all gene classes were included, in accordance with previous phylogenomic studies<sup>5,11</sup>. We also performed an analysis based on very conservative orthology determination using only the 243 genes for which our method and InParanoid identified the same *Lottia* sequence as orthologous to the primer taxon (*Drosophila*) sequence (see Methods). Branching order (Supplementary Fig. 10) was identical to the tree based on all 308 genes (Fig. 2). Our ML analyses differ from other phylogenomic studies by using gene-specific amino acid substitution models rather than a single model across the entire matrix. Thus, for comparative reasons, we also ran single-model



**Table 1 | Ancestral states affected by placement of Monoplacophora**

Character	Inferred plesiomorphic state of Mollusca		
	Monoplacophora not considered	Monoplacophora basal in Conchifera	Monoplacophora sister to Polyplacophora
Shell by shell gland	Absent	Absent	Equivocal
Periostracum	Absent	Absent	Equivocal
Position of mantle cavity	Equivocal	Circumpedal	Equivocal
Number of D-V muscles	Equivocal	Eight or more	Equivocal
Pedal ganglia	Equivocal	Absent	Equivocal
Cerebral (pretrochal) eyes	Equivocal	Absent	Equivocal

Only six of 60 characters were affected by the placement of Monoplacophora. See Supplementary Table 7 for additional characters and coding for all characters.

ML analyses using the WAG + CAT + F model (Supplementary Fig. 11) and the LG + CAT + F model (Supplementary Fig. 12). These analyses yielded the same relationships as the ML analysis using the best-fitting model for each gene (Supplementary Fig. 5) with similar overall support in all three analyses. We also assessed the effect of model selection by performing a BI analysis using the CAT-GTR model on the data set of the 100 best-sampled genes (Supplementary Fig. 7); this model is too computationally intensive for the full 308 gene data set. Except for the placement of *Pleurobranchaea*, this analysis yielded the same branching order as the analysis using the CAT model (Fig. 2) with similar support values. Finally, even an approximately ML analysis (Supplementary Fig. 13), which is less computationally intensive, yielded the same relationships among major lineages as the fully parameterized ML analysis.

A primary goal of resolving molluscan phylogeny is to improve our understanding of their early evolutionary history. Perhaps more than any other animal group, understanding of molluscan early evolution has been constrained by the notion of a generalized bauplan or 'archetype' which is still propagated by some invertebrate zoology textbooks. Arguably, such a viewpoint has hindered our ability to consider how individual characters have evolved within Mollusca. Using a modified version of a morphological character matrix<sup>4</sup>, we performed ancestral state reconstruction using maximum parsimony and a simplified topology based on our results (Fig. 4) to infer ancestral states for 60 characters across Mollusca (Supplementary Table 7). Even though monoplacophoran transcriptome data were unavailable herein, we were able to evaluate how placement of Monoplacophora influences our understanding of early molluscan evolution. Ancestral state reconstruction of most characters for the last common ancestor of Mollusca was unaffected by the placement of monoplacophorans. We considered three possibilities: (1) Monoplacophora basal within Conchifera, (2) sister to Polyplacophora, and (3) absent from the analysis. In all three cases, only 6 out of 60 characters were influenced (Table 1). For example, ancestral state reconstruction for shell(s) secreted by a shell gland and periostracum changed between absent (Monoplacophora basal conchiferan) and equivocal (Monoplacophora sister to Polyplacophora, or not considered).

Results of these ancestral state reconstructions shed light on the early evolution of Mollusca. *Odontogriphus*, a Middle Cambrian form proposed to be a stem-group mollusc, showed character states consistent with our reconstructions (ventral muscular foot, dorsal cuticular mantle, mantle cavity containing ctenidia or gills, and regionalized gut)<sup>23</sup>. However, whereas *Odontogriphus* and *Wiwaxia* (another Middle Cambrian putative stem-group mollusc) apparently had a narrow, distichous (bipartite, aplacophoran-like) radula<sup>23,24</sup>, ancestral state reconstruction indicates that the plesiomorphic state of the radula was broad and rasping with multiple teeth per row attached to a flexible radular membrane supported by muscular and cartilage-like bolsters as in chitons and most conchiferans.

The origin and evolution of molluscan epidermal hardparts (shells and sclerites) is another contentious issue. Although aculiferan sclerites, chiton valves and conchiferan shells are all calcareous secretions of the mantle, developmental and structural differences indicate that these structures are not homologous<sup>16</sup>. Sclerites are only present in aculiferans, and shells secreted by a shell gland are only present in conchiferans. Moreover, fossil taxa do not help clarify the plesiomorphic state of the molluscan scleritome as *Odontogriphus* lacked both sclerites and shells<sup>23</sup>,

*Wiwaxia* had uncalcified, chitinous sclerites, and other putative stem-group molluscs had calcareous sclerites and/or shells<sup>7</sup>. Therefore, organization of the ancestral scleritome, if present, remains ambiguous.

In summary, our robustly supported evolutionary framework for Mollusca consists of two major clades: Aculifera, which includes a monophyletic Aplacophora sister to Polyplacophora, and Conchifera (as sampled), including a gastropod/bivalve clade we term Pleiostomolusca. Neomeniomorpha was not placed as the basal-most molluscan lineage as previously suggested nor is the Testaria hypothesis supported. Thus, several aplacophoran features commonly argued to be molluscan plesiomorphies (for example, non-muscular foot, organization of midgut, primarily distichous radula without subradular membrane) are reinterpreted as aplacophoran synapomorphies, whereas others are reinterpreted as neomenioid apomorphies (for example, prepedal cirri, pericalymma-type larva). Within Conchifera, our results show that gastropods are sister to bivalves (not cephalopods), a result that has important implications for molluscan model systems. Also, possible independent evolution of highly cephalized morphologies in gastropods and cephalopods suggests additional work addressing neural features across conchiferans is needed<sup>20</sup>.

## METHODS SUMMARY

RNA was extracted from 20 mollusc species representing 18 OTUs, reverse transcribed to cDNA, and sequenced using 454 GS-FLX or Titanium (Roche; Supplementary Table 2). Sanger expressed sequence tag (EST) libraries generated for *Scutopus* and *Wirenia* were also included in this study. These data were augmented with publicly available data (Supplementary Table 3). ESTs were cleaned, assembled and translated using EST2Uni<sup>25</sup>. Unigenes (contigs and singletons) were parsed into putatively orthologous groups (OGs) with HaMStr<sup>26</sup>.

Each OG was aligned and manually evaluated to trim out obviously mis-translated regions, screen for paralogues and combine two or more incomplete sequences representing the same orthologue into a consensus sequence. For each OG, ML trees were inferred in RAXML 7.27 (ref. 27) using the best fitting amino acid substitution model. For OGs with apparent paralogues, suspect sequences were removed or the OG was excluded from further analysis. Additional filtering was used on the neomenioid aplacophoran data sets to identify and remove cnidarian contamination (see Methods).

Phylogenetic analyses of the final matrix were performed using ML with the best fitting model for each gene in RAXML and BI with the CAT model in Phylobayes 2.3 (ref. 28) on the Alabama Supercomputer Authority's Dense Memory Cluster (<http://www.asc.edu/>). Stability of each OTU was calculated using the leaf stability index implemented in Phytutility<sup>29</sup> and alternative hypotheses of molluscan relationships were evaluated using AU tests<sup>30</sup> with the WAG +  $\Gamma$  + F model in RAXML. Ancestral state reconstructions were performed based on a modified morphological matrix<sup>4</sup> using maximum parsimony in Mesquite 2.74 (<http://mesquiteproject.org/>).

**Full Methods** and any associated references are available in the online version of the paper at [www.nature.com/nature](http://www.nature.com/nature).

**Received 23 February; accepted 22 July 2011.**

**Published online 4 September 2011.**

1. Passamanek, Y. J., Schander, C. & Halanych, K. M. Investigation of molluscan phylogeny using large-subunit and small-subunit nuclear rRNA sequences. *Mol. Phylogenet. Evol.* **32**, 25–38 (2004).
2. Giribet, G. *et al.* Evidence for a clade composed of molluscs with serially repeated structures: Monoplacophorans are related to chitons. *Proc. Natl. Acad. Sci. USA* **103**, 7723–7728 (2006).

3. Wilson, N. G., Rouse, G. W. & Giribet, G. Assessing the molluscan hypothesis Serialia (Monoplacophora + Polyplacophora) using novel molecular data. *Mol. Phylogenet. Evol.* **54**, 187–193 (2010).
4. Haszprunar, G. Is the Aplacophora monophyletic? A cladistic point of view. *Am. Malacol. Bull.* **15**, 115–130 (2000).
5. Dunn, C. W. *et al.* Broad phylogenomic sampling improves resolution of the animal tree of life. *Nature* **452**, 745–749 (2008).
6. Haszprunar, G., Schander, C. & Halanych, K. M. In *Phylogeny and Evolution of the Mollusca* (eds Ponder, W. & Lindberg, D. R.) 19–32 (Univ. of California Press, 2008).
7. Todt, C., Okusu, A., Schander, C. & Schwabe, E. In *Phylogeny and evolution of the Mollusca* (eds Ponder, W. & Lindberg, D. R.) 105–141 (Univ. of California Press, 2008).
8. Scheltema, A. H. Aplacophora as progenetic aculiferans and the coelomate origin of mollusks as the sister taxon of Sipuncula. *Biol. Bull.* **184**, 57–78 (1993).
9. Salvini-Plawen, L. On the phylogenetic significance of the aplacophoran Mollusca. *Iberus* **21**, 67–97 (2003).
10. Meyer, A., Todt, C., Mikkelsen, N. & Lieb, B. Fast evolving 18S rRNA sequences from Solenogastres (Mollusca) resist standard PCR amplification and give new insights into mollusk substitution rate heterogeneity. *BMC Evol. Biol.* **10**, 70 (2010).
11. Struck, T. H. *et al.* Phylogenomic analyses unravel annelid evolution. *Nature* **471**, 95–98 (2011).
12. Sigwart, J. D. & Sutton, M. D. Deep molluscan phylogeny: synthesis of palaeontological and neontological data. *Proc. R. Soc. B* **274**, 2413–2419 (2007).
13. Scheltema, A. H. & Ivanov, D. L. An aplacophoran postlarva with iterated dorsal groups of spicules and skeletal similarities to Paleozoic fossils. *Invertebr. Biol.* **121**, 1–10 (2002).
14. Nielsen, C., Haszprunar, G., Ruthensteiner, B. & Wanninger, A. Early development of the aplacophoran mollusc *Chaetoderma*. *Acta Zool.* **88**, 231–247 (2007).
15. Todt, C. & Wanninger, A. Of tests, trochs, shells, and spicules: Development of the basal mollusk *Wirenia argentea* (Solenogastres) and its bearing on the evolution of trochozoan larval key features. *Front. Zool.* **7**, 6 (2010).
16. Scheltema, A. H. & Schander, C. Exoskeletons: tracing molluscan evolution. *Venus* **65**, 19–26 (2006).
17. Meyer, A., Witek, A. & Lieb, B. Selecting ribosomal protein genes for invertebrate phylogenetic inferences: how many genes to resolve the Mollusca? *Method. Ecol. Evol.* **2**, 34–42 (2011).
18. Wanninger, A. & Haszprunar, G. Muscle development in *Antalis entalis* (Mollusca, Scaphopoda) and its significance for scaphopod relationships. *J. Morphol.* **254**, 53–64 (2002).
19. Lundin, K., Schander, C. & Todt, C. Ultrastructure of epidermal cilia and ciliary rootlets in Scaphopoda. *J. Molluscan Stud.* **75**, 69–73 (2008).
20. Moroz, L. L. On the independent origins of complex brains and neurons. *Brain Behav. Evol.* **74**, 177–190 (2009).
21. Simone, L. R. L. *Filogenia das superfamílias de Caenogastropoda (Mollusca) com base em morfologia comparativa*. PhD thesis, Univ. São Paulo (2000).
22. Jörger, K. M. *et al.* On the origin of Acochlidia and other enigmatic euthyneuran gastropods, with implications for the systematics of Heterobranchia. *BMC Evol. Biol.* **10**, 323 (2010).
23. Caron, J. B., Scheltema, A., Schander, C. & Rudkin, D. A soft-bodied mollusc with radula from the Middle Cambrian Burgess Shale. *Nature* **442**, 159–163 (2006).
24. Scheltema, A. H., Kerth, K. & Kuzirian, A. M. Original molluscan radula: comparisons among Aplacophora, Polyplacophora, Gastropoda, and the Cambrian fossil *Wiwaxia corrugata*. *J. Morphol.* **257**, 219–245 (2003).
25. Forment, J. *et al.* EST2uni: an open, parallel tool for automated EST analysis and database creation, with a data mining web interface and microarray expression data integration. *BMC Bioinformatics* **9**, 5 (2008).
26. Ebersberger, I., Strauss, S. & Von Haeseler, A. HaMStR: Profile hidden markov model based search for orthologs in ESTs. *BMC Evol. Biol.* **9**, 157 (2009).
27. Stamatakis, A. RAxML-VI-HPC: maximum likelihood-based phylogenetic analyses with thousands of taxa and mixed models. *Bioinformatics* **22**, 2688–2690 (2006).
28. Lartillot, N. & Philippe, H. A Bayesian mixture model for across-site heterogeneities in the amino-acid replacement process. *Mol. Biol. Evol.* **21**, 1095–1109 (2004).
29. Smith, S. A. & Dunn, C. W. Phyutility: a phylogenetics tool for trees, alignments and molecular data. *Bioinformatics* **24**, 715–716 (2008).
30. Shimodaira, H. An approximately unbiased test of phylogenetic tree selection. *Syst. Biol.* **51**, 492–508 (2002).

**Supplementary Information** is linked to the online version of the paper at [www.nature.com/nature](http://www.nature.com/nature).

**Acknowledgements** We thank W. Jones and K. T. Fielman for help with cDNA library preparation, R. M. Jennings, N. Mikkelsen, and the crews of the RV *Håkon Mosby*, RV *Hans Brattstrom* and RV *Laurence M. Gould* for assistance collecting aplacophorans, and J. C. Havird, P. J. Krug, S. C. Kempf, D. R. Lindberg, M. V. Matz, L. R. Page and T. H. Struck for discussions. D. Speiser kindly shared the photo of *Argopecten*. F. W. Goetz, A. Gracey and M. L. Blaxter kindly provided sequence quality data for *Dreissena rostriformis*, *Mytilus californianus* and *Lumbricus rubellus*, respectively. We thank A. Di Cosmo, P. Burbach, V. Rehder, W. Wright and R. Gillette for providing samples of *Octopus*, *Loligo*, *Helisoma*, *Dolabrifera* and *Pleurobranchaea* as well as sharing some sequencing cost for these species. We also thank D. Young and the Alabama Supercomputer Authority for access to computational resources. The genomes of *Capitella teleta*, *Helobdella robusta*, *Lottia gigantea* and *Nematostella vectensis* were produced by the US Department of Energy Joint Genome Institute in collaboration with the user community. This work was supported by National Science Foundation (NSF) grants (0744649 and 0821622) to K.M.H., National Institute of Health (NIH) grants (1R01NS06076, 1R01GM097502, R21 RR025699, R21DA030118) and the McKnight Brain Research Foundation to L.L.M., the Deep Metazoan Phylogeny (DMP) program of the German Science Foundation (Li 998/9-1) to B.L., and The University of Bergen (Norway) free researcher initiated project grant to C.T. (project no. 226270). This work represents contributions 82 and 4 to the Auburn University (AU) Marine Biology Program and Molette Biology Laboratory for Environmental and Climate Change Studies, respectively.

**Author Contributions** K.M.H., C.T., B.L., C.S. and K.M.K. conceived and designed this study. K.M.H., L.L.M., B.L. and C.T. supervised cDNA preparation and sequencing. L.L.M., A.B.K., K.M.K., J.T.C. and A.M. prepared and sequenced cDNA. K.M.K., J.T.C., S.R.S. and M.R.C. developed the bioinformatics pipeline. K.M.K. performed phylogenetic and ancestral state reconstruction analyses. K.M.K. and J.T.C. prepared the figures. C.S., C.T. and K.M.K. modified the morphological character matrix. A.B.K., K.M.K. and A.M. submitted sequences to GenBank. All authors contributed in preparing the Letter.

**Author Information** Capillary sequence data are available from the NCBI EST database (<http://www.ncbi.nlm.nih.gov/projects/dbEST>) under accession numbers JG454968.1–JG456874.1 and 454 sequence data are available from the NCBI SRA database (<http://www.ncbi.nlm.nih.gov/sra>) accession number SRA030407.1. Matrices and trees from this study are available from TreeBASE (<http://www.treebase.org>) accession number S11762. Reprints and permissions information is available at [www.nature.com/reprints](http://www.nature.com/reprints). The authors declare no competing financial interests. Readers are welcome to comment on the online version of this article at [www.nature.com/nature](http://www.nature.com/nature). Correspondence and requests for materials should be addressed to K.M.K. ([krmkocot@auburn.edu](mailto:krmkocot@auburn.edu)) and K.M.H. ([ken@auburn.edu](mailto:ken@auburn.edu)).

## METHODS

**Overview.** Data and analyses were conducted in four basic steps: (1) RNA was extracted from mollusc species, cDNA was prepared and then sequenced; (2) EST data were processed with a bioinformatics pipeline incorporating EST2Uni<sup>25</sup> and HaMStr<sup>26</sup>; (3) trees were reconstructed with RAxML 7.27 (ref. 27) and Phylobayes 2.3 (ref. 28). (4) Additional measures, including leaf stability with Phyutility<sup>29</sup> and Approximately Unbiased (AU) tests<sup>30</sup> were used to assess robustness of the results.

**Molecular techniques.** Complementary DNA was prepared using standard protocols and sequenced using either 454 GS-FLX or Titanium. Sanger EST libraries generated for *Scutopus* and *Wirenia* were also included in this study. See Supplementary Methods for detailed laboratory methods.

**Sequence processing.** Raw ESTs were processed and assembled using the EST2uni pipeline<sup>25</sup>. This software removes low-quality regions with Lucy<sup>31</sup>, removes vector sequences with Lucy and SeqClean (<http://compbio.dfci.harvard.edu/tgi/software/>), masks low complexity regions with RepeatMasker (<http://www.repeatmasker.org>), and assembles contigs with CAP3 (ref. 32). Data on sequence quality were used by CAP3 when available. Unigenes were translated with ESTScan<sup>33</sup> and sequences shorter than 100 amino acids were deleted. Manual BLAST searches of samples of unigenes for vector sequences as well as examination of contig assembly diagrams generated by EST2uni indicated that these programs performed well at removing vector and low-quality sequences and assembling contigs, respectively.

To reduce the amount of missing data per taxon, sequences from two or more closely related taxa were combined to create the following 11 chimaerical OTUs: *Chitonida*, *Crassostrea*, *Dreissena*, *Haliothis*, *Helicoidea*, *Loligo*, *Mytilus*, *Pectinidae*, *Pedicellina*, *Sipuncula* and *Venerupis*.

**Orthology assignment and data set assembly.** OG identification used HaMStr local 7 (ref. 26), which uses profile hidden Markov models (pHMMs) generated from completely sequenced reference taxa in the InParanoid database<sup>34</sup>. Translated unigenes were searched against the 1,032 single-copy OGs of HaMStr's 'model organism' pHMMs derived from *Homo*, *Ciona*, *Drosophila*, *Caenorhabditis* and *Saccharomyces*. Translated unigenes matching an OG's pHMM were then compared to the proteome of *Drosophila* using BLASTP. If the *Drosophila* protein contributing to the pHMM was the best BLASTP hit, the unigene was then placed in that OG.

If one of the first or last 20 characters of an amino acid sequence was an X (corresponding to a codon with an ambiguity, gap, or missing data), all characters between the X and that end of the sequence were deleted and treated as missing data. This step was important as ends of singletons were occasionally, but obviously, mistranslated. Each OG was aligned with MAFFT<sup>35</sup> using the default alignment strategy. Aligned OGs were then manually inspected and subjected to trimming or deleting of partially mistranslated sequences, screening for paralogues, and combining incomplete sequences from the same OTU into one, more complete consensus sequence. These alignments were then trimmed with Aliscore and Alicut<sup>36</sup> to remove regions with ambiguous alignment or little to no phylogenetic signal. Lastly, any alignments less than 25 amino acids in length were discarded.

Maximum likelihood (ML) trees were inferred for each OG using RAxML 7.2.7 (ref. 27) using the best-fitting amino acid substitution model as determined using the RAxML amino acid substitution model selection Perl script. OGs with strongly supported deep nodes suggesting the inclusion of paralogs were edited to delete obviously paralogous sequences or discarded. To reduce missing data in the final matrices, only OGs with sequences from at least ten molluscs were retained for analysis.

If an OG still possessed more than one sequence from one or more OTUs (inparalogues), the sequence with the shortest average pairwise distance to all others was retained. Pairwise distances were calculated using a gamma distribution with four rate categories as implemented in SCAFoS<sup>37</sup>. If two or more sequences from the same taxon were >10% divergent, all sequences from that taxon were discarded from that OG. To visualize the amount of data sampled for each taxon, a gene sampling diagram (Fig. 3) was created using MARE (<http://mare.zfink.de>).

**Contamination screening.** Neomenioids have been reported to harbour nucleic acid contamination from their prey<sup>38</sup>. Given this, specimens of *Wirenia argentea* (which feed on cnidarians) were starved for 2 months before RNA extraction. Gut content analysis of *Neomenia* sp. confirmed that this undescribed Antarctic species (see Supplementary Results) also feeds on cnidarians. Therefore, *Neomenia* unigenes were compared to predicted transcripts of *Lottia* and *Nematostella* using TBLASTX and sequences with a lower *E*-value for *Nematostella* than *Lottia* (that is, sequences more similar to a sequence in the proteome of *Nematostella* than *Lottia*) were discarded. ML trees for each gene were manually evaluated and any remaining cnidarian contamination in the neomenioid data sets was removed by deleting sequences which either formed a clade with *Nematostella* or were part of a polytomy that included *Nematostella*. Finally, *Nematostella* was included in analyses with broad outgroup sampling (Supplementary Figs 3 and 4) to demonstrate that there is no obvious attraction between it and either neomenioid.

**Phylogenetic analyses.** Phylogenetic analyses were conducted using ML in RAxML 7.2.7 (ref. 27) and BI in PhyloBayes 2.3 (ref. 28) on the Alabama Supercomputer Authority Dense Memory Cluster (<http://www.asc.edu/>). For ML analyses, the best fitting amino acid substitution model for each gene was determined using the RAxML model selection Perl script. This script tests the fit of each available model of amino acid substitution by optimizing model parameters and branch lengths on a JTT start tree for each OG. Additionally, for comparative purposes, ML analyses using one model for the entire matrix were performed using the WAG + CAT + F and LG + CAT + F models in RAxML (Supplementary Figs 11 and 12) and an approximately ML analysis was performed using the JTT + CAT model in FastTree 2.1 (ref. 39, Supplementary Fig. 13). Topological robustness (that is, nodal support) for all ML analyses was assessed with 100 replicates of nonparametric bootstrapping. Stabilities of OTUs among the bootstrapped trees were calculated using the leaf stability index in Phyutility<sup>29</sup>. Competing hypotheses of mollusc phylogeny were evaluated using the AU test<sup>30</sup> with the best-fitting model for each partition. For all BI analyses, the CAT model was used to account for site-specific rate heterogeneity<sup>28</sup>. Unless otherwise noted, all BI analyses were conducted with five parallel chains run for 15,000 cycles each, with the first 5,000 trees discarded as burn-in. A 50% majority rule consensus tree was computed from the remaining 10,000 trees from each chain. Topological robustness was assessed using posterior probabilities. Maxdiff values below 0.3 indicated that all chains in a run had converged.

**Ancestral state reconstruction.** Ancestral character state reconstruction was performed using an updated and modified version of the morphological matrix from ref. 4 in Mesquite 2.74 (<http://mesquiteproject.org/>) using maximum parsimony as the reconstruction method.

- Chou, H. H. & Holmes, M. H. DNA sequence quality trimming and vector removal. *Bioinformatics* **17**, 1093–1104 (2001).
- Huang, X. & Madan, A. CAP3: a DNA sequence assembly program. *Genome Res.* **9**, 868–877 (1999).
- Lottaz, C., Iseli, C., Jongeneel, C. V. & Bucher, P. Modeling sequencing errors by combining Hidden Markov models. *Bioinformatics* **19**, (2003).
- O'Brien, K. P., Remm, M. & Sonnhammer, E. L. InParanoid: a comprehensive database of eukaryotic orthologs. *Nucleic Acids Res.* **33**, D476–D480 (2005).
- Katoh, K., Kuma, K., Toh, H. & Miyata, T. MAFFT version 5: improvement in accuracy of multiple sequence alignment. *Nucleic Acids Res.* **33**, 511–518 (2005).
- Misof, B. & Misof, K. A Monte Carlo approach successfully identifies randomness in multiple sequence alignments: a more objective means of data exclusion. *Syst. Biol.*, (2009).
- Roure, B., Rodríguez-Ezpeleta, N. & Philippe, H. SCAFoS: a tool for selection, concatenation and fusion of sequences for phylogenomics. *BMC Evol. Biol.* **7**, (2007).
- Okusu, A. & Giribet, G. New 18S rRNA sequences from neomenioid aplousobranchs and the possible origin of persistent exogenous contamination. *J. Molluscan Stud.* **69**, 385–387 (2003).
- Price, M. N., Dehal, P. S. & Arkin, A. P. FastTree 2 – approximately maximum-likelihood trees for large alignments. *PLoS ONE* **5**, (2010).



# Antibiotic resistance is ancient

Vanessa M. D'Costa<sup>1,2\*</sup>, Christine E. King<sup>3,4\*</sup>, Lindsay Kalan<sup>1,2</sup>, Mariya Morar<sup>1,2</sup>, Wilson W. L. Sung<sup>4</sup>, Carsten Schwarz<sup>3</sup>, Duane Froese<sup>5</sup>, Grant Zazula<sup>6</sup>, Fabrice Calmels<sup>5</sup>, Regis Debruyne<sup>7</sup>, G. Brian Golding<sup>4</sup>, Hendrik N. Poinar<sup>1,3,4</sup> & Gerard D. Wright<sup>1,2</sup>

The discovery of antibiotics more than 70 years ago initiated a period of drug innovation and implementation in human and animal health and agriculture. These discoveries were tempered in all cases by the emergence of resistant microbes<sup>1,2</sup>. This history has been interpreted to mean that antibiotic resistance in pathogenic bacteria is a modern phenomenon; this view is reinforced by the fact that collections of microbes that predate the antibiotic era are highly susceptible to antibiotics<sup>3</sup>. Here we report targeted metagenomic analyses of rigorously authenticated ancient DNA from 30,000-year-old Beringian permafrost sediments and the identification of a highly diverse collection of genes encoding resistance to  $\beta$ -lactam, tetracycline and glycopeptide antibiotics. Structure and function studies on the complete vancomycin resistance element VanA confirmed its similarity to modern variants. These results show conclusively that antibiotic resistance is a natural phenomenon that predates the modern selective pressure of clinical antibiotic use.

Recent studies of modern environmental and human commensal microbial genomes have a much larger concentration of antibiotic resistance genes than has been previously recognized<sup>4–6</sup>. In addition, metagenomic studies have revealed diverse homologues of known resistance genes broadly distributed across environmental locales. This widespread dissemination of antibiotic resistance elements is inconsistent with a hypothesis of contemporary emergence and instead suggests a richer natural history of resistance<sup>2</sup>. Indeed, estimates of the origin of natural product antibiotics range from 2 Gyr to 40 Myr ago<sup>7,8</sup>, suggesting that resistance should be similarly old. Previous publications claim to have cultured resistant bacteria from Siberian permafrost (for example ref. 9), but these results remain contentious (see Supplementary Information).

To determine whether contemporary resistance elements are modern or whether they originated before our use of antibiotics, we analysed DNA sequences recovered from Late Pleistocene permafrost sediments. The samples were collected east of Dawson City, Yukon, at the Bear Creek (BC) site (Fig. 1); prominent forms of ground ice (ice wedges and surface icings) are preserved in the exposure, immediately overlain by a distinctive volcanic ash layer, the Dawson tephra<sup>10,11</sup> (Supplementary Table 1 and Supplementary Figs 1 and 2). The tephra has been dated at several sites in the area to about 25,300 radiocarbon (<sup>14</sup>C) years BP, or about 30,000 calendar years<sup>10,12</sup>. The cryostratigraphic context is similar to other sites in the area preserving relict permafrost and indicates that the permafrost has not thawed since the time of deposition (Supplementary Information). In the absence of fluid leaching, the site represents an ideal source of uncontaminated and securely dated ancient DNA.

Two frozen sediment cores (BC1 and BC4), 10 cm apart, were obtained 50 cm below the tephra. In accordance with appropriate protocols<sup>13</sup>, we monitored contamination introduced during coring by spraying the drilling equipment and the outer surface of the cores

with high concentrations of *Escherichia coli* harbouring the *gfp* (green fluorescent protein) gene from *Aequorea victoria* (Supplementary Information).

After fracturing of the samples (Supplementary Fig. 3), total DNA was extracted from a series of five subsamples taken along the radius of each core (Supplementary Information). Quantitative polymerase

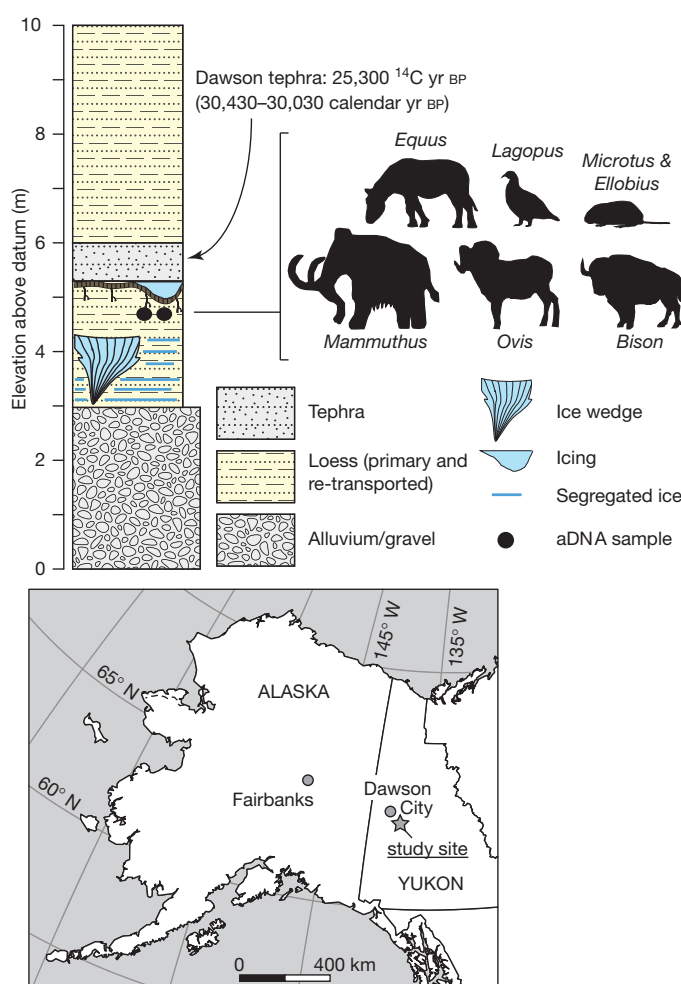


**Figure 1 | Stratigraphic profile and location of Bear Creek site.** Elevation is given in metres above base of exposure. Permafrost samples from below Dawson tephra were dated to about 30 kyr BP. Preservation of the ice below and above the sample indicates that the sediments have not thawed since deposition. Silhouettes represent mammals and birds identified from ancient DNA sequences that are typical of the regional Late Pleistocene environment. aDNA, ancient DNA.

<sup>1</sup>Michael G. DeGroot Institute for Infectious Disease Research, McMaster University, Hamilton, Ontario, Canada, L8N 3Z5. <sup>2</sup>Department of Biochemistry and Biomedical Sciences, McMaster University, Hamilton, Ontario, Canada, L8N 3Z5. <sup>3</sup>McMaster Ancient DNA Centre, Department of Anthropology, McMaster University, Hamilton, Ontario, Canada, L8S 4L9. <sup>4</sup>Department of Biology, McMaster University, Hamilton, Ontario, Canada, L8S 4K1. <sup>5</sup>Department of Earth and Atmospheric Sciences, University of Alberta, Edmonton, Alberta, Canada, T6G 2E3. <sup>6</sup>Yukon Palaeontology Program, Department of Tourism and Culture, Yukon Government, PO Box 2703, Whitehorse, Yukon, Canada, Y1A 2C6. <sup>7</sup>Muséum National d'Histoire Naturelle, UMR 7206 Eco-anthropologie, 57 rue Cuvier, CP139, 75231 Paris cedex 05, France.

\*These authors contributed equally to this work.

chain reaction (qPCR) analysis confirmed extremely high yields of *gfp* on both core exteriors, with 0.1% or less of this amount at the centre (Supplementary Information and Supplementary Fig. 4). This supports negligible leaching or cross-contamination during subsampling.

A crucial step lending support for the authenticity of the ancient DNA was to confirm the presence of DNA derived from flora and fauna characteristic of a late Pleistocene age, and the absence of common modern or Holocene floral and faunal sources. To explore the vertebrate and plant diversity, we amplified fragments of the mitochondrial 12S rRNA and chloroplast *trnL* and *rbcL* genes (Supplementary Table 3). Amplicons were sequenced with the 454 GS-FLX platform and identified by BLAST analysis of GenBank sequences (Supplementary Information).

The vertebrate sequences included abundant Late Pleistocene megafauna such as *Bison*, *Equus* and *Ovis*, as well as rodents (*Microtus* and *Ellobius*) and the rock ptarmigan, *Lagopus mutus* (Supplementary Fig. 6 and Supplementary Table 5). *Mammuthus* was detectable at low copy numbers with the use of a mammoth-specific qPCR assay, which is consistent with the low ratio of these fossils relative to bison and horse in the region<sup>11,14</sup>. The *rbcL* and *trnL* sequences revealed many plant groups that are also well documented in Beringia, including the grasses *Poa* and *Festuca*, sage (*Artemisia*) and willow (*Salix*)<sup>15</sup> (Supplementary Figs 7 and 8, and Supplementary Tables 6 and 7). No sequences of common Holocene vertebrates (for example elk or moose) or plants (for example spruce) were identified despite sequence conservation across the primer-binding sites; these results are consistent with other reports<sup>16</sup> that have argued against DNA leaching in permafrost sediments.

We focused our investigation of bacterial 16S rRNA sequences on the Actinobacteria, known for their ability to synthesize diverse secondary metabolites and for harbouring antibiotic resistance genes<sup>4</sup>. Deep sequencing of 16S amplicons (Supplementary Information) revealed genera commonly found in soil and permafrost microbial communities<sup>17</sup>, including *Aeromicrobium*, *Arthrobacter* and *Frankia* (Supplementary Fig. 9 and Supplementary Table 8). Analysis of contaminant 16S sequences derived from extraction and PCR control reactions (Supplementary Table 4) suggested that these do not contribute to the ancient DNA data set; in fact not only were the copy numbers 1,000–30,000-fold lower than from the permafrost extracts, but with the exception of unclassified bacteria there was also very little overlap in the genera identified (Supplementary Fig. 9 and

Supplementary Table 8). Querying the permafrost sequences against the contaminant data set with the use of BLAST further confirmed their disparity: only 1% of the reads had 95–100% identity to a contaminant sequence, with a single sequence showing 100% identity.

We next developed a series of assays to detect genes encoding resistance to several major classes of antibiotic and representing diverse strategies of drug evasion (for example target modification, target protection and enzymatic drug inactivation) (Supplementary Information). Determinants included the ribosomal protection protein TetM, which confers resistance to tetracycline antibiotics by weakening the interaction between the drug and the ribosome; the D-Ala-D-Ala dipeptide hydrolase VanX, which is a component of the vancomycin resistance operon; the aminoglycoside-antibiotic-modifying acetyltransferase AAC(3); a penicillin-inactivating  $\beta$ -lactamase Bla (a member of the TEM group of  $\beta$ -lactamases); and the ribosome methyltransferase Erm, which blocks the binding of macrolide, lincosamide and type B streptogramin antibiotics. Amplification of *vanX*, *tetM* and *bla* fragments was successful, and triplicate PCR products from multiple extracts were cloned and multiple clones were sequenced.

The  $\beta$ -lactamase sequences demonstrated amino-acid identities between 53% and 84% with known determinants and clustered with one of two groups of enzymes: characterized  $\beta$ -lactamases from streptomycetes and uncharacterized  $\beta$ -lactamase-like hydrolytic proteins (Fig. 2a and Supplementary Fig. 14). We identified several *tetM*-related genes in the permafrost, most of which were most closely related to the actinomycete subset of ribosomal protection proteins, including the biochemically characterized self-resistance element OtrA from the oxytetracycline producer *Streptomyces rimosus*<sup>18</sup> (Fig. 2b). Most intriguing was the identification of *vanX* gene fragments, which spanned the entire phylogenetic space of characterized vancomycin resistance determinants found in the clinic and in the environment. These branch away from the cellular dipeptidases that are the likely progenitors the *vanX* family (Supplementary Fig. 10).

Vancomycin resistance took the clinical community by surprise when it emerged in pathogenic enterococci in the late 1980s<sup>19</sup>. In both clinical pathogens<sup>19</sup> and contemporary soil environments<sup>4</sup>, resistance results from the acquisition of a three-gene operon *vanH-vanA-vanX* (*vanHAX*). These enzymes collectively reconstruct bacterial peptidoglycan to terminate in D-alanine-D-lactate in place of the canonical D-alanine-D-alanine, which is required for vancomycin binding and

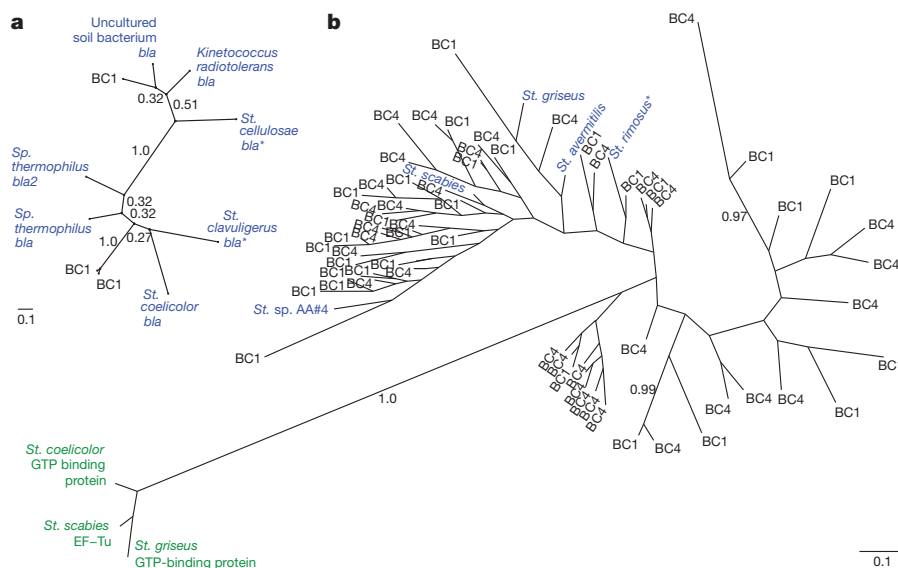


**Figure 2 | Genetic diversity of ancient antibiotic resistance elements.** a, b, Unrooted Bayesian phylogenies of translated  $\beta$ -lactamase (*bla*) (a) and tetracycline resistance (*tetM*) (b). Blue denotes predicted resistance enzymes, and green those associated with other functions; permafrost-derived sequences are labelled with the originating core name. Sequences in which resistance

activity has been biochemically verified are noted with a single asterisk (Supplementary Information). The scale bar represents 0.1 substitutions per site. Posterior probabilities are shown for a, and those of 0.7 or more are indicated for b. All unlabelled tips derive from ancient sequences. BC1, Bear Creek sample 1; BC4, Bear Creek sample 4.

subsequent antibiotic action. Although most forms of resistance are attributed to a single gene, this complex mechanism is exclusively associated with resistance and thus its presence provides unambiguous confirmation of its role as a resistance determinant.

With few exceptions, the *vanHAX* operon is invariant in genetic organization; it therefore offers a matchless template for confirming its presence with PCR assays that span the *vanHA* and *vanAX* boundaries. Two short qPCR assays were designed to confirm this contiguity

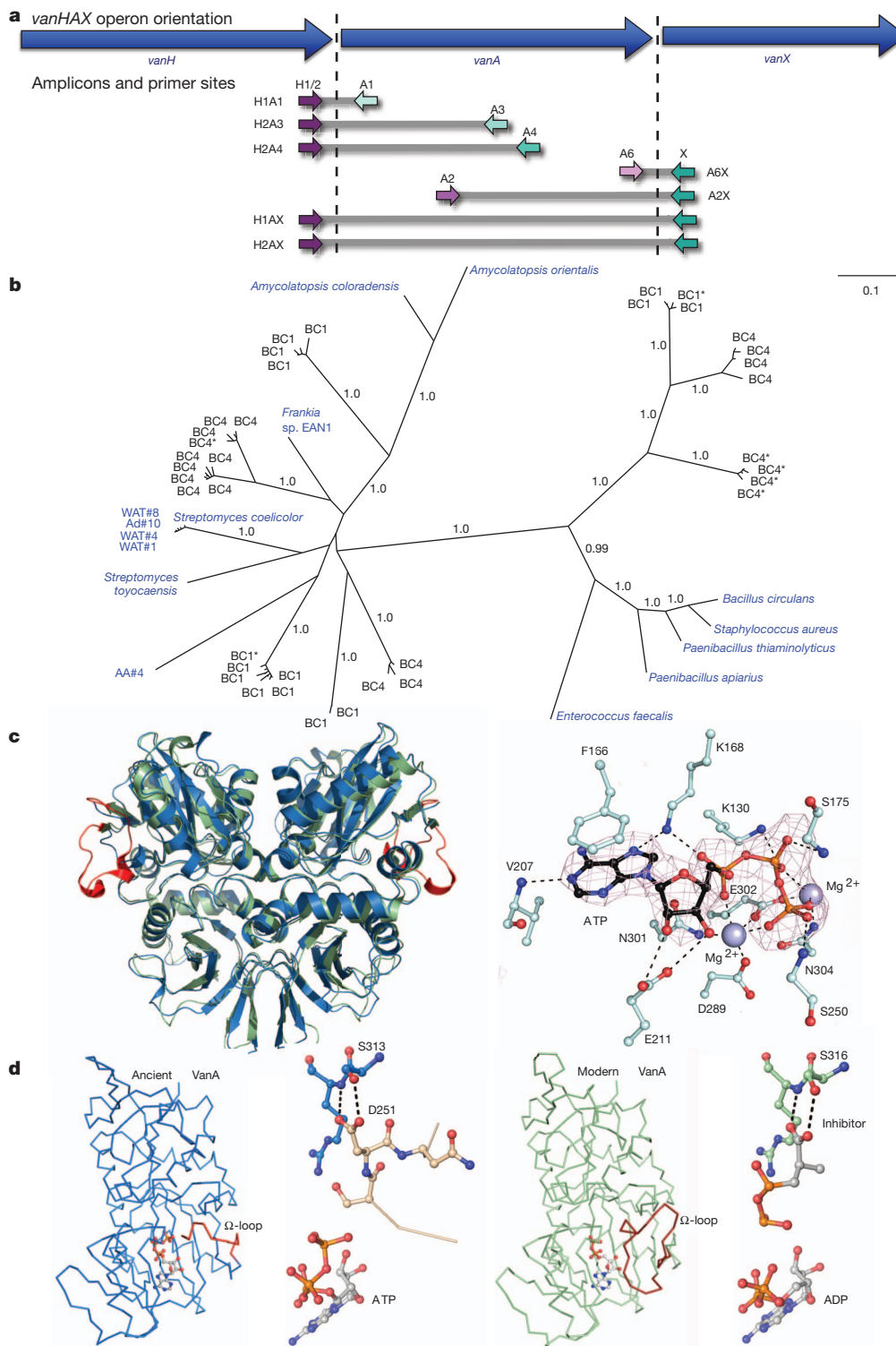


**Figure 3 | Ancient vancomycin resistance elements.** **a**, *vanHAX* amplicons used in this study, with primer names noted above each arrow. **b**, Unrooted Bayesian phylogeny of translated *vanA* sequences; blue denotes strains with *vanHAX* clusters confirmed to confer resistance; sequences containing stop codons but homology throughout are noted with a single asterisk (Supplementary Information). BC1, Bear Creek sample 1; BC4, Bear Creek sample 4. **c**, VanA<sub>A2</sub> structure. Left: ribbon diagram of the VanA<sub>A2</sub> dimer (blue)

overlaid with modern VanA (green), where the  $\Omega$ -loop is coloured red; right: ball-and-stick representation of ATP binding. The electron density shown is an  $F_o - F_c$  map contoured at  $3\sigma$ . **d**, Comparison of modern and ancient VanA monomer structures. The  $\Omega$ -loop is coloured red and detailed in the ball-and-stick figures. Ligands are shown in grey. Dashed lines represent hydrogen bonds.



**Table 1 | *vanHAX* permutation tests**

Amplicon	Number	Length (base pairs)	Probability of similarity by chance alone to <i>Streptomyces coelicolor</i> genes		
			<i>vanH</i>	<i>vanA</i>	<i>vanX</i>
H1A1	164	203–213	$3.59 \times 10^{-3}$	$4.39 \times 10^{-17}$	0.24
H1A1*	12	209–216	$2.83 \times 10^{-3}$	$8.16 \times 10^{-16}$	0.28
H2A3	24	573–605	$9.83 \times 10^{-3}$	$1.27 \times 10^{-54}$	0.22
H2A4	79	666–681	$4.33 \times 10^{-3}$	$6.15 \times 10^{-53}$	0.18
A6X	159	170–179	0.11	$6.87 \times 10^{-8}$	$5.64 \times 10^{-9}$
A6X*	11	176–179	0.04	$2.96 \times 10^{-8}$	$3.63 \times 10^{-9}$
A2X	96	735–796	0.11	$1.80 \times 10^{-59}$	$1.35 \times 10^{-6}$
HAX†	40	1,173–1,204	$5.95 \times 10^{-3}$	$9.32 \times 10^{-92}$	$6.47 \times 10^{-7}$

\*Clones from independent replication in France. †Includes both H1AX and H2AX.

(Fig. 3a and Supplementary Information). Positive results, including particularly high yields of the smallest amplicon, A6X (Supplementary Table 9), encouraged us to attempt amplification across both boundaries (that is, the complete *vanA* gene) in a single 1.2-kilobase amplicon. We also targeted fragments anchored on either boundary and extending as far as possible into *vanA*. None of the sequences from these products, or those generated by an independent laboratory (Supplementary Information), were present in GenBank. No contaminants were detected in more than 300 control reactions.

Phylogenetic analyses showed that many of the ancient *vanHAX* sequences cluster with characterized glycopeptide-resistant strains of Actinobacteria containing *vanHAX* cassettes (for example streptomycetes, glycopeptide-producing *Amycolatopsis* species and the nitrogen-fixing *Frankia* sp. EAN1pec) (Fig. 3b and Supplementary Figs 11 and 12). Another group falls between the actinobacterial sequences and the Firmicutes-derived cluster, which includes environmental *Paenibacillus* isolates and the pathogenic *Enterococci*, and may reflect an intermediate group.

Permutation tests were performed with the PRSS algorithm<sup>20</sup> (1,000 permutations each) to confirm that the sequences were statistically similar to those of vancomycin resistance genes (*vanHAX*) present in modern *Streptomyces*. As shown in Table 1, all *vanHA*-spanning clones have significant similarity to *vanH* and *vanA*, and all *vanAX*-spanning clones have significant similarity to *vanA* and *vanX*.

To ascertain whether the complete *vanA* sequences are indeed functional and do not represent PCR artefacts or pseudogenes, we synthesized four open reading frames from the 40 H1AX/H2AX sequences (Supplementary Information). Two of these generated soluble proteins suitable for purification to homogeneity. Enzymatic characterization indicated that these ligases were indeed D-alanine-D-lactate-specific (Supplementary Fig. 13), and analysis revealed steady-state kinetic parameters consistent with contemporary enzymes derived from both the clinic and the environment (Supplementary Table 10). These results clearly show that the *vanHAX* genes identified in the ancient samples encode enzymes capable of genuine antibiotic resistance.

We further confirmed the link between 30,000-year-old VanA and contemporary enzymes by determining the three-dimensional structure of VanA<sub>A2</sub> by X-ray crystallography (Supplementary Table 11 and Supplementary Information). The quaternary and tertiary structures of VanA<sub>A2</sub>, crystallized in the ATP-bound form, show the overall D-Ala-D-X ligase fold of modern enzymes including VanA from vancomycin-resistant *Enterococcus faecium* (Fig. 3c, d). Superposition of ancient and modern VanA (Fig. 3c, d) reveals conservation of quaternary and tertiary structure with minor differences in Mg<sup>2+</sup> and ATP γ-phosphate coordination. The Ω-loop comprises the biggest structural change; 13 amino-terminal residues (233–246) are absent from the electron density map of VanA<sub>A2</sub>, including His 241 (His 244 in modern VanA), responsible for the lactate selectivity. The last seven Ω-loop residues (247–253) have clear electron density, undergoing a drastic 13 Å shift. These structural differences, however, are not reflected in enzyme function.

This work firmly establishes that antibiotic resistance genes predate our use of antibiotics and offers the first direct evidence that antibiotic

resistance is an ancient, naturally occurring phenomenon widespread in the environment. This is consistent with the rapid emergence of resistance in the clinic and predicts that new antibiotics will select for pre-existing resistance determinants that have been circulating within the microbial pangenome for millennia. This reality must be a guiding principle in our stewardship of existing and new antibiotics.

## METHODS SUMMARY

Permafrost cores were collected at Bear Creek, Yukon, then shipped frozen to the McMaster Ancient DNA Centre and stored at  $-40^{\circ}\text{C}$ . All subsequent procedures before PCR/qPCR amplification were performed in dedicated clean rooms, physically separated from laboratories containing modern DNA, bacterial cultures and amplification products. Contaminant leaching into the centre of cores after sampling was monitored by qPCR assays designed to detect *E. coli* DNA encoding the jellyfish green fluorescent protein sprayed onto coring equipment and the external surfaces of all collected cores. DNA was extracted from the centre of subsampled permafrost cores. PCR assays were designed to target vertebrates, plants, bacteria and specific antibiotic resistance elements. All products were sequenced with either the 454 GS-FLX platform or by standard cloning and sequencing procedures (GenBank accession numbers JN316287–JN366376). The ancient *vanA* gene identified from the permafrost was synthesized and expressed in *E. coli*, and the His<sub>6</sub>-tagged protein was purified by immobilized metal-affinity chromatography. This protein was used in enzymatic studies to determine steady-state kinetics and was also studied by crystallography using the vapour-diffusion hanging-drop method. Data were collected at the National Synchrotron Light Source, Brookhaven National Laboratory, beamline X25 (PDB 1E4E).

Received 28 March; accepted 22 July 2011.

Published online 31 August 2011.

- Livermore, D. M. Has the era of untreatable infections arrived? *J. Antimicrob. Chemother.* **64**, i29–i36 (2009).
- Wright, G. D. The antibiotic resistome: the nexus of chemical and genetic diversity. *Nature Rev. Microbiol.* **5**, 175–186 (2007).
- Hughes, V. M. & Datta, N. Conjugative plasmids in bacteria of the 'pre-antibiotic' era. *Nature* **302**, 725–726 (1983).
- D'Costa, V. M., McGrann, K. M., Hughes, D. W. & Wright, G. D. Sampling the antibiotic resistome. *Science* **311**, 374–377 (2006).
- Dantas, G., Sommer, M. O. A., Oluwasegun, R. D. & Church, G. M. Bacteria subsisting on antibiotics. *Science* **320**, 100–103 (2008).
- Sommer, M. O. A., Dantas, G. & Church, G. M. Functional characterization of the antibiotic resistance reservoir in the human microflora. *Science* **325**, 1128–1131 (2009).
- Baltz, R. H. Antibiotic discovery from actinomycetes: will a renaissance follow the decline and fall? *SIM News* **55**, 186–196 (2005).
- Hall, B. G. & Barlow, M. Evolution of the serine β-lactamases: past, present and future. *Drug Resist. Updat.* **7**, 111–123 (2004).
- Mindlin, S. Z., Soina, V. S., Petrova, M. A. & Gorlenko, Z. M. Isolation of antibiotic resistance bacterial strains from Eastern Siberia permafrost sediments. *Russ. J. Genet.* **44**, 27–34 (2008).
- Froese, D. G., Zazula, G. D. & Reyes, A. V. Seasonality of the late Pleistocene Dawson tephra and exceptional preservation of a buried riparian surface in central Yukon Territory, Canada. *Quat. Sci. Rev.* **25**, 1542–1551 (2006).
- Froese, D. G. et al. The Klondike goldfields and Pleistocene environments of Beringia. *GSA Today* **19**, 4–10 (2009).
- Brock, F., Froese, D. G. & Roberts, R. G. Low temperature (LT) combustion of sediments does not necessarily provide accurate radiocarbon ages for site chronology. *Quat. Geochronol.* **5**, 625–630 (2010).
- Willerslev, E., Hansen, A. J. & Poinar, H. N. Isolation of nucleic acids and cultures from fossil ice and permafrost. *Trends Ecol. Evol.* **19**, 141–147 (2004).
- Harington, C. R. & Clulow, F. V. Pleistocene mammals from Gold Run Creek, Yukon Territory. *Can. J. Earth Sci.* **10**, 697–759 (1973).
- Zazula, G. D. et al. Ice-age steppe vegetation in east Beringia. *Nature* **423**, 603 (2003).

16. Haile, J. *et al.* Ancient DNA reveals late survival of mammoth and horse in interior Alaska. *Proc. Natl Acad. Sci. USA* **106**, 22352–22357 (2009).
17. Gilichinsky, D. *et al.* in *Psychrophiles: From Biodiversity to Biotechnology* (eds Margesin, R., Schinner, F., Marx, J.-C. & Gerday, C.) 83–102 (Springer, 2008).
18. Doyle, D., McDowall, K. J., Butler, M. J. & Hunter, I. S. Characterization of an oxytetracycline-resistance gene, *otrA*, of *Streptomyces rimosus*. *Mol. Microbiol.* **5**, 2923–2933 (1991).
19. Courvalin, P. Vancomycin resistance in gram-positive cocci. *Clin. Infect. Dis.* **42**, S25–S34 (2006).
20. Pearson, W. R. & Lipman, D. J. Improved tools for biological sequence comparison. *Proc. Natl Acad. Sci. USA* **85**, 2444–2448 (1988).

**Supplementary Information** is linked to the online version of the paper at [www.nature.com/nature](http://www.nature.com/nature).

**Acknowledgements** We thank A. Guarné for assistance in X-ray data collection. This work was supported by Canada Research Chairs to D.F., H.N.P. and G.D.W., a Canadian Institutes of Health Research operating grant to G.D.W. (MOP-79488) and a scholarship to V.M.D., and by grants from the Natural Sciences and Engineering Research Council of Canada to D.F. and H.N.P. and scholarship to C.E.K.

**Author Contributions** D.F., G.Z. and F.C. collected permafrost cores and performed geochemical analyses followed by subsampling by C.S., V.M.D. and C.E.K. C.E.K. performed ancient DNA laboratory work and 454 sequencing. V.M.D. designed primers for resistance genes, 16S and *gfp*. V.M.D. and C.E.K. designed and optimized the qPCR assays, and cloned and sequenced the resistance gene products. R.D. independently confirmed the results in France. L.K. purified and characterized VanA, and M.M. crystallized VanA and determined the three-dimensional structure. W.S., G.B.G., C.E.K. and H.N.P. processed and analysed the floral/faunal data; V.M.D. and G.B.G. performed phylogenetic and bioinformatic analyses of the resistance gene sequences. H.N.P. and G.D.W. conceived the project, and V.M.D., C.E.K., D.F., H.N.P. and G.D.W. wrote the manuscript. All authors edited the final draft.

**Author Information** The metagenomic sequences determined from permafrost are deposited in GenBank under accession numbers JN316287–JN366376. Reprints and permissions information is available at [www.nature.com/reprints](http://www.nature.com/reprints). The authors declare no competing financial interests. Readers are welcome to comment on the online version of this article at [www.nature.com/nature](http://www.nature.com/nature). Correspondence and requests for materials should be addressed to G.D.W. ([wrightge@mcmaster.ca](mailto:wrightge@mcmaster.ca)) or H.N.P. ([poinarh@mcmaster.ca](mailto:poinarh@mcmaster.ca)).

# Evidence for several waves of global transmission in the seventh cholera pandemic

Ankur Mutreja<sup>1\*</sup>, Dong Wook Kim<sup>2,3\*</sup>, Nicholas R. Thomson<sup>1\*</sup>, Thomas R. Connor<sup>1</sup>, Je Hee Lee<sup>2,4</sup>, Samuel Kariuki<sup>5</sup>, Nicholas J. Croucher<sup>1</sup>, Seon Young Choi<sup>2,4</sup>, Simon R. Harris<sup>1</sup>, Michael Lebens<sup>6</sup>, Swapan Kumar Niyogi<sup>7</sup>, Eun Jin Kim<sup>2</sup>, T. Ramamurthy<sup>7</sup>, Jongsik Chun<sup>4</sup>, James L. N. Wood<sup>8</sup>, John D. Clemens<sup>2</sup>, Cecil Czerkinsky<sup>2</sup>, G. Balakrish Nair<sup>7</sup>, Jan Holmgren<sup>6</sup>, Julian Parkhill<sup>1</sup> & Gordon Dougan<sup>1</sup>

*Vibrio cholerae* is a globally important pathogen that is endemic in many areas of the world and causes 3–5 million reported cases of cholera every year. Historically, there have been seven acknowledged cholera pandemics; recent outbreaks in Zimbabwe and Haiti are included in the seventh and ongoing pandemic<sup>1</sup>. Only isolates in serogroup O1 (consisting of two biotypes known as ‘classical’ and ‘El Tor’) and the derivative O139 (refs 2, 3) can cause epidemic cholera<sup>2</sup>. It is believed that the first six cholera pandemics were caused by the classical biotype, but El Tor has subsequently spread globally and replaced the classical biotype in the current pandemic<sup>1</sup>. Detailed molecular epidemiological mapping of cholera has been compromised by a reliance on sub-genomic regions such as mobile elements to infer relationships, making El Tor isolates associated with the seventh pandemic seem superficially diverse. To understand the underlying phylogeny of the lineage responsible for the current pandemic, we identified high-resolution markers (single nucleotide polymorphisms; SNPs) in 154 whole-genome sequences of globally and temporally representative *V. cholerae* isolates. Using this phylogeny, we show here that the seventh pandemic has spread from the Bay of Bengal in at least three independent but overlapping waves with a common ancestor in the 1950s, and identify several transcontinental transmission events. Additionally, we show how the acquisition of the SXT family of antibiotic resistance elements has shaped pandemic spread, and show that this family was first acquired at least ten years before its discovery in *V. cholerae*.

Whole-genome analysis is perhaps the ultimate approach to building a robust phylogeny in recently emerged pathogens, through the identification of SNPs and other rare genetic variants<sup>4</sup>. Therefore, we sequenced the genomes of 136 isolates of *V. cholerae*, the causative agent of several million cholera cases each year (<http://www.who.int/mediacentre/factsheets/fs107/en/>). These sequences, including 113 isolates from the seventh pandemic, were added to 18 previously published genomes<sup>1,2,5</sup> to produce a global genomic database from isolates collected in the course of a century. We included representative El Tor isolates collected in the past four decades and compared these to previously reported and novel genome sequences of both classical and non-O1 types<sup>1,2</sup>.

The sequence reads were mapped to the reference sequence of El Tor N16961 (ref. 6), a seventh-pandemic *V. cholerae* that was isolated in Bangladesh in 1975 (see footnote to Supplementary Table 1) and the resulting consensus tree identified eight distinct phyletic lineages (L1–L8, see Supplementary Fig. 1 and Supplementary Table 1 for strain and lineage information), six of which incorporated O1 clinical isolates. The classical isolates formed a distinct, highly clustered group (L1), distant from the El Tor isolates of the seventh pandemic (L2). It is clear

from Supplementary Fig. 1 that the classical and El Tor clades did not originate from a recent common ancestor and instead seem to be independent derivatives with distinct phylogenetic histories, consistent with previous proposals<sup>2</sup>. Isolates of L4 share a common ancestor with previously reported non-conventional O1 isolates<sup>2</sup> (Supplementary Fig. 2), and are likely to have acquired the O1 antigen genes by a recombination event onto a genetically distinct genome backbone. Isolates of L7 also have a distinct backbone, whereas L2, L3 (USA gulf coast strains), L5, L6 and L8 share a more ‘El-Tor-like’ genome backbone, and the L1 backbone is of the ‘classical’ type.

Genome-wide SNP analysis showed that the 123 El Tor isolates in the L2 cluster (Supplementary Fig. 1) differed from the reference by only 50–250 SNPs. With this large sample size we were able to construct a high-resolution phylogeny that shows unequivocally that the current pandemic is monophyletic and originated from a single source, providing a framework for future epidemiological and phenotypic analysis of *V. cholerae*, including transmission-tracking and typing.

Predicted recombined regions were identified, and along with genomic islands and mobile genetic elements, these were initially excluded from the phylogenetic analysis of seventh-pandemic isolates, to determine the underlying phylogeny. Notably, analysis of the tree (Fig. 1; see Supplementary Fig. 3 for a tree with strain names) provides clear evidence of a clonal expansion of the lineage, with a strong temporal signature. This is most clearly illustrated by the fact that the most divergent isolates from the N16961 reference are represented by the oldest seventh-pandemic isolate in our collection, A6, collected in 1957, together with the most recent Haitian isolates<sup>5</sup> from late 2010. We performed a linear regression analysis on all the L2 isolates to calculate the rate of SNP accumulation on the basis of the date of isolation and the root-to-tip distance. The shape of the tree and temporal signatures in Fig. 1 show a very consistent rate of SNP accumulation, 3.3 SNPs year<sup>-1</sup> ( $R^2 = 0.73$ , Supplementary Fig. 4) in the core genome, emphasizing the tree’s robustness and utility for transmission studies. The only exception to this is *V. cholerae* A4, a repeatedly passaged laboratory strain that was originally isolated in 1973 (Supplementary Figs 3 and 4). The estimated rate of mutation for our seventh-pandemic *V. cholerae* collection was  $8.3 \times 10^{-7}$  SNPs site<sup>-1</sup> year<sup>-1</sup>: between 5 and 2.5 times slower than the rate estimated for recent clonal expansions of some other human-pathogenic bacteria<sup>4,7</sup>.

The seventh-pandemic tree can be subdivided into three major groups or clades by clustering using Bayesian analysis of population structure<sup>8,9</sup> (shown as waves 1–3 in Fig. 1); this clustering is mostly consistent with the cholera toxin (CTX) type of the three clades, which represent independent waves of transmission. Although examples of

<sup>1</sup>Wellcome Trust Sanger Institute, Wellcome Trust Genome Campus, Hinxton, Cambridge CB10 1SA, UK. <sup>2</sup>International Vaccine Institute, SNU Research Park, Bongchun 7 dong, Kwanak, Seoul 151-919, Korea. <sup>3</sup>Department of Pharmacy, College of Pharmacy, Hanyang University, Kyeonggi-do 426-791, Korea. <sup>4</sup>Seoul National University, 1 Gwanak-ro, Gwanak-gu, Seoul 151-742, Korea. <sup>5</sup>Centre for Microbiology Research, KEMRI at Kenyatta Hosp Compound, Off Ngong Road, PO Box 43640-00100, Kenya. <sup>6</sup>Department of Microbiology and Immunology and University of Gothenburg Vaccine Research Institute, The Sahlgrenska Academy at the University of Gothenburg, Box 435, 40530 Göteborg, Sweden. <sup>7</sup>National Institute of Cholera and Enteric Diseases, P-33, CIT Scheme XM, Beliaghata, Kolkata 700 010, India. <sup>8</sup>University of Cambridge, Department of Veterinary Medicine, Madingley Road, Cambridge CB3 0ES, UK.

\*These authors contributed equally to this work.



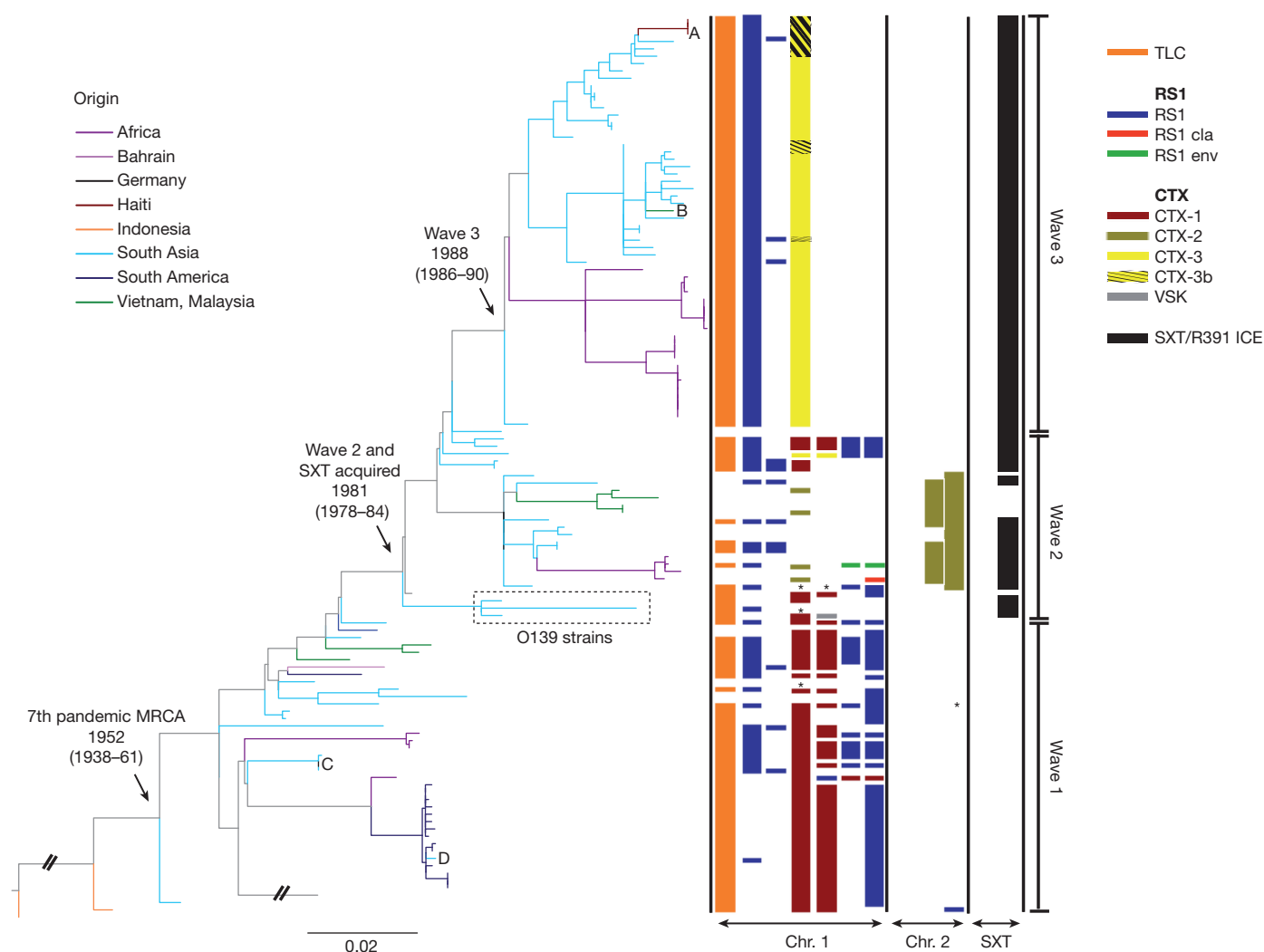


**Figure 1** | A maximum-likelihood phylogenetic tree of the seventh pandemic lineage of *V. cholerae* based on SNP differences across the whole core genome, excluding probable recombination events. The pre-seventh-pandemic isolate M66 was used as an outgroup to root the tree. Branches are coloured on the basis of the region of isolation of the strains. The branches representing the three major waves are indicated on the far right. The nodes representing the MRCAs of the seventh pandemic, and subsequent waves 2 and 3, are indicated with arrows and labelled with inferred dates. The presence and

type of CTX and SXT elements in each strain are shown to the right of the tree. The presence of toxin-linked cryptic (TLC) and repeated sequence 1 (RS1) elements is shown, but their number and position, respectively, are arbitrarily assigned. Cases of sporadic intercontinental transmission are marked A–D. The dates shown are the median estimates for the indicated nodes, taken from the results of the BEAST analysis. The scale is given as the number of substitutions per variable site; asterisks indicate that no data were available.

genetic determinants differentiating these three CTX types have previously been published<sup>10</sup>, they have not been put into a phylogenetic context, undermining efforts to investigate the evolutionary aspects of their emergence. Perhaps as a result, there has been substantial uncertainty in naming new CTX types as they have been discovered. Our data shows that the first CTX type is canonical CTX El Tor and we propose that it is renamed CTX-1; for the other two we propose a new expandable nomenclature and class them as CTX-2 and CTX-3 (Supplementary Table 2).

Isolates spanning A18 to PRL5 (the lower clade in Fig. 1) represent wave 1, covering about 16 years (1977–1992). All isolates in this group lack the integrative and conjugative element (ICE) of the SXT/R391 family, encoding resistance to several antibiotics<sup>11,12</sup>. It is within this time period that seventh-pandemic cholera occurred in South America<sup>6</sup>. Our data show that the South American isolates form a discrete cluster, which also includes a single Angolan isolate collected in 1989. The position of the Angolan isolate at the base of the South American group indicates that transmission to South America may have been via Africa, as previously proposed<sup>13</sup>. We used BEAST<sup>14</sup> to translate evolutionary distance in SNPs into time (Supplementary

Fig. 5) and this indicated that transmission to South America is likely to have occurred between 1981 and 1985. The branch harbouring this West African–South American (WASA) clade is distinguished from all other *V. cholerae* by the acquisition of novel VSP-2 genes<sup>15</sup> and a novel genomic island that we have denoted WASA1 (Supplementary Table 3). Notably, the Angolan isolate A5 and all the South American isolates are discriminated by just ten SNPs. Based on the accumulation rate of 3.3 SNPs year<sup>-1</sup> (Supplementary Fig. 4), the 3-year time period between the isolation of A5 and the oldest South American isolate included in this study, A32, is consistent with previous studies indicating that cholera spread as a single epidemic<sup>13</sup>.

The first acquisition of an SXT/R391 ICE lies at the point of transition from the wave-1 cluster to the wave-2 cluster. Using our dated phylogeny (Supplementary Fig. 5)<sup>14</sup>, we were able to date this transition and the first acquisition of SXT/R391 ICE to 1978–84, ten years before its discovery in O139 strains, which also fits with the otherwise surprising discovery of SXT in a Vietnamese strain isolated before 1992 (ref. 16). This date would also correspond to the most recent common ancestor (MRCA) of the O1 and O139 serogroup isolates. Analysis of the diversity of the common regions of SXT/R391 ICEs in

our seventh-pandemic collection (Supplementary Fig. 6) shows that they are discriminated by 3,161 SNPs, compared to only 1,757 SNPs used to define the core whole-genome phylogeny in Fig. 1. This indicates either that there have been several recombination events within these ICEs, or that they have been acquired independently several times on the tree<sup>11</sup>. Isolates from wave 2 represent a discrete cluster that shows a complex pattern of accessory elements in the CTX locus (Fig. 1) and a wide phylogeographical distribution. It is also notable that isolates collected in Vietnam in 1995–2004 and strain A109 are the only wave-2 isolates studied from this time period that lack an SXT/R391 ICE. We examined the genomic locus in these clones that marks the point of insertion of SXT/R391 ICE in all other *V. cholerae* isolates and found no remnants of this conjugative element, which may have been lost from this lineage (no ‘scar’ in DNA sequence is expected after the precise excision of SXT/R391 ICE).

Ignoring the CTX-related genomic regions, the seventh-pandemic L2 isolates show relatively little evidence of recombination either within or from outside the tree. On the basis of the SNP distribution, 1,930 out of 2,027 SNPs (Supplementary Table 4) are congruent with the tree, leaving 97 homoplasies that could be due to selection or homologous recombination among the L2 isolates. Only 270 SNPs were predicted to be due to homologous recombination from outside the tree. The only two branches in which the SNP distribution indicated considerable recombination were those leading to the WASA cluster (Supplementary Fig. 7) and the O139 serogroup. Aside from the acquisitions of CTX and the SXT/R391 ICEs, we found evidence of gene flux affecting only 155 other genes (Supplementary Figs 8 and 9 and Supplementary Table 3).

Also represented in our collection are two isolates of serogroup O139, which are known to have arisen from a homologous replacement of their O-antigen determinant into an El Tor genomic backbone<sup>2,3,13</sup>. CTX types that are different from El Tor, classical, CTX-2 and CTX-3 have been reported for the O139 serogroup<sup>17–20</sup>; however, the phylogenetic position of the two strains included in this study shows that O139 was derived from O1 El Tor and therefore represents another distinct but spatially restricted wave from the common source.

We were also able to date the ancestor of the El Tor seventh-pandemic lineage, L2, as having existed in 1827–1936 (Supplementary Fig. 5), which is consistent with the predicted date of origin from the linear regression plot (1910, Supplementary Fig. 4). This also

corresponds well with the date of isolation of the first El Tor biotype strain in 1905 (ref. 21).

It is apparent from Fig. 1 that *V. cholerae* wave 1, which spread globally, was later replaced by the more geographically restricted wave 2 and wave 3, a phenomenon supported by local clinical observations and phage analysis<sup>10</sup>. This also reflects the fact that *V. cholerae* epidemics since 2003–2010 have been restricted to Africa and south Asia. Notably, the rates of SNP accumulation calculated independently for wave 1, wave 3 and wave 2 (2.3, 2.6 and 3.5 SNPs year<sup>-1</sup> respectively) are consistent with the rate calculated over the whole collection period (Supplementary Fig. 4).

The clonal clustering of L2 isolates, the constant rate of SNP accumulation and the temporal and geographical distribution support the concept that the seventh pandemic has spread by periodic radiation from a single source population located in the Bay of Bengal, followed by local evolution and ultimately local extinction in non-endemic areas. This is evidenced by the disappearance of wave-1 isolates, followed by the independent expansion of waves 2 and 3, both derived from the same original population, occurring within seven years of each other. These two waves are clearly distinguished from the first by the acquisition of SXT/R391 ICEs (Fig. 1). Plotting the intercontinental spread of each wave onto the world map (Fig. 2) clearly shows that the *V. cholerae* seventh pandemic is sourced from a single, restricted geographical location but has spread in overlapping waves. In these ancestral waves, there are at least four recent long-range transmission events (A–D in Fig. 1), in which isolates clearly share a common ancestor with recent strains at distant locations, indicating that such events are not uncommon. The most recent example of this is the Haitian outbreak, in which strains share a very recent common ancestor with south-Asian strains at the tip of wave 3. The number of SNP differences, even at whole-genome resolution, between the Haitian and the most closely related Indian and Bangladeshi strains is very low. This demonstrates that the Haitian strains must have come from south Asia, at most within the last six years. However, the limited discrimination means that it may prove challenging to make country-specific inferences as to the origins of the Haitian strains on the basis of DNA sequence alone. For such conclusions to be robust, great care must be taken in the selection of samples for analysis.

Despite clear evidence of sporadic long-range transmission events that are likely to be associated with direct human carriage, the overall pattern seen in our data is one of continued local evolution of *V. cholerae* in the

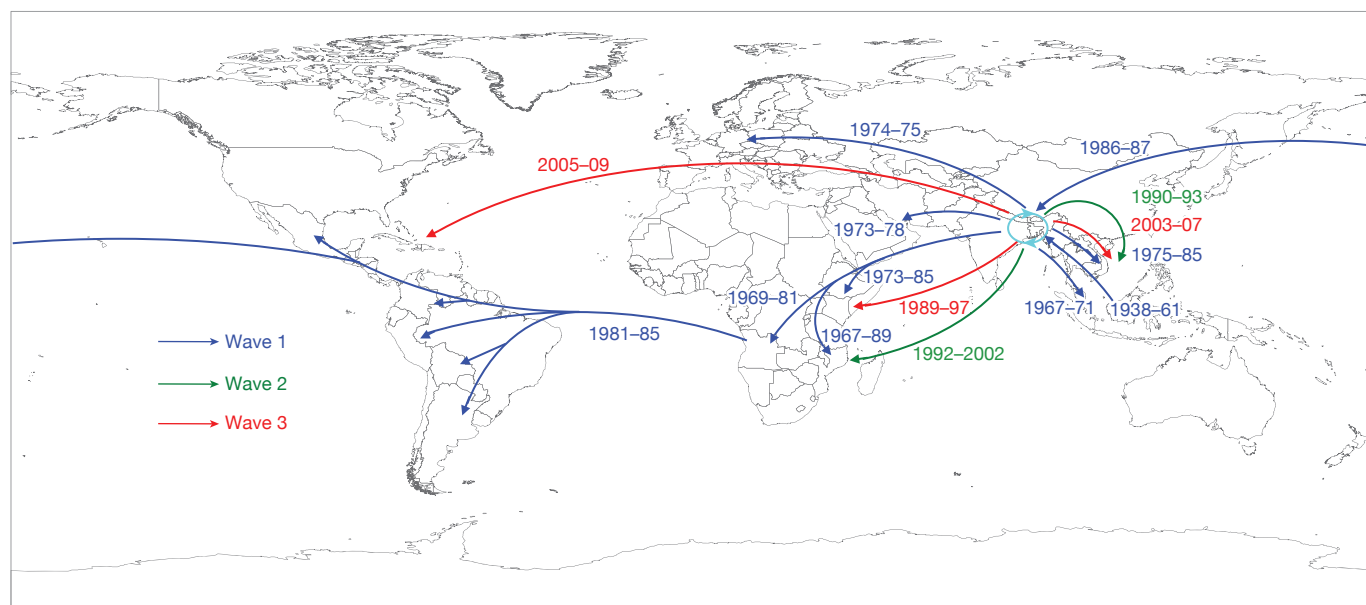


**Figure 2 | Transmission events inferred for the seventh-pandemic phylogenetic tree, drawn on a global map.** The date ranges shown for transmission events are taken from the BEAST analysis, and represent the

median values for the MRCA of the transmitted strains (later bound), and the MRCA of the transmitted strains and their closest relative from the source location (earlier bound).

Bay of Bengal, with several independent waves of global transmission resulting in short-term epidemics in non-endemic countries. Although our sample set is substantial, there are clearly areas where geographical coverage is limited. However, the structure of the tree, with deep branches between the major waves, means that increasing the number of strains and the resolution further should only identify further independent waves of transmission. Indeed, we cannot rule out the possibility of an El Tor population persisting or evolving as a new wave of the seventh pandemic; for example, in areas such as China that were not sampled in this study.

One notable factor in the ongoing evolution of pandemic cholera was the acquisition of the SXT/R391-family antibiotic resistance element. The clinical use of the antibiotics tetracycline and furazolidone for cholera treatment started in 1963 and 1968 respectively, about 15 years before our prediction of the first acquisition of an SXT/R391 ICE (1978–1984). Our analysis provides a robust framework for elucidating the evolution of the seventh pandemic further, and for studying the local evolution, particularly in the Bay of Bengal, that has such a key role in the evolution of cholera.

## METHODS SUMMARY

Genomic libraries were created for each sample, followed by multiplex sequencing on an Illumina GAIIX analyser. The 54-base paired-end reads obtained were mapped against N16961 El Tor as a reference and SNPs in the core genome were identified as described in Methods. The SNPs were used to draw a whole core-genome phylogeny as described in ref. 4. The final SNP alignment was used to perform BEAST<sup>14</sup> analysis and to confirm the output of linear regression analysis. The three cholera waves reported in the seventh-pandemic phylogeny were confirmed using BAPS<sup>8,9</sup>. The raw Illumina data were also assembled *de novo* (see Methods) so that pairwise genome comparisons could be made. A new and expandable nomenclature system describing the CTX trends seen in the last 40 years was proposed following the rationale described in Methods.

**Full Methods** and any associated references are available in the online version of the paper at [www.nature.com/nature](http://www.nature.com/nature).

**Received 3 June; accepted 26 July 2011.**

**Published online 24 August 2011.**

- Chin, C. S. *et al.* The origin of the Haitian cholera outbreak strain. *N. Engl. J. Med.* **364**, 33–42 (2011).
- Chun, J. *et al.* Comparative genomics reveals mechanism for short-term and long-term clonal transitions in pandemic *Vibrio cholerae*. *Proc. Natl Acad. Sci. USA* **106**, 15442–15447 (2009).
- Hochhut, B. & Waldor, M. K. Site-specific integration of the conjugal *Vibrio cholerae* SXT element into *prfC*. *Mol. Microbiol.* **32**, 99–110 (1999).
- Harris, S. R. *et al.* Evolution of MRSA during hospital transmission and intercontinental spread. *Science* **327**, 469–474 (2010).
- Update: cholera outbreak—Haiti, 2010. *MMWR Morb. Mortal Wkly Rep.* **59**, 1473–1479 (2010).
- Heidelberg, J. F. *et al.* DNA sequence of both chromosomes of the cholera pathogen *Vibrio cholerae*. *Nature* **406**, 477–483 (2000).
- Croucher, N. J. *et al.* Rapid pneumococcal evolution in response to clinical interventions. *Science* **331**, 430–434 (2011).

- Corander, J., Marttinen, P., Siren, J. & Tang, J. Enhanced Bayesian modelling in BAPS software for learning genetic structures of populations. *BMC Bioinformatics* **9**, 539 (2008).
- Corander, J., Waldmann, P. & Sillanpää, M. J. Bayesian analysis of genetic differentiation between populations. *Genetics* **163**, 367–374 (2003).
- Safa, A., Nair, G. B. & Kong, R. Y. Evolution of new variants of *Vibrio cholerae* O1. *Trends Microbiol.* **18**, 46–54 (2010).
- Garriss, G., Waldor, M. K. & Burrus, V. Mobile antibiotic resistance encoding elements promote their own diversity. *PLoS Genet.* **5**, e1000775 (2009).
- Wozniak, R. A. *et al.* Comparative ICE genomics: insights into the evolution of the SXT/R391 family of ICEs. *PLoS Genet.* **5**, e1000786 (2009).
- Lam, C., Octavia, S., Reeves, P., Wang, L. & Lan, R. Evolution of seventh cholera pandemic and origin of 1991 epidemic, Latin America. *Emerg. Infect. Dis.* **16**, 1130–1132 (2010).
- Drummond, A. J., Ho, S. Y., Phillips, M. J. & Rambaut, A. Relaxed phylogenetics and dating with confidence. *PLoS Biol.* **4**, e88 (2006).
- O'Shea, Y. A. *et al.* The *Vibrio* seventh pandemic island-II is a 26.9 kb genomic island present in *Vibrio cholerae* El Tor and O139 serogroup isolates that shows homology to a 43.4 kb genomic island in *V. vulnificus*. *Microbiology* **150**, 4053–4063 (2004).
- Bani, S. *et al.* Molecular characterization of ICEVchVie0 and its disappearance in *Vibrio cholerae* O1 strains isolated in 2003 in Vietnam. *FEMS Microbiol. Lett.* **266**, 42–48 (2007).
- Basu, A. *et al.* *Vibrio cholerae* O139 in Calcutta, 1992–1998: incidence, antibiograms, and genotypes. *Emerg. Infect. Dis.* **6**, 139–147 (2000).
- Faruque, S. M. & Mekalanos, J. J. Pathogenicity islands and phages in *Vibrio cholerae* evolution. *Trends Microbiol.* **11**, 505–510 (2003).
- Faruque, S. M. *et al.* The O139 serogroup of *Vibrio cholerae* comprises diverse clones of epidemic and non-epidemic strains derived from multiple *V. cholerae* O1 or non-O1 progenitors. *J. Infect. Dis.* **182**, 1161–1168 (2000).
- Nair, G. B., Bhattacharya, S. K. & Deb, B. C. *Vibrio cholerae* O139 Bengal: the eighth pandemic strain of cholera. *Indian J. Public Health* **38**, 33–36 (1994).
- Cvijetanic, B. & Barua, D. The seventh pandemic of cholera. *Nature* **239**, 137–138 (1972).

**Supplementary Information** is linked to the online version of the paper at [www.nature.com/nature](http://www.nature.com/nature).

**Acknowledgements** This work was supported by The Wellcome Trust grant 076964. The IVI is supported by the Governments of Korea, Sweden and Kuwait. D.W.K. was partially supported by grant RTI05-01-01 from the Ministry of Knowledge and Economy (MKE), Korea and by R01-2006-000-10255-0 from the Korea Science and Engineering Foundation; and J.L.N.W. was supported by the Alborada Trust and the RAPIDD program of the Science & Technology Directorate, Department of Homeland Security. Thanks to A. Camilli at Tufts University Medical School for providing the corrected N16961 sequence, to B.M. Nguyen at NIHE, Vietnam and M. Ansaruzzaman at ICDDR, Bangladesh for providing strains, and to M. Fookes at WTSI for training support.

**Author Contributions** A.M., D.W.K. and N.R.T. collected the data, analysed it and performed phylogenetic analyses and comparative genomics. J.H.L., S.Y.C., E.J.K. and J.C. analysed the CTX types. S.K., S.K.N. and T.R. were involved in strain collection and serogroup analysis. T.R.C. performed Bayesian analysis; N.J.C. and S.R.H. did the computational coding. J.L.N.W., J.D.C., C.C., G.B.K., J.H., N.R.T., J.P. and G.D. were involved in the study design. A.M., N.R.T., J.P., G.D., J.H., G.B.K., N.J.C., S.R.H., T.R.C., D.W.K. and M.L. contributed to the manuscript writing.

**Author Information** Reprints and permissions information is available at [www.nature.com/reprints](http://www.nature.com/reprints). All the genomic sequences have been submitted to the European Nucleotide Archive with the accession numbers listed in Supplementary Table 1. The authors declare no competing financial interests. Readers are welcome to comment on the online version of this article at [www.nature.com/nature](http://www.nature.com/nature). Correspondence and requests for materials should be addressed to J.P. ([parkhill@sanger.ac.uk](mailto:parkhill@sanger.ac.uk)).



## METHODS

**Genomic library creation and multiplex sequencing.** Unique index-tagged libraries for each sample were created, and up to 12 separate libraries were sequenced in each of eight channels in Illumina Genome Analyser GAI cells with 54-base paired-end reads. The index-tag sequence information was used for downstream processing to assign reads to the individual samples<sup>4</sup>.

**Detection of SNPs in the core genome.** The 54-base paired-end reads were mapped against the N16961 El Tor reference (accession numbers AE003852 and AE003853) and SNPs were identified as described in ref. 7. The unmapped reads and the sequences that were not present in all genomes were not considered a part of the core genome, and therefore SNPs from these regions were not included in the analysis. Appropriate SNP cutoffs were chosen to minimize the number of false-positive and false-negative calls; SNPs were filtered to remove those at sites with a SNP quality score lower than 30, and SNPs at sites with heterogeneous mappings were filtered out if the SNP was present in fewer than 75% of reads at that site. From the seventh-pandemic data set, high-density SNP clusters indicating possible recombination were excluded<sup>7</sup>. In total, 2,027 SNPs were detected in the core genome of the El Tor lineage. Of these, 270 SNPs were predicted to be due to recombination. Removing these provided a data set characterized by 1,757 SNPs: these were used to produce the final phylogeny.

**Comparative genomics.** Raw Illumina data were split to generate paired-end reads, and assembled using a *de novo* genome-assembly program, Velvet v0.7.03 (ref. 22), to generate a multi-contig draft genome for each of 133 *V. cholerae* strains<sup>4</sup>. The overlap parameters were optimized to give the highest N50 value. Because seventh-pandemic *V. cholerae* strains are closely related in the core, Abacas<sup>23</sup> was used to order the contigs using the N16961 El Tor strain as a reference, followed by annotation transfer from the reference strain to each draft genome<sup>4</sup>. Using the N16961 sequence as a database to perform a TBLASTX<sup>24</sup> for each draft genome, a genome comparison file was generated that was subsequently used in the Artemis comparison tool<sup>25</sup> to compare the genomes manually and search for novel genomic islands.

**Phylogenetic analysis.** A phylogeny was drawn for *V. cholerae* using RAxML v0.7.4 (ref. 26) to estimate the trees for all SNPs called from the core genome. The general time-reversible model with gamma correction was used for among-site rate variation for ten initial trees<sup>4</sup>. USA gulf coast strains A215 and A325, which have substantially different core genomes from all other strains in our collection, were used as an outgroup to root the global phylogeny (Supplementary Fig. 1), whereas a pre-seventh-pandemic strain, M66 (accession numbers CP001233 and CP001234), and strain A6 (from our collection), were used to root the seventh-pandemic phylogenetic tree (Fig. 1).

**CTX prophage analysis.** For each strain, the CTX structure and the sequence of *rstA*, *rstR* and *ctxB* was determined as in refs 27 and 28.

**Linear regression and Bayesian analysis.** The phylogram for the seventh pandemic was exported to Path-O-Gen v1.3 (<http://tree.bio.ed.ac.uk/software/pathogen/>) and a linear regression plot for isolation date versus root-to-tip distance was generated. The same plot was also constructed individually for the three waves, but A4, being a laboratory strain, was excluded from the latter analysis.

The presence of three waves was checked, and their makeup was determined, using a BAPS analysis performed on the SNP alignment containing the unique SNP patterns from the seventh-pandemic isolates. The program was run using the BAPS individual mixture model and three independent iterations were performed using an upper limit for the number of populations of 20, 21 and 22 to obtain

optimal partitioning of the sample. The dates for the acquisition of SXT and the ancestors of the three waves were inferred using the Bayesian Markov chain Monte Carlo framework BEAST<sup>29</sup>. We used the final SNP alignment with recombinant sites removed and fixed the tree topology to the phylogeny produced by RAxML, as described above. We used BEAST to estimate the rates of evolution on the branches of the tree using a relaxed molecular clock<sup>14</sup>, which allows rates of evolution to vary amongst the branches of the tree. BEAST produced estimates for the dates of branching events on the tree by sampling dates of divergence between isolates from their joint posterior distribution, in which the sequences are constrained by their known date of isolation. The data were analysed using a coalescent constant population size and a general time-reversible model with gamma correction. The results were produced from three independent chains of 50 million steps each, sampled every 10,000 steps to ensure good mixing. The first 5 million steps of each chain were discarded as a burn-in. The results were combined using Log Combiner, and the maximum clade credibility tree was generated using Tree Annotator, both parts of the BEAST package (<http://tree.bio.ed.ac.uk/software/beast/>). Convergence and the effective sample-size values were checked using Tracer 1.5 (available from <http://tree.bio.ed.ac.uk/software/tracer/>). ESS values in excess of 200 were obtained for all parameters.

**Nomenclature.** The seventh-pandemic cholera strains were clearly distinguished by three waves and we therefore propose their CTX types to be CTX-1, CTX-2 and CTX-3 under the new nomenclature scheme (see Supplementary Table 2). Our nomenclature system is expandable and would be suitable for naming any new seventh-pandemic *V. cholerae* strains. With CTX-1 representing canonical El Tor, we followed the rationale: (1) For CTX-1 to CTX-2, because there was a shift of *rstR*<sup>El Tor</sup> to *rstR*<sup>Classical</sup>, *rstA*<sup>El Tor</sup> to *rstA*<sup>Classical + El Tor</sup> and *ctxB*<sup>El Tor</sup> to *ctxB*<sup>Classical</sup>, we called it CTX-2; (2) for CTX-1 to CTX-3, because there was a shift of *ctxB*<sup>El Tor</sup> to *ctxB*<sup>Classical</sup>, we called it CTX-3; (3) for CTX-3 to CTX-3b, because there was only one SNP mutation in *ctxB*<sup>Classical</sup> from CTX-2 and rest was identical, we called it the next variant of CTX-3, which is CTX-3b.

In summary, if there is a shift of any gene from one biotype to another, the new CTX will be called CTX-n: thus the next strains fitting these criteria will be called CTX-4. However, if there is a mutation(s) that does not lead to a shift of the gene to another biotype gene, CTX-1b, CTX-1c or CTX-2b; CTX-2c or CTX-3b; CTX-3c and so on should be followed as appropriate.

22. Zerbino, D. R. & Birney, E. Velvet: algorithms for *de novo* short read assembly using de Bruijn graphs. *Genome Res.* **18**, 821–829 (2008).
23. Assefa, S., Keane, T. M., Otto, T. D., Newbold, C. & Berriman, M. ABACAS: algorithm-based automatic contiguation of assembled sequences. *Bioinformatics* **25**, 1968–1969 (2009).
24. Altschul, S. F., Gish, W., Miller, W., Myers, E. W. & Lipman, D. J. Basic local alignment search tool. *J. Mol. Biol.* **215**, 403–410 (1990).
25. Carver, T. *et al.* Artemis and ACT: viewing, annotating and comparing sequences stored in a relational database. *Bioinformatics* **24**, 2672–2676 (2008).
26. Stamatakis, A. RAxML-VI-HPC: maximum likelihood-based phylogenetic analyses with thousands of taxa and mixed models. *Bioinformatics* **22**, 2688–2690 (2006).
27. Lee, J. H. *et al.* Classification of hybrid and altered *Vibrio cholerae* strains by CTX prophage and RS1 element structure. *J. Microbiol.* **47**, 783–788 (2009).
28. Nguyen, B. M. *et al.* Cholera outbreaks caused by an altered *Vibrio cholerae* O1 El Tor biotype strain producing classical cholera toxin B in Vietnam in 2007 to 2008. *J. Clin. Microbiol.* **47**, 1568–1571 (2009).
29. Drummond, A. J. & Rambaut, A. BEAST: Bayesian evolutionary analysis by sampling trees. *BMC Evol. Biol.* **7**, 214 (2007).

# Broad neutralization coverage of HIV by multiple highly potent antibodies

Laura M. Walker<sup>1\*</sup>, Michael Huber<sup>1,2\*</sup>, Katie J. Doores<sup>1,2\*</sup>, Emilia Falkowska<sup>1,2</sup>, Robert Pejchal<sup>3</sup>, Jean-Philippe Julien<sup>3</sup>, Sheng-Kai Wang<sup>4</sup>, Alejandra Ramos<sup>1</sup>, Po-Ying Chan-Hui<sup>5</sup>, Matthew Moyle<sup>5</sup>, Jennifer L. Mitcham<sup>5</sup>, Phillip W. Hammond<sup>5</sup>, Ole A. Olsen<sup>5</sup>, Pham Phung<sup>6</sup>, Steven Fling<sup>7</sup>, Chi-Huey Wong<sup>4</sup>, Sanjay Phogat<sup>7</sup>, Terri Wrinn<sup>6</sup>, Melissa D. Simek<sup>7</sup>, Protocol G. Principal Investigators†, Wayne C. Koff<sup>7</sup>, Ian A. Wilson<sup>3</sup>, Dennis R. Burton<sup>1,2</sup> & Pascal Poignard<sup>1,7</sup>

**Broadly neutralizing antibodies against highly variable viral pathogens are much sought after to treat or protect against global circulating viruses. Here we probed the neutralizing antibody repertoires of four human immunodeficiency virus (HIV)-infected donors with remarkably broad and potent neutralizing responses and rescued 17 new monoclonal antibodies that neutralize broadly across clades. Many of the new monoclonal antibodies are almost tenfold more potent than the recently described PG9, PG16 and VRC01 broadly neutralizing monoclonal antibodies and 100-fold more potent than the original prototype HIV broadly neutralizing monoclonal antibodies<sup>1–3</sup>. The monoclonal antibodies largely recapitulate the neutralization breadth found in the corresponding donor serum and many recognize novel epitopes on envelope (Env) glycoprotein gp120, illuminating new targets for vaccine design. Analysis of neutralization by the full complement of anti-HIV broadly neutralizing monoclonal antibodies now available reveals that certain combinations of antibodies should offer markedly more favourable coverage of the enormous diversity of global circulating viruses than others and these combinations might be sought in active or passive immunization regimes. Overall, the isolation of multiple HIV broadly neutralizing monoclonal antibodies from several donors that, in aggregate, provide broad coverage at low concentrations is a highly positive indicator for the eventual design of an effective antibody-based HIV vaccine.**

Most successful antiviral vaccines elicit neutralizing antibodies as a correlate of protection<sup>4,5</sup>. For highly variable viruses—such as HIV, hepatitis C virus (HCV) and, to a lesser extent, influenza—vaccine design efforts have been hampered by the difficulties associated with eliciting neutralizing antibodies that are effective against the enormous diversity of global circulating isolates (that is, broadly neutralizing antibodies)<sup>6,7</sup>. However, for HIV for example, 10–30% of infected individuals do, in fact, develop broadly neutralizing sera and protective broadly neutralizing monoclonal antibodies have been isolated from infected donors<sup>1,2,8–12</sup>. It has been suggested that, given the appropriate immunogen<sup>13</sup> and understanding the properties of broadly neutralizing monoclonal antibodies has become a major goal in research on highly variable viruses.

We have previously screened sera from approximately 1,800 HIV-infected donors for neutralization breadth and potency, designating the top 1% as ‘elite neutralizers’, based on a score incorporating both breadth and potency<sup>14</sup>. In this study, we set out to isolate broadly neutralizing monoclonal antibodies from the top four elite neutralizers (Supplementary Table 1) by screening antibody-containing memory B cell supernatants for broad neutralizing activity using a recently

described high-throughput functional approach<sup>2</sup>. Antibody variable genes were rescued from B-cell cultures that showed cross-clade neutralizing activity and expressed as full-length IgGs. Analysis of the sequences revealed that all of the monoclonal antibodies isolated from each individual donor belong to a distant, but clonally related cluster of antibodies (Supplementary Table 2). Because it has been proposed that antibodies from HIV-infected patients are often polyreactive<sup>15,16</sup>, we tested the new monoclonal antibodies for binding to a panel of antigens and showed that they were not polyreactive (Supplementary Fig. 2).

The potency and breadth of the monoclonal antibodies were next assessed on a 162-pseudovirus panel representing all major circulating HIV subtypes (Fig. 1 and Supplementary Tables 3 and 4)<sup>2</sup>. All of the monoclonal antibodies exhibited cross-clade neutralizing activity, but more strikingly, several showed exceptional potency. The median antibody concentrations required to inhibit HIV activity by 50% or 90% (IC<sub>50</sub> and IC<sub>90</sub> values), of PGT monoclonal antibodies 121–123 and 125–128 were almost tenfold lower (that is, more potent) than the recently described PG9, PG16, VRC01 and PGV04 broadly neutralizing monoclonal antibodies<sup>1,2</sup> (E. Falkowska *et al.*, manuscript in preparation, X. Wu *et al.*, *Science*, in the press), and approximately 100-fold lower than other broadly neutralizing monoclonal antibodies

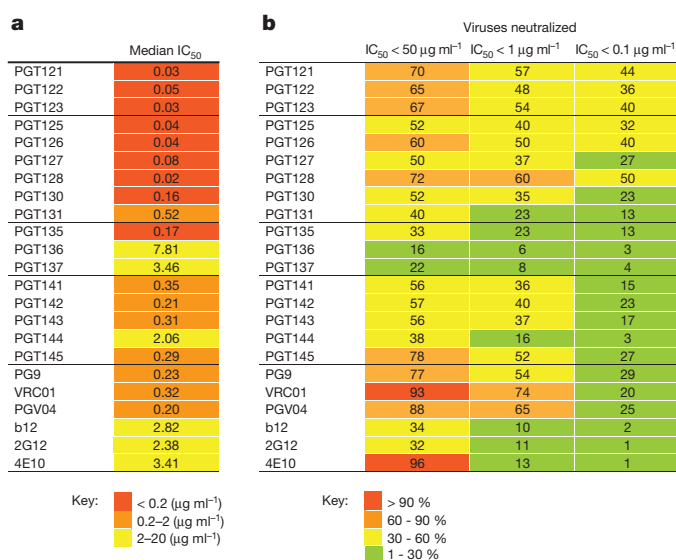


**Figure 1 | Neutralization activity of the newly identified PGT antibodies.** **a**, Median neutralization potency against viruses neutralized with an IC<sub>50</sub> < 50 μg ml<sup>-1</sup>. **b**, Neutralization breadth at different IC<sub>50</sub> cut-offs.

<sup>1</sup>Department of Immunology and Microbial Science and IAVI Neutralizing Antibody Center, The Scripps Research Institute, La Jolla, California 92037, USA. <sup>2</sup>Ragon Institute of MGH, MIT, and Harvard, Cambridge, Massachusetts 02129, USA. <sup>3</sup>Department of Molecular Biology, Skaggs Institute for Chemical Biology, and IAVI Neutralizing Antibody Center, The Scripps Research Institute, La Jolla, California 92037, USA. <sup>4</sup>Department of Chemistry, The Scripps Research Institute, La Jolla, California 92037, USA. <sup>5</sup>Theracell Sciences, Inc., Seattle, Washington 98104, USA. <sup>6</sup>Monogram Biosciences, Inc., South San Francisco, California 94080, USA. <sup>7</sup>International AIDS Vaccine Initiative, New York, New York 10038, USA.

\*These authors contributed equally to this work.

†Lists of authors and affiliations appear in Supplementary Information.

described earlier (Fig. 1). At concentrations less than  $0.1 \mu\text{g ml}^{-1}$ , these monoclonal antibodies still neutralized 27% to 50% of viruses in the panel (Fig. 1). Although PGT monoclonal antibodies 135, 136 and 137 showed a lesser neutralization breadth than the other monoclonal antibodies, they all still potentially neutralized over 30% of the clade C viruses on the panel (Supplementary Fig. 2 and Supplementary Table 3b). This result is significant considering that HIV clade C predominates in sub-Saharan Africa and accounts for more than 50% of all HIV infections worldwide.

Interestingly, many of the clonally related monoclonal antibodies exhibited differing degrees of overall neutralization potency. For example, the median  $\text{IC}_{50}$  values of PGT monoclonal antibodies 131, 136, 137 and 144 were approximately 10- to 50-fold higher than those of their somatically related sister clones (Fig. 1). Also, in some cases, the somatically related monoclonal antibodies exhibited similar neutralization potency but differing degrees of neutralization breadth against the panel of viruses tested (Fig. 1 and Supplementary Tables 3 and 4). For example, PGT 128 neutralized with comparable overall potency but significantly greater neutralization breadth than the clonally related PGT 125, 126 and 127 monoclonal antibodies (Fig. 1 and Supplementary Tables 3 and 4). Overall, these observations suggest that serum neutralization breadth may develop from the successive selection of somatic variants that bind to a modified epitope or a slightly different Env conformation expressed on virus escape variants. Comparison of the neutralization profiles of the monoclonal antibodies isolated from a given donor with that from the corresponding serum revealed that the isolated monoclonal antibodies could largely recapitulate the serum neutralization breadth and potency (Fig. 2 and Supplementary Fig. 3).

We next sought to gain information on the epitopes recognized by the newly isolated broadly neutralizing monoclonal antibodies. Enzyme-linked immunosorbent (ELISA) assays indicated that PGT monoclonal antibodies 121–123, 125–128, 130, 131 and 135–137 bound to monomeric gp120 (Supplementary Table 5). In contrast, the PGT 141–145 broadly neutralizing monoclonal antibodies exhibited a strong preference for membrane-bound, trimeric HIV Env (Supplementary Fig. 4). On the basis of this result, we postulated that these broadly neutralizing monoclonal antibodies bound to quaternary epitopes similar to those of the recently described PG9 and PG16 broadly neutralizing monoclonal antibodies<sup>2</sup>. Indeed, this hypothesis was confirmed by competition studies, N160K sensitivity and, for PGT monoclonal antibodies 141–144, an inability to neutralize JR-CSF pseudoviruses expressing homogenous  $\text{Man}_9\text{GlcNAc}_2$  glycans<sup>17</sup> (Supplementary Fig. 5).

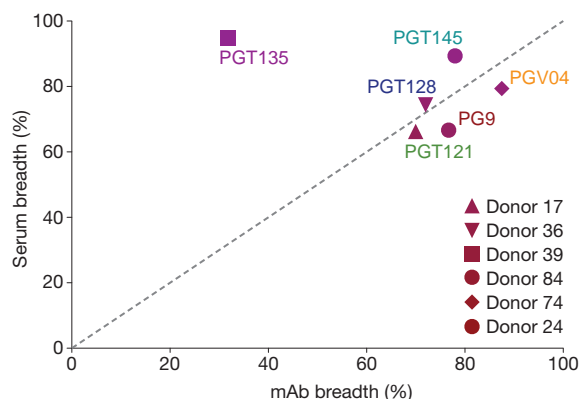
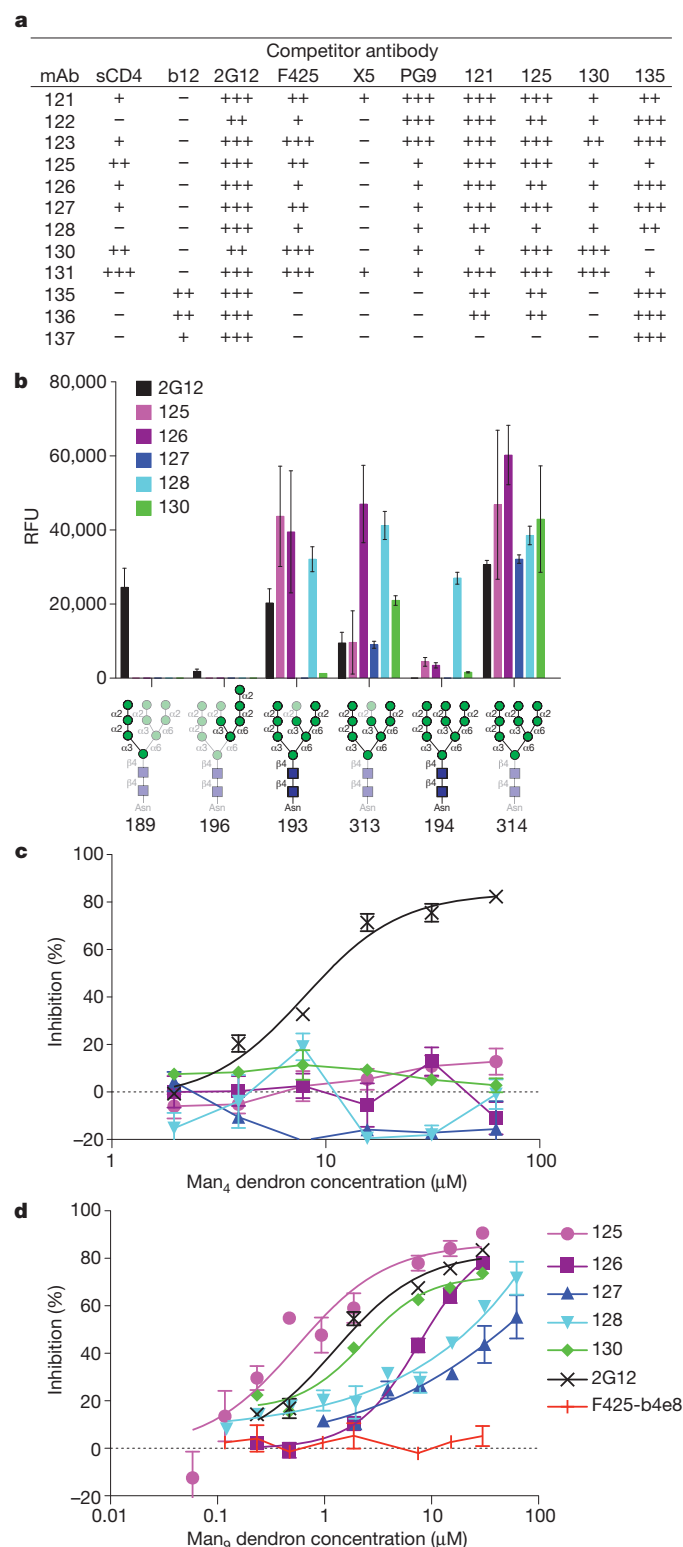


**Figure 2 | Key monoclonal antibodies fully recapitulate serum neutralization by the corresponding donor serum.** Serum breadth was correlated with the breadth of the broadest monoclonal antibody (mAb) for each donor (percentage of viruses neutralized at 50% neutralizing titre ( $\text{NT}_{50}$ ) > 100 or  $\text{IC}_{50}$  <  $50 \mu\text{g ml}^{-1}$ , respectively). Of note, monoclonal antibodies isolated from donor 39 could not completely recapitulate the serum neutralization breadth.

To define the epitopes recognized by the remaining PGT antibodies, competition ELISA assays were carried out with a panel of well-characterized neutralizing and non-neutralizing antibodies (Fig. 3a). Unexpectedly, all of the remaining antibodies (PGT monoclonal antibodies 121–123, 125–128, 130, 131 and 135–137) competed with the glycan-specific broadly neutralizing monoclonal antibody 2G12. This result was surprising given that 2G12 had previously formed its own unique competition group. All of the monoclonal antibodies, except for PGT monoclonal antibodies 135, 136 and 137, also





competed with a V3-loop-specific monoclonal antibody and failed to bind to gp120 $\Delta$ V3, suggesting that their epitopes were in proximity to or contiguous with V3 (Fig. 3a and Supplementary Table 5). Deglycosylation of gp120 with Endo H abolished binding by all the monoclonal antibodies, indicating that certain oligomannose glycans were important for epitope recognition (Supplementary Table 5). Competition of these monoclonal antibodies with 2G12 and lack of binding to deglycosylated gp120 prompted us to investigate whether these antibodies contacted glycans directly. Glycan array analysis revealed that PGT monoclonal antibodies 125–128 and 130 bound specifically to both Man<sub>8</sub>GlcNAc<sub>2</sub> and Man<sub>9</sub>GlcNAc<sub>2</sub>, whereas the remaining antibodies showed no detectable binding to high-mannose glycans (Fig. 3b). Interestingly, binding of PGT monoclonal antibodies 125–128 and 130 to gp120 was competed by Man<sub>9</sub> but, unlike 2G12, was not competed by monomeric mannose or Man<sub>4</sub> (D1 arm of Man<sub>9</sub>GlcNAc<sub>2</sub>) (Fig. 3c, d), suggesting a different mode of glycan recognition. Furthermore, in contrast to 2G12, no evidence was found for domain exchange and monomeric Fab fragments still exhibited potent neutralizing activity (Supplementary Fig. 7 and data not shown).

To define further the epitopes recognized by the monoclonal antibodies, neutralizing activity against a large panel of HIV-1<sub>JR-CSF</sub> variants incorporating single alanine substitutions was assessed using a single round of replication pseudovirus assay (Supplementary Table 6). In the panel of mutants, the N-linked glycans at positions 332 and/or 301 were important for neutralization by PGT monoclonal antibodies 125–128, 130 and 131, suggesting their direct involvement in epitope formation. The apparent dependency on so few glycans indicates that, although these PGT monoclonal antibodies contact Man<sub>8-9</sub>GlcNAc<sub>2</sub> glycans directly, their arrangement in the context of gp120 is critical for high-affinity glycan recognition and neutralization potency. This is further highlighted by the inability of the PGT monoclonal antibodies to neutralize simian immunodeficiency virus (SIV) strain SIV<sub>MAC239</sub>, HIV-2 or HCV, which show a high level of glycosylation (data not shown). Interestingly, although PGT monoclonal antibodies 121–123 failed to exhibit detectable binding to high-mannose glycans and be competed by mannose sugars (Supplementary Fig. 6), the only substitutions that completely abolished neutralization by these monoclonal antibodies were those that resulted in removal of the glycan at position 332. Although structural studies will be required to fully define the epitopes recognized by these antibodies, the above results indicate either that the PGT monoclonal antibodies 121–123 bind to a protein epitope along the gp120 polypeptide backbone that is conformationally dependent on the N332 glycan or that the glycan contributes more strongly to binding in the context of the intact protein.

Vaccines against pathogens with low antigenic diversity, such as hepatitis B virus or measles, commonly achieve 90–95% efficacy<sup>18</sup>. Similarly, the influenza vaccine achieves 85–90% efficacy in years

when the vaccine and circulating seasonal strain are well matched<sup>19,20</sup>. However, efficacy drops severely in years when there is a mismatch between the vaccine and circulating strain. In the case of HIV, the global diversity of circulating viruses is such that the match between the prophylactic antibodies and the circulating viruses—that is, the antibody viral coverage—will be crucial for the degree of efficacy of active or passive prophylaxis approaches. As yet, although the recent

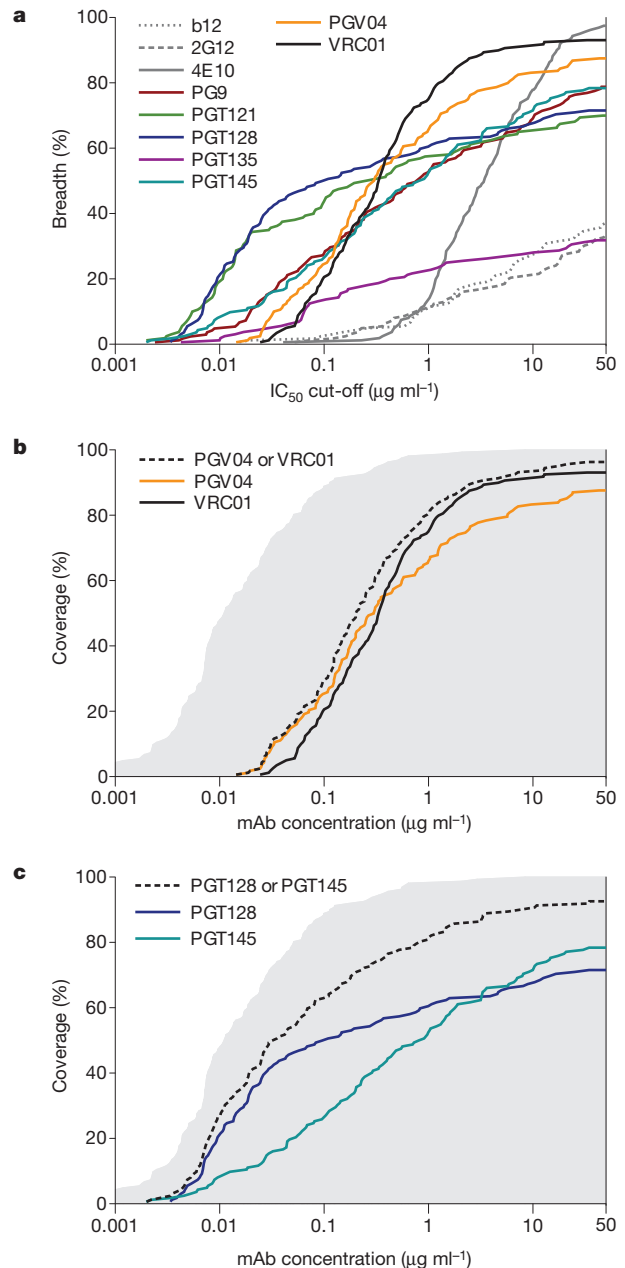


**Figure 3 | Epitope mapping of PGT antibodies.** **a**, Competition of PGT monoclonal antibodies with sCD4 (soluble CD4), b12 (anti-CD4 binding site), 2G12 (anti-glycan), F425/b4e8 (anti-V3), X5 (CD4-induced), PG9 (anti-V1/V2 and V3, quaternary) and each other. Competition assays were performed by ELISA using gp120<sub>Bal</sub> or gp120<sub>JR-FL</sub>, except for the PG9 competition assay, which was performed on the surface of JR-FL<sub>E168K</sub> or JR-CSF transfected cells. Boxes are coded as follows: + + +, 75–100% competition; + +, 50–75% competition; +, 25–50% competition; –, <25% competition. Experiments were performed in duplicate, and data represent an average of at least two independent experiments. **b**, Glycan microarray analysis (Consortium for Functional Glycomics (CFG), version 5.0) reveals that PGT monoclonal antibodies 125, 126, 127, 128 and 130 contact Man<sub>8</sub> (313), Man<sub>8</sub>GlcNAc<sub>2</sub> (193), Man<sub>9</sub> (314) and Man<sub>9</sub>GlcNAc<sub>2</sub> (194) glycans directly. Only glycan structures with RFU (relative fluorescent units) > 3,000 are shown. PGT-131 showed no detectable binding to the CFG glycan array but bound to Man<sub>9</sub>-oligodendrons<sup>30</sup> (data not shown). Error bars represent standard deviation. **c**, **d**, Binding of PGT monoclonal antibodies 125, 126, 127, 128 and 130 to gp120 is competed by Man<sub>9</sub> oligodendrons but not Man<sub>4</sub> oligodendrons. Binding of 131 to immobilized gp120 was too low to measure any competition. Error bars represent standard error of the mean.

**Figure 4 | Certain antibodies or antibody combinations are able to cover a broad range of HIV isolates at low, vaccine-achievable concentrations.**

**a**, Cumulative frequency distribution of IC<sub>50</sub> values of broadly neutralizing monoclonal antibodies tested against a 162-virus panel. The y-axis shows the cumulative frequency of IC<sub>50</sub> values up to the concentration shown on the x-axis and can therefore also be interpreted as the breadth at a specific IC<sub>50</sub> cut-off. **b**, **c**, Percentage of viruses covered by single monoclonal antibodies (solid lines) or by at least one of the monoclonal antibodies in dual combinations of breadth (dashed black lines) dependent on individual concentrations. The grey area in both panels is the coverage of 26 monoclonal antibodies tested on the 162-virus panel (PGT121–123, PGT125–128, PGT130–131, PGT135–137, PGT141–145, PG9, PG16, PGC14, VRC01, PGV04, b12, 2G12, 4E10, 2F5) and depicts the theoretical maximal achievable coverage known to date.

RV144 trial has led to speculation that some degree of protection against HIV may be achieved through extra-neutralizing activities of antibodies, such as antibody-dependent cell-mediated cytotoxicity or phagocytosis, the strongest evidence for protection is for neutralizing antibodies in non-human primate models using simian-human immunodeficiency virus (SHIV) challenge<sup>21–25</sup>. Passive administration of neutralizing antibodies in these models suggests that a serum antibody concentration of approximately or greater than 100 times the *in vitro* pseudovirus assay IC<sub>50</sub> is required to achieve a meaningful level of protection<sup>21–25</sup>. Therefore, if a vaccine elicits a serum broadly neutralizing antibody concentration on the order of 10 µg ml<sup>-1</sup> (ref. 26) and if an IC<sub>50</sub>:protective-serum-concentration ratio of 1:100 is assumed, then protection would be only achieved against viruses for which the broadly neutralizing antibody IC<sub>50</sub> is lower than 0.1 µg ml<sup>-1</sup>. As a second more conservative scenario, for an IC<sub>50</sub>:protective-serum-concentration ratio of 1:500, protection would be achieved against viruses for which the broadly neutralizing antibody IC<sub>50</sub> is lower than 0.02 µg ml<sup>-1</sup>. As shown in Fig. 4, although various broadly neutralizing monoclonal antibodies show breadth at high concentrations, viral coverage often drops sharply at lower concentrations. Therefore, if elicited or delivered singly, only the most potent antibodies, such as 121 and 128, would be able to achieve a meaningful level of viral coverage, in particular at concentrations corresponding to the more conservative scenario given above. As broadly neutralizing monoclonal antibodies show different and in some cases complementary breadth, we further looked at the theoretical coverage achieved by antibody combinations. For the two IC<sub>50</sub>:protective-serum-concentration ratios above, a combination of PGV04 and VRC01, the two most potent CD4 binding site broadly neutralizing monoclonal antibodies, would provide protection against 29% and 2% of viruses, respectively (Fig. 4b). In contrast, for a vaccine eliciting antibodies with high potency and favourable non-overlapping breadth, such as 128 and 145, coverage would be achieved against 63% and 40% of viruses for the two scenarios (Fig. 4c). Several combinations of two broadly neutralizing monoclonal antibodies, including those directed to overlapping epitopes, can yield this degree of coverage (Supplementary Fig. 8). In addition, a combination of all of the broadly neutralizing monoclonal antibodies would cover 89% and 62% of viruses, correspondingly. Coverage against such a large proportion of viruses would probably have an important impact on the pandemic.

An effective vaccine against HIV will probably require the elicitation of a combination of complementary potent neutralizing antibodies. The demonstration that large numbers of potent and diverse broadly neutralizing monoclonal antibodies can be isolated from several different individuals provides grounds for renewed optimism that an antibody-based vaccine may be achievable.

## METHODS SUMMARY

Activated memory B-cell supernatants were screened in a high-throughput format for neutralization activity using a micro-neutralization assay, as described<sup>2</sup>. Heavy- and light-chain variable regions were isolated from B-cell lysates of selected neutralizing hits by reverse transcription from RNA followed by multiplex PCR amplification using family-specific V-gene primer sets. For some antibodies, traditional cloning methods were used for antibody isolation, as described<sup>2</sup>. For other antibodies, amplicons from each lysate were uniquely tagged with multiplex identifier (MID) sequences and 454 sequencing regions (Roche). Single rounds of replication pseudovirus neutralization assays and cell surface binding assays were performed as described previously<sup>2,27,28</sup>. Glycan reactivities were profiled on a printed glycan microarray (version 5.0 from the Consortium for Functional Glycomics) as described previously<sup>29</sup>.

**Full Methods** and any associated references are available in the online version of the paper at [www.nature.com/nature](http://www.nature.com/nature).

Received 20 April; accepted 14 July 2011.

Published online 17 August; corrected 22 September 2011 (see full-text HTML version for details).

1. Wu, X. *et al.* Rational design of envelope identifies broadly neutralizing human monoclonal antibodies to HIV-1. *Science* **329**, 856–861 (2010).

2. Walker, L. M. *et al.* Broad and potent neutralizing antibodies from an African donor reveal a new HIV-1 vaccine target. *Science* **326**, 285–289 (2009).
3. Binley, J. M. *et al.* Comprehensive cross-clade neutralization analysis of a panel of anti-human immunodeficiency virus type 1 monoclonal antibodies. *J. Virol.* **78**, 13232–13252 (2004).
4. Amanna, I. J., Messaoudi, I. & Slifka, M. K. Protective immunity following vaccination: how is it defined? *Hum. Vaccin.* **4**, 316–319 (2008).
5. Plotkin, S. A. Immunologic correlates of protection induced by vaccination. *Pediatr. Infect. Dis. J.* **20**, 63–75 (2001).
6. Barouch, D. H. Challenges in the development of an HIV-1 vaccine. *Nature* **455**, 613–619 (2008).
7. Karlsson Hedestam, G. B. *et al.* The challenges of eliciting neutralizing antibodies to HIV-1 and to influenza virus. *Nature Rev. Microbiol.* **6**, 143–155 (2008).
8. Stamatatos, L., Morris, L., Burton, D. R. & Mascola, J. R. Neutralizing antibodies generated during natural HIV-1 infection: good news for an HIV-1 vaccine? *Nature Med.* **15**, 866–870 (2009).
9. Trkola, A. *et al.* Cross-clade neutralization of primary isolates of human immunodeficiency virus type 1 by human monoclonal antibodies and tetrameric CD4-IgG. *J. Virol.* **69**, 6609–6617 (1995).
10. Stiegler, G. *et al.* A potent cross-clade neutralizing human monoclonal antibody against a novel epitope on gp41 of human immunodeficiency virus type 1. *AIDS Res. Hum. Retroviruses* **17**, 1757–1765 (2001).
11. Burton, D. R. *et al.* Efficient neutralization of primary isolates of HIV-1 by a recombinant human monoclonal antibody. *Science* **266**, 1024–1027 (1994).
12. Kwong, P. D. & Wilson, I. A. HIV-1 and influenza antibodies: seeing antigens in new ways. *Nature Immunol.* **10**, 573–578 (2009).
13. Schief, W. R., Ban, Y. E. & Stamatatos, L. Challenges for structure-based HIV vaccine design. *Curr. Opin. HIV AIDS* **4**, 431–440 (2009).
14. Simek, M. D. *et al.* Human immunodeficiency virus type 1 elite neutralizers: individuals with broad and potent neutralizing activity identified by using a high-throughput neutralization assay together with an analytical selection algorithm. *J. Virol.* **83**, 7337–7348 (2009).
15. Haynes, B. F. *et al.* Cardiophilic polyspecific autoreactivity in two broadly neutralizing HIV-1 antibodies. *Science* **308**, 1906–1908 (2005).
16. Mouquet, H. *et al.* Polyreactivity increases the apparent affinity of anti-HIV antibodies by heterologation. *Nature* **467**, 591–595 (2010).
17. Walker, L. M. *et al.* A limited number of antibody specificities mediate broad and potent serum neutralization in selected HIV-1 infected individuals. *PLoS Pathog.* **6**, e1001028 (2010).
18. Plotkin, S. A. Orenstein, W. A. & Offit, P. A. *Vaccines* (Elsevier Health Sciences, Philadelphia, 2008).
19. Bridges, C. B. *et al.* Effectiveness and cost-benefit of influenza vaccination of healthy working adults: a randomized controlled trial. *J. Am. Med. Assoc.* **284**, 1655–1663 (2000).
20. Herrera, G. A. *et al.* Influenza vaccine effectiveness among 50–64-year-old persons during a season of poor antigenic match between vaccine and circulating influenza virus strains: Colorado, United States, 2003–2004. *Vaccine* **25**, 154–160 (2007).
21. Parren, P. W. *et al.* Antibody protects macaques against vaginal challenge with a pathogenic R5 simian/human immunodeficiency virus at serum levels giving complete neutralization *in vitro*. *J. Virol.* **75**, 8340–8347 (2001).
22. Nishimura, Y. *et al.* Determination of a statistically valid neutralization titre in plasma that confers protection against simian-human immunodeficiency virus challenge following passive transfer of high-titered neutralizing antibodies. *J. Virol.* **76**, 2123–2130 (2002).
23. Hessel, A. J. *et al.* Effective, low-titer antibody protection against low-dose repeated mucosal SHIV challenge in macaques. *Nature Med.* **15**, 951–954 (2009).
24. Hessel, A. J. *et al.* Broadly neutralizing human anti-HIV antibody 2G12 is effective in protection against mucosal SHIV challenge even at low serum neutralizing titers. *PLoS Pathog.* **5**, e1000433 (2009).
25. Willey, R., Nason, M. C., Nishimura, Y., Follmann, D. A. & Martin, M. A. Neutralizing antibody titers conferring protection to macaques from a simian/human immunodeficiency virus challenge using the TZM-bl assay. *AIDS Res. Hum. Retroviruses* **26**, 89–98 (2010).
26. Martell, B. A. *et al.* Cocaine vaccine for the treatment of cocaine dependence in methadone-maintained patients: a randomized, double-blind, placebo-controlled efficacy trial. *Arch. Gen. Psychiatry* **66**, 1116–1123 (2009).
27. Pantophlet, R. *et al.* Fine mapping of the interaction of neutralizing and nonneutralizing monoclonal antibodies with the CD4 binding site of human immunodeficiency virus type 1 gp120. *J. Virol.* **77**, 642–658 (2003).
28. Li, M. *et al.* Human immunodeficiency virus type 1 *env* clones from acute and early subtype B infections for standardized assessments of vaccine-elicited neutralizing antibodies. *J. Virol.* **79**, 10108–10125 (2005).
29. Blixt, O. *et al.* Printed covalent glycan array for ligand profiling of diverse glycan binding proteins. *Proc. Natl Acad. Sci. USA* **101**, 17033–17038 (2004).
30. Wang, S. K. *et al.* Targeting the carbohydrates on HIV-1: interaction of oligomannose dendrons with human monoclonal antibody 2G12 and DC-SIGN. *Proc. Natl Acad. Sci. USA* **105**, 3690–3695 (2008).

**Supplementary Information** is linked to the online version of the paper at [www.nature.com/nature](http://www.nature.com/nature).

**Acknowledgements** We thank N. Schultz, K. Le and V. Thane for technical assistance at The Scripps Research Institute. We also thank C. Corbaci, S. M. Eagol and C. Williams for assistance with Fig. 3. We would also like to thank the research staff members of the Theraclone I-STAR Discovery and Antibody Purification Team, and K. Limoli, S. Jauregui, K. Tran, P. Sitou, J. Perea, B. Huang and P. Guinto at Monogram

BioSciences. We thank R. McBride for assistance with the glycan array and are grateful to W. Olson for providing purified KHN1144 SOSIP trimer, R. Wyatt for providing the YU2 Foldon trimer and J. Mascola for providing monoclonal antibody VRC01. In addition, we would like to thank all of the International AIDS Vaccine Initiative (IAVI) Protocol G project, clinical and site team members, the IAVI Human Immunology Laboratory (HIL) and all of the Protocol G clinical investigators, specifically, G. Miir, A. Pozniak, D. McPhee, O. Manigart, E. Karita, A. Inwoley, W. Jaoko, J. DeHovitz, L.-G. Bekker, P. Pitisuttithum, R. Paris, J. Serwanga and S. Allen. This work was supported by IAVI, NIAID, the Ragon Institute and the United States for International Development (USAID). The contents are the responsibility of the authors and do not necessarily reflect the views of USAID or the United States Government.

**Author Contributions** Project planning was performed by L.M.W., M.H., K.J.D., E.F., P.-Y.C.-H., R.P., J.-P.J., T.W., S.P., M.D.S., W.K., I.A.W., M.M., S.F., D.R.B. and P.P.;

experimental work by L.M.W., M.H., K.J.D., E.F., R.P., J.-P.J., P.-Y.C.-H., S.-K.W., A.R., J.L.M., P.W.H., O.A.O. and T.W.; data analysis by M.H., L.M.W., K.J.D., E.F., T.W., P.-Y.C.-H., D.R.B. and P.P.; composition of the first draft of the manuscript by L.M.W. and D.R.B.; manuscript layout and major manuscript revisions by M.H., K.J.D. and P.P.; revisions by R.P., J.-P.J., E.F., W.C.K. and I.A.W.

**Author Information** Gene sequences of the reported antibodies and the primers used for antibody isolation have been deposited under GenBank accession numbers JN201894–JN201927. Reprints and permissions information is available at [www.nature.com/reprints](http://www.nature.com/reprints). The authors declare competing financial interests: details accompany the full-text HTML version of the paper at [www.nature.com/nature](http://www.nature.com/nature). Readers are welcome to comment on the online version of this article at [www.nature.com/nature](http://www.nature.com/nature). Correspondence and requests for materials should be addressed to D.R.B. ([burton@scripps.edu](mailto:burton@scripps.edu)) or P.P. ([poignard@scripps.edu](mailto:poignard@scripps.edu)).



## METHODS

**Antibodies and antigens.** The following antibodies and reagents were procured by the IAVI Neutralizing Antibody Consortium: antibody 2G12 (Polymun Scientific), antibody F425/b4E8 (provided by L. Cavacini, Beth Israel Deaconess Medical Center), soluble CD4 (Progenics), HxB2 gp120, SF162 gp120, BaL gp120, JR-FL gp120, JR-CSF gp120 and YU2 gp120 (provided by G. Stewart-Jones, Oxford University). Purified ADA gp120 was produced in the laboratory of R. Doms, University of Pennsylvania. Fab X5 was expressed in *Escherichia coli* and purified using an anti-human Fab specific affinity column. Deglycosylated gp120 JRFL was expressed in HEK 293S GnTI<sup>-/-</sup> cells and treated with Endo H (Roche).

**Donors.** The donors identified for this study were selected from the IAVI sponsored study, Protocol G<sup>14</sup>. Eligibility for enrolment into Protocol G was defined as: male or female at least 18 years of age with documented HIV infection for at least three years, clinically asymptomatic at the time of enrolment and not currently receiving antiretroviral therapy. Selection of individuals for monoclonal antibody generation was based on a rank-order high-throughput screening and analytical algorithm<sup>14</sup>. Volunteers were identified as elite neutralizers based on broad and potent neutralizing activity against a cross-clade pseudovirus panel<sup>14</sup>.

**Isolation of monoclonal antibodies.** The method for isolating human monoclonal antibodies from memory B cells in circulation has previously been described<sup>2</sup>. Surface IgG<sup>+</sup> B cells seeded at near-clonal density in 384-well microplates were activated in short-term culture. Supernatants were screened for neutralization activity against 2–4 pseudotyped viruses for which neutralization activity was detected at high titres in the donor serum. Heavy- and light-chain variable regions were isolated from B-cell lysates of selected neutralizing hits by reverse transcription from RNA followed by multiplex PCR amplification using family-specific V-gene primer sets. Amplicons from each lysate were uniquely tagged with multiplex identifier (MID) sequences and 454 sequencing regions (Roche). A normalized pooling of gamma, kappa and lambda chains was performed based on agarose gel image quantitation and the pool was analysed by 454 Titanium sequencing. Consensus sequences of the VH and VL chains were generated using the Amplicon Variant Analyser (Roche) and assigned to specific B-cell culture wells by decoding the MID tags. Selected VH and VL chains were synthesized and cloned in expression vectors with the appropriate IgG1, Ig kappa or Ig lambda constant domain. Monoclonal antibodies were reconstituted by transient transfection in HEK293 cells followed by purification from serum-free culture supernatants.

**PGT antibody expression and purification.** Antibody genes were cloned into an expression vector and transiently expressed with the FreeStyle 293 Expression System (Invitrogen). Antibodies were purified using affinity chromatography (Protein A Sepharose Fast Flow, GE Healthcare) and purity and integrity checked with SDS-PAGE.

**Neutralization assays.** Neutralization by monoclonal antibodies and donor sera was performed by Monogram Biosciences using a single round of replication pseudovirus assay as previously described<sup>31</sup>. Briefly, pseudoviruses capable of a single round of infection were produced by co-transfection of HEK293 cells with a subgenomic plasmid, pHIV-1luc3, that incorporates a firefly luciferase indicator gene and a second plasmid, pCXAS, which expressed HIV-1 Env libraries or clones. Following transfection, pseudoviruses were harvested and used to infect U87 cell lines expressing co-receptors CCR5 or CXCR4. Pseudovirus neutralization assays using HIV-1JR-CSF alanine mutants are fully described elsewhere<sup>2</sup>. Neutralization activity of monoclonal antibodies against HIV-1JR-CSF alanine mutants was measured using a TZM-BL assay, as described<sup>2</sup>. Kifunensine-treated pseudoviruses were produced by treating 293T cells with 25  $\mu$ M kifunensine on the day of transfection. Memory B-cell supernatants were screened in a micro-neutralization assay against a cross-clade panel of HIV-1 isolates and SIV<sub>MAC239</sub> (negative control). This assay was based on the 96-well pseudotyped HIV-1 neutralization assay (Monogram Biosciences) and was modified for screening 15  $\mu$ l of B-cell culture supernatants in a 384-well format.

**Cell surface binding assays.** Titrating amounts of antibodies were added to HIV-1 Env-transfected 293T cells, incubated for 1 h at 37 °C, washed with FACS buffer, and stained with goat anti-human IgG F(ab')<sub>2</sub> conjugated to phycoerythrin (Jackson ImmunoResearch). Binding was analysed using flow cytometry, and binding curves were generated by plotting the mean fluorescence intensity of

antigen binding as a function of antibody concentration. For competition assays, titrating amounts of competitor antibodies were added to the cells 30 min before adding biotinylated PGT monoclonal antibodies at a concentration required to give half-maximum effective concentration (EC<sub>50</sub>).

**ELISA assays.** For antigen-binding ELISAs, serial dilutions of monoclonal antibodies were added to antigen-coated wells and binding was probed with alkaline-phosphatase-conjugated goat anti-human IgG F(ab')<sub>2</sub> antibody (Pierce). For competition ELISAs, titrating amounts of competitor monoclonal antibodies were added to gp120-coated ELISA wells and incubated for 30 min before adding biotinylated PGT monoclonal antibodies at a concentration required to give IC<sub>70</sub>. Biotinylated PGT monoclonal antibodies were detected using alkaline-phosphatase-conjugated streptavidin (Pierce) and visualized using p-nitrophenol phosphate substrate (Sigma).

**Glycan microarray analysis.** Monoclonal antibodies were screened on a printed glycan microarray version 5.0 from the CFG as described previously<sup>29</sup>. Antibodies were used at a concentration of 30  $\mu$ g ml<sup>-1</sup> and were precomplexed with 15  $\mu$ g ml<sup>-1</sup> secondary antibody (goat anti-human-Fc-rPE, Jackson ImmunoResearch) before addition to the slide. Complete glycan array data sets for all antibodies can be found at <http://www.functionallyglycomics.org> in the CFG data archive under "cfg\_rRequest\_2250".

**Oligomannose dendron synthesis.** The oligomannose dendrons (Man<sub>4</sub>D and Man<sub>9</sub>D) were synthesized by Cu(I) catalysed alkyne-azide cycloaddition between azido oligomannose and the second generation of AB<sub>3</sub> type alkynyl dendron. Detailed procedures and characterization were previously reported<sup>30</sup>.

**Fabrication of gp120 microarray.** NHS-activated glass slides (Nexterion slide H, Schott North American) were printed with robotic pin (Arrayit 946) to deposit gp120 JRFL at concentrations of 750 or 250  $\mu$ g ml<sup>-1</sup> in printing buffer (120 mM phosphate, pH 8.5; containing 5% glycerol and 0.01% Tween 20). Twelve replicates were used for each concentration. The printed slides were incubated in relative humidity 75% chamber overnight and treated with blocking solution (superblock blocking buffer in PBS, Thermo) at 25 °C for 1 h. The slides were then rinsed with PBS-T (0.05% Tween 20) and PBS buffer, and centrifuged at 200g to remove residual solution from slide surface.

**Oligomannose dendron-gp120 competition assay with monoclonal antibodies.** Serial diluted oligomannose dendrons were mixed with monoclonal antibody (40  $\mu$ g ml<sup>-1</sup>) in PBS-BT buffer (1% BSA and 0.05% Tween 20 in PBS). The mixtures were applied directly to each sub-array on slide. After incubation in a humidified chamber for 1 h at 25 °C, the slides were rinsed sequentially with PBS-T (0.05% Tween 20 in PBS) and PBS buffer, and then centrifuged at 200g. Each sub-array was then stained with Cy3-labelled goat anti-human Fc IgG (7.5  $\mu$ g ml<sup>-1</sup> in PBS-BT) for 1 h in a humidified chamber. The slides were then rinsed sequentially with PBS-T and deionized water and centrifuged at 200g. The fluorescence of the final arrays was imaged at 10  $\mu$ m resolution (excitation: 540 nm; emission: 595 nm) with an ArrayWorx microarray reader (Applied Precision).

**Sequence analysis.** Germline genes were predicted using the immunoglobulin sequence alignment tools IMGT/V-QUEST<sup>32</sup> and SoDA2<sup>33</sup>. Clonally related sequences were identified by common germline V-genes and long stretches of identical N-nucleotides.

**Statistics.** Statistical analyses were done with Prism 5.0 for Mac (GraphPad). Viruses that are not neutralized at an IC<sub>50</sub> or IC<sub>90</sub> < 50  $\mu$ g ml<sup>-1</sup> were given a value of 50  $\mu$ g ml<sup>-1</sup> for median calculations. For combinations of antibodies, a virus was counted as covered if at least one of the monoclonal antibodies was neutralized depending on individual concentrations (IC<sub>50</sub>). This approach does not take additivity into account and therefore underestimates the neutralization potency of antibody combinations.

- Richman, D. D., Wrinn, T., Little, S. J. & Petropoulos, C. J. Rapid evolution of the neutralizing antibody response to HIV type 1 infection. *Proc. Natl Acad. Sci. USA* **100**, 4144–4149 (2003).
- Brochet, X., Lefranc, M. P. & Giudicelli, V. IMGT/V-QUEST: the highly customized and integrated system for IG and TR standardized V-J and V-D-J sequence analysis. *Nucleic Acids Res.* **36**, W503–W508 (2008).
- Munshaw, S. & Kepler, T. B. SoDA2: a Hidden Markov Model approach for identification of immunoglobulin rearrangements. *Bioinformatics* **26**, 867–872 (2010).

# Synthetic chromosome arms function in yeast and generate phenotypic diversity by design

Jessica S. Dymond<sup>1,2†</sup>, Sarah M. Richardson<sup>1,3</sup>, Candice E. Coombes<sup>1,2</sup>, Timothy Babatz<sup>1,3</sup>, H  lo  se Muller<sup>4</sup>, Narayana Annaluru<sup>4</sup>, William J. Blake<sup>5†</sup>, Joy W. Schwerzmann<sup>4†</sup>, Junbiao Dai<sup>1,2†</sup>, Derek L. Lindstrom<sup>6†</sup>, Annabel C. Boeke<sup>1†</sup>, Daniel E. Gottschling<sup>6</sup>, Srinivasan Chandrasegaran<sup>4</sup>, Joel S. Bader<sup>1,7</sup> & Jef D. Boeke<sup>1,2</sup>

Recent advances in DNA synthesis technology have enabled the construction of novel genetic pathways and genomic elements, furthering our understanding of system-level phenomena<sup>1–7</sup>. The ability to synthesize large segments of DNA allows the engineering of pathways and genomes according to arbitrary sets of design principles. Here we describe a synthetic yeast genome project, Sc2.0, and the first partially synthetic eukaryotic chromosomes, *Saccharomyces cerevisiae* chromosome synIXR, and semi-synVIL. We defined three design principles for a synthetic genome as follows: first, it should result in a (near) wild-type phenotype and fitness; second, it should lack destabilizing elements such as tRNA genes or transposons<sup>8,9</sup>; and third, it should have genetic flexibility to facilitate future studies. The synthetic genome features several systemic modifications complying with the design principles, including an inducible evolution system, SCRaMbLE (synthetic chromosome rearrangement and modification by loxP-mediated evolution). We show the utility of SCRaMbLE as a novel method of combinatorial mutagenesis, capable of generating complex genotypes and a broad variety of phenotypes. When complete, the fully synthetic genome will allow massive restructuring of the yeast genome, and may open the door to a new type of combinatorial genetics based entirely on variations in gene content and copy number.

The first phase of any genome engineering project is design (Supplementary Text 1). We designed the right arm of chromosome IX (IXR) according to the three principles outlined above and in Box 1. IXR is the smallest chromosome arm in the genome and features several genomic elements of interest (Fig. 1a), making it suitable for a pilot study. The designed sequence, synIXR, is based on a native IXR sequence extending from open reading frame (ORF) *YIL002W* through the centromere and the remainder of chromosome IXR, an 89,299-base-pair (bp) sequence (native IXR position 350,585–438,993 (ref. 10)). In accordance with the second design principle, a transfer RNA gene, a Ty1 long terminal repeat (LTR), and telomeric sequences were removed. The final synIXR sequence, 91,010 bp, is slightly longer than the native sequence owing to the inclusion of 43 loxP sites, and it replaces 20.3% of the native chromosome. A 30-kilobase (kb) telomeric segment of the left arm of chromosome VI (semi-synVIL) was similarly designed (Fig. 1b and Supplementary Text 2), and replaced 15.7% of the native chromosome. Of the original sequence lengths, 17% was changed by base substitution, deleted, or inserted during design of the two synthetic segments (Supplementary Table 1). Sequences were submitted to GenBank (sequences synIXR:JN020955 and semi-synVIL:JN020956 are also available in Supplementary Information).

We systematically introduced two sets of changes *in silico* using the genome editing suite BioStudio (S.M.R., J.S.D., J.D.B. and J.S.B., unpublished data): TAG/TAA stop-codon swaps and PCRTags sequences (see Supplementary Text 1). In recognition of the third design principle, the elimination of the TAG stop codon by recoding to TAA frees a codon for future expansion of the genetic code (for example, by adding a twenty-first, unnatural amino acid<sup>11,12</sup>), and could serve as a future mechanism of reproductive isolation and control. PCRTags are short pairs of recoded sequences, unique to either the wild-type or synthetic genome. They serve as convenient, low-cost, closely spaced genetic markers for verifying the introduction of synthetic sequence and the removal of native sequence by allowing the design of PCR primers for rapid evaluation of the presence of synthetic sequences and absence of native sequences. This is critical for evaluating the incorporation of synthetic DNA (see below and Supplementary Text 2). PCRTags, designed *in silico*, were tested in triplicate to verify specificity (Supplementary Fig. 1 and Supplementary Tables 2 and 3).

LoxPsyn sequences are nondirectional loxP sites that are capable of recombining in either orientation<sup>13</sup>. Theoretically, they produce inversions or deletions with equal probability. Under the third design principle, these sites form the substrate for the inducible SCRaMbLE system and are intended to generate combinatorial diversity. We inserted loxPsyn sites 3 bp after the stop codon of each nonessential gene and at major landmarks, such as sites of LTR and tRNA deletions, flanking the centromere *CEN9*, and adjacent to telomeres (Fig. 1 and Supplementary Text 1). LoxPsyn sites inserted at equivalent positions genome-wide will allow the formation of many structurally distinct genomes.

After completion of chromosome design and construction, ‘arm-swap’ strains, wherein the wild-type sequence was replaced with synthetic sequence, were generated. The synIXR chromosome, cloned in a circular bacterial artificial chromosome (BAC) vector, includes all sequences needed for propagation in yeast and bacteria (Fig. 1a). We introduced synIXR into a diploid strain by transformation (Fig. 2a); typically, about 10–15% of the synIXR transformants obtained were positive for all PCRTags pairs tested (Fig. 2d). We chose one such transformant, strain A (Fig. 2a), and truncated one native IXR homologue (IX  R) by transforming with a suitably designed linear DNA fragment<sup>14</sup>, introducing a selectable marker (*URA3*) and a telomere seed sequence, generating strain C (Fig. 2b). Chromosome truncation was confirmed by pulsed-field gel electrophoresis analysis (Fig. 2c), and strain C was sporulated to generate haploids carrying synIXR and

<sup>1</sup>High Throughput Biology Center, Johns Hopkins University School of Medicine, 733 North Broadway, Baltimore, Maryland 21205, USA. <sup>2</sup>Department of Molecular Biology and Genetics, Johns Hopkins University School of Medicine, 725 North Wolfe Street, Baltimore, Maryland 21205, USA. <sup>3</sup>McKusick-Nathans Institute of Genetic Medicine, Johns Hopkins University School of Medicine, 733 North Broadway, Baltimore, Maryland 21205, USA. <sup>4</sup>Bloomberg School of Public Health, Johns Hopkins University, 615 North Wolfe Street, Baltimore, Maryland 21205, USA. <sup>5</sup>Codon Devices, 99 Erie Street, Cambridge, Massachusetts 02139, USA. <sup>6</sup>Fred Hutchinson Cancer Research Center, Mailstop A3-025, PO Box 19024, Seattle, Washington 98109, USA. <sup>7</sup>Department of Biomedical Engineering, Whiting School of Engineering, Johns Hopkins University, 3400 North Charles Street, Baltimore, Maryland 21218, USA. †Present addresses: Animal Biosciences and Biotechnology Laboratory, Agricultural Research Service, USDA, 10300 Baltimore Avenue, Beltsville, Maryland 20705, USA (J.S.D.); GreenLight Biosciences, Inc., 196 Boston Avenue, Suite 2400, Medford, Massachusetts 02155, USA (W.J.B.); Battelle Memorial Institute, 2987 Clairmont Road NE, Atlanta, Georgia 30329, USA (J.W.S.); School of Life Sciences, Tsinghua University, Beijing 100084, China (J.D.); Agilent Laboratories, 5301 Stevens Creek Boulevard, Mailstop 53L-IB, Santa Clara, California 95051, USA (D.L.L.); Bowdoin College, 5000 College Station, Brunswick, Maine 04011, USA (A.C.B.).

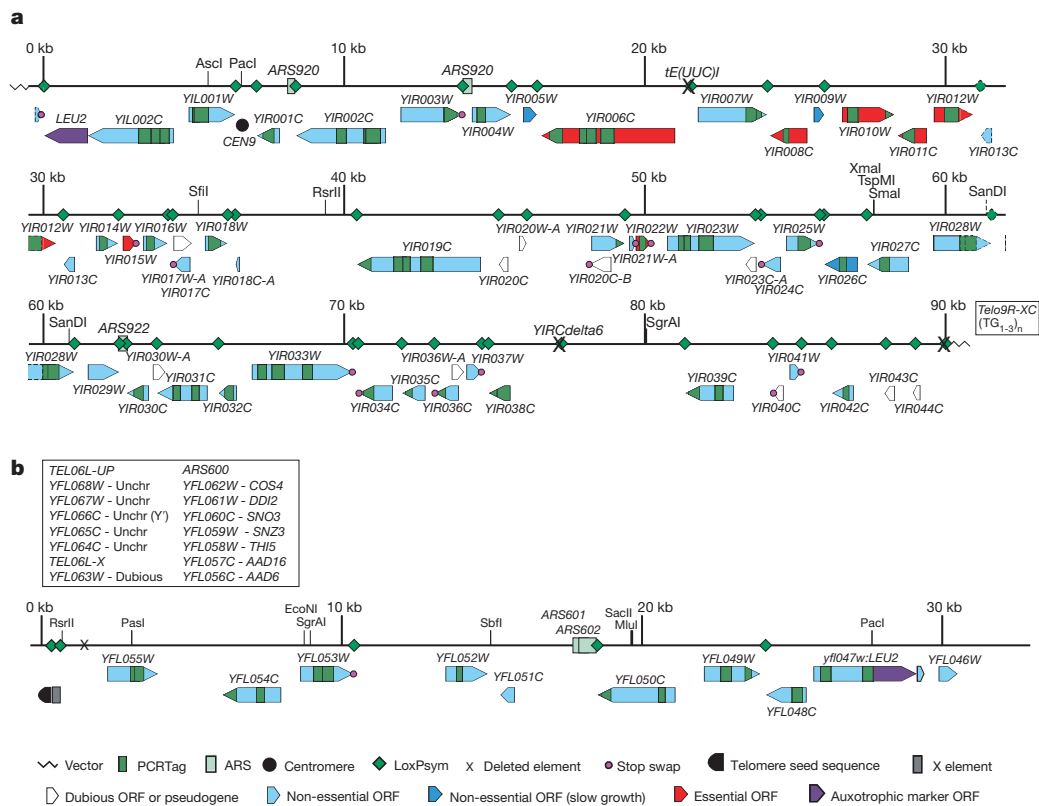


**Figure 1 | Maps of synIXR and semi-synVII.** Boxed text indicates elements deleted in the synthetic chromosomes. Vertical green bars inside ORFs indicate PCRTag amplicons; only sequences at the outside edges of these are recorded.

IXΔR. We observed more spore lethality than in control crosses, presumably owing to segregation of synIXR away from IXΔR; cells bearing only synIXR or only IXΔR would lack many essential genes and would not survive. PCRTag analysis of 14 synIXR candidate arm-swap strains revealed ten haploids with all synthetic PCRTags and no native PCRTags present (Fig. 2d and Supplementary Fig. 2). The remaining

ARS, autonomously replicating sequence. **a**, SynIXR. Vector is circular. **b**, Semi-synVIL.

four strains carried BACs with patchworks of synthetic and native sequences indicative of meiotic gene-conversion events (Supplementary Fig. 2). Sanger sequencing and structural analyses (Supplementary Fig. 3, Supplementary Table 4 and Supplementary Text 3) of recovered synIXR BACs revealed that no mutations had occurred in the synthetic chromosome. Thus, the synthetic sequence is replicated faithfully.

Whereas synIXR was incorporated in a circular form, we used an alternate strategy to integrate the semi-synVII chromosome fragment into native chromosome VI (Supplementary Fig. 4): a linear synthetic fragment marked with *LEU2* was transformed into a *YFL054C::kanMX* strain. Approximately 13% of transformants (75 of 586) had the  $\text{Leu}^+\text{G418}^S$  phenotype expected for the desired integrant. PCRTag analysis showed that 10 of 12 such strains contained only synthetic PCRTags, as expected for full replacement (Supplementary Fig. 5).

The first design principle prioritizes a wild-type phenotype and a high level of fitness despite the incorporated modifications. SynIXR has a designed sequence alteration approximately every 500 bp, 2.64% of total sequence is altered, and it carries 43 loxPsym sites. To check for negative effects of modifications on fitness, we examined colony size and morphology under various conditions, and also performed transcript profiling. We inspected colony size and morphology of synIXR swap strains under six distinct growth conditions. It was impossible to

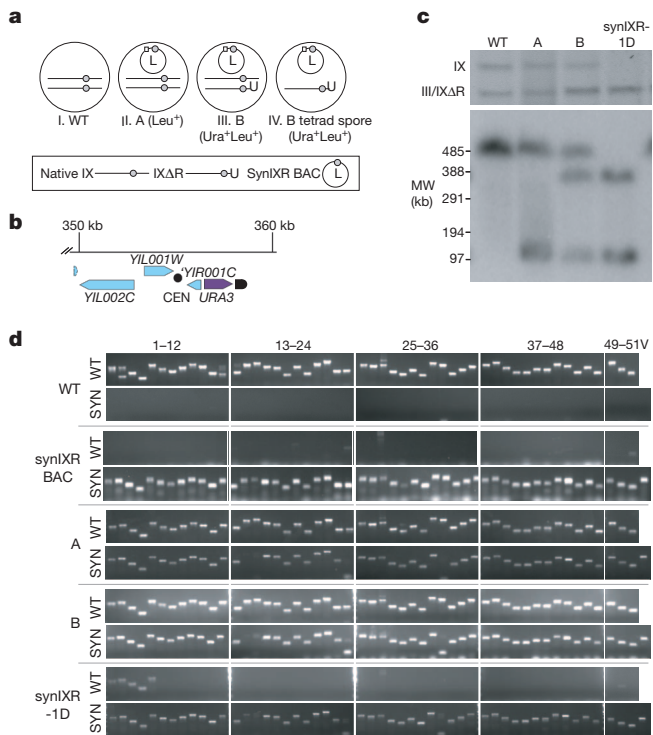


**Figure 2 | Strain construction and verification.** **a**, Generation of synIXR haploids. The synIXR BAC (L) was transformed into the wild-type strain BY4743 (WT, step I) to generate strain A (step II). One copy of native IXR in A was replaced with a *URA3*-telomere seed cassette (U), generating IXΔR in strain B (step III). B was sporulated to produce haploids (step IV). Circle, centromere; small square, *LEU2* gene. **b**, Structure of IXΔR. **c**, Electrophoretic karyotype (top panel) and Southern blot of NotI digest (bottom panel) of the wild-type, strain A, strain B and synIXR-1Δ genomes. Linearized synIXR migrates as a discrete band of ~100 kb. The probe (*YIL002C*) detects all isoforms of chromosome IX. \*, native IXR; \*\*, IXΔR. **d**, PCRTag analysis. SYN, synIXR BAC; V, vector amplicon.



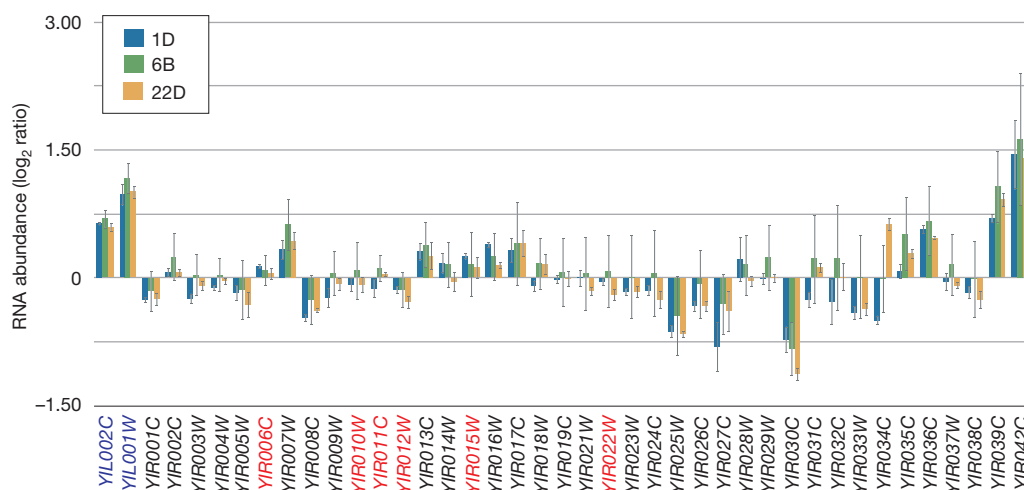


**Figure 3 | Transcript profiling of wild-type and synIXR strains.** Transcript profiling of synIXR-1D, -6B, and -22D. The log<sub>2</sub> ratio of RNA abundance relative to wild type (BY4741 or BY4742) is shown. YIL002C and YIL001W (blue) exist in two copies. Essential genes are labelled in red. Error bars, s.d.

distinguish swap strains from the wild type (BY4741) under these conditions, indicating that any fitness defect attributable to synIXR is modest; fitness tests on semi-synVIL gave similar results (Supplementary Fig. 6).

Synonymous substitutions, introduction of loxPsym sites or other changes might change gene expression. We performed transcript profiling on the swap strains synIXR-1D, synIXR-6B, and synIXR-22D (Supplementary Text 4); these studies revealed notable but predictable trends (Fig. 3). As expected, genes present in two copies (*YIL001W* and *YIL002C*, present on both synIXR and IXAR) were approximately doubled in transcript abundance. Most genes showed no substantial expression change, although a few showed modest decreases; however, the subtelomeric genes *YIR039C* and *YIR042C* showed increased expression. We speculate that in the circular synthetic chromosome, these are released from telomeric silencing, resulting in their overexpression. Overall, synIXR genes show relatively normal expression, indicating that loxPsym sites and PCRTags affect expression only minimally. Similarly, no substantial changes were observed by RNA blotting (Supplementary Fig. 7a). To detect possible compensatory transcriptome changes, we profiled transcripts genome-wide. Except for trivial differences attributable to slightly different configurations of selectable markers in the strains, there were no consistent, statistically significant differences outside IXR itself (Supplementary Fig. 7b). Thus, modifications present in synIXR and semi-synVIL do not produce major fitness effects or compensatory transcriptomic alterations.

A central feature of the synthetic yeast genome is the incorporated conditional genome instability system, SCRaMbLE. The design principles dictate that SCRaMbLE should be available for use on demand, yet should lie dormant until intentional Cre recombinase induction, at which point generation of genetic diversity is desirable. To complete the SCRaMbLE toolkit, we incorporated an engineered Cre recombinase fused to the murine oestrogen binding domain (EBD). This recently described Cre-EBD variant<sup>15</sup> is oestradiol-inducible, has low basal activity and is controlled by the daughter-cell-specific promoter *SCW11* (Supplementary Fig. 8). The plasmid *pSCW11-Cre-EBD* should produce a pulse of recombinase activity once and only once in each cell's lifetime, and should depend on oestradiol exposure. The uninduced, integrated construct is well tolerated even in swap strains, which, with 43 loxPsym sites, are expected to be Cre-hypersensitive. Upon oestradiol addition, rearrangements were induced at the loxPsym sites and viability dropped by 100-fold in synIXR strains (Fig. 4a and Supplementary Fig. 9). This loss of viability probably results from loss of synIXR essential genes. In contrast, viability in semi-synVIL, which lacks essential genes, is not affected by Cre induction (Fig. 1b and Supplementary Fig. 9d).

Semi-synVIL contains just five loxPsym sites, including one immediately adjacent to the telomeric TG<sub>1-3</sub> repeats (Fig. 1b). This simple configuration allows comprehensive PCR-based mapping of rearrangements of four of the loxPsym sites in SCRaMbLEd strains. A SCRaMbLEd semi-synVIL population was analysed by PCR for most of the possible rearranged configurations, revealing a large variety of deletions and inversions (Fig. 4b); most predicted rearrangements were readily detected.

The symmetry of loxPsym sites allows alignment in two orientations, theoretically giving rise to deletions and inversions with equal frequency. SynIXR contains 43 loxPsym sites, allowing more than 3,600 potential pairwise interactions between synIXR loxPsym sites. We reasoned that SCRaMbLEd synIXR clones should display high phenotypic diversity. Indeed, SCRaMbLEd swap strains show more growth-rate heterogeneity than wild-type controls (Fig. 4c and Supplementary Fig. 10). These SCRaMbLEd clones show many different phenotypes (Supplementary Fig. 11 and Supplementary Text 5). In summary, SCRaMbLE is sufficient to generate substantial genetic heterogeneity and complex phenotypes.

To characterize the utility of SCRaMbLE further, we performed a mutagenesis study. SynIXR encodes both *MET28* and *LYS1*, genes required for biosynthesis of amino acids<sup>16,17</sup>. Null mutants result in auxotrophy, and can be detected easily by replica-plating. We introduced episomal Cre-EBD (*pSCW11-Cre-EBD-URA3MX* cloned in a CEN plasmid) into strain C that was previously made *LYS2*<sup>+</sup> (strain D, yJS587), and performed SCRaMbLE. We screened 20,242 colonies and 3% (604 of 20,242) were candidate *lys1* and/or *met28* auxotrophs. Of 360 candidates tested more rigorously, 295 (81.9%) were confirmed: we found 212 *Lys*<sup>−</sup> auxotrophs (1.37%), 66 *Met*<sup>−</sup> auxotrophs (0.43%) and, notably, 17 *Lys*<sup>−</sup> *Met*<sup>−</sup> double auxotrophs (0.11%). PCRTag profiles of 24 *Met*<sup>−</sup> auxotrophs, 35 *Lys*<sup>−</sup> auxotrophs and seven double auxotrophs (Fig. 4d) showed that all *Met*<sup>−</sup> auxotrophs had deletions in the loxPsym-flanked segment containing *MET28* and *YAP5*, whereas all *Lys*<sup>−</sup> auxotrophs had deletions in the loxPsym-flanked segment containing *LYS1*. The deletion profiles of many SCRaMbLEd auxotrophs were highly variable and more than one segment was often missing.

To confirm that the observed SCRaMbLE phenotypes resulted solely from deletions in synIXR, we recovered the synIXR chromosomes from two *Met*<sup>−</sup> auxotrophs into *Escherichia coli*, and then introduced them to a clean genetic background. In both cases, the auxotrophic phenotype was associated with the presence of the SCRaMbLEd chromosomes (Supplementary Fig. 12 and Supplementary Text 6). Thus, the SCRaMbLE system is a highly effective method of mutagenesis, giving rise to mutants with different genetic backgrounds and generating a wide variety of double mutants.

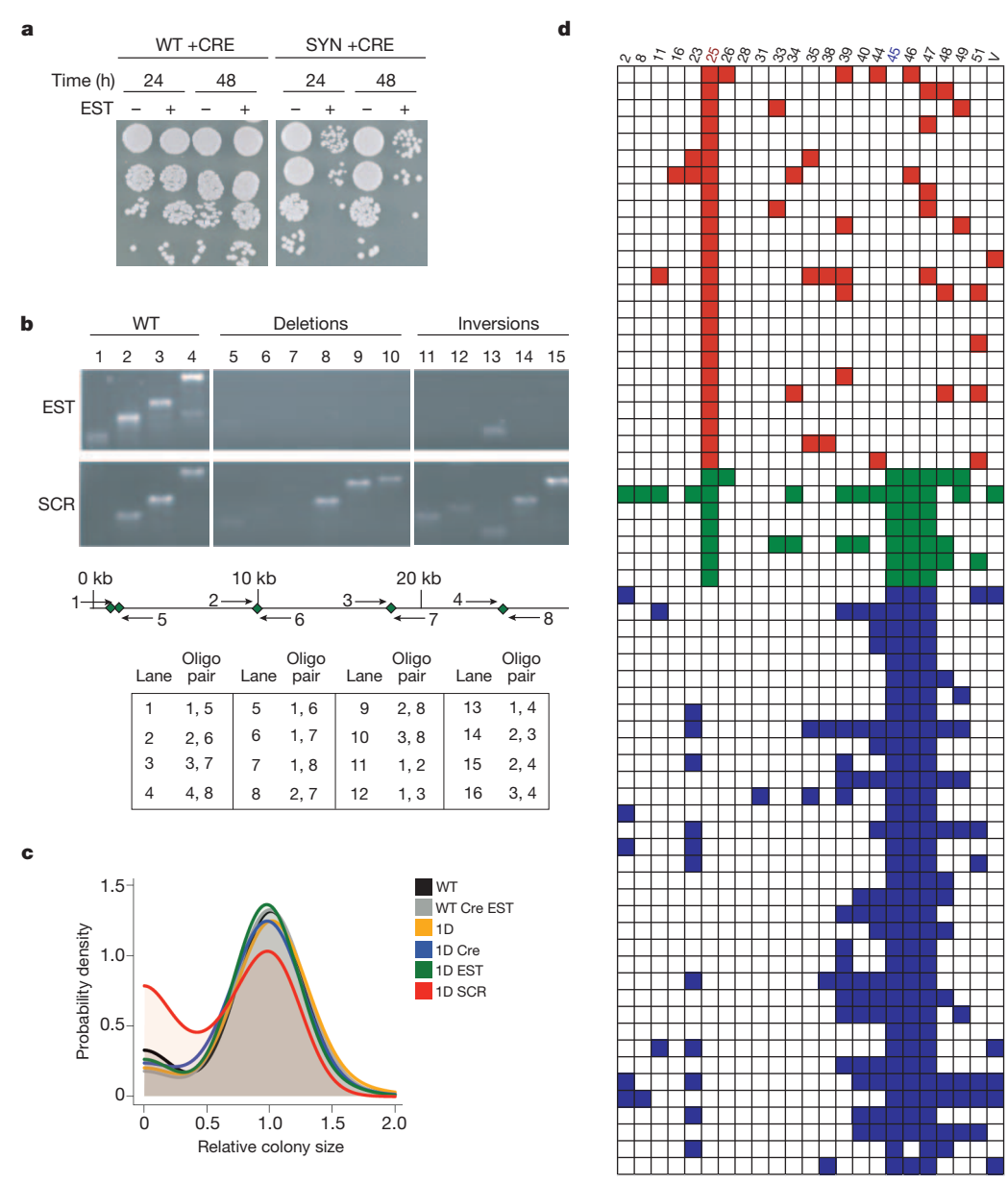


**Figure 4 | SCRaMbLE rearranges genomes. a**, Cre induction reduces the fitness of the synIXR strain (SYN) but not the wild type (WT; BY4741). EST, oestradiol; time, oestradiol exposure time. **b**, PCR analysis of semi-synVIL SCRaMbLE. The map shows primer positions. Amplicon 13 is spurious (wrong size). SCR, SCRaMbLE. **c**, Shifted colony-size distribution in SCRaMbLE survivors (wild type and the swap strain synIXR-1D). **d**, PCRTAG analysis of

We have shown there does not seem to be any major theoretical impediment to extending the design strategy outlined here to the entire yeast genome, apart from the challenge of 12-megabase DNA synthesis. Whether or not fitness defects will accumulate as design and synthesis are scaled up remains to be seen; however, the overall high fitness of the swap strains described here validates the design strategy. Furthermore, the iterative, bottom-up approach will allow identification of potential ‘problem regions’ in synthetic sequences as synthesis moves forward. If a given swap experiment results in only transformants with reduced fitness (or if no transformants are obtainable), then the underlying defect can be mapped by introducing subsegments, facilitated by strategic placement of unique restriction sites throughout synthetic chromosome arms. Also, because a subset of transformants consist of patchworks of native and synthetic sequence (Supplementary Figs 2 and 5), analysis of such strains can be used to map phenotypic defects rapidly. The stability and sequence fidelity of

Met<sup>-</sup> (red), Lys<sup>-</sup> (blue) and Met<sup>-</sup> Lys<sup>-</sup> (green) auxotrophs using PCRTags. PCRTAG pairs are numbered for each column (see Supplementary Table 2); MET28, pair 25; LYS1, pair 45. Each row represents one clone. Shaded boxes indicate presumed deletions. Panels a–c show strains with integrated Cre-EBD; d shows episomal Cre-EBD.

large circular chromosomes seen here and elsewhere<sup>5–7</sup> bode well for the use of yeast as a host platform for synthetic biology. SCRaMbLE may become a useful general strategy for analysing genome structure, content and function. One important feature of SCRaMbLE is its potential for customization: expression of different Cre-EBD variants from various promoters at distinct levels of inducer (oestradiol) should produce distinct SCRaMbLE dynamics. Use of weaker promoters than pSCW11, use of promoters expressed at different phases of the cell cycle, performing SCRaMbLE in diploids, and lowering the inducer concentration should all contribute to decreased lethality of SCRaMbLE strains, an important consideration as additional segments of the genome are replaced with synthetic counterparts and the proportion of essential genes that can be lost by SCRaMbLEing increases. As shown here, SCRaMbLE mutagenesis is efficient and generates mutants with a wide variety of different genetic backgrounds. It is possible that different combinations of gene deletions will give rise

## BOX 1

## Modifications in synthetic sequence

**Elements removed**

**Retrotransposons:** The *S. cerevisiae* genome contains both active retrotransposons and retrotransposon-derived sequences. These highly repetitive sequences are known to contribute to genome instability<sup>22</sup>. Because retrotransposons are presumed to be nonessential in yeast, we are eliminating these sequences from the synthetic genome.

**Subtelomeric repeats:** Two major types of subtelomeric repeats, Y' and X elements, reside in the genome. Y' elements are of unknown function, and are present at some, but not all, *S. cerevisiae* chromosome ends<sup>23</sup>. In contrast, X elements are present in a single copy at all *S. cerevisiae* chromosome ends; they are more highly divergent, and function in telomeric silencing and possibly in chromosome segregation<sup>23</sup>. To create a more streamlined genome, all Y' elements will be deleted from the synthetic genome; extant X elements will be replaced with the consensus core X-element sequence, as in semi-synVIL.

**Introns:** The yeast genome is estimated to contain approximately 285 introns. Based on a previous intron-deletion study<sup>24</sup> we do not anticipate that removal of introns will result in fitness defects; however, in some cases these introns house small non-coding RNAs (snoRNAs) that can be expressed ectopically in the synthetic yeast.

**Elements relocated to extrachromosomal array**

**tRNA genes:** tRNA genes (tDNAs) are highly redundant, with 275 nuclear tDNAs encoding only 42 tRNA species<sup>25</sup>. In addition, these genes are known regions of genome instability<sup>8,9</sup>. They will therefore be relocated to a dedicated chromosome to contain any instability resulting from their presence.

**Elements replaced**

**TAG stop codons replaced by TAA:** Removal of the TAG stop codon from the synthetic genome will allow future genetic code manipulation. The 'free' codon may be used to incorporate artificial amino acids<sup>11,12</sup>; alternatively, the TAG codon may be placed in essential genes, and, exploiting an engineered orthogonal synthetase/tRNA pair, specify a non-genetically encoded amino acid, thereby providing a mechanism of reproductive isolation and an additional level of control over the synthetic yeast.

**Individual synonymous codons:** The synthetic genome is fabricated in fragments as small as 750 bp<sup>26</sup>. Unique restriction sites are necessary within the synthetic fragment to facilitate construction of these building blocks into large contigs of up to 100 kb. Short stretches of fewer than four codons may therefore be synonymously recoded to introduce or eliminate restriction sites.

**Strings of synonymous codons:** Although several modifications exist between the native and synthetic genomes, the presence of a dedicated mechanism to distinguish between the two sequence types is invaluable. Short stretches of fewer than ten codons are therefore recoded to generate 'PCRTags', synonymous sequences used as the basis for PCR primer design to amplify selectively from wild-type or synthetic genomes.

**Elements introduced**

**LoxPsym sites:** Symmetrical loxP sites<sup>13</sup> are inserted in the 3' UTR of all non-essential genes, as well as at synthetic landmarks. LoxPsym sites lack the directionality of canonical loxP sites, and can therefore align in two orientations. As a result, both inversions and deletions are predicted at equal probability. These loxPsym sites and an inducible Cre recombinase<sup>15</sup> form the basis of the SCRaMbLE toolkit.

**Elements not changed**

**Gene order:** Gene order is preserved in the synthetic yeast to prevent incorporation of a non-permissible configuration in the design phase. Induction of SCRaMbLE results in changes in gene order and chromosome structure; all recovered SCRaMbLEd yeast have viable genome structures.

**Noncoding regions:** Except where noted, noncoding regions have not been modified. The yeast genome is well annotated; however, it is of paramount importance that the synthetic yeast be as fit as wild type until SCRaMbLE is induced. We therefore eschewed changes of noncoding regions to avoid disrupting unannotated critical elements. The few modifications that are made in noncoding sequence are kept to a minimum.

to a variety of subtly different phenotypes that can be mapped rapidly by PCRTag analysis; more extensive analysis by deep sequencing will reveal changes in genome structure and content. As the synthetic yeast genome grows, opportunities for genome rearrangement will increase exponentially. In principle, changes in chromosome number, ploidy, content and structure are all possible, increasing the utility of the SCRaMbLE system. For example, there may be many different routes to a minimal genome, and exploring all of them by a hit or miss predictive approach is impractical and unlikely to yield comprehensive results. Using SCRaMbLE, many independent routes of genome minimization can be explored at one time, under many environmental conditions, for instance by growing yeast cells long-term in serially transferred batch cultures, or in a chemostat or turbidostat under conditions in which Cre is minimally active. Such an approach may also lead to derivatives that are more fit than the parent, for example, by gene duplication events facilitated by the Cre-EBD/loxPsym system.

**METHODS SUMMARY**

**DNA preparation.** BAC DNA was prepared using the Qiagen plasmid midi kit or alkaline lysis<sup>18</sup>. The following protocol modifications were made: cells were diluted 1:100 from an overnight culture into 50 ml, grown in Luria broth with 50 µg ml<sup>-1</sup> carbenicillin, and grown at 30 °C for 14–16 h. Qiagen-purified DNA was treated with 60 µg ml<sup>-1</sup> proteinase K at 37 °C overnight, then extracted with phenol/chloroform. DNAs prepared without a column were phenol/chloroform extracted, and then treated with RNase immediately before use.

Yeast genomic DNA for use in PCRTag analysis was prepared by standard methods<sup>19</sup>. DNA preparation for recovery of the synIXR BAC into bacteria was as previously reported<sup>20</sup>.

**PCR conditions.** PCRTags were amplified using Taq polymerase (New England Biolabs). Template concentrations were 1 ng µl<sup>-1</sup> for genomic DNA and 10 pg µl<sup>-1</sup> for purified BAC DNA. The following program was used: 94 °C 3 min; 30 cycles of 94 °C 30 s, 65 °C 30 s, 72 °C 30 s; 72 °C 3 min.

**RNA analysis.** Total RNA was isolated by hot acid phenol extraction. Microarray hybridization and data analysis were performed at the Johns Hopkins Microarray Core Facility (<http://www.microarray.jhmi.edu>). Dubious ORFs and pseudogenes were omitted from synIXR transcript analysis.

**Pulsed-field gels.** DNAs were prepared as described elsewhere<sup>21</sup>. The identity of the chromosomes was inferred from the known molecular karyotype of wild type (BY4743), and from lambda ladders run on the same gel.

**Full Methods** and any associated references are available in the online version of the paper at [www.nature.com/nature](http://www.nature.com/nature).

Received 10 December 2010; accepted 28 June 2011.

Published online 14 September 2011.

1. Han, J. S. & Boeke, J. D. A highly active synthetic mammalian retrotransposon. *Nature* **429**, 314–318 (2004).
2. Richardson, S. M., Wheelan, S. J., Yarrington, R. M. & Boeke, J. D. GeneDesign: rapid, automated design of multikilobase synthetic genes. *Genome Res.* **16**, 550–556 (2006).
3. Chan, L. Y., Kosuri, S. & Endy, D. Refactoring bacteriophage T7. *Mol. Syst. Biol.* **1**, 2005.0018 (2005).



4. Stricker, J. *et al.* A fast, robust and tunable synthetic gene oscillator. *Nature* **456**, 516–519 (2008).
5. Gibson, D. G. *et al.* One-step assembly in yeast of 25 overlapping DNA fragments to form a complete synthetic *Mycoplasma genitalium* genome. *Proc. Natl Acad. Sci. USA* **105**, 20404–20409 (2008).
6. Gibson, D. G. *et al.* Creation of a bacterial cell controlled by a chemically synthesized genome. *Science* **329**, 52–56 (2010).
7. Lartigue, C. *et al.* Creating bacterial strains from genomes that have been cloned and engineered in yeast. *Science* **325**, 1693–1696 (2009).
8. Ji, H. *et al.* Hotspots for unselected Ty1 transposition events on yeast chromosome III are near tRNA genes and LTR sequences. *Cell* **73**, 1007–1018 (1993).
9. Admire, A. *et al.* Cycles of chromosome instability are associated with a fragile site and are increased by defects in DNA replication and checkpoint controls in yeast. *Genes Dev.* **20**, 159–173 (2006).
10. Churcher, C. *et al.* The nucleotide sequence of *Saccharomyces cerevisiae* chromosome IX. *Nature* **387**, 84–87 (1997).
11. Park, H. *et al.* Expanding the genetic code of *Escherichia coli* with phosphoserine. *Science* **333**, 1151–1154 (2011).
12. Isaacs, F. J. *et al.* Precise manipulation of chromosomes *in vivo* enables genome-wide codon replacement. *Science* **333**, 348–353 (2011).
13. Hoess, R. H., Wierzbicki, A. & Abremski, K. The role of the loxP spacer region in P1 site-specific recombination. *Nucleic Acids Res.* **14**, 2287–2300 (1986).
14. Vollrath, D., Davis, R. W., Connelly, C. & Hieter, P. Physical mapping of large DNA by chromosome fragmentation. *Proc. Natl Acad. Sci. USA* **85**, 6027–6031 (1988).
15. Lindstrom, D. L. & Gottschling, D. E. The mother enrichment program: a genetic system for facile replicative life span analysis in *Saccharomyces cerevisiae*. *Genetics* **183**, 413–422 (2009).
16. Kuras, L., Cherest, H., Surdin-Kerjan, Y. & Thomas, D. A heteromeric complex containing the centromere binding factor 1 and two basic leucine zipper factors, Met4 and Met28, mediates the transcription activation of yeast sulfur metabolism. *EMBO J.* **15**, 2519–2529 (1996).
17. Ogawa, H. & Fujioka, M. Purification and characterization of saccharopine dehydrogenase from baker's yeast. *J. Biol. Chem.* **253**, 3666–3670 (1978).
18. Sambrook, J. & Russell, D. W. Isolation of BAC DNA from small-scale cultures. *Cold Spring Harb. Protoc.* doi:10.1101/pdb.prot4006 (2006).
19. Hoffman, C. S. Preparation of yeast DNA. *Curr. Protoc. Mol. Biol.* Ch. 13, Unit 13.11 (2001).
20. Boeke, J. D., Garfinkel, D. J., Styles, C. A. & Fink, G. R. Ty elements transpose through an RNA intermediate. *Cell* **40**, 491–500 (1985).
21. Schwartz, D. C. & Cantor, C. R. Separation of yeast chromosome-sized DNAs by pulsed field gradient gel electrophoresis. *Cell* **37**, 67–75 (1984).
22. Lemoine, F. J., Degtyareva, N. P., Lobachev, K. & Petes, T. D. Chromosomal translocations in yeast induced by low levels of DNA polymerase: a model for chromosome fragile sites. *Cell* **120**, 587–598 (2005).
23. Louis, E. J. The chromosome ends of *Saccharomyces cerevisiae*. *Yeast* **11**, 1553–1573 (1995).
24. Parenteau, J. *et al.* Deletion of many yeast introns reveals a minority of genes that require splicing for function. *Mol. Biol. Cell* **19**, 1932–1941 (2008).
25. Percudani, R., Pavesi, A. & Ottonello, S. Transfer RNA gene redundancy and translational selection in *Saccharomyces cerevisiae*. *J. Mol. Biol.* **268**, 322–330 (1997).
26. Dymond, J. S. *et al.* Teaching synthetic biology, bioinformatics and engineering to undergraduates: the interdisciplinary build-a-genome course. *Genetics* **181**, 13–21 (2009).

**Supplementary Information** is linked to the online version of the paper at [www.nature.com/nature](http://www.nature.com/nature).

**Acknowledgements** We thank G. Church for suggesting the global substitution of TAG codons with TAA codons, C. Connelly for sharing technical expertise and V. Huang for generating a sequence visualizer. We are grateful to B. Cormack, G. Seydoux and J. Nathans for offering helpful advice, to Y. Cai and J. Peccoud for suggesting methods to validate the sequence data, and to E. Louis for providing expert advice on telomeres. The work was supported by National Science Foundation grant MCB0718846 to J.D.B., J.S.B. and S.C.; by a grant from Microsoft to J.S.B. and J.D.B.; by Department of Energy Fellowship DE-FG02097ER25308 to S.M.R.; by National Institutes of Health grant AG023779 to D.E.G.; and by a fellowship from Fondation pour la Recherche Médicale to H.M.

**Author Contributions** J.S.D., S.M.R., S.C., J.S.B. and J.D.B. designed experiments. J.S.D., S.M.R., C.E.C., T.B., H.M., N.A., J.W.S., J.D. and A.C.B. performed experiments. W.J.B. built the synIXR chromosome. D.L.L. and D.E.G. generated the integrated CRE-EBD cassette. J.S.D., S.M.R., J.S.B. and J.D.B. analysed data and wrote the manuscript.

**Author Information** SynIXR and semi-synVIL sequences have been deposited to GenBank with the accession codes: synIXR, JN020955; semi-synVIL, JN020956. Microarray data have been submitted to Gene Expression Omnibus under accession number GSE31326. Reprints and permissions information is available at [www.nature.com/reprints](http://www.nature.com/reprints). The authors declare no competing financial interests. Readers are welcome to comment on the online version of this article at [www.nature.com/nature](http://www.nature.com/nature). Correspondence and requests for materials should be addressed to J.D.B. ([jboeke@jhmi.edu](mailto:jboeke@jhmi.edu)).

## METHODS

**DNA preparation.** BAC DNA was prepared using the Qiagen plasmid midi kit or alkaline lysis<sup>18</sup>. The following protocol modifications were made: cells were diluted 1:100 from an overnight culture into 50 ml, grown in Luria broth with 50 µg ml<sup>-1</sup> carbenicillin, and grown at 30 °C for 14–16 h. Qiagen-purified DNA was treated with 60 µg ml<sup>-1</sup> proteinase K at 37 °C overnight, then extracted with phenol/chloroform. DNAs prepared without a column were phenol/chloroform extracted, and then treated with RNase immediately before use.

Yeast genomic DNA for use in PCRTAG analysis was prepared by standard methods<sup>19</sup>. DNA preparation for recovery of the synIXR BAC into bacteria was as previously reported<sup>20</sup>.

**PCR conditions.** PCRTags were amplified using Taq polymerase (New England Biolabs). Template concentrations were 1 ng µl<sup>-1</sup> for genomic DNA and 10 pg µl<sup>-1</sup> for purified BAC DNA. The following program was used: 94 °C 3 min; 30 cycles of 94 °C 30 s, 65 °C 30 s, 72 °C 30 s; 72 °C 3 min.

**RNA analysis.** Total RNA was isolated by hot acid phenol extraction. Microarray hybridization and data analysis were performed at the Johns Hopkins Microarray Core Facility (<http://www.microarray.jhmi.edu>). Dubious ORFs and pseudogenes were omitted from synIXR transcript analysis.

**Pulsed-field gels.** DNAs were prepared as described elsewhere<sup>21</sup>. The identity of the chromosomes was inferred from the known molecular karyotype of wild type (BY4743), and from lambda ladders run on the same gel.

**Yeast strains, transformation and tetrad analysis.** Strains ABY7 and ABY8 were derived from strain BY4743; ABY7 (*MATa*) and ABY8 (*MATα*) otherwise share the genotype *his3Δ1 leu2Δ0 ura3Δ0 lys2Δ0 met15Δ0 yil001::URA3 yir039::kanMX*. All strain genotypes are listed in Supplementary Table 8.

BY4743 spheroplasts were transformed with synIXR. The strain *YFL054C::kanMX* was transformed with synVII restriction fragments by standard lithium acetate transformation.

The synIXR-1D strain and others were backcrossed to strains ABY7 and ABY8; the resultant diploids were sporulated and genotyped to identify synIXR segregants. **Phenotypic screening.** Single colonies were picked into 96-well plates and grown for 48 h in yeast peptone dextrose (YPD) at 30 °C. (SCRaMbLE strains were grown for 72 h in YPD at 30 °C, diluted 1:10 and grown for 4 h before plating.) Tenfold dilutions were spotted on various types of agar medium and selective conditions in OmniTrays (NUNC), as previously described<sup>27</sup>. Most cells were grown for 72 h (except those grown on yeast extract/peptone/glycerol/ethanol (YPGE) plates, which were grown for 108 h), then scored for growth and photographed.

**Yeast growth and media.** Unless otherwise indicated, all experiments were performed at 30 °C. YPGE was supplemented with 2% ethanol and 2% glycerol. Concentrations of drugs were as follows: hydroxyurea, 0.2 M; methylmethane

sulphonate, 0.05%; 6-azauracil, 100 µg ml<sup>-1</sup>; benomyl, 15 µg ml<sup>-1</sup>; hydrogen peroxide, 1 mM; cycloheximide, 10 µg ml<sup>-1</sup>. Resistance to cycloheximide and hydrogen peroxide was assayed by growing cells in treated medium for 2 h, then plating on YPD. Other phenotypes were assayed by growing cells to mid-log phase in rich media, then spotting tenfold dilutions on selective media.

**Colony size measurements.** Cells were plated at various dilutions so that similar numbers of colonies were observed on control and experimental (oestradiol-treated) plates. Colony size was measured using ImageJ software<sup>28</sup>, and normalized against the total number of colonies on each plate. Sample sizes for data presented in Fig. 4c are as follows: wild-type, *n* = 488 colonies; wild-type + Cre + oestradiol, *n* = 486; 1D, *n* = 395; 1D + Cre, *n* = 251; 1D + oestradiol, *n* = 416; 1D + Cre + oestradiol, *n* = 394.

**SynIXR BAC sequence analysis.** The original synIXR BAC was sequenced by the manufacturer, Codon Devices<sup>29</sup>. SynIXR BACs were recovered into bacteria and sequenced by Agencourt (Beckman Coulter Genomics), using sequencing primers listed in Supplementary Table 5. Repetitive sequences, including the highly internally repetitive *MUC1* open reading frame, were PCR-amplified before sequencing when necessary.

**Pulsed-field gels.** Samples were run on a 1.0% agarose gel in ×0.5 TBE (pH 8.0) for 20 h at 14 °C on a clamped homogenous electric field (CHEF) gel apparatus. The voltage was 3.5 V cm<sup>-1</sup>, at an angle of 120° and a switch time of 60–120 s, ramped over 20 h.

NotI (Promega) digests were performed on whole chromosomes embedded in agarose plugs. Agarose plugs were removed from the 0.5 M EDTA storage buffer, washed with 0.05 M EDTA for 1 h at room temperature (~23 °C), and then washed with ×0.1 restriction enzyme buffer, followed by ×1 buffer, under the same conditions.

**Probe preparation for northern and Southern blots.** Probes were prepared using the Prime-It II kit (Stratagene) and hybridized using Ultrahyb hybridization solution (Ambion) according to the manufacturer's instructions.

**SCRaMbLE.** Cre activity was induced by exposure to 1 µM β-oestradiol (Sigma-Aldrich) in rich media for either 48 h (integrated Cre) or 4 h (episomal Cre), except where indicated otherwise. PCRTAG analysis of Met<sup>-</sup> and Lys<sup>-</sup> auxotrophs was performed with a non-redundant array, using one primer pair per loxPsym-flanked segment.

27. Hampsey, M. A review of phenotypes in *Saccharomyces cerevisiae*. *Yeast* **13**, 1099–1133 (1997).
28. Abramoff, M. D., Magelhaes, P. J. & Ram, S. J. Image processing with ImageJ. *Biophotonics Int.* **11**, 36–42 (2004).
29. Blake, W. J. *et al.* Pairwise selection assembly for sequence-independent construction of long-length DNA. *Nucleic Acids Res.* **38**, 2594–2602 (2010).

# Antidiabetic actions of a non-agonist PPAR $\gamma$ ligand blocking Cdk5-mediated phosphorylation

Jang Hyun Choi<sup>1\*</sup>, Alexander S. Banks<sup>1\*</sup>, Theodore M. Kamenecka<sup>2,4\*</sup>, Scott A. Busby<sup>3\*</sup>, Michael J. Chalmers<sup>3</sup>, Naresh Kumar<sup>3</sup>, Dana S. Kuruvilla<sup>3</sup>, Youseung Shin<sup>2</sup>, Yuanjun He<sup>2</sup>, John B. Bruning<sup>5</sup>, David P. Marciano<sup>3</sup>, Michael D. Cameron<sup>2,3,4</sup>, Dina Laznik<sup>1</sup>, Michael J. Jurczak<sup>6</sup>, Stephan C. Schürer<sup>7</sup>, Dušica Vidović<sup>7</sup>, Gerald I. Shulman<sup>6</sup>, Bruce M. Spiegelman<sup>1</sup> & Patrick R. Griffin<sup>2,3,4</sup>

PPAR $\gamma$  is the functioning receptor for the thiazolidinedione (TZD) class of antidiabetes drugs including rosiglitazone and pioglitazone<sup>1</sup>. These drugs are full classical agonists for this nuclear receptor, but recent data have shown that many PPAR $\gamma$ -based drugs have a separate biochemical activity, blocking the obesity-linked phosphorylation of PPAR $\gamma$  by Cdk5 (ref. 2). Here we describe novel synthetic compounds that have a unique mode of binding to PPAR $\gamma$ , completely lack classical transcriptional agonism and block the Cdk5-mediated phosphorylation in cultured adipocytes and in insulin-resistant mice. Moreover, one such compound, SR1664, has potent antidiabetic activity while not causing the fluid retention and weight gain that are serious side effects of many of the PPAR $\gamma$  drugs. Unlike TZDs, SR1664 also does not interfere with bone formation in culture. These data illustrate that new classes of antidiabetes drugs can be developed by specifically targeting the Cdk5-mediated phosphorylation of PPAR $\gamma$ .

PPAR $\gamma$  is a member of the nuclear receptor family of transcription factors and is a dominant regulator of adipose cell differentiation and development<sup>3,4</sup>. It is also the functioning receptor for the thiazolidinedione (TZD) class of antidiabetic drugs such as rosiglitazone and pioglitazone<sup>1,5</sup>. These antidiabetes drugs were developed specifically to have high affinity and full agonism towards PPAR $\gamma$  before their molecular modes of action were known<sup>6</sup>. It has therefore been assumed that their therapeutic actions result from their functional agonism on this receptor. From a clinical perspective, rosiglitazone (Avandia) and pioglitazone (Actos) are both highly effective oral medications for type 2 diabetes and are well tolerated by the majority of patients<sup>7</sup>. Unfortunately, a substantial number of patients experience side effects from these drugs, including fluid retention, weight gain, congestive heart failure and loss of bone mineral density<sup>8,9</sup>. Whereas some of the non-TZD full agonists have good antidiabetic activity, they also cause many of the same side effects, including fluid retention.

The therapeutic role of classical agonism of PPAR $\gamma$  was made somewhat confusing by the development of several compounds that have less than full agonist properties (partial agonists) but retain substantial insulin-sensitizing and antidiabetic actions in experimental models<sup>10,11</sup>. Furthermore, we have recently shown that many antidiabetic PPAR $\gamma$  ligands have a second, distinct biochemical function: blocking the obesity-linked phosphorylation of PPAR $\gamma$  by cyclin-dependent kinase 5 (Cdk5) at serine 273 (ref. 2). This is a direct action of the ligands and requires binding to the PPAR $\gamma$  ligand binding domain (LBD), causing a conformational change that interferes with the ability of Cdk5 to phosphorylate serine 273. Rosiglitazone and MRL24 (a selective partial agonist towards PPAR $\gamma$ ) both modulate serine 273 phosphorylation at therapeutic doses in mice. Furthermore, a small clinical trial of newly diagnosed type 2 diabetics showed a remarkably close

association between the clinical effects of rosiglitazone and the blocking of this phosphorylation of PPAR $\gamma$ . Thus, the contribution made by classical agonism to the therapeutic effects of these drugs and to their side effects is not clear.

These data indicate that it might be possible to develop entirely new classes of antidiabetes drugs optimized for the inhibition of Cdk5-mediated phosphorylation of PPAR $\gamma$  while lacking classical agonism. Here we describe the development of synthetic small molecules that bind tightly to PPAR $\gamma$ , yet are completely devoid of classical agonism and effectively inhibit phosphorylation at serine 273. These compounds have a unique binding mode in the ligand binding pocket of PPAR $\gamma$ . An example from this series, SR1664, shows potent and dose-dependent antidiabetic effects in obese mice. Unlike TZDs and other PPAR $\gamma$  agonists, this compound does not cause fluid retention or weight gain *in vivo* or reduce osteoblast mineralization in culture.

To develop a suitable ligand, we optimized compounds for (1) high binding affinity for PPAR $\gamma$ , (2) blocking the Cdk5-mediated PPAR $\gamma$  phosphorylation and (3) lacking classical agonism. We first identified published compounds that bind tightly to PPAR $\gamma$  and have favourable properties as a scaffold for extensive chemical modifications. Classical agonism is defined here, as is standard in the nuclear receptor field, as an increased level of transcription through a tandem PPAR response element luciferase reporter. Of particular interest was compound **7b** described previously as an extremely potent and selective PPAR $\gamma$  partial agonist (30% activation compared to rosiglitazone)<sup>12</sup>. A modular synthesis approach was used to make a series of analogues of compound **7b**; these compounds were tested *in vitro* and in adipose cells (Supplementary Fig. 1c, d). Using a Lanthascreen competitive binding assay, SR1664 (Fig. 1a) had a half-maximum inhibitory concentration (IC<sub>50</sub>) of 80 nM (Supplementary Fig. 1a, b). As shown in Fig. 1b, when compared to rosiglitazone or MRL24 (a partial agonist) in a classical transcriptional activity assay, SR1664 had essentially no transcriptional agonism at any concentration. Rosiglitazone and SR1664 both effectively blocked the Cdk5-mediated phosphorylation of PPAR $\gamma$  *in vitro* with half-maximal effects between 20 and 200 nM (Fig. 1c). In contrast, they had no effect on the phosphorylation of a well-characterized Cdk5 substrate, the Rb protein (Fig. 1d)<sup>13</sup>. This indicated that these compounds do not disrupt the basic protein kinase function of Cdk5. In addition, SR1664 was also effective at blocking Cdk5-mediated phosphorylation of PPAR $\gamma$  in differentiated fat cells (Fig. 1e) with no measurable difference in phosphorylation of Rb (Supplementary Fig. 1e). Additional analogues were synthesized and four compounds were identified that have similar *in vitro* profiles (Supplementary Fig. 1b). SR1824 (Fig. 1a) was further characterized for its ability to block Cdk5-dependent phosphorylation of PPAR $\gamma$  (Fig. 1b–e). These data demonstrate that ligands can be made that potentially block Cdk5-dependent

<sup>1</sup>Department of Cancer Biology and Division of Metabolism and Chronic Disease, Dana-Farber Cancer Institute and Department of Cell Biology, Harvard Medical School, Boston, Massachusetts 02115, USA.

<sup>2</sup>Translational Research Institute, The Scripps Research Institute, Scripps Florida, Jupiter, Florida 33458, USA. <sup>3</sup>Department of Molecular Therapeutics, The Scripps Research Institute, Scripps Florida, Jupiter, Florida 33458, USA. <sup>4</sup>The Scripps Research Molecular Screening Center (SRMSC), The Scripps Research Institute, Scripps Florida, Jupiter, Florida 33458, USA. <sup>5</sup>Department of Biochemistry and Biophysics, Texas A&M University, College Station, Texas 77843-2128, USA. <sup>6</sup>Howard Hughes Medical Institute, Departments of Internal Medicine and Cellular & Molecular Physiology, Yale University School of Medicine, New Haven, Connecticut 06510, USA. <sup>7</sup>Center for Computational Science, University of Miami, Miami, Florida 33136, USA.

\*These authors contributed equally to this work.



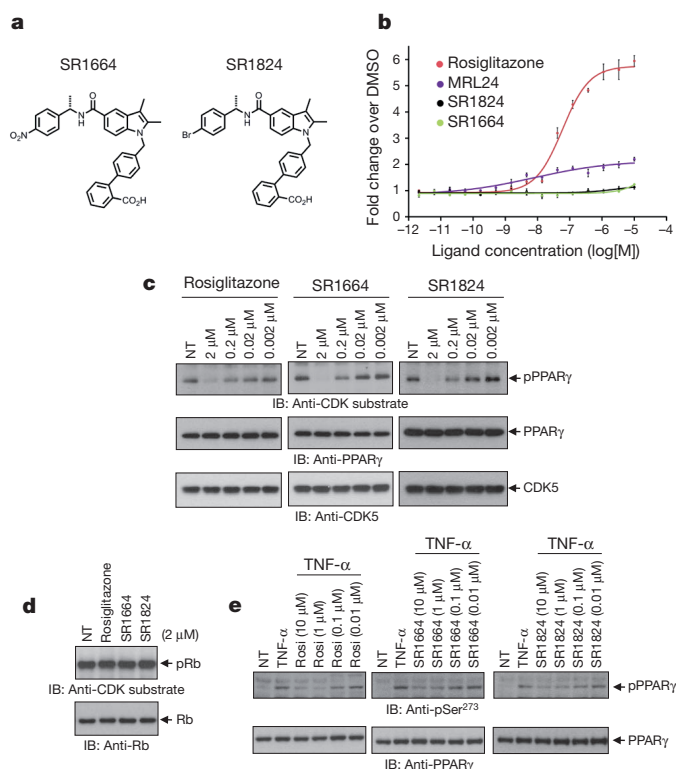


**Figure 1 | Novel PPAR $\gamma$  ligands lack classical agonism, block phosphorylation at Ser 273.** **a**, Chemical structures of SR1664 and SR1824. **b**, Transcriptional activity of a PPAR-derived reporter gene in COS-1 cells following treatment with rosiglitazone, SR1664 or SR1824 ( $n = 3$ ). **c**, *In vitro* Cdk5 assay with rosiglitazone, SR1664 or SR1824 with PPAR $\gamma$  or Rb substrates. IB, immunoblot; NT, not treated; pPPAR $\gamma$ , phosphorylated PPAR $\gamma$ ; pRb, phosphorylated Rb. **e**, TNF- $\alpha$ -induced phosphorylation of PPAR $\gamma$  in differentiated PPAR $\gamma$  knock-out MEFs expressing wild-type PPAR $\gamma$  treated with rosiglitazone, SR1664 or SR1824. Error bars are s.e.m.

phosphorylation of PPAR $\gamma$  in cells while demonstrating little to no classical agonism.

Of the four compounds identified as non-agonist inhibitors of Cdk5-mediated PPAR $\gamma$  phosphorylation, SR1664 had adequate pharmacokinetic properties to move forward to biological and therapeutic assays. Adipogenesis was the first known biological function of PPAR $\gamma$ <sup>3</sup> and agonist ligands for PPAR $\gamma$  have been shown to stimulate potently the differentiation of pre-adipose cell lines; this response has been widely used as a sensitive cellular test for PPAR $\gamma$  agonism<sup>1,14,15</sup>. As shown in Fig. 2a, rosiglitazone potently stimulated fat cell differentiation, as evidenced by Oil Red O staining of the cellular lipid. In contrast, SR1664 did not stimulate increased lipid accumulation or changes in morphology characteristic of differentiating fat cells. The stimulation of fat cell gene expression was also apparent with rosiglitazone, as illustrated by an increased expression of genes linked to adipogenesis. In contrast, SR1664 induced little or no change in the expression of these genes (Fig. 2b).

Another well-known effect of both rosiglitazone and pioglitazone is that they decrease bone formation and bone mineral density leading to an increase in fracture risk<sup>8,16</sup>. TZDs have also been shown to decrease bone mineralization in cultured osteoblasts<sup>17</sup>. As shown in Fig. 2c, rosiglitazone treatment reduced the mineralization of mouse osteoblastic cells, as measured by Alizarin red staining. Moreover, the expression of genes involved in the differentiation of these cells was impaired (see Supplementary Fig. 2). Importantly, treatment with SR1664 did not affect the extent of calcification or the expression of this osteoblast gene set in MC3T3-E1 cells.

Co-crystallography, mutagenesis and hydrogen/deuterium exchange (HDX) have all demonstrated that full agonists of PPAR $\gamma$  affect critical

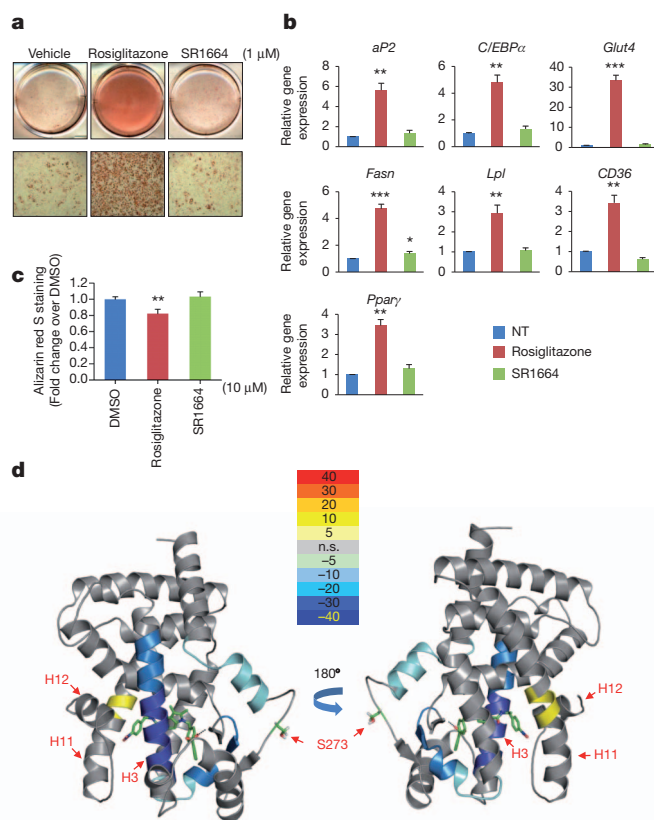


**Figure 2 | Structural and *in vitro* functional analysis of SR1664.** **a**, Lipid accumulation in differentiated 3T3-L1 cells treated with rosiglitazone or SR1664 following Oil Red O staining. **b**, Expression of adipocyte-enriched genes in these cells was analysed by qPCR ( $n = 3$ ). **c**, Mineralization of MC3T3-E1 osteoblast cells as determined by Alizarin Red-S. Error bars are s.e.m.; \* $P < 0.05$ , \*\* $P < 0.01$ , \*\*\* $P < 0.001$ . NT, no treatment. **d**, Overlay of differential HDX data onto the docking model of 2hfp bound to SR1664 (see Supplementary Fig. 3). This overlay depicts the difference in HDX between ligand-free and SR1664 bound PPAR $\gamma$  LBD. Perturbation data are colour coded and plotted onto the backbone of the PDB file according to the key. n.s., not significant. Observed changes in HDX were statistically significant ( $P < 0.05$ ) in a two-tailed  $t$ -test ( $n = 3$ ).

hydrogen bonds within the C-terminal helix (H12) of the receptor<sup>18–21</sup>. This interaction stabilized the AF2 surface (helix 3–4 loop, C-terminal end of H11 and H12) of the receptor facilitating co-activator interactions. Interestingly, high affinity partial agonists have been identified that do not make these interactions yet still possess some level of classical agonism, and several of these have been shown to bind the backbone amide of S342 (S370 in PPAR $\gamma$ 2) within the  $\beta$ -sheet of the LBD<sup>18</sup>. More recently, we demonstrated that the proximity of ligand to the amide of S342 correlated with increased stability of the helix 2-helix 2' loop, the region of the receptor containing S273 (S245 in PPAR $\gamma$ 1) as determined by HDX<sup>2</sup>. Surprisingly, HDX analysis of SR1664 and SR1824 increased the conformational mobility of the C-terminal end of H11, a helix that abuts H12 (Fig. 2d); in contrast, the full and partial agonists stabilized the same region of H11 (Supplementary Fig. 3).

*In silico* docking studies were carried out to understand the structural basis of SR1664 interactions in the PPAR $\gamma$ 1 ligand binding domain (Supplementary Fig. 4). In this model, the phenyl-substituted nitro group of SR1664 clashes with hydrophobic side chains of H11 such as Leu 452 and Leu 453 (Leu 480 and Leu 481 in PPAR $\gamma$ 2, respectively) as well as Leu 469 and Leu 465 (corresponding to Leu 497 and Leu 493 in PPAR $\gamma$ 2) of the loop N-terminal to H12. This potentially explains the lack of stabilization of H12 and the destabilization of the region of H11 near His 449 as seen by HDX. Despite the altered mode of

binding, SR1664 and rosiglitazone both bind to the same core residues within the PPAR $\gamma$  LBD. This is demonstrated by the ability of SR1664 to attenuate the transcriptional activity of rosiglitazone on PPAR $\gamma$  in the context of a competitive ligand binding assay (Supplementary Fig. 4b).

To determine whether the altered transcriptional activity of SR1664 may be attributed to differences in DNA binding or coactivator recruitment, we compared the chromatin association of PPAR $\gamma$  or steroid receptor co-activator-1 (SRC1) within the  $\alpha$ P2 promoter. As expected, rosiglitazone significantly increased SRC1 occupancy without affecting PPAR $\gamma$  occupancy. However, SR1664 treatment did not influence the occupancy of PPAR $\gamma$  or SRC1 recruitment to the  $\alpha$ P2 promoter, indicating that SR1664 has a very different activity of co-regulator recruitment (Supplementary Fig. 4c).

We next asked whether SR1664 had antidiabetic properties *in vivo*. Wild-type mice fed a high-fat high-sugar diet become obese and insulin-resistant, with activation of Cdk5 in their adipose tissues<sup>2</sup>. Figure 3a demonstrates that SR1664, injected twice daily for 5 days, caused a dose-dependent decrease in the Cdk5-mediated phosphorylation of PPAR $\gamma$  at serine 273 in adipose tissue. Moreover, SR1664 treatment also caused a trend towards lowered (and normalized) glucose levels, and a significant reduction in the fasting insulin levels. Insulin resistance, as

computed by HOMA-IR, showed a clear and dose-dependent improvement with SR1664 (Fig. 3b). These changes occurred without significant differences in body weight compared to vehicle-treated mice (Supplementary Fig. 5).

The most accurate method for measuring changes in insulin sensitivity *in vivo* is the hyperinsulinaemic-euglycaemic clamp<sup>22</sup>. As shown in Fig. 3c and in Supplementary Fig. 6, the glucose infusion rate (GIR) needed to maintain euglycaemia in the mice treated with SR1664 was significantly greater than in animals treated with the vehicle alone, indicating improved whole-body insulin sensitivity. Suppression of hepatic glucose production (HGP), an important component of insulin action, was improved by SR1664. Whereas no difference in whole-body glucose disposal was detected from calculations of <sup>3</sup>H-glucose turnover, analysis of tissue-specific <sup>14</sup>C-2-deoxyglucose transport demonstrated improved insulin-stimulated glucose disposal in adipose tissue of SR1664-treated mice. Similarly, reductions in both basal and clamped plasma free fatty acids levels, as well as a 20% greater suppression of lipolysis in response to insulin, indicated improved adipose tissue insulin sensitivity in SR1664-treated mice. Together, these data indicate that SR1664 improves insulin sensitivity.

Using cells expressing the S273A mutant of PPAR $\gamma$ , we previously defined a gene set in cultured adipose cells that was most sensitive to the phosphorylation at this site<sup>2</sup>. Treatment of mice with SR1664 caused changes in the expression of 11/17 (65%) of these genes, all in the direction predicted for the inhibition of the PPAR $\gamma$  S273 phosphorylation (Fig. 3d). Adiponectin and adipisin, genes long recognized as being reduced in obesity<sup>23,24</sup>, are both induced by SR1664. We also defined a separate set of genes reflective of a full agonist (rosiglitazone) on cultured fat cells. SR1664 caused changes in expression of 6/19 genes in this 'agonist' gene set; importantly, three of these changes were in the same direction as expected for an agonist, but three were changed in the opposite direction (Fig. 3e). Taken together, these data show that SR1664 has an insulin-sensitizing effect with preferential regulation of the gene set sensitive to the phosphorylation of PPAR $\gamma$  by Cdk5.

A more severe model of obesity is the leptin-deficient ob/ob mouse. These animals are very obese and insulin-resistant, with substantial compensatory hyperinsulinaemia. Preliminary pharmacokinetic and pharmacodynamic experiments showed comparable drug exposures at 40 mg kg<sup>-1</sup> for SR1664 and 8 mg kg<sup>-1</sup> for rosiglitazone, both injected twice daily (Supplementary Fig. 7). Functional analyses were performed at days 5 and 11 after the start of treatments. As shown in Fig. 4a, both drugs caused a similar reduction in PPAR $\gamma$  phosphorylation at S273. After 5 days of treatment, there were no overt differences in fasting body weight or glucose levels (Fig. 4b). Control mice receiving only the vehicle remained hyperinsulinaemic, but both rosiglitazone and SR1664 substantially reduced these insulin levels (Fig. 4b). Glucose tolerance tests were markedly improved with both rosiglitazone and SR1664, and the areas under these glucose excursion curves were statistically indistinguishable, without changing body weight (Fig. 4c).

Weight gain and fluid retention caused by TZD drugs like rosiglitazone are suspected to be key factors in their increased cardiac risk<sup>9,25</sup>. After recovering from the glucose tolerance test on day 5, rosiglitazone-treated mice began to show an increase in body weight (Fig. 4d). This increased mass is accounted for primarily by fluid retention, quantified by a decrease in haematocrit seen with haemodilution (Fig. 4f). However, an increase in body fat was also observed by magnetic resonance imaging (Fig. 4e, f). Importantly, SR1664 treatment did not cause the weight gain seen with the rosiglitazone treatment. Furthermore, SR1664 treatment showed no decrease in the haematocrit or change in body adiposity. These results were confirmed by measurements showing a decreased concentration of haemoglobin in the mice treated with rosiglitazone, but not in those treated with SR1664 (Supplementary Fig. 8). Taken together, these data indicate that SR1664, a non-agonist PPAR $\gamma$  ligand, has antidiabetic actions in two murine models

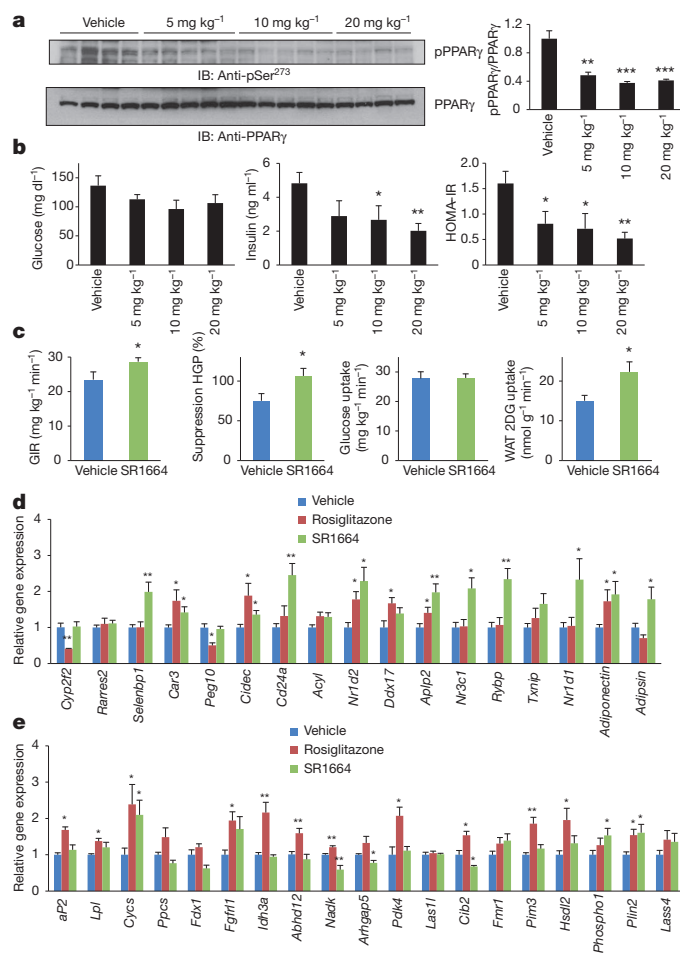


**Figure 3 | Antidiabetic activity of SR1664 in high-fat diet (HFD) mice.**

**a**, Dose-dependent inhibition of phosphorylation of PPAR $\gamma$  by SR1664 in white adipose tissue (WAT). Quantification of PPAR $\gamma$  phosphorylation compared to total PPAR $\gamma$  (right). **b**, *Ad libitum*-fed glucose ( $P = 0.062$  at 10 mg kg<sup>-1</sup>), insulin and HOMA-IR in HFD mice. **c**, Glucose infusion rate (GIR), suppression of hepatic glucose production (HGP), whole body glucose disposal and WAT 2-deoxyglucose tracer uptake during hyperinsulinaemic-euglycaemic clamps. **d**, Expression of a gene set regulated by PPAR $\gamma$  phosphorylation in WAT. **e**, Expression of an agonist gene set (see Methods) in WAT. Error bars are s.e.m.; \* $P < 0.05$ , \*\* $P < 0.01$ .

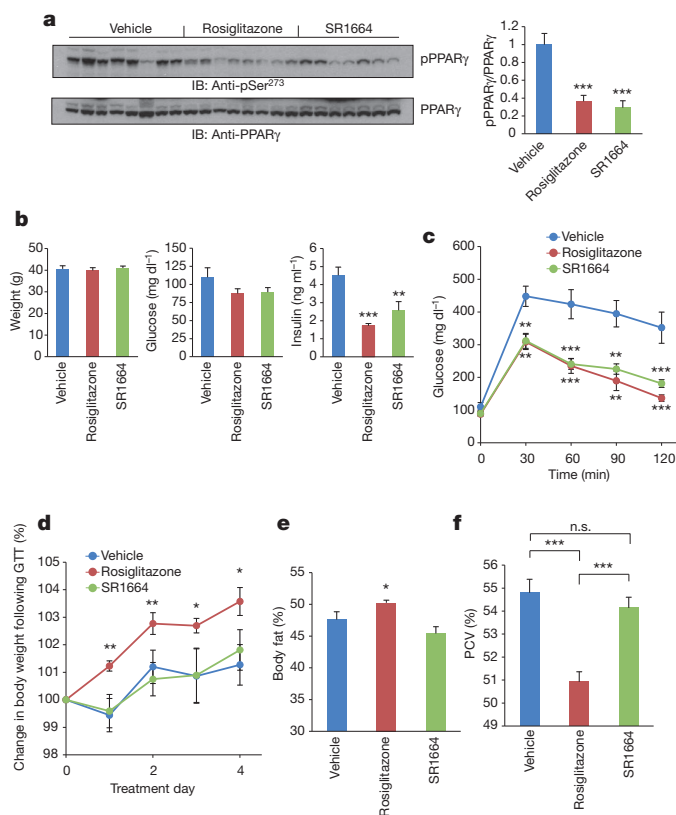


**Figure 4 | SR1664 has potent antidiabetic activity and does not promote fluid retention in ob/ob mice.** **a**, Phosphorylation of PPAR $\gamma$  in WAT (left). Quantification of PPAR $\gamma$  phosphorylation compared to total PPAR $\gamma$  (right). **b**, **c**, Fasting body weight, blood glucose and insulin levels before glucose-tolerance tests (GTT) in ob/ob mice treated with vehicle, rosiglitazone or SR1664 ( $n = 8$ ). Whole-body weight (**d**) and fat change (**e**) with continued drug administration following the GTT. **f**, Packed cell volume (PCV) in whole blood from ob/ob mice treated with vehicle, rosiglitazone or SR1664. Error bars are s.e.m.; \* $P < 0.05$ , \*\* $P < 0.01$ , \*\*\* $P < 0.001$ . n.s., not significant.

of insulin-resistance. Furthermore, this non-agonist does not stimulate two of the best documented side-effects of the PPAR $\gamma$  agonist drugs *in vivo*.

The TZD class of drugs has been important for the treatment of type 2 diabetes<sup>26</sup>. Whereas these drugs function as full agonists for PPAR $\gamma$ , the role of agonism in their therapeutic effects has been called into question recently. Rosiglitazone and partial agonists like MRL24 both block the obesity-linked phosphorylation of PPAR $\gamma$  at serine 273 (ref. 2). The tight correlation between inhibition of this phosphorylation and the therapeutic effects of these drugs in both mouse and man suggested that it might be possible to create new classes of non-agonist ligands for PPAR $\gamma$  which are effective for the treatment of diabetes and cause fewer side effects. Hence, this paper addresses three key questions: first, is it possible to create novel PPAR $\gamma$  ligands that block Cdk5-mediated PPAR $\gamma$  phosphorylation yet have no classical agonism? Second, would such compounds have robust antidiabetic activity? Finally, would non-agonist compounds have fewer side effects than classical full agonists like rosiglitazone?

We show here that it is possible to create new ligands that have high affinity for PPAR $\gamma$ , block the Cdk5-mediated phosphorylation and completely lack classical agonism. SR1664 does not function as an agonist and has no adipogenic action *in vitro*. The structural requirements for the non-agonist actions of SR1664 and SR1824 are particularly interesting. Ligands that function as classical full agonists, like rosiglitazone, have been shown to alter the conformation and HDX kinetics of H12, the major agonist helix. Surprisingly, ligands that do not affect the conformational dynamics of H12 are not non-agonists,

rather they seem to function as partial agonists<sup>18,21,27</sup>. This strongly suggests that when engaged by ligands, other structural features of the AF2 surface such as H3, H3-H4 loops and the C-terminal end of H11 contribute to partial agonism of the receptor. As expected SR1664 and SR1824 do not interact with H12 in any detectable way, but unexpectedly both ligands cause an increase in the conformational mobility of H11, which is part of the AF2 surface and directly abuts H12. Hence, it seems likely that the destabilization of H11 distorts the AF2 surface enough to block partial agonism. Whether there are other alternative modes of ligand binding that would lead to a complete lack of classical agonism remains to be determined.

That classical agonism is not required for strong antidiabetic actions of a PPAR $\gamma$  ligand is now clear. In both diet-induced and genetically obese animals, SR1664 has strong antidiabetic actions. The ability to improve adipose tissue insulin sensitivity is similar to the effects shown for rosiglitazone<sup>28</sup>. SR1664 has inferior pharmacokinetic properties compared to rosiglitazone, so an absolute quantitative comparison of their efficacy is difficult. However, using our best calculations to get approximately equal exposure to the two drugs *in vivo*, SR1664 has very robust antidiabetic activity, roughly equivalent to rosiglitazone in the experiments shown here. The unfavourable pharmacokinetic properties of SR1664 strongly suggest that this compound will never be administered to patients but it proves that non-agonist compounds can have robust therapeutic effects.

Analysis of the side effects of PPAR $\gamma$  ligands can be difficult because some of these (like cardiovascular disorders) do not occur in mice whereas others (like loss of bone mineral density) take many months of treatment to manifest. However, weight gain and fluid retention occur rapidly in both humans and mice. Increased body weight, increased accretion of fat tissues and increased fluid retention all occur in mice within 11 days of treatment with rosiglitazone (Fig. 4). The non-agonist SR1664 shows none of these side effects, even as it effectively improves glucose homeostasis. Unlike rosiglitazone, SR1664 does not affect bone cell mineralization in culture (Fig. 2c). Taken together, these data indicate that many of the known side effects of the TZD drugs occur as a consequence of classical agonism on target genes. Whether ligands directed at the Cdk5-mediated phosphorylation have their own problems remains to be determined. Still, these studies illustrate that the development of entirely new classes of PPAR $\gamma$ -targeted drugs is feasible.

## METHODS SUMMARY

**Cell culture.** Adipocyte differentiation in 3T3-L1 or PPAR $\gamma$ -null mouse embryonic fibroblasts (MEFs) expressing PPAR $\gamma$ <sup>2</sup> was induced by treating cells with 1  $\mu$ M dexamethasone, 0.5 mM isobutylmethylxanthine, and 850 nM insulin for 48 h and cells were switched to the maintenance medium containing 850 nM insulin for 6 days.

**Gene expression analysis.** Total RNA was isolated from cells or tissues using TRIzol reagent (Invitrogen). The RNA was reverse-transcribed using ABI reverse transcription kit. Quantitative PCR (qPCR) reactions were performed with SYBR green fluorescent dye using an ABI9300 PCR machine. Relative mRNA expression was determined by the  $\Delta\Delta$ -C<sub>t</sub> method using TATA-binding protein (TBP) levels.

**Animals.** All animal experiments were performed according to procedures approved by Beth Israel Deaconess Medical Center's Institutional Animal Care and Use Committee. Male C57BL/6J and C57BL/6J-*Lep<sup>ob/ob</sup>* mice (4- to 5-week-old) were obtained from the Jackson Laboratory. C57BL/6J mice were fed a high-fat, high-sucrose diet (60% kcal fat, D12492, Research Diets Inc.). For glucose tolerance tests, mice were injected intraperitoneally (i.p.) with rosiglitazone or SR1664 for 5 days, and fasted overnight before i.p. injection of 1 g kg<sup>-1</sup> D-glucose.

**Full Methods** and any associated references are available in the online version of the paper at [www.nature.com/nature](http://www.nature.com/nature).

Received 16 May; accepted 22 July 2011.

Published online 4 September 2011.

- Lehmann, J. M. *et al.* An antidiabetic thiazolidinedione is a high affinity ligand for peroxisome proliferator-activated receptor  $\gamma$  (PPAR $\gamma$ ). *J. Biol. Chem.* **270**, 12953–12956 (1995).



2. Choi, J. H. *et al.* Anti-diabetic drugs inhibit obesity-linked phosphorylation of PPAR $\gamma$  by Cdk5. *Nature* **466**, 451–456 (2010).
3. Tontonoz, P., Hu, E. & Spiegelman, B. M. Stimulation of adipogenesis in fibroblasts by PPAR $\gamma$ 2, a lipid-activated transcription factor. *Cell* **79**, 1147–1156 (1994).
4. Willson, T. M., Lambert, M. H. & Kliewer, S. A. Peroxisome proliferator-activated receptor gamma and metabolic disease. *Annu. Rev. Biochem.* **70**, 341–367 (2001).
5. Forman, B. M. *et al.* 15-Deoxy- $\Delta^{12,14}$ -prostaglandin  $J_2$  is a ligand for the adipocyte determination factor PPAR $\gamma$ . *Cell* **83**, 803–812 (1995).
6. Henke, B. R. *et al.* *N*-(2-Benzoylphenyl)-L-tyrosine PPAR $\gamma$  agonists. 1. Discovery of a novel series of potent antihyperglycemic and antihyperlipidemic agents. *J. Med. Chem.* **41**, 5020–5036 (1998).
7. Parulkar, A. A., Pendergrass, M. L., Granda-Ayala, R., Lee, T. R. & Fonseca, V. A. Nonhypoglycemic effects of thiazolidinediones. *Ann. Intern. Med.* **134**, 61–71 (2001).
8. Kahn, S. E. *et al.* Rosiglitazone-associated fractures in type 2 diabetes. *Diabetes Care* **31**, 845–851 (2008).
9. Nesto, R. W. *et al.* Thiazolidinedione use, fluid retention, and congestive heart failure: a consensus statement from the American Heart Association and American Diabetes Association. *Diabetes Care* **27**, 256–263 (2004).
10. Rocchi, S. *et al.* A unique PPAR $\gamma$  ligand with potent insulin-sensitizing yet weak adipogenic activity. *Mol. Cell* **8**, 737–747 (2001).
11. Berger, J. P. *et al.* Distinct properties and advantages of a novel peroxisome proliferator-activated protein  $\gamma$  selective modulator. *Mol. Endocrinol.* **17**, 662–676 (2003).
12. Lamotte, Y. *et al.* Synthesis and biological activities of novel indole derivatives as potent and selective PPAR $\gamma$  modulators. *Bioorg. Med. Chem. Lett.* **20**, 1399–1404 (2010).
13. Grana, X. *et al.* PITALRE, a nuclear CDC2-related protein kinase that phosphorylates the retinoblastoma protein *in vitro*. *Proc. Natl Acad. Sci. USA* **91**, 3834–3838 (1994).
14. Kliewer, S. A. *et al.* A prostaglandin  $J_2$  metabolite binds peroxisome proliferator-activated receptor  $\gamma$  and promotes adipocyte differentiation. *Cell* **83**, 813–819 (1995).
15. Chawla, A., Schwarz, E. J., Dimaculangan, D. D. & Lazar, M. A. Peroxisome proliferator-activated receptor (PPAR) gamma: adipose-predominant expression and induction early in adipocyte differentiation. *Endocrinology* **135**, 798–800 (1994).
16. Grey, A. *et al.* The peroxisome proliferator-activated receptor-gamma agonist rosiglitazone decreases bone formation and bone mineral density in healthy postmenopausal women: a randomized, controlled trial. *J. Clin. Endocrinol. Metab.* **92**, 1305–1310 (2007).
17. Lecka-Czernik, B. *et al.* Inhibition of Osf2/Cbfa1 expression and terminal osteoblast differentiation by PPAR $\gamma$ 2. *J. Cell. Biochem.* **74**, 357–371 (1999).
18. Bruning, J. B. *et al.* Partial agonists activate PPAR $\gamma$  using a helix 12 independent mechanism. *Structure* **15**, 1258–1271 (2007).
19. Hamuro, Y. *et al.* Hydrogen/deuterium-exchange (H/D-Ex) of PPAR $\gamma$  LBD in the presence of various modulators. *Protein Sci.* **15**, 1883–1892 (2006).
20. Nolte, R. T. *et al.* Ligand binding and co-activator assembly of the peroxisome proliferator-activated receptor- $\gamma$ . *Nature* **395**, 137–143 (1998).
21. Chalmers, M. J., Busby, S. A., Pascal, B. D., Southern, M. R. & Griffin, P. R. A two-stage differential hydrogen deuterium exchange method for the rapid characterization of protein/ligand interactions. *J. Biomol. Tech.* **18**, 194–204 (2007).
22. DeFronzo, R. A., Tobin, J. D. & Andres, R. Glucose clamp technique: a method for quantifying insulin secretion and resistance. *Am. J. Physiol.* **237**, E214–E223 (1979).
23. Flier, J. S., Cook, K. S., Usher, P. & Spiegelman, B. M. Severely impaired adipin expression in genetic and acquired obesity. *Science* **237**, 405–408 (1987).
24. Hu, E., Liang, P. & Spiegelman, B. M. AdipoQ is a novel adipose-specific gene dysregulated in obesity. *J. Biol. Chem.* **271**, 10697–10703 (1996).
25. Kahn, B. B. & McGraw, T. E. Rosiglitazone, PPAR $\gamma$ , and type 2 diabetes. *N. Engl. J. Med.* **363**, 2667–2669 (2010).
26. Nolan, J. J., Ludvik, B., Beerdson, P., Joyce, M. & Olefsky, J. Improvement in glucose tolerance and insulin resistance in obese subjects treated with troglitazone. *N. Engl. J. Med.* **331**, 1188–1193 (1994).
27. Hamuro, Y. *et al.* Hydrogen/deuterium-exchange (H/D-Ex) of PPAR $\gamma$  LBD in the presence of various modulators. *Protein Sci.* **15**, 1883–1892 (2006).
28. Mayerson, A. B. *et al.* The effects of rosiglitazone on insulin sensitivity, lipolysis, and hepatic and skeletal muscle triglyceride content in patients with type 2 diabetes. *Diabetes* **51**, 797–802 (2002).

**Supplementary Information** is linked to the online version of the paper at [www.nature.com/nature](http://www.nature.com/nature).

**Acknowledgements** We are grateful for support from S. Novick for assistance in the HDX studies and from R. D. Garcia-Ordóñez in protein production and mutagenesis. We are grateful for support from B. Pascal and S. Willis for software analysing the HDX data. We are grateful to R. Gupta and P. Cohen for their critical comments on the manuscript. This work was supported in part by the Intramural Research Program of the National Institutes of Health (NIH), National Institute of Mental Health (grant U54-MH074404, H. Rosen principal investigator), the National Institute of General Medical Sciences (grant R01-GM084041, P.R.G.) and the National Institute of Diabetes and Digestive and Kidney Diseases (grant 1RC4DK090861, B.M.S.). This work also supported by NIH DK31405 to B.M.S.

**Author Contributions** B.M.S. and P.R.G. conceived the project and designed research; J.H.C., A.S.B., T.M.K., S.A.B., M.J.C., N.K., D.S.K., Y.S., Y.H., J.B.B., D.P.M., M.D.C., D.L., M.J.J., S.C.S., and D.V. performed research; J.H.C., A.S.B., T.M.K., S.A.B., M.J.C., N.K., D.K., J.B.B., D.M., M.D.C., D.L., M.J.J., S.C.S., D.V., G.I.S., B.M.S. and P.R.G. analysed data; and B.M.S., A.S.B. and P.R.G. wrote the paper with contributions from all authors.

**Author Information** Reprints and permissions information is available at [www.nature.com/reprints](http://www.nature.com/reprints). The authors declare no competing financial interests. Readers are welcome to comment on the online version of this article at [www.nature.com/nature](http://www.nature.com/nature). Correspondence and requests for materials should be addressed to B.M.S. ([bruce\\_spiegelman@dfci.harvard.edu](mailto:bruce_spiegelman@dfci.harvard.edu)) or P.R.G. ([pgriffin@scripps.edu](mailto:pgriffin@scripps.edu)).

## METHODS

**SR1664.** (S)-4'-((5-((1-(4-nitrophenyl)ethyl)carbamoyl)-1H-indol-1-yl)methyl)-[1,1'-biphenyl]-2-carboxylic acid. Commercially available ethyl 2,3-dimethyl-1H-indole-5-carboxylate was *N*-alkylated with commercially available *tert*-butyl 4'-(bromomethyl)biphenyl-2-carboxylate using NaH in DMF. The corresponding ethyl ester was hydrolysed using aqueous NaOH in ethanol to give the acid, which was coupled to (S)-1-(4-nitrophenyl)ethanamine using 2-(3H-[1,2,3]triazolo [4,5-*b*]pyridin-3-yl)-1,1,3,3-tetramethylisouronium hexafluorophosphate(V) (HATU) and diisopropylethylamine in CH<sub>2</sub>Cl<sub>2</sub> to give the amide. Final deprotection of the *tert*-butyl ester using 30% trifluoroacetic acid in CH<sub>2</sub>Cl<sub>2</sub> and purification by flash chromatography (ethyl acetate/hexanes 10–100%) afforded SR1664. Electrospray ionisation coupled with mass spectrometry (ESI-MS; *m/z*): 576 [M+H]<sup>+</sup>; <sup>1</sup>H NMR (400 MHz, dimethylsulphoxide (DMSO)-*d*<sub>6</sub>):  $\delta$  (p.p.m.) 8.83 (d, *J* = 7.6 Hz, 1H), 8.25 (m, 1H), 8.16 (d, *J* = 1.2 Hz, 1H), 7.74–7.68 (m, 4H), 7.57 (dt, *J* = 1.6, 7.2 Hz, 1H), 7.51 (d, *J* = 8.4 Hz, 1H), 7.46 (dt, *J* = 1.2, 7.2 Hz, 1H), 7.36 (dd, *J* = 0.8, 7.6 Hz, 1H), 7.28 (m, 2H), 7.03 (m, 2H), 5.52 (s, 2H), 5.32 (quint, *J* = 7.2 Hz, 1H), 2.36 (s, 3H), 2.34 (s, 3H), 1.57 (d, *J* = 6.8 Hz, 3H); <sup>13</sup>C NMR (400 MHz, DMSO-*d*<sub>6</sub>):  $\delta$  (p.p.m.) 170.5, 167.9, 154.5, 147.2, 141.5, 140.7, 138.7, 138.2, 135.1, 133.2, 131.8, 131.5, 130.0, 129.6, 128.6, 128.2, 128.1, 126.8, 125.8, 124.4, 121.4, 118.8, 109.7, 108.3, 49.4, 46.7, 22.9, 11.0, 9.7.

**SR1824.** (S)-4'-((5-((1-(4-bromophenyl)ethyl)carbamoyl)-2,3-dimethyl-1H-indol-1-yl)methyl)biphenyl-2-carboxylic acid (1824) was synthesized in the same manner using (S)-1-(4-bromophenyl)ethanamine. ESI-MS (*m/z*): 581/583 [M+H]<sup>+</sup>; <sup>1</sup>H NMR (400 MHz, DMSO-*d*<sub>6</sub>):  $\delta$  (p.p.m.) 1.48 (d, *J* = 6.8 Hz, 3H, CH<sub>3</sub> (4-bromophenyl)ethylcarbamoyl), 2.28 (s, 3H, CH<sub>3</sub> indole), 2.32 (s, 3H, CH<sub>3</sub> indole), 5.17 (quintuplet, *J* = 7.6 Hz, 1H, CH (4-bromophenyl)ethylcarbamoyl), 5.47 (s, 2H, CH<sub>2</sub>-biphenyl), 6.99 (d, *J* = 8 Hz, 2H, H<sub>7</sub> and H<sub>9</sub> biphenyl), 7.24 (d, *J* = 8 Hz, 2H, H<sub>6</sub> and H<sub>10</sub> biphenyl), 7.31 (d, *J* = 7.6 Hz, 1H, H<sub>7</sub> indole), 7.36–7.55 (m, 7H, H<sub>2</sub>, H<sub>3</sub> and H<sub>4</sub> biphenyl, H<sub>6</sub> indole and H 4-bromophenyl), 8.10 (d, *J* = 1.6 Hz, 1H, H<sub>4</sub> indole), 8.65 (d, *J* = 8 Hz, 1H, NH amide). <sup>13</sup>C NMR (400 MHz, DMSO-*d*<sub>6</sub>):  $\delta$  (p.p.m.) 169.5, 166.7, 144.9, 140.5, 139.7, 137.6, 137.3, 134.0, 132.2, 131.0, 130.8, 130.4, 129.0, 128.6, 128.4, 127.6, 127.2, 125.9, 125.0, 120.3, 119.4, 117.7, 108.7, 107.3, 47.9, 45.7, 22.1, 10.1, 8.6.

**Cell culture.** COS-1, 3T3-L1 and HEK-293 cells were obtained from ATCC. Adipocyte differentiation in 3T3-L1 or PPAR $\gamma$ -null mouse embryonic fibroblasts (MEFs) expressing PPAR $\gamma^2$  was induced by treating cells with 1  $\mu$ M dexamethasone, 0.5 mM isobutylmethylxanthine, and 850 nM insulin with 10% FBS in DMEM for 48 h and cells were switched to the maintenance medium containing 10% FBS and 850 nM insulin. Lipid accumulation in the cells was detected by Oil Red O staining. All chemicals for cell culture were obtained from Sigma unless otherwise indicated.

**In vitro kinase assay.** Active Cdk5/p35 was purchased from Millipore. *In vitro* CDK kinase assay was performed according to the manufacturer's instructions (Cell Signaling Technology). Purified PPAR $\gamma$  (0.5  $\mu$ g; Cayman Chemicals) were incubated with active CDK kinase in assay buffer (25 mM Tris-HCl pH 7.5, 5 mM beta-glycerophosphate, 2 mM dithiothreitol (DTT), 0.1 mM Na<sub>3</sub>VO<sub>4</sub>, 10 mM MgCl<sub>2</sub>) containing 20  $\mu$ M ATP for 15 min at 30 °C. PPAR $\gamma$  ligands were pre-incubated with the specified substrates for 30 min before the assay was performed. Rb (Cell Signaling Technology) was used as a positive control.

**LanthaScreen.** PPAR $\gamma$  competitive binding assay (Invitrogen) was performed according to the manufacturer's protocol. A mixture of 5 nM glutathione S-transferase fused with the PPAR $\gamma$  ligand binding domain (GST-PPAR $\gamma$ -LBD), 5 nM Tb-GST-antibody, 5 nM Fluormone Pan-PPAR Green, and serial dilutions of SR1664 beginning at 10  $\mu$ M downwards was added to wells of black 384-well low-volume plates (Greiner) to a total volume of 18  $\mu$ L. All dilutions were made in TR-FRET assay buffer C. DMSO at 2% final concentration was used as a no-ligand control. Experiments were performed in triplicate and incubated for 2 h in the dark before analysis in Perkin Elmer ViewLux ultra HTS microplate reader. The FRET signal was measured by excitation at 340 nm and emission at 520 nm for fluorescein and 490 nm for terbium. The fold change over DMSO was calculated by 520 nm/490 nm ratio. Graphs were plotted as fold change of FRET signal for each compound over DMSO-only control.

**Cell-based transactivation assay.** COS-1 cells were cotransfected in batch by adding 4.5  $\mu$ g full-length murine PPAR $\gamma$ 2-pSV Sport or full-length human PPAR $\gamma$ 2-pSport6, with 4.5  $\mu$ g 3 $\times$  multimerized pPRE-luciferase reporter and 27  $\mu$ L X-treme Gene 9 transfection reagent in serum-free Opti-mem reduced serum media (Gibco). After 18-h incubation at 37 °C in a 5% CO<sub>2</sub> incubator, transfected cells were plated in triplicate in white 384-well plates (Perkin Elmer) at a density of 10,000 cells per well. After replating, cells were treated with either DMSO vehicle only or the indicated compounds in increasing doses from 2 pM–10  $\mu$ M for mouse receptor or 220 pM–2  $\mu$ M for the human receptor. After 18-h incubation, treated cells were developed with Brite Lite Plus (Perkin Elmer) and read in 384-well Luminescence Perkin Elmer EnVision Multilabel plate reader. Graphs were plotted in triplicate as fold change of treated cells over DMSO-treated control cells.

**Ensemble docking.** PPAR $\gamma$  co-crystal structures (68 in total) with unique ligands were identified in the Protein Data Bank (PDB) (as of 3 January 2011). Four structures were selected based on the maximum similarity of the co-crystal ligands to SR1664; specifically 3kmg (ligand 538, 0.98 similarity), 2hfp (ligand NSI, similarity of 0.91), 1fm9 (ligand 570, 0.90 similarity), 2pob (ligand GW4, 0.88 similarity). SR1664 was prepared using Schrodinger LigPrep generating tautomers and ionization states (pH range 7  $\pm$  2). Flexible ligand docking of SR1664 against the four structures was performed using Schrodinger Glide. At least one of the two constraints Arg 288 and Ser 342 (Arg 316 and Ser 370 in PPAR $\gamma^2$ ) was required to score docking poses. The best docking score (Glide docking scores are meant to correspond to binding affinity) of –9.21 was achieved with the PPAR $\gamma$  structure 2hfp and SR1664 forms a hydrogen bond to Ser 342 (shown in Fig. 2). Unconstrained docking produced almost the same docking pose with the preserved hydrogen bonding to Ser 342 and a slightly less favourable docking score of –8.99 indicating Ser 342 as a critical ligand binding element.

**Differentiation of MC3T3-E1.** After reaching confluence, cells were grown in  $\alpha$ -MEM supplemented with 10% FBS, 1% penicillin-streptomycin, 200  $\mu$ M ascorbic acid and 10 mM  $\beta$ -glycerophosphate. The cells were treated with either rosiglitazone (10  $\mu$ M) or SR1664 (10  $\mu$ M) or left in vehicle at the start of differentiation. The cells were collected 7 days post-differentiation for gene expression analysis and 21 days post-differentiation for mineralization. The mineralization of MC3T3-E1 cells was determined by Alizarin red S staining (Millipore catalogue no. ECM815) as per manufacturer's instructions.

**Preparation of cell or tissue lysates and immunoblotting.** Differentiated adipocytes were pre-treated with PPAR $\gamma$  ligands for 45 min, and incubated with TNF- $\alpha$  for 30 min. For tissue lysates, WAT from mice was homogenized in RIPA buffer (50 mM Tris pH 7.5, 150 mM NaCl, 1% NP-40, 0.5% sodium deoxycholate, 0.1% SDS with protease and phosphatase inhibitors). For western blotting, a phospho-specific antibody against PPAR $\gamma$  Ser 273 was used<sup>2</sup>. Total tissue lysates were analysed with an anti-PPAR $\gamma$  antibody (Santa Cruz).

**Gene expression analysis.** Total RNA was isolated from cells or tissues using TRIzol reagent (Invitrogen). The RNA was reverse-transcribed using the ABI reverse transcription kit. Quantitative PCR reactions were performed with SYBR green fluorescent dye using an ABI9300 PCR machine. Relative mRNA expression was determined by the  $\Delta\Delta$ -C<sub>t</sub> method normalized to TATA-binding protein (TBP) levels. The sequences of primers used in this study are found in Supplementary Table 1.

**ChIP.** Differentiated 3T3-L1 adipocytes were treated on day 6 with 1  $\mu$ M of compounds or vehicle for 24 h. The samples were prepared using manufacturer's protocol (ChampionChIP One-Day Kit, Qiagen). Briefly, cross-linked chromatin was sonicated and 5  $\mu$ g of antibody was used to immunoprecipitate the pre-cleared samples. The following antibodies were used: normal rabbit IgG, PPAR $\gamma$  (Santa Cruz), SRC-1 (Abcam). The promoter region of aP2 for PPAR- $\gamma$  binding was amplified using PCR with reverse transcription (RT-PCR). The primers used for aP2 were aP2 forward 5'-AAATTCAGAAGAAAGTAAACACATTATT-3'; aP2 reverse 5'-ATGCCCTGACCATGTGA-3'.

**Gene sets from microarray.** We performed a microarray with total RNA isolated from PPAR $\gamma$ -null fibroblasts expressing wild-type or S273A mutant of PPAR $\gamma$  or WT cells treated with 1  $\mu$ M rosiglitazone for 24 h (ref. 2). To create refined gene sets regulated by phosphorylation of PPAR $\gamma$  or rosiglitazone, we first calculated *P*-values as well as fold-change of gene expression in wild-type versus S273A mutant cells or wild-type versus wild-type/Rosiglitazone cells, and we plotted –log *P*-value versus log<sub>2</sub> fold-change. From this list of genes, we selected genes which were changed in magnitude ( $\geq 1.4$  fold difference) and statistical significance (*P* < 0.05). The selected genes were validated in cells by using qPCR, the resulting gene sets (phosphorylation-dependent or agonist-dependent gene sets) were analysed in WAT of mice using qPCR.

**Animals.** All animal experiments were performed according to procedures approved by Beth Israel Deaconess Medical Center's Institutional Animal Care and Use Committee. Male C57BL/6J or C57BL/6J-*Lep<sup>ob/ob</sup>* mice (4- to 5-week-old) were obtained from the Jackson Laboratory. C57BL/6J mice were fed a regular diet (10% kcal fat, D12450B, Research Diets Inc.) or a high-fat, high-sugar diet (60% kcal fat, D12492, Research Diets Inc.) for either 8, 10 or 18 weeks. The mice were intraperitoneally (i.p.) injected twice daily with 4 mg kg<sup>–1</sup> rosiglitazone or 20 mg kg<sup>–1</sup> SR1664 for 6 days before gene expression analysis or hyperinsulinaemic-euglycaemic clamp experiments. Clamps were performed essentially as previously described with one exception to the standard protocol<sup>29</sup>. As the mice were fed a high-fat diet for 8 weeks before the clamp studies, a higher insulin infusion rate of 4 mU (kg-min)<sup>–1</sup> was used instead of the typical 3 mU (kg-min)<sup>–1</sup> for standard chow studies. For glucose tolerance tests, 6-week-old male C57BL/6J-*Lep<sup>ob/ob</sup>* mice were i.p. injected twice daily with 8 mg kg<sup>–1</sup> rosiglitazone or 40 mg kg<sup>–1</sup> SR1664 for 6 days, and fasted overnight before i.p. injection of 1 g kg<sup>–1</sup> D-glucose. Glucose was measured by tail vein bleeds at the indicated intervals using a TruTrack

- glucometer. Serum insulin concentrations were determined by ELISA (Crystal Chem).
29. Kim, H. J. *et al.* Differential effects of interleukin-6 and -10 on skeletal muscle and liver insulin action *in vivo*. *Diabetes* **53**, 1060–1067 (2004).



# Absence of effects of Sir2 overexpression on lifespan in *C. elegans* and *Drosophila*

Camilla Burnett<sup>1\*</sup>, Sara Valentini<sup>1\*</sup>, Filipe Cabreiro<sup>1\*</sup>, Martin Goss<sup>1</sup>, Milán Somogyvári<sup>2</sup>, Matthew D. Piper<sup>1</sup>, Matthew Hoddinott<sup>1</sup>, George L. Sutphin<sup>3,4</sup>, Vid Leko<sup>5</sup>, Joshua J. McElwee<sup>1</sup>, Rafael P. Vazquez-Manrique<sup>6,7</sup>, Anne-Marie Orfila<sup>6,7</sup>, Daniel Ackerman<sup>1</sup>, Catherine Au<sup>1</sup>, Giovanna Vinti<sup>1</sup>, Michèle Riesen<sup>1</sup>, Ken Howard<sup>8</sup>, Christian Neri<sup>6,7</sup>, Antonio Bedalov<sup>5</sup>, Matt Kaeberlein<sup>3,4</sup>, Csaba Söti<sup>2</sup>, Linda Partridge<sup>1,9</sup> & David Gems<sup>1</sup>

Overexpression of sirtuins (NAD<sup>+</sup>-dependent protein deacetylases) has been reported to increase lifespan in budding yeast (*Saccharomyces cerevisiae*), *Caenorhabditis elegans* and *Drosophila melanogaster*<sup>1–3</sup>. Studies of the effects of genes on ageing are vulnerable to confounding effects of genetic background<sup>4</sup>. Here we re-examined the reported effects of sirtuin overexpression on ageing and found that standardization of genetic background and the use of appropriate controls abolished the apparent effects in both *C. elegans* and *Drosophila*. In *C. elegans*, outcrossing of a line with high-level *sir-2.1* overexpression<sup>1</sup> abrogated the longevity increase, but did not abrogate *sir-2.1* overexpression. Instead, longevity co-segregated with a second-site mutation affecting sensory neurons. Outcrossing of a line with low-copy-number *sir-2.1* overexpression<sup>2</sup> also abrogated longevity. A *Drosophila* strain with ubiquitous overexpression of *dSir2* using the UAS-GAL4 system was long-lived relative to wild-type controls, as previously reported<sup>3</sup>, but was not long-lived relative to the appropriate transgenic controls, and nor was a new line with stronger overexpression of *dSir2*. These findings underscore the importance of controlling for genetic background and for the mutagenic effects of transgene insertions in studies of genetic effects on lifespan. The life-extending effect of dietary restriction on ageing in *Drosophila* has also been reported to be *dSir2* dependent<sup>3</sup>. We found that dietary restriction increased fly lifespan independently of *dSir2*. Our findings do not rule out a role for sirtuins in determination of metazoan lifespan, but they do cast doubt on the robustness of the previously reported effects of sirtuins on lifespan in *C. elegans* and *Drosophila*.

The role of sirtuins in ageing was discovered in budding yeast, where overexpression of *SIR2* increases replicative lifespan<sup>5</sup>. It was then reported that elevated sirtuin levels increase lifespan in the nematode *C. elegans*<sup>1,2,6</sup> and the fruitfly *Drosophila*<sup>3</sup>, indicating an evolutionarily ancient role of sirtuins in longevity assurance<sup>7</sup>. Dietary restriction (reduced food intake short of starvation) extends lifespan in organisms ranging from yeast to mammals<sup>8</sup>, and initial studies indicated that dietary restriction increases lifespan by activating sirtuins in yeast<sup>9</sup>, *C. elegans*<sup>10</sup> and *Drosophila*<sup>3</sup>. Pharmacological activation of sirtuins has therefore been widely promulgated as a potential means to mimic dietary restriction and slow ageing in humans<sup>11</sup>. However, several aspects of the role of sirtuins in ageing have proved controversial<sup>12</sup>. Subsequent studies have indicated that sirtuins do not mediate the effects of dietary restriction on ageing, at least in budding yeast and *C. elegans*<sup>13,14</sup>. The plant-derived polyphenol resveratrol and other compounds have been reported to activate sirtuins and extend lifespan<sup>15,16</sup>, but more recent findings have challenged both effects<sup>17–20</sup>. We therefore re-examined the effects of sirtuin overexpression on lifespan in *C. elegans* and *Drosophila*. In particular, we wished to

exclude the possibility that the increased longevity observed in strains with overexpression of sirtuin genes is caused by differences in genetic background, or by the mutagenic effects of transgene insertion, which frequently confound studies of the genetics of ageing<sup>4</sup>.

We first examined a high-copy-number *sir-2.1* transgenic *C. elegans* strain (LG100) carrying the integrated transgene array *gelIn3* [*sir-2.1 rol-6(su1006)*] (ref. 1). As expected, this strain was long-lived (Fig. 1a and Supplementary Table 1). However, outcrossing (×5) of *gelIn3* to wild type (N2) abrogated the increase in longevity (Fig. 1a and Supplementary Table 1) without affecting SIR-2.1 protein levels (Fig. 1b). This loss of longevity upon outcrossing was verified by an independent research team (Supplementary Table 2).

LG100 showed a neuronal dye-filling (Dyf) defect<sup>21</sup> that did not segregate with the transgene upon outcrossing (Supplementary Fig. 2a). Dyf mutants often show extended lifespan<sup>22</sup>. To determine whether the longevity of LG100 might be attributable to a *dyf* mutation, we derived from this strain three Dyf, non-Rol lines (lacking *gelIn3*) and three non-Dyf, Rol lines (carrying *gelIn3*). Dyf, non-Rol lines were long-lived and showed wild-type SIR-2.1 protein levels (Fig. 1c, d and Supplementary Table 3). Non-Dyf, Rol lines showed elevated SIR-2.1 protein levels but had wild-type lifespans. Dyf mutant longevity seemed to be partially dependent on *daf-16* (Supplementary Fig. 2b), as seen previously for other Dyf mutants<sup>22</sup>. The co-segregation of longevity with this *dyf* mutation, but not with *gelIn3*, was previously noted by another research team (S. S. Lee, personal communication). Furthermore, knockdown of *sir-2.1* expression in LG100 using RNA-mediated interference did not suppress longevity, despite lowering SIR-2.1 protein to wild-type levels (Fig. 1e, f and Supplementary Table 4). Taken together, these results indicate that the longevity of LG100 is attributable to an unidentified *dyf* mutation (or possibly another mutation closely linked to the *dyf* locus), and that high-level overexpression of *sir-2.1* is not sufficient to increase lifespan in these strains.

A low-copy-number transgenic strain (NL3909) overexpressing *sir-2.1* (ref. 7) is also long-lived<sup>2</sup>. We confirmed the increased lifespan of NL3909 (*pkIs1642* [*sir-2.1 unc-119*] *unc-119(ed3)*) relative to the control strain NL3908 (*pkIs1641* [*unc-119*] *unc-119(ed3)*) (Fig. 1g and Supplementary Table 5). We also observed an apparent increase in SIR-2.1 protein levels in NL3909 relative to NL3908 (Fig. 1h). Outcrossing (×6) of NL3909 once again abrogated longevity (Fig. 1g and Supplementary Table 5) without affecting SIR-2.1 protein levels (Fig. 1h and Supplementary Fig. 1c). This effect of outcrossing was independently verified (Supplementary Table 6). Thus, the longevity of NL3909 also seems to be attributable to effects of genetic background rather than to *pkIs1642*.

The duplication *mDp4* includes the *sir-2.1* locus, and the *mDp4*-containing strain DR1786 is long-lived<sup>1</sup>. We found that DR1786 is

<sup>1</sup>Institute of Healthy Ageing and Department of Genetics, Evolution and Environment, University College London, Gower Street, London WC1E 6BT, UK. <sup>2</sup>Department of Medical Chemistry, Semmelweis University, Tűzoltó Street 37–47, 1094 Budapest, Hungary. <sup>3</sup>Department of Pathology, University of Washington, Seattle, Washington 98195, USA. <sup>4</sup>Molecular and Cellular Biology Program, University of Washington, Seattle, Washington 98195, USA. <sup>5</sup>Fred Hutchinson Cancer Research Center, Seattle, Washington 98109, USA. <sup>6</sup>Inserm, Unit 894, Laboratory of Neuronal Cell Biology and Pathology, 75014 Paris, France. <sup>7</sup>Université Paris Descartes, 75014 Paris, France. <sup>8</sup>MRC Laboratory for Molecular Cell Biology, University College London, Gower Street, London WC1E 6BT, UK. <sup>9</sup>Max Planck Institute for Biology of Ageing, Gleueler Strasse 50a, 50931 Köln, Germany.

\*These authors contributed equally to this work.

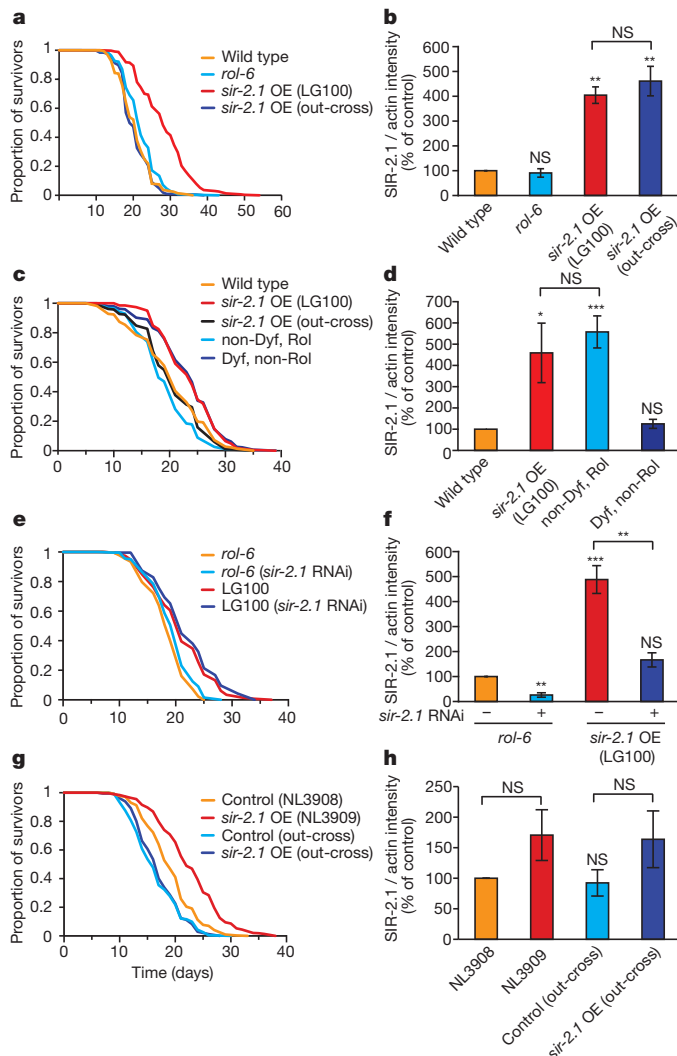


**Figure 1 | Longevity of LG100 and NL3909 is not attributable to *sir-2.1* overexpression in *C. elegans*.** **a, b**, Outcrossing of LG100 removes lifespan extension without affecting SIR-2.1 protein levels. Data in **b** are derived from western blots (mean of three trials, each using an independent protein preparation). A representative western blot is shown in Supplementary Fig. 1a. Quantitative reverse transcriptase PCR showed that *sir-2.1* mRNA is also elevated in both strains (data not shown). **c**, LG100-derived Dyf, non-Rol segregant lines are long-lived whereas non-Dyf, Rol lines are not. **d**, Non-Dyf Rol segregant lines have elevated SIR-2.1 levels, whereas Dyf, non-Rol lines do not. **e, f**, *sir-2.1* RNAi does not suppress LG100 longevity, but reduces SIR-2.1 protein levels. **g, h**, Outcrossing of NL3909 removes lifespan extension without affecting SIR-2.1 protein levels. See Supplementary Tables 1–5 for lifespan statistics for **a, c, e** and **g**, respectively. OE, overexpression. All error bars represent s.e.m. \*,  $0.01 < P < 0.05$ ; \*\*,  $0.001 < P < 0.01$ ; \*\*\*,  $P < 0.001$ ; NS, not significant; Student's *t*-test (two-tailed). One remaining possibility is that the outcrossed *sir-2.1* strains both contain second-site mutations that suppress longevity effects. However, *daf-2* RNAi strongly induced longevity in both strains (data not shown), arguing against the presence of a general suppressor of longevity in each case.

indeed long-lived, and also shows elevated *sir-2.1* expression. However, longevity was not suppressed by *sir-2.1* RNA interference (RNAi) (Supplementary Fig. 3 and Supplementary Table 7) indicating causation by factors other than *sir-2.1*, either on *mDp4* or elsewhere in the genome.

In *Drosophila*, overexpression of *dSir2* reportedly increases lifespan relative to wild-type controls<sup>3</sup>. Overexpression was achieved using the GAL4-UAS binary system<sup>23</sup>, with the largest increases in lifespan being produced by the combination of EP-UAS-*dSir2* (*dSir2*<sup>EP2300</sup>) with a ubiquitously expressed tubulin-GAL4 driver. We outcrossed these

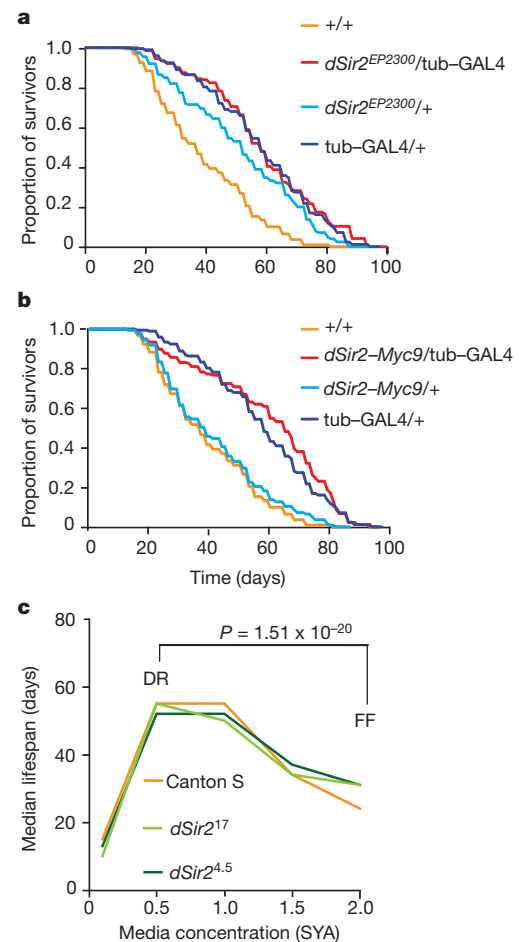


**Figure 2 | Absence of effects of *dSir2* on lifespan in *Drosophila*.** All lines were outcrossed into *w*<sup>Dah</sup> (*+/+*). **a**, Lifespan in flies overexpressing *dSir2*<sup>EP2300</sup> driven via tubulin-GAL4 (tub-GAL4) is longer than in the wild type, but not longer than in the *tubulin-GAL4*/+ genetic control. Median lifespans: *+/+*, 39 days; *dSir2*<sup>EP2300</sup>/tubulin-GAL4, 59 days; *dSir2*<sup>EP2300</sup>/+, 53 days, *tubulin-GAL4*/+, 60 days.  $P = 0.0006$  for comparison of *dSir2*<sup>EP2300</sup>/tubulin-GAL4 versus *dSir2*<sup>EP2300</sup>/+;  $P = 0.9295$  for *dSir2*<sup>EP2300</sup>/tubulin-GAL4 versus *tubulin-GAL4*/+;  $P < 0.0001$  for *dSir2*<sup>EP2300</sup>/tubulin-GAL4 versus *+/+*. **b**, Lifespan in flies overexpressing *dSir2-Myc9* is longer than in wild type, but not longer than in the *tubulin-GAL4* control. Median lifespans: *+/+*, 39 days; *dSir2-Myc9*/tubulin-GAL4, 67 days; *dSir2-Myc9*/+, 41 days; *tubulin-GAL4*/+, 60 days. *dSir2-Myc9*/tubulin-GAL4 versus *dSir2-Myc9*/+,  $P = 0.0001$ ; *dSir2-Myc9*/tubulin-GAL4 versus *tubulin-GAL4*/+,  $P = 0.1354$ ; *dSir2-Myc9*/tubulin-GAL4 versus *+/+*,  $P < 0.0001$ . All comparisons were made using log-rank tests,  $n = 200$ . **c**, The effect of dietary restriction on *Drosophila* lifespan is not *dSir2*-dependent. Flies were assayed over five concentrations of SYA media and data are presented as the median lifespan on each food concentration. All lines were outcrossed into Canton S (*+/+*).  $P$  values confirm that all flies respond normally to dietary restriction when median lifespans are compared for dietary restriction (DR) versus fully-fed (FF) conditions<sup>30</sup>.

two transgenes ( $\times 6$ ) into the control white Dahomey (*w*<sup>Dah</sup>) background. When assayed on a medium similar to that used in the original study, EP-UAS-*dSir2*/tubulin-GAL4 flies were longer-lived than wild-type controls, as previously reported<sup>3</sup> (Fig. 2a). However, they did not live longer than the *tubulin-GAL4*/+ control flies (Fig. 2a). This implies that lifespan extension is due to transgene-linked genetic effects other than the overexpression of *dSir2*. Lifespan was assayed on a range of food media (see Methods for details) to test for nutrient dependence of any effect. However, in no case were EP-UAS-*dSir2*/tubulin-GAL4 flies longer-lived than one or both transgenic controls (Supplementary Fig. 4).

The lack of an observable effect on lifespan could reflect the relatively modest increase in *dSir2* expression in EP-UAS-*dSir2*/tubulin-GAL4

flies, both in terms of messenger RNA levels (Supplementary Fig. 5) and protein levels (increased by 35% relative to wild type; Supplementary Fig. 6). We therefore created lines with a higher level of overexpression of *dSir2* (UAS-*dSir2-Myc9/tubulin-GAL4*). Here, *dSir2* mRNA and protein levels were robustly increased relative to wild type (an increase of 318% relative to wild-type protein levels; Supplementary Figs 5 and 6). We examined recombinant protein raised in *Escherichia coli* to check that the presence of the Myc tag did not interfere with *dSir2* histone deacetylase activity, as measured by deacetylation of the fluorophore-containing p53 substrate (Fluor de Lys) or of native acetylated histone H4 substrates, and it did not (Supplementary Fig. 7). We also found that *dSir2* histone deacetylase activity was unaffected by addition of resveratrol in either assay (Supplementary Fig. 7). We saw no increase in lifespan in UAS-*dSir2-Myc9/tubulin-GAL4* flies relative to *tubulin-GAL4/+* controls, either on a food medium similar to that used in the original study (Fig. 2b), or relative to either control on a range of other media (Supplementary Fig. 4b, c, f). An independent research team also saw no increase in lifespan in UAS-*dSir2-Myc9/tubulin-GAL4* flies (Supplementary Fig. 8). These results indicate that the previously observed longevity of EP-UAS-*dSir2/tubulin-GAL4* flies was not attributable to elevated expression of *dSir2*, and that stronger, ubiquitous overexpression of *dSir2* also does not extend fly lifespan.

The role of sirtuins in the extension of lifespan by dietary restriction in yeast and *C. elegans* is controversial, with several groups reporting that sirtuins are not required for lifespan extension via dietary restriction in both organisms<sup>8</sup>. In *Drosophila*, it was reported that dietary restriction does not increase lifespan in *dSir2* deletion-mutant flies<sup>3</sup>. We tested this too, using the deletion alleles *dSir2*<sup>4,5</sup> (tested previously<sup>3</sup>) and *dSir2*<sup>17</sup>. We first outcrossed these alleles (Supplementary Fig. 9a) into the Canton S wild type (see Methods), which was used in the previous dietary-restriction study<sup>3</sup>. We then checked the effect of each allele on *dSir2* gene expression. The allele *dSir2*<sup>17</sup> abrogated *dSir2* mRNA, indicating that this is a null allele. By contrast, *dSir2*<sup>4,5</sup>, which contains a relatively small deletion at the 5' end of the gene, did not reduce *dSir2* mRNA levels (Supplementary Fig. 9b, c).

To reassess the role of *dSir2* in dietary restriction in *Drosophila*, we compared lifespans of wild-type (Canton S), *dSir2*<sup>4,5</sup> and *dSir2*<sup>17</sup> homozygotes. All genotypes responded similarly and normally to dietary restriction in trials conducted by two independent research teams (Fig. 2c and Supplementary Fig. 10), hence the effect of dietary restriction on lifespan did not require *dSir2*.

In this study, we were unable to verify the effect of sirtuin overexpression on lifespan in either *C. elegans* or *Drosophila*. Increased lifespan was seen in two *C. elegans* lines with elevated *sir-2.1* expression, derived from independent studies, as previously reported, but in each case this was abrogated by outcrossing. Overexpression of *sir-2.1* does exert effects on traits other than lifespan. For example, *gel-3* is neuroprotective in a worm model of neuron dysfunction in Huntington's disease<sup>24</sup> and, notably, this effect is not attributable to the *dyf* mutation (Supplementary Fig. 11). Moreover, both NL3909 and its outcrossed derivative are thermotolerant (M. Somogyvári and C. Söti, unpublished data). In *Drosophila*, lines overexpressing *dSir2* were longer-lived than wild-type controls, as previously reported, but they were not longer-lived than lines containing the appropriate transgenic controls. The fact that all transgenic lines were longer-lived than the Dahomey wild type into which they had been outcrossed could reflect heterosis in the vicinity of the transgene inserts, or a mutagenic effect of the GAL4 insert.

Lifespan was not increased either by overexpression of *sir-2.1* from its own promoter in *C. elegans*, or by ubiquitous overexpression of *dSir2* from a heterologous promoter in *Drosophila*. Our findings call into question the robustness of earlier reports of a role for sirtuins in longevity assurance on the basis of overexpression in *C. elegans* and *Drosophila*, and also the role of *dSir2* in the response to dietary restriction in *Drosophila*. However, sirtuins can affect lifespan in animals

under certain conditions: *C. elegans daf-2(e1370)* mutants are hypersensitive to genetic effects on lifespan<sup>25</sup>, and in these mutants, deletion of *sir-2.1* reproducibly increases lifespan<sup>6</sup> (Supplementary Fig. 12).

Our finding that resveratrol does not activate the histone deacetylase activity of *dSir2* using a native histone H4 peptide is consistent with earlier findings using yeast SIR2 and mammalian SirT1 (refs 17, 18). Resveratrol increased *Drosophila* lifespan in one study<sup>26</sup> but not in another<sup>27</sup>. In principle, this could reflect sensitivity of resveratrol effects to subtle differences in culture conditions. If this were the case, our findings would indicate that such effects are not attributable to direct activation of *dSir2* by resveratrol.

## METHODS SUMMARY

**Nematode strains and maintenance.** Nematodes were maintained on nematode-growth-medium agar at 20 °C, with *E. coli* OP50 bacteria as a food source. Nematode strains used included: wild type (N2), GA707 *wuEx166 [rol-6(su1006)]* (*rol-6* control), LG100 *gel-3 [sir-2.1 rol-6(su1006)] dyf-2(wu250)*, NL3909 *pkIs1642 [sir-2.1 unc-119] unc-119(ed3)* and the control strain NL3908 *pkIs1641 [unc-119] unc-119(ed3)*.

**Nematode lifespan measurements.** These were performed as previously described<sup>28</sup>, at 20 °C. To prevent progeny production, 5-fluoro-2'-deoxyuridine (FUDR) was added to seeded plates, to a final concentration of 10, 40 or 50 µM. Before testing the effects of RNAi on lifespan, worms were kept for two generations on the RNAi bacteria. The statistical significance of effects on lifespan was estimated using the log-rank test, performed using JMP, Version 7 (SAS Institute).

**Drosophila stocks and maintenance.** *Tubulin-GAL4* and *dSir2*<sup>EP2300</sup> were obtained from the Bloomington Stock Center. The *dSir2-Myc2* and *dSir2-Myc9* lines were generated by germline transformation into strain *w*<sup>04</sup>. The *dSir2*<sup>4,5</sup>/*SM6B*, *dSir2*<sup>17</sup>/*Cyo* and Canton S lines were gifts from S. Pletcher, J. Rine and S. Helfand. All lines were outcrossed at least six times into the relevant controls. Experiments were performed at 25 °C on a 12 h:12 h light:dark cycle at constant humidity.

**Drosophila lifespan assays.** Flies were bred at standard density, allowed to mate for 48 h after emerging, then sorted into ten females per vial. Vials were changed every 48 h, and deaths per vial were scored until all flies were dead. In overexpression studies, *n* = 200. In *dSir2*-mutant studies, *n* = 100. For statistical methodology, see earlier.

**dSir2 deacetylation assays.** We used both the SirT1 Fluorimetric Drug Discovery Kit (Enzo Life Sciences) and an HPLC-based acetyl-histone-H4 deacetylation assay<sup>29</sup>. *dSir2* and *dSir2-Myc* were cloned into pET SUMO (Invitrogen) and proteins were purified on HisPur cobalt spin columns (Thermo Scientific).

**Full Methods** and any associated references are available in the online version of the paper at [www.nature.com/nature](http://www.nature.com/nature).

Received 27 October 2010; accepted 10 June 2011.

1. Tissenbaum, H. A. & Guarente, L. Increased dosage of a *sir-2* gene extends lifespan in *Caenorhabditis elegans*. *Nature* **410**, 227–230 (2001).
2. Viswanathan, M., Kim, S. K., Berdichevsky, A. & Guarente, L. A role for SIR-2.1 regulation of ER stress response genes in determining *C. elegans* life span. *Dev. Cell* **9**, 605–615 (2005).
3. Rogina, B. & Helfand, S. Sir2 mediates longevity in the fly through a pathway related to calorie restriction. *Proc. Natl Acad. Sci. USA* **101**, 15998–16003 (2004).
4. Partridge, L. & Gems, D. Benchmarks for ageing studies. *Nature* **450**, 165–167 (2007).
5. Kaeberlein, M., McVey, M. & Guarente, L. The SIR2/3/4 complex and SIR2 alone promote longevity in *Saccharomyces cerevisiae* by two different mechanisms. *Genes Dev.* **13**, 2570–2580 (1999).
6. Berdichevsky, A., Viswanathan, M., Horvitz, H. R. & Guarente, L. *C. elegans* SIR-2.1 interacts with 14-3-3 proteins to activate DAF-16 and extend life span. *Cell* **125**, 1165–1177 (2006).
7. Guarente, L. Sirtuins in aging and disease. *Cold Spring Harb. Symp. Quant. Biol.* **72**, 483–488 (2007).
8. Mair, W. & Dillin, A. Aging and survival: the genetics of life span extension by dietary restriction. *Annu. Rev. Biochem.* **77**, 727–754 (2008).
9. Lin, S., Defossez, P. & Guarente, L. Requirement of NAD and SIR2 for life-span extension by calorie restriction in *Saccharomyces cerevisiae*. *Science* **289**, 2126–2128 (2000).
10. Wang, Y. & Tissenbaum, H. A. Overlapping and distinct functions for a *Caenorhabditis elegans* SIR2 and DAF-16/FOXO. *Mech. Ageing Dev.* **127**, 48–56 (2006).
11. Haigis, M. C. & Sinclair, D. A. Mammalian sirtuins: biological insights and disease relevance. *Annu. Rev. Pathol.* **5**, 253–295 (2010).
12. Garber, K. A mid-life crisis for aging theory. *Nature Biotechnol.* **26**, 371–374 (2008).



13. Kaerberlein, M. Lessons on longevity from budding yeast. *Nature* **464**, 513–519 (2010).
14. Kenyon, C. The genetics of ageing. *Nature* **464**, 504–512 (2010).
15. Howitz, K. T. *et al.* Small molecule activators of sirtuins extend *Saccharomyces cerevisiae* lifespan. *Nature* **425**, 191–196 (2003).
16. Milne, J. *et al.* Small molecule activators of SIRT1 as therapeutics for the treatment of type 2 diabetes. *Nature* **450**, 712–716 (2007).
17. Kaerberlein, M. *et al.* Substrate-specific activation of sirtuins by resveratrol. *J. Biol. Chem.* **280**, 17038–17045 (2005).
18. Borra, M., Smith, B. & Denu, J. Mechanism of human SIRT1 activation by resveratrol. *J. Biol. Chem.* **280**, 17187–17195 (2005).
19. Behr, D. *et al.* Resveratrol is not a direct activator of SIRT1 enzyme activity. *Chem. Biol. Drug Des.* **74**, 619–624 (2009).
20. Pacholec, M. *et al.* SRT1720, SRT2183, SRT1460, and resveratrol are not direct activators of SIRT1. *J. Biol. Chem.* **285**, 8340–8351 (2010).
21. Hedgecock, E., Culotti, J., Thomson, J. & Perkins, L. Axonal guidance mutants of *Caenorhabditis elegans* identified by filling sensory neurons with fluorescein dyes. *Dev. Biol.* **111**, 158–170 (1985).
22. Apfeld, J. & Kenyon, C. Regulation of lifespan by sensory perception in *Caenorhabditis elegans*. *Nature* **402**, 804–809 (1999).
23. Brand, A. & Perrimon, N. Targeted gene expression as a means of altering cell fates and generating dominant phenotypes. *Development* **118**, 401–415 (1993).
24. Parker, J. A. *et al.* Resveratrol rescues mutant polyglutamine cytotoxicity in nematode and mammalian neurons. *Nature Genet.* **37**, 349–350 (2005).
25. Patel, D. S. *et al.* Clustering of genetically defined allele classes in the *Caenorhabditis elegans* DAF-2 insulin/IGF-1 receptor. *Genetics* **178**, 931–946 (2008).
26. Wood, J. *et al.* Sirtuin activators mimic caloric restriction and delay ageing in metazoans. *Nature* **430**, 686–689 (2004).
27. Bass, T., Weinkove, D., Houthoofd, K., Gems, D. & Partridge, L. Effects of resveratrol on lifespan in *Drosophila melanogaster* and *Caenorhabditis elegans*. *Mech. Ageing Dev.* **128**, 546–552 (2007).
28. Gems, D. *et al.* Two pleiotropic classes of *daf-2* mutation affect larval arrest, adult behavior, reproduction and longevity in *Caenorhabditis elegans*. *Genetics* **150**, 129–155 (1998).
29. Borra, M. T. & Denu, J. M. Quantitative assays for characterization of the Sir2 family of NAD<sup>+</sup>-dependent deacetylases. *Methods Enzymol.* **376**, 171–187 (2003).
30. Grandison, R. C., Wong, R., Bass, T. M., Partridge, L. & Piper, M. D. Effect of a standardised dietary restriction protocol on multiple laboratory strains of *Drosophila melanogaster*. *PLoS ONE* **4**, e4067 (2009).

**Supplementary Information** is linked to the online version of the paper at [www.nature.com/nature](http://www.nature.com/nature).

**Acknowledgements** We thank A. Gartner for providing an antibody against *C. elegans* SIR-2.1; D. Chen, P. Kapahi, S. Pletcher and D. Skurupa for providing data; S. S. Lee for permission to cite unpublished results; S. Helfand and J. Rine for providing fly strains; W. Mair for performing preliminary trials and R. Baumeister for useful discussion. Some nematode strains were provided by the *Caenorhabditis* Genetics Center, which is funded by the National Institutes of Health National Center for Research Resources. We acknowledge funding from the European Union (FP6-036894 to C.B., D.G., L.P. and S.V. and FP6-518230 to D.G. and C.S.), the Hungarian Science Foundation and Norway Grants (NNF-78794 to C.S.), INSERM and ANR, Paris (R.V., A.-M.O. and C.N.), the National Institutes of Health (CA129132 to A.B., R01AG031108 to M.K. and T32AG000057 to G.L.S.) and the Wellcome Trust (Strategic Award to C.A., F.C., D.G., L.P. and M.R.). C.S. is a Bolyai Research Scholar of the Hungarian Academy of Sciences and M.K. is an Ellison Medical Foundation New Scholar in Aging.

**Author Contributions** The project was conceived by D.G. and L.P. and the experiments were designed by A.B., C.B., F.C., D.G., K.H., M.K., J.J.M., C.N., L.P., C.S. and S.V. The experiments were performed and analysed by C.A., D.A., C.B., F.C., J.J.M., M.G., M.H., A.-M.O., M.D.P., M.R., G.L.S., M.S., G.V., R.P.V.-M., S.V. and V.L. The manuscript was written by C.B., F.C., D.G., L.P. and S.V.

**Author Information** Reprints and permissions information is available at [www.nature.com/reprints](http://www.nature.com/reprints). The authors declare no competing financial interests. Readers are welcome to comment on the online version of this article at [www.nature.com/nature](http://www.nature.com/nature). Correspondence and requests for materials should be addressed to D.G. ([david.gems@ucl.ac.uk](mailto:david.gems@ucl.ac.uk)).

## METHODS

**Nematode strains and maintenance.** *Caenorhabditis elegans* were cultured under standard monoxenic conditions<sup>31,32</sup>. Strains used included N2 (wild type), GA707 *wuEx166 [rol-6(su1006)]*, HT1593 *unc-119(ed3)*, LG100 *geln3 [sir-2.1 rol-6(su1006)] dyf-?(wu250)*, NL3908 *pkl1641 [unc-119] unc-119(ed3)* and NL3909 *pkl1642 [sir-2.1 unc-119] unc-119(ed3)*.

**Outcrossing of nematode strains.** LG100 was outcrossed with N2 and the Rol trait was used to detect the presence of *geln3*. NL3908 and NL3909 were outcrossed using HT1593 *unc-119(ed3)*. Rescue of Unc (uncoordinated movement) was used to detect the presence of the transgene array.

**Isolation of Dyf, non-Rol and non-Dyf, Rol lines.** LG100 was crossed with N2 and lines were established from individual F<sub>2</sub> animals with Dyf, non-Rol or non-Dyf, Rol phenotypes. The Dyf phenotype was identified by staining with the dye 1,1'-diiodo-3,3',3'-tetramethylindocarbocyanine perchlorate (DiI) and looking for absence of dye uptake into the amphid and phasmid neurons. Non-Dyf, Rol F<sub>2</sub> animals that were heterozygous for the *geln3* transgene array (the *rol-6* marker is dominant) were identified by the presence of non-Rol animals in the F<sub>3</sub>, and were excluded.

**RNAi in *C. elegans*.** Animals were fed *E. coli* containing the HT115 vector, either with or without a portion of the *sir-2.1* gene cloned into it. The *sir-2.1* feeding strain was obtained from the Ahringer RNAi library<sup>33</sup>. Worms were maintained on RNAi feeding strains for two generations before lifespan measurements. One day before starting measurements, FUDR was applied to seeded plates at 10 µM to prevent progeny production.

**Analysis of SIR-2.1 protein levels in *C. elegans*.** Protein was prepared from synchronous nematode cultures (L4 larvae and young adults) raised on *E. coli* OP50 or RNAi bacteria for two generations. Western blots were performed with anti-actin monoclonal antibodies (Santa-Cruz Biotechnology) and an anti-SIR-2.1 polyclonal antibody (provided by A. Gartner<sup>34</sup>). For all assays, 3–5 replicate worm cultures were used.

**Neuroprotection assays in *C. elegans*.** To test for sir-2-mediated protection from expanded polyglutamines (polyQs), we crossed GA919 (*geln3* dissociated from *dyf-?(wu250)*) to strains carrying integrated polyQ arrays. These polyQ strains co-express the first 57 amino acids of human huntingtin with either 19 or 128 Gln residues fused to cyan fluorescent protein and expressed from the *mec-3* promoter, and YFP expressed from the *mec-7* promoter in touch-receptor neurons<sup>24</sup>. The response to touch at the tail was tested as previously described<sup>24</sup>. Three trials were performed and 150–200 animals were tested per genotype.

**Lifespan analysis in *C. elegans*.** Lifespans of synchronized population cohorts were measured as previously described<sup>28</sup>. FUDR was applied to the plates at 10, 40 or 50 µM (see Supplementary Tables). Lifespan experiments were performed at 20 °C. A small proportion of animals were censored, usually due to uterine rupture, which mainly occurred at mid-adulthood (~day 9–11).

**Statistical analysis of *C. elegans* data.** The statistical significance of effects on lifespan was estimated using the log-rank test, performed using JMP, Version 7 (SAS Institute).

***Drosophila* stocks and maintenance.** *Tubulin-GAL4* and *dSir2<sup>EP2300</sup>* lines were obtained from the Bloomington Stock Center. *dSir2-Myc2* and *dSir2-Myc9* lines were generated by germline transformation. These were outcrossed into white Dahomey (*w<sup>Dah</sup>*). The strains *dSir2<sup>4.5</sup>/SM6B* (ref. 35) and *dSir2<sup>17</sup>/Cyo* (ref. 36), provided by S. Pletcher and J. Rine, were outcrossed into Canton S. All lines were outcrossed at least six times. The presence of the deletion was detected by PCR using the following primers: 149F (5'-AGATATGACATAAGGCAGTGGC-3'), 1427R (5'-TCCCGTTAGCACAAATGATCTTC-3') and 3909R (5'-GAAGGCGG TAGCAATGG TGACAA-3'). Flies were maintained at 25 °C on a 12 h:12 h light:dark cycle at constant humidity.

**Myc-tagged *dSir2*.** The Myc tag was added to RE27621 (Riken) using standard techniques and cloned into pUASP. The construct was microinjected into *w<sup>04</sup>* and the transformant lines *dSir2-Myc2* and *dSir2-Myc9* were recovered. Primers were: Sir5'R2 (5'-CAAGAATTCCAACGAGAATTTTACACAGGTCGTGTG-3'), Sir3'Xba (5'-ATC GAGTCTAGACACTGCTGCTAACTGTCTGGAGG-3') and MYC3'Xba (5'-GAGCT ATCTAGAGGATCCGAGGAGCAGAAGCTGATC-3').

**Lifespan assays in *Drosophila*.** Flies were bred at standard density (~300 flies per 200-ml bottle), allowed to mate for 48 h after emerging (once mated) and then

sorted into ten females per vial (experiments performed at University College London) or 35 per vial on 15% SYA (experiments performed at University of Michigan). Vials were changed every 48 h and deaths per vial were scored until all flies were dead. The numbers of flies used in lifespan assays were: overexpression studies, *n* ≈ 200 (UCL) or *n* ≈ 350 (U. Michigan); dietary-restriction studies, *n* = 100. For the overexpression studies, the fly-food recipes were as follows: SYA (100 g yeast, 50 g sugar, 15 g agar, 30 ml nipagin and, in most trials, 3 ml propionic acid per litre of food); ASG (20 g yeast, 85 g sugar, 10 g agar and 60 g maize per litre of food); ASG<sup>1</sup> (31 g yeast, 124 g sugar, 9 g agar, 53 g cornmeal and 25 ml nipagin per litre of food); 15% SYA (150 g yeast, 150 g sugar, 21 g agar and 15 ml tegosept). For the dietary-restriction trials, the food dilutions used were as follows: 15 g agar, 30 ml nipagin, 3 ml propionic acid, with yeast and sugar both altered to final concentrations of 10 g, 50 g, 100 g, 150 g or 200 g per litre of food. All food was prepared as previously described<sup>27</sup>.

**Genetic crosses in *Drosophila*.** *Tubulin-GAL4/TM3* males were crossed to *dSir2<sup>EP2300</sup>*, *dSir2-Myc2* or *dSir2-Myc9* virgin females, and *dSir2<sup>EP2300</sup>/+*; *tubulin-GAL4/+*, *dSir2-Myc2/+*; *tubulin-GAL4/+* or *dSir2-Myc9/+*; and *tubulin-GAL4/+* females were selected from the progeny. For the controls, *tubulin-GAL4/TM3* males or *dSir2<sup>EP2300</sup>*, *dSir2-Myc2* or *dSir2-Myc9* virgin females were crossed to *w<sup>Dah</sup>* and *dSir2<sup>EP2300</sup>/+*, *tubulin-GAL4/+*, *dSir2-Myc2/+* or *dSir2-Myc9/+* females were selected from the progeny.

**Quantitative reverse transcriptase PCR in *Drosophila*.** RNA was extracted from ten females at 10 days of age using standard techniques and transcribed into cDNA. Four biological replicates were run per genotype, each in triplicate. Samples were normalized to either actin5C or ribosomal protein 49 (RP49). Primers used were: Sir2-4 5'-GCTCTCCACCGTTGTCTGAGGGCC-3' (ref. 3), Sir2-5 5'-GGCGGCAGCTGTGCTGCGATGAG-3' (ref. 3), Actin5CF 5'-CAC ACCAAATCTTACAAAATGTGTGA-3', ActinCR 5'-AATCCGGCCTTGACATG-3', RP49F 5'-ATGACCATCCGCCAGCATCAGG-3' and RP49R 5'-ATCTCCGCCGAGTAAACG-3'.

**Analysis of *dSir2* protein levels.** Protein was extracted from 30 females at 7 days of age. Western blots were performed using antibodies c-myc 9E10 (Santa Cruz Biotechnology), p2E2 (Developmental Studies Hybridoma Bank) and tubulin (Sigma).

***dSir2* deacetylation assays.** Sequences encoding *dSir2* (RE27621) and *dSir2-Myc* were cloned into pET SUMO (Invitrogen) and proteins were purified on HisPur cobalt spin columns (Thermo Scientific). For the Fluor de Lys assay, using the SirT1 Fluorimetric Drug Discovery Kit (Enzo Life Sciences), results presented are the mean ± s.e.m. of three biological replicates. In each biological replicate, samples were run in triplicate. Final concentrations were: resveratrol and suramin, 0.2 mM; NAD<sup>+</sup> 0.1 mM. Deacetylation of native acetyl-histone-H4 peptide was monitored by HPLC<sup>29</sup>. Deacetylation of histone H4 amino-terminal peptide (SGRGKGGKGLGKGA(acetyl-K)RHRC) (Biomatik) was carried out using 500 µM NAD<sup>+</sup>, 100 mM Tris-HCl (pH 8.0), 150 mM NaCl, 0.5 mM dithiothreitol and 0.05% Triton X-100, and monitored by HPLC (Agilent 1100) with an ACE C8-300 150 × 3.0 mm column. The elution profiles were analysed using Chemstation for LC 3D software.

**Statistical analysis of *Drosophila* data.** Survivorships and the response to dietary restriction were compared using the log-rank test and analyses were performed using JMP, Version 7 (SAS Institute).

- Brenner, S. The genetics of *Caenorhabditis elegans*. *Genetics* **77**, 71–94 (1974).
- Sulston, J. & Hodgkin, J. in *The Nematode Caenorhabditis elegans* (ed. Wood, W. B.) 587–606 (Cold Spring Harbor, 1988).
- Kamath, R. et al. Systematic functional analysis of the *Caenorhabditis elegans* genome using RNAi. *Nature* **421**, 231–237 (2003).
- Greiss, S., Hall, J., Ahmed, S. & Gartner, A. C. *C. elegans* SIR-2.1 translocation is linked to a proapoptotic pathway parallel to cep-1/p53 during DNA damage-induced apoptosis. *Genes Dev.* **22**, 2831–2842 (2008).
- Newman, B. L., Lundblad, J. R., Chen, Y. & Smolik, S. M. A *Drosophila* homologue of Sir2 modifies position-effect variegation but does not affect life span. *Genetics* **162**, 1675–1685 (2002).
- Astrom, S. U., Cline, T. W. & Rine, J. The *Drosophila melanogaster* sir2<sup>+</sup> gene is nonessential and has only minor effects on position-effect variegation. *Genetics* **163**, 931–937 (2003).

# Structures of the RNA-guided surveillance complex from a bacterial immune system

Blake Wiedenheft<sup>1,2\*</sup>, Gabriel C. Lander<sup>3\*</sup>, Kaihong Zhou<sup>1,2</sup>, Matthijs M. Jore<sup>4</sup>, Stan J. J. Brouns<sup>4</sup>, John van der Oost<sup>4</sup>, Jennifer A. Doudna<sup>1,2,5,6</sup> & Eva Nogales<sup>1,2,3</sup>

Bacteria and archaea acquire resistance to viruses and plasmids by integrating short fragments of foreign DNA into clustered regularly interspaced short palindromic repeats (CRISPRs). These repetitive loci maintain a genetic record of all prior encounters with foreign transgressors<sup>1–6</sup>. CRISPRs are transcribed and the long primary transcript is processed into a library of short CRISPR-derived RNAs (crRNAs) that contain a unique sequence complementary to a foreign nucleic-acid challenger<sup>7–12</sup>. In *Escherichia coli*, crRNAs are incorporated into a multisubunit surveillance complex called Cascade (CRISPR-associated complex for antiviral defence), which is required for protection against bacteriophages<sup>13,14</sup>. Here we use cryo-electron microscopy to determine the subnanometre structures of Cascade before and after binding to a target sequence. These structures reveal a sea-horse-shaped architecture in which the crRNA is displayed along a helical arrangement of protein subunits that protect the crRNA from degradation while maintaining its availability for base pairing. Cascade engages invading nucleic acids through high-affinity base-pairing interactions near the 5' end of the crRNA. Base pairing extends along the crRNA, resulting in a series of short helical segments that trigger a concerted conformational change. This conformational rearrangement may serve as a signal that recruits a *trans*-acting nuclease (Cas3) for destruction of invading nucleic-acid sequences.

The CRISPR RNA-guided adaptive immune system in *Escherichia coli* K12 consists of eight *cas* genes and a downstream CRISPR locus (Fig. 1a). Cascade is a 405-kDa ribonucleoprotein complex composed of 11 subunits of five functionally essential Cas proteins (one CasA protein, two CasB proteins, six CasC proteins, one CasD protein and one CasE protein) and a 61-nucleotide crRNA<sup>13,14</sup>. Previous structural and biochemical studies have determined the composition and general morphology of the Cascade complex<sup>14</sup>. However, the arrangement of subunits and the mechanism of target recognition remain largely unknown. Using single-particle cryo-electron microscopy (cryo-EM), we determined the structure of Cascade at a resolution of ~8 Å (Fig. 1, Supplementary Fig. 1 and Supplementary Movie 1). This structure provides a detailed description of the subunit organization with sufficient resolution to observe secondary structure elements within each of the 11 protein components and the crRNA.

Overall, Cascade has a sea-horse-shaped architecture with a helical backbone, as suggested by two-dimensional electron microscopy<sup>14</sup>. The backbone is capped at its ends by two prominent features representing the 'head' (CasE) and 'tail' (CasA) of the sea-horse anatomy. The resolution of the cryo-EM reconstruction, together with crystal structures of two individual subunits and previously established subunit stoichiometries, allowed us to delineate the molecular boundaries of all the individual components. The resulting model provides detailed insight into Cascade organization (Fig. 1, Supplementary Fig. 2 and Supplementary Movie 2).

The backbone of Cascade consists of six copies of CasC organized in a helical stack. Integral to the spine, the crRNA lies in a groove on the concave surface of the CasC helix. The extended conformation of the crRNA explains its importance for complex assembly and suggests that it has a structural role as a template for CasC subunit association.

The crRNA is anchored at both ends of the Cascade complex by specific protein–RNA interactions that can be seen in the cryo-EM structure. CasE is the endoribonuclease that specifically binds to a stem-loop in the CRISPR transcript, and cleavage results in a 61-nucleotide crRNA<sup>13,14</sup>. A co-crystal structure of the CasE homologue from *Thermus thermophilus* in complex with the crRNA stem-loop fits with high fidelity into the head structure of the complex<sup>9,11</sup> (Supplementary Fig. 2). After CRISPR cleavage, CasE remains bound to the 3' end of the mature crRNA and the RNA stem-loop protrudes like a 'beak' from the head of the Cascade complex (Fig. 1 and Supplementary Fig. 2). The crRNA loops around the base of CasE and extends ~45 nucleotides along the binding groove in the helical backbone. The 5' end of the crRNA terminates within the tail of the complex, forming a hook-like structure in a pocket between CasC6 (C6, the sixth CasC subunit) and CasA (Fig. 1b). CasD is adjacent to this interface, sits at the midpoint of CasA and makes extensive contacts with the neighbouring domain of C6 (Fig. 1).

The two CasB subunits form an elongated dimer positioned along the inner surface of the crRNA–CasC spine, connecting the head (CasE) and tail (CasA) of the Cascade complex. CasB1 sits next to the head, and has limited interactions with CasE and the first two CasC subunits (C1 and C2). The CasB2 subunit makes similar contacts with CasC subunits C3 and C4. The extended conformation of the CasB dimer creates a deep cleft that cradles the 3' half of the crRNA spacer sequence (Fig. 1).

The three-dimensional structure of Cascade reveals how six identical CasC polypeptides assemble into an asymmetric helix that is programmed to terminate at C6. The first five CasC subunits are structurally similar, forming a right-handed helix with a pitch of 135 Å (Fig. 2a). However, this symmetry is perturbed between C5 and C6 owing to the interaction of C6 with the hook-like structure at the 5' end of the crRNA (Fig. 2b). This interaction results in a ~160° rotation of the distal domain of C6 (Fig. 2). This rotation flips the distal domain out of the vertical axis of the CasC helix, breaking the helical arrangement. CasD and CasA stabilize this distinct structure and orientation of C6. The flipped-out conformation of the distal domain in C6 results in a larger gap between the C5 and C6 subunits, exposing a segment of crRNA in the 5' region of the spacer sequence.

Cascade engages invading nucleic acids with high affinity when they bear sequence complementary to the 5' end of the crRNA spacer sequence<sup>15,16</sup> (the 'seed' sequence: nucleotides 1–5, 7–8). Bacteriophages containing a single-nucleotide mutation in the seed region escape Cascade-mediated immunity, whereas point mutations outside the

<sup>1</sup>Howard Hughes Medical Institute, University of California, Berkeley, California 94720, USA. <sup>2</sup>Department of Molecular and Cell Biology, University of California, Berkeley, California 94720, USA. <sup>3</sup>Life Sciences Division, Lawrence Berkeley National Laboratory, Berkeley, California 94720, USA. <sup>4</sup>Laboratory of Microbiology, Department of Agrotechnology and Food Sciences, Wageningen University, Dreijenplein 10, 6703 HB Wageningen, The Netherlands. <sup>5</sup>Department of Chemistry, University of California, Berkeley, California 94720, USA. <sup>6</sup>Physical Biosciences Division, Lawrence Berkeley National Laboratory, Berkeley, California 94720, USA.

\*These authors contributed equally to this work.



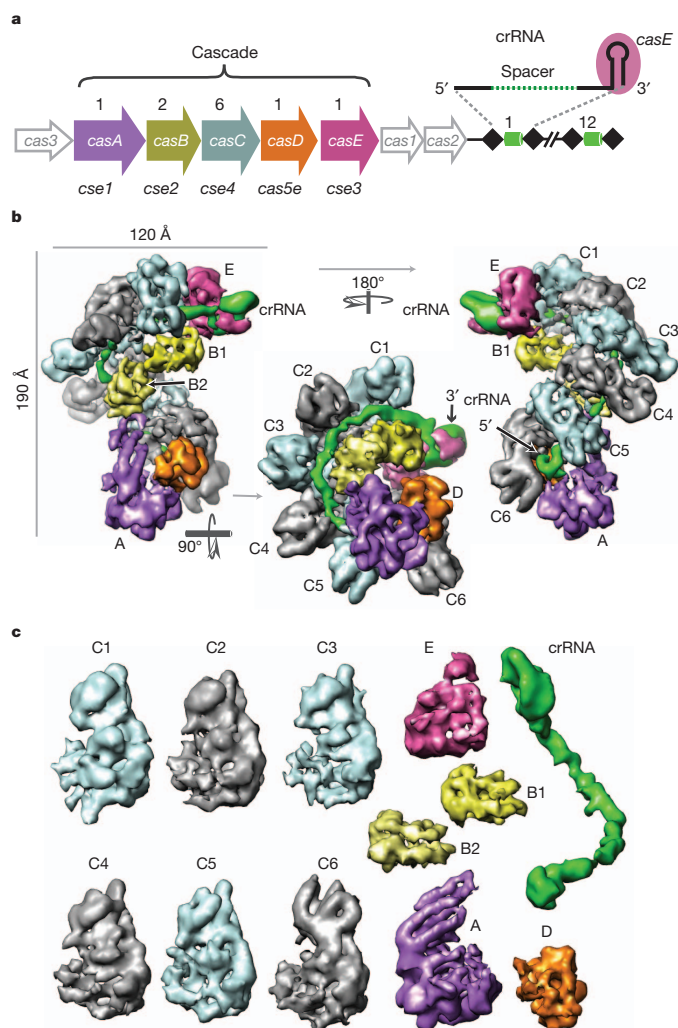


**Figure 1 | Structure of the Cascade complex from *E. coli*.** **a** The CRISPR system in *E. coli* K12 (Cse-type) consists of eight *cas* genes and a downstream CRISPR locus. *casA* to *casE* are members of large gene families, referred to as *cse1*, *cse2*, *cse4*, *cas5e* and *cse3*, respectively<sup>28,29</sup>. The CRISPR consists of a series of 29-nucleotide repeats (black diamonds) separated by 32-nucleotide spacer sequences (green cylinders). CasE (magenta) is an endoribonuclease that specifically binds to a stable stem-loop in the CRISPR RNA repeat and cleaves 8 nucleotides away from the spacer sequence in the 5' direction<sup>9,11,14</sup>. **b**, Cascade assembles into a sea-horse-shaped architecture where the crRNA (green) is positioned along a helical arrangement of six CasC subunits (C1–C6). The helical spine is capped at its ends by two prominent features that represent the head (E, CasE) and tail (A, CasA) of the sea-horse anatomy. D, CasD. **c**, Cascade consists of unequal numbers of Cas proteins and a crRNA (CasA<sub>1</sub>B<sub>2</sub>C<sub>6</sub>D<sub>1</sub>E<sub>1</sub>crRNA<sub>1</sub>). The first five CasC subunits (C1–C5) are structurally similar, whereas CasC6 is distinct. B1, CasB1; B2, CasB2.

seed region do not facilitate escape<sup>15</sup>. Despite these observations, little is known about the mechanism of target binding and the extent to which base pairing occurs between the crRNA and a target sequence. To address these issues, we determined the structure of Cascade bound to a 32-nucleotide single-stranded RNA (ssRNA) that is complementary to the spacer sequence of the crRNA. Although Cascade is thought to target DNA, it has also been shown to bind ssRNA targets with high affinity. *In vitro*, Cascade makes specific and nonspecific interactions with double-stranded DNA substrates but interacts with RNA in a strictly sequence-specific fashion<sup>13,14</sup>. We chose a ssRNA substrate to achieve maximal target site occupancy and sample homogeneity. Notably, RNA and DNA targets induce similar structural changes in the Cascade complex as detected by partial proteolysis (Supplementary Fig. 3).

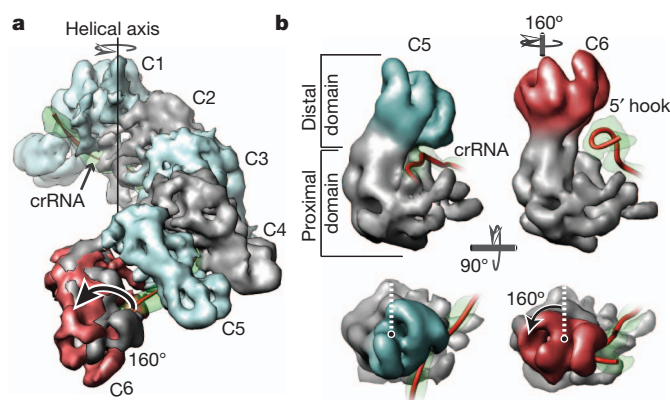


**Figure 2 | Programmed capping of the CasC helix.** **a**, C1–C5 form a right-handed helix with a pitch of 135 Å. The two domains of each CasC subunit are referred to as proximal and distal, relative to the helical axis of the CasC subunits. The different conformation of C6 (red) relative to the other CasC subunits interrupts the helical symmetry (black arrow). **b**, The crRNA is positioned along a contiguous groove on the concave surface of the C1–C5 helix. The 5' end of the crRNA forms a hook-like structure that interacts with C6. This interaction correlates with the distinct conformation of C6 and the termination of the helix. Although the proximal domains of C5 and C6 have the same orientation, the distal domain of C6 is rotated by ~160° relative to the other CasC subunits (black arrow). The centre of rotation is indicated by a black dot.

The ~9 Å target-bound structure maintains the sea-horse morphology observed for the unbound complex, in which the CasC subunits can be superimposed on the unbound structure (Fig. 3a and Supplementary Fig. 4). However, examination of the other subunits reveals several significant differences that occur on target binding (Fig. 3b). The width of the crRNA density approximately doubles along the entire length of the spacer sequence, suggestive of duplex formation. Strikingly, however, the crRNA and target RNA strands do not form one contiguous double-stranded helix. Instead, we observe density consistent with five short duplex segments, each accommodating four or five base pairs of double-stranded RNA (Fig. 3b–e). The helical segments are connected by short (1–2-nucleotide) non-helical regions that seem to be the contact sites for individual CasC subunits (Fig. 3e).

In addition to changes in the RNA, we observed a concerted conformational change in the locations and orientations of CasE, CasB and CasA. CasE remains bound to the 3' crRNA stem-loop, and target binding results in a clockwise rotation (~15°) consistent with a shortening of the crRNA spacer (Fig. 3b). This motion is coupled with movement of the CasB dimer, which forms a protein bridge between the head (CasE) and the tail (CasA) of the complex (Supplementary Movies 3 and 4). The two CasB subunits move ~17 Å along the crRNA binding groove, towards the tail. CasB2 interacts with a four-helix bundle in CasA, inducing a ~30° rotation of CasA. This rotation is centred around CasD, which functions as a hinge that connects CasA to C6. The distinct orientation of C6 relative to C1–C5 is conserved in the target-bound Cascade complex (Fig. 3c, d). However, duplex formation on target binding seems to alter the interaction between C6 and the 5' hook. Base pairing in the crRNA spacer is concomitant with a disruption of the hook-like structure at the 5' end of the crRNA and results in a decrease in resolvable density for the distal domain of C6 (Fig. 3c, d and Supplementary Movie 5).

The target-bound structure of Cascade reveals segments of density along the length of the crRNA spacer that accommodate short regions of double-stranded helix. This structural observation indicates that the entire spacer sequence is available for base pairing to a complementary target sequence. However, previous genetic and biochemical assays have identified a preferred high-affinity binding site in the 5' seed region of the crRNA that is essential for phage protection<sup>15</sup>. To test the relative binding affinities of discrete regions of the crRNA, we

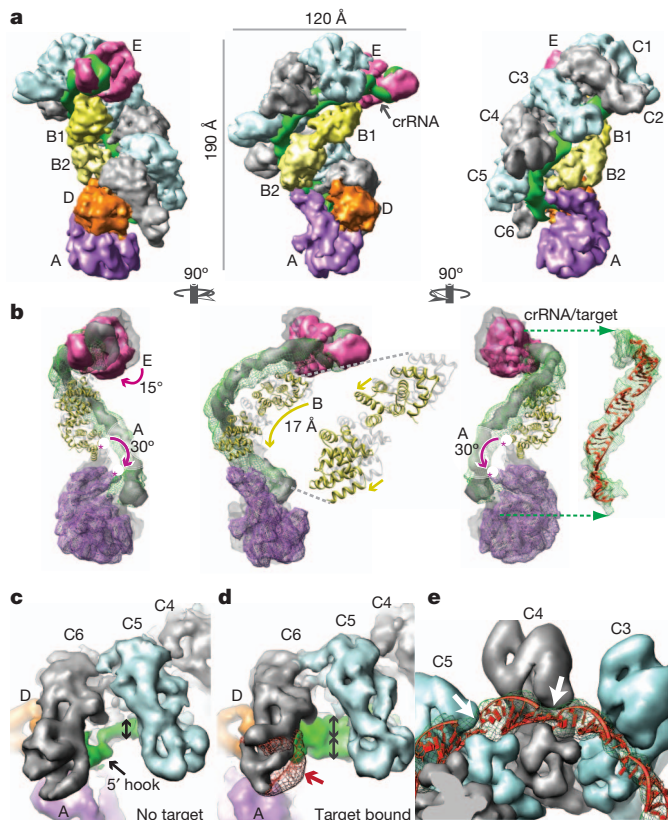


**Figure 3 | Target binding triggers a concerted conformational change.**

**a**, Structure of Cascade bound to a 32-nucleotide target RNA complementary to the crRNA spacer sequence, at a resolution of  $\sim 9$  Å. **b**, Removing the CasC subunits reveals significant structural differences between the unbound and target-bound structures. CasE, CasA and the crRNA from the unbound structure are shown as grey volumes. The same subunits from the target bound complex are shown in magenta, green mesh and purple mesh, respectively. Models of the CasB crystal structure are shown docked into the cryo-EM map before (grey) and after (yellow) target binding. Four or five base pairs of double-stranded RNA (red) fit with high fidelity into the crRNA density. On target binding, CasE rotates by  $\sim 15^\circ$  (magenta arrow), both CasB subunits move  $\sim 17$  Å along the concave surface of the CasC backbone (yellow arrow) and CasA rotates by  $\sim 30^\circ$  (purple arrow). The purple asterisks indicate the positions of the four-helix bundle on CasA before and after target binding. **c**, In the unbound structure, CasC6 is rotated out of the CasC helix, exposing the 5' region of the crRNA (double-headed arrow indicates density for the single-stranded crRNA). **d**, Additional density corresponding to the target nucleic acid is clearly visible in the target-bound complex (double-headed arrows). Base pairing in the crRNA spacer disrupts the hook-like structure at the 5' end of the crRNA, and a difference map reveals a significant loss of resolvable density in the distal domain of C6 following target binding (red mesh and arrow). **e**, The short segments of double-stranded helices are connected by short, non-helical regions located at pinch points of the CasC subunits (white arrows).

designed a series of 16-nucleotide target DNAs that tile across the crRNA in 8-nucleotide steps (Supplementary Fig. 5). Using native gel mobility shift assays, we observed high-affinity interactions for targets that include the seed region, and that binding affinities decrease with increasing steps in the 3' direction (Supplementary Fig. 5). This indicates that each portion of the crRNA spacer is accessible for target binding, but that the unique structural context of the 5' region of the crRNA results in a higher binding affinity for this region. A high-affinity seed binding site, of approximately the same length, has also been observed in other gene silencing systems<sup>16,17</sup>. In eukaryotes, Argonaute proteins enhance target recognition by pre-ordering the microRNA seed sequence in a helical configuration, and we speculate that Cascade may use a similar mechanism<sup>17</sup>.

Overall, our data suggest a model in which Cascade-mediated surveillance initially relies on high-affinity binding to the seed region of

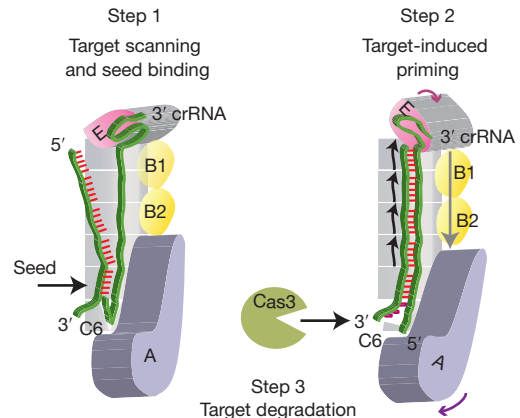


**Figure 4 | A model for pathogen surveillance and signalling by Cascade.**

Efficient surveillance and detection of invading nucleic acids is mediated by base pairing in the seed sequence (nucleotides 1–5, 7–8) of the crRNA<sup>15</sup>. Duplex formation may proceed in the 3' direction (four curved black arrows), resulting in a series of short helical duplexes that shorten the crRNA; this in turn causes a concerted conformational change in CasA, CasB and CasE (coloured arrows) that coincides with a disruption of the 5' hook and results in a decrease in resolvable density for the distal domain of C6. Cascade binds single-stranded and double-stranded substrates. Here we depict the target as a single strand for simplicity.

the crRNA (Fig. 4). Following a seed match, duplex formation then proceeds in the 3' direction along the length of the crRNA in increments of four or five base pairs. These helical segments reduce the overall length of the crRNA, triggering the concerted conformational change that may serve as a signal to recruit Cas3 for target destruction (Fig. 4 and Supplementary Movies 3, 4 and 5).

## METHODS SUMMARY

**Cascade preparation.** Proteins of the CRISPR system in *E. coli* (CasA–E) and the synthetic CRISPR RNA were co-expressed in *E. coli* BL21(DE3). Cascade was affinity-purified on Strep-Tactin Superflow Plus resin (Qiagen) using an amino-terminal Strep-II tag on the CasB subunit. The Strep-II peptide was removed from CasB by cleavage with PreScission protease, and the complex was further purified by gel filtration. The purified protein was used for native gel mobility shift assays using standard methods.

**Cryo-EM and image analysis.** Purified complexes were applied to glow-discharged C-flats (Protochips Inc.), blotted and plunged into liquid ethane. Data were acquired using a Tecnai F20 Twin transmission electron microscope at  $20\text{ e}^- \text{Å}^{-2}$  on a Gatan  $4,000 \times 4,000$ -pixel charge-coupled-device camera using the LEGION data collection software<sup>18</sup>. Data preprocessing was performed using functionalities within the APPION electron microscopy processing environment<sup>19</sup>.

The contrast transfer function (CTF) of each image was estimated during data collection using ACE2 and CTFFIND<sup>20</sup>. Particles were initially selected using a difference-of-Gaussians particle picker, extracted using a box size of  $280 \times 280$  pixels, and classified two dimensionally using the IMAGIC package<sup>21–23</sup>. The resulting reference-free class averages were used for template-based automatic particle selection<sup>24</sup>. Three-dimensional maps were calculated using an iterative projection-matching approach with libraries from the EMAN2 and SPARX software packages<sup>25,26</sup>. Volume segmentation, docking and visualization of molecular models were performed using CHIMERA<sup>27</sup>.

**Full Methods** and any associated references are available in the online version of the paper at [www.nature.com/nature](http://www.nature.com/nature).

Received 7 May; accepted 27 July 2011.

- Barrangou, R. *et al.* CRISPR provides acquired resistance against viruses in prokaryotes. *Science* **315**, 1709–1712 (2007).
- Garneau, J. E. *et al.* The CRISPR/Cas bacterial immune system cleaves bacteriophage and plasmid DNA. *Nature* **468**, 67–71 (2010).
- Andersson, A. F. & Banfield, J. F. Virus population dynamics and acquired virus resistance in natural microbial communities. *Science* **320**, 1047–1050 (2008).
- Bolotin, A., Quinquis, B., Sorokin, A. & Ehrlich, S. D. Clustered regularly interspaced short palindromic repeats (CRISPRs) have spacers of extrachromosomal origin. *Microbiology* **151**, 2551–2561 (2005).



5. Jansen, R., van Embden, J. D. A., Gaastra, W. & Schouls, L. M. Identification of genes that are associated with DNA repeats in prokaryotes. *Mol. Microbiol.* **43**, 1565–1575 (2002).
6. Mojica, F. J., Diez-Villasenor, C., Garcia-Martinez, J. & Soria, E. Intervening sequences of regularly spaced prokaryotic repeats derive from foreign genetic elements. *J. Mol. Evol.* **60**, 174–182 (2005).
7. Carte, J., Wang, R., Li, H., Terns, R. M. & Terns, M. P. Cas6 is an endoribonuclease that generates guide RNAs for invader defense in prokaryotes. *Genes Dev.* **22**, 3489–3496 (2008).
8. Deltcheva, E. *et al.* CRISPR RNA maturation by trans-encoded small RNA and host factor RNase III. *Nature* **471**, 602–607 (2011).
9. Gesner, E. M., Schellenberg, M. J., Garside, E. L., George, M. M. & MacMillan, A. M. Recognition and maturation of effector RNAs in a CRISPR interference pathway. *Nature Struct. Mol. Biol.* **18**, 688–692 (2011).
10. Haurwitz, R. E., Jinek, M., Wiedenheft, B., Zhou, K. & Doudna, J. A. Sequence- and structure-specific RNA processing by a CRISPR endonuclease. *Science* **329**, 1355–1358 (2010).
11. Sashital, D. G., Jinek, M. & Doudna, J. A. An RNA-induced conformational change required for CRISPR RNA cleavage by the endonuclease Cse3. *Nature Struct. Mol. Biol.* **18**, 680–687 (2011).
12. Wang, R., Preamplume, G., Terns, M. P., Terns, R. M. & Li, H. Interaction of the Cas6 ribonuclease with CRISPR RNAs: recognition and cleavage. *Structure* **19**, 257–264 (2011).
13. Brouns, S. J. *et al.* Small CRISPR RNAs guide antiviral defense in prokaryotes. *Science* **321**, 960–964 (2008).
14. Jore, M. M. *et al.* Structural basis for CRISPR RNA-guided DNA recognition by Cascade. *Nature Struct. Mol. Biol.* **18**, 529–536 (2011).
15. Semenova, E. *et al.* A crRNA seed sequence governs CRISPR interference. *Proc. Natl Acad. Sci. USA* **108**, 10098–10103 (2011).
16. Wiedenheft, B. *et al.* RNA-guided complex from a bacterial immune system enhances target recognition through seed sequence interactions. *Proc. Natl Acad. Sci. USA* **108**, 10092–10097 (2011).
17. Parker, J. S., Parizotto, E. A., Wang, M., Roe, S. M. & Barford, D. Enhancement of the seed-target recognition step in RNA silencing by a PIWI/MID domain protein. *Mol. Cell* **33**, 204–214 (2009).
18. Suloway, C. *et al.* Automated molecular microscopy: the new Leginon system. *J. Struct. Biol.* **151**, 41–60 (2005).
19. Lander, G. C. *et al.* Appion: an integrated, database-driven pipeline to facilitate EM image processing. *J. Struct. Biol.* **166**, 95–102 (2009).
20. Mindell, J. A. & Grigorieff, N. Accurate determination of local defocus and specimen tilt in electron microscopy. *J. Struct. Biol.* **142**, 334–347 (2003).
21. Voss, N. R., Yoshioka, C. K., Radermacher, M., Potter, C. S. & Carragher, B. DoG Picker and TiltPicker: software tools to facilitate particle selection in single particle electron microscopy. *J. Struct. Biol.* **166**, 205–213 (2009).
22. Ludtke, S. J., Baldwin, P. R. & Chiu, W. EMAN: semiautomated software for high-resolution single-particle reconstructions. *J. Struct. Biol.* **128**, 82–97 (1999).
23. van Heel, M., Harauz, G., Orlova, E. V., Schmidt, R. & Schatz, M. A new generation of the IMAGIC image processing system. *J. Struct. Biol.* **116**, 17–24 (1996).
24. Roseman, A. M. FindEM—a fast, efficient program for automatic selection of particles from electron micrographs. *J. Struct. Biol.* **145**, 91–99 (2004).
25. Tang, G. *et al.* EMAN2: an extensible image processing suite for electron microscopy. *J. Struct. Biol.* **157**, 38–46 (2007).
26. Hohn, M. *et al.* SPARX, a new environment for Cryo-EM image processing. *J. Struct. Biol.* **157**, 47–55 (2007).
27. Goddard, T. D., Huang, C. C. & Ferrin, T. E. Visualizing density maps with UCSF Chimera. *J. Struct. Biol.* **157**, 281–287 (2007).
28. Haft, D. H., Selengut, J., Mongodin, E. F. & Nelson, K. E. A guild of 45 CRISPR-associated (Cas) protein families and multiple CRISPR/Cas subtypes exist in prokaryotic genomes. *PLoS Comput. Biol.* **1**, e60 (2005).
29. Makarova, K. S., Grishin, N. V., Shabalina, S. A., Wolf, Y. I. & Koonin, E. V. A putative RNA-interference-based immune system in prokaryotes: computational analysis of the predicted enzymatic machinery, functional analogies with eukaryotic RNAi, and hypothetical mechanisms of action. *Biol. Direct* **1**, 7 (2006).

**Supplementary Information** is linked to the online version of the paper at [www.nature.com/nature](http://www.nature.com/nature).

**Acknowledgements** We are grateful to the Doudna and Nogales lab members for their reading of this manuscript, and to P. Grob, S. Hill, R. Hall and T. Houweling for technical support. This project was funded by a National Science Foundation grant to J.A.D., a Veni grant to S.J.J.B. (863.08.014) and a NWO Vici grant to J.v.d.O. (865.05.001). G.C.L. is a Damon Runyon Fellow supported by the Damon Runyon Cancer Research Foundation. B.W. is a Howard Hughes Medical Institute Fellow of the Life Sciences Research Foundation. E.N. and J.A.D. are Howard Hughes Medical Institute investigators.

**Author Contributions** M.M.J., S.J.J.B. and J.v.d.O. designed expression constructs. B.W. and K.Z. purified samples. B.W., K.Z., M.M.J. and S.J.J.B. performed assays. B.W. and G.C.L. carried out the cryo-electron microscopy. G.C.L. performed the electron microscopy processing and segmentation analysis. All authors contributed to experimental design, data analysis and manuscript preparation.

**Author Information** The cryo-electron microscopy density maps for Cascade and Cascade bound to a 32-nucleotide target have been deposited at the Electron Microscopy Data Bank under accession numbers 5314 and 5315, respectively. Reprints and permissions information is available at [www.nature.com/reprints](http://www.nature.com/reprints). The authors declare no competing financial interests. Readers are welcome to comment on the online version of this article at [www.nature.com/nature](http://www.nature.com/nature). Correspondence and requests for materials should be addressed to J.A.D. ([doudna@berkeley.edu](mailto:doudna@berkeley.edu)) and E.N. ([enogales@lbl.gov](mailto:enogales@lbl.gov)).



## METHODS

**Cascade preparation.** The Cas proteins (CasA–E) and the synthetic CRISPR RNA were co-expressed in *E. coli* BL21(DE3) cells that were induced with 0.5 mM isopropyl- $\beta$ -D-thiogalactopyranoside at  $D_{600\text{ nm}} = 0.5$  in overnight cultures grown at 16 °C (refs 13, 14). Cells from the overnight expression cultures were collected by centrifugation (5,000g for 10 min). The cell pellet was resuspended in lysis buffer (100 mM Tris, pH 8.0, 300 mM KCl, 1 mM EDTA, 1 mM tris(2-carboxyethyl) phosphine hydrochloride (TCEP) and 5% glycerol), supplemented with protease inhibitors (Roche), and the slurry was sonicated on ice for 2 min in 10-s bursts. The lysate was clarified by centrifugation (22,000g for 20 min) and the complex was affinity-purified on Strep-Tactin Superflow Plus resin (Qiagen) using an N-terminal Strep-II tag on the CasB subunit. The complex was eluted from the resin in 50 ml lysis buffer containing 2.5 mM desthiobiotin. The Strep-II peptide was removed from CasB by cleavage with PreScission protease during dialysis at 4 °C overnight against gel filtration buffer (25 mM Hepes, pH 7.5, 100 mM KCl, 1 mM TCEP). The liberated Strep-II tag was removed using a second Strep-Tactin Superflow Plus column (Qiagen). The protein was concentrated (Amicon) for further purification on a Superose 6 size-exclusion column (GE Healthcare) equilibrated in gel filtration buffer. The target-bound complex was prepared by adding fivefold molar excess of an oligoribonucleotide complementary to the crRNA. The mixture was incubated at 37 °C for 15 min. The unbound oligoribonucleotide was separated from the target-bound complex on a Superdex 200 size-exclusion column (GE Healthcare).

**Cryo-electron microscopy.** Preservation of nucleoprotein complexes in vitreous ice was performed in the same manner for both unbound and target-bound specimens. Aliquots (4  $\mu$ l) of purified sample ( $\sim 1.2\text{ mg ml}^{-1}$ ) were placed onto C-flats (Protochips Inc.) that had been just glow-discharged in a nitrogen atmosphere for 60 s using an Edwards carbon evaporator. Grids were loaded into an FEI Vitrobot whose incubation chamber maintained an environment of 4 °C and 100% humidity. The grids were blotted for 3 s using a blotting offset of  $-1$ , and were then plunged into liquid ethane and stored in liquid nitrogen until being loaded into the electron microscope. Data were acquired using a Tecnai F20 Twin transmission electron microscope operating at 120 keV at a nominal magnification of  $\times 100,000$  (1.15 Å at the specimen level) using low-dose exposures ( $\sim 20\text{ e}^{-}\text{Å}^{-2}$ ) with a randomly set focus ranging from  $-0.8$  to  $-2.5\text{ }\mu\text{m}$ . A total of 2,370 images of unbound Cascade and 1,406 images of target-bound Cascade were automatically recorded on a Gatan  $4,000 \times 4,000$ -pixel charge-coupled-device camera (15- $\mu\text{m}$  pixel size) using the LEGION data collection software<sup>18</sup>.

**Single-particle pre-processing.** All data preprocessing leading to three-dimensional reconstruction was performed using functionalities within the APPION processing environment<sup>19</sup>. Concurrent with data collection, carbon edges were manually masked from the acquired images, and particles were initially extracted automatically using a difference-of-Gaussians particle picker<sup>21</sup>. The contrast transfer function (CTF) was additionally estimated automatically during data collection using both the ACE2 program and the CTFFIND program<sup>20</sup>. Particle image stacks were generated by extracting selected particles with a box size of  $288 \times 288$  (performed with the 'batchboxer' program<sup>22</sup>) from images whose estimated CTF confidence value was greater than 80%. The stack was reduced by a factor of four, and reference-free, two-dimensional classification was performed using iterative multivariate statistical analysis and multireference alignment analysis (MSA–MRA) within the IMAGIC software package<sup>23</sup>. The resulting class averages showing detailed structural information at a high signal-to-noise ratio were selected for use as templates for template-based automatic particle selection using FINDEM<sup>24</sup>, resulting in a total of 498,137 and 389,166 particle selections for the unbound and target-bound particles, respectively. Particles were extracted in the same manner as previously described, and reference-free, two-dimensional classifications were again performed with the MSA–MRA methodology. The resulting gallery of 5,000 class averages was manually curated to remove ice contamination, false positives and damaged Cascade complexes. Another round of MSA–MRA was performed on the resulting 'cleaned' stack, and the resulting class averages were again inspected to remove false or damaged particle selections. Only particles contained in the final set of class averages were re-extracted from phase-flipped micrographs to generate the final stack for the data sets. The particle image stacks, which contained 275,573 and 176,090 particles for the unbound

and target-bound complexes, respectively, were binned by a factor of two to a pixel size of 2.3 Å for three-dimensional reconstructions.

Initial models for three-dimensional reconstruction were determined using a low-resolution SAXS reconstruction<sup>30</sup>. The SAXS reconstruction was low-pass-filtered to a resolution of 60 Å and forward-projected at an angular increment of 15°, and a multireference alignment was performed using the final 5,000 reference-free class averages of each of the Cascade complexes. The aligned class averages were back-projected to generate a new density model, which was then used for another iteration of projection matching. Ten iterations of projection matching at an angular increment of 15° were performed using the EMAN reconstruction software to arrive at the unbound and target-bound Cascade densities, which were used as starting points for refinement using single particles.

**Three-dimensional reconstruction and analysis.** The unbound and target-bound data sets were processed separately, each using their corresponding initial model. Three-dimensional refinements of the starting densities were performed using an iterative projection-matching approach with libraries from the EMAN2 and SPARX software packages<sup>25,26</sup>. Projection matching began at an angular increment of 25°, progressing down to 0.8° over the course of dozens of iterations. The reconstruction algorithm dictated that the reconstruction was only allowed to proceed to the next smaller angular increment once >95% of the particles had a pixel error of less than one pixel. The resolution was estimated by splitting the data set into two separate halves and calculating the Fourier shell correlation between the resulting volumes. The density was conservatively low-pass-filtered to this estimated resolution before proceeding to the next iteration. The estimated resolutions based on the Fourier shell correlation for the unbound Cascade density were 8.8 Å at a correlation of 0.5 and 7.7 Å at a correlation of 0.143. The estimated resolutions based on the Fourier shell correlation for the target-bound Cascade density were 9.2 Å at a correlation of 0.5 and 8.0 Å at a correlation of 0.143.

To dampen predominant low-resolution amplitudes, the density Fourier amplitudes of the two final reconstructed densities were adjusted to match experimental one-dimensional SAXS curves using the SPIDER software package<sup>30</sup>. Segmentation of the densities was performed manually using the 'volume tracer' tool of the UCSF CHIMERA visualization software<sup>27</sup>. UCSF CHIMERA was also used for rigid-body docking of crystal structures into the segmented densities, as well as for generation of all surface renderings of cryo-EM densities. To assess the difference in position of CasC6 relative to the other CasC subunits, helical models of CasC and the RNA were generated by using two components of the iterative helical real-space reconstruction method<sup>31</sup>. Cryo-EM density corresponding to C1–5, as well as their associated nucleic-acid densities, were first segmented from the asymmetric reconstructions. A rough estimate of the axial rise and rotation of the subunits was determined manually, and were used as initial parameters for the 'hsearch\_lorentz' program, which determined the true axial parameters. The 'himpose\_long' program was then used to impose the helical symmetry on the segmented density, generating the helical structure.

**Electrophoretic mobility shift assays.** Binding assays were performed by incubating Cascade with 5' <sup>32</sup>P-labelled single-stranded DNAs. Each reaction included 25 mM HEPES, pH 7.5, 100 mM KCl, 1 mM TCEP, 1% glycerol, 1 mM MgCl<sub>2</sub> and 1 mg ml<sup>-1</sup> transfer RNA. All reactions were incubated for 15 min at 37 °C before electrophoresis on 6% polyacrylamide gels. Gels were dried and exposed using phosphor storage screens, scanned with a phosphorimager (GE Healthcare) and quantified using KALEIDAGRAPH (Synergy software).

**Limited proteolysis.** Preparations of Cascade were annealed to ssRNA or single-stranded DNA substrates complementary to the spacer sequence, spacer plus the 5' handle (self) or spacer with a protospacer-adjacent motif. Limited proteolysis was performed at room temperature (25 °C) in a total reaction volume of 100  $\mu$ l. Each reaction mixture contained 30  $\mu$ M trypsin (Sigma), 3.7  $\mu$ M Cascade, 25 mM Hepes, pH 7.5, 100 mM KCl, 5% glycerol and 1 mM TCEP. Aliquots (20  $\mu$ l) of the reaction were sampled at each time point and added directly to  $\times 5$  SDS-loading buffer at 95 °C for 5 min. Reaction products were separated by sodium dodecyl sulphate polyacrylamide gel electrophoresis using 12% gels.

30. Frank, J. *et al.* SPIDER and WEB: processing and visualization of images in 3D electron microscopy and related fields. *J. Struct. Biol.* **116**, 190–199 (1996).

31. Egelman, E. H. Single-particle reconstruction from EM images of helical filaments. *Curr. Opin. Struct. Biol.* **17**, 556–561 (2007).

# Polyamine sensing by nascent ornithine decarboxylase antizyme stimulates decoding of its mRNA

Leo Kurian<sup>1†\*</sup>, R. Palanimurugan<sup>1\*</sup>, Daniela Gödderz<sup>1†</sup> & R. Jürgen Dohmen<sup>1</sup>

Polyamines are essential organic polycations with multiple cellular functions relevant for cell division, cancer and ageing<sup>1–3</sup>. Regulation of polyamine synthesis is mainly achieved by controlling the activity of ornithine decarboxylase (ODC) through an unusual mechanism involving ODC antizyme<sup>1,4</sup>, the binding of which disrupts homodimeric ODC and targets it for ubiquitin-independent degradation by the 26S proteasome<sup>5</sup>. Whereas mammals express several antizyme genes<sup>6</sup>, we have identified a single orthologue, termed *OAZ1*, in *Saccharomyces cerevisiae*<sup>7</sup>. Similar to its mammalian counterparts, *OAZ1* synthesis is induced with rising intracellular polyamine concentrations, which also inhibit ubiquitin-dependent degradation of the *OAZ1* protein<sup>7</sup>. Together, these mechanisms contribute to a homeostatic feedback regulation of polyamines<sup>1,7,8</sup>. Antizyme synthesis involves a conserved +1 ribosomal frameshifting (RFS) event at an internal STOP codon during decoding of its messenger RNA<sup>6–10</sup>. Here we used *S. cerevisiae OAZ1* to dissect the enigmatic mechanism underlying polyamine regulation of RFS. In contrast with previous assumptions, we report here that the nascent antizyme polypeptide is the relevant polyamine sensor that operates *in cis* to negatively regulate upstream RFS on the polysomes, where its own mRNA is being translated. At low polyamine levels, the emerging antizyme polypeptide inhibits completion of its synthesis causing a ribosome pile-up on antizyme mRNA, whereas polyamine binding to nascent antizyme promotes completion of its synthesis. Thus, our study reveals a novel autoregulatory mechanism, in which binding of a small metabolite to a nascent sensor protein stimulates the latter's synthesis co-translationally.

Our dissection of the elements controlling decoding of *OAZ1* mRNA involving RFS shows that it is negatively regulated within a polyribosome unit by nascent *OAZ1* polypeptide, which serves as the sensor of polyamines in this system (Supplementary Fig. 1). To identify the elements in *OAZ1* mRNA important for polyamine regulation of RFS, we generated constructs that either carried the authentic RFS site bearing a TGA codon or a deletion of a T nucleotide in this STOP codon, yielding an in-frame fusion (Fig. 1)<sup>7</sup>. Expression of all constructs was monitored in a mutant impaired in proteasomal activity to minimize effects of polyamines or the truncations on the stability of *OAZ1* (refs 7 and 11). Polyamine levels and truncations had no significant effects on the abundance of *OAZ1* transcripts (Supplementary Fig. 2). Quantitative western blot analyses were performed to determine 'relative RFS efficiency' by comparing levels for the constructs carrying the RFS site to those of the corresponding in-frame controls. In the absence of added polyamines, the wild-type RFS construct yielded approximately 3% RFS efficiency (Fig. 1a). Addition of 10  $\mu$ M or higher concentrations of the polyamine spermidine to the growth media had no detectable effect on the in-frame control but led to a ~fourfold induction (~13% RFS efficiency) for the RFS construct (Fig. 1a and Supplementary Fig. 3).

Truncations at the 5' end of the *OAZ1* coding sequence had marked effects, yielding RFS efficiencies up to approximately 62%, with a

gradual loss of polyamine regulation. These observations indicated that translation of *OAZ1* mRNA bearing the RFS site is inhibited by sequences close to its 5' end (Fig. 1a). A different scenario was observed for the 3' end of *OAZ1* mRNA, where deletions of 57 or more nucleotides resulted in a complete loss of polyamine regulation (Fig. 1b). In contrast to the 5' deletions, however, the 3' deletions caused RFS rates (~20%) that were only moderately higher than those of spermidine-induced wild-type *OAZ1* (~13%). These findings demonstrated that a segment of the *OAZ1* mRNA downstream of the RFS site is essential for negative regulation at low polyamine levels. Next, we asked whether the effects observed for 5' or 3' truncations were synthetic or epistatic. We observed a loss of polyamine regulation of all constructs bearing deletions at the 5' end when combined with 3' $\Delta$ 150. Both in the absence or presence of externally applied polyamines, RFS rates detected for all of these constructs were remarkably high (~65%), indicating that 5' and 3' truncations had a synthetic effect in eliminating negative regulation of RFS (Fig. 1c). Together these experiments surprisingly revealed that RFS during decoding of *OAZ1* is strongly inhibited by *OAZ1* elements 5' and 3' to the RFS site, both of which are also required to sense polyamines.

To test whether the element provided by the 5' portion of *OAZ1* is an mRNA secondary structure motif, silent mutations were introduced at all possible positions within the first 24 or 51 nucleotides of the *OAZ1* coding sequence. These mutations had no effects on RFS, indicating that mRNA structure motifs in this area are not relevant for polyamine sensing (Supplementary Fig. 4a). To investigate whether instead the encoded polypeptide is mediating the regulation, we caused drastic changes to the polypeptide sequence close to the amino terminus by introducing two frameshift mutations (Fig. 2a). Despite the only small changes to the mRNA sequence, this 'shift of frames' variant (5'SF) had completely lost negative regulation of RFS in the absence of spermidine, indicating that the coding capacity rather than the mRNA structure of the 5' portion of *OAZ1* mRNA is critical for the observed inhibition of RFS. This notion was further supported by an *OAZ1* mutant that showed constitutive inhibition of RFS unresponsive to the addition of polyamines (Supplementary Fig. 5). The underlying mutation was a change of an Ile (I) codon at position 5 to a Phe (F) codon (I5F). Inhibition of RFS was obtained with both Phe codons tested, whereas all other permutations of codon 5 yielding Ile or Leu codons had no effect, showing that the relevant parameter is the encoded amino acid residue rather than specificity for a certain transfer RNA. Together, these findings led to the unexpected conclusion that the *OAZ1* N terminus mediates a negative control of RFS during decoding of *OAZ1* mRNA.

Next we asked whether the N-terminal inhibitory element of *OAZ1* could act independently of the polyamine-regulated element that depends on sequences downstream of the RFS site. Therefore, we generated a set of constructs, in which *OAZ1* variants extending only until 30 nucleotides downstream of the RFS site were fused to the mouse *Dhfr* open reading frame (ORF) (Fig. 2b). The much lower

<sup>1</sup>Institute for Genetics, University of Cologne, Cologne Biocenter, Zùlpicher Strasse 47a, D-50674 Cologne, Germany. <sup>†</sup>Present addresses: Salk Institute for Biological Studies, 10010 North Torrey Pines Road, La Jolla, California 92037-1099, USA (L.K.); Department for Cell and Molecular Biology, Karolinska Institutet, Von Eulers väg 3, S-17177 Stockholm, Sweden (D.G.).

\*These authors contributed equally to this work.

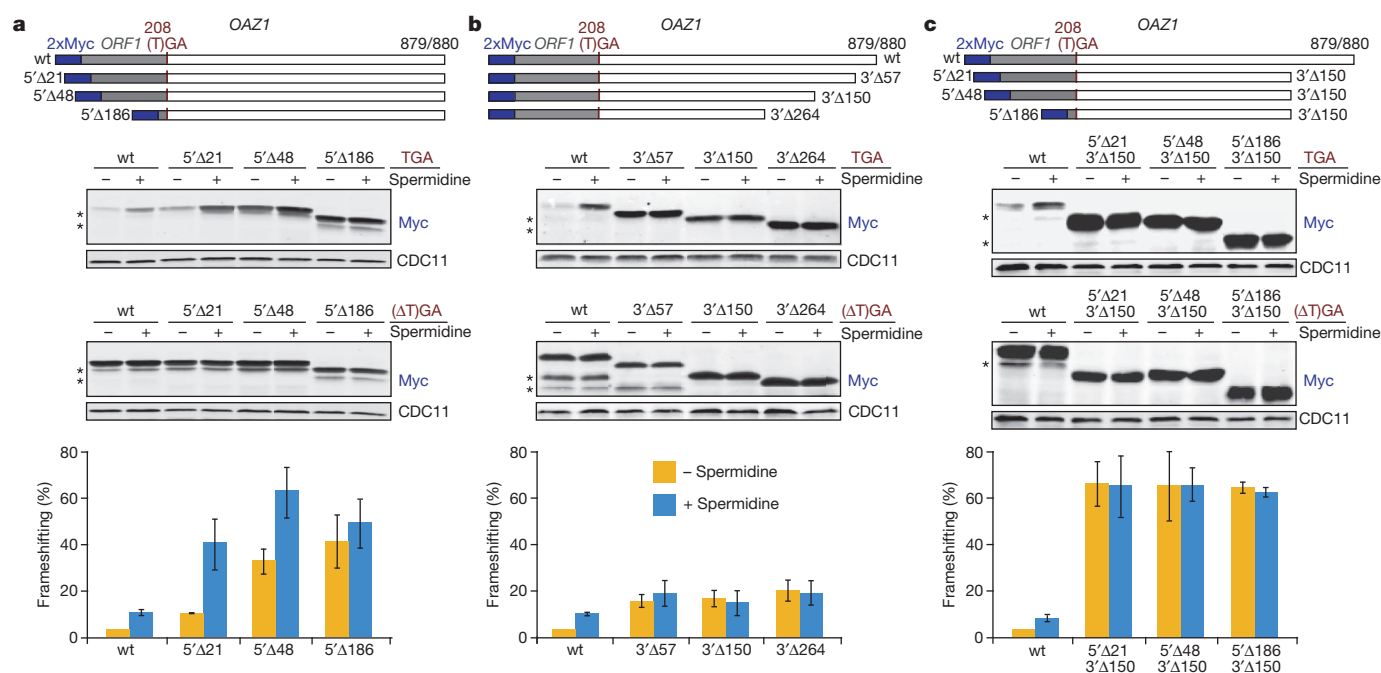


**Figure 1 | Mapping of elements in *OAZ1* that regulate its decoding.**

**a**, Analysis of the effects of *OAZ1* 5' truncations. Top, schematic representation of constructs used, all of which encoded 2×Myc-tagged *OAZ1* variants. Truncations were introduced at the 5' end removing the indicated number of nucleotides starting from the ATG start codon. Two versions of each construct were generated, one that contained the RFS site with the TGA STOP codon, and one in-frame control construct, in which the first nucleotide of this codon was deleted. Middle, western blot analysis of Myc–*OAZ1* levels in yeast *pre1-1* cells expressing constructs either with RFS site ('TGA') or without ('(ΔT)GA'),

grown either in the absence or presence of 10 μM spermidine. CDC11 was simultaneously detected as a loading control. *OAZ1* degradation products are indicated by asterisks. Bottom, relative RFS efficiencies (% *OAZ1* protein obtained with a construct bearing the RFS site relative to the corresponding in-frame construct) calculated from quantification of western blot signals. wt, wild type. **b**, As in panel **a**, but with 3' truncated *OAZ1* constructs. **c**, As in panel **a**, but with *OAZ1* constructs combining the indicated 5' and 3' truncations. See also Supplementary Fig. 1 for an RT–PCR analysis of selected constructs. Error bars, s.d.; *n* = 3.

RFS rates obtained for the construct bearing an intact *ORF1* in comparison to the corresponding 5'Δ48 and 5'SF constructs demonstrated that the N-terminal element is a strong inhibitor of RFS even in the absence of the sequence 3' of the RFS site. This notion was further supported by the observation that the I5F mutation caused an even lower RFS rate in this context. These results therefore clearly demonstrated that the N-terminal inhibitory element can operate independently of the 3' element, and that it is not directly regulated by polyamines. Whereas the exact mechanism by which the N terminus of nascent *OAZ1* inhibits RFS remains to be explored, it is in line with an increasing number of examples of nascent polypeptides that inhibit their own synthesis<sup>12</sup> (see also Supplementary Discussion).

To characterize the polyamine-regulated element, which depends on sequence downstream of the RFS site, we used strategies analogous to the ones applied for the characterization of the upstream element. Whereas silent mutations affecting the 3' end of the *OAZ1* ORF had no effect on RFS (Supplementary Fig. 4b), a mutant version, in which the C-terminal eight amino acids are changed by two frameshift mutations, yielded constitutive RFS similar to constructs bearing carboxy-terminal truncations (Fig. 2a). These observations led us to the striking conclusion that the polyamine-regulated element also resides in the nascent polypeptide. To determine how close to the end of the *OAZ1* ORF this element is located, we individually mutated its last four codons to STOP codons (Fig. 3a). Whereas mutation of the last two codons had no effect on the decoding efficiency, mutating the third (9stop) or the fourth (12stop) codon from the C terminus resulted in constitutive RFS. These results indicated that residues very close to the *OAZ1* C terminus are critically important for the function of the polyamine-responsive element. Perturbation of this element results in constitutive RFS with an efficiency that is only slightly higher than that of wild-type *OAZ1* upon polyamine induction. We note that drastic depletion of cellular polyamines leads to a reduction in translation

and RFS also for *OAZ1* constructs lacking these elements, indicating that translation across the RFS site shows an additional sensitivity to very low concentrations of polyamines (see Supplementary Discussion).

The experiments described so far revealed the remarkable finding that RFS during decoding of *OAZ1* mRNA is under negative control by distinct elements within the *OAZ1* polypeptide. Their inactivation resulted in an up to 20-fold increase of RFS at low polyamine levels (Fig. 1c). The observation that residues very close to the C terminus of *OAZ1* polypeptide are required for an inhibitory effect on decoding of the *OAZ1* mRNA was surprising because this sequence emerges from the ribosome only after the RFS event. This raised the possibility that the *OAZ1* polypeptide influences *OAZ1* decoding *in trans*, that is, after its release from the ribosome. Co-expression of an *OAZ1* in-frame construct, however, had no effect on the decoding of an RFS reporter construct demonstrating that *OAZ1* protein does not inhibit RFS *in trans* (Supplementary Fig. 6). These results indicated that the elements residing in the nascent *OAZ1* polypeptide inhibit RFS *in cis* within the context of an *OAZ1* mRNA–polyribosome complex. To determine whether there is a correlation of the association of nascent *OAZ1* polypeptides with ribosomes and the efficiency of RFS, ribosomal complexes were affinity-purified from a strain bearing a Flag-tagged version of ribosomal subunit RPL25 (ref. 13). Strikingly, higher levels of incompletely synthesized Myc–*OAZ1* polypeptides of various sizes were associated with ribosomes in cells grown in the absence of polyamines than in those grown in their presence (Fig. 3b). This result illustrated that polyamine induction of RFS promotes completion of *OAZ1* synthesis and its release from the ribosomes. Consistent with this notion, either high or low levels of *OAZ1* peptides were pulled down with ribosomes, respectively, when mutants were used that either repressed or induced RFS constitutively (I5F or cRFS, respectively, in Fig. 3b). We conclude that inhibition of RFS results in a





was added to the cultures, OAZ1 levels obtained with the RTI construct were induced approximately twofold, whereas levels remained unchanged for the wild-type construct. Introduction of the 3' SF mutation described above, which impairs the polyamine-responsive element, also resulted in a loss of polyamine regulation of the RTI in-frame construct, with OAZ1 levels in the absence of polyamines rising to those observed in their presence (Fig. 3c). We conclude that the same element in nascent OAZ1 is conferring polyamine regulation to the RFS reporter and the RTI in-frame construct. When polyamine concentration is low, this element, which requires a relatively low ribosome density, can therefore either be activated by translational pausing caused by the RFS site or, even though not with full efficiency, by reduced translation initiation rates (see also Supplementary discussion).

Our observation that regulation of RFS during OAZ1 decoding involves the nascent OAZ1 peptide prompted us to ask whether the OAZ1 protein senses polyamines directly. We previously observed that high polyamine levels inhibit ubiquitin-dependent degradation of OAZ1 protein. It was also noted that OAZ1 has homology to the polyamine-binding enzyme spermidine/spermine-acetyltransferase (SSAT)<sup>7</sup>, which was supported by structural similarity between antizyme and acetyltransferases, including SSAT<sup>16</sup>. To test for polyamine binding to OAZ1, we developed a filtration-based assay using 6His-OAZ1 purified from *Escherichia coli* and radiolabelled spermidine or spermine. 6His-OAZ1 was incubated at approximately equimolar concentration together with polyamines followed by centrifugal ultrafiltration. 6His-OAZ1 showed a strong retention of spermidine (~50%) and spermine (84%), whereas neither material from mock preparations (Supplementary Fig. 8) nor several control proteins showed any values significantly above background (Fig. 4). We conclude that OAZ1 specifically binds to both polyamines, apparently with a higher affinity for spermine. To address whether polyamine binding is a conserved property of antizyme, we produced human AZ1 as a fusion to maltose binding protein (MBP). In contrast to the MBP control, human MBP-AZ1 specifically bound spermidine with similar efficiency as yeast OAZ1, indicating that polyamine sensing by antizyme is conserved from yeast to humans (Supplementary Fig. 9).

What might be the mechanism by which binding of polyamines to nascent OAZ1 regulates its synthesis? The element in the C-terminal portion of nascent OAZ1 could arrest translation during elongation or at the termination step. The former would be reminiscent of the regulated elongation arrest caused by a specific sequence in nascent *E. coli* SecM (secretion monitor) protein<sup>17</sup>. The observation that residues so close to the OAZ1 C terminus that they must still be in the ribosome exit tunnel are critical for this arrest to occur, indicates that interactions between these residues with inner surfaces of the ribosome contribute to the arrest, similar to what has been shown for SecM<sup>18</sup>. Based on our findings, we propose a model (Supplementary Fig. 1), wherein nascent OAZ1

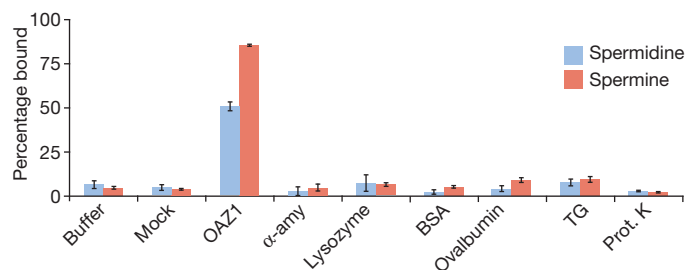


**Figure 4 | Polyamines bind to OAZ1 protein.** Shown are the results of measurements that determined the retention of radiolabelled polyamines during ultrafiltration. Retention of [<sup>3</sup>H]-spermidine or [<sup>14</sup>C]-spermine by 6His-OAZ1 from three independent preparations was compared to that observed with buffer only, with material from Ni-NTA mock preparations from an *E. coli* strain not expressing 6His-OAZ1, as well as with *Bacillus subtilis*  $\alpha$ -amylase ( $\alpha$ -amy), chicken egg lysozyme, bovine serum albumin (BSA), ovalbumin, thyroglobulin (TG), and proteinase K (each at 10  $\mu$ M). Error bars, s.d.;  $n = 3$ .

assumes a conformation that, together with the residues located inside the exit tunnel, promotes an arrest of translation at low cellular polyamine concentrations, whereas binding of polyamines to OAZ1 prevents formation of this inhibitory conformation. We found that various mutations downstream of the RFS site inactivated the polyamine-regulated element (Supplementary Fig. 10), indicating that the downstream inhibitory element involves a larger structural domain. Formation of this element apparently requires translational pausing at the RFS site (Supplementary discussion). In our model, the N-terminal inhibitory element and the RFS site are cooperating to achieve the required translational pausing resulting in low ribosome density.

A key finding of our study is that ribosome-associated nascent OAZ1 polypeptide acts as a direct sensor of intracellular polyamine concentrations. Therefore, this system provides an intriguing novel type of co-translational control mechanism, in which a metabolite binds to a nascent, ribosome-associated autoregulatory sensor protein that regulates the decoding of its own mRNA. Similar types of co-translational mechanisms are likely to control the expression of other autoregulatory proteins, including metabolic enzymes. One possible example is the expression of mammalian SSAT, an enzyme involved in polyamine catabolism, which is known to bind polyamines (see above). Translation of SSAT mRNA is induced by polyamines and depends on sequences close to both ends of its ORF<sup>19</sup>. Polyamine binding to nascent SSAT might regulate its expression co-translationally, similar to what we observed for OAZ1, except that RFS is not involved. Beyond the control of ODC, antizyme was reported to have multiple additional cellular targets with relevance to cancer, such as the polyamine uptake system, Aurora A kinase, and the anti-apoptotic protein DeltaNp73 (refs 2, 20–22). The identification of antizyme as a polyamine sensor therefore may provide an interesting drug target to simultaneously stimulate downregulation of polyamine synthesis and uptake, as well as downregulation of cell cycle regulators.

## METHODS SUMMARY

**Determination of relative frameshifting efficiency.** *S. cerevisiae* YHI29/1 (pre1-1)<sup>11</sup> (a gift from D. H. Wolf) transformants expressing OAZ1 constructs either with the RFS site or the corresponding in-frame variants (see plasmid table in the Supplementary information) were grown in SD medium supplemented with 10  $\mu$ M spermidine where indicated. RFS efficiency (given in percentage of concentration obtained for the in-frame construct) was calculated as follows. First, steady-state signals obtained for OAZ1 expressed from the corresponding RFS and in-frame constructs as well as for CDC11 were quantified. Second, the OAZ1 levels were normalized for protein loading differences using the corresponding CDC11 values. RFS efficiency was then calculated from the normalized OAZ1 levels obtained with the RFS construct and the corresponding in-frame constructs in at least three independent experiments.

**Ribosome pull-down assay.** To analyse ribosome-associated nascent OAZ1 polypeptides, strain LEY1 expressing RPL25-Flag-6His was used. Extracts from transformants of this strain encoding 2 $\times$ Myc-OAZ1 variants were subjected to anti-Flag pull-down and western blot analysis.

**In vitro polyamine binding assay.** Polyamine binding was assayed with recombinant affinity purified 6His-OAZ1 and [<sup>3</sup>H]-spermidine or [<sup>14</sup>C]-spermine by an ultrafiltration protocol. Purified 6His-OAZ1 (~10  $\mu$ M) was incubated with 10  $\mu$ M spermidine or spermine for 1 h on ice. Unbound polyamines were then separated from bound ones by ultrafiltration. Samples of the filtrate and the retentate were subjected to scintillation counting. The resulting values from at least three independent measurements were used to calculate the percentage of bound polyamines with the formula %C<sub>B</sub> = 100  $\times$  (C<sub>R</sub> - C<sub>F</sub>)/C<sub>R</sub>; where C<sub>F</sub> is the concentration of free polyamines detected in the filtrate, and C<sub>R</sub> the total concentration of soluble polyamines in the retentate.

**Full Methods** and any associated references are available in the online version of the paper at [www.nature.com/nature](http://www.nature.com/nature).

Received 23 August 2010; accepted 27 July 2011.

Published online 7 September 2011.

1. Coffino, P. Regulation of cellular polyamines by antizyme. *Nature Rev. Mol. Cell Biol.* **2**, 188–194 (2001).
2. Wallace, H. M., Fraser, A. V. & Hughes, A. A perspective of polyamine metabolism. *Biochem. J.* **376**, 1–14 (2003).

3. Eisenberg, T. *et al.* Induction of autophagy by spermidine promotes longevity. *Nature Cell Biol.* **11**, 1305–1314 (2009).
4. Hayashi, S., Murakami, Y. & Matsufuji, S. Ornithine decarboxylase antizyme: a novel type of regulatory protein. *Trends Biochem. Sci.* **21**, 27–30 (1996).
5. Murakami, Y. *et al.* Ornithine decarboxylase is degraded by the 26S proteasome without ubiquitination. *Nature* **360**, 597–599 (1992).
6. Ivanov, I. P. & Atkins, J. F. Ribosomal frameshifting in decoding antizyme mRNAs from yeast and protists to humans: close to 300 cases reveal remarkable diversity despite underlying conservation. *Nucleic Acids Res.* **35**, 1842–1858 (2007).
7. Palanimurugan, R., Scheel, H., Hofmann, K. & Dohmen, R. J. Polyamines regulate their synthesis by inducing expression and blocking degradation of ODC antizyme. *EMBO J.* **23**, 4857–4867 (2004).
8. Matsufuji, S. *et al.* Autoregulatory frameshifting in decoding mammalian ornithine decarboxylase antizyme. *Cell* **80**, 51–60 (1995).
9. Rom, E. & Kahana, C. Polyamines regulate the expression of ornithine decarboxylase antizyme *in vitro* by inducing ribosomal frame-shifting. *Proc. Natl Acad. Sci. USA* **91**, 3959–3963 (1994); erratum **91**, 9195 (1994).
10. Rato, C., Amirova, S. R., Bates, D. G., Stansfield, I. & Wallace, H. M. Translational recoding as a feedback controller: systems approaches reveal polyamine-specific effects on the antizyme ribosomal frameshift. *Nucleic Acids Res.* **39**, 4587–4597 (2011).
11. Heinemeyer, W., Kleinschmidt, J. A., Saidowsky, J., Escher, C. & Wolf, D. H. Proteinase yscE, the yeast proteasome/multicatalytic-multifunctional proteinase: mutants unravel its function in stress induced proteolysis and uncover its necessity for cell survival. *EMBO J.* **10**, 555–562 (1991).
12. Tenson, T. & Ehrenberg, M. Regulatory nascent peptides in the ribosomal tunnel. *Cell* **108**, 591–594 (2002).
13. Inada, T. *et al.* One-step affinity purification of the yeast ribosome and its associated proteins and mRNAs. *RNA* **8**, 948–958 (2002).
14. Arava, Y., Boas, F. E., Brown, P. O. & Herschlag, D. Dissecting eukaryotic translation and its control by ribosome density mapping. *Nucleic Acids Res.* **33**, 2421–2432 (2005).
15. Baim, S. B. & Sherman, F. mRNA structures influencing translation in the yeast *Saccharomyces cerevisiae*. *Mol. Cell. Biol.* **8**, 1591–1601 (1988).
16. Hoffman, D. W., Carroll, D., Martinez, N. & Hackert, M. L. Solution structure of a conserved domain of antizyme: a protein regulator of polyamines. *Biochemistry* **44**, 11777–11785 (2005).
17. Nakatogawa, H. & Ito, K. The ribosomal exit tunnel functions as a discriminating gate. *Cell* **108**, 629–636 (2002).
18. Woolhead, C. A., Johnson, A. E. & Bernstein, H. D. Translation arrest requires two-way communication between a nascent polypeptide and the ribosome. *Mol. Cell* **22**, 587–598 (2006).
19. Butcher, N. J., Broadhurst, G. M. & Minchin, R. F. Polyamine-dependent regulation of spermidine-spermine N1-acetyltransferase mRNA translation. *J. Biol. Chem.* **282**, 28530–28539 (2007).
20. Basuroy, U. K. & Gerner, E. W. Emerging concepts in targeting the polyamine metabolic pathway in epithelial cancer chemoprevention and chemotherapy. *J. Biochem.* **139**, 27–33 (2006).
21. Lim, S. K. & Gopalan, G. Antizyme1 mediates AURKAIP1-dependent degradation of Aurora-A. *Oncogene* **26**, 6593–6603 (2007).
22. Dulloo, I., Gopalan, G., Melino, G. & Sabapathy, K. The antiapoptotic DeltaNp73 is degraded in a c-Jun-dependent manner upon genotoxic stress through the antizyme-mediated pathway. *Proc. Natl Acad. Sci. USA* **107**, 4902–4907 (2010).

**Supplementary Information** is linked to the online version of the paper at [www.nature.com/nature](http://www.nature.com/nature).

**Acknowledgements** We thank M. Hochstrasser for comments, D. Richardson for critical reading of the manuscript, and D. H. Wolf for the *pre1-1* strain. L.K. and D.G. were supported by the NRW Graduate School in Genetics and Functional Genomics. This work was supported by a grant from the Deutsche Forschungsgemeinschaft (Do 649/4) to R.J.D.

**Author Contributions** All authors contributed to the design of experiments. L.K. and R.P. generated constructs, performed RFS assays and analysed data. L.K. performed ribosome pull-down experiments. D.G. established expression and purification of 6His-OAZ1. R.P. established and performed polyamine binding assays (with help from D.G.), and performed all experiments in the revision process (Supplementary Figs. 3, 7, 8, 9 and 10). R.P. and R.J.D. wrote the manuscript with contributions from L.K. and D.G.

**Author Information** Reprints and permissions information is available at [www.nature.com/reprints](http://www.nature.com/reprints). The authors declare no competing financial interests. Readers are welcome to comment on the online version of this article at [www.nature.com/nature](http://www.nature.com/nature). Correspondence and requests for materials should be addressed to R.J.D. ([j.dohmen@uni-koeln.de](mailto:j.dohmen@uni-koeln.de)).



## METHODS

**Growth of strains and western blot analysis for determination of RFS efficiency.** Yeast rich (YPD) and synthetic minimal media with 2% dextrose (SD) were prepared as described<sup>7</sup>. YH129/1 (*pre1-1*)<sup>11</sup> transformants expressing OAZ1 variants from the copper-inducible  $P_{CUP1}$  promoter were grown in SD medium supplemented with 100  $\mu$ M  $\text{CuSO}_4$  (ref. 7). Spermidine (Sigma-Aldrich) was added when the precultures were diluted into fresh media. Cells were grown at 30 °C from an attenuation measured at 600 nm ( $D_{600}$ ) of approximately 0.2 until they reached a  $D_{600}$  of 0.6–0.8. Equal amounts of cells were harvested by pelleting them at 4,000g for 5 min. Cell extracts were prepared by boiling the pellets in an appropriate volume of loading buffer (62.5 mM Tris-HCl, pH 6.8, 2% SDS, 1%  $\beta$ -mercaptoethanol, 10% glycerol, and 0.002% bromophenol blue) for 5 min at 100 °C. Extracts from cells corresponding to  $0.5 \times D_{600}$  (~15  $\mu$ g protein) for the in-frame constructs and from  $1.0 \times D_{600}$  (~30  $\mu$ g protein) for the RFS constructs were used for SDS-PAGE and quantitative two-colour western blot analysis using the Odyssey Infrared Imaging System (Li-Cor). Anti-Myc (9B11, Cell Signaling Technology) and anti-haemagglutinin (16B12, HISS Diagnostics) monoclonal antibodies were used for detecting tagged versions of various OAZ1 proteins. Anti-rabbit polyclonal antibody (Santa Cruz Biotechnology) was used to detect CDC11, which served as an internal protein loading control. Western blotting procedure as well as anti-mouse and anti-rabbit secondary antibodies coupled to fluorophores were used as described before<sup>7</sup>.

**Ribosome pull-down assay.** We used a ribosome-tagged strain similar to one described by others<sup>13</sup>. Strain LEY1, which expressed genomically tagged *RPL25-Flag-6His*, is a derivative of YH129/1 generated using the integrative plasmid pLE133. LEY1 transformants expressing *2xMyc-OAZ1* variants were grown from a starting  $D_{600}$  of 0.2 in a volume of 100 ml selective SD medium to a  $D_{600}$  of approximately 0.8. Cells were harvested and resuspended in 600  $\mu$ l of ice cold lysis buffer (20 mM HEPES, pH 7.4, 2 mM  $\text{Mg}(\text{CH}_3\text{COO})_2$ , 100 mM  $\text{KCH}_3\text{COO}$ , 0.5 mM DTT) containing a protease inhibitor mix (complete, EDTA free, from Roche), and lysed with an equal volume of acid-washed glass beads (0.4–0.6 mm diameter) by vortexing five times for 30 s with 1 min intervals on ice. Lysates were clarified by an initial centrifugation at 10,000g for 5 min at 4 °C. The supernatant was again cleared by centrifugation for 20 min at 10,000g at 4 °C. For affinity purification of ribosomes, lysates containing 1 mg of total protein were mixed with an equal volume of ice-cold 2 $\times$  binding buffer (100 mM Tris-HCl pH 7.5, 24 mM  $\text{Mg}(\text{CH}_3\text{COO})_2$ , 1 mM DTT, 1 mM PMSF, 50 U ml<sup>-1</sup> RNasin). To this mix, 100  $\mu$ l of anti-Flag M2-agarose affinity resin (Sigma-Aldrich) was added followed by an incubation for 4 h at 4 °C with end-over-end rotation. The resin was then washed five times with 1 ml of ice-cold washing buffer (50 mM Tris-HCl, pH 7.5, 100 mM KCl, 12 mM  $\text{Mg}(\text{CH}_3\text{COO})_2$ , 1 mM DTT, 1 mM PMSF). After washing, the bound proteins were eluted by incubating the resin in 50  $\mu$ l of washing buffer containing 300  $\mu$ g ml<sup>-1</sup> Flag peptide, and analysed by western blotting.

**Sucrose density gradient fractionation and quantification of OAZ1 mRNA.** Yeast strain LEY1 carrying the plasmid pPM318 was grown in approximately 300 ml of synthetic medium without leucine and uracil containing 200  $\mu$ M  $\text{CuSO}_4$  at 30 °C. Spermidine (10  $\mu$ M) was added to the indicated cultures approximately 3 h before harvesting. Cells were harvested when the cultures reached a  $D_{600}$  of 0.6–0.8. Culture volumes corresponding to 100  $D_{600}$  units were centrifuged at 2,800g for 5 min at 4 °C. Cell pellets were washed once in 5 ml of ice-cold lysis buffer (30 mM HEPES-KOH (pH 7.4), 100 mM  $\text{KCH}_3\text{COO}$ , 30 mM  $\text{Mg}(\text{CH}_3\text{COO})_2$ , 0.5 mM DTT, Protease inhibitor cocktail without EDTA (Roche), 200  $\mu$ g ml<sup>-1</sup> heparin). Cell pellets were resuspended in ice-cold lysis buffer (1 ml final volume) containing 5  $\mu$ l RNasin (Promega). Cells were lysed by vortexing five times for 30 s at full speed in the presence of 500  $\mu$ l 0.5-mm glass beads with 30 s intervals on ice. The lysates were clarified by three 5 min centrifugation steps, first at 5,200g, then at 10,600g, and finally at 20,800g. Extracts present in 450  $\mu$ l of the final supernatant were loaded on top of an 11 ml 10–50% w/v sucrose gradient prepared in ice-cold gradient buffer (30 mM HEPES-KOH (pH 7.4), 50 mM  $\text{KCH}_3\text{COO}$ , 12 mM  $\text{Mg}(\text{CH}_3\text{COO})_2$ , 0.5 mM DTT and Protease inhibitor cocktail without EDTA (Roche)). Polyosomes were separated by centrifugation at 100,000g for 105 min at 4 °C in a Beckman SW40Ti rotor. After the centrifugation, 750  $\mu$ l fractions were collected from the sucrose gradient. Each fraction was mixed with 2.5 volume ice-cold ethanol and kept at –20 °C for 15 h or longer for RNA precipitation. To isolate total RNA from the fractions, they

were centrifuged at 20,800g for 20 min. Supernatants were carefully removed from all the samples and the pellets were dried at room temperature for 15 min. After drying, the pellets were resuspended in 100  $\mu$ l RNase-free water and placed on ice. RNA from each fraction was isolated using Qiagen's RNeasy mini kit. RNA was eluted from each column with 25  $\mu$ l RNase-free water. RNA samples isolated from each fraction were transferred onto ice immediately after elution. Ten microlitre of the eluted RNA samples were used for cDNA synthesis using the High-Capacity cDNA Reverse Transcription kit (Applied Biosystems). *OAZ1* and *TPI1* transcripts from each fraction were quantified by Q-PCR using TaqMan Gene Expression Master Mix (Applied Biosystems) and gene-specific TaqMan probes (Eurogentec).

**Affinity purification of 6His-OAZ1.** A plasmid expressing codon-optimized *6His-OAZ1* was constructed based on the pET11a vector (Merck) to obtain pDG240. *E. coli* strain Rosetta (Merck) was transformed either with pDG240 or the empty pET11a (mock) plasmid. Expression was induced for 4 h at 30 °C with 1 mM IPTG. Cell pellets corresponding to approximately 550  $D_{600}$  units were resuspended in 10 ml binding buffer (50 mM Tris, pH 7.8 at 4 °C). In order to purify 6 $\times$ His-tagged OAZ1, frozen cell pellets were thawed at 25 °C, then 20 mg of lysozyme from chicken egg (Sigma-Aldrich), 2 mg of DNase I (Roche) and protease inhibitor mix (Roche) were added. Lysis was initiated by vortexing six times for 10 s at 25 °C followed by incubation on ice for 45 min. Later, the lysate was clarified by centrifugation at 25,000g for 30 min at 4 °C. Imidazole was added to the supernatant to a final concentration of 20 mM, followed by addition of 250  $\mu$ l of pre-equilibrated Ni-NTA Sepharose (GE healthcare). Binding was carried out by keeping the suspension at 4 °C for 2 h with mild rotation. Unbound material was removed by centrifugation at 200g for 3 min at 4 °C. The beads were washed four times with 10 ml lysis buffer containing 20 mM imidazole. Bound protein was eluted in 350  $\mu$ l lysis buffer containing 250 mM imidazole for 1 h. Protein concentration was determined using the Bradford assay (Bio-Rad).

**Affinity purification of MBP-hAZ1.** A plasmid expressing codon-optimized human AZ1 (hAZ1) as a fusion to maltose binding protein (MBP-hAZ1) was constructed based on the pMAL-c2 vector (New England Biolabs (NEB)) to obtain pJD633. *E. coli* strain Rosetta (Merck) was transformed either with pJD633 or the empty pMAL-c2 plasmid. Expression was induced overnight in Overnight Express Instant TB Medium (Novagen). Cell pellets were frozen in liquid nitrogen and stored at –80 °C. For lysis, pellets were thawed on ice overnight and resuspended in 10 ml binding buffer (50 mM Tris, pH 7.8 at 4 °C). To purify MBP or MBP-hAZ1, 10 mg of lysozyme from chicken egg (Sigma-Aldrich), 1 mg of DNase I (Roche) and protease inhibitor mix (Roche) were added. Lysis was initiated by vortexing six times for 10 s at 25 °C followed by incubation on ice for 45 min. Later, the lysate was clarified by centrifugation at 25,000g for 30 min at 4 °C. Amylose resin (200  $\mu$ l; NEB) equilibrated with binding buffer was added to the supernatant. Binding was carried out by keeping the suspension at 4 °C for 2 h with mild rotation. Unbound material was removed by centrifugation at 200g for 3 min at 4 °C. The beads were washed four times with 5 ml binding buffer. Bound protein was eluted in 350  $\mu$ l binding buffer containing 10 mM maltose for 90 min.

**Polyamine binding assay.** To establish an ultrafiltration-based binding assay, we first tested whether spermidine and spermine passed freely and without retention through low protein binding (10K cutoff) centrifugal filtration devices with modified polyethersulphone membranes (VWR). Samples (100  $\mu$ l) were subjected to centrifugal filtration at 2,500g for 4 min at 4 °C. These conditions yielded a filtrate of approximately 15  $\mu$ l. Samples (10  $\mu$ l) of the filtrate and the retentate were then used to determine the concentration of radioactive polyamines by scintillation counting. Retention of polyamines was 5% or less as shown in Fig. 4. To detect polyamine binding to proteins, purified 6His-OAZ1, MBP-hAZ1, or control proteins were diluted to a final volume of 100  $\mu$ l (~10  $\mu$ M) using binding buffer (50 mM Tris, pH 7.8 at 4 °C) containing 10  $\mu$ M [<sup>3</sup>H]-spermidine (PerkinElmer) or [<sup>14</sup>C]-spermine (GE Healthcare). After 1 h of binding on ice, these samples were analysed by centrifugal filtration and scintillation counting as described above. The percentage of bound polyamines was calculated with the formula  $\%C_B = 100 \times (C_R - C_F)/C_R$ ; where  $C_F$  is the concentration of free polyamines detected in the filtrate, and  $C_R$  the total concentration of soluble polyamines in the retentate. Control proteins used were *B. subtilis*  $\alpha$ -amylase, chicken egg lysozyme, bovine serum albumin, chicken egg ovalbumin, bovine thyroglobulin, and proteinase K (all from Sigma-Aldrich).



# CAREERS

**EUROPEAN UNION** A universal patent system could ease researcher mobility **p.501**

**GRADUATE STUDENTS** Study seeks to reveal career options for aspiring scientists **p.501**

**NATUREJOBS** For the latest career listings and advice [www.naturejobs.com](http://www.naturejobs.com)

IMAGES.COM/CORBIS



## EDUCATION

# Time to teach

*Young scientists want to concentrate on their research, but teaching can bring rewards.*

BY PAUL SMAGLIK

**K**ostas Pagiamtzis's experiences as a student motivated him to be an effective teaching assistant. "I was actually a big critic of teaching assistants when I was an undergraduate," says Pagiamtzis. "I had both really good ones and really bad ones." The bad ones didn't even seem to be trying. Then he had to take on the role himself, while studying for a PhD in electrical and computer engineering at the University of Toronto in Canada. "I thought I'd better not be one of the bad ones", he says. At the time, the University of Toronto had no formal training for teaching assistants.

So Pagiamtzis looked to his adviser, his colleagues and the Internet for advice.

His diligence paid off: Pagiamtzis won three departmental teaching awards and gained interpersonal 'soft skills', such as communication and time management, that prepared him for a career as a microchip designer with Gennum in Burlington, Canada.

Making the time and effort to teach can be difficult for young scientists — especially when mentors, advisers and other faculty members tell them to concentrate on their research. Training varies wildly in content and quality. Some institutions mandate training only in topics such as sexual harassment and ethnic discrimination.

Others offer voluntary courses on how to teach. Some provide course- or topic-specific instruction. And a few, such as Emory University in Atlanta, Georgia, and, now, the University of Toronto, mandate detailed training, in which teaching assistants or young instructors learn to teach first during discussion sessions with small groups of students, then in lab courses and, finally, in large lectures. Whether they are autodidacts like Pagiamtzis or have had formal training like graduate students at Emory, good teachers learn the iterative process of preparing relevant lessons and presenting information effectively, then assessing the effectiveness of their efforts (see 'Pedagogical pointers'). ►



## EXPERT TIPS

*Pedagogical pointers*

Early-career researchers are often unpractised at teaching, and can get distracted by their lab responsibilities. Here, experienced teachers offer some tips to help novices and their students get the most out of the classroom experience.

**Prepare**

Send your syllabus to your peers for feedback. Ask others who have taught a similar class to share their materials.

Set aside time to develop course materials — it often takes longer than you think.

Find a mentor whose philosophy and teaching style you would like to emulate. If possible, visit their classes before you begin teaching, to understand how they structure time, interact with students and promote learning. Talk to your mentor about what works and what doesn't.

Think about the skills and knowledge that you want your students to gain — and make sure that you are allowing time for your students to practise using them.

**Interact**

Focus less on content mastery than on skill mastery. You can't expect your students to think critically in an exam if you haven't asked the same in class.

Don't do for students what they can and should be doing for themselves. Teach them how to find the answers to their own questions, either alone or in groups.

Don't feel that you have to cover every topic that falls under the heading of your course. What does it matter that students know every definition in the textbook if they can't do anything with that information?

**Assess**

Make sure to provide students with ample feedback, so that they and you recognize when they need improvement.

Make sure you and your students have clear, measurable goals. Write them down and provide copies to your students. Revisit these goals throughout the teaching period and assess whether you've attained them.

Be transparent with your students. Let them know what you expect, what you are doing and why you are doing it. Honesty will go a long way towards building a successful learning community. **P.S.**

► Teaching can benefit an academic's career whether or not it is their main focus. Bouncing between teaching and research can help to identify research questions, improve academic writing and hone presentation skills — particularly those required for audiences with varying knowledge and skill levels. Teaching can also be a laboratory in which to learn the soft skills that will be vital to a professional career.

**PREPARATION**

One of the most important aspects of teaching is also one of the most misunderstood: preparation. Many new teachers think that preparation means having a basic understanding of the course material, but mere familiarity is only the beginning. "I aimed to understand the material one level deeper than what I was teaching," says Pagiamtzis. "But go as deep as you can in the time you have allotted for preparation."

To prepare course materials, Diane Ebert-May, a plant biologist at Michigan State University in East Lansing, suggests thinking about the core skills or knowledge that teachers want their students to gain, then reverse engineering the syllabus to ensure that pupils get the desired benefits. "Then you have to practise those competencies with them," says Ebert-May, who also trains biology postdocs in scientific teaching through an inter-university programme called FIRST IV.

Students are often told to put in two hours of work outside the classroom for every one they spend in it; teachers should devote at least as much time to their own preparation, says Ebert-May. And that doesn't include marking work, advising students or other administrative tasks.

Committing to that level of preparation means mastering time management, especially for graduate students or postdocs doing their own research. "Academic expectations keep going up. There just isn't enough time," says Alison Roark, a biologist at Hood College in Frederick, Maryland, who is a former teaching assistant and a participant in FIRST IV. To deal with the crunch, she reverse engineers her schedule in the same way as she does her syllabuses — by setting goals, then carving out time to meet them. What works best, she says, is to set aside blocks of time for specific activities: academic writing, teaching preparation and correcting her students' work.

"It gets better," Roark tells new teaching appointees. The first two years in an academic

job are the toughest; teachers are simultaneously developing curricula, writing grants and setting up a lab. "My first year is something I don't want to repeat. You're developing everything *de novo*," says Roark. Having become established, she is now able to spend a bit less time on preparation and a bit more on research.

Some programmes ease teachers in. For example, at Emory, graduate students work their way up from supervising lab courses to teaching independently, and so have time to get used to juggling different aspects of their career. They also have the option to focus on research rather than on teaching for a semester.

Although Pagiamtzis didn't have formal training in teaching, he did have an advice network. His PhD supervisor, Ali Sheikholeslami, an electrical engineer at Toronto, recommended that he ask random students questions throughout labs or discussions — not to put them on the spot, but to check whether they were getting the material. Pagiamtzis also looked to other teaching assistants for support — for example, someone teaching an earlier section of the same course might be able to tell him that they had had a particular problem, alerting him that he might require extra time and attention for his own section.

Good teaching, like good science, requires observation. Novice teachers should watch others, then get colleagues and peers to observe them and offer feedback, recommends Emily Rauscher, a postdoc in plant ecology at Pennsylvania State University in State College, who had some pedagogy training and took part in FIRST IV. Many formal teacher-training programmes video-record practice teaching sessions; people who aren't in such a programme can get a friend or colleague to record a lecture, then review it with them, suggests Sidney Omelon, an engineer at the University of Ottawa.

**PRESENTATION**

Part of being an effective teacher involves being able to grab students' attention — even being a showman of sorts. Young teachers should look at the day's lesson as a story, with a beginning, middle and end, says Pagiamtzis. For example, he traces the history of computing from the invention of the transistor to the formation of technology giants such as Intel and Google by talking about how William Shockley, co-inventor of the transistor, "was a jerk". Pagiamtzis interweaves the story of how transistor technology morphed into microchips with tales of how Shockley's abrasive personality drove away eight top scientists, some of whom went on to form a venture-capital firm that funded Google, Amazon and others. Intermingling science with the personalities behind it helps to hold students' attention, says Pagiamtzis. Nanda Dimitrov, associate director of the Teaching Support Centre at the University of Western Ontario in London, Canada, agrees. "A lot of great researchers know the material very well,



**"I was a big critic of teaching assistants when I was an undergraduate. I thought I'd better not be one of the bad ones."**

Kostas Pagiamtzis

I. GOLDTHORPE





Biologist Diane Ebert-May suggests teachers spend twice as long preparing classes as teaching them.

but do not know how to engage the students,” she says. “You need to understand the learner, understand the learner’s prior knowledge and understand how to motivate the learner.” The best teachers, says Dimitrov, use various approaches, including active learning and frequent assessments. That philosophy sums up a technique called ‘scientific teaching’, which builds on the standard lecture format.

“The notion that ‘If I cover it, they learn it’ is fatally flawed,” says Ebert-May. Her research shows that students retain more when lectures are enhanced by interactive lessons and lots of feedback (D. Ebert-May *et al. Bioscience* 47, 601–608; 1997). The best way for researchers to teach science, says Ebert-May, is to treat the classroom as if it were a lab, getting students to ask research questions, do literature reviews, conduct research, analyse data and present results. “You want to have people working together to solve complex problems,” she says.

### EXERCISING THE BRAIN

Roark uses this approach when teaching about how nerves drive muscle-cell function in her introductory biology course. She gives each student a ‘neuron token’ with a voltage value, then arranges the students into ‘neural networks’. They must work out whether a particular muscle cell in that network will contract. “The students have to turn on their brains in my classroom,” says Roark. “They can’t just sit there and take notes.”

Pagiamtzis likes to challenge his students with problems that have unexpected solutions. For example, as part of the standard electronics curriculum, he asks them to calculate the level of amplification of a two-pole amplifier. They usually use a simplified formula called the Miller approximation, and most come up with the wrong answer. But with enough prodding, students come to understand that the usual formula is not valid at high frequencies. They will remember the lesson better for having discovered it

for themselves than they would for having been taught it directly, says Pagiamtzis.

Although coming up with challenges requires a lot of effort, the work pays off — and not just for the students. Pagiamtzis has found that searching for special cases and exceptions to use in exercises deepens his own knowledge and understanding of the subject. His experience agrees with the conclusions of a study published last month, which quantitatively shows that teaching helps to enhance graduate students’ scientific skill sets (D. F. Feldon *et al. Science* 333, 1037–1039; 2011). The authors suggest that coming up with multiple study designs and research premises for use in the classroom honed the graduate students’ own thought processes.

Tobias Langenhan, a physiologist at the University of Würzburg in Germany, finds that teaching and testing his students helps him to think about where to put his future research efforts, as well as how to refine his teaching. “You realize that some of the principles you teach are very well substantiated in terms of experimental results and that others are not,” says Langenhan. “Flipping back and forth between teaching and research tells me where I should invest more time in explaining, and also where the pieces in the dogma we are trying to explain to the students are missing.”

Not only did Pagiamtzis’s classroom experiences force him to gain technical mastery of his subject matter, but the interpersonal skills that he learned have been invaluable to his industry job. He uses those skills when he explains the intricacies of computer chips to marketing people, or technical problems to managers. An important part of that exchange, he says, is being a good student by actively listening. “In essence,” says Pagiamtzis, “we are always learning from and teaching each other.” ■

**Paul Smaglik** is a freelance writer in Milwaukee, Wisconsin.

## EUROPEAN UNION

### Single patent system

The European Union (EU) should adopt a universal patent system with English as its official language, suggests a white paper released by the Charles III University of Madrid on 12 September. In *The EU Patent System: To Be or Not To Be*, researchers argue that the existing system impedes innovation. Currently, patents can be filed in any language, and every EU nation has different stipulations, legal requirements and costs. Marco Giarratana, an associate professor in business strategy at Bocconi University in Milan, Italy, and a co-author of the report, says that a universal system in English would encourage innovation by lowering translation and other costs. He also argues that a shared language for patents would boost mobility among young scientists.

## GRADUATE STUDENTS

### Career options clarified

A new group aims to help graduate students to learn about their options for scientific and other careers, particularly outside of academia. Announced on 8 September, the Commission on Pathways through Graduate School and into Careers has been formed by the US Council of Graduate Schools and the Educational Testing Service. Patrick Osmer, chairman of the commission and vice-provost for graduate studies at the Ohio State University in Columbus, says that the group is polling students about their knowledge of career options, questioning those who have graduated about their career paths and asking employers in various sectors about their needs. The findings will be out in April 2012.

## UNITED KINGDOM

### Home enrolment lagging

Meagre growth in postgraduate science, technology, engineering and maths enrolment by UK natives could put courses at English universities in long-term jeopardy, says a report from the Higher Education Funding Council for England, out on 9 September. The low growth coincides with large rises in international enrolment, says the report. Any decrease in overseas enrolment could threaten the “future viability of courses and the overall sustainability of these disciplines” by reducing university income. But the council says that recent rises in native undergraduate enrolment should carry over into postgraduate totals.



Biologist Diane Ebert-May suggests teachers spend twice as long preparing classes as teaching them.

but do not know how to engage the students,” she says. “You need to understand the learner, understand the learner’s prior knowledge and understand how to motivate the learner.” The best teachers, says Dimitrov, use various approaches, including active learning and frequent assessments. That philosophy sums up a technique called ‘scientific teaching’, which builds on the standard lecture format.

“The notion that ‘If I cover it, they learn it’ is fatally flawed,” says Ebert-May. Her research shows that students retain more when lectures are enhanced by interactive lessons and lots of feedback (D. Ebert-May *et al. Bioscience* 47, 601–608; 1997). The best way for researchers to teach science, says Ebert-May, is to treat the classroom as if it were a lab, getting students to ask research questions, do literature reviews, conduct research, analyse data and present results. “You want to have people working together to solve complex problems,” she says.

### EXERCISING THE BRAIN

Roark uses this approach when teaching about how nerves drive muscle-cell function in her introductory biology course. She gives each student a ‘neuron token’ with a voltage value, then arranges the students into ‘neural networks’. They must work out whether a particular muscle cell in that network will contract. “The students have to turn on their brains in my classroom,” says Roark. “They can’t just sit there and take notes.”

Pagiamtzis likes to challenge his students with problems that have unexpected solutions. For example, as part of the standard electronics curriculum, he asks them to calculate the level of amplification of a two-pole amplifier. They usually use a simplified formula called the Miller approximation, and most come up with the wrong answer. But with enough prodding, students come to understand that the usual formula is not valid at high frequencies. They will remember the lesson better for having discovered it

for themselves than they would for having been taught it directly, says Pagiamtzis.

Although coming up with challenges requires a lot of effort, the work pays off — and not just for the students. Pagiamtzis has found that searching for special cases and exceptions to use in exercises deepens his own knowledge and understanding of the subject. His experience agrees with the conclusions of a study published last month, which quantitatively shows that teaching helps to enhance graduate students’ scientific skill sets (D. F. Feldon *et al. Science* 333, 1037–1039; 2011). The authors suggest that coming up with multiple study designs and research premises for use in the classroom honed the graduate students’ own thought processes.

Tobias Langenhan, a physiologist at the University of Würzburg in Germany, finds that teaching and testing his students helps him to think about where to put his future research efforts, as well as how to refine his teaching. “You realize that some of the principles you teach are very well substantiated in terms of experimental results and that others are not,” says Langenhan. “Flipping back and forth between teaching and research tells me where I should invest more time in explaining, and also where the pieces in the dogma we are trying to explain to the students are missing.”

Not only did Pagiamtzis’s classroom experiences force him to gain technical mastery of his subject matter, but the interpersonal skills that he learned have been invaluable to his industry job. He uses those skills when he explains the intricacies of computer chips to marketing people, or technical problems to managers. An important part of that exchange, he says, is being a good student by actively listening. “In essence,” says Pagiamtzis, “we are always learning from and teaching each other.” ■

**Paul Smaglik** is a freelance writer in Milwaukee, Wisconsin.

## EUROPEAN UNION

### Single patent system

The European Union (EU) should adopt a universal patent system with English as its official language, suggests a white paper released by the Charles III University of Madrid on 12 September. In *The EU Patent System: To Be or Not To Be*, researchers argue that the existing system impedes innovation. Currently, patents can be filed in any language, and every EU nation has different stipulations, legal requirements and costs. Marco Giarratana, an associate professor in business strategy at Bocconi University in Milan, Italy, and a co-author of the report, says that a universal system in English would encourage innovation by lowering translation and other costs. He also argues that a shared language for patents would boost mobility among young scientists.

## GRADUATE STUDENTS

### Career options clarified

A new group aims to help graduate students to learn about their options for scientific and other careers, particularly outside of academia. Announced on 8 September, the Commission on Pathways through Graduate School and into Careers has been formed by the US Council of Graduate Schools and the Educational Testing Service. Patrick Osmer, chairman of the commission and vice-provost for graduate studies at the Ohio State University in Columbus, says that the group is polling students about their knowledge of career options, questioning those who have graduated about their career paths and asking employers in various sectors about their needs. The findings will be out in April 2012.

## UNITED KINGDOM

### Home enrolment lagging

Meagre growth in postgraduate science, technology, engineering and maths enrolment by UK natives could put courses at English universities in long-term jeopardy, says a report from the Higher Education Funding Council for England, out on 9 September. The low growth coincides with large rises in international enrolment, says the report. Any decrease in overseas enrolment could threaten the “future viability of courses and the overall sustainability of these disciplines” by reducing university income. But the council says that recent rises in native undergraduate enrolment should carry over into postgraduate totals.



# EVERY GIRL DREAMS OF FALLING IN LOVE

*For the good of the nation.*

BY SHELLY LI

Every girl dreams of falling in love. When I was five, I decided that my future husband would have a smile that could brighten a room.

At twelve, I dreamt of a husband who was tall and slim, with dark, clean-cut hair and a well-defined jawline. He would have green eyes that reminded me of evergreen trees.

At sixteen, I wanted to date a guy with blonde curls that swept over his eyes. He would be a witty but tortured soul, perhaps a poet. He would be shy around everyone else, but with me, he would open up and make me laugh, and he would make my skin tingle when he kissed me.

But when I entered the dating world, the faces of all three of the men I once thought I would marry began to fade into the ceiling of my empty bedroom.

The future never turns out the way we think it will: the cruellest thing God ever gave children was the gift of imagination.

Ten years passed, twenty years, and still, I never once got the chance to answer the question: "Will you marry me?"

To this day, the closest I've ever got to a marriage proposal was when a man in a suit knocked on my door and asked: "Will you serve your country?"

This was five days after the bombing of the railroad out of the Wisconsin River Basin. Like everyone, I wanted to help in any way, and so I agreed. Three days later, Bobby came to me. Bobby was a programmed war machine, the newest and the most human-like model ever designed.

"Introduce him to the neighbours," said the man. "Say the two of you eloped. You don't have to do anything except acknowledge your relationship with him, if ever questioned. He'll come home only in the winter, when he needs a place to hide out."

Bobby looked like a classic American hero, straight off the poster. His hair was cut short, and his ears stuck out. His eyes were hazel, and he had big cheeks, and when he smiled, dimples appeared on his face.

He was pretty laid back when we were alone, but around the neighbours, he was plenty charming, and the story we fabricated

went off without a hitch. The way he looked at me when other people were watching ... it actually made me feel loved.

I knew that it wasn't real love. Bobby was a robot who went off and fought in nightmarish places when the neighbours thought — and I pretended — that he was going on a business retreat.

Living a lie like that, with a husband who was not even a real man, initially I thought I'd be bothered. But when he was away, and I sat around with the other married women on the porch, the lie became the reality.

We're all living a lie in our own way, after all.



When Bobby came home in the winter, there would never be a scratch on him. The factory repaired him before they let him return, so that no one would see the cuts down his back, or bullet dents up and down his leg.

In this sense, I learned so much from Bobby. He would tell me stories, when we were alone, if I asked. "Bobby's Bedtime Tales," I would jokingly call them. He laughed because he was programmed to laugh when I was laughing, but he didn't understand humour.

I was fascinated by the things he couldn't understand. Sometimes, I would even watch him sleep at night. Bobby always slept soundly, even though sleep was probably as foreign to him

as gunfire was to me. How could I not love Bobby, even if he couldn't love me back? Bobby would always be the unrecognized hero of the country, the robot that carried out the tasks that humans did not have the stomach to perform.

More years passed and, like clockwork on every December 15th, a taxi would pull up to the driveway, and Bobby would emerge with a big suitcase. He would pretend it was heavy as he lugged it into the house, but it was always empty when he opened it.

The routine was something I had come to accept, no matter how lonely I felt in the springtime, when I saw husbands helping their wives clean out the garage.

It wasn't Bobby's strength that I missed. I could mow my own lawn. I could throw my own steaks on the grill. I could make my own repairs on the house.

It was his company I missed. I missed hearing the breathing of another person, before I drifted off to sleep.

Nevertheless, no matter how many times I whispered under my breath for him to come back, be it spring, summer or autumn, he never returned. I kept telling myself that it was nothing I could change. When I signed up for this, I signed up with the desire to help my country. Somewhere along the way, that desire began to fade just as the faces of my fairytale husbands faded.

One day, I was trimming the tree in the front yard, the one that was tall enough to brush the second-floor windows. The leaves provided a lot of shade in the summer, but it was now autumn, and time for the branches to go.

I climbed to the top of the tree and reached out to clip off a branch. Somehow, my foot slipped, and before I knew it, the grass was zooming towards me.

I stuck out my hands to break the fall, but I ended up knocking into something else before hitting the ground.

Gasping, I blinked and looked up at the man whose arms in which I was cradled.

"Be careful," Bobby said with a smile. ■ [SEE COMMENT P.399](#)

Shelly Li's online home is [www.shelly-li.com](http://www.shelly-li.com). Her first novel, *The Royal Hunter*, will be out this autumn, from Philomel Books.

JACEY



# Regulation of *Caenorhabditis elegans* lifespan by *sir-2.1* transgenes

ARISING FROM H. A. Tissenbaum & L. Guarente *Nature* **410**, 227–230 (2001)

Tissenbaum and Guarente<sup>1</sup> identified the first metazoan Sir2 homologue shown to affect lifespan, *Caenorhabditis elegans sir-2.1*. Independent transgenic lines harbouring extrachromosomal DNA arrays containing *sir-2.1* and the dominant transgene marker *rol-6(su1006)* were reported to extend mean lifespan between 15% and 50%<sup>1</sup>. Similar extensions in mean lifespan were also found for lines in which the *sir-2.1* transgenic arrays were integrated into the genome following  $\gamma$ -irradiation<sup>1</sup>. However, the extension of lifespan was overestimated in a high-copy *sir-2.1* transgene-containing worm strain because of an unlinked mutation.

One long-lived integrated transgenic line, LG100 *gels3* (formerly known as *geIn3*, ref. 1), was out-crossed four times to wild-type N2 worms along with *gels101*, an integrated *rol-6(su1006)* transgene control allele, creating LG269 and LG268, respectively. LG269 has a 50% increase in mean lifespan relative to LG268 (Fig. 1). Subsequently, we were made aware of a mutation in LG100 that prevented dye filling (Dyf<sup>−</sup>) of sensory neurons (exposed to the environment) with the amphipathic fluorescent dye DiO (S. Lee, personal communication). Dyf<sup>−</sup> is indicative of a sensory neuron defect and mutations that confer sensory neuron defects can extend lifespan<sup>2</sup>. By chance, we found LG269 to be Dyf<sup>−</sup>, prompting us to outcross the strain two more times thus segregating the Dyf<sup>−</sup> mutation from *gels3*. The resulting strain, LG389 (*gels3* Dyf<sup>+</sup>), has a shorter mean lifespan relative to its Dyf<sup>−</sup> progenitor, LG269, but is still long-lived (9.7%  $P < 0.0001$ ) relative to the similarly outcrossed control strain LG390 *gels101* (Fig. 1). Further

outcross of *gels3* resulted in lines (LG391–LG394) with a 14.3% ( $P < 0.0001$ ) increase in lifespan compared to similarly outcrossed control lines (LG395–LG398) (Fig. 1). All strains harbouring *gels3* show increases in *sir-2.1* mRNA of 10–30-fold (Fig. 1, right inset). Outcrossed strains (LG433–LG434) containing the Dyf<sup>−</sup> mutation, but not *gels3*, were also long-lived (10–16%) (Fig. 1, left inset), indicating that both alleles probably contributed to the larger extension seen in the *gels3* Dyf<sup>−</sup> strains LG100 and LG269.

We now know that *sir-2.1* is the second gene in an operon with R11A8.5. Its expression is regulated by two different promoters:  $P_{int}$ , an intergenic promoter that regulates expression of *sir-2.1* in the hypodermis and nerve cells, and  $P_0$ , an upstream operon promoter that regulates its expression in muscle cells and intestine<sup>3</sup>. The original *sir-2.1* transgenic lines<sup>1</sup>, *gels3* and *geX1-3*, contain only 500 bases of DNA upstream of the start of *sir-2.1* and therefore lack  $P_0$ . An independently derived low-copy *sir-2.1* transgenic line containing  $P_0$  was reported to extend lifespan by 26%<sup>4</sup>—an extension that was abolished by *sir-2.1* RNA interference<sup>5</sup>. In conclusion, our original paper<sup>1</sup> overestimated the extension of lifespan in a high-copy *sir-2.1* transgene-containing worm strain due to an unlinked mutation. However, we still observe 10–14% lifespan extension by *sir-2.1* overexpression in the absence of the unlinked Dyf<sup>−</sup> mutation. Finally, lifespan extension by *sir-2.1* overexpression can be greater in strains bearing *sir-2.1* in the context of its operonic promoter  $P_0$ <sup>4,5</sup>.

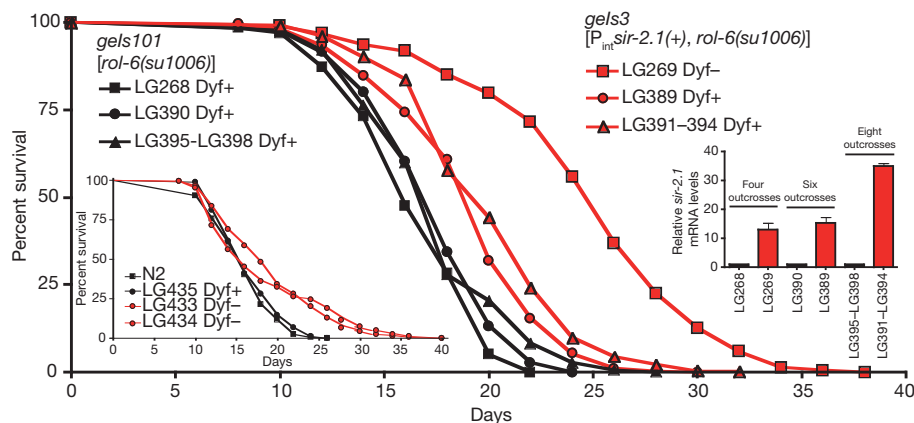


**Figure 1 | Integrated transgene *gels3*, expressing *sir-2.1* from its intergenic promoter ( $P_{int}$ ), extends *C. elegans* lifespan following outcross of a linked dye-filling mutation.** Strains LG269 *gels3*[ $P_{int}$  *sir-2.1*(+) *rol-6(su1006)*] and LG268 *gels101*[*rol-6(su1006)*] were outcrossed to wild-type N2 worms four times (four outcrosses) before the discovery of a dye-filling mutation in LG269 (not present in LG268). Both lines were further outcrossed four times, uncoupling the dye-filling (Dyf<sup>−</sup>) mutation from the *gels3* transgene in the sixth outcross (six outcrosses). Lifespan assays were performed as described previously<sup>5</sup>. Kaplan–Meyer survival curves are presented along with expression levels of *sir-2.1* transcript relative to actin in the various strains as determined by quantitative reverse transcription PCR from two independent samples of each strain performed in duplicate (right inset), standard error of the mean reported. Lifespan of the eight outcross strains represents the combined survival data of four independent segregants of the eighth outcross for both the *gels3* and *gels101* transgenes. No statistical lifespan differences were found among the four independent *gels3* or *gels101* lines from the final outcross.

Following separation from *gels3* in the sixth outcross the Dyf<sup>−</sup> mutation was outcrossed to N2 one additional time (seven outcrosses); two independent Dyf<sup>−</sup> segregants were tested for lifespan along with a Dyf<sup>+</sup> sibling control and N2 worms were used for the outcross. Four outcrosses: LG268 *gels101*,  $n = 197$ ,  $m = 16.7$  days; LG269 *gels3*  $n = 222$ ,  $m = 25.1$  days (50.2%),  $P < 0.0001$ . Six outcrosses: LG390 *gels101*,  $n = 287$ ,  $m = 17.6$  days; LG389 *gels3*  $n = 278$ ,  $m = 19.3$  days (9.7%),  $P < 0.0001$ . Eight outcrosses: LG395–LG398 *gels101*,  $n = 511$ ,  $m = 17.7$  days; LG391–LG394 *gels3*  $n = 517$ ,  $m = 20.3$  days (14.3%),  $P < 0.0001$ . Left inset: N2,  $n = 165$ ,  $m = 16.1$  days; LG435,  $n = 175$ ,  $m = 16.7$  days,  $P = 0.1476$  (relative to N2); LG433,  $n = 129$ ,  $m = 19.4$  days (16.2%),  $P < 0.0001$  (relative to LG435); LG434,  $n = 146$ ,  $m = 18.7$  days (12%),  $P = 0.0002$  (relative to LG435),  $P = 0.8818$  (relative to LG433).  $n$  = number of worms tested,  $m$  = mean day of survival, parenthetical values are the per cent change in mean lifespan relative to control.  $P$  values are relative to outcross control unless otherwise stated. Note: all transgenic strains listed in Fig. 1 have been deposited at the *Caenorhabditis* Genetics Center.

*Note added in proof:* A new report from the laboratories of S. Lee and C. Murphy independently confirms that our low-copy *sir-2.1* overexpression strain has an extended lifespan that is abolished by *sir-2.1* RNA interference<sup>6</sup>. This report also reaffirms the conclusion that *sir-2.1* interacts with DAF-16 (ref. 5) by showing that more than 1,000 DAF-16-regulated genes are upregulated in the *sir-2.1* overexpression strain.

**Mohan Viswanathan<sup>1</sup> & Leonard Guarente<sup>1</sup>**

<sup>1</sup>Massachusetts Institute of Technology, Department of Biology, Cambridge, Massachusetts 02139, USA.  
e-mail: leng@mit.edu

**Received 22 March; accepted 10 August 2011.**

1. Tissenbaum, H. A. & Guarente, L. Increased dosage of a *sir-2* gene extends lifespan in *Caenorhabditis elegans*. *Nature* **410**, 227–230 (2001).

2. Apfeld, J. & Kenyon, C. Regulation of lifespan by sensory perception in *Caenorhabditis elegans*. *Nature* **402**, 804–809 (1999).
3. Bamps, S., Wirtz, J., Savory, F. R., Lake, D. & Hope, I. A. The *Caenorhabditis elegans* sirtuin gene, *sir-2.1*, is widely expressed and induced upon caloric restriction. *Mech. Ageing Dev.* **130**, 762–770 (2009).
4. Viswanathan, M., Kim, S. K., Berdichevsky, A. & Guarente, L. A role for SIR-2.1 regulation of ER stress response genes in determining *C. elegans* life span. *Dev. Cell* **9**, 605–615 (2005).
5. Berdichevsky, A., Viswanathan, M., Horvitz, H. R. & Guarente, L. C. *elegans* SIR-2.1 interacts with 14-3-3 proteins to activate DAF-16 and extend life span. *Cell* **125**, 1165–1177 (2006).
6. Rizki, G. *et al.* The evolutionarily conserved longevity determinants HCF-1 and SIR-2.1/SIRT1 collaborate to regulate DAF-16/FOXO. *PLoS Genet.* **7**, e1002235 (2011).

**Author Contributions** M.V. and L.P.G. planned experiments. M.V. performed experiments and analysed data.

**Competing financial interests:** LG is co-chair of the SAB of Sirtris/GSK.  
**doi:**10.1038/nature10440

# Crystal structure of nucleotide-free dynamin

Katja Faelber<sup>1</sup>, York Posor<sup>2\*</sup>, Song Gao<sup>1,2\*</sup>, Martin Held<sup>3\*</sup>, Yvette Roske<sup>1\*</sup>, Dennis Schulze<sup>1</sup>, Volker Haucke<sup>2</sup>, Frank Noé<sup>3</sup> & Oliver Daumke<sup>1,4</sup>

**Dynamin is a mechanochemical GTPase that oligomerizes around the neck of clathrin-coated pits and catalyses vesicle scission in a GTP-hydrolysis-dependent manner. The molecular details of oligomerization and the mechanism of the mechanochemical coupling are currently unknown. Here we present the crystal structure of human dynamin 1 in the nucleotide-free state with a four-domain architecture comprising the GTPase domain, the bundle signalling element, the stalk and the pleckstrin homology domain. Dynamin 1 oligomerized in the crystals via the stalks, which assemble in a criss-cross fashion. The stalks further interact via conserved surfaces with the pleckstrin homology domain and the bundle signalling element of the neighbouring dynamin molecule. This intricate domain interaction rationalizes a number of disease-related mutations in dynamin 2 and suggests a structural model for the mechanochemical coupling that reconciles previous models of dynamin function.**

Dynamin, the founding member of the dynamin superfamily, is a 100-kDa mechanochemical enzyme (Fig. 1a) involved in the scission of clathrin-coated vesicles from the plasma membrane<sup>1</sup>. The brain-specific isoform dynamin 1 mediates uptake of synaptic vesicles in presynaptic terminals<sup>2–4</sup>, whereas a function of dynamin 3 at the post-synaptic density has been described<sup>5</sup>. Dynamin 2 is ubiquitously expressed<sup>6</sup>, and mutations in its middle domain (MD), pleckstrin homology (PH) domain and GTPase effector domain (GED) are linked

to human diseases, for example, rare forms of centronuclear myopathy and Charcot-Marie-Tooth peripheral neuropathy<sup>7</sup>. Upon recruitment via the carboxy-terminal proline-rich domain (PRD), dynamin oligomerizes into helical structures around the neck of budding vesicles and catalyses vesicle scission in a GTP-hydrolysis-dependent manner<sup>8,9</sup>. Different mechanisms for the scission reaction have been proposed, including GTP-hydrolysis-dependent constriction<sup>10</sup>, extension<sup>11</sup> and twisting<sup>9</sup> of the vesicle neck. Other models suggest that the GTP-bound

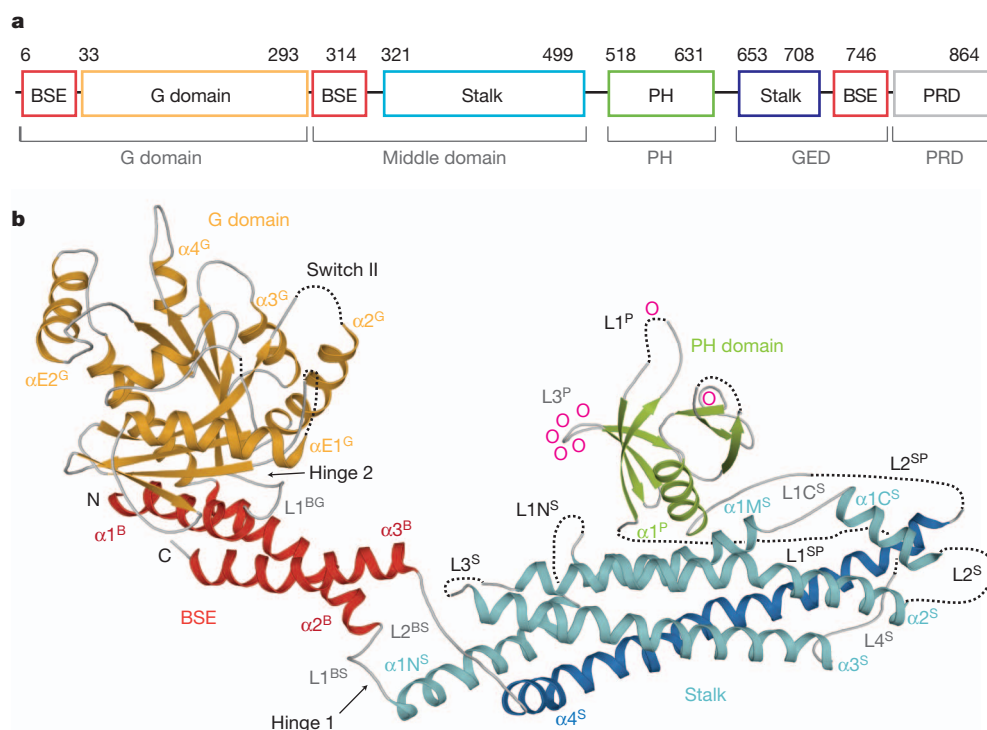


**Figure 1 | Structure of nucleotide-free human dynamin 1.**

**a**, Structure-based domain architecture of human dynamin 1. The classical domain assignment is indicated below. **b**, Ribbon-type representation of human dynamin 1. Regions not resolved in the crystal structure are indicated by dotted lines. Domains, distinct secondary structure elements and N and C termini are labelled. Lipid-binding residues are indicated as o.

<sup>1</sup>Crystallography, Max-Delbrück-Centrum for Molecular Medicine, Robert-Rössle-Straße 10, 13125 Berlin, Germany. <sup>2</sup>Institute for Chemistry and Biochemistry, Freie Universität Berlin, Takustraße 6, 14195 Berlin, Germany. <sup>3</sup>Institute for Mathematics, Freie Universität Berlin, Arnimallee 6, 14195 Berlin, Germany. <sup>4</sup>Institute for Medical Physics and Biophysics, Charité, Ziegelstraße 5-9, 10117 Berlin, Germany. \*These authors contributed equally to this work.



dynamins oligomer induces hemifusion of the inner membrane leaflet followed by complete membrane scission after GTP-hydrolysis-dependent release<sup>12,13</sup>. To resolve the detailed molecular mechanism, high-resolution structural data for full-length dynamins are required which, to date, are available only for the isolated PH domain<sup>14,15</sup> and the GTPase (G) domain<sup>16,17</sup>. Low-resolution electron microscopy reconstructions of dynamins oligomers showed that nucleotide binding leads to constriction of helical assemblies through rearrangements in the stalk region composed of the MD and GED<sup>18</sup>. Furthermore, G domain dimerization via a conserved interface across the nucleotide-binding site was shown to mediate the stimulated GTPase activity<sup>19</sup>. We recently described the structure of the stalk of the dynamins-like antiviral myxovirus resistance protein 1 (MxA) GTPase and elucidated its mode of oligomerization, which involves three distinct interfaces and two loop regions in the stalk<sup>20</sup>. Using this information, we succeeded to determine the structure of dynamins 1.

### The structure of human dynamins 1

We reasoned that the propensity of dynamins to oligomerize at high protein concentrations might interfere with the formation of protein crystals. On the basis of our previous MxA study<sup>20</sup>, we assayed a number of mutants in a human dynamins 1 construct (amino acids 6–746, Fig. 1a) for oligomerization defects. Indeed, a five-amino-acid exchange (IHGIR395–399AAAAA) in a conserved motif mapping to loop L2 of the MxA stalk<sup>20</sup> interfered with higher-order assembly and resulted in a monodisperse dimeric dynamins 1 species (Supplementary Fig. 1, see also ref. 21). Crystals of a construct containing additionally the K562E mutation were obtained in the absence of nucleotides and diffracted to a maximal resolution of 3.7 Å (Supplementary Table 1). The structure was solved by molecular replacement and refined to  $R_{\text{work}}/R_{\text{free}}$  of 28.4%/33.5% (Supplementary Table 1). To verify the sequence, the positions of 19 internal methionines were assigned by a single anomalous dispersion approach (Supplementary Fig. 2).

Dynamins 1 ( $\Delta$ PRD) has a four-domain architecture, composed of the G domain, the bundle signalling element (BSE), the stalk and the PH domain (annotated as superscript G, B, S and P, respectively), which does not strictly follow the sequence-derived domain boundaries (Fig. 1 and

Supplementary Fig. 3). The structure of the amino-terminal G domain is very similar to that of the isolated nucleotide-free G domain<sup>17</sup> (root-mean-square deviation (r.m.s.d.) of 1.4 Å for 287 C $\alpha$  atoms) and shows a curved central  $\beta$ -sheet surrounded by  $\alpha$ -helices at both sides. The two switch regions known to mediate nucleotide-dependent conformational changes and the *cis* stabilizing loop, involved in G domain dimerization<sup>19</sup>, are partly disordered. At the N and C termini of the G domain, helices  $\alpha 1^B$  and  $\alpha 2^B$ , together with  $\alpha 3^B$  from the C-terminal part of the GED of the same molecule, form a three-helix bundle, the BSE<sup>19,22</sup> (Fig. 1 and Supplementary Fig. 4). Compared to the previously described G domain-BSE construct in the GDP•AlF<sub>4</sub><sup>−</sup>-bound form<sup>19</sup>,  $\alpha 1^B$  is shifted by two turns relative to  $\alpha 2^B/\alpha 3^B$  (Supplementary Figs 2 and 4), whereas it interacts with the G domain in a similar fashion in both structures.

At the C-terminal end of  $\alpha 2^B$ , the BSE connects to the stalk of dynamins 1. The stalk is composed of a four-helix bundle where three helices,  $\alpha 1^S$ – $\alpha 3^S$ , are provided by the MD and  $\alpha 4^S$  by the N-terminal part of the GED (Fig. 1 and Supplementary Fig. 5a).  $\alpha 1^S$  in dynamins 1 is subdivided into  $\alpha 1N^S$ ,  $\alpha 1M^S$  and  $\alpha 1C^S$  by two disordered loops, L1N<sup>S</sup> and L1C<sup>S</sup>, compared to a single break of the corresponding helix in MxA. Furthermore,  $\alpha 3^S$  in dynamins 1 is extended by a highly conserved loop L4<sup>S</sup>. At the C terminus of the stalk,  $\alpha 4^S$  closely packs against  $\alpha 1^S$ – $\alpha 3^S$  via hydrophobic contacts and leads the polypeptide chain back to the BSE. Despite an overall sequence identity of only 16%, the architecture of the dynamins 1 and MxA stalk is remarkably similar (r.m.s.d. of 2.6 Å for 160 aligned C $\alpha$  atoms, Supplementary Fig. 5).

The PH domain is interconnected between  $\alpha 3^S$  and  $\alpha 4^S$  of the stalk by two disordered loops, L1<sup>SP</sup> and L2<sup>SP</sup>, and shows only minor deviations from the isolated PH domain of dynamins 1 (refs 14, 15; r.m.s.d. of 0.8 Å for 102 C $\alpha$  atoms). The three lipid binding loops<sup>23–25</sup> are only partially resolved and point towards the solvent (Fig. 1b and Supplementary Fig. 3).

### Dynamins assembly via the stalk

Similarly to the MxA stalks<sup>20</sup>, the dynamins 1 stalks in the crystals were arranged in a criss-cross fashion resulting in a linear stalk filament. The highly conserved symmetric interface-2 of 1,200 Å<sup>2</sup> is located in the centre of the stalk (according to the MxA nomenclature, Fig. 2 and

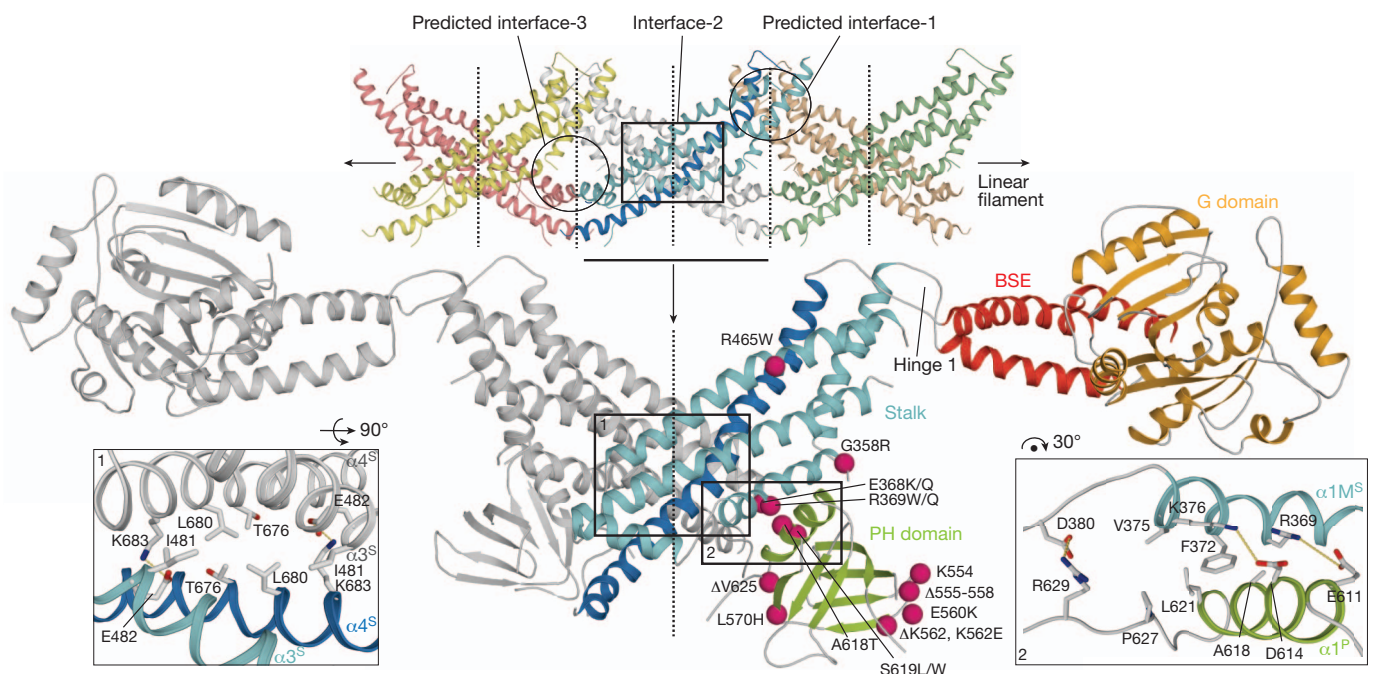


**Figure 2 | The dynamins 1 dimer.** In the crystals, stalks were arranged in a criss-cross fashion via crystallographic two-fold axis (black dotted lines). Assembly via the central interface-2 leads to an extended dynamins 1 dimer. Black rectangles indicate stalk interfaces shown in detail in the insets (see

Supplementary Fig. 2 for PH domain assignment). Disease-related dynamins 2 mutations causing centronuclear myopathy or Charcot–Marie–Tooth<sup>7</sup> are represented by pink spheres, with the amino acid exchange indicated.

Supplementary Figs 3 and 5). Assembly via this interface results in an extended dynamin dimer that serves as building block for dynamin oligomers<sup>26</sup>. Shape and dimension of this dimer agree well with a small-angle X-ray scattering study<sup>27</sup>.

We previously showed that a second hydrophobic interface in the MxA stalk, interface-1, mediates assembly of higher-order oligomers<sup>20</sup>. In dynamin 1, however, the stalks do not contact each other directly at the predicted interface-1 (minimal distance 4.5 Å, Supplementary Fig. 5). This difference is caused by a 5° tilt of the dynamin 1 stalks relative to the stalk axis. The hydrophobic nature of this surface in dynamin 1 and its conservation in the dynamin family (Supplementary Fig. 5c) is indicative of a similar function as in MxA as an oligomerization site. Closure of interface-1 might induce a pitch in the dynamin assemblies leading to helical oligomers rather than to ring-like structures as in MxA<sup>28</sup>.

L2<sup>S</sup> containing the disruptive IHGIR395–399AAAAA mutation and L1N<sup>S</sup> are not ordered in the linear dynamin 1 oligomer (Supplementary Fig. 5). The corresponding loops in the MxA stalk form a third interface (interface-3) which also contributes to the assembly of oligomers (Fig. 2). Accordingly, mutations in both loops in dynamin 1 (ref. 21), MxA<sup>20</sup> and in L1 of dynamin 1-like protein<sup>29,30</sup> prevent oligomerization. Interestingly, Ser 347 and Tyr 354 in loop L1N<sup>S</sup> in dynamin 1 are phosphorylated *in vivo*<sup>31,32</sup> and might control the assembly status.

## Interactions of the BSE

The BSE interacts with the central  $\beta$ -sheet of the G domain via a mostly hydrophilic interface of 1,100 Å<sup>2</sup> (Supplementary Figs 4 and 6). In contrast, the BSE and concomitantly the G domain are only loosely associated with the stalk of the same molecule via loops L1<sup>BS</sup> and L2<sup>BS</sup> constituting a flexible hinge (hinge 1), as observed in other dynamin related proteins<sup>33</sup> (Figs 1b and 2, and Supplementary Fig. 2).

Interestingly, Asp 744 at the C terminus of  $\alpha 3^B$  of the BSE contacts Arg 440 in  $\alpha 2^S$  of the neighbouring, parallel dynamin 1 stalk (Fig. 3a). A similar intermolecular interaction mediates oligomerization and the antiviral function of MxA (S.G., K.F., O.D., unpublished observation). We tested the importance of this contact experimentally. The wild-type dynamin 1 construct bound efficiently to liposomes resulting in an approximately 200-fold stimulation of GTPase activity (Supplementary Fig. 7). The single R440A and D744A mutants behaved as wild type in these assays. To analyse the role of these residues for clathrin-mediated endocytosis, dynamin 2–eGFP mutants (a fusion of dynamin 2 with enhanced green fluorescent protein) were re-expressed in HeLa cells depleted of endogenous dynamin 2. Both R440A and D744A mutants localized similarly as wild-type dynamin 2 to the plasma membrane (Supplementary Fig. 8), but transferrin internalization was increased (Fig. 3b and Supplementary Fig. 9). Thus, the salt bridge has an inhibitory and/or control function in dynamin-based endocytosis.

## The stalk–PH domain interface

$\alpha 1M^S$  of the stalk forms a conserved surface of 370 Å<sup>2</sup> with the PH domain (Figs 1b and 2, and Supplementary Figs 3 and 5c). Interestingly, 19 unique mutations causing centronuclear myopathy or Charcot–Marie–Tooth disease<sup>7</sup> cluster in the stalk or the PH domain of dynamin 2, but none localizes to the G domain or BSE (Fig. 2). For example, mutations E368K/Q and R369W/Q in the stalk and A618T and S619L/W in the PH domain are directly in or in close vicinity to the interface between the two domains. Mutations A618T and S619L/W lead to increased oligomerization rates of dynamin in solution<sup>27,34</sup>, suggesting that the stalk–PH interface controls oligomerization. In gel filtration, the disease-related stalk mutant E368K also eluted as high molecular weight species. Consistently, this mutant showed a 20-fold increased basal GTPase rate, whereas the liposome-stimulated GTPase reaction and transferrin uptake were unchanged (Fig. 3b and Supplementary Fig. 7). In contrast, the R369W mutant behaved as wild-type dynamin in biochemical and endocytosis assays. Mutations at the periphery of

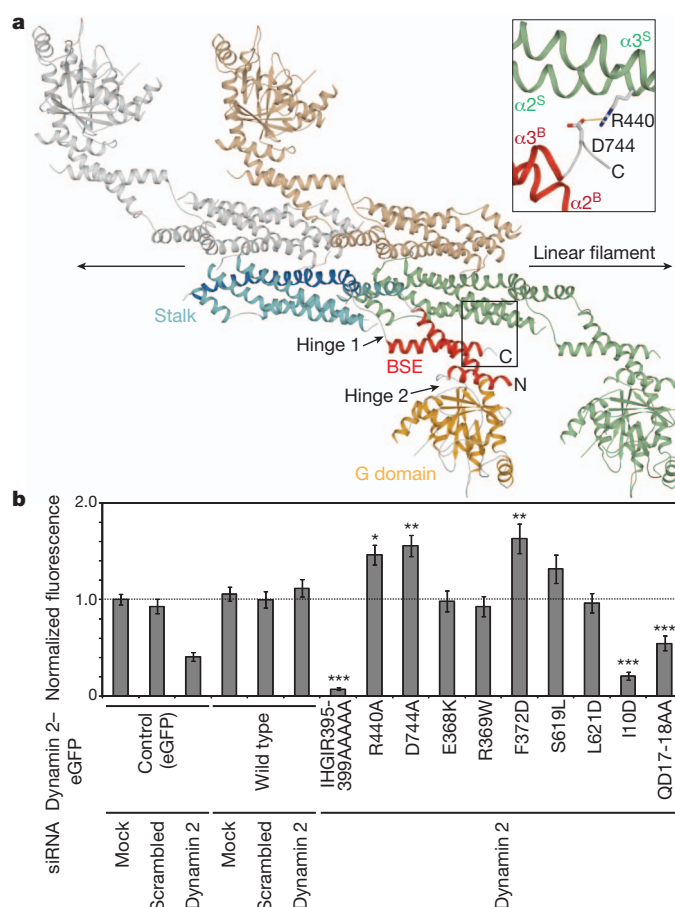


**Figure 3 | Stalk interactions with the BSE and PH domain.** **a**, Top view on the dynamin 1 oligomer. The PH domains are not drawn for clarity. The insert shows a close view of the intermolecular BSE–stalk interaction. **b**, HeLa cells depleted of endogenous dynamin 2 by short interfering RNA (siRNA) were transfected with a plasmid encoding siRNA-resistant dynamin 2–eGFP and allowed to endocytose fluorescently labelled transferrin. In transfected cells, fluorescence was quantified and normalized to mock-treated cells expressing eGFP. Data shown represent mean  $\pm$  standard error, \* $P < 0.05$ ; \*\* $P < 0.01$ ; \*\*\* $P < 0.0001$  for wild-type versus mutant dynamin 2–eGFP, as determined by *t*-test.

this interface (S619L, L621D) also did not compromise dynamin 2-based endocytic activity (Fig. 3b), indicating that more subtle changes lead to the disease-phenotype. Interestingly, the F372D mutant in the centre of the interface showed significantly higher transferrin uptake compared to wild-type dynamin 2, pointing also to an inhibitory and/or control function of this interface for dynamin-based endocytosis.

## Conformational changes during dynamin assembly

Based on the isolated BSE and PH domain (Fig. 1b), the stalk dimer (Fig. 2), the GDP•AlF<sub>4</sub><sup>−</sup>-bound G domain dimer<sup>19</sup>, and electron microscopy reconstructions of oligomerized dynamin 1 in the constricted state<sup>18</sup>, we generated a molecular model for self-assembly of dynamin into helical structures (Fig. 4a and Supplementary Fig. 10). The resulting dynamin dimer spans a length of more than 260 Å and covers 95° of a dynamin ring, thereby placing G domain and BSE above the neighbouring stalk. According to this model, oligomerization of dynamin proceeds along the central stalk, whereas the G domains mediate contacts between neighbouring turns (see ref. 20 for a similar MxA model).

When comparing the linear structure of dynamin 1 in the crystal with the helical assembly, large-scale domain movements are apparent (Supplementary Fig. 11). The G domain–BSE unit is shifted and rotated



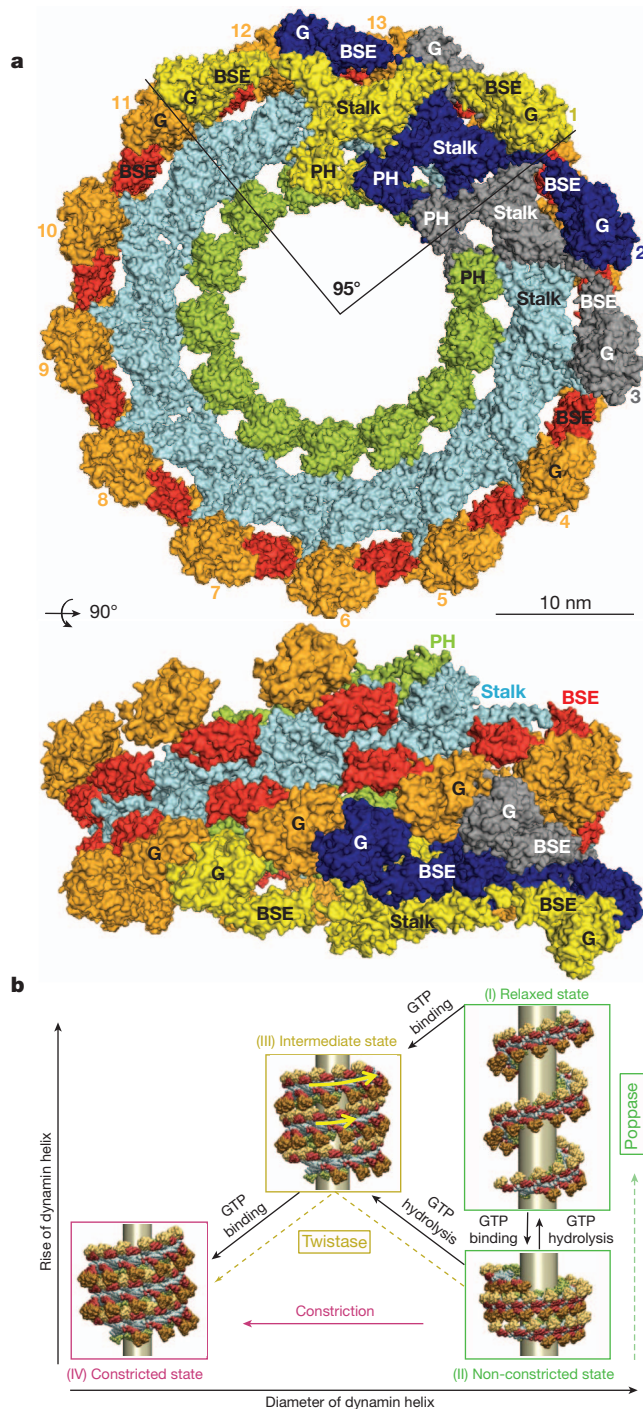


**Figure 4 | Model for dynamin oligomerization and function.** **a**, Model of the oligomerized dynamin helix in the constricted state, in top and side view (see also Supplementary Fig. 10). Three dimers (1–3) are uniformly coloured. Whereas 13 stalk dimers complete one turn, the G domain of dimer (*i*) associates with the G domain of dimer (*i* + 10). **b**, Structure-based illustration for the proposed mechanism of the dynamin oligomer. Variations in the assembly of consecutive dynamin molecules lead to dynamin helices of different rise and diameter. For further explanation, see main text and Supplementary Fig. 12.

around hinge 1 upon oligomerization. Additionally, the G domain separates from the BSE by a rotation around the invariant Pro 32 and Pro 294 (Supplementary Fig. 6). The corresponding residues Gly 68 and Gly 309 in BDLP<sup>33,35</sup> and Pro 342 in atlastin<sup>36,37</sup> have also been suggested to act as a hinge (hinge 2). Integrity of the G domain–BSE interface is crucial for the function of dynamin, as indicated by the

aggregation of the I10D interface mutant *in vivo* (Supplementary Figs 6 and 8). Furthermore, I10D behaved as a dominant-negative mutant in transferrin uptake assays (Fig. 3b). Moreover, the QD17–18AA mutation rendered dynamin 2 largely inactive in endocytosis assays, despite localizing correctly to clathrin-coated pits at the plasma membrane (Fig. 3b and Supplementary Fig. 8).

The PH domains also undergo a pronounced rearrangement, to a position below the stalk, with the lipid-binding loops<sup>23–25</sup> oriented towards the membrane (Supplementary Fig. 11a). We suggest that the stalk PH domain interface is disrupted by binding of the PH domain to high-affinity, phosphatidylinositol-4,5-bisphosphate-containing membranes such as the plasma membrane<sup>23–25</sup>, thereby promoting dynamin oligomerization.

Finally, we suggest that rotation of stalk dimers via the flexible interface-1 and/or interface-3, leaving interface-2 unchanged, leads to bending of the linear oligomer and allows helix formation (Supplementary Figs 11b and 12). Interestingly, the IHGIR395–399AAAAA mutation in interface-3 prevented liposome binding and, consequently, the liposome-stimulated GTPase activity (Supplementary Fig. 7). This mutant further behaved in a dominant-negative fashion in transferrin uptake assays (Fig. 3b) and displayed a diffuse localization and reduced recruitment to clathrin-coated pits (Supplementary Fig. 8). These results point to the central role of interface-3 for the function of dynamin.

## Discussion

The present work, combined with prior studies<sup>18–20,38</sup>, suggests a structural model for the mechanochemical coupling in dynamin that is consistent with previous models<sup>9–11</sup>. Our structural analysis indicates that the diameter of helical dynamin assemblies is controlled by the angle between two stalk dimers (Supplementary Figs 11b and 12f–h). We suggest that this angle is adjusted in response to GTP-dependent dimerization of the G domains: a relaxed conformation of interface-1 is adopted in the absence of G domain constraints, whereas GTP-triggered dimerization of the G domains constrains rotation in interface-1 and induces a bent, constricted conformation (Supplementary Fig. 11b), possibly via the BSE–stalk interface (Fig. 3a). Interestingly, in molecular dynamics simulations of two stalk dimers, the bent conformation of interface-1 rapidly converts towards a relaxed state, concomitant with an opening of the helical oligomer (Fig. 4b and Supplementary Fig. 12). This supports our assumption that constraints from G domains dimerization are required for the stabilization of the constricted state.

Accordingly, dynamin initially assembles via the stalks with interface-1 in a relaxed conformation, allowing the filament to adopt a range of different diameters<sup>12</sup> (state I in Fig. 4b and Supplementary Fig. 12). When the filament has embraced its template, GTP-loaded G domains of adjacent turns dimerize, the inhibitory stalk–BSE interface (Fig. 3a) is disrupted and the bent conformation of interface-1 is induced. This will result in constriction of the filament if the lipid template is flexible (state IV in Fig. 4b, constrictase model<sup>10</sup>) or compaction of the dynamin helix if the lipid template is rigid (state II in Fig. 4b, poppase model<sup>11</sup>). Constriction of a long dynamin helix will induce a sliding of neighbouring filaments until a new constricted equilibrium position of the oligomer is reached. This sliding is observed as a rotary movement of the dynamin helix upon addition of GTP in real-time imaging assays (twistase model<sup>9</sup>). To reach the constricted state along the whole assembly, several cycles of local release and rebinding of neighbouring dynamin turns might be triggered by GTP-dependent dimerization of G domains and dissociation after GTP hydrolysis (state III in Fig. 4b). Accordingly, GTP binding and hydrolysis are both required for the mechanochemical function of dynamin<sup>8,39</sup> and might induce local opening or twisting of the constricted dynamin helix. The resulting shear forces could tear the underlying membrane.



The complex domain interplay in dynamin rationalizes the high degree of structural conservation in the dynamin superfamily, sheds light on the molecular mechanisms of disease-associated mutations and highlights structural features of the nucleotide-free state as a prerequisite to understand dynamin's mechanochemical function.

## METHODS SUMMARY

A human dynamin 1 construct (residues 6–746) containing the IHGIR395–399AAAAA and K562E mutations was expressed as a His<sub>6</sub>-tag-fusion in *Escherichia coli* and purified to homogeneity. Crystals were obtained using PEG400 and isopropanol as precipitants. The structure was solved by molecular replacement. To verify the model, the positions of 19 out of 26 methionines were determined by an anomalous data set of SeMet-substituted crystals. Liposome binding assays were carried out as described (<http://www.endocytosis.org>). GTPase assays were carried out at 37 °C using 20 mM HEPES/NaOH, pH 7.5, 150 mM NaCl, 2 mM KCl, 2 mM MgCl<sub>2</sub> as reaction buffer. Uptake of fluorescently labelled transferrin was monitored in HeLa cells depleted of endogenous dynamin 2 by siRNA and transfected with the indicated siRNA-resistant dynamin 2 constructs.

**Full Methods** and any associated references are available in the online version of the paper at [www.nature.com/nature](http://www.nature.com/nature).

**Received 8 March; accepted 17 July 2011.**

**Published online 18 September 2011.**

- Praefcke, G. J. & McMahon, H. T. The dynamin superfamily: universal membrane tubulation and fission molecules? *Nature Rev. Mol. Cell Biol.* **5**, 133–147 (2004).
- van der Bliek, A. M. & Meyerowitz, E. M. Dynamin-like protein encoded by the *Drosophila shibire* gene associated with vesicular traffic. *Nature* **351**, 411–414 (1991).
- Ferguson, S. M. *et al.* A selective activity-dependent requirement for dynamin 1 in synaptic vesicle endocytosis. *Science* **316**, 570–574 (2007).
- Robinson, P. J. *et al.* Dynamin GTPase regulated by protein kinase C phosphorylation in nerve terminals. *Nature* **365**, 163–166 (1993).
- Lu, J. *et al.* Postsynaptic positioning of endocytic zones and AMPA receptor cycling by physical coupling of dynamin-3 to Homer. *Neuron* **55**, 874–889 (2007).
- Cook, T. A., Urrutia, R. & McNiven, M. A. Identification of dynamin 2, an isoform ubiquitously expressed in rat tissues. *Proc. Natl Acad. Sci. USA* **91**, 644–648 (1994).
- Durieux, A. C. *et al.* Dynamin 2 and human diseases. *J. Mol. Med.* **88**, 339–350 (2010).
- Marks, B. *et al.* GTPase activity of dynamin and resulting conformation change are essential for endocytosis. *Nature* **410**, 231–235 (2001).
- Roux, A. *et al.* GTP-dependent twisting of dynamin implicates constriction and tension in membrane fission. *Nature* **441**, 528–531 (2006).
- Hinshaw, J. E. & Schmid, S. L. Dynamin self-assembles into rings suggesting a mechanism for coated vesicle budding. *Nature* **374**, 190–192 (1995).
- Stowell, M. H. B. *et al.* Nucleotide-dependent conformational changes in dynamin: evidence for a mechanochemical molecular spring. *Nature Cell Biol.* **1**, 27–32 (1999).
- Bashkurov, P. V. *et al.* GTPase cycle of dynamin is coupled to membrane squeeze and release, leading to spontaneous fission. *Cell* **135**, 1276–1286 (2008).
- Pucadyil, T. J. & Schmid, S. L. Real-time visualization of dynamin-catalyzed membrane fission and vesicle release. *Cell* **135**, 1263–1275 (2008).
- Timm, D. *et al.* Crystal structure of the pleckstrin homology domain from dynamin. *Nature Struct. Biol.* **1**, 782–788 (1994).
- Ferguson, K. M. *et al.* Crystal structure at 2.2 Å resolution of the pleckstrin homology domain from human dynamin. *Cell* **79**, 199–209 (1994).
- Niemann, H. H. *et al.* Crystal structure of a dynamin GTPase domain in both nucleotide-free and GDP-bound forms. *EMBO J.* **20**, 5813–5821 (2001).
- Reubold, T. F. *et al.* Crystal structure of the GTPase domain of rat dynamin 1. *Proc. Natl Acad. Sci. USA* **102**, 13093–13098 (2005).
- Mears, J. A., Ray, P. & Hinshaw, J. E. A corkscrew model for dynamin constriction. *Structure* **15**, 1190–1202 (2007).
- Chappie, J. S. *et al.* G domain dimerization controls dynamin's assembly-stimulated GTPase activity. *Nature* **465**, 435–440 (2010).
- Gao, S. *et al.* Structural basis of oligomerization in the stalk region of dynamin-like MxA. *Nature* **465**, 502–506 (2010).
- Ramachandran, R. *et al.* The dynamin middle domain is critical for tetramerization and higher-order self-assembly. *EMBO J.* **26**, 559–566 (2007).
- Chappie, J. S. *et al.* An intramolecular signaling element that modulates dynamin function *in vitro* and *in vivo*. *Mol. Biol. Cell* **20**, 3561–3571 (2009).
- Vallis, Y. *et al.* Importance of the pleckstrin homology domain of dynamin in clathrin-mediated endocytosis. *Curr. Biol.* **9**, 257–263 (1999).
- Zheng, J. *et al.* Identification of the binding site for acidic phospholipids on the pH domain of dynamin: implications for stimulation of GTPase activity. *J. Mol. Biol.* **255**, 14–21 (1996).
- Salim, K. *et al.* Distinct specificity in the recognition of phosphoinositides by the pleckstrin homology domains of dynamin and Bruton's tyrosine kinase. *EMBO J.* **15**, 6241–6250 (1996).
- Zhang, P. & Hinshaw, J. E. Three-dimensional reconstruction of dynamin in the constricted state. *Nature Cell Biol.* **3**, 922–926 (2001).
- Kenniston, J. A. & Lemmon, M. A. Dynamin GTPase regulation is altered by PH domain mutations found in centronuclear myopathy patients. *EMBO J.* **29**, 3054–3067 (2010).
- Kochs, G. *et al.* Assay and functional analysis of dynamin-like Mx proteins. *Methods Enzymol.* **404**, 632–643 (2005).
- Ingerman, E. *et al.* Dnm1 forms spirals that are structurally tailored to fit mitochondria. *J. Cell Biol.* **170**, 1021–1027 (2005).
- Chang, C. R. *et al.* A lethal *de novo* mutation in the middle domain of the dynamin-related GTPase Drp1 impairs higher order assembly and mitochondrial division. *J. Biol. Chem.* **285**, 32494–32503 (2010).
- Graham, M. E. *et al.* The *in vivo* phosphorylation sites of rat brain dynamin I. *J. Biol. Chem.* **282**, 14695–14707 (2007).
- Rush, J. *et al.* Immunoaffinity profiling of tyrosine phosphorylation in cancer cells. *Nature Biotechnol.* **23**, 94–101 (2004).
- Low, H. H. & Lowe, J. Dynamin architecture—from monomer to polymer. *Curr. Opin. Struct. Biol.* **20**, 791–798 (2010).
- Wang, L. *et al.* Dynamin 2 mutants linked to centronuclear myopathies form abnormally stable polymers. *J. Biol. Chem.* **285**, 22753–22757 (2010).
- Low, H. H. *et al.* Structure of a bacterial dynamin-like protein lipid tube provides a mechanism for assembly and membrane curving. *Cell* **139**, 1342–1352 (2009).
- Byrnes, L. J. & Sondermann, H. Structural basis for the nucleotide-dependent dimerization of the large G protein atlastin-1/SPG3A. *Proc. Natl Acad. Sci. USA* **108**, 101073/pnas.1012792108 (10 January 2011).
- Bian, X. *et al.* Structures of the atlastin GTPase provide insight into homotypic fusion of endoplasmic reticulum membranes. *Proc. Natl Acad. Sci. USA* **108**, 3976–3981 (2011).
- Klockow, B. *et al.* The dynamin A ring complex: molecular organization and nucleotide-dependent conformational changes. *EMBO J.* **21**, 240–250 (2002).
- Morlot, S. *et al.* Deformation of dynamin helices damped by membrane friction. *Biophys. J.* **99**, 3580–3588 (2010).

**Supplementary Information** is linked to the online version of the paper at [www.nature.com/nature](http://www.nature.com/nature).

**Acknowledgements** This project was supported by a grant from the Deutsche Forschungsgemeinschaft (SFB 740/C7 and SFB958/A12 to O.D., SFB740/D7 and SFB958/A04 to F.N., SFB740/C8 and SFB 958/A7 to V.H.), by a Career Development Fellowship of The International Human Frontier Science Program Organization and by the EMBO Young Investigator Program to O.D. We would like to thank S. Werner, M. Papst and S. Kraft for technical assistance, the BESSY staff at BL14.1 for help during data collection, G. Schröder for advice in DEN refinement and U. Heinemann for discussions.

**Author Contributions** K.F., Y.P., D.S. and Y.R. performed experiments, K.F., Y.P., S.G., M.H., V.H., F.N. and O.D. designed research, M.H. and F.N. conducted and analysed molecular modelling and molecular dynamics simulations. K.F. and O.D. wrote the manuscript.

**Author Information** The atomic coordinates of human dynamin 1 have been deposited in the Protein Data Bank with accession number 3SNH. Reprints and permissions information is available at [www.nature.com/reprints](http://www.nature.com/reprints). The authors declare no competing financial interests. Readers are welcome to comment on the online version of this article at [www.nature.com/nature](http://www.nature.com/nature). Correspondence and requests for materials should be addressed to O.D. ([oliver.daumke@mdc-berlin.de](mailto:oliver.daumke@mdc-berlin.de)) or K.F. ([katja.faelber@mdc-berlin.de](mailto:katja.faelber@mdc-berlin.de)).

## METHODS

**Protein expression and purification.** Human dynamin 1 (residues 6–746) and indicated mutants of this construct were expressed from pET46-EK/LIC (Novagen) as N-terminal His<sub>6</sub>-tag fusion followed by a PreScission cleavage site. The crystallized construct contained mutations IHGIR395–399AAAAA which prevented oligomerization and K562E which reduced DNA contaminations during purification. Proteins were expressed in *Escherichia coli* host strain Rosetta2-BL21-DE3, and bacteria were cultured in autoinduction medium (Novagen) for 7.5 h at 37 °C followed by temperature shift to 20 °C for overnight expression. Selenomethionine (SeMet)-substituted human dynamin 1 was expressed in M9 minimal medium, supplemented with L-amino acids Lys, Phe, Thr (100 mg l<sup>-1</sup>), Ile, Leu, Val, SeMet (50 mg l<sup>-1</sup>), using the same vector and host strain as for native protein expression<sup>40</sup>. Cells were resuspended in buffer A (25 mM HEPES/NaOH (pH 7.9), 500 mM NaCl, 2 mM MgCl<sub>2</sub>, 1 μM DNase (Roche), 500 μM Pefabloc (Roht)) and disrupted by a microfluidizer (Microfluidics). Cleared lysates (95,000g, 1 h, 4 °C) were incubated with Benzonase (Novagen) for 30 min at 4 °C before application to a Co<sup>2+</sup>-Talon column (Clontech). Protein was eluted with buffer A containing additional 100 mM imidazole. Fractions containing human dynamin 1 were incubated with 2.4 mM β-mercaptoethanol and His<sub>6</sub>-tagged PreScission protease overnight at 4 °C. Using 50 kDa molecular weight cut-off concentrators (Amicon), imidazole, β-mercaptoethanol and the free His<sub>6</sub>-tag were removed by washing with buffer A, before a second application to a Co<sup>2+</sup>-Talon column to remove non-cleaved His-tagged dynamin 1 and protease. The flow-through and four column volumes of washing buffer A were collected and concentrated. Finally, dynamin 1 was purified by size exclusion chromatography on a Superdex200 column (GE) in buffer containing 25 mM HEPES/NaOH (pH 7.5), 300 mM NaCl, 2 mM MgCl<sub>2</sub>. Fractions containing dynamin 1 were pooled, concentrated and flash-frozen in liquid nitrogen (Supplementary Fig. 1). SeMet-substituted protein was purified using the same protocol.

**Crystallization and structure determination.** Crystallization trials by the sitting-drop vapour-diffusion method were performed at 4 °C using a Hydra-plus-One pipetting robot (Matrix Technologies Corporation) and Rock Imager storage system (Formulatrix). The human dynamin 1 construct (300 nl at a concentration of 12 mg ml<sup>-1</sup>) was mixed with an equal volume of reservoir solution containing 9% PEG400, 6% isopropanol, 100 mM HEPES/NaOH (pH 7.3), 10 mM MgCl<sub>2</sub> and 10 mM KCl. Crystals of the native protein appeared after 2 weeks and had dimensions of 0.2 mm × 0.05 mm × 0.02 mm. Crystals of SeMet protein were obtained in 6% MPD, 10% isopropanol, 0.1 M HEPES/NaOH (pH 7.5). During flash-cooling of the crystals in liquid nitrogen, a cryo-solution containing additionally 20% ethylene glycol was used. All data were recorded at BL14.1 at BESSY II, Berlin. One native data set was collected from a single crystal and processed and scaled using the XDS program suite<sup>41</sup>. Phase information was obtained by molecular replacement with Phaser<sup>42</sup> using the structure of the nucleotide-free rat dynamin 1 G domain<sup>16</sup>, the stalk of human Mxα<sup>20</sup> and the human PH domain<sup>15</sup> as search models. The model was built using COOT<sup>43</sup> and iteratively refined using CNS1.3 with a deformable elastic network<sup>44</sup>, followed by 10 cycles of TLS refinement using 1 TLS group per domain in refmac5 (ref. 45). To confirm the amino acid sequence, a data set of a SeMet-substituted protein crystal was recorded at the selenium peak wavelength. Owing to non-isomorphism of the native and SeMet crystals, molecular replacement with the refined native structure was performed. The positions of 19 out of 26 selenium atoms in the dynamin 1 construct were determined by calculating an anomalous difference map with the CCP4 program suite<sup>46</sup> using the calculated phases after refinement. The final native model comprises amino acids 6–746. Residues 63–64, 110–112, 143–149, 347–356, 394–404, 446–447, 500–517, 534–537, 578–581 and 632–652 are disordered. Electron density for loop L2<sup>BS</sup> (amino acids 709–715) was only visible in the SeMet derivative structure and was therefore not modelled in the native structure. However, L2<sup>BS</sup> was included for figure preparation. Of all residues, 86.9% are in the most favoured regions of the Ramachandran plot and no residue in the disallowed regions, as analysed with Procheck<sup>47</sup>. Figures were prepared with PyMol<sup>48</sup>. Buried surface areas (per molecule) were calculated using CNS<sup>44</sup>. Solvent-accessible areas per residue were calculated using areaimol<sup>46</sup>. Domain superpositions were performed with lsqkab<sup>46</sup>. Sequences were aligned using CLUSTAL W<sup>49</sup> and adjusted by hand.

**Liposome co-sedimentation assays.** Liposomes were prepared as previously described (<http://www.endocytosis.org>). Folch liposomes (total bovine brain lipids fraction I from Sigma) in 20 mM HEPES/NaOH (pH 7.5), 150 mM NaCl, 2 mM KCl were extruded through a 0.1 μm filter. Liposomes (0.1 mg ml<sup>-1</sup>) were incubated at room temperature with 4.0 μM of the indicated dynamin 1 construct for 10 min in 40 μl reaction volume, followed by a 70,000g spin for 10 min at 20 °C.

**GTP hydrolysis assay.** GTPase activities of 1 μM of the indicated dynamin 1 constructs were determined at 37 °C in 20 mM HEPES/NaOH (pH 7.5), 150 mM

NaCl, 2 mM KCl, 2 mM MgCl<sub>2</sub>, in the absence and presence of 0.1 mg ml<sup>-1</sup> 0.1-μm-filtered Folch liposomes, using saturating concentrations of GTP as substrate (1 mM for the basal and 3 mM for the stimulated reactions). Reactions were initiated by the addition of protein to the reaction. At different time points, reaction aliquots were diluted 15-fold in GTPase buffer and quickly transferred to liquid nitrogen. Nucleotides in the samples were separated via a reversed-phase Hypersil ODS-2 C18 column (250 × 4 mm), with 10 mM tetrabutylammonium bromide, 100 mM potassium phosphate (pH 6.5), 7.5% acetonitrile as running buffer. Denatured proteins were adsorbed at a C18 guard column. Nucleotides were detected by absorption at 254 nm and quantified by integration of the corresponding peaks. Rates were derived from a linear fit to the initial reaction (<40% GTP hydrolysed).

**Transferrin uptake in HeLa cells.** HeLa cells were transfected with siRNA using Oligofectamine (Invitrogen) on day 1. The sequence of the siRNA against human dynamin 2 is 5'-GCAACUGACCAACCACAUC-3', targeting nucleotides 849–867. On day 2, cells were transfected with pEGFP-N1 (Clontech) or siRNA-resistant rat dynamin 2-pEGFP-N1 using lipofectamine 2000 (Invitrogen) and seeded on coverslips. On day 3, cells were serum-starved and incubated with 20 μg ml<sup>-1</sup> transferrin-Alexa568 (Molecular Probes, Invitrogen) for 10 min at 37 °C. After four PBS washes on ice, cells were paraformaldehyde-fixed for 20 min at room temperature. Transferrin uptake was analysed using a Zeiss Axiovert200M microscope and Slidebook imaging software (3i Inc.). Internalized transferrin was quantified from transfected cells only and normalized to the value of eGFP-transfected, mock-treated cells (*n* = 28–83 images, five independent experiments; IHGVR395–399AAA, 110D, QD17–18AA: three independent experiments; E368K, R369W, S619L, F372D: two independent experiments). Knockdown of dynamin 2 and expression levels of dynamin 2-eGFP mutants were assessed by immunoblotting using antibodies to dynamin 2 (a gift of M. A. McNiven), β-actin (clone ac-15, Sigma-Aldrich) and eGFP (clone j1-8, Clontech).

**Localization of dynamin 2-eGFP mutants.** HeLa cells were transfected with dynamin 2-pEGFP-N1 wild-type or mutant constructs 20 h before fixation in 4% paraformaldehyde for 12 min at room temperature. Cells were blocked and permeabilized in 10% goat serum, 0.3% Triton X-100, 100 mM NaCl in phosphate buffer and stained for endogenous adaptor complex AP-2 using an antibody to α-adaptin (clone AP-6, Abcam). Total internal reflection fluorescence (TIRF) imaging was performed using a Zeiss Axiovert200M microscope equipped with a ×100 TIRF objective and a dual-colour TIRF setup from Visitron Systems using Slidebook imaging software (3i Inc.).

**Loop modelling and molecular dynamics simulations.** For modelling of the unresolved loop regions L1N<sup>S</sup> and L2<sup>S</sup>, two stalk dimers in the constricted state served as scaffold. Using Modeller (9v8)<sup>50</sup>, the scaffold was fixed in position, whereas L1N<sup>S</sup> and L2<sup>S</sup> could freely sample the empirical potential function. To reduce the conformational search space, additional harmonic distance restraints were added between conserved residues Arg 399–Asp 406 and Glu 355–Arg 361. Based on the modelled stalk tetramer, five independent all-atom molecular dynamics simulations (NVT ensemble), each of 90 ns, were conducted at *T* = 300 K in a periodic boundary setting using Gromacs 4.5.3 (ref. 51). The model was immersed in a rectangular 20 nm × 10 nm × 9 nm box, containing approximately 56,400 water molecules, 21 sodium and 17 chloride ions to neutralize the system, resulting in a total number of 185,857 atoms. As force fields, Amber99 (protein and ions)<sup>52</sup> and TIP3P (water)<sup>53</sup> were applied. To treat long-range interactions, the Particle-mesh Ewald method<sup>54,55</sup> was used. A cut-off of 1 nm was used for the real parts of electrostatic and van der Waals interactions. All hydrogen bonds were constrained by using the LINCS<sup>56</sup> algorithm, allowing for an integration time-step of 2 fs. For the thermostatted integration, Langevin dynamics were used as implemented by the Gromacs s.d. integrator (tau<sub>t</sub> = 1).

For the calculation of bending and twisting angles, each of the four stalk monomers was represented by two geometric centres, defined as the mean position of Cα atoms of residues 366–377, 420–430, 468–481 and 671–683 for position A and residues 360–365, 428–445, 457–472 and 686–701 for position B (Supplementary Fig. 12d). The stalk bending angle α was defined as the mean angle between parallel stalks, and the twisting angle β by the minimal angle between the planes spanned by each dimer (positions A, B, B' in Supplementary Fig. 12f).

For each simulation time step, the corresponding stalk tetramer structure describes a linear transformation of the first dimer onto the second dimer, consisting of a translation vector and a rotation matrix. This linear transformation was used to reconstruct the structure of an ideal dynamin helix by applying it to the dynamin dimer model in the constricted state. The diameter, *d*, and the rise per turn, *r*, of these helices were measured by using the geometric centres of the stalk coordinates and obtaining trajectories in (*d*, *r*). Based on these trajectories, the free energy surface of stalk helix conformations was calculated: the two-dimensional space (*d*, *r*) was discretized into boxes of size 25 × 25 Å. Based on the simulation trajectories, the transition probability between all pairs of boxes was computed,

which allowed the calculation of an equilibrium probability of finding a single stalk tetramer in a given box,  $p_1(d,r)^{57}$ . When more than two stalk dimers are assembled, non-cooperative behaviour of neighbouring dimers has to be considered, for example, the assembled stalk dimers can almost independently switch between different conformations. The resulting equilibrium distribution of two independent tetrameric units would be given by the convolution of two single-tetramer distributions,  $p_2(d,r)$ . It was found that for only about three such convolutions, the resulting probability distribution converges to  $p_3(d,r) \approx p(d,r)$ . Thus, assuming that the helix has at least three independently switching subunits, the free energy landscape is unique, and is given by  $F(d,r) = -kT \ln(p(d,r))$ , where  $k$  is the Boltzmann constant and  $T$  the temperature.

40. Van Duyne, G. D. *et al.* Atomic structures of the human immunophilin FKBP-12 complexes with FK506 and rapamycin. *J. Mol. Biol.* **229**, 105–124 (1993).
41. Kabsch, W. Automatic processing of rotation diffraction data from crystals of initially unknown symmetry and cell constants. *J. Appl. Cryst.* **26**, 795–800 (1993).
42. McCoy, A. J. *et al.* Phaser crystallographic software. *J. Appl. Cryst.* **40**, 658–674 (2007).
43. Emsley, P. & Cowtan, K. Coot: model-building tools for molecular graphics. *Acta Crystallogr. D* **60**, 2126–2132 (2004).
44. Schröder, G. F., Levitt, M. & Brunger, A. T. Super-resolution biomolecular crystallography with low-resolution data. *Nature* **464**, 1218–1222 (2010).
45. Murshudov, G. N., Vagin, A. A. & Dodson, E. J. Refinement of macromolecular structures by the maximum-likelihood method. *Acta Crystallogr. D* **53**, 240–255 (1997).
46. Collaborative Computational Project, Number 4. The CCP4 suite: programs for protein crystallography. *Acta Crystallogr. D* **50**, 760–763 (1994).
47. Laskowski, R. A. *et al.* PROCHECK: a program to check the stereochemical quality of protein structures. *J. Appl. Cryst.* **26**, 283–291 (1993).
48. DeLano, W. L. *The PyMol Molecular Graphics System* version 1.4.1 (Schrödinger, 2011).
49. Thompson, J. D., Higgins, D. G. & Gibson, T. J. CLUSTAL W: improving the sensitivity of progressive multiple sequence alignment through sequence weighting, position-specific gap penalties and weight matrix choice. *Nucleic Acids Res.* **22**, 4673–4680 (1994).
50. Fiser, A., Do, R. K. & Sali, A. Modeling of loops in protein structures. *Protein Sci.* **9**, 1753–1773 (2000).
51. Van Der Spoel, D. *et al.* GROMACS: fast, flexible, and free. *J. Comput. Chem.* **26**, 1701–1718 (2005).
52. Wang, J. M., Cieplak, P. & Kollman, P. A. How well does a restrained electrostatic potential (RESP) model perform in calculating conformational energies of organic and biological molecules? *J. Comput. Chem.* **21**, 1049–1074 (2000).
53. Jorgensen, W. *et al.* Comparison of simple potential functions for simulating liquid water. *J. Chem. Phys.* **79**, 926–935 (1983).
54. Essmann, U. *et al.* A smooth particle mesh Ewald method. *J. Chem. Phys.* **103**, 8577–8593 (1995).
55. Darden, T., York, D. & Pedersen, L. Particle mesh Ewald: an  $N$ -log( $N$ ) method for Ewald sums in large systems. *J. Chem. Phys.* **98**, 10089–10092 (1993).
56. Hess, B. *et al.* LINCS: a linear constraint solver for molecular simulations. *J. Comput. Chem.* **18**, 1463–1472 (1997).
57. Prinz, J. H. *et al.* Markov models of molecular kinetics: generation and validation. *J. Chem. Phys.* **134**, 174105 (2011).



# High-fidelity projective read-out of a solid-state spin quantum register

Lucio Robledo<sup>1\*</sup>, Lilian Childress<sup>2\*</sup>, Hannes Bernien<sup>1\*</sup>, Bas Hensen<sup>1</sup>, Paul F. A. Alkemade<sup>1</sup> & Ronald Hanson<sup>1</sup>

**Initialization and read-out of coupled quantum systems are essential ingredients for the implementation of quantum algorithms<sup>1,2</sup>. Single-shot read-out of the state of a multi-quantum-bit (multi-qubit) register would allow direct investigation of quantum correlations (entanglement), and would give access to further key resources such as quantum error correction and deterministic quantum teleportation<sup>1</sup>. Although spins in solids are attractive candidates for scalable quantum information processing, their single-shot detection has been achieved only for isolated qubits<sup>3–6</sup>. Here we demonstrate the preparation and measurement of a multi-spin quantum register in a low-temperature solid-state system by implementing resonant optical excitation techniques originally developed in atomic physics. We achieve high-fidelity read-out of the electronic spin associated with a single nitrogen-vacancy centre in diamond, and use this read-out to project up to three nearby nuclear spin qubits onto a well-defined state<sup>7</sup>. Conversely, we can distinguish the state of the nuclear spins in a single shot by mapping it onto, and subsequently measuring, the electronic spin<sup>5,8</sup>. Finally, we show compatibility with qubit control: we demonstrate initialization, coherent manipulation and single-shot read-out in a single experiment on a two-qubit register, using techniques suitable for extension to larger registers. These results pave the way for a test of Bell's inequalities on solid-state spins and the implementation of measurement-based quantum information protocols.**

The electronic spin of the nitrogen-vacancy centre (NV) in diamond constitutes an exceptional solid-state system for investigating quantum phenomena, combining excellent spin coherence<sup>9–12</sup> with a robust optical interface<sup>13–16</sup>. Furthermore, the host nitrogen nuclear spin (typically <sup>14</sup>N, with nuclear spin  $I = 1$ ) and nearby isotopic impurity <sup>13</sup>C nuclei ( $I = 1/2$ ) have hyperfine interactions with the NV's electronic spin ( $S = 1$ ), allowing development of few-spin quantum registers that have been suggested as building blocks for quantum repeaters<sup>17</sup>, cluster state computation<sup>18</sup> and distributed quantum computing<sup>19</sup>. All of these applications require high-fidelity preparation, manipulation and measurement of multiple spins. There have been significant advances in coherent control over few-spin systems in diamond<sup>20,21</sup>, but no method exists for the simultaneous preparation<sup>22,23</sup> and single-shot read-out<sup>5</sup> of multi-spin registers, which impedes progress towards multi-qubit protocols. Here we remove this obstacle by exploiting resonant excitation techniques, as pioneered in atomic physics<sup>24,25</sup>, in microstructured diamond devices that allow high photon collection efficiency (Fig. 1a). These new methods enable us to initialize multiple nuclear spin qubits and to perform single-shot read-out of a few-qubit register, clearing the way towards implementation of quantum algorithms with solid-state spins.

Our preparation and read-out techniques rely on resonant excitation of spin-selective optical transitions of the NV, which can be spectrally resolved at low temperatures<sup>26</sup>. We use the  $E_x$  and  $A_1$  transitions in our experiments (Fig. 1b):  $A_1$  connects the ground states with spin projection  $m_S = \pm 1$  to an excited state with a primarily

$m_S = \pm 1$  character, whereas  $E_x$  connects states with  $m_S = 0$ . A typical spectrum of NV A, one of the two NVs we study, is shown in Fig. 1c (see Supplementary Information for NV B). Under resonant excitation of a single transition, the fluorescence decays with time owing to a slight spin mixing within the excited states that induces shelving into the other spin state (Fig. 1d). This optical pumping mechanism allows high-fidelity spin state initialization<sup>24,27</sup>: from the data in Fig. 1d, we estimate a preparation error into the  $m_S = 0$  ground state of  $0.3 \pm 0.1\%$ , which is a drastic reduction of the  $11 \pm 3\%$  preparation

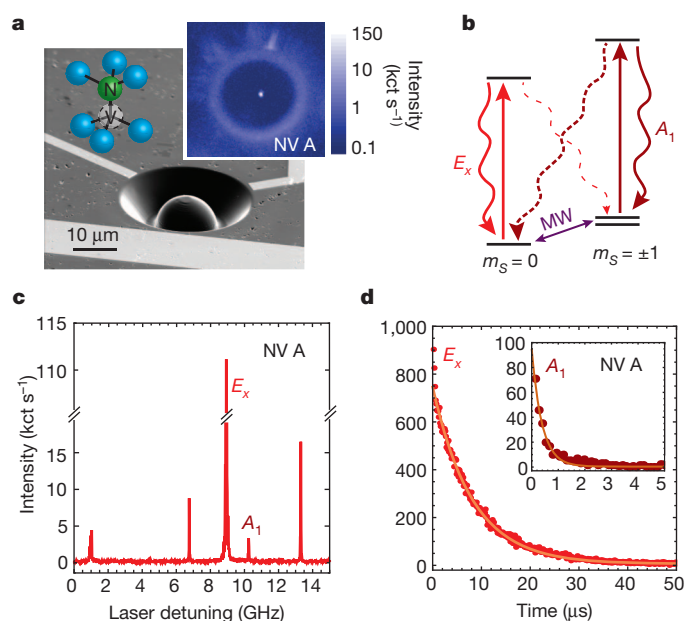


**Figure 1 | Resonant excitation and electronic spin preparation of a nitrogen-vacancy centre.** **a**, Scanning electron microscope image of a solid immersion lens representative of those used in the experiments (for details, see Supplementary Information). The overlaid sketch shows the substitutional nitrogen and the adjacent vacancy that form the NV. Inset, scanning confocal microscope image of NV A (logarithmic colour scale). kct, 1,000 counts. **b**, Energy levels used to prepare and read out the NV's electronic spin ( $S = 1$  in the ground and optically excited states); transitions are labelled according to the symmetry of their excited states. Dashed lines indicate spin-non-conserving decay paths. MW, microwave transition. **c**, Photoluminescence excitation spectrum of NV A; frequency is given relative to 470.443 THz. **d**, Fluorescence time trace of NV A, initially prepared in  $m_S = 0$  ( $E_x$  excitation, 4.8-nW power) and  $m_S = \pm 1$  ( $A_1$  excitation, 7.4-nW power; inset), with a saturation power  $P_{\text{sat}} \approx 6$  nW. Spin flips in the excitation cycle lead to nearly exponential decay of fluorescence, with fitted spin-flip times of  $1/\gamma_0 = 8.1 \pm 0.1$   $\mu\text{s}$  for  $E_x$  and  $0.39 \pm 0.01$   $\mu\text{s}$  for  $A_1$ , and initial respective intensities of  $740 \pm 5$  and  $95 \pm 2$  kct  $\text{s}^{-1}$ , giving a lower limit of  $99.7 \pm 0.1\%$  to the  $m_S = 0$  preparation fidelity and one of  $99.2 \pm 0.1\%$  to the  $m_S = \pm 1$  preparation fidelity. The low initial intensity for  $A_1$  is associated with a fast intersystem crossing to metastable singlet states (Supplementary Information).

<sup>1</sup>Kavli Institute of Nanoscience Delft, Delft University of Technology, PO Box 5046, 2600 GA Delft, The Netherlands. <sup>2</sup>Department of Physics and Astronomy, Bates College, 44 Campus Avenue, Lewiston, Maine 04240, USA.

\*These authors contributed equally to this work.

error observed with conventional off-resonant initialization (Supplementary Information).

Spin-dependent resonant excitation also allows single-shot electronic spin read-out: the presence or absence of fluorescence under  $E_x$  excitation reveals the spin state. By working with low-strain NVs at low temperature ( $T = 8.6$  K), we suppress spin mixing<sup>26,28</sup> and phonon-induced transitions<sup>29</sup> within the excited states, extending the spin relaxation time under  $E_x$  excitation to several microseconds. Together with a high collection efficiency due to the use of solid immersion lenses<sup>30</sup> fabricated around pre-selected, low-strain NVs, and efficient rejection of resonant excitation from the measured phonon-sideband emission, this highly spin-preserving transition allows the detection of several photons before the spin flips.

We demonstrate single-shot read-out by initializing the electronic spin to have  $m_S = 0$  or  $m_S = \pm 1$ , followed by resonant excitation of the  $E_x$  read-out transition for  $t_{ro} = 100$   $\mu$ s (Fig. 2a). The resulting histograms of the number of detected photons are given in Fig. 2b. As expected, for  $m_S = \pm 1$  we observe negligible excitation, with a 98.3%

probability of not measuring any photons during the probe interval. By stark contrast, after initializing the spin to have  $m_S = 0$  we detect an average of  $\langle n_0 \rangle = 6.4$  photons per shot. We assign the state  $m_S = 0$  to detection of one or more photons, and  $m_S = \pm 1$  to the detection of no photons. After truncating our integration window to the optimal duration of 40  $\mu$ s, we find an average fidelity of

$$F_{\text{avg}} = \frac{1}{2} (F_{m_S=0} + F_{m_S=\pm 1}) = 93.2 \pm 0.5\%$$

where  $F_{m_S}$  is the probability of obtaining the measurement outcome  $m_S$  after optical pumping into  $m_S$ . To verify that these measurement outcomes indeed correspond to the electronic spin states, we use single-shot read-out to observe spin Rabi oscillations and microwave-induced quantum jumps<sup>25</sup> (Fig. 2d,e).

Whereas the full read-out optically pumps the spin, shorter read-out durations can be non-destructive, albeit at lower fidelity. By optimizing integration windows, we obtain a fidelity of  $83.4 \pm 0.5\%$  for each of two successive read-out segments (Fig. 2c). Correlations

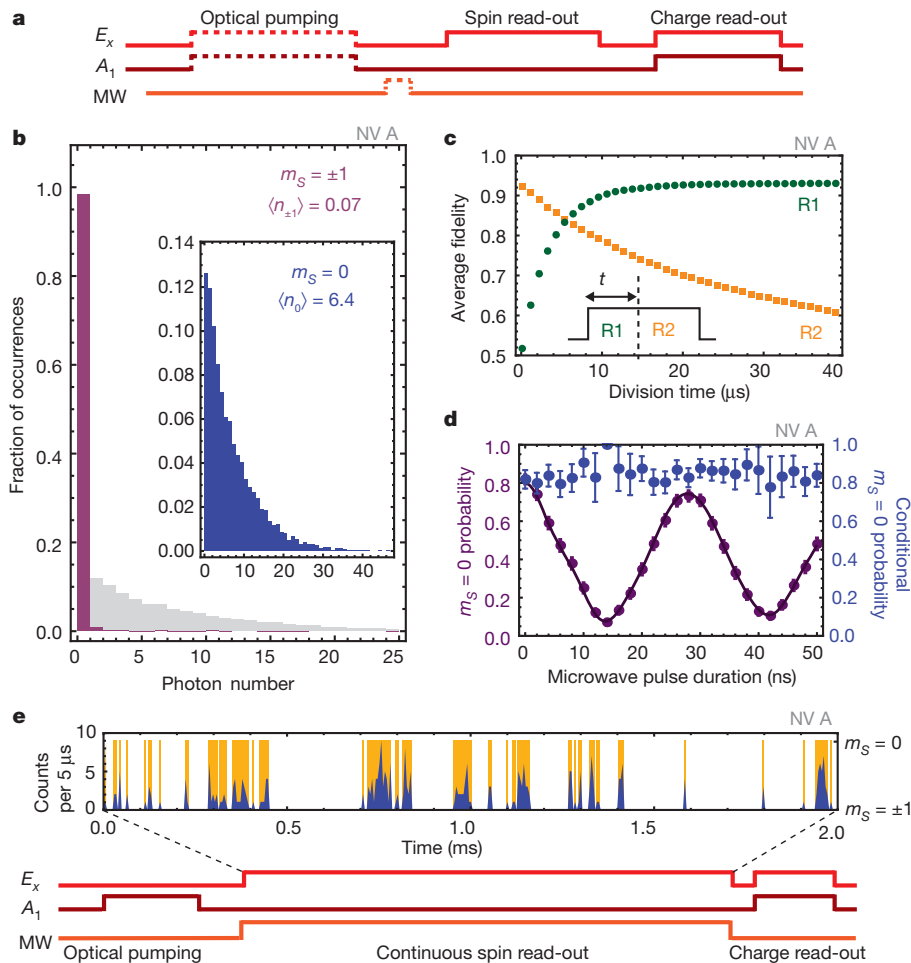


**Figure 2 | Projective single-shot read-out of the NV's electronic spin.**

**a**, Pulse sequence used for electronic spin read-out: after charge initialization (532 nm; not shown) the electron is pumped into the  $m_S = 0$  ( $A_1$ , dark red) or  $m_S = \pm 1$  ( $E_x$ , bright red) state, and then undergoes optional microwave spin manipulation and spin read-out by a pulse resonant with  $E_x$ . Conditioning on simultaneous resonance during the final charge- and detuning-sensing stage eliminates effects of local electric field fluctuations or ionization (Supplementary Information). **b**, Statistics of photon counts detected during a  $t_{ro} = 100$ - $\mu$ s electronic spin read-out after initialization into the respective  $m_S = \pm 1$  (red) and  $m_S = 0$  (superimposed light grey and inset) states, obtained from 10,000 measurement repetitions. **c**, When the 100- $\mu$ s read-out pulse is divided into two read-out segments, R1 and R2, with a variable division point, the fidelity of two consecutive segments reaches  $83.4 \pm 0.5\%$  for an optimal

division time of 5.5  $\mu$ s; the probability of identical sequential outcomes is  $82.0 \pm 0.7\%$ . Error bars (2 s.e.,  $n = 10,000$ ) are smaller than the symbols.

**d**, Electronic spin Rabi oscillations between  $m_S = 0$  and  $m_S = -1$  at axial magnetic field  $B_z \approx 15$  G (purple): each data point comes from 1,000 single-shot read-out repetitions. The fit, which includes the detailed hyperfine level structure, yields a visibility of  $78 \pm 8\%$ , where a maximum of 84% can be expected. Blue data points show the measurement outcome after projection into  $m_S = 0$  by selecting only read-out events with photons detected within the first 400 ns (Supplementary Information). All errors and error bars, 2 s.e.

**e**, Quantum jumps in the fluorescence time trace during continuous spin read-out. Durations of dark periods depend on the microwave Rabi frequency (Supplementary Information). Blue data indicates the counts per 5- $\mu$ s read-out bin, and the deduced spin state is shown in orange.

between measurement outcomes indicate that the read-out is projective. Following preparation of a superposition of spin states, we condition on detection of at least one photon (that is, measurement outcome  $m_S = 0$ ) during a first short read-out pulse, and probe the resulting spin state with a second read-out (Fig. 2d, blue data points). Regardless of the initial spin state, we observe a constant high probability of obtaining  $m_S = 0$  in the second read-out. This shows that the read-out method is strongly projective and well suited for application in measurement-based quantum protocols.

We use projective read-out of the electronic spin in combination with quantum gate operations for initialization and read-out of a few-qubit nuclear spin register. We first demonstrate the concept of measurement-based preparation on a single nuclear qubit. The electronic spin resonance spectrum for NV B (Fig. 3a, green trace) reveals the coupling to the host  $I = 1$   $^{14}\text{N}$  nuclear spin: two partly overlapping sets of three hyperfine lines correspond to the  $m_S = 0 \leftrightarrow -1$  and

$m_S = 0 \leftrightarrow +1$  electronic spin transitions, Zeeman-split by  $\sim 2$  MHz in Earth's magnetic field. The outermost transitions are associated with a specific nuclear spin state with spin projection  $m_I$ , for example  $(m_S, m_I) = (0, -1) \leftrightarrow (-1, -1)$  at 2.874 GHz. Our initialization procedure works as follows (Fig. 3a, circuit diagram). First we prepare the electronic spin in  $m_S = \pm 1$ . We then perform a nuclear-spin-controlled NOT operation on the electronic spin by applying a  $\pi$ -pulse at 2.874 GHz; this operation rotates the electronic spin into  $m_S = 0$  only when  $m_I = -1$ . Finally we read out the electronic spin for 400 ns. If one or more photons are detected during this interval, the two-spin system is projected into  $(m_S, m_I) = (0, -1)$ . Alternatively, if we run the same protocol with initial electronic spin state  $m_S = 0$ , we prepare the nuclear spin with  $m_I = \{0, +1\}$ .

The efficiency of the nuclear spin initialization is evidenced by its drastic effect on the electronic spin resonance spectrum (Fig. 3a). Whereas before preparation the depths of the different hyperfine lines

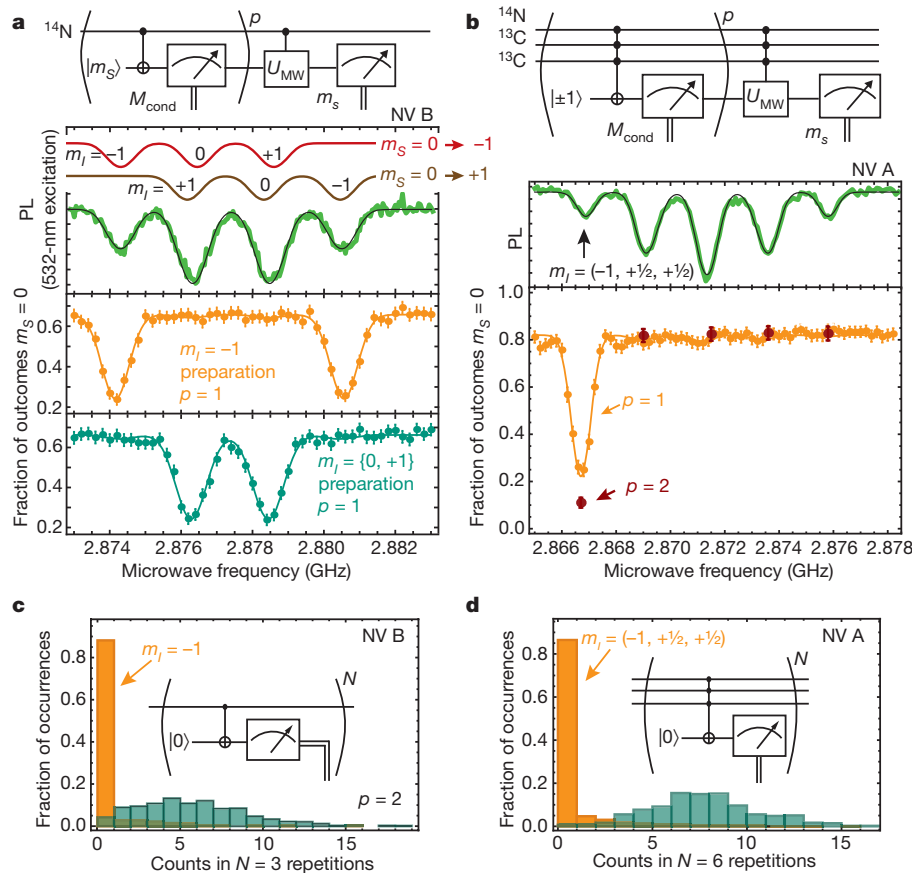


**Figure 3 | Nuclear spin preparation and read-out.** **a**, Measurement-based preparation of a single  $^{14}\text{N}$  nuclear spin. In Earth's ambient magnetic field of  $\sim 0.5$  G, without nuclear spin polarization we observe four resonances in the hyperfine spectrum (green trace) for NV B; the outer two correspond to the nuclear spin state with  $m_I = -1$  and the central two are combinations of the states with  $m_I = \{0, +1\}$ . PL, photoluminescence intensity. Red and brown traces indicate transitions to the  $m_S = +1$  and  $m_S = -1$  states, respectively. As indicated in the circuit diagram, to initialize the nuclear spin we entangle it with the electronic spin and then read out the latter;  $p$  denotes the number of preparation steps, each of which is one iteration of the section of the circuit diagram enclosed in parentheses.  $M_{\text{cond}}$  indicates the conditioning measurement,  $M_e$  the electron spin read-out and  $U_{\text{MW}}$  the microwave spin manipulation. Data for the  $m_I = -1$  preparation is shown in orange; data for the  $m_I = \{0, +1\}$  preparation is shown in cyan. Fits to Gaussian spectra show an amplitude ratio of  $96 \pm 4\%$  in the desired nuclear spin state. **b**, Measurement-based preparation of a three-nuclear-spin register. Using a similar sequence (circuit diagram), we prepare a well-defined state for all three nuclear spins. A portion of the uninitialized hyperfine spectrum (green) contains 12 partly superposed lines, of which we prepare the single line corresponding to

$m_I = (-1, 1/2, 1/2)$  (orange). Gaussian fits constrained to known hyperfine splittings yield an amplitude ratio of  $88 \pm 10\%$ . The observed visibility can be improved by performing two preparation steps and electronic spin repumping ( $p = 2$ ; five red data points), yielding a contrast of 82% of the expected visibility from known read-out fidelity (Supplementary Information). Uncertainties and error bars, 2 s.e. ( $n = 1,000$  for **a** and **b** with  $p = 1$ ; selected from 10,000 measurement runs for **b** with  $p = 2$ ). **c**, Single-shot measurement of the  $^{14}\text{N}$  nuclear spin, preceded by two preparation steps ( $p = 2$ ). Read-out (three repetitions) conditioned on successful preparation distinguishes  $m_I = -1$  (orange; threshold  $< 1$  count) from  $m_I = \{0, +1\}$  (cyan) with an average fidelity of  $92 \pm 2\%$  (Supplementary Information). **d**, Multiple-nuclear-spin read-out. Using a sequence similar to that in **c** (inset), we distinguish one of the 12 hyperfine states associated with NV A. To prepare nuclear spin states, we perform the read-out procedure seven times and keep only data with zero total counts (identified as  $m_I = (-1, 1/2, 1/2)$ ) or  $\geq 2$  counts per initialization step (other states). Subsequent read-out with six repetitions ( $m_I = (-1, 1/2, 1/2)$ ; state discrimination threshold,  $< 3$  total counts) achieves a  $96.7 \pm 0.8\%$  average fidelity for preparation and detection of the nuclear spin configuration.



indicate an equal mixture of the nuclear spin states (green trace), after preparation only the hyperfine lines corresponding to the prepared states are visible ( $m_I = -1$  for the orange trace and  $m_I = \{0, +1\}$  for the cyan trace).

The same nuclear spin initialization scheme can be applied to multi-qubit registers. Figure 3b shows the electronic spin resonance spectrum of NV A (green trace), whose electronic spin is coupled to both the host  $^{14}\text{N}$  nuclear spin and two nearby  $^{13}\text{C}$  nuclei (Supplementary Information). The lowest-frequency line corresponds to a single state of the three nuclear spins. A  $\pi$ -pulse on this transition therefore implements a triple-controlled NOT operation on the electronic spin (Fig. 3b, circuit diagram), allowing the initialization of all three nuclear spins (Fig. 3b, orange trace). The initialization can be further improved by repeating the preparation step (Fig. 3b, red data points).

The nuclear qubits can be read out in a single shot by applying a nuclear-spin-controlled NOT operation to the electronic spin and subsequently reading out the electronic spin (Fig. 3c, d, inset circuit diagrams). Because the back-action of the electronic spin measurement on the nuclear spin is weak, we can repeat the process to obtain higher read-out fidelity<sup>5,8</sup>. Figure 3c compares the resulting photon statistics for NV B after initialization into the single nuclear spin state  $m_I = -1$  with those obtained for  $m_I = \{0, +1\}$ , and indicates an average read-out fidelity of  $92 \pm 2\%$ . This number is a lower bound on the true read-out fidelity, as it includes errors in state preparation.

A straightforward extension of this scheme can be used to read out the complete state of a register of multiple nuclear spins. By using a

multiply controlled NOT gate in the read-out sequence, we can measure in a single shot whether the register is in a particular configuration. We demonstrate this procedure on NV A, where we identify the three-nuclear-spin state  $m_I = (-1, 1/2, 1/2)$  (Fig. 3d and Supplementary Information). The other possible configurations can be probed by sequential application of this read-out scheme to different spectrally resolved hyperfine transitions, or, alternatively, by systematically flipping the nuclear spin qubits and repeating the read-out on the same hyperfine transition.

Electronic–nuclear flip-flop processes in the optically excited state, which reduce the nuclear spin read-out fidelity, pose a significant hurdle to scaling the read-out to more qubits. Critically, resonant read-out allows selection of which states undergo optical excitation. By starting with the electronic spin in an  $m_S = \pm 1$  state, optical excitation will occur only when the register is in the state being probed; therefore, no optically induced nuclear spin flips will occur during measurement of any of the other states. Thus, by contrast with schemes depending on off-resonant excitation where each additional read-out step degrades the fidelity, resonant excitation allows scaling of high-fidelity read-out to larger registers.

Finally, we demonstrate the compatibility of all the different techniques discussed here by implementing them in a single experiment: we initialize, coherently manipulate and then read out a two-qubit register consisting of the electronic spin and  $^{14}\text{N}$  nuclear spin of NV B. After initializing it to have  $(m_S, m_I) = (0, -1)$ , we rotate the nuclear spin using a radio-frequency pulse and subsequently rotate the

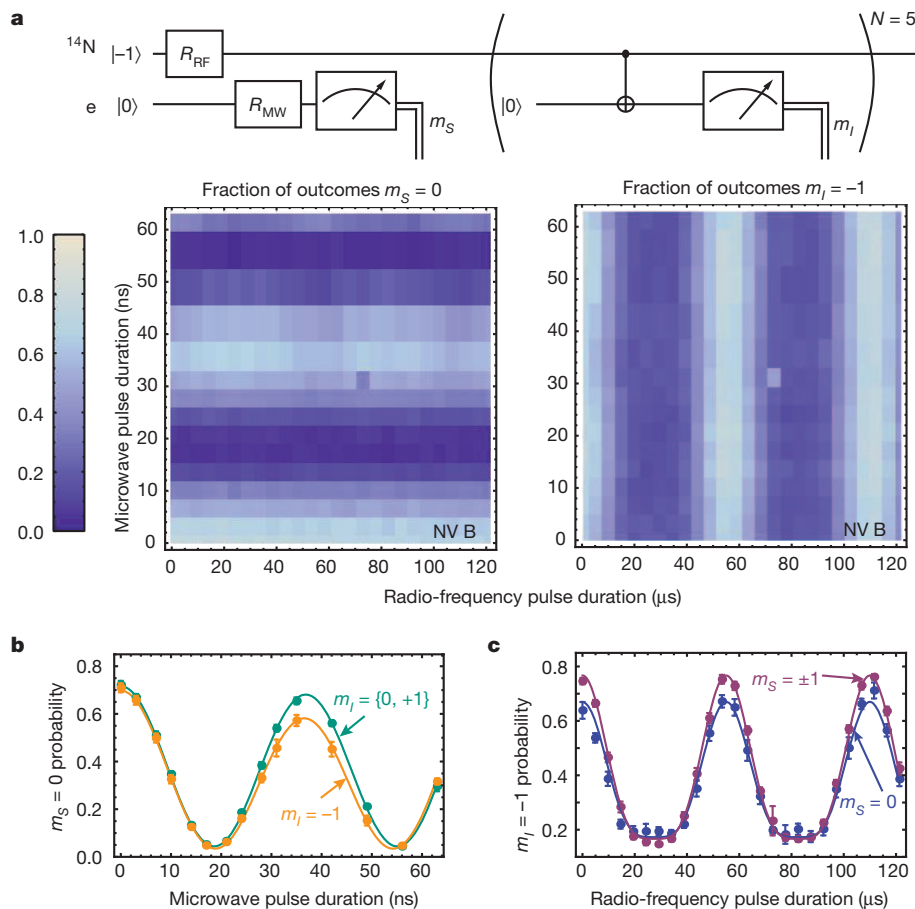


**Figure 4 | Initialization, manipulation and read-out of a two-qubit register.** **a**, After initialization of NV B into the  $(m_S, m_I) = (0, -1)$  state, we use radio-frequency excitation (spin rotation  $R_{\text{RF}}$  at 4.9464 MHz) to drive the nuclear spin and then microwaves (spin rotation  $R_{\text{MW}}$  at 2.8774 GHz) to drive the electronic spin. The electronic spin state is subsequently measured for 15  $\mu\text{s}$ , and this is followed by five read-out steps (each of 10  $\mu\text{s}$ ) of the  $^{14}\text{N}$  nuclear spin state. **b**, Probability of observing  $m_S = 0$  conditional on the measured nuclear

spin state and averaged over all radio-frequency pulse durations, as a function of microwave pulse duration (Supplementary Information). **c**, Probability of observing  $m_I = -1$  conditional on the observed electronic spin state and averaged over all microwave pulse durations, as a function of radio-frequency pulse duration (Supplementary Information). Error bars and uncertainties, 2 s.e.; data in **a** are based on 1,000 measurements per pixel.

electronic spin with a microwave pulse. We then read out the electronic spin and, subsequently, the  $^{14}\text{N}$  nuclear spin state (Fig. 4a, circuit diagram). The left-hand plot in Fig. 4a shows the read-out results for the electronic spin qubit, showing Rabi oscillations as a function of microwave pulse length. By contrast, the read-out results for the nuclear spin qubit (right-hand plot of Fig. 4a) show Rabi oscillations as a function of the radio-frequency pulse length.

To quantify crosstalk, we closely examine correlations between the two measurement outcomes. We observe that the electronic spin Rabi oscillation depends on the outcome of the nuclear read-out (Fig. 4b), but this dependence can be fully accounted for by the finite microwave power used in this experiment (Supplementary Information). The observed correlations thus arise from imperfect manipulation rather than from measurement crosstalk. For the nuclear spin read-out, however, true measurement crosstalk appears: nuclear Rabi oscillation amplitudes decrease when the electronic spin is measured to be in  $m_S = 0$  (Fig. 4c) because optical excitation during electronic spin read-out (which only succeeds for  $m_S = 0$ ) induces nuclear spin relaxation (see Supplementary Information for details). This effect can be mitigated by improving the collection efficiency (thus reducing the read-out duration), for example by integrating the NV into an optical cavity. Also, application of moderate magnetic fields can decrease the optically induced nuclear spin relaxation rate by orders of magnitude<sup>5</sup>.

Our results have implications for a broad range of spin-based applications. Single-shot electronic spin read-out can drastically improve NV-based sensors by allowing fast, quantum-projection-limited detection, creating opportunities in low-temperature magnetometry<sup>31,32</sup>. Extension of nuclear spin preparation techniques to remote nuclei in the spin bath may permit line-narrowing for enhanced sensitivity to d.c. magnetic fields. Furthermore, the preparation, manipulation and single-shot read-out of two spins opens the door to the exploration of two-particle quantum correlations, such as Bell's inequalities, and elementary quantum information processing protocols. Importantly, the techniques we describe are extendable to larger spin registers, and can be combined with precise spin qubit control and dynamical decoupling to give coherence protection<sup>10–12</sup>. The preparation and read-out fidelities reported here are sufficient for demonstrating measurement-based entanglement generation and quantum teleportation of spin qubits, and for exploring elementary quantum error correction schemes<sup>1</sup>. Ultimately, the integration of multi-spin registers with quantum optical channels by means of spin-photon entanglement<sup>13</sup> may allow their application as few-qubit nodes in long-distance quantum communication protocols or distributed quantum information processing networks.

## METHODS

All data were obtained by detecting photons emitted into the phonon sideband (wavelength, 650–750 nm). For photoluminescence excitation spectroscopy, excitation with 5.5-nW red light is applied while microwaves at 2.878 GHz, coupled through an on-chip stripline, drive the electronic spin transitions to prevent optical pumping. Scans are recorded in a single laser frequency sweep at  $\sim 200\text{ MHz s}^{-1}$ , and are preceded by a 10- $\mu\text{s}$  pulse of 532-nm excitation (50  $\mu\text{W}$ ). The green light is necessary to reset the negative-charge state of the NV, which can be photoionized by continuous resonant excitation. For all other experiments, 532-nm-induced spectral diffusion must also be controlled: to ensure that the NV is on resonance with the red excitation lasers, we condition our data on strong fluorescence upon simultaneous  $E_x$  and  $A_1$  excitation following the experimental sequence (details in Supplementary Information). All errors and error bars are 2 s.e. statistical uncertainty in the mean (95% confidence interval).

Received 11 June; accepted 28 July 2011.

Published online 21 September 2011.

- Nielsen, M. A. & Chuang, I. L. *Quantum Computation and Quantum Information* (Cambridge Univ. Press, 2000).
- Raussendorf, R., Browne, D. E. & Briegel, H. J. Measurement-based quantum computation on cluster states. *Phys. Rev. A* **68**, 022312 (2003).
- Elzerman, J. M. *et al.* Single-shot read-out of an individual electron spin in a quantum dot. *Nature* **430**, 431–435 (2004).

- Vamivakas, A. N. *et al.* Observation of spin-dependent quantum jumps via quantum dot resonance fluorescence. *Nature* **467**, 297–300 (2010).
- Neumann, P. *et al.* Single-shot readout of a single nuclear spin. *Science* **329**, 542–544 (2010).
- Morello, A. *et al.* Single-shot readout of an electron spin in silicon. *Nature* **467**, 687–691 (2010).
- Giedke, G., Taylor, J. M., D'Alessandro, D., Lukin, M. D. & Imamoglu, A. Quantum measurement of a mesoscopic spin ensemble. *Phys. Rev. A* **74**, 032316 (2006).
- Jiang, L. *et al.* Repetitive readout of a single electronic spin via quantum logic with nuclear spin ancillae. *Science* **326**, 267–272 (2009).
- Balasubramanian, G. *et al.* Ultralong spin coherence time in isotopically engineered diamond. *Nature Mater.* **8**, 383–387 (2009).
- Naydenov, B. *et al.* Dynamical decoupling of a single-electron spin at room temperature. *Phys. Rev. B* **83**, 081201(R) (2011).
- de Lange, G., Wang, Z. H., Ristè, D., Dobrovitski, V. V. & Hanson, R. Universal dynamical decoupling of a single solid-state spin from a spin bath. *Science* **330**, 60–63 (2010).
- Ryan, C. A., Hodges, J. S. & Cory, D. G. Robust decoupling techniques to extend quantum coherence in diamond. *Phys. Rev. Lett.* **105**, 200402 (2010).
- Togan, E. *et al.* Quantum entanglement between an optical photon and a solid-state spin qubit. *Nature* **466**, 730–734 (2010).
- Batalov, A. *et al.* Temporal coherence of photons emitted by single nitrogen-vacancy defect centers in diamond using optical Rabi-oscillations. *Phys. Rev. Lett.* **100**, 077401 (2008).
- Buckley, B. B., Fuchs, G. D., Bassett, L. C. & Awschalom, D. D. Spin-light coherence for single-spin measurement and control in diamond. *Science* **330**, 1212–1215 (2010).
- Robledo, L., Bernien, H., van Weperen, I. & Hanson, R. Control and coherence of the optical transition of single nitrogen vacancy centers in diamond. *Phys. Rev. Lett.* **105**, 177403 (2010).
- Childress, L., Taylor, J. M., Sørensen, A. S. & Lukin, M. D. Fault-tolerant quantum communication based on solid-state photon emitters. *Phys. Rev. Lett.* **96**, 070504 (2006).
- Barrett, S. D. & Kok, P. Efficient high-fidelity quantum computation using matter qubits and linear optics. *Phys. Rev. A* **71**, 060310(R) (2005).
- Jiang, L., Taylor, J. M. & Lukin, M. D. Fast and robust approach to long-distance quantum communication with atomic ensembles. *Phys. Rev. A* **76**, 012301 (2007).
- Dutt, M. V. G. *et al.* Quantum register based on individual electronic and nuclear spin qubits in diamond. *Science* **316**, 1312–1316 (2007).
- Neumann, P. *et al.* Multiparticle entanglement among single spins in diamond. *Science* **320**, 1326–1329 (2008).
- Fuchs, G. D. *et al.* Excited-state spectroscopy using single spin manipulation in diamond. *Phys. Rev. Lett.* **101**, 117601 (2008).
- Jacques, V. *et al.* Dynamic polarization of single nuclear spins by optical pumping of nitrogen-vacancy color centers in diamond at room temperature. *Phys. Rev. Lett.* **102**, 057403 (2009).
- Happer, W. Optical pumping. *Rev. Mod. Phys.* **44**, 169–249 (1972).
- Blatt, R. & Zoller, P. Quantum jumps in atomic systems. *Eur. J. Phys.* **9**, 250–256 (1988).
- Tamarat, P. *et al.* Spin-flip and spin-conserving optical transitions of the nitrogen-vacancy centre in diamond. *N. J. Phys.* **10**, 045004 (2008).
- Atature, M. *et al.* Quantum-dot spin-state preparation with near-unity fidelity. *Science* **312**, 551–553 (2006).
- Manson, N. B., Harrison, J. P. & Sellars, M. J. Nitrogen-vacancy center in diamond: model of the electronic structure and associated dynamics. *Phys. Rev. B* **74**, 104303 (2006).
- Fu, K.-M. C. *et al.* Observation of the dynamic Jahn-Teller effect in the excited states of nitrogen-vacancy centers in diamond. *Phys. Rev. Lett.* **103**, 256404 (2009).
- Hadden, J. P. *et al.* Strongly enhanced photon collection from diamond defect centers under microfabricated integrated solid immersion lenses. *Appl. Phys. Lett.* **97**, 241901 (2010).
- Degen, C. L. Scanning magnetic field microscope with a diamond single-spin sensor. *Appl. Phys. Lett.* **92**, 243111 (2008).
- Taylor, J. M. *et al.* High-sensitivity diamond magnetometer with nanoscale resolution. *Nature Phys.* **4**, 810–816 (2008).

Supplementary Information is linked to the online version of the paper at [www.nature.com/nature](http://www.nature.com/nature).

**Acknowledgements** L.R. acknowledges support by a Marie Curie Intra European Fellowship within the 7th European Community Framework Programme. L.R., H.B., B.H. and R.H. acknowledge support from the Dutch Organization for Fundamental Research on Matter (FOM) and the European Commission (SOLID). L.C. acknowledges support from Research Corporation for Science Advancement (RCSA).

**Author Contributions** L.R., L.C. and H.B. conducted the experiments. L.R., L.C., H.B., B.H. and R.H. analysed the data. H.B. and P.F.A.A. fabricated the devices. L.R., L.C. and R.H. wrote the paper. All authors commented on the manuscript.

**Author Information** Reprints and permissions information is available at [www.nature.com/reprints](http://www.nature.com/reprints). The authors declare no competing financial interests. Readers are welcome to comment on the online version of this article at [www.nature.com/nature](http://www.nature.com/nature). Correspondence and requests for materials should be addressed to R.H. ([r.hanson@tudelft.nl](mailto:r.hanson@tudelft.nl)).

# A reserve stem cell population in small intestine renders *Lgr5*-positive cells dispensable

Hua Tian<sup>1</sup>, Brian Biehs<sup>2</sup>, Søren Warming<sup>1</sup>, Kevin G. Leong<sup>3</sup>, Linda Rangell<sup>4</sup>, Ophir D. Klein<sup>2</sup> & Frederic J. de Sauvage<sup>1</sup>

The small intestine epithelium renews every 2 to 5 days, making it one of the most regenerative mammalian tissues. Genetic inducible fate mapping studies have identified two principal epithelial stem cell pools in this tissue. One pool consists of columnar *Lgr5*-expressing cells that cycle rapidly and are present predominantly at the crypt base<sup>1</sup>. The other pool consists of *Bmi1*-expressing cells that largely reside above the crypt base<sup>2</sup>. However, the relative functions of these two pools and their interrelationship are not understood. Here we specifically ablated *Lgr5*-expressing cells in mice using a human diphtheria toxin receptor (*DTR*) gene knocked into the *Lgr5* locus. We found that complete loss of the *Lgr5*-expressing cells did not perturb homeostasis of the epithelium, indicating that other cell types can compensate for the elimination of this population. After ablation of *Lgr5*-expressing cells, progeny production by *Bmi1*-expressing cells increased, indicating that *Bmi1*-expressing stem cells compensate for the loss of *Lgr5*-expressing cells. Indeed, lineage tracing showed that *Bmi1*-expressing cells gave rise to *Lgr5*-expressing cells, pointing to a hierarchy of stem cells in the intestinal epithelium. Our results demonstrate that *Lgr5*-expressing cells are dispensable for normal intestinal homeostasis, and that in the absence of these cells, *Bmi1*-expressing cells can serve as an alternative stem cell pool. These data provide the first experimental evidence for the interrelationship between these populations. The *Bmi1*-expressing stem cells may represent both a reserve stem cell pool in case of injury to the small intestine epithelium and a source for replenishment of the *Lgr5*-expressing cells under non-pathological conditions.

Two types of stem cells have been described in the small intestine based on location and cycling dynamics<sup>1–4</sup>. Fast-cycling stem cells express markers including *Lgr5*, *Cd133* (also known as *Prom1*) and *Sox9* (refs 1, 5, 6) and are present throughout the intestine. Also known as crypt base columnar cells (CBCs), these slender cells populate the crypt and villi within 3 days, and are interspersed among the Paneth cells that support them<sup>7,8</sup>. Slower-cycling stem cells, marked by enriched expression of *Bmi1* or mouse *Tert* (*mTert*), represent a rarer cell population<sup>2,9</sup>. These cells form a descending gradient from proximal to distal regions of the intestine, such that they are more prevalent in the duodenum than in the colon. Despite their rarity, *Bmi1*-expressing stem cells are crucial for crypt maintenance<sup>2</sup>.

To study the function of *Lgr5*-expressing cells, we replaced the first coding exon of *Lgr5* with two distinct cassettes. The first consisted of a dsRED-IRES-CreERT2 sequence to enable genetic lineage tracing studies by tamoxifen (TAM)-inducible expression of Cre in *Lgr5*-expressing cells (Supplementary Fig. 1a, *Lgr5*<sup>CreER</sup> allele). The second cassette contained enhanced green fluorescent protein (EGFP) linked in frame to a human DTR cDNA (Supplementary Fig. 1a, *Lgr5*<sup>DTR</sup> allele), producing a fusion protein. Consistent with previous reports<sup>1</sup>, one injection of TAM in *Lgr5*<sup>CreER</sup>;R26R mice marked *Lgr5*-expressing stem cells in a mosaic fashion and led to generation of labelled progeny for more than 60 days (Supplementary Fig. 1b). Expression of DTR-EGFP

in *Lgr5*<sup>DTR</sup> mice functioned as a reporter for *Lgr5* expression (Fig. 1a) and also conferred diphtheria toxin (DT) sensitivity on CBCs. Expression of EGFP in mice carrying the *Lgr5*<sup>DTR</sup> allele was detected at the membrane of cycling CBCs in every crypt (Supplementary Fig. 1c–e, CBCs are marked by asterisks).

We next set out to test the effects of eliminating *Lgr5*-expressing cells by administering DT to *Lgr5*<sup>DTR</sup> mice. Twenty-four hours after DT administration, all EGFP-positive cells were depleted, including CBCs (Fig. 1a, b, j, k, p, q). Loss of *Lgr5*-expressing cells was further confirmed by the absence of *Lgr5* messenger RNA (Fig. 1d, e) and was accompanied by extensive apoptosis at the base of the crypts, with shedding of dead cells into the lumen (Fig. 1m, n).

After sustained DT exposure for 10 days, both the EGFP reporter and *Lgr5* mRNA were completely absent from the base of the crypts (Fig. 1c, f and Supplementary Fig. 2) but, notably, crypt architecture was comparable to controls (Fig. 1g, i, j, l). Proliferating CBCs were absent from the crypt (Fig. 1l, r), such that the crypt base was occupied mostly or entirely by Paneth cells (Supplementary Fig. 3a, b). The extensive apoptosis detected 24 h after DT treatment had significantly decreased by day 10 (compare Fig. 1n with o) but was still detectable. No increase in crypt fission after DT treatment was observed by haematoxylin and eosin staining at any time point (Fig. 1g–i).

Because *Lgr5*-expressing cells have been proposed to have a critical role in renewal of the intestine, it was surprising that the architecture of the intestinal epithelium was essentially intact after ablation of *Lgr5*-expressing CBCs (Fig. 1g–i). Within the villi, very little change in the total number of endocrine cells was observed (Supplementary Fig. 3c, d), and goblet cells were abundant in the crypts and villi (Supplementary Fig. 3g, h, j). Upon CBC ablation, Paneth cells were found at the bottom of the crypts and in some cases were mislocalized to the villi (Supplementary Fig. 3a, b and data not shown); additionally, migration of cells as assessed by BrdU pulse-chase labelling was normal (Supplementary Fig. 4). The only major difference from controls that we observed was in the secretory cell lineage; the number of chromogranin-A-positive enteroendocrine cells in the crypts doubled after DT administration for 10 days (Supplementary Fig. 3e, f, i).

We did not detect any *Lgr5*-expressing CBCs using either the EGFP reporter or *in situ* hybridization after 10 days of DT (Fig. 1c, f and Supplementary Fig. 2), but it was still possible that a few CBCs could have escaped ablation and repopulated the epithelium, as a similar scenario was reported in *c-Myc* and *Ascl2* conditional null mice<sup>10,11</sup>. To address this possibility directly, we visualized *Lgr5*-expressing cell activity during DT selection by producing *Lgr5*<sup>DTR/CreER</sup>;R26R mice. These mutant mice carried two null alleles at the *Lgr5* locus, of which one enabled ablation of *Lgr5*-expressing cells and the other enabled lineage tracing of any possibly remaining *Lgr5*-expressing cells. These mice died at postnatal day (P)1, consistent with previous reports that *Lgr5* null mice are not viable<sup>12</sup>. To analyse the postnatal gut, we grew pieces of small intestine from embryonic day (E)15 *Lgr5*<sup>DTR/CreER</sup>;R26R embryos under the kidney capsule of immunocompromised mice for

<sup>1</sup>Department of Molecular Biology, Genentech Inc., 1 DNA Way, South San Francisco, California 94080, USA. <sup>2</sup>Departments of Orofacial Sciences and Pediatrics, Institute for Human Genetics and Program in Craniofacial and Mesenchymal Biology, UCSF, 513 Parnassus Avenue, San Francisco, California 94143-0442, USA. <sup>3</sup>Department of Research Oncology, Genentech Inc., 1 DNA Way, South San Francisco, California 94080, USA. <sup>4</sup>Department of Pathology, Genentech Inc., 1 DNA Way, South San Francisco, California 94080, USA.



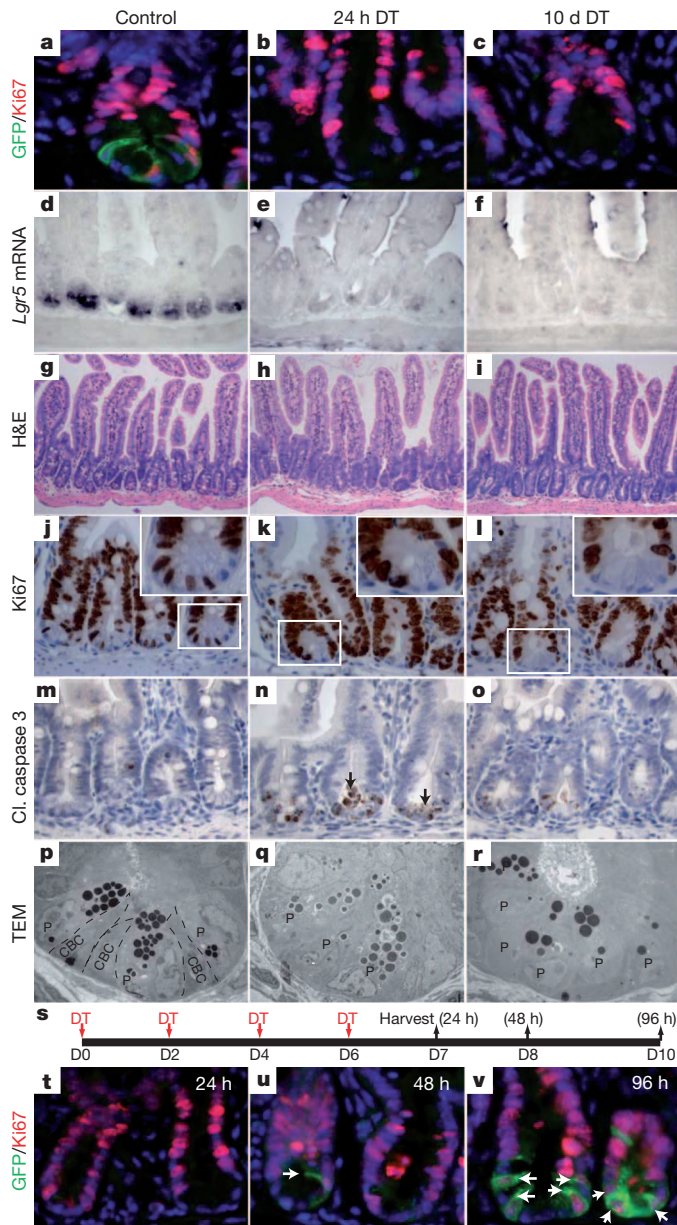


**Figure 1 | Characterization of DT-mediated CBC ablation.** **a**, EGFP is detected on the membrane of Ki67<sup>+</sup> proliferating CBCs in saline-treated *Lgr5*<sup>DTR/+</sup> mice. **b**, One dose of DT eliminates all DTR-EGFP-positive cells at 24 h. **c**, DT treatment for up to 10 days prevents reappearance of *Lgr5*-expressing cells. **d–f**, *Lgr5* mRNA is normally present at the bottom of the crypts (**d**) and is not detected after 24 h (**e**) or 10 days of DT treatment (**f**). **g–i**, Crypt architecture is intact after ablation of *Lgr5*-expressing CBCs. H&E, haematoxylin and eosin. **j–l**, Proliferation above the crypt base is normal after ablation of *Lgr5*-expressing CBCs. **m–o**, Extensive apoptosis is observed at the crypt base 24 h after DT and tapers off by 10 days, but is still higher than controls. 'Cl. caspase 3' is cleaved caspase 3. **p–r**, Electron microscopy shows that CBCs in controls are characterized by slender nuclei and scant cytoplasm. No CBCs remain at the crypt base after one dose or 10 days of DT treatment. The crypt base is filled with granule-rich Paneth cells. TEM, transmission electron microscopy. **s**, Dosing regimen for study of the recovery of *Lgr5*-expressing CBCs. **t**, No CBCs are detected 24 h after DT administration. **u**, A few *Lgr5*<sup>+</sup>/Ki67<sup>+</sup> CBCs (arrow) were detected 48 h after the last dose of DT. **v**, More *Lgr5*<sup>+</sup>/Ki67<sup>+</sup> CBCs (arrows) recovered after 96 h. Original magnification for panels: **a–f**, **m–o** and **t–v** at 40×; **g–i** at 20×; **j–l** at 63×; and **p–r** at 2,650×.

three weeks, at which point they formed crypts comparable to P17 intestine (Fig. 2a–e)<sup>13</sup>. After 10 days of TAM treatment, columns of blue cells emanated from the crypt base, and progeny of *Lgr5*-expressing cells differentiated into all four major cell types of the intestinal

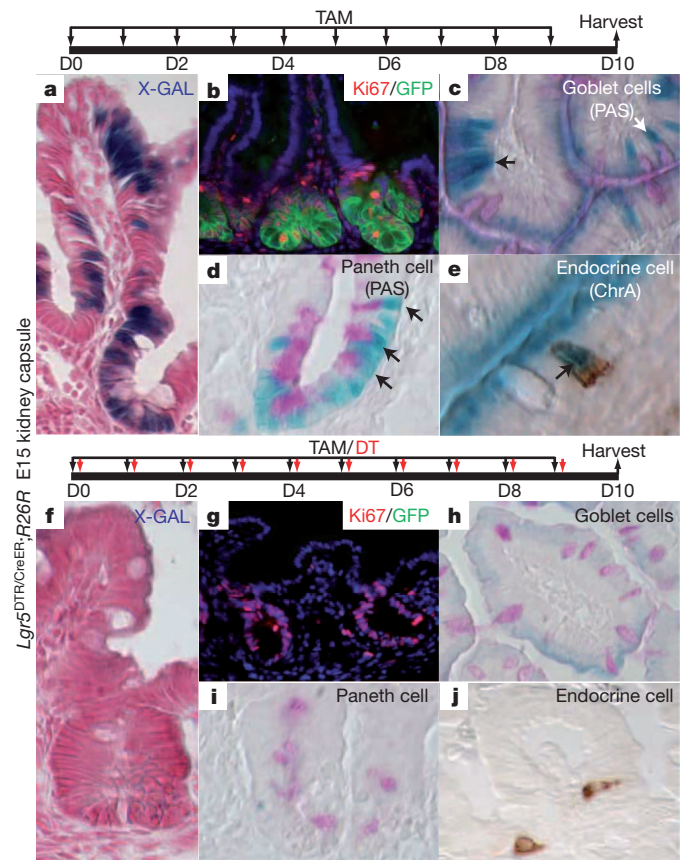


**Figure 2 | Maintenance of normal crypt architecture is not mediated by *Lgr5*-positive cells that have escaped ablation.** **a**, Ten-day lineage tracing of descendants of *Lgr5*-expressing stem cells shows a blue ribbon emanating from the base of the crypt in a grafted intestine piece from E15 *Lgr5*<sup>DTR/CreER</sup> embryos. **b–e**, Normal proliferation and differentiation of intestinal epithelium after loss of *Lgr5* gene function. *Lgr5*-expressing stem cells can give rise to all four major differentiated cell types (arrows). X-GAL-positive cells mark *Lgr5*-positive stem cell progeny, which overlap with differentiated cell markers for goblet (**c**), Paneth (**d**) and endocrine cell (**e**) lineages. PAS, periodic acid Schiff; ChrA, Chromogranin A. **f**, Concurrent TAM and DT treatment kills all *Lgr5*-expressing cells. No progeny of *Lgr5*-expressing cells (blue) are detected in the grafted intestine. **g–j**, No GFP-positive cells are detected but proliferation and differentiation are normal after DT-mediated ablation of *Lgr5*-expressing CBCs. Original magnification for panels: **a**, **b**, **f**, **g** at 40×; **c–e**, **h–j** at 63×.

epithelium (Fig. 2a–e). Concomitant administration of DT and TAM for 10 days eradicated all EGFP-positive CBCs (Fig. 2g), and no cells descended from *Lgr5*-expressing cells were observed (Fig. 2f), confirming that the *Lgr5*<sup>DTR</sup> allele leads to complete elimination of these cells. Importantly, no abnormalities in graft morphology, differentiation or proliferation were observed in these mice compared to controls (Fig. 2a–j).

Although *Lgr5*-expressing cells were completely depleted within 24 h of DT treatment, persistence of apoptotic bodies at the crypt base throughout the 10-day DT treatment suggested that *Lgr5*-expressing CBCs were continuously generated and eliminated during the treatment (Fig. 1n, o). This notion was supported by the quick recovery of *Lgr5*-expressing cells between 48 to 96 h after the final dose of DT (Fig. 1s–v). To follow the fate of the newly generated *Lgr5*-expressing cells, mice implanted with *Lgr5*<sup>DTR/CreER</sup>;R26R embryonic intestine fragments in the kidney capsule were allowed to recover for 6 days in the presence of TAM following 6 days of DT treatment. A row of blue cells emanated from the crypt base (Supplementary Fig. 5a), indicating that the newly formed *Lgr5*-expressing stem cells (Supplementary Fig. 5b, GFP-positive cells) gave rise to progeny that migrated out of the crypt. When the converse experiment was performed by



injecting TAM for 6 days and then dosing with DT from days 6 to 12, blue cells were only present in the upper region of the villi (Supplementary Fig. 5c), indicating that progeny of *Lgr5*-expressing cells marked between day 1 and 6 migrated out of the crypts into the villi, but that during DT treatment between days 6 and 12, *Lgr5*-expressing stem cells were no longer available (Supplementary Fig. 5d, absence of GFP signal) to supply labelled (blue) progeny to replenish the epithelium.

To study the long-term effects of CBC ablation, we isolated crypts from *Lgr5*<sup>DTR/+</sup> mice to perform *in vitro* crypt organoid cultures<sup>14</sup>. Crypts depleted of *Lgr5*-expressing CBCs by treatment for 10 days with DT, as indicated by absence of GFP expression, gave rise to organoids with similar efficiency as wild-type controls (Supplementary Fig. 6a, b). These could be passaged *in vitro* in DT for up to 2 months without losing their ability to expand and proliferate. No *Lgr5*-expressing (GFP-positive) cells were detected in organoid epithelium as long as the organoids were maintained in medium containing DT (Supplementary Fig. 6d). However, when DT was removed from the culture medium, *Lgr5*-expressing cells reappeared at the bottom of crypt-like structures within 3 days (Supplementary Fig. 6c, GFP-positive cells).

Because we found that *Lgr5*-expressing CBCs were dispensable for crypt maintenance, we next asked whether *Bmi1*-expressing stem cells were mobilized to compensate for the loss of *Lgr5*-expressing stem cells. Mouse BMI1 regulates self-renewal of haematopoietic and neuronal stem cells<sup>15</sup>. We used a GFP knock-in allele (*Bmi1*<sup>GFP/+</sup>) to monitor *Bmi1* gene expression<sup>16</sup>. *Bmi1*-expressing GFP-positive cells were most commonly observed at positions 3 to 6 above the crypt base (Fig. 3a), consistent with the *Bmi1* mRNA expression pattern in the small intestine<sup>2</sup>. Upon depletion of *Lgr5*-expressing CBCs in *Lgr5*<sup>DTR/+</sup>; *Bmi1*<sup>GFP/+</sup> mice after 9 days of DT treatment, the number of GFP-positive cells per crypt increased three fold (Fig. 3a–d and Supplementary Fig. 7a), and the proportion of crypts containing either single or multiple GFP-expressing cells increased by 40% compared to control animals (Supplementary Fig. 7b). Of note, 55% of the total number of GFP-positive crypts in *Lgr5*<sup>DTR/+</sup>; *Bmi1*<sup>GFP/+</sup> mice now contained multiple GFP-positive cells (Fig. 3d and Supplementary Fig. 7b), compared with only 22% in *Bmi1*<sup>GFP/+</sup> control animals.

To trace the fate of cells descended from *Bmi1*-expressing cells after elimination of *Lgr5*-expressing CBCs, we generated a *Bmi1*CreER bacterial artificial chromosome (BAC) transgenic allele (Supplementary Fig. 8). Labelling kinetics using the *Bmi1*-CreER transgenic line crossed with the R26R reporter were identical to previously reported results using the *Bmi1*<sup>CreER</sup> knock-in allele<sup>2</sup> (Fig. 3f). *Bmi1*-CreER;R26R;*Lgr5*<sup>DTR/+</sup> animals were treated with alternating doses of DT and TAM per day for 7 days (Fig. 3e). Because *Bmi1*-expressing cells are most abundant in the first 5 cm of the duodenum, we focused our analysis on this region. Consistent with the increased number of *Bmi1*-expressing cells (Supplementary Fig. 7a), the proportion of LacZ-positive crypts (either partially or fully labelled) also increased 34% upon loss of *Lgr5*-expressing CBCs (Supplementary Fig. 7c). The most marked difference was in the number of fully labelled crypts. Only 2.3% of crypts were fully labelled in *Bmi1*CreER;R26R control mice during a 6-day lineage tracing period, which was comparable with previous studies using a *Bmi1*<sup>CreER</sup> knock-in allele<sup>2</sup>. Upon loss of *Lgr5*-expressing CBCs, the number of fully labelled crypts increased approximately 15-fold (Fig. 3h, i and Supplementary Fig. 7c). These results indicate that in the absence of *Lgr5*-expressing cells, *Bmi1*-expressing cells are capable of directly giving rise to all intestinal cell types without going through *Lgr5*-positive intermediate cells. However, *Bmi1*-expressing stem cells did not give rise to an increased number of labelled crypts in more distal regions of small intestine and colon upon loss of *Lgr5*-expressing CBCs (Fig. 3f, g), indicating that alternative stem cell pools must compensate for the loss of *Lgr5*-expressing stem cells in distal regions of the gut.

Lastly, we tested whether *Bmi1*-expressing cells give rise to *Lgr5*-expressing cells under normal conditions. Because *Bmi1*- and *Lgr5*-expressing cells represent distinct although overlapping cell populations, we carried out a series of short-term pulse-chase experiments

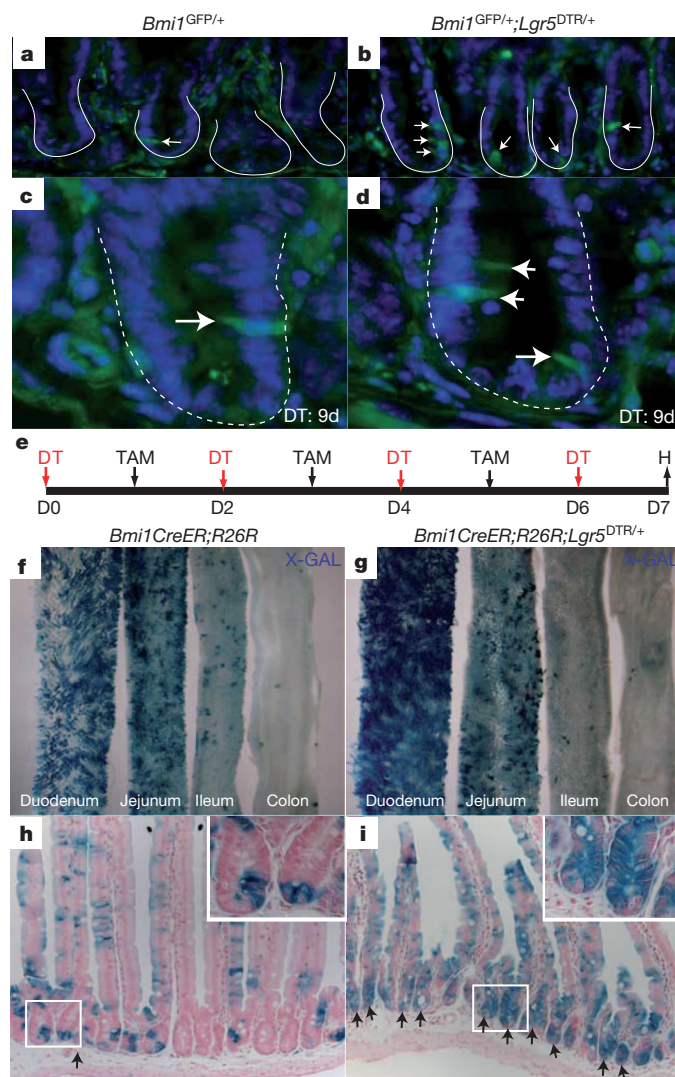


**Figure 3 | *Bmi1*-expressing stem cells are mobilized to compensate for the loss of *Lgr5*-expressing CBCs.** **a**, Rare *Bmi1*-expressing cells (arrows) are detected at positions 3 to 6 of the crypt base in the duodenum of *Bmi1*<sup>GFP/+</sup> reporter mice. **b**, Increased *Bmi1*-expressing cells appear at the crypt base upon ablation of *Lgr5*-expressing CBCs. **c**, Higher magnification showing a *Bmi1*-expressing cell at position 4 of crypt base in *Bmi1*<sup>GFP/+</sup> reporter mice. **d**, Close-up view of a crypt with multiple *Bmi1*-expressing cells after ablation of *Lgr5*-expressing cells. Arrows in **a–d** indicate (*Bmi1*)-expressing cells. **e**, Dosing regimen for lineage tracing of *Bmi1*-expressing cell progeny after ablation of *Lgr5*-expressing CBCs. H, harvest. **f**, **g**, Whole-mount X-GAL staining of the gastrointestinal tract. In both control mice and after ablation of *Lgr5*-expressing CBCs, *Bmi1*-expressing cells produce more progeny in the proximal than in the distal intestine. **h**, **i**, Close-up view of X-GAL-positive crypts in duodenum. Most of the labelled crypts have less than five X-GAL-positive cells in *Bmi1*-CreER;R26R control animals. Ablation of *Lgr5*-expressing CBCs stimulates production of progeny by *Bmi1*-expressing cells. 36% of the crypts in the first 5 cm of duodenum now become fully labelled (marked by arrows). Original magnification for panels: **a–d** at 40×; **f**, **g** at 1.2×; **h**, **i** at 20×.

using *Bmi1*-CreER;R26R;*Lgr5*<sup>DTR/+</sup> mice. Twenty-four hours after TAM administration, most of the  $\beta$ -galactosidase ( $\beta$ -gal)-positive cells appeared as individuals, reflecting the normal pattern of *Bmi1* expression (Fig. 4a) in the initially labelled cells. *Bmi1*-expressing cells ( $\beta$ -gal positive) overlapped with *Lgr5*-expressing cells (GFP positive) between positions 1 to 6 at the crypt base; the double-positive cells peaked at positions 3 and 4 (Fig. 4a–c). This observation is consistent with a previous report stating that *Bmi1* mRNA expression (via quantitative polymerase chain reaction (qPCR) analysis) was readily detectable in *Lgr5*-positive cells<sup>11</sup>. Later, between 48–72 h, clonal expansion

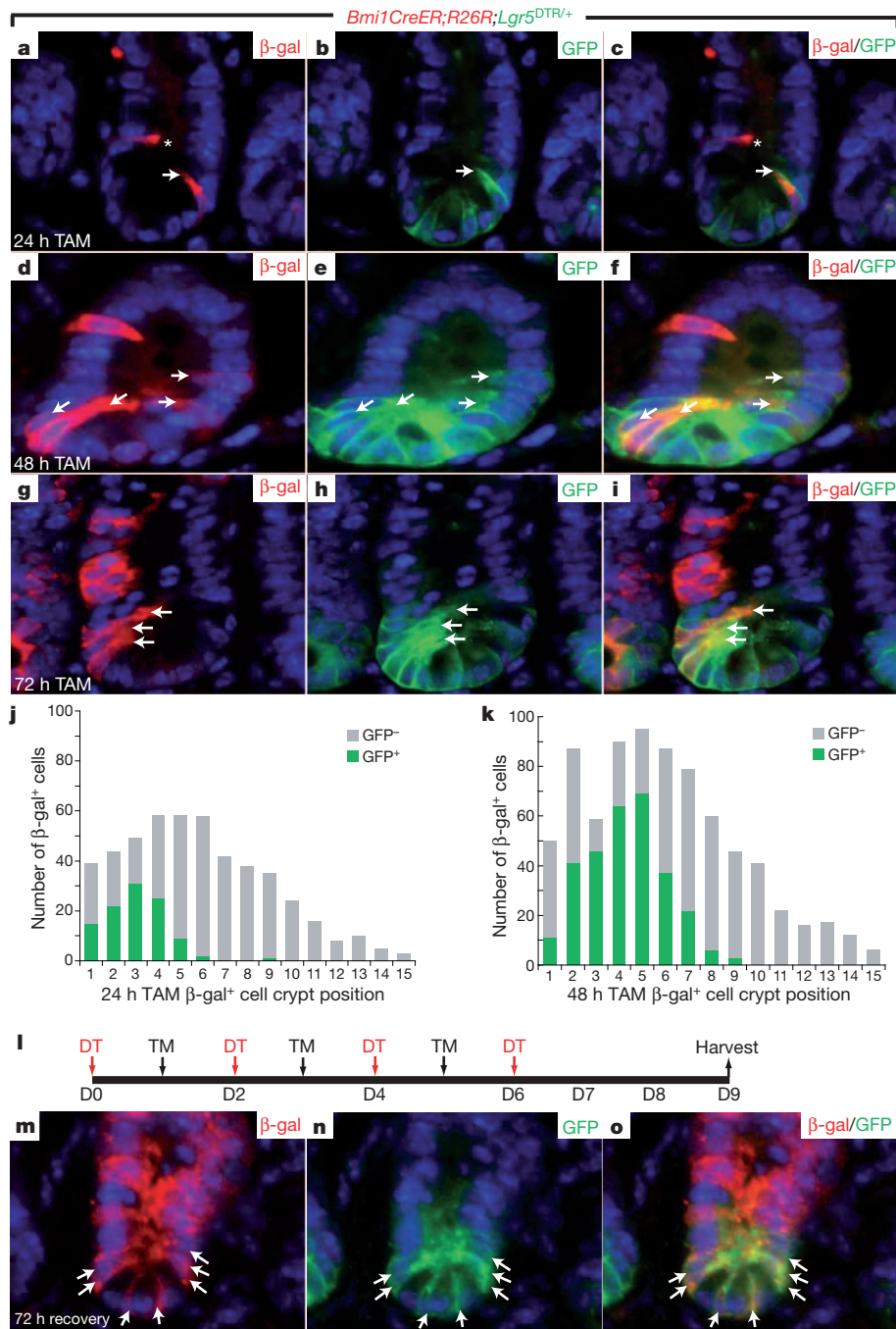


**Figure 4 | *Bmi1*-expressing cells give rise to *Lgr5*-expressing CBCs under normal and injury conditions.** **a–c**, *Bmi1*-*CreER*; *R26R*; *Lgr5*<sup>DTR/+</sup> mice were dosed with 5 mg TAM and harvested 24 h later.  $\beta$ -Gal-positive cells (red) derived from *Bmi1*-expressing cells overlap with *Lgr5*-expressing CBCs (GFP-positive, green) at position 4 (arrow). A non-overlapping  $\beta$ -gal-positive cell was detected at position 7 in the same crypt (asterisk). **d–f**, More  $\beta$ -gal-positive cells (red) show overlapping expression (marked by arrow) with *Lgr5*-expressing CBCs (GFP<sup>+</sup>, green) at 48 h. **g–i**, At 72 h, clonal expansion from *Bmi1*-positive stem cells is now evident by a streak of  $\beta$ -gal-positive cells migrating upward (red).  $\beta$ -Gal-positive clones at lower crypt positions overlap with *Lgr5*-

expressing CBCs (arrow). **j, k**, Distribution of the *Bmi1*-positive stem cell progeny ( $\beta$ -gal<sup>+</sup> cells) within the crypt at 24 and 48 h after TAM induction. **j**, *Bmi1*-expressing cells appear as singles throughout the crypt base between positions 1 to 15. **k**, More cells are derived from *Bmi1*-expressing stem cells at 48 h. A significant portion of  $\beta$ -gal<sup>+</sup> cells also express *Lgr5* (GFP<sup>+</sup>, green column), at positions 1 to 6. Overlapping cells (green) peak around positions 3, 4 or 5. **l**, Dosing regimen used to study the recovery of *Lgr5*-expressing CBCs from *Bmi1*-positive cells. **m–o**, *Bmi1*-positive cells give rise to a fully labelled crypt (red), including newly formed *Lgr5*-expressing CBCs (GFP<sup>+</sup>, arrows). The original magnification for all panels is 40 $\times$ .

from *Bmi1*-expressing cells was evident, as  $\beta$ -gal/GFP double-positive cells now appeared as doublets or triplets (Fig. 4d–i). We scored a total of 500 crypts at each time point and found that although a few cells were  $\beta$ -gal/GFP double positive (that is, expressing both *Bmi1* and *Lgr5*) at 24 h after TAM induction, this number doubled at 48 h (Fig. 4j, k). Similarly, lineage tracing from *Bmi1*-expressing cells carried out in mice treated for 6 days with DT and allowed to recover

for 72 h (Fig. 4l) demonstrated that newly formed *Lgr5*-positive cells at the bottom of the crypts arose from *Bmi1*-expressing cells (Fig. 4m–o). Together, these data show that *Bmi1*-expressing cells can give rise to *Lgr5*-expressing cells both under normal physiological conditions and after insults that deplete CBCs. Similar to our observation, *mTert*-expressing stem cells could also give rise to *Lgr5*-positive cells over a 5-day lineage tracing period<sup>9</sup>.



Our data support the existence of two stem cell pools in the epithelium of the small intestine: an actively proliferating stem cell compartment responsible for the daily maintenance of the intestine epithelium that is characterized by the expression of *Lgr5*, *Ascl2* and *Olfm4* (refs 1, 11, 17) and a distinct pool of stem cells expressing *Bmi1*. Our results lend support to the two-stem-cell pool model that is based on computational approaches<sup>18</sup>, and provide experimental evidence for recent models predicting that the intestine could fully recover after complete elimination of cellular subpopulations deemed to be functional stem cells<sup>19</sup>. Our data do not support the recent proposal that *Bmi1*-expressing cells are exclusively a subset of *Lgr5*-expressing cells<sup>11</sup>; rather they indicate that under normal circumstances, *Bmi1*-positive stem cells are upstream of rapidly cycling, *Lgr5*-expressing stem cells and replenish the pool of active stem cells, either to avoid exhaustion of actively cycling stem cells or to prevent the accumulation of damaged cells that may lead to the development of tumours. Importantly, we also demonstrate that when the *Lgr5*-expressing cell compartment is eliminated by DT treatment, *Bmi1*-expressing cells can increase in number, presumably as a compensatory mechanism. Under these conditions, *Bmi1*-expressing cells contribute directly to the generation of all cell types of the intestinal epithelium to produce a functional organ until the rapidly cycling stem cell compartment is able to recover. Although it has been proposed that *Bmi1*-expressing stem cells are quiescent<sup>2</sup>, this remains to be conclusively demonstrated.

Distinct stem cell pools with differing cycling dynamics have previously been observed in the hair follicle and in blood, organs that, like the intestine, undergo regular bouts of proliferation and regeneration<sup>20–22</sup>. The factors that regulate the interplay between discrete populations of stem cells, and the precise hierarchical relationships among such populations, remain to be characterized. Although we have found that loss of *Lgr5*-positive cells is sustainable under short-term conditions *in vivo*, it remains to be determined whether such a scenario can persist for longer periods of time. Interestingly, depletion of Paneth cells, which are thought to be important for the maintenance of CBCs<sup>7</sup>, can be tolerated by mice for over 6 months without significant structural defects of the epithelium<sup>23,24</sup>, supporting the idea that the intestine can function normally in the absence of CBCs. It will be important to determine how different stem cell populations sense the activity of other populations, whether rapidly cycling cells can repopulate more quiescent stem cell populations, and whether additional subpopulations of stem cells exist.

## METHODS SUMMARY

**Mice.** *Lgr5*<sup>DTR/+</sup>, *Lgr5*<sup>CreER/+</sup> and *Bmi1*-*CreER* alleles were generated as described in Methods. *Bmi1*<sup>GFP/+</sup> mice were provided by I. Weissman<sup>16</sup>. All studies and procedures involving animal subjects were approved by the Institutional Animal Care and Use Committees of Genentech and the University of California, San Francisco, and were conducted strictly in accordance with the approved animal handling protocol.

**Full Methods** and any associated references are available in the online version of the paper at [www.nature.com/nature](http://www.nature.com/nature).

Received 19 April; accepted 1 August 2011.

Published online 18 September 2011.

1. Barker, N. *et al.* Identification of stem cells in small intestine and colon by marker gene *Lgr5*. *Nature* **449**, 1003–1007 (2007).
2. Sangiorgi, E. & Capecchi, M. R. *Bmi1* is expressed *in vivo* in intestinal stem cells. *Nature Genet.* **40**, 915–920 (2008).

3. Li, L. & Clevers, H. Coexistence of quiescent and active adult stem cells in mammals. *Science* **327**, 542–545 (2010).
4. Fuchs, E. The tortoise and the hair: slow-cycling cells in the stem cell race. *Cell* **137**, 811–819 (2009).
5. Zhu, L. *et al.* Prominin 1 marks intestinal stem cells that are susceptible to neoplastic transformation. *Nature* **457**, 603–607 (2009).
6. Furuyama, K. *et al.* Continuous cell supply from a Sox9-expressing progenitor zone in adult liver, exocrine pancreas and intestine. *Nature Genet.* **43**, 34–41 (2011).
7. Sato, T. *et al.* Paneth cells constitute the niche for *Lgr5* stem cells in intestinal crypts. *Nature* **469**, 415–418 (2011).
8. Cheng, H. & Leblond, C. P. Origin, differentiation and renewal of the four main epithelial cell types in the mouse small intestine. V. Unitarian Theory of the origin of the four epithelial cell types. *Am. J. Anat.* **141**, 537–561 (1974).
9. Montgomery, R. K. *et al.* Mouse telomerase reverse transcriptase (mTert) expression marks slowly cycling intestinal stem cells. *Proc. Natl Acad. Sci. USA* **108**, 179–184 (2011).
10. Muncan, V. *et al.* Rapid loss of intestinal crypts upon conditional deletion of the Wnt/Tcf-4 target gene *c-Myc*. *Mol. Cell. Biol.* **26**, 8418–8426 (2006).
11. van der Flier, L. G. *et al.* Transcription factor achaete scute-like 2 controls intestinal stem cell fate. *Cell* **136**, 903–912 (2009).
12. Garcia, M. I. *et al.* LGR5 deficiency deregulates Wnt signaling and leads to precocious Paneth cell differentiation in the fetal intestine. *Dev. Biol.* **331**, 58–67 (2009).
13. Crosnier, C., Stamatakis, D. & Lewis, J. Organizing cell renewal in the intestine: stem cells, signals and combinatorial control. *Nature Rev. Genet.* **7**, 349–359 (2006).
14. Sato, T. *et al.* Single *Lgr5* stem cells build crypt-villus structures *in vitro* without a mesenchymal niche. *Nature* **459**, 262–265 (2009).
15. Park, I. K., Morrison, S. J. & Clarke, M. F. *Bmi1*, stem cells, and senescence regulation. *J. Clin. Invest.* **113**, 175–179 (2004).
16. Hosen, N. *et al.* *Bmi-1*-green fluorescent protein-knock-in mice reveal the dynamic regulation of *bmi-1* expression in normal and leukemic hematopoietic cells. *Stem Cells* **25**, 1635–1644 (2007).
17. van der Flier, L. G., Haeghebarth, A., Stange, D. E., van de Wetering, M. & Clevers, H. OLFM4 is a robust marker for stem cells in human intestine and marks a subset of colorectal cancer cells. *Gastroenterology* **137**, 15–17 (2009).
18. Lobachevsky, P. N. & Radford, I. R. Intestinal crypt properties fit a model that incorporates replicative ageing and deep and proximate stem cells. *Cell Prolif.* **39**, 379–402 (2006).
19. Buske, P. *et al.* A comprehensive model of the spatio-temporal stem cell and tissue organisation in the intestinal crypt. *PLoS Comput. Biol.* **7**, e1001045 (2011).
20. Wilson, A. *et al.* Hematopoietic stem cells reversibly switch from dormancy to self-renewal during homeostasis and repair. *Cell* **135**, 1118–1129 (2008).
21. Ito, M. *et al.* Stem cells in the hair follicle bulge contribute to wound repair but not to homeostasis of the epidermis. *Nature Med.* **11**, 1351–1354 (2005).
22. Hsu, Y. C., Pasolli, H. A. & Fuchs, E. Dynamics between stem cells, niche, and progeny in the hair follicle. *Cell* **144**, 92–105 (2011).
23. Bastide, P. *et al.* Sox9 regulates cell proliferation and is required for Paneth cell differentiation in the intestinal epithelium. *J. Cell Biol.* **178**, 635–648 (2007).
24. Garabedian, E. M., Roberts, L. J., McNevin, M. S. & Gordon, J. I. Examining the role of Paneth cells in the small intestine by lineage ablation in transgenic mice. *J. Biol. Chem.* **272**, 23729–23740 (1997).

**Supplementary Information** is linked to the online version of the paper at [www.nature.com/nature](http://www.nature.com/nature).

**Acknowledgements** We gratefully acknowledge efforts by all the members of the Genentech mouse facility, in particular R. Ybarra and G. Morrow. We are grateful to N. Strauli, D.-K. Tran and A. Rathnayake for assistance with mouse breeding. We thank M. Roose-Girma, X. Rairdan and the members of the embryonic stem cell and microinjection groups for embryonic stem cell work and transgenic line generation and members of the F.J.d.S. laboratory for discussions and ideas. This work was funded in part by the National Institutes of Health through the NIH Director's New Innovator Award Program, 1-DP2-OD007191 and by R01-DE021420, both to O.D.K.

**Author Contributions** H.T., B.B., S.W., K.G.L. and L.R. designed, performed experiments and collected data. H.T., B.B., O.D.K. and F.J.d.S. designed experiments, analysed the data and wrote the manuscript. O.D.K. and F.J.d.S. are joint senior authors. All authors discussed results and edited the manuscript.

**Author Information** Reprints and permissions information is available at [www.nature.com/reprints](http://www.nature.com/reprints). The authors declare competing financial interests: details accompany the full-text HTML version of the paper at [www.nature.com/nature](http://www.nature.com/nature). Readers are welcome to comment on the online version of this article at [www.nature.com/nature](http://www.nature.com/nature). Correspondence and requests for materials should be addressed to F.J.d.S. ([desauvage.fred@gene.com](mailto:desauvage.fred@gene.com)) or O.D.K. ([ophir.klein@ucsf.edu](mailto:ophir.klein@ucsf.edu)).

## METHODS

***Lgr5* and *Bmi1* vector construction.** The constructs for targeting the C57BL/6 *Lgr5* locus and the *Bmi1* BAC transgene were made using a combination of recombineering, DNA synthesis and standard molecular cloning techniques<sup>25,26</sup>.

For *Lgr5*, a 7,213 bp fragment (assembly NCBI37/mm9, chr10:115,020,315–115,027,527) from a C57BL/6 BAC (RP23 library) was first retrieved into plasmid pBlight-TK<sup>25</sup>. To generate the DTR–EGFP KI vector for *Lgr5*, a DTR–EGFP–pA–loxP–Neo–loxP cassette was synthesized (Blue Heron/Origene, DTR–EGFP sequence was based on that described previously<sup>27</sup>, and inserted right after the ATG of *Lgr5* (chr10:115,024,547, reverse strand), deleting the remainder of exon 1 and splice donor of intron 1 (a 212 bp deletion). To generate the CreERT2 KI vector, a dsRed2–IRES–CreERT2–pA–Frt–neo–Frt cassette was synthesized (Blue Heron/Origene) and inserted at the same position as the DTR–EGFP cassette. The final vectors were confirmed by DNA sequencing.

The *Lgr5* KI vectors were linearized with NotI and C57BL/6 C2 embryonic stem cells were targeted using standard methods (G418-positive and gancyclovir-negative selection). Positive clones were identified using PCR and taqman analysis, and confirmed by sequencing of the modified locus. Correctly targeted embryonic stem cells were transfected with a Cre or Flpe plasmid, respectively, to remove the Neo cassette. The modified embryonic stem cells were then injected into blastocysts using standard techniques, and germline transmission was obtained after crossing the resulting chimaeras with C57BL/6N females.

For *Bmi1*, a 210 kb C57BL/6 BAC (RP23-181D14, assembly NCBI37/mm9, chr2:18,464,619–18,674,471) was obtained and characterized by DNA fingerprinting. The BAC contains the *Bmi1* locus and considerable 5' and 3' flanking sequence. An IRES–CreERT2–pA–Frt–Neo–Frt cassette was synthesized (Blue Heron/Origene) and inserted, using recombineering, 85 bp 3' of the *Bmi1* stop codon (after position chr2:18,606,193). Neo was then removed by transforming the modified BAC into arabinose-induced, SW105 cells<sup>28,29</sup> expressing the yeast protein Flp. C57BL/6 transgenic mice carrying the modified *Bmi1* BAC were obtained using standard pronuclear microinjection methods<sup>30</sup> and characterized.

We analysed the *Lgr5*<sup>DTR/+</sup> mice at 24 h after DT administration (50 µg kg<sup>-1</sup>, intraperitoneal injection, *n* = 3), at 10 days of DT treatment (50 µg kg<sup>-1</sup> every other day for 10 days, *n* = 5), 48 h recovery (*n* = 3) and 96 h recovery time points after four doses of DT (*n* = 2). The DT treatment could not be extended beyond 10 days due to severe liver toxicity apparently mediated by a subset of *Lgr5*–DTR–EGFP-expressing hepatocytes. We analysed *Bmi1*CreER;R26R;*Lgr5*<sup>DTR/+</sup> at 24 h (*n* = 2), 48 h (*n* = 2) and 72 h (*n* = 2) after TAM injection. Two-hundred and fifty β-gal-positive crypts were scored per mouse.

**Renal capsule explants.** 3–5-mm small intestine pieces from E15 *Lgr5*<sup>DTR/CreER</sup> embryos (*n* = 3) were grafted under the renal capsule of 6–8-week-old athymic nu/nu mice and allowed to develop for 3 weeks. We treated *Lgr5*<sup>DTR/CreER</sup>;R26R renal grafts with 10 days TAM (*n* = 5), 10 days DT/TAM (*n* = 5), 6 days DT followed by 6 days TAM (*n* = 5) and 6 days TAM followed by 6 days DT

(*n* = 5). Some GFP expression was seen outside of the CBC region due to perdurance of GFP protein as well as upregulation of the *Lgr5* locus when *Lgr5* is deleted<sup>12</sup>. **DT cell ablation.** Mice (between 6 and 12 weeks old) were given DT at 50 µg kg<sup>-1</sup> every 48 h through intraperitoneal injections.

**TAM labelling experiments.** Mice (between 6 and 12 weeks old) were given 5 mg TAM in corn oil through intraperitoneal injection.

**Transmission electron microscopy.** The tissues were fixed in 1/2 Karnovsky's fixative (2% paraformaldehyde (PFA), 2.5% glutaraldehyde in 0.1 M sodium cacodylate buffer, pH 7.2), washed in the same buffer, and post-fixed in 1% osmium tetroxide. The samples were then dehydrated through a series of ethanol, followed by propylene oxide and embedded in Eponate 12 (Ted Pella). Thin sections were stained with uranyl acetate and lead citrate and examined using a Philips CM12 or JEOL JEM-1400 TEM.

**Histology, immunohistochemistry and immunofluorescence.** Animals were perfused with 2% PFA. Small intestine and colon were flushed with 2% PFA and fixed in 4% PFA overnight. Half of the materials were cryo-protected, embedded in OCT, and sectioned at 6 µm for immunofluorescence. The other half of the materials were paraffin embedded, sectioned at 3 µm for histology and immunohistochemistry. Antibodies: Ki67 (Neomarker), cleaved caspase 3 (Cell Signaling), GFP (Novus), chromogranin A (Neomarkers), β-gal (Cappel).

**In situ hybridization and X-GAL staining.** Full-length *Lgr5* cDNA was cloned into the pGEM vector to make anti-sense DIG-probe. Protocols for *in vitro* transcription and *in situ* hybridization were as described previously<sup>31</sup>. Whole-mount X-GAL staining was performed as described<sup>3</sup>.

**Crypt organoid culture.** Crypt isolation and culture were performed as described<sup>14</sup>.

25. Warming, S., Rachel, R. A., Jenkins, N. A. & Copeland, N. G. *Zfp423* is required for normal cerebellar development. *Mol. Cell. Biol.* **26**, 6913–6922 (2006).
26. Liu, P., Jenkins, N. A. & Copeland, N. G. A highly efficient recombineering-based method for generating conditional knockout mutations. *Genome Res.* **13**, 476–484 (2003).
27. Kissenpfennig, A. *et al.* Dynamics and function of Langerhans cells *in vivo*: dermal dendritic cells colonize lymph node areas distinct from slower migrating Langerhans cells. *Immunity* **22**, 643–654 (2005).
28. Warming, S., Costantino, N., Court, D. L., Jenkins, N. A. & Copeland, N. G. Simple and highly efficient BAC recombineering using galK selection. *Nucleic Acids Res.* **33**, e36 (2005).
29. Lee, E. C. *et al.* A highly efficient *Escherichia coli*-based chromosome engineering system adapted for recombinogenic targeting and subcloning of BAC DNA. *Genomics* **73**, 56–65 (2001).
30. Van Keuren, M. L., Gavrilina, G. B., Filipiak, W. E., Zeidler, M. G. & Saunders, T. L. Generating transgenic mice from bacterial artificial chromosomes: transgenesis efficiency, integration and expression outcomes. *Transgenic Res.* **18**, 769–785 (2009).
31. Gregorieff, A. & Clevers, H. *In situ* hybridization to identify gut stem cells. *Curr. Protoc. Stem Cell Biol.* Ch. 2, Unit 2F.1 (2010).

# ATP-induced helicase slippage reveals highly coordinated subunits

Bo Sun<sup>1,2\*</sup>, Daniel S. Johnson<sup>1,2,†\*</sup>, Gayatri Patel<sup>3</sup>, Benjamin Y. Smith<sup>1,2</sup>, Manjula Pandey<sup>3</sup>, Smita S. Patel<sup>3</sup> & Michelle D. Wang<sup>1,2</sup>

Helicases are vital enzymes that carry out strand separation of duplex nucleic acids during replication, repair and recombination<sup>1,2</sup>. Bacteriophage T7 gene product 4 is a model hexameric helicase that has been observed to use dTTP, but not ATP, to unwind double-stranded (ds)DNA as it translocates from 5' to 3' along single-stranded (ss)DNA<sup>2–6</sup>. Whether and how different subunits of the helicase coordinate their chemo-mechanical activities and DNA binding during translocation is still under debate<sup>1,7</sup>. Here we address this question using a single-molecule approach to monitor helicase unwinding. We found that T7 helicase does in fact unwind dsDNA in the presence of ATP and that the unwinding rate is even faster than that with dTTP. However, unwinding traces showed a remarkable sawtooth pattern where processive unwinding was repeatedly interrupted by sudden slippage events, ultimately preventing unwinding over a substantial distance. This behaviour was not observed with dTTP alone and was greatly reduced when ATP solution was supplemented with a small amount of dTTP. These findings presented an opportunity to use nucleotide mixtures to investigate helicase subunit coordination. We found that T7 helicase binds and hydrolyses ATP and dTTP by competitive kinetics such that the unwinding rate is dictated simply by their respective maximum rates  $V_{\max}$ , Michaelis constants  $K_M$  and concentrations. In contrast, processivity does not follow a simple competitive behaviour and shows a cooperative dependence on nucleotide concentrations. This does not agree with an uncoordinated mechanism where each subunit functions independently, but supports a model where nearly all subunits coordinate their chemo-mechanical activities and DNA binding. Our data indicate that only one subunit at a time can accept a nucleotide while other subunits are nucleotide-ligated and thus they interact with the DNA to ensure processivity. Such subunit coordination may be general to many ring-shaped helicases and reveals a potential mechanism for regulation of DNA unwinding during replication.

Despite the fact that most motor proteins use ATP as a fuel source, previous bulk studies have shown that T7 helicase does not unwind DNA efficiently in the presence of ATP, although it is capable of ATP hydrolysis<sup>5,6,8</sup>. To investigate why ATP seemed not to support T7 helicase unwinding, we used a single-molecule optical trapping assay that we previously developed to measure unwinding of dsDNA or translocation on ssDNA (Fig. 1a and Supplementary Fig. 1)<sup>9</sup>. Briefly, two strands of a DNA fork junction were held under tension that was not sufficient to mechanically unwind the junction without a helicase. Helicase unwinding of the junction resulted in an increase in the ssDNA length, permitting tracking of the helicase location. When experiments were conducted with 2 mM ATP, we were surprised to find that ATP supported not only dsDNA unwinding but that it also supported it at a significantly faster rate than with dTTP (Fig. 1b–c). However, processive unwinding was interrupted by slippage events, resulting in a remarkable sawtooth pattern in the unwinding trace

(Fig. 1b). Control experiments verified that each trace was the action of a single helicase (Supplementary Fig. 2). We attribute this pattern to helicase losing its grip on the ssDNA, sliding backwards under the influence of the reannealing DNA fork, and then regaining its grip and resuming unwinding (Fig. 1d). In contrast, slippage behaviour was essentially absent with 2 mM dTTP alone (Fig. 1b). These results resolve the mystery of the apparent lack of significant unwinding activity seen in bulk studies<sup>4–6,8</sup>; unwinding and slippage could not be separated, so unwinding was masked by unobservable slips that prevented helicase from moving over a substantial distance. Our work is the first direct observation, to our knowledge, of helicase nucleotide-specific slippage. Previous studies of non-ring-shaped helicases have reported reverse motions of the unwinding fork attributable to helicase reaching the end of the DNA or encountering a barrier<sup>10,11</sup>, dissociating from the DNA<sup>12,13</sup>, or moving in the reverse direction<sup>9,12,13</sup>. These are of a somewhat different nature than what we have observed. The only slippage behaviour that may resemble ours is from non-helicase bacteriophage motors<sup>14,15</sup>, but their slippage is not a result of the use of a specific nucleotide.

Slippage was not observed with dTTP alone (Fig. 1b) and therefore seems to be sensitive either to the base composition of the bound nucleotide (for example, adenosine versus thymidine) or the type of sugar (ribose versus deoxyribose). We compared slippage for all four NTPs and their dNTP counterparts (Supplementary Fig. 3). For each nucleotide we measured processivity, defined as the mean distance between slips (Supplementary Fig. 4). The results indicate that the additional 2'-OH group on the ribose sugar makes the helicase more prone to slipping. Examination of the helicase structure at the nucleotide-binding pocket<sup>16</sup> reveals that the 2'-OH group of a bound nucleotide may displace the -OH group on the side chain of residue Y535 (Supplementary Fig. 5a). We thus generated a Y535F mutant to remove the -OH group and it showed significantly increased processivity in the presence of ATP, albeit still less than that seen for dATP (Supplementary Fig. 5b).

Although ATP caused helicase to slip more frequently, it supported a much faster unwinding rate between slips, consistent with an earlier finding of a faster rate of ATP hydrolysis<sup>17</sup>. Because ATP and dTTP support different unwinding rates and processivities, we used nucleotide mixtures to understand how multiple subunits of the helicase coordinate unwinding activity. We approximated the *in vivo* concentrations of ATP and dTTP of *Escherichia coli*<sup>18</sup> by using 2.0 mM ATP and a small amount of dTTP, 0.2 mM (Fig. 1b, c). Although the unwinding rate between slips was close to the value observed with 2 mM ATP alone, the processivity increased by approximately threefold. When the converse experiment was performed (0.2 mM ATP and 2.0 mM dTTP), the unwinding rate was comparable to that with 2 mM dTTP alone and minimal slippage was observed (Fig. 1b, c). These results imply that even a small fraction of helicase subunits, when bound with dTTP, reduce slippage and substantially increase processivity. This finding was further substantiated by bulk experiments using ATP alone, and an ATP/dTTP mixture (Supplementary Fig. 6). To determine if T7

<sup>1</sup>Department of Physics - Laboratory of Atomic and Solid State Physics, Cornell University, Ithaca, New York 14853, USA. <sup>2</sup>Howard Hughes Medical Institute, Cornell University, Ithaca, New York 14853, USA.

<sup>3</sup>Department of Biochemistry, UMDNJ-Robert Wood Johnson Medical School, Piscataway, New Jersey 08854, USA. <sup>†</sup>Present address: Rockefeller University, New York, New York 10065, USA.

\*These authors contributed equally to this work.



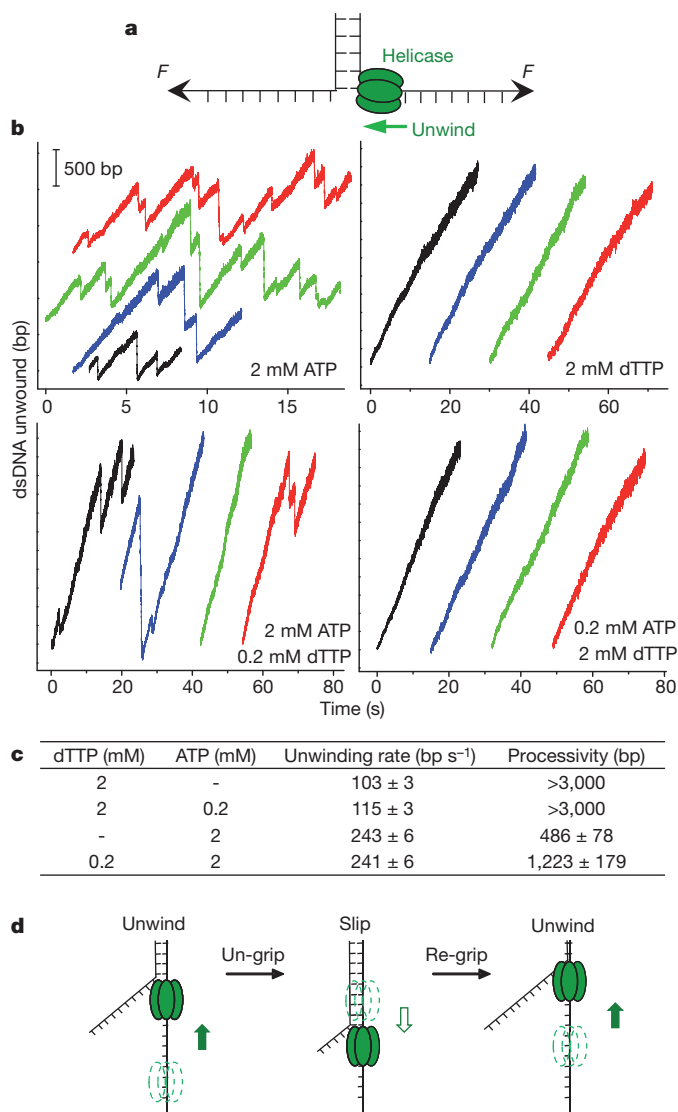


**Figure 1 | Comparison of helicase unwinding behaviours with different nucleotides.** **a**, Schematic of the single-molecule configuration (not to scale). The single-stranded ends of a dsDNA were held at a constant unzipping force of 8 pN while T7 helicase unwound the dsDNA by translocating on ssDNA. **b**, Representative traces showing the number of unwound base pairs versus time in the presence of various concentrations of nucleotides. For clarity, traces have been arbitrarily shifted along both axes. **c**, A summary of unwinding rates and processivities. Uncertainties are s.e.m. **d**, Cartoon illustrating slippage behaviour. The helicase unwinds, loses grip, slips, re-grips and resumes unwinding. Dotted helicase indicates a previous location of the helicase.

helicase binds DNA with different affinities in the presence of dTTP and ATP, bulk binding studies were carried out using fluorescence anisotropy with dTTP and ATP analogues (Supplementary Fig. 7). The results show that T7 helicase binds ssDNA 100-fold more tightly with dTMP-PCP than with AMP-PCP, and indicate that the greater slippage in the presence of ATP is probably due to weaker binding to DNA.

The discovery of helicase slippage and the ability to directly measure helicase processivity provided a unique opportunity to explore the following: (1) how ATP and dTTP compete for binding to helicase subunits; (2) how nucleotide binding regulates helicase affinity to DNA; and (3) how multiple subunits of helicase coordinate their activities.

To understand how ATP and dTTP compete for binding to helicase subunits, we determined the unwinding rates between slippage events (Fig. 2a) as a function of nucleotide concentration. For each nucleotide alone, the unwinding rate followed Michaelis–Menten-like kinetics, yielding  $V_{\max}$  and  $K_M$  values that were both higher for ATP than for

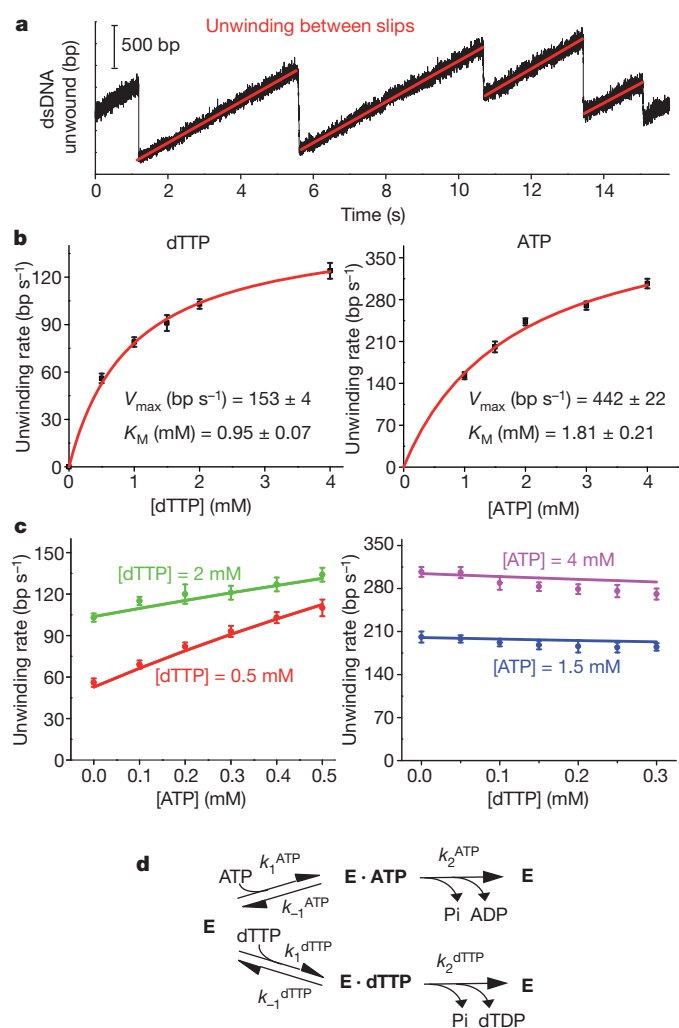


**Figure 2 | Helicase unwinding kinetics.** **a**, Example of unwinding with ATP to illustrate the method of determining unwinding rate by analysing data between slips. **b**, Kinetic constants for unwinding under a constant unzipping tension of 8 pN in the presence of either ATP (right) or dTTP (left). For each nucleotide,  $K_M$  and  $V_{\max}$  were obtained by fitting the unwinding rates as a function of NTP concentration to the Michaelis–Menten equation. **c**, Measured unwinding rates at either fixed [dTTP] and varying [ATP], or fixed [ATP] and varying [dTTP], and comparison with direct predictions (not fits) from the competitive nucleotide binding model using kinetic constants  $K_M$  and  $V_{\max}$  shown in **b**. Error bars indicate s.e.m. **d**, Kinetic pathway of a competitive binding model where ATP and dTTP compete for binding and hydrolysis by the helicase (denoted by E here).

dTTP (Fig. 2b). These kinetics indicated that there was no cooperativity in NTP binding and hydrolysis. Next, we conducted experiments in which the concentration of one nucleotide was fixed while that of the other nucleotide was varied. The resulting unwinding rates could be explained by competitive kinetics: ATP and dTTP compete for binding based on their respective affinities and the resulting reaction rate is determined by their concentrations,  $V_{\max}$ , and  $K_M$  (Fig. 2c, d; Methods Summary and Supplementary Discussion). A comparison of unwinding rates with mixed nucleotides and direct predictions (not fits) from the competitive binding kinetics showed excellent agreement. These results were further substantiated by ssDNA translocation rate experiments (Supplementary Fig. 8). This also explains why in Fig. 1b, c the unwinding rate was minimally altered when 0.2 mM of dTTP was added to 2 mM ATP. Under those conditions, only about 16% of the nucleotide bound to the helicase hexamer was dTTP.

The competitive binding kinetics for nucleotides, however, does not explain the observed slippage behaviour with mixed nucleotides (Fig. 1b, c). That is, it is unclear how the 16% bound dTTP resulted

in a threefold increase in processivity. If only a single nucleotide can be bound by the helicase at a time and the type of the bound nucleotide determines the helicase's affinity to the DNA, then processivity should only increase by 7% (Supplementary Discussion). In addition, it has previously been shown that the helicase subunits do not bind to ssDNA in the absence of a nucleotide<sup>19</sup>. However, we found minimal slippage even at [dTTP] much below its  $K_M$ . These observations indicate participation of multiple subunits in both nucleotide and DNA binding, where each subunit would have a nucleotide-specific DNA binding affinity. Our data indicate that helicase may not slip if at least one subunit of the hexamer is in a deoxythymidine-ligated state, which has a higher affinity for the DNA.

Two models may be consistent with this idea. In an uncoordinated model<sup>1,2,7</sup>, each helicase subunit functions independently in its nucleotide binding/hydrolysis, and DNA binding/release (Supplementary Discussion). Conversely, coordinated models have been proposed for T7 helicase<sup>1,2,7</sup>, but details of the coordination remain unclear. Biochemical and structural studies indicate that nucleotide hydrolysis may occur sequentially around the hexameric ring<sup>16,20,21</sup>, that roughly four subunits are nucleotide-ligated at any given time<sup>20</sup>, and that DNA binding to the helicase might involve one-to-two helicase subunits<sup>16,20–22</sup>. A model based on structural studies has been proposed for ring-shaped helicases E1 (ref. 23) and Rho<sup>24</sup>, where all or some of the subunits coordinate their chemo-mechanical activities (Fig. 3d). Coordination

could occur sequentially around the hexameric ring with the leading subunit poised for NTP binding and each successive subunit having a bound nucleotide in states of progression along the chemical reaction pathway (NTP, NDP + Pi, NDP, and so on). Depending on the state and type of nucleotide bound each subunit may have a different affinity to DNA. Once the leading subunit binds to an NTP and reels in the DNA, the remaining subunits progress to their next reaction states. Product release by the last participating subunit results in release of DNA from that subunit, and thus completes a single cycle.

We formulated quantitative descriptions for the uncoordinated and coordinated models (Supplementary Discussion). The observed rate of unwinding as a function of [ATP] or [dTTP] is consistent with both models, which predict an apparent Michaelis–Menten-like kinetics. The observed unwinding rate with ATP and dTTP mixtures is also consistent with the competitive binding kinetics for both models as long as, in the case of the coordinated model, the rates are treated as averages over time (Supplementary Discussion). Although the two models cannot be distinguished based on rate measurement studies, they do yield different predictions for DNA slippage behaviour. The uncoordinated model (Supplementary Discussion) requires that each subunit binds and hydrolyses nucleotides independently with an affinity to DNA dependent on the state and type of nucleotide bound. This model is not consistent with the processivity data taken with mixed nucleotides at concentrations near or lower than their respective  $K_M$  values (Supplementary Fig. 9).

On the other hand, the coordinated model requires that subunits participating in coordination bind and hydrolyse nucleotide in coordination, with only one subunit poised to bind a nucleotide at a time and with each subunit having an affinity to DNA dependent on the state and type of nucleotide bound. This model predicts that processivity should increase linearly with [NTP] in the presence of a single type of NTP. Indeed, our data show that the processivity increases linearly with increasing [ATP] (Fig. 3a, b). If multiple helicase subunits coordinate in their chemo-mechanical activities, what is the degree of coordination as measured by the number of participating subunits at any given time ( $n$ )? This is a key parameter that characterizes the mechanism of the helicase. Previous studies indicate that only one or two subunits are involved in significant DNA binding, suggesting a lower degree of coordination of  $n = 1$  or 2 (refs. 16, 20–22). However, subunits may participate in the coordination even if they have lower affinity to ssDNA. The coordinated model formulated (Supplementary Discussion) is rather general and naturally takes this into account. Interestingly, it predicts that processivity sensitively depends on  $n$  as [dTTP] is increased in the presence of a fixed [ATP]—the larger  $n$ , the more subunits participate in DNA binding, and the more steeply processivity increases with [dTTP]. Therefore we measured processivity with mixtures of ATP and dTTP (Fig. 3c). A global fit to the processivity data in Fig. 3b, c yielded  $n = 5.2 \pm 0.4$  (Methods Summary). In contrast,  $n = 2$  does not agree with the measurements. These findings are further substantiated by experiments using UTP instead of ATP (Supplementary Fig. 10,  $n = 5.0 \pm 0.3$ ), experiments under a different unzipping force (Supplementary Fig. 11,  $n = 5.4 \pm 0.3$ ), and data on time between slips (Supplementary Fig. 12,  $n = 5.5 \pm 0.4$ ). Because  $n \leq 6$  is expected for a hexamer, this finding indicates that nearly all subunits participate in the coordination ( $n = 5$  or 6) (Fig. 3d). Our findings suggest that only one subunit at a time can accept an incoming nucleotide, while the rest of the subunits are already nucleotide bound and coordinate to prevent slippage and maintain high processivity.

The work presented here provides a quantitative description of nucleotide binding/hydrolysis and its coupling to DNA binding and translocation for T7 helicase. This was possible because unwinding and slippage events are clearly distinguishable in single-molecule traces. The slippage behaviour is explained by a multiple-site coordinated model. For helicase to slip, all six subunits must simultaneously lose their grip on the DNA. This happens more often when helicase subunits are bound only to ribose nucleotides. Our data demonstrate

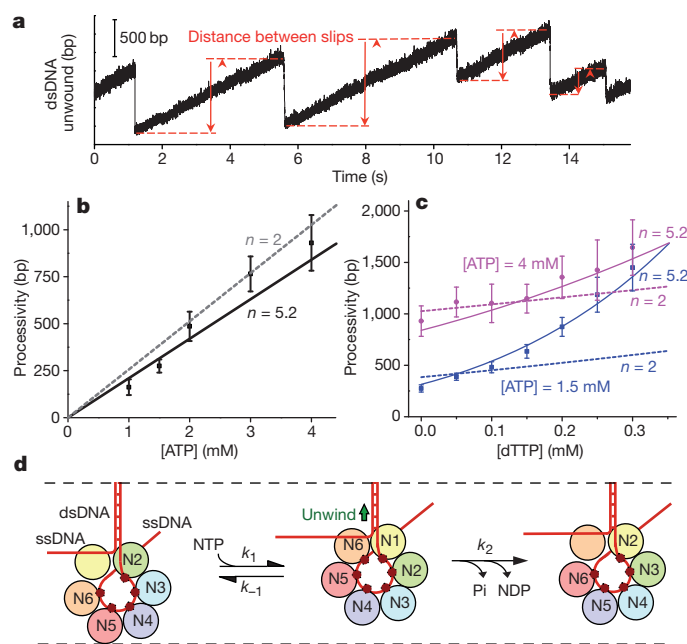


**Figure 3 | Processivity dependence on nucleotides and a proposed coordinated model.** **a**, An example of unwinding with ATP to illustrate the method of determining distance between slips. **b**, **c**, Measured processivity (mean distance between slipping events) as a function of [ATP] alone, and as functions of [dTTP] at two fixed concentrations of ATP. Note processivity increased substantially when a small amount of dTTP was added to the reaction. Solid lines are global fits using the coordinated model, yielding  $n = 5.2 \pm 0.4$ . For comparison, fits using  $n = 2$  are also shown. Error bars indicate s.e.m. **d**, An interpretation of the proposed coordinated model. Each subunit is uniquely labelled with a different colour and has a potential ssDNA-binding site (small red dot). Nucleotide binding and subsequent hydrolysis occur sequentially around the ring. If a subunit is nucleotide-ligated (the state of hydrolysis indicated by Ni), it has a non-zero probability of being bound to ssDNA. During unwinding, the leading subunit can bind to a nucleotide (N) and thus acquire affinity to the upstream ssDNA. This stimulates the last nucleotide-bound subunit to release its nucleotide and ssDNA. Then the cycle proceeds again around the ring. Slippage occurs when all subunits simultaneously release ssDNA, as determined by the joint probability of detachment for all subunits (Supplementary Discussion).

that T7 helicase has a very weak DNA binding affinity in the presence of ATP but the addition of a small amount of dTTP to the ATP reaction increases the binding affinity of helicase to DNA. As a consequence, the presence of a single deoxythymidine-ligated subunit significantly decreases the chance of slippage so that helicase can still effectively unwind dsDNA with ATP. Thus T7 helicase, like most other helicases<sup>2</sup>, could still use ATP as a main power source *in vivo*, under conditions such as those during phage infection of *E. coli*<sup>18</sup> where ATP is most abundant. ATP could be used for rapid unwinding and dTTP for high processivity. Although we focus here on a comparison of dTTP with ATP for helicase unwinding, other deoxyribose nucleotides may also reduce the frequency of slippage (Supplementary Fig. 3). We speculate that slippage may also provide an evolutionary advantage for replication: when dNTP concentrations are low, slippage can slow down helicase to allow its synchronization with a slow-moving DNA polymerase.

## METHODS SUMMARY

Single-molecule assays were performed as described previously<sup>9</sup>. If dTTP and ATP compete for binding to helicase according to the kinetic pathway outlined in Fig. 2d, then the resulting unwinding rate is:  $V_{\text{tot}} = \left( V_{\text{max}}^{\text{ATP}} \frac{[\text{ATP}]}{K_M^{\text{ATP}}} + V_{\text{max}}^{\text{dTTP}} \frac{[\text{dTTP}]}{K_M^{\text{dTTP}}} \right) / \left( 1 + \frac{[\text{ATP}]}{K_M^{\text{ATP}}} + \frac{[\text{dTTP}]}{K_M^{\text{dTTP}}} \right)$ , where for each type of nucleotide  $K_M = \frac{k_{-1} + k_2}{k_1}$  and  $V_{\text{max}} = sk_2$  with  $s$  being the step size (in nucleotides) (see Supplementary Discussion). In the presence of dTTP and ATP, if  $n$  helicase subunits coordinate in their chemo-mechanical activities and DNA binding, then the resulting distance between slips (processivity) is:  $d_{\text{processivity}} = c \left( V_{\text{max}}^{\text{ATP}} \frac{[\text{ATP}]}{K_M^{\text{ATP}}} + V_{\text{max}}^{\text{dTTP}} \frac{[\text{dTTP}]}{K_M^{\text{dTTP}}} \right) / \left( \frac{[\text{ATP}]/K_M^{\text{ATP}}}{[\text{ATP}]/K_M^{\text{ATP}} + [\text{dTTP}]/K_M^{\text{dTTP}}} \right)^{n-1}$  (Supplementary Discussion), with  $c$  being a proportionality constant. This expression was used to fit data in Fig. 3b, c with  $c$  and  $n$  as fit parameters.

**Full Methods** and any associated references are available in the online version of the paper at [www.nature.com/nature](http://www.nature.com/nature).

**Received 24 December 2010; accepted 1 August 2011.**

**Published online 18 September 2011.**

1. Singleton, M. R., Dillingham, M. S. & Wigley, D. B. Structure and mechanism of helicases and nucleic acid translocases. *Annu. Rev. Biochem.* **76**, 23–50 (2007).
2. Patel, S. S. & Picha, K. M. Structure and function of hexameric helicases. *Annu. Rev. Biochem.* **69**, 651–697 (2000).
3. Donmez, I. & Patel, S. S. Mechanisms of a ring shaped helicase. *Nucleic Acids Res.* **34**, 4216–4224 (2006).
4. Matson, S. W., Tabor, S. & Richardson, C. C. The gene 4 protein of bacteriophage T7. Characterization of helicase activity. *J. Biol. Chem.* **258**, 14017–14024 (1983).
5. Matson, S. W. & Richardson, C. C. DNA-dependent nucleoside 5'-triphosphatase activity of the gene 4 protein of bacteriophage T7. *J. Biol. Chem.* **258**, 14009–14016 (1983).
6. Hingorani, M. M. & Patel, S. S. Cooperative interactions of nucleotide ligands are linked to oligomerization and DNA binding in bacteriophage T7 gene 4 helicases. *Biochemistry* **35**, 2218–2228 (1996).
7. Lyubimov, A. Y., Strycharska, M. & Berger, J. M. The nuts and bolts of ring-translocase structure and mechanism. *Curr. Opin. Struct. Biol.* **21**, 240–248 (2011).

8. Lee, S. J. & Richardson, C. C. Molecular basis for recognition of nucleoside triphosphate by gene 4 helicase of bacteriophage T7. *J. Biol. Chem.* **285**, 31462–31471 (2010).
9. Johnson, D. S., Bai, L., Smith, B. Y., Patel, S. S. & Wang, M. D. Single-molecule studies reveal dynamics of DNA unwinding by the ring-shaped T7 helicase. *Cell* **129**, 1299–1309 (2007).
10. Myong, S., Rasnik, I., Joo, C., Lohman, T. M. & Ha, T. Repetitive shuttling of a motor protein on DNA. *Nature* **437**, 1321–1325 (2005).
11. Myong, S., Bruno, M. M., Pyle, A. M. & Ha, T. Spring-loaded mechanism of DNA unwinding by hepatitis C virus NS3 helicase. *Science* **317**, 513–516 (2007).
12. Sun, B. *et al.* Impediment of *E. coli* UvrD by DNA-destabilizing force reveals a strained-inchworm mechanism of DNA unwinding. *EMBO J.* **27**, 3279–3287 (2008).
13. Dessinges, M. N., Lionnet, T., Xi, X. G., Bensimon, D. & Croquette, V. Single-molecule assay reveals strand switching and enhanced processivity of UvrD. *Proc. Natl Acad. Sci. USA* **101**, 6439–6444 (2004).
14. Chemla, Y. R. *et al.* Mechanism of force generation of a viral DNA packaging motor. *Cell* **122**, 683–692 (2005).
15. Tsay, J. M., Sippy, J., Feiss, M. & Smith, D. E. The Q motif of a viral packaging motor governs its force generation and communicates ATP recognition to DNA interaction. *Proc. Natl Acad. Sci. USA* **106**, 14355–14360 (2009).
16. Singleton, M. R., Sawaya, M. R., Ellenberger, T. & Wigley, D. B. Crystal structure of T7 gene 4 ring helicase indicates a mechanism for sequential hydrolysis of nucleotides. *Cell* **101**, 589–600 (2000).
17. Patel, S. S., Rosenberg, A. H., Studier, F. W. & Johnson, K. A. Large scale purification and biochemical characterization of T7 primase/helicase proteins. Evidence for homodimer and heterodimer formation. *J. Biol. Chem.* **267**, 15013–15021 (1992).
18. Mathews, C. K. Biochemistry of deoxyribonucleic acid-defective amber mutants of bacteriophage T4. 3. Nucleotide pools. *J. Biol. Chem.* **247**, 7430–7438 (1972).
19. Hingorani, M. M. & Patel, S. S. Interactions of bacteriophage T7 DNA primase/helicase protein with single-stranded and double-stranded DNAs. *Biochemistry* **32**, 12478–12487 (1993).
20. Liao, J. C., Jeong, Y. J., Kim, D. E., Patel, S. S. & Oster, G. Mechanochemistry of T7 DNA helicase. *J. Mol. Biol.* **350**, 452–475 (2005).
21. Crampton, D. J., Mukherjee, S. & Richardson, C. C. DNA-induced switch from independent to sequential dTTP hydrolysis in the bacteriophage T7 DNA helicase. *Mol. Cell* **21**, 165–174 (2006).
22. Yu, X., Hingorani, M. M., Patel, S. S. & Egelman, E. H. DNA is bound within the central hole to one or two of the six subunits of the T7 DNA helicase. *Nature Struct. Biol.* **3**, 740–743 (1996).
23. Enemark, E. J. & Joshua-Tor, L. Mechanism of DNA translocation in a replicative hexameric helicase. *Nature* **442**, 270–275 (2006).
24. Thomsen, N. D. & Berger, J. M. Running in reverse: the structural basis for translocation polarity in hexameric helicases. *Cell* **139**, 523–534 (2009).

**Supplementary Information** is linked to the online version of the paper at [www.nature.com/nature](http://www.nature.com/nature).

**Acknowledgements** We thank members of the Wang laboratory for critical reading of the manuscript. We also thank M. A. Hall for assistance with single-molecule assays, data acquisition and data analysis. We wish to acknowledge support from National Institutes of Health grants (GM059849 to M.D.W.; GM55310 to S.S.P.), National Science Foundation grant (MCB-0820293 to M.D.W.) and Cornell's Molecular Biophysics Training Grant (T32GM008267) Traineeship (to D.S.J. and B.Y.S.).

**Author Contributions** B.S., D.S.J., S.S.P. and M.D.W. designed the experiments. D.S.J. found the helicase slippage with ATP. B.S. carried out all single-molecule work and, together with B.Y.S. analysed and interpreted single-molecule data. G.P. performed all the ensemble experiments. M.P. and G.P. purified and analysed the wild-type and mutant T7 gp4 proteins. M.D.W. formulated the theoretical models. B.S., D.S.J., B.Y.S., S.S.P. and M.D.W. wrote the manuscript.

**Author Information** Reprints and permissions information is available at [www.nature.com/reprints](http://www.nature.com/reprints). The authors declare no competing financial interests. Readers are welcome to comment on the online version of this article at [www.nature.com/nature](http://www.nature.com/nature). Correspondence and requests for materials should be addressed to M.D.W. ([mwang@physics.cornell.edu](mailto:mwang@physics.cornell.edu)) or S.S.P. ([patels@umdndj.edu](mailto:patels@umdndj.edu)).



## METHODS

**Protein and DNA preparations.** Wild-type T7 helicase (gp4A') and Y535F 4A' were expressed and purified as described previously<sup>17</sup>. A 5.2 kb DNA was constructed as described elsewhere<sup>9,25</sup>, with minor modifications. Briefly, a ~1.1 kb anchoring segment was prepared by PCR from pRL574 using a digoxigenin-labelled primer, and then digested with BstXI (NEB) to produce a 3 bp overhang. A ~4.1 kb unzipping/translocation/unwinding segment was derived from pCP681 by digestion with EarI (NEB) and ligated to a biotin-labelled 37 bp segment lacking a 5' phosphate on the distal end. The anchoring segment and unzipping segment were then ligated, with a nick due to the missing phosphate. For ssDNA translocation experiments (Supplementary Fig. 8), the ~4.1 kb segment was capped with a hairpin (5'-TAGGGCGACCTAGCTCTATGCTAGGTCGCC-3').

**Single-molecule assays.** Sample preparation was similar to that previously described<sup>9</sup>. Briefly, helicase was prepared by first incubating 2  $\mu$ M of the helicase monomer for 20 min in the unwinding buffer. This solution was then further diluted to obtain the final experimental concentration of helicase monomer, nucleotides and  $\text{MgCl}_2$ . DNA tethers were formed by first non-specifically coating the sample chamber surface with anti-digoxigenin (Roche), followed by an incubation with digoxigenin tagged DNA. Streptavidin-coated 0.48  $\mu$ m polystyrene microspheres were then added to the chamber. Finally, helicase solution was flowed in just before data acquisition. The helicase unwinding buffer was 20 mM Tris-HCl (pH 7.5), 3 mM EDTA, 0.02% Tween 20, 50 mM NaCl, NTPs or dNTPs at the concentrations specified in the text, and  $\text{MgCl}_2$  at a concentration 5 mM in excess of the total nucleotide concentration (Supplementary Fig. 13). The helicase monomer concentration was adjusted between 1–500 nM for each buffer condition so that the average unwinding initiation time (defined as the time between when the DNA was initially mechanically unzipped and when the helicase began to unwind) was approximately the same for all experiments (Supplementary Fig. 3).

Experiments were conducted in a climate-controlled room at a temperature of 23.3 °C, but owing to local laser trap heating the temperature increased slightly to  $25 \pm 1$  °C (ref. 26). Each experiment was conducted in the following steps (Supplementary Fig. 1). First, several hundred base pairs of dsDNA were mechanically unzipped, at a constant velocity of  $1,400 \text{ bp s}^{-1}$ , to produce a ssDNA loading region for helicase. Second, after the force dropped owing to helicase loading and initiation of unwinding, several hundred more base pairs were mechanically unzipped to generate ssDNA for helicase translocation. Third, the fork position was maintained until the force dropped again, indicating that the helicase had again reached the junction, at which point the force was allowed to drop to

8 pN and then maintained at this level as helicase unwound the remaining ~3 kb of dsDNA. Measurements of ssDNA translocation rates and dsDNA unwinding rates by T7 helicase were thus obtained for each tether.

**Data collection and analysis.** Data were low-pass filtered to 5 kHz and digitized at 12 kHz, then were further averaged to 110 Hz. The acquired data signals were converted into unwound base pairs as previously described<sup>9,25</sup>. To improve positional accuracy and precision, the data were then aligned to a theoretical unzipping curve for the mechanically unzipped section of the DNA<sup>27</sup>. Slippage events were identified by a threshold on the instantaneous unwinding rate at each sequence position (Supplementary Fig. 4). We used a threshold of  $2,000 \text{ bp s}^{-1}$  in the reverse velocity for identifying slippage. Unwinding rates from each trace were found from linear fits to the unwinding between adjacent slippage events. An average unwinding rate was obtained from a number of traces. Distances travelled between slips were compiled to determine processivity. These distances followed an exponential distribution, indicating a stochastic process in slippage<sup>28</sup>. Processivity is defined as the mean distance of the distribution (Supplementary Fig. 4b).

**Modeling.** If dTTP and ATP compete for binding to helicase according to the kinetic pathway outlined in Fig. 2d, then the resulting unwinding rate is:  $V_{\text{tot}} = \left( V_{\text{max}}^{\text{ATP}} \frac{[\text{ATP}]}{K_M^{\text{ATP}}} + V_{\text{max}}^{\text{dTTP}} \frac{[\text{dTTP}]}{K_M^{\text{dTTP}}} \right) / \left( 1 + \frac{[\text{ATP}]}{K_M^{\text{ATP}}} + \frac{[\text{dTTP}]}{K_M^{\text{dTTP}}} \right)$ , where for each type of nucleotide  $K_M = \frac{k_{-1} + k_2}{k_1}$  and  $V_{\text{max}} = sk_2$  with  $s$  being the step size (in nucleotides) (see Supplementary Discussion). In the presence of dTTP and ATP, if  $n$  helicase subunits coordinate in their chemo-mechanical activities and DNA binding, then the resulting distance between slips (processivity) is:  $d_{\text{processivity}} = c \left( V_{\text{max}}^{\text{ATP}} \frac{[\text{ATP}]}{K_M^{\text{ATP}}} + V_{\text{max}}^{\text{dTTP}} \frac{[\text{dTTP}]}{K_M^{\text{dTTP}}} \right) / \left( \frac{[\text{ATP}]/K_M^{\text{ATP}}}{[\text{ATP}]/K_M^{\text{ATP}} + [\text{dTTP}]/K_M^{\text{dTTP}}} \right)^{n-1}$  (Supplementary Discussion), with  $c$  being a proportionality constant. This expression was used to fit data in Fig. 3b, c with  $c$  and  $n$  as fit parameters.

25. Koch, S. J., Shundrovsky, A., Jantzen, B. C. & Wang, M. D. Probing protein-DNA interactions by unzipping a single DNA double helix. *Biophys. J.* **83**, 1098–1105 (2002).
26. Peterman, E. J., Gittes, F. & Schmidt, C. F. Laser-induced heating in optical traps. *Biophys. J.* **84**, 1308–1316 (2003).
27. Shundrovsky, A., Smith, C. L., Lis, J. T., Peterson, C. L. & Wang, M. D. Probing SWI/SNF remodeling of the nucleosome by unzipping single DNA molecules. *Nature Struct. Mol. Biol.* **13**, 549–554 (2006).
28. Lohman, T. M., Tomko, E. J. & Wu, C. G. Non-hexameric DNA helicases and translocases: mechanisms and regulation. *Nature Rev. Mol. Cell Biol.* **9**, 391–401 (2008).

# Deep sequencing reveals 50 novel genes for recessive cognitive disorders

Hossein Najmabadi<sup>1,2</sup>, Hao Hu<sup>3\*</sup>, Masoud Garshasbi<sup>1,3\*</sup>, Tomasz Zemojtel<sup>4</sup>, Seyedeh Sedigheh Abedini<sup>1</sup>, Wei Chen<sup>3,5</sup>, Masoumeh Hosseini<sup>1</sup>, Farkhondeh Behjati<sup>1</sup>, Stefan Haas<sup>4</sup>, Payman Jamali<sup>6</sup>, Agnes Zecha<sup>3</sup>, Marzieh Mohseni<sup>1</sup>, Lucia Püttmann<sup>3</sup>, Leyla Nouri Vahid<sup>1</sup>, Corinna Jensen<sup>3</sup>, Lia Abbasi Moheb<sup>1,3</sup>, Melanie Bienek<sup>3</sup>, Farzaneh Larti<sup>1</sup>, Ines Mueller<sup>3</sup>, Robert Weissmann<sup>3</sup>, Hossein Darvish<sup>1</sup>, Klaus Wrogemann<sup>3,7</sup>, Valeh Hadavi<sup>2</sup>, Bettina Lipkowitz<sup>3</sup>, Sahar Esmaeeli-Nieh<sup>3</sup>, Dagmar Wiczorek<sup>8</sup>, Roxana Kariminejad<sup>2</sup>, Saghar Ghasemi Firouzabadi<sup>1</sup>, Monika Cohen<sup>9</sup>, Zohreh Fattahi<sup>1</sup>, Imma Rost<sup>10</sup>, Faezeh Mojahedi<sup>11</sup>, Christoph Hertzberg<sup>12</sup>, Atefeh Dehghan<sup>13</sup>, Anna Rajab<sup>14</sup>, Mohammad Javad Soltani Banavandi<sup>1</sup>, Julia Hoffer<sup>3</sup>, Masoumeh Falah<sup>1</sup>, Luciana Musante<sup>3</sup>, Vera Kalscheuer<sup>3</sup>, Reinhard Ullmann<sup>3</sup>, Andreas Walter Kuss<sup>3†</sup>, Andreas Tzschach<sup>3</sup>, Kimia Kahrizi<sup>1</sup> & H. Hilger Ropers<sup>3</sup>

Common diseases are often complex because they are genetically heterogeneous, with many different genetic defects giving rise to clinically indistinguishable phenotypes. This has been amply documented for early-onset cognitive impairment, or intellectual disability, one of the most complex disorders known and a very important health care problem worldwide. More than 90 different gene defects have been identified for X-chromosome-linked intellectual disability alone, but research into the more frequent autosomal forms of intellectual disability is still in its infancy. To expedite the molecular elucidation of autosomal-recessive intellectual disability, we have now performed homozygosity mapping, exon enrichment and next-generation sequencing in 136 consanguineous families with autosomal-recessive intellectual disability from Iran and elsewhere. This study, the largest published so far, has revealed additional mutations in 23 genes previously implicated in intellectual disability or related neurological disorders, as well as single, probably disease-causing variants in 50 novel candidate genes. Proteins encoded by several of these genes interact directly with products of known intellectual disability genes, and many are involved in fundamental cellular processes such as transcription and translation, cell-cycle control, energy metabolism and fatty-acid synthesis, which seem to be pivotal for normal brain development and function.

Early-onset cognitive impairment, or intellectual disability, is an unresolved health care problem and an enormous socio-economic burden. Most severe forms of intellectual disability are due to chromosomal abnormalities or defects in specific genes. For many years, research into the genetic causes of intellectual disability and related disorders has focused on X-chromosome-linked intellectual disability (XLID). It has become clear, however, that X-linked forms account for only 10% of intellectual disability cases, which means that the vast majority of the underlying genetic defects must be autosomal<sup>1</sup>. For severe forms of intellectual disability, autosomal-dominant inheritance is rare because most affected individuals do not reproduce, but recent observations suggest that in outbred Caucasian populations, a significant portion of the sporadic cases may be due to dominant *de novo* mutations<sup>2–4</sup>. So far, relatively little is known about the role of autosomal recessive intellectual disability (ARID), because in Western societies, where most of the research takes place, its investigation has been hampered by infrequent parental consanguinity and small family sizes.

In most Northern African countries, and also in the Near and Middle East, parental consanguinity and large families are common; for example, in Iran, 40% of the families are consanguineous and about two-thirds of the population is 30 years of age or younger.

Since 2004, we have performed systematic array-based consanguinity mapping in 272 consanguineous Iranian families. In several dozen families, we have defined single linkage intervals and mapped the underlying gene defects<sup>5,6</sup>, and by subsequent mutation screening of candidate genes from these intervals, we and others identified several novel ARID genes (for review see refs 1, 7).

Recently, exome enrichment and next-generation sequencing have been introduced as a cost-effective and fast strategy for comprehensive mutation screening and disease-gene identification in the coding portion of the human genome<sup>8–10</sup>. To unravel the molecular basis of ARID in a systematic fashion, we have now used a related, but more targeted, approach. Instead of sequencing entire exomes in consanguineous families, we have focused on the exons from homozygous linkage intervals known to carry the genetic defect. Before sequencing, these exons were enriched by hybrid capture using custom-made oligonucleotide arrays as baits. All patients had cognitive impairment (mostly moderate or severe, see Supplementary Table 1), and in a subset of the families there were signs of autism spectrum disorder. More information about the families and their clinical features, quality controls performed to validate the sequence variants observed and to assess their pathogenicity, as well as other methodological details are provided in Supplementary Information.

<sup>1</sup>Genetics Research Center, University of Social Welfare and Rehabilitation Sciences, 19857 Tehran, Iran. <sup>2</sup>Kariminejad-Najmabadi Pathology & Genetics Centre, 14667 Tehran, Iran. <sup>3</sup>Department Human Molecular Genetics, Max Planck Institute for Molecular Genetics, 14195 Berlin, Germany. <sup>4</sup>Department of Computational Molecular Biology, Max Planck Institute for Molecular Genetics, 14195 Berlin, Germany. <sup>5</sup>Max-Planck-Centrum für Molekulare Medizin, 13092 Berlin, Germany. <sup>6</sup>Shahroud Welfare Organization, 36156 Semnan, Iran. <sup>7</sup>Department of Biochemistry and Medical Genetics, University of Manitoba, Winnipeg, Manitoba R3E0J9, Canada. <sup>8</sup>Institut fuer Humangenetik, Universitaetsklinikum, 45122 Essen, Germany. <sup>9</sup>Kinderzentrum Muenchen, 81377 Muenchen, Germany. <sup>10</sup>Zentrum fuer Humangenetik und Laboratoriumsmedizin Dr Klein und Dr Rost, 82152 Martinsried, Germany. <sup>11</sup>Mashhad Medical Genetic Counseling Center, 91767 Mashhad, Iran. <sup>12</sup>Kinderneurologie und Sozialpaediatric, Vivantes-Klinikum Neukölln, 12351 Berlin, Germany. <sup>13</sup>Yazd Welfare Organization, 89178 Yazd, Iran. <sup>14</sup>Genetics Unit, Ministry of Health, Directorate General of Health Affairs, Royal Hospital, Muscat 113, Oman. <sup>†</sup>Present address: Institute for Human Genetics, University Medicine Greifswald & Interfaculty Institute for Genetics and Functional Genomics, Ernst Moritz Arndt University, 17489 Greifswald, Germany.

\*These authors contributed equally to this work.

## Mutations in known and novel intellectual disability genes

In 115 out of 136 families studied, plausible causal defects were observed, and in 78 of these, a single, apparently disease-causing mutation could be identified (see Supplementary Fig. 1, Tables 1 and 2 and Supplementary Table 2). Twenty-eight protein-truncating changes were found, including frameshift, splice-site and nonsense mutations, as well as whole-exon deletions, plus several smaller in-frame deletions of varying size. In 26 families listed in Table 1, we identified known, mostly syndromic forms of ARID, including rare metabolic defects and storage disorders, such as an atypical form of Tay–Sachs' disease and Sanfilippo's syndrome (mucopolysaccharidosis IIIB), as well as intellectual disability with congenital abnormalities, such as a Joubert-like syndrome resulting from *AHI1* mutations, observed in two unrelated families. Two families were also found with allelic *PRKCG* mutations, implicated previously in spinocerebellar ataxia, and two families carried different allelic mutations in the *SRD5A3* gene, associated with Kahrizi's syndrome, a recently elucidated congenital glycosylation disorder<sup>11,12</sup>.

Two mutations involving the adaptor protein complex 4 were observed, namely in the *AP4M1* and *AP4E1* genes, which encode different AP-4 subunits. AP-4 is involved in the recognition and sorting of cargo protein transported from the trans-Golgi network to the endosomal-lysosomal system. Another possibly pathogenic change was found in the *AP4B1* gene, but its effect may be obscured by a *PEX6* mutation in the same family, which causes a severe peroxisome biosynthesis disorder<sup>13</sup> and probably accounts for most of the clinical features. In highly inbred families, coexistence of two different recessive defects is not unexpected and is the most plausible explanation for the complex phenotypes in at least two families with novel forms of ARID (M154 and M189, see Table 2).

Mutations in the *SLC2A1* gene, which encodes a glucose transporter, the *PRKRA* gene with a role in dysautonomia, and the *MED13L* gene, previously associated with intellectual disability and cardiac symptoms, were the only plausible causes of intellectual disability in three families with non-syndromic intellectual disability. None of the respective families showed signs of dysautonomia or cardiac abnormalities. In all other families, the phenotype was characteristic for the molecular defect, including family M198 with folate receptor deficiency, a rare syndromic form of ARID that can often be

treated by oral administration of folinic acid<sup>14</sup>. Further details are provided in Table 1.

Apparently pathogenic changes were also found in 50 genes that had not been previously implicated in ARID (see Table 2). Thirty of the relevant families had non-syndromic forms of intellectual disability, whereas 22 exhibited syndromic forms. Only two of the novel ARID genes were mutated in more than a single family. Two different missense mutations with high pathogenicity scores were detected in *ZNF526*, which encodes a krüppel-type zinc-finger protein. One of these changes was observed in DNA samples collected from two distinct families with non-syndromic intellectual disability, but closer inspection revealed that these families, which live in the same city in the northwestern part of Iran, share a common haplotype and thus must be distantly related. In these families, no other potentially disease-causing and co-segregating change could be identified. Zinc-finger proteins are transcriptional regulators, and other krüppel-type zinc-finger genes have been implicated in intellectual disability before<sup>15</sup>. Recent protein interaction studies have indicated a role for *ZNF526* in promoting messenger RNA translation and cell growth (N. Hubner *et al.*, personal communication). Another gene within which disease-causing mutations were found in two families was *ELP2*. It encodes a subunit of the RNA polymerase II elongator complex, which is a histone acetyltransferase component of RNA polymerase II. This gene is involved in the acetylation of histones H3 and probably H4, and it may have a role in chromatin remodelling.

## Mutations affecting housekeeping genes

In the *LARP7* gene, we found a frameshift mutation in a family with intellectual disability and microcephaly. *LARP7* is a negative transcriptional regulator of polymerase II genes, acting by means of the 7SK RNP system. Within the 7SK RNP complex, the positive transcription elongation factor b (P-TEFb) is sequestered in an inactive form, preventing RNA polymerase II phosphorylation and subsequent transcriptional elongation. Hitherto, no disease association has been reported for *LARP7*.

Presumably causative homozygous mutations were also found in *KDM5A* and *KDM6B*. These genes encode histone demethylases that specifically demethylate histone H3 at lysine 4 and lysine 27, respectively, and they both have a central role in the histone code. We have

**Table 1 | Mutations identified in known genes for intellectual disability or related disorders**

Family	Gene	Mutation	LOD score	Length (Mb)	OMIM no.	Diagnosis, clinical features
8500306	<i>AHI1</i>	R329X	2.65	10.35	608629	Joubert's syndrome 3
M332	<i>AHI1</i>	R495H	3.2	11.1	608629	Joubert's syndrome 3
M254	<i>AP4E1</i>	V454fs	2.5	13.57	607244	Microcephaly, paraplegia
M004	<i>AP4M1</i>	E193K	1.9	16.75	602296	Microcephaly, paraplegia
M324	<i>BBS7</i>	533del2aa	3.24	8.2	209900	Bardet–Biedl's syndrome
M107	<i>CA8</i>	R237Q	2.4	4.02	613227	Ataxia, cerebellar hypoplasia
M175	<i>COL18A1</i>	L1587fs	2.1	9.8	267750	Knobloch's syndrome (eye and brain development)
G026	<i>FAM126A</i>	Splice site*	2.4	15.46	610532	Hypomyelination-cataract
M198	<i>FOLR1</i>	Splice site*	2.1	16.95	136430	Folate receptor deficiency
M165	<i>HEXA</i>	C58Y	2.7	15.91	272800	Psychomotor delay, mild Tay–Sachs' disease
8600276†	<i>L2HGDH</i>	R335X	5.1	13.39	609584	Hydroxyglutaric aciduria
M142	<i>MED13L</i>	R1416H	1.9	9.17	608808	Non-syndromic ID, no cardiac involvement
8600486	<i>NAGLU</i>	R565Q	2.8	13.25	252920	Sanfilippo's syndrome, MPS IIIB
8500234	<i>PDHX</i>	R15H	3.13	35.17	245349	Pyruvate dehydrogenase defect
M331	<i>PEX6</i>	L534P	3.8	10.83	601498	Peroxisome biogenesis disorder
8307998	<i>PMM2</i>	Y106F	2.67	6.71	212065	Glycosylation disorder CDG Ia
8600273	<i>PRKCG</i>	V177fs	2.53	0.72	605361	Spinocerebellar ataxia 14
M146	<i>PRKCG</i>	D480Y	2.1	7.45	605361	Spinocerebellar ataxia 14
8600162	<i>PRKRA</i>	S235T	2.1	40.02	612067	Non-syndromic ID
8600042	<i>SLC2A1</i>	V237M	3.73	16.7	606777	Non-syndromic ID
8700017	<i>SRD5A3</i>	Y169C	4.8	10.5	612713	Kahrizi's syndrome, CDG
M069†	<i>SRD5A3</i>	A68fs	3.01	10.44	612713	Kahrizi's syndrome, CDG
G008	<i>SURF1</i>	W227R	1.8	4.59	185620	Leigh's syndrome, very mild form
8600041	<i>TH</i>	R202H	2.1	7.23	605407	infantile parkinsonism, Segawa's syndrome
M017N	<i>VRK1</i>	R133C	3.4	3	607596	Pontocerebellar hypoplasia
M196	<i>WDR62</i>	G705G	2.1	18.33	600176	Microcephaly, cerebellar atrophy

CDG, congenital disorder of glycosylation; fs, frameshift; ID, intellectual disability; LOD, logarithm of the odds; MPS, mucopolysaccharidosis; OMIM, Online Mendelian Inheritance in Man.

\* See Supplementary Information for further details.

† Remotely related, degree of consanguinity is not clear, analysis performed under conservative assumption of second degree consanguinity.



**Table 2 | Apparently causative variants in novel (candidate) genes for intellectual disability**

Family	Phenotype	Gene	Mutation	LOD score	Length (Mb)	Supporting evidence
M008† M173	S NS, ASD	<i>ACBD6</i> <i>ADK</i>	G22fs H324R	2.65 5.1	6.46 9.68	P; binds long-chain acyl-CoA molecules, role in fatty acid synthesis or turnover <sup>44</sup> . S, P; only change in family. Adenosine kinase, regulates adenosine levels in the brain. Overexpression leads to learning impairment in mice <sup>45</sup> ; knockout mice develop lethal neonatal liver steatosis <sup>30</sup> . In human, a different gene defect has been found in this condition.
M266-2	NS	<i>ADRA2B</i>	R440G	2.53	24.97	S, P; GPCR regulating adrenergic neurons in the CNS. Associates with EIF2B, a GEF regulating translation <sup>19</sup> . Also associates with 14-3-3, which interacts with RGS7, mutated in family 8700136.
M226	NS	<i>ASCC3</i>	S1564P	3.2	62.80	S, P, E; helicase that is part of the activating signal co-integrator complex, enhances NF-κB and AP1. Interacts with RARS2, implicated in pontocerebellar hypoplasia 6 <sup>46</sup> .
M007L‡	NS	<i>ASCL1</i>	A41S	2.4	18.13	Encodes the bHLH factor MASH1, critical role in neuronal commitment and differentiation <sup>47,48</sup> .
M182	NS	<i>C11orf46</i>	R236H	2.1	12.39	P, E; encodes subunit of the Triple T complex, role in regulation of DNA damage response <sup>22</sup> .
G001	NS	<i>C12orf57</i>	M1V	2.5	11.19	S; function hitherto unknown. May overlap neighbouring <i>ANT1</i> (DRPLA) gene (see UCSC Genome Browser, hg18; OMIM 125370).
M100	NS	<i>C8orf41</i>	P367L	3.3	6.44	S, P, E; C8orf41 associates with RUVBL2 <sup>49</sup> , which is involved in regulation of transcription and interacts with HDACs <sup>50</sup> .
G015	NS	<i>C9orf86</i>	A562P	3.3	2.17	P; encodes Rab-like GTP-binding protein PARF, which interacts with ARF (or CDKN2A). Other Rab has been implicated in ID <sup>49</sup> .
8500031	S	<i>CACNA1G</i>	S1346fs	2.7	18.76	P, E; encodes a low-voltage-activated calcium channel which may also modulate the firing patterns of neurons <sup>23,24</sup> .
8600057	S	<i>CAPN10</i>	138ins5aa	2.1	2.09	E; calcium-regulated non-lysosomal endopeptidase with a role in cytoskeletal remodelling and signal transduction, involved in long-term potentiation <sup>51</sup> .
8600495	NS	<i>CASP2</i>	Q392X	2.5	29.62	P; caspase 2, role in apoptosis, abnormal in CASP2-deficient mice, particularly for motor and sympathetic neurons <sup>52</sup> . Motor abnormalities not observed in family.
M346	NS	<i>CCNA2</i>	Splice site*	3.3	52.17	S, P; cyclin A2 is essential for cell cycle control <sup>53</sup> . In mice, targeted deletion of this gene is lethal <sup>54</sup> . Regulated by <i>SCAPER</i> , mutated in family 8600277.
8500235‡	S	<i>CNKSR1</i>	T282fs	2.53	15.83	P; regulates Raf in the MAPK pathway, acts as scaffold protein linking Ras and Rho signal transduction pathways <sup>29</sup> . Interacts with RALGDS, which is mutated in family 8500155.
M144	NS	<i>COQ5</i>	G118S	1.8	15.10	P, E; methyltransferase with pivotal role in coenzyme Q biosynthesis. Interacts with NAB2 which controls length of poly(A) tail (see <a href="http://thebiogrid.org/35094/summary/saccharomyces-cerevisiae/coq5.html">http://thebiogrid.org/35094/summary/saccharomyces-cerevisiae/coq5.html</a> ). The human orthologue of NAB2 is implicated in ARID <sup>32</sup> .
M178	NS	<i>EEF1B2</i>	Splice site*	2.6	13.84	S, P, E; controls translation by transferring aminoacyl-tRNAs to the ribosome. Interacts with UNC51-like kinase 2 which is involved in axonal elongation translation <sup>55</sup> .
G017	NS	<i>ELP2</i>	T555P	2.4	14.33	P, E; encodes subunit of the RNA polymerase II elongator complex <sup>56</sup> . ELP3 subunit implicated in motor neuron degeneration. Allelic <i>ELP2</i> mutation found in family M8500061.
8500061	NS	<i>ELP2</i>	R462L	2.7	16.98	P, E; involved in transcriptional elongation, see also family G017 with allelic <i>ELP2</i> mutation.
M263	NS	<i>ENTPD1</i>	Y65C	2.65	12.12	P, E; ectonucleoside triphosphate diphosphohydrolase, expressed in CNS; knockout mice display abnormal transmitter release <sup>57</sup> .
M050†	S	<i>ERLIN2</i>	R36K	3.73	12.72	S, P, E; involved in the ER-associated degradation of inositol 1,4,5-triphosphate receptors <sup>58</sup> .
8500058	NS	<i>FASN</i>	R1819W	3.3	4.50	P; gene product synthesizes long-chain fatty acids from acetyl-CoA and malonyl-CoA. Expressed in post-synaptic density. In mice, <i>FASN</i> deficiency leads to embryonic lethality <sup>59</sup> .
M269	S	<i>FRY</i>	R1197X	2.8	12.68	P; regulates actin cytoskeleton, limits dendritic branching. In HeLa cells, <i>FRY</i> binds to microtubules and localizes on the spindle and is crucial for the alignment of mitotic chromosomes <sup>60</sup> .
M251	S	<i>GON4L</i>	Splice site*	3.01	40.19	P, E; cloned from brain. Encodes a transcription factor thought to function in cell cycle control <sup>61</sup> .
M189‡	S	<i>HIST1H4B</i>	K9fs	2.1	48.87	P, E; encodes a member of the histone H4 family; analogy to histone H3 mutation in family G002. Ehlers–Danlos-related symptoms are probably due to <i>TNXB</i> mutation.
G002	NS	<i>HIST3H3</i>	R130C	2.53	26.74	P; role in spindle assembly and chromosome bi-orientation <sup>62–64</sup> . See also family M189 with <i>HIST1H4B</i> mutation.
8500064	NS	<i>INPP4A</i>	D915fs	2.4	46.16	P, E; encodes inositol polyphosphate-4-phosphatase, only plausible change in family. Regulates localization of synaptic NMDA receptors, protects neurons from excitotoxic cell death <sup>65</sup> . Knockout mice develop locomotor instability; not observed in this family.
M061	S	<i>KDM5A</i>	R719G	2.3	6.06	P, E; encodes histone demethylase specific for Lys 4 of histone H3, role in transcriptional regulation <sup>66</sup> . Other histone demethylase has been implicated in X-linked ID <sup>16</sup> . See also family M8303971 with <i>KDM6B</i> mutation.

previously shown that mutations in another lysine-specific histone demethylase, *KDM5C* (also called *JARID1C*), are a relatively frequent cause of X-linked intellectual disability<sup>16</sup>. In two other families, we observed apparently pathogenic mutations that involved histones directly: a frameshift mutation in the *HIST1H4B* gene which belongs to the histone 4 family, and a *HIST3H3* missense mutation with high pathogenicity scores that was the only plausible change in a family with non-syndromic intellectual disability. Together, at least ten of the novel candidate genes for ARID involve histone structure, histone modification, chromatin remodelling or the regulation of transcription, and many of these genes are functionally linked to known and novel intellectual disability genes, as shown in Fig. 1a.

Several other mutated genes are directly or indirectly involved in the regulation of translation. A homozygous frameshift mutation

inactivating the *TRMT1* gene was detected in a family with non-syndromic intellectual disability. *TRMT1* is an RNA methyltransferase that dimethylates a single guanine residue at position 26 of most tRNAs. Previously we and others have shown that inactivation of the X-linked gene *FTSJ1*, another RNA methyltransferase, also gives rise to non-syndromic intellectual disability<sup>17,18</sup>, and we have recently identified several ARID families with truncating mutations in a third RNA methyltransferase (L.A.M. *et al.*, manuscript in preparation). A large deletion in the *EEF1B2* gene was the only detectable defect in another family with non-syndromic intellectual disability. *EEF1B2* encodes the elongation factor 1β, which is involved in the transport of aminoacyl-tRNAs to the ribosomes. In yet another family with non-syndromic intellectual disability, a missense change was found in *ADRA2B*. This gene encodes a brain-expressed G-protein-coupled receptor that

Table 2 | Continued

Family	Phenotype	Gene	Mutation	LOD score	Length (Mb)	Supporting evidence
8303971	S	<i>KDM6B</i>	P888S	3.1	5.08	S, P; demethylase 6B specifically targeting Lys 27 of histone H3, has a central role in regulation of posterior development by regulating HOX gene expression <sup>67</sup> . Mutation of <i>KDM5A</i> gives rise to ID (see family M061).
M154	S	<i>KIF7</i>	E758K	2.1	7.46	P, E; knockout mouse model with complex picture involving brain and other neurological abnormalities <sup>68</sup> . Stickler-like clinical features in this family can be explained by co-existing <i>COL9A1</i> mutation.
M183	S	<i>LAMA1</i>	G1572fs	2.1	5.82	S, P; codes for subunit of laminin, role in attachment, migration and organization of cells during embryonic development. Required for normal retinal development in mice <sup>69</sup> .
G030	S	<i>LARP7</i>	K276fs	1.93	8.94	S,P; encodes negative transcriptional regulator of polymerase II genes <sup>70</sup> .
7903104	S	<i>LINS1</i>	H329fs	2.65	7.87	S, P; similar to <i>lin</i> , a <i>Drosophila</i> gene having important roles in the development of the epidermis and the hindgut. Link with ID unclear.
8600060†	NS	<i>MAN1B1</i>	R334C	3.13	2.49	P, E; encodes mannosidase that targets misfolded glycoproteins for degradation. <i>MAN1B1</i> frameshift mutation observed in another ARID family by Canadian group (J. Vincent, personal communication).
8600277	NS	<i>NDST1</i>	R709Q	2.1	10.18	S, P; only change in family. Encodes heparan <i>N</i> -deacetylase/ <i>N</i> -sulphotransferase, deficiency is lethal in mice due to respiratory distress <sup>71</sup> . No obvious link with ID.
M158	S	<i>PARP1</i>	L293F	1.8	16.76	P; poly(ADP-ribose) polymerase involved in histone 1 modification; role in memory stabilization in mice <sup>72</sup> .
M194	NS, ASD	<i>PECR</i>	L57V	2.5	11.27	P; brain-expressed peroxisomal <i>trans</i> -2-enoyl-CoA reductase involved in the biosynthesis of unsaturated fatty acids <sup>73</sup> .
8401214	S	<i>POLR3B</i>	T199K	1.93	24.89	E; second-largest core component of RNA polymerase III, which synthesizes small RNAs such as tRNAs and 5S rRNAs <sup>21</sup> .
8500302	NS	<i>PRMT10</i>	G189R	2.65	9.75	P, E; protein arginine methyltransferase 10. Protein arginine methylation affects chromatin remodelling leading to transcriptional regulation, RNA processing, DNA repair and cell signalling <sup>74</sup> .
M010	NS	<i>PRRT2</i>	A214fs	5.2	25.59	P; interacts with SNAP25 which in turn assembles with syntaxin-1 and synaptobrevin to form exocytotic fusion complex in neurons <sup>55</sup> .
8500155	NS	<i>RALGDS</i>	A706V	4.0	5.56	S, E; effector of Ras-related RalA and RalB GTPases, role in synaptic plasticity <sup>26</sup> . Interacts with CNKSR1, inactivated in family 8500235.
8700136	NS, ASD	<i>RGS7</i>	N304fs	2.53	24.34	P; regulator of G protein signalling. Interacts with 14-3-3 protein, tau and snapin, a component of the SNARE complex required for synaptic vesicle docking and fusion <sup>75</sup> . Indirectly linked with <i>ADRA2B</i> , mutated in family M266_2.
8600086	NS	<i>SCAPER</i>	Y118fs	3.9	17.45	S, E; interacts with CCNA2/CDK2 complex, transiently maintains CCNA2 in cytoplasm <sup>76</sup> . CCNA2 is mutated in family M346.
8600012	S	<i>SLC31A1</i>	R90G	2.1	13.85	P, E; encodes one of two genes involved in copper import. Deficiency of the SLC31A1 orthologue in mice is early lethal, heterozygotes have progressive neurological disorder <sup>77</sup> , similar to patients in this family.
M177	S	<i>TAF2</i>	W649R	2.1	19.16	P, E; TATA-box-associated gene is very important regulator of transcription (see OMIM 604912). Other TAF genes have been implicated in X-linked ID (V.K. <i>et al.</i> , manuscript in preparation). MAL2 is another, less likely, candidate in this family.
M160	S	<i>TMEM135</i>	C228S	2.4	16.89	S, P, E; transmembrane protein involved in fat metabolism and energy expenditure <sup>78</sup> .
M300	NS	<i>TRMT1</i>	I230fs	3.4	10.34	P, E; encodes dimethylguanosine tRNA methyltransferase <sup>79</sup> . At least two other RNA methyltransferases have been implicated in ID (ref. 17 and L.A.M., manuscript in preparation).
M168	NS, ASD	<i>UBR7</i>	N124S	2.5	8.78	P, E; encodes n-regognin 7, a component of E3 ubiquitin ligase <sup>80</sup> . Involved in protein degradation, which has been implicated in ID.
8500320	S	<i>WDR45L</i>	R109Q	1.93	2.55	P, E; WD repeat domain, phosphoinositide-interacting protein 3, ILF1-like <sup>81</sup> , specific function unknown.
M169	S	<i>ZBTB40</i>	Q525X	3.5	14.56	S, P, E; krüppel-type zinc finger, highly expressed in brain. Regulator of glia differentiation <sup>25</sup> .
M156	NS	<i>ZCCHC8</i>	L90X	2.3	7.64	P; zinc-finger protein, identified in the spliceosome C complex. Interacts with BRCA1 and RBM7 <sup>82,83</sup> . RBM10 has been implicated in X-linked ID (V.K. <i>et al.</i> , manuscript in preparation).
M025	NS	<i>ZNF526</i>	R459Q	4.5	6.13	P; zinc-finger protein, only remaining change in family. Functional relevance supported by 3D modelling. Probable activator of mRNA translation. Allelic <i>ZNF526</i> mutation observed in family 8500156.
8500156	NS	<i>ZNF526</i>	Q539H	4.04	11.33	P; see family M025 with allelic <i>ZNF526</i> mutation.

References 44–83 are listed in Supplementary Information. E, high evolutionary conservation score; P, high pathogenicity score, includes truncating mutations; S, only change found in family. ASD, autism spectrum disorder; GPCR, G-protein-coupled receptor; ID, intellectual disability; NS, non-syndromic; S, syndromic.

\* See Supplementary Information for further details.

† Parents are distantly related. LOD scores provided are minimum estimates, calculated on the assumption that they are second cousins.

‡ In ethnically matching healthy controls a single heterozygous carrier was found (for details, see Supplementary Table 3).

associates with EIF2B, a guanine exchange factor regulating translation<sup>19</sup>; notably, *ADRA2B* also interacts with the 14-3-3 protein, which in turn associates with RGS7, another novel ARID gene product that regulates G-protein signalling. Finally, in a family with a syndromic form of intellectual disability, a missense change was found in the *POLR3B* gene, involving a nucleotide with a very high conservation score and predicted to be pathogenic by Mutation Taster<sup>20</sup>. *POLR3B* encodes the second-largest core component of RNA polymerase III, which synthesizes small RNAs such as tRNAs and 5S rRNAs<sup>21</sup> and also interacts with ENTPD1, the product of a novel candidate gene for intellectual disability (see GeneCards, <http://www.genecards.org/cgi-bin/cardsearch.pl?search=POLR3B> and Table 2). Together, these observations

indicate that gene defects interfering with transcription and translation are particularly important causes of intellectual disability.

However, we also found pathogenic mutations affecting other fundamental cellular functions and pathways such as cell-cycle control, as illustrated by a mutation inactivating *CCNA2*, and another one truncating *SCAPER*, a specific regulator of the CCNA2–CDK2 complex (see Fig. 1b). The *C11orf46* gene encodes TTI2, a subunit of the Triple T complex, which is required for the establishment of cell-cycle checkpoints and for DNA-damage signalling<sup>22</sup>. Other mutations involved fatty-acid synthesis and turnover (*ACBD6*, *FASN* and *PECR*; see Table 2), protein degradation (*UBR7*), splicing (*ZCCHC8*) and cell migration (*LAMA1*).

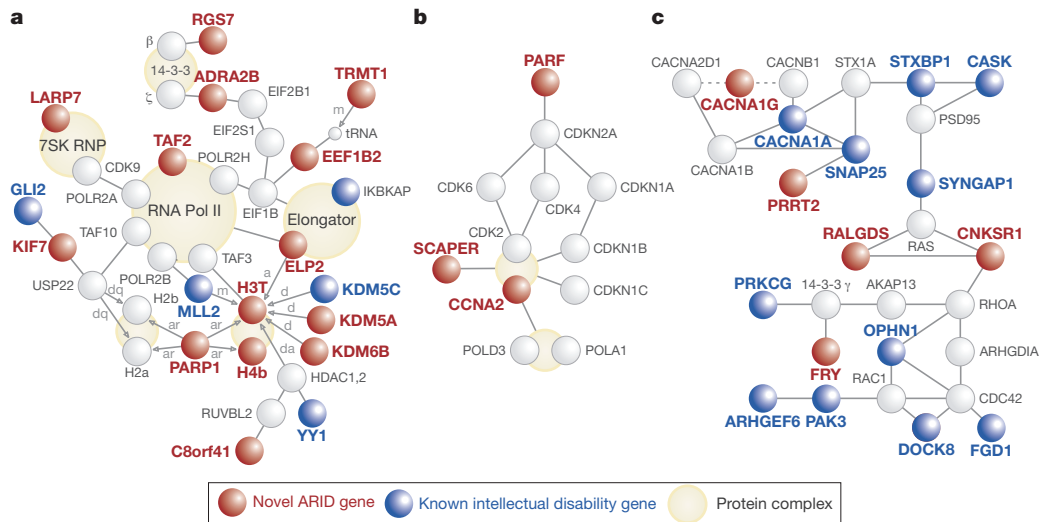


**Figure 1 | Known and novel intellectual disability genes form protein and regulatory networks.** **a**, Transcriptional/translational network. **b**, Cell-cycle-related network. **c**, Ras/Rho/PSD95 network. Connecting edges in the figure stand for protein–protein interactions. Arrows define direction of post-translational protein modifications: a, acetylation; ar, ADP-ribosylation; d,

demethylation; da, deacetylation; dq, deubiquitination; m, methylation. Dotted lines indicate modulation of gene function. Data were obtained in part by using the INGENUITY software package (<http://www.ingenuity.com>) and by literature mining. More details about these proteins and their interactions are provided in Table 2 and in Supplementary Information.

### Intellectual disability genes with brain-specific functions

Not surprisingly, several mutations involved genes with neuron- or brain-specific functions. For example, we found a frameshift mutation abolishing the function of *CACNA1G*, a T-type calcium channel with a critical role in the generation of GABA<sub>B</sub> receptor-mediated spike and wave discharges in the thalamocortical pathway<sup>23,24</sup>. A nonsense mutation inactivated *ZBTB40*, which has a role in glia cell differentiation<sup>25</sup>, and other observed changes are expected to interfere with the regulation of neurotransmission, exocytosis or neurotransmitter release. Our study also adds several novel intellectual-disability-associated genes to the Ras and Rho pathway (see Fig. 1c); for example, a convincing missense mutation in the *RALGDS* gene was the only variant detected in one family with non-syndromic intellectual disability. This gene encodes an effector of the Ras-related GTPase Ral, which stimulates the dissociation of GDP from the Ras-related RalA and RalB GTPases, thereby allowing GTP binding and activation of the GTPases<sup>26</sup>. Regulators of small GTPases were among the first genes to be implicated in non-syndromic intellectual disability<sup>27,28</sup>. We also found a homozygous frameshift mutation in *CNKSRI*, which is physically associated with *RALGDS*. Homozygous carriers of this mutation have a severe syndromic phenotype with quadrupedal gait. *CNKSRI* binds to rhophilin (Online Mendelian Inheritance in Man (OMIM) 601031), a Rho effector, suggesting that it acts as a scaffold protein and mediates crosstalk between the Ras and Rho GTPase signalling pathways<sup>29</sup>. Neither *RALGDS* nor *CNKSRI* had been implicated in intellectual disability so far; thus, both are novel ARID genes.

### Genes without obvious link to intellectual disability

For several of the sequence variants, there is no obvious functional link between the molecular defect and intellectual disability. This applies to *LINS1* and *NDST1*, and it is not easy to understand why in humans, adenosine kinase deficiency should lead to intellectual disability, whereas in the mouse, overexpression of *Adk* causes neurological symptoms, and *Adk* deficiency gives rise to early lethal liver steatosis<sup>30</sup>. Nothing is known yet about the function of the *C12orf57* gene, apart from its apparent overlap with *ATN1* (see UCSC Genome Browser, NCBI36/hg18). CAG trinucleotide expansion in the *ATN1* gene is the cause of dentatorubral pallidolysian atrophy (DRPLA), another syndromic form of intellectual disability. A comprehensive list of families with single, probably disease-causing mutations is shown in Table 2.

Despite exhaustive validation of our data and stringent filtering against all known neutral and pathogenic sequence variants (see Supplementary Information and Supplementary Tables 3–6), it is still possible that not all of these changes will turn out to be causative. Particularly for the numerous missense mutations observed, functional studies will be required to rule out rare polymorphisms that are unrelated to intellectual disability. In a previous study, 1% of the protein-truncating mutations on the X chromosome were found to be unrelated to disease<sup>31</sup>, and in our study, 12 observed inactivating mutations did not co-segregate with intellectual disability (see Supplementary Table 4). However, we believe that the vast majority of the changes presented here as probably pathogenic will be confirmed, even if they have been observed only once, because most of the proteins encoded by these novel candidate genes interact with the products of known or novel genes associated with intellectual disability, as shown in Fig. 1.

### Most ARID genes are not synapse specific

We have previously shown that ARID is an extremely heterogeneous disorder<sup>6</sup>. In contrast to non-syndromic hearing impairment or X-linked intellectual disability, common forms of ARID do not seem to exist, although there is evidence for regional clustering of the underlying gene defects<sup>5</sup>. Extrapolating from the number of known X-chromosomal intellectual disability genes argues for the involvement of several hundred genes in non-syndromic ARID, and the total number of ARID genes may well run into the thousands<sup>1</sup>. Identification of most or all of these genes is a prerequisite for early diagnosis, prevention and, eventually, therapy of intellectual disability, but at the present pace, many years would be required to accomplish this task. Here, we have combined homozygosity mapping, targeted exon enrichment and next-generation sequencing to speed up the molecular elucidation of ARID. In 78 out of 136 consanguineous families investigated, we have found apparently pathogenic mutations in single genes. Fifty of these genes had not been implicated in ARID before, and only two of these novel intellectual disability genes were found to be mutated in two independent families. None of the ~10 previously known genes for non-syndromic ARID, including those that were identified in Iranian families<sup>32–36</sup>, was observed in our present cohort, thereby corroborating previous evidence that ARID is extremely heterogeneous.

Much of the research into the molecular causes of intellectual disability has focused on the synapse and synapse-specific genes (for



example, see refs 2, 37). In the present study, relatively few of the novel defects identified involve synapse- or neuron-specific genes, and they are vastly outnumbered by ubiquitously expressed genes with indispensable cellular functions, such as DNA transcription and translation, protein degradation, mRNA splicing, energy metabolism as well as fatty-acid synthesis and turnover. Many of these defects were found to be associated with non-syndromic ARID. It is not immediately clear why the clinical consequences of defects involving such a wide spectrum of basic cellular processes should be confined to the brain, but this conceivably reflects the complexity of the central nervous system which may render it particularly vulnerable to damage.

We expect that these findings will have direct implications for the diagnosis and prevention of intellectual disability, and perhaps also for autism, schizophrenia and epilepsy, which often co-exist in intellectual disability patients and are frequently associated with mutations in the same genes (for example, see ref. 38; reviewed in ref. 1). Further investigation of the novel genes and networks presented here should significantly deepen our insight into the pathogenesis of intellectual disability and related disorders. Moreover, this study illustrates the power of large-scale next-generation sequencing in families as a general strategy to shed light on the aetiology of complex disorders and on the function of the underlying genes.

**Note added in proof:** While this work was in the press, two unrelated groups reported on inactivating ERLIN2 mutations in patients with recessive intellectual disability and progressive motor dysfunction<sup>39,40</sup>. Moreover, syndromic forms of intellectual disability have been described in patients with AP4B1 and AP4E1 (ref. 41) and MAN1B1 (ref. 42) mutations, respectively. Finally, mutations inactivating the KIF7 gene were identified as the cause of the recessive fetal hydrolethals and acrocallosal syndromes that include brain malformations<sup>43</sup>.

## METHODS SUMMARY

Most families studied were from Iran, and less than 10% had a Turkish or Arabic background. Wechsler Intelligence Scales for Children (WISC) and WAIS were used to assess the IQ in children and parents. Many of the pedigrees, as well as the methods used for autozygosity mapping, have been described previously.

Exons from homozygous intervals were enriched with custom-made Agilent SureSelect DNA capture arrays and sequenced on an Illumina Genome Analyser II yielding 76-bp single reads. >98% of the targeted exons were covered by at least four non-redundant sequence reads, each with a PHRED-like quality score of 20 or above (mean, 0.984; median, 0.993; for details, see Supplementary Table 5).

To assess the reliability of this procedure for calling homozygous mutations, we looked up SNP markers from homozygous intervals of five selected families that had been analysed with high-resolution SNP arrays. For 773 out of 776 markers, next-generation sequencing and array-based SNP typing yielded identical results.

To detect single nucleotide variants, high-quality reads were aligned to the human reference genome (hg18) by SOAP2.20 with default settings, typically gap-free. Homozygous exon-spanning deletions were assumed if the sequence coverage of the relevant exon(s) was reduced to <5% of the mean. Details about the detection of smaller deletions and insertions are provided in Methods. All variants were validated by high-resolution array CGH, Sanger sequencing, or both.

Homozygous variants were filtered against dbSNP130/131, whole genomes from 185 healthy individuals studied by the 1000 Genomes Project and exomes from 200 Danish individuals, and found to be absent in at least 100 chromosomes from Iranian controls (see Supplementary Tables 1 and 3). To select and prioritize apparently disease-causing variants, various criteria were used (for more details, see Methods). All putative mutations co-segregated with intellectual disability in the respective families.

Received 9 March; accepted 5 August 2011.

Published online 21 September 2011.

1. Ropers, H. H. Genetics of early onset cognitive impairment. *Annu. Rev. Genomics Hum. Genet.* **11**, 161–187 (2010).
2. Hamdan, F. F. *et al.* Excess of *de novo* deleterious mutations in genes associated with glutamatergic systems in nonsyndromic intellectual disability. *Am. J. Hum. Genet.* **88**, 306–316 (2011).
3. Hamdan, F. F. *et al.* Mutations in SYNGAP1 in autosomal nonsyndromic mental retardation. *N. Engl. J. Med.* **360**, 599–605 (2009).

4. Vissers, L. E. *et al.* A *de novo* paradigm for mental retardation. *Nature Genet.* **42**, 1109–1112 (2010).
5. Najmabadi, H. *et al.* Homozygosity mapping in consanguineous families reveals extreme heterogeneity of non-syndromic autosomal recessive mental retardation and identifies 8 novel gene loci. *Hum. Genet.* **121**, 43–48 (2007).
6. Kuss, A. W. *et al.* Autosomal recessive mental retardation: homozygosity mapping identifies 27 single linkage intervals, at least 14 novel loci and several mutation hotspots. *Hum. Genet.* **129**, 141–148 (2011).
7. Kaufman, L., Ayub, M. & Vincent, J. B. The genetic basis of non-syndromic intellectual disability: a review. *J. Neurodev. Disord.* **2**, 182–209 (2010).
8. Ng, S. B. *et al.* Exome sequencing identifies MLL2 mutations as a cause of Kabuki syndrome. *Nature Genet.* **42**, 790–793 (2010).
9. Ng, S. B. *et al.* Exome sequencing identifies the cause of a mendelian disorder. *Nature Genet.* **42**, 30–35 (2010).
10. Lupski, J. R. *et al.* Whole-genome sequencing in a patient with Charcot-Marie-Tooth neuropathy. *N. Engl. J. Med.* **362**, 1181–1191 (2010).
11. Cantagrel, V. *et al.* SRD5A3 is required for converting polyprenol to dolichol and is mutated in a congenital glycosylation disorder. *Cell* **142**, 203–217 (2010).
12. Kahrizi, K. *et al.* Next generation sequencing in a family with autosomal recessive Kahrizi syndrome (OMIM 612713) reveals a homozygous frameshift mutation in SRD5A3. *Eur. J. Hum. Genet.* **19**, 115–117 (2011).
13. Raas-Rothschild, A. *et al.* A PEX6-defective peroxisomal biogenesis disorder with severe phenotype in an infant, versus mild phenotype resembling Usher syndrome in the affected parents. *Am. J. Hum. Genet.* **70**, 1062–1068 (2002).
14. Steinfeld, R. *et al.* Folate receptor alpha defect causes cerebral folate transport deficiency: a treatable neurodegenerative disorder associated with disturbed myelin metabolism. *Am. J. Hum. Genet.* **85**, 354–363 (2009).
15. Shoichet, S. A. *et al.* Mutations in the ZNF41 gene are associated with cognitive deficits: identification of a new candidate for X-linked mental retardation. *Am. J. Hum. Genet.* **73**, 1341–1354 (2003).
16. Jensen, L. R. *et al.* Mutations in the JARID1C gene, which is involved in transcriptional regulation and chromatin remodeling, cause X-linked mental retardation. *Am. J. Hum. Genet.* **76**, 227–236 (2005).
17. Freude, K. *et al.* Mutations in the FTSJ1 gene coding for a novel S-adenosylmethionine-binding protein cause nonsyndromic X-linked mental retardation. *Am. J. Hum. Genet.* **75**, 305–309 (2004).
18. Ramser, J. *et al.* A splice site mutation in the methyltransferase gene FTSJ1 in Xp11.23 is associated with non-syndromic mental retardation in a large Belgian family (MRX9). *J. Med. Genet.* **41**, 679–683 (2004).
19. Klein, U., Ramirez, M. T., Kobilka, B. K. & von Zastrow, M. A novel interaction between adrenergic receptors and the  $\alpha$ -subunit of eukaryotic initiation factor 2B. *J. Biol. Chem.* **272**, 19099–19102 (1997).
20. Schwarz, J. M., Rodelsperger, C., Schuelke, M. & Seelow, D. MutationTaster evaluates disease-causing potential of sequence alterations. *Nature Methods* **7**, 575–576 (2010).
21. Geiduschek, E. P. & Kassavetis, G. A. The RNA polymerase III transcription apparatus. *J. Mol. Biol.* **310**, 1–26 (2001).
22. Hurov, K. E., Cotta-Ramusino, C. & Elledge, S. J. A genetic screen identifies the Triple T complex required for DNA damage signaling and ATM and ATR stability. *Genes Dev.* **24**, 1939–1950 (2010).
23. Zamponi, G. W., Lory, P. & Perez-Reyes, E. Role of voltage-gated calcium channels in epilepsy. *Pflügers Arch.* **460**, 395–403 (2010).
24. Singh, B. *et al.* Mutational analysis of CACNA1G in idiopathic generalized epilepsy. *Hum. Mutat.* **28**, 524–525 (2007).
25. Södersten, E., Lilja, T. & Hermanson, O. The novel BTB/POZ and zinc finger factor Zbtb45 is essential for proper glial differentiation of neural and oligodendrocyte progenitor cells. *Cell Cycle* **9**, 4866–4875 (2010).
26. Zhu, X. *et al.* Disruption of PC1/3 expression in mice causes dwarfism and multiple neuroendocrine peptide processing defects. *Proc. Natl Acad. Sci. USA* **99**, 10293–10298 (2002).
27. Billuart, P. *et al.* Oligophrenin-1 encodes a rhoGAP protein involved in X-linked mental retardation. *Nature* **392**, 923–926 (1998).
28. D'Adamo, P. *et al.* Mutations in GDI1 are responsible for X-linked non-specific mental retardation. *Nature Genet.* **19**, 134–139 (1998).
29. Jaffe, A. B., Aspenstrom, P. & Hall, A. Human CNK1 acts as a scaffold protein, linking Rho and Ras signal transduction pathways. *Mol. Cell. Biol.* **24**, 1736–1746 (2004).
30. Boison, D. *et al.* Neonatal hepatic steatosis by disruption of the adenosine kinase gene. *Proc. Natl Acad. Sci. USA* **99**, 6985–6990 (2002).
31. Tarpey, P. S. *et al.* A systematic, large-scale resequencing screen of X-chromosome coding exons in mental retardation. *Nature Genet.* **41**, 535–543 (2009).
32. Pak, C. *et al.* Mutation of the conserved polyadenosine RNA binding protein, ZC3H14/dNab2, impairs neural function in *Drosophila* and humans. *Proc. Natl Acad. Sci. USA* **108**, 12390–12395 (2011).
33. Garshasbi, M. *et al.* A defect in the TUSC3 gene is associated with autosomal recessive mental retardation. *Am. J. Hum. Genet.* **82**, 1158–1164 (2008).
34. Mir, A. *et al.* Identification of mutations in TRAPPC9, which encodes the NIK- and IKK- $\beta$ -binding protein, in nonsyndromic autosomal-recessive mental retardation. *Am. J. Hum. Genet.* **85**, 909–915 (2009).
35. Moheb, L. A. *et al.* Identification of a nonsense mutation in the very low-density lipoprotein receptor gene (VLDLR) in an Iranian family with dysequilibrium syndrome. *Eur. J. Hum. Genet.* **16**, 270–273 (2008).
36. Motazacker, M. M. *et al.* A defect in the ionotropic glutamate receptor 6 gene (GRIN2) is associated with autosomal recessive mental retardation. *Am. J. Hum. Genet.* **81**, 792–798 (2007).
37. Laumonnier, F., Cuthbert, P. C. & Grant, S. G. The role of neuronal complexes in human X-linked brain diseases. *Am. J. Hum. Genet.* **80**, 205–220 (2007).

38. Ullmann, R. *et al.* Array CGH identifies reciprocal 16p13.1 duplications and deletions that predispose to autism and/or mental retardation. *Hum. Mutat.* **28**, 674–682 (2007).
39. Yildirim, Y. *et al.* A frameshift mutation of ERLIN2 in recessive intellectual disability, motor dysfunction and multiple joint contractures. *Hum. Mol. Genet.* **20**, 1886–1892 (2011).
40. Alazami, A. M., Adly, N., Al Dhalaan, H. & Alkuraya, F. S. A nullimorphic *ERLIN2* mutation defines a complicated hereditary spastic paraplegia locus (SPG18). *Neurogenetics* doi:10.1007/s10048-011-0291-8 (2011).
41. Abou Jamra, R. *et al.* Adaptor protein complex 4 deficiency causes severe autosomal-recessive intellectual disability, progressive spastic paraplegia, shy character, and short stature. *Am. J. Hum. Genet.* **88**, 788–795 (2011).
42. Rafiq, M. A. *et al.* Mutations in the alpha 1,2-mannosidase gene, *MAN1B1*, cause autosomal-recessive intellectual disability. *Am. J. Hum. Genet.* **89**, 176–182 (2011).
43. Putoux, A. *et al.* KIF7 mutations cause fetal hydrolethrus and acrocallosal syndromes. *Nature Genet.* **43**, 601–606 (2011).

**Supplementary Information** is linked to the online version of the paper at [www.nature.com/nature](http://www.nature.com/nature).

**Acknowledgements** We express our gratitude to the patients and their families for their participation in the study. We thank S. Nakhee and K. Javan for their support; S. Arzhang, S. Banihashemi, M. Kasiri, H. Khodae, M. Schlicht and M. Gerloff for contributing to this project in various ways; G. Eder for her assistance with the

preparation of the manuscript; and S. Shoichet for critically reading the manuscript. This work was supported by the Max Planck Innovation Funds, the German Federal Ministry of Education and Research through the MRNET (grant 01GS08161, to H.H.R.), the Iranian National Science Foundation and the EU-FP7 project GENCODYS.

**Author Contributions** H.H.R. and H.N. initiated and directed this study. H.H., M.G., W.C., S.H., K.W., V.K., R.U., K.K. and A.W.K. contributed to its design and coordination. H.N., K.K., A.T., P.J., V.H., D.W., M.C., I.R., F.M., C.H., A.D., A.R., M.J.S.B., M.F. and H.D. recruited patients and families, and K.K. and A.T. were responsible for the clinical investigations. F.B., S.G.F. and R.K. did the karyotyping. M.G. performed the linkage analyses and together with R.W. and H.H., he established data management tools. R.U. and I.M. performed exon enrichments, and C.J. and M.B. did the deep sequencing experiments. H.H. analysed the sequencing data and provided bioinformatics support. M.G., S.S.A., M.H., A.Z., M.M., L.P., L.N.V., L.A.M., F.L., B.L., S.E.-N., Z.F., J.H., L.M. and A.W.K. participated in the validation of the results and the segregation analyses. T.Z. performed the pathway analyses. H.H., M.G., A.Z., L.P., R.W., T.Z., L.M., A.W.K., A.T., K.K., H.N. and H.H.R. evaluated and interpreted the results, and H.H.R., H.H. and M.G. wrote the manuscript.

**Author Information** Raw sequencing data can be retrieved from the Sequence Read Archive (SRA), accession number SRA036250. Reprints and permissions information is available at [www.nature.com/reprints](http://www.nature.com/reprints). The authors declare no competing financial interests. Readers are welcome to comment on the online version of this article at [www.nature.com/nature](http://www.nature.com/nature). Correspondence and requests for materials should be addressed to H.H.R. ([ropers@molgen.mpg.de](mailto:ropers@molgen.mpg.de)) or K.K. ([kkahrizi@uswr.ac.ir](mailto:kkahrizi@uswr.ac.ir)).

# Mechanical strain in actin networks regulates FilGAP and integrin binding to filamin A

A. J. Ehrlicher<sup>1,2</sup>, F. Nakamura<sup>1</sup>, J. H. Hartwig<sup>1</sup>, D. A. Weitz<sup>2</sup> & T. P. Stossel<sup>1</sup>

Mechanical stresses elicit cellular reactions mediated by chemical signals. Defective responses to forces underlie human medical disorders<sup>1–4</sup> such as cardiac failure<sup>5</sup> and pulmonary injury<sup>6</sup>. The actin cytoskeleton's connectivity enables it to transmit forces rapidly over large distances<sup>7</sup>, implicating it in these physiological and pathological responses. Despite detailed knowledge of the cytoskeletal structure, the specific molecular switches that convert mechanical stimuli into chemical signals have remained elusive. Here we identify the actin-binding protein filamin A (FLNA)<sup>8,9</sup> as a central mechanotransduction element of the cytoskeleton. We reconstituted a minimal system consisting of actin filaments, FLNA and two FLNA-binding partners: the cytoplasmic tail of  $\beta$ -integrin, and FilGAP. Integrins form an essential mechanical linkage between extracellular and intracellular environments, with  $\beta$ -integrin tails connecting to the actin cytoskeleton by binding directly to filamin<sup>4</sup>. FilGAP is an FLNA-binding GTPase-activating protein specific for RAC, which *in vivo* regulates cell spreading and bleb formation<sup>10</sup>. Using fluorescence loss after photoconversion, a novel, high-speed alternative to fluorescence recovery after photobleaching<sup>11</sup>, we demonstrate that both externally imposed bulk shear and myosin-II-driven forces differentially regulate the binding of these partners to FLNA. Consistent with structural predictions, strain increases  $\beta$ -integrin binding to FLNA, whereas it causes FilGAP to dissociate from FLNA, providing a direct and specific molecular basis for cellular mechanotransduction. These results identify a molecular mechanotransduction element within the actin cytoskeleton, revealing that mechanical strain of key proteins regulates the binding of signalling molecules.

The composite cytoskeleton network *in vivo* provides dynamic cellular structure and actively generates movement. A physiological reconstituted *in vitro* network of actin and FLNA creates an elastic gel mechanically dominated by the rod-like actin filaments and cross-linked by flexible FLNA molecules. Applying strain to this network readily deforms FLNA crosslinks (Fig. 1a, b), and the specific structure and actin binding of FLNA suggest how these deformations might affect FLNA's interaction of with some of its 90 or so other currently identified binding partners<sup>9</sup>.

FLNA is an extended homodimer composed of two identical subunits, each having an amino-terminal actin-binding domain followed by 24 immunoglobulin repeats<sup>12</sup> (Fig. 1c, d). The actin-binding domains and repeats 1–15 are designated 'rod 1' and form a linear structure that binds actin filaments. Repeats 16–23, comprising 'rod 2', however, form compact globular clusters that do not interact with actin filaments and contain most of FLNA's binding-partner sites. Strain-dependent reversible straightening of these domains contributes to FLNA-actin network flexibility and may regulate local binding-partner affinity (Supplementary Fig. 1). Here we examine the effects of mechanical strain on FLNA's interactions with two key rod-2 binding partners; cytoplasmic  $\beta$ -tail integrin, which nucleates an extensively characterized signalling<sup>13</sup> and adhesion<sup>14</sup> complex, and FilGAP, which is a GTPase specific for RAC, a regulator of cellular activity such as actin

assembly<sup>10</sup>. Mechanical strain may regulate partner binding, and we propose that stretching FLNA crosslinks not only causes FilGAP to unbind, but also causes integrin to bind more strongly (Fig. 1c, d and Supplementary Fig. 1). Neighbouring immunoglobulin repeats cover integrin binding sites on FLNA repeats 19 and 21 (refs 15, 16), but computational simulations suggest that rod 2 of FLNA is highly flexible and that physiological forces are sufficient to expose these cryptic sites, allowing integrin to bind<sup>17,18</sup> (Supplementary Fig 1a, b). FilGAP binding occurs on each repeat 23, suggesting that FilGAP is able to bind repeat 23 on both subunits simultaneously when unstressed, providing sufficient avidity to promote FilGAP association with FLNA (Fig. 1c and Supplementary Fig. 1c). Mechanical stretching of FLNA spatially separates repeats 23, preventing FilGAP from binding simultaneously to both<sup>19</sup>, thus causing it to dissociate (Fig. 1d and Supplementary Fig. 1d).

To test these hypotheses and measure the effect of mechanical stress on binding-partner interactions with FLNA, we reconstituted networks of polymerized actin (F-actin) and FLNA containing the binding-partner FilGAP or  $\beta_7$ -integrin. To quantify the strain-dependent

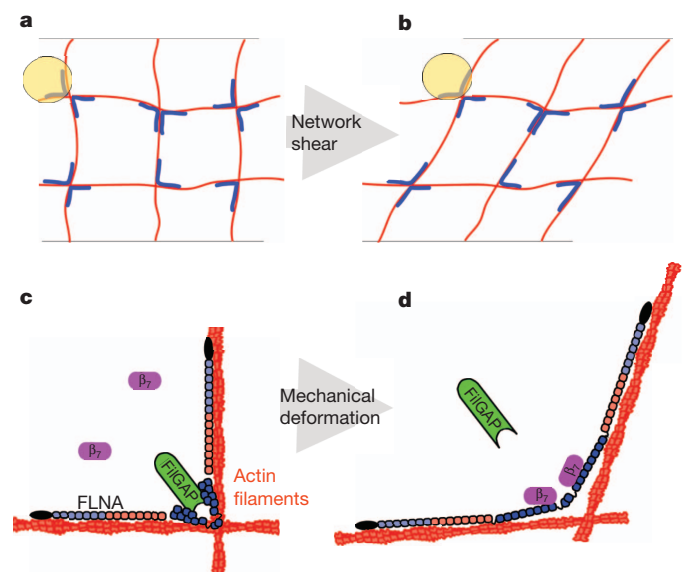


**Figure 1 | Differential mechanotransduction in FLNA occurs through spatial separation of binding sites and opening cryptic sites.** **a**, A gel of actin (red) crosslinked with filamin (blue) forms an orthogonal network. **b**, When this network is strained, crosslinks are deformed. **c**, The actin-binding domain of FLNA is shown in black, and is followed by repeats 1–7 (light blue) and 8–15 (red/orange), which form the linear rod-1 region. Repeats 16–23 (dark blue) form the compact rod-2 region. FilGAP (green) binds repeats 23 and the cytoplasmic domain of  $\beta_7$ -integrin (purple) is unbound. **d**, When FLNA is mechanically deformed, the cryptic integrin site on repeat 21 is exposed allowing  $\beta_7$ -integrin to bind, whereas repeats 23 are spatially separated, preventing FilGAP from binding them both.

<sup>1</sup>Translational Medicine Division, Department of Medicine, Brigham and Women's Hospital, Harvard Medical School, Boston, Massachusetts 02115, USA. <sup>2</sup>School of Engineering and Applied Sciences, Department of Physics, Harvard University, Cambridge, Massachusetts 02138, USA.



kinetics of these partners of FLNA, we developed fluorescence loss after photoconversion (FLAC), which takes advantage of the rapid photoactivation or conversion of photoactivatable fluorescent proteins (PAFPs) as a high-speed analogue to fluorescence recovery after photobleaching<sup>11</sup>. In FLAC, a sample with an initially non-fluorescent binding partner is locally illuminated with a 50-ms pulse of 405-nm light, rapidly and permanently activating PAFP-conjugated partner fluorescence (Supplementary Figs 4 and 5). Photoactivation fluorescently marks the sample faster than conventional photobleaching, and without the requirement of high excitation flux. After activation, unbound PAFP rapidly diffuses away, decreasing the fluorescence signal, whereas bound PAFP dissociates more slowly. The time-dependent decay of PAFP intensity reveals the kinetics of the FLNA binding partner, as slower decay indicates slower unbinding, and thus provides a direct, high-speed assay of dissociation.

We tested the utility of these PAFP constructs in assaying binding kinetics by reconstituting F-actin and the PAFP-labelled binding partner with different forms of FLNA that have higher or lower affinities for  $\beta_7$ -integrin or FilGAP. Consistent with immunoprecipitation data (Supplementary Fig. 3b, c), the fluorescence decay of  $\beta_7$ -integrin labelled with photoactivatable green fluorescent protein (PA-GFP  $\beta_7$ -integrin) was faster in wild-type FLNA networks than in the del41 variant (Supplementary Movie 1), demonstrating relatively stronger binding in the del41 mutant than in wild type. The fluorescence decay of PA-GFP FilGAP was slower in wild-type FLNA networks than in the M2474E mutant (Supplementary Movie 2), also in agreement with immunoprecipitation data (Supplementary Fig. 3a).

We then applied the FLAC methodology to measure the mechanosensitive aspect of interactions between PAFP-labelled binding partners and FLNA. We sheared networks of F-actin and FLNA containing PAFP-tagged FilGAP or  $\beta_7$ -integrin in a precise and highly controlled fashion using a microscope stage comprising a stationary coverslip for the bottom of the sample and a piezo-controlled linear actuator for the top. When the FLNA/F-actin network was not strained,  $\beta_7$ -integrin had a characteristic exponential decay time of  $1.3 \pm 0.1$  s. The application of a shear strain,  $\gamma = 0.28$ , increased this time to  $3.5 \pm 0.3$  s (Fig. 2a). The change in fluorescence decay rate under strain describes how the geometric state of FLNA affects dissociation of  $\beta_7$ -integrin; thus, mechanically stretching FLNA molecules enhanced the  $\beta_7$ -integrin binding. By contrast, FilGAP behaved qualitatively oppositely: unstrained networks had a characteristic fluorescence decay time of  $3.6 \pm 0.7$  s, which decreased to  $0.6 \pm 0.1$  s when a shear strain of  $\gamma = 0.28$  was applied (Fig. 2b). FLNA does not permanently crosslink actin, and by unbinding and rebinding on the timescale of  $\sim 6$  min (Supplementary Fig. 6), it dynamically allows the network to relax to an unstressed state. After 10 min under strain, the network had sufficient time to dissipate

internal stress through FLNA remodelling, and the fluorescence decay time increased to  $6.1 \pm 0.7$  s, demonstrating the reversibility of strain-modulated FilGAP binding to FLNA (Fig. 2b).

The application of unidirectional shear reveals the effects of strain on partner binding to FLNA; however, cells commonly generate internal stresses using molecular motors such as myosin. To examine the effects of cytoskeleton-induced stress, and as a physiological technique complementary to external shear, we included myosin II in the networks to generate contractile stress<sup>20</sup> (Supplementary Fig. 9 and Supplementary Movie 3). We allowed the composite network to assemble and come to an unstressed equilibrium state over  $\sim 6$  h, after which time the incorporated myosin II had ceased contracting, by enzymatically exhausting the pool of added ATP, and dynamic FLNA remodelling had dissipated internal stresses. For unstressed FLNA, we measured  $\beta_7$ -integrin and FilGAP fluorescence decay times of  $1.6 \pm 0.1$  and  $1.5 \pm 0.1$  s, respectively (Fig. 3a, c). Including photo-labile ‘caged’ ATP in the sample allowed us to release fresh ATP and restart myosin motor activity<sup>21,22</sup>, which contracts the actin network and strains FLNA crosslinks. In myosin-stressed FLNA, the integrin unbinding time increased to  $2.5 \pm 0.2$  s but the FilGAP unbinding time decreased to  $0.9 \pm 0.1$  s (Fig. 3b, d). The application of either external shear or myosin contraction resulted in increased integrin binding and decreased FilGAP binding, demonstrating the robust, opposite behaviours of these FLNA binding partners.

The FLNA-crosslinked actin cytoskeleton is a large, percolated network that, owing to its filamentous actin structure, can readily transmit large mechanical deformations over long intracellular distances, yet FLNA is mechanosensitive to nanometre-scale molecular deformations. This range of length scales contrasts with that of focal adhesion mechanosensitivity, which detects local mechanics and is limited to small spatial and strain scales owing to their size and connectivity<sup>23,24</sup>.

In conclusion, we have developed *in vitro* systems to study quantitatively protein–protein interactions under mechanical force. Using PAFPs with the FLAC technique provides the increases in time resolution necessary for measuring transient kinetics, without the harsh intensity or duration of bleaching exposure required for fluorescence recovery after photobleaching. The results presented here establish FLNA as a mechanotransductive substrate within the cytoskeleton and highlight the utility of *in vitro* systems, in combination with FLAC, to determine quantitative responses of specific proteins.

Mechanotransduction *in vitro* provides the biological specificity necessary for understanding how these complex regulatory signals may operate *in vivo*. Cellular mechanotransduction has been shown to induce rapid biochemical activity over long distances<sup>25</sup>. Because mechanical stimuli induce relatively large local deformations that decrease in magnitude with distance from the site of application,

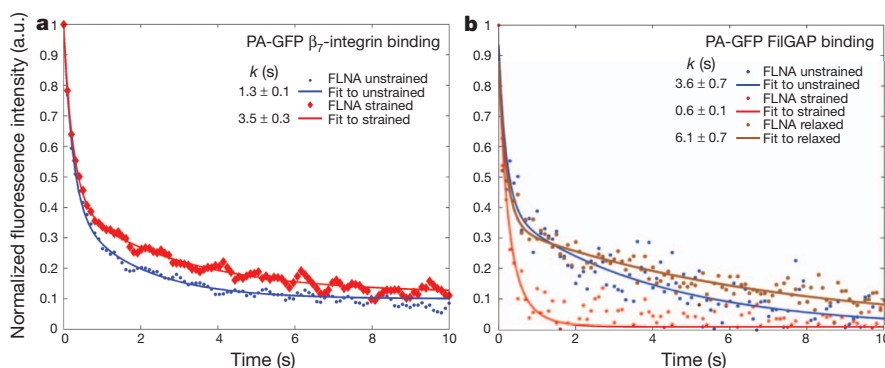


**Figure 2 | External bulk shear of F-actin/FLNA networks alters FLNA's binding affinity for  $\beta_7$ -integrin and FilGAP.** **a**, Fluorescence intensity of PA-GFP  $\beta_7$ -integrin as a function of time after photoactivation. When unstrained (blue), fluorescence of  $\beta_7$ -integrin decays with a characteristic time constant of  $k = 1.3$  s. Following the application of a shear strain of  $\gamma = 0.28$ , the time constant increases to 3.5 s, as the integrin dissociates more slowly from FLNA

( $n = 18$ ). a.u., arbitrary units. **b**, Fluorescence intensity of PA-GFP FilGAP as a function of time after photoactivation. Unstrained (blue) FilGAP's fluorescence decay time is  $k = 3.6$  s. A shear strain of  $\gamma = 0.28$  (red) decreased  $k$  to 0.6 s. This behaviour is reversible, and after allowing the network to relax for 10 min, removing all strain,  $k$  increases to 6.1 s (brown) ( $n = 10$ ).

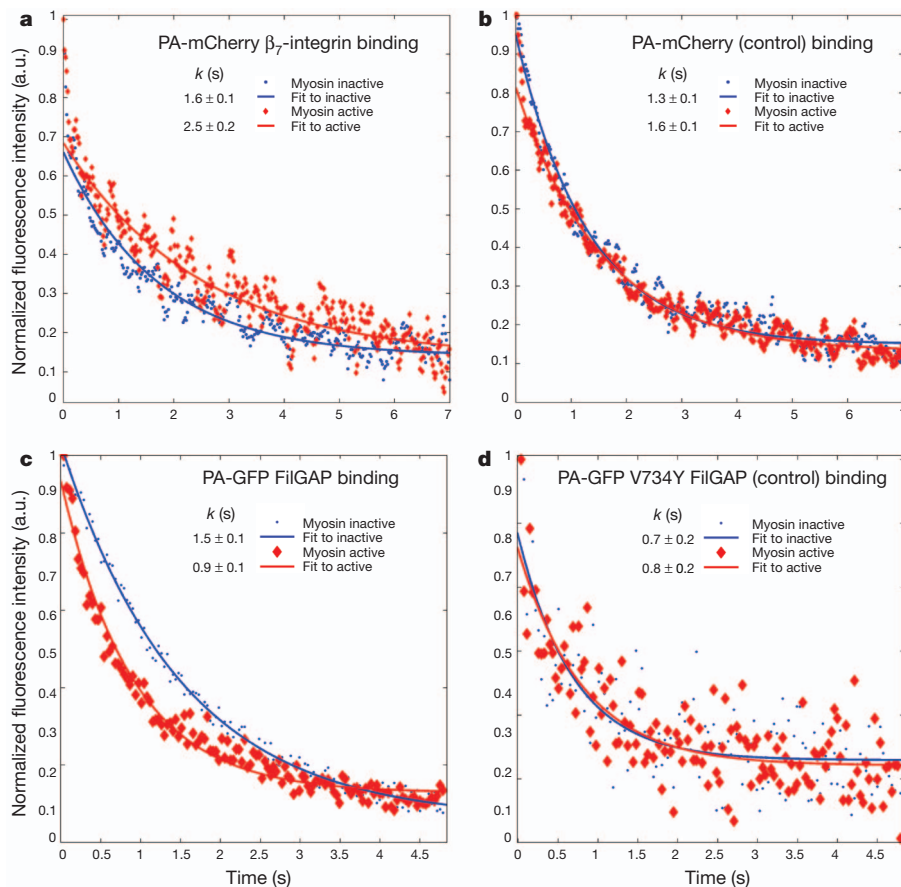


**Figure 3 | Myosin II forces applied to F-actin/FLNA networks change FLNA's binding affinity to  $\beta_7$ -integrin and FilGAP.** **a**, When depleted of ATP, myosin is in a rigor state. The FLNA within the network is not stressed and PA-GFP  $\beta_7$ -integrin fluorescence decays with a characteristic time constant of  $k = 1.6$  s (blue). After caged ATP is released, myosin reactivates, straining FLNA crosslinks. The decay time constant increases to 2.5 s because the integrin dissociates more slowly from FLNA under stress. **b**, PA-mCherry

FLNA mechanotransduction *in vivo* probably provides a rapid, distance-sensitive biphasic response by binding or unbinding integrins or FilGAP, respectively, as a result of the transmitted strain. Physiologically, the localization and binding of these proteins determine their activity. Strain-induced binding of integrin to FLNA may compete with talin binding to integrin<sup>26</sup>, thus providing a mechanosensitive switch for integrin activation and adhesion. FLNA's homodimer structure may induce clustering of integrin, thereby reinforcing adhesion and concentrating signalling molecules at a specific location. FilGAP, when unbound from FLNA, relocates to the plasma membrane, where it inactivates RAC<sup>10</sup>. Active RAC levels profoundly affect cell movement<sup>27</sup>, and increased RAC activity in FLNA-deficient cells correlates with increased apoptosis<sup>28</sup>. Moreover, our measurements are consistent with *in vivo* studies demonstrating that RAC activity and expression seem to be force-regulated by FilGAP–FLNA interactions, because inhibiting FLNA or FilGAP increases RAC activity but applying local forces to wild-type cells causes FilGAP to decrease RAC activity<sup>28</sup>. Because FLNA does not change FilGAP's catalytic activity, mechanically induced redistribution alone might explain its regulation *in vivo*. Force-dependent conformational changes in structure required for mechanical regulation have been observed in many proteins, including FLNA *in vivo*<sup>29,30</sup>. By identifying FLNA as a mechanosensitive element within the cytoskeleton, we have clarified how RAC and integrin activity may be regulated by a specific molecular mechanotransduction pathway. Identifying mechanotransduction elements may direct novel, targeted therapeutic approaches by correcting or modulating mechanosensitive binding.

alone as a control shows no significant difference between the unstrained and strained states. **c**, Fluorescence intensity of PA-GFP FilGAP as a function of time after photoactivation. **d**, In the ATP-depleted state, FilGAP's fluorescence decay time is  $k = 1.5$  s, and after release of the caged ATP (red),  $k$  decreases to 0.9 s. In PA-GFP V734Y FilGAP, a non-FLNA binding mutant used as a control, the decay time in the unstrained state (0.7 s) is not significantly different from that in the strained state (0.8 s) ( $n = 20$ ).

## METHODS SUMMARY

**PAFP fluorophore synthesis.** PAFP fluorophore was genetically tagged to binding partners, creating PAFP-labelled  $\beta_7$ -integrin and FilGAP. Solubility and correct binding of labelled partners was confirmed using western blots (Supplementary Fig. 3).

**FLAC methodology.** An external 405-nm laser was coupled into a Leica SP5 confocal microscope and used to illuminate a central,  $\sim 2\text{-}\mu\text{m}$  spot for 50 ms, converting the PAFP from its dark state to its fluorescent state (Supplementary Figs 4 and 5). The decay in the fluorescence intensity,  $I(t)$ , of the activated fluorophores was monitored and fitted with the exponential  $I(t) = ae^{-t/k} + c$ , where  $k$  is the time constant of characteristic dissociation. Given  $k$  values represent best fits plus 95% confidence intervals. In the case of single-step uniaxial strain presented in Fig. 2, data were fitted to  $I(t) = ae^{-t/k} + 0.5e^{-t/(0.15s)} + c$  to provide a more accurate fit and compensate for the rapid diffusion of free fluorophore.

**Sample cell composition.** Shear cell samples consisted of 24  $\mu\text{M}$  actin, 0.12  $\mu\text{M}$  FLNA,  $\times 1$  F-actin polymerization buffer (Methods), 2  $\mu\text{M}$  Alexa 546 phalloidin and either PA-GFP FilGAP or PA-GFP  $\beta_7$ -integrin, and were sheared in a piezo-driven shear cell (Supplementary Information). Sheared FLAC measurements for strained networks were acquired approximately 5–10 s after shear. Myosin samples included 24  $\mu\text{M}$  actin, 0.12  $\mu\text{M}$  FLNA, 1  $\mu\text{M}$  myosin II,  $\times 1$  activity buffer (Methods) and 2  $\mu\text{M}$  caged ATP, along with 2  $\mu\text{M}$  Alexa 546 phalloidin and PA-GFP FilGAP or 2  $\mu\text{M}$  Alexa 488 phalloidin and PA-mCherry  $\beta_7$ -integrin. Samples were allowed to polymerize and consume available ATP over  $\sim 6$  h. FLAC measurements were then performed on the ATP-free unstrained network. Subsequently, the caged ATP (Sigma) was released by a 4-s exposure to a diffuse 50-mW, 365-nm light-emitting diode (Prizmatix), and within 3 s the network could be seen to homogenize under myosin contraction (Supplementary Fig. 9 and Supplementary Movie 3). FLAC measurements were then repeated in this active myosin-stressed network to quantify the strain-dependent binding activity.

**Full Methods** and any associated references are available in the online version of the paper at [www.nature.com/nature](http://www.nature.com/nature).

**Received 12 April; accepted 5 August 2011.**

**Published online 18 September 2011.**

1. Ingber, D. E. Mechanobiology and diseases of mechanotransduction. *Ann. Med.* **35**, 564–577 (2003).
2. Discher, D. E., Janmey, P. & Wang, Y. L. Tissue cells feel and respond to the stiffness of their substrate. *Science* **310**, 1139–1143 (2005).
3. Moore, S. W., Roca-Cusachs, P. & Sheetz, M. P. Stretchy proteins on stretchy substrates: the important elements of integrin-mediated rigidity sensing. *Dev. Cell* **19**, 194–206 (2010).
4. Hoffman, B. D. *et al.* Dynamic molecular processes mediate cellular mechanotransduction. *Nature* **475**, 316–323 (2011).
5. Krüger, M. & Linke, W. A. Titin-based mechanical signalling in normal and failing myocardium. *J. Mol. Cell. Cardiol.* **46**, 490–498 (2009).
6. Birukov, K. G. Small GTPases in mechanosensitive regulation of endothelial barrier. *Microvasc. Res.* **77**, 46–52 (2009).
7. Wang, N., Tytell, J. D. & Ingber, D. E. Mechanotransduction at a distance: mechanically coupling the extracellular matrix with the nucleus. *Nature Rev. Mol. Cell Biol.* **10**, 75–82 (2009).
8. Stossel, T. P. *et al.* Filamins as integrators of cell mechanics and signalling. *Nature Rev. Mol. Cell Biol.* **2**, 138–145 (2001).
9. Nakamura, F., Stossel, T. P. & Hartwig, J. H. The filamins: organizers of cell structure and function. *Cell Adh. Migr.* **5**, 160–169 (2011).
10. Ohta, Y., Hartwig, J. H. & Stossel, T. P. FilGAP, a Rho- and ROCK-regulated GAP for Rac binds filamin A to control actin remodelling. *Nature Cell Biol.* **8**, 803–814 (2006).
11. Sprague, B. L., Pego, R. L., Stavreva, D. A. & McNally, J. G. Analysis of binding reactions by fluorescence recovery after photobleaching. *Biophys. J.* **86**, 3473–3495 (2004).
12. Nakamura, F., Osborn, T. M., Hartemink, C. A., Hartwig, J. H. & Stossel, T. P. Structural basis of filamin A functions. *J. Cell Biol.* **179**, 1011–1025 (2007).
13. Wang, N., Butler, J. P. & Ingber, D. E. Mechanotransduction across the cell surface and through the cytoskeleton. *Science* **260**, 1124–1127 (1993).
14. Calderwood, D. A. *et al.* Increased filamin binding to  $\beta$ -integrin cytoplasmic domains inhibits cell migration. *Nature Cell Biol.* **3**, 1060–1068 (2001).
15. Lad, Y. *et al.* Structure of three tandem filamin domains reveals auto-inhibition of ligand binding. *EMBO J.* **26**, 3993–4004 (2007).
16. Heikkinen, O. K. *et al.* Atomic structures of two novel immunoglobulin-like domain pairs in the actin cross-linking protein filamin. *J. Biol. Chem.* **284**, 25450–25458 (2009).
17. Penttinen, U. & Ylanne, J. The regulation mechanism for the auto-inhibition of binding of human filamin A to integrin. *J. Mol. Biol.* **393**, 644–657 (2009).
18. Chen, H. S., Kolahi, K. S. & Mofrad, M. R. Phosphorylation facilitates the integrin binding of filamin under force. *Biophys. J.* **97**, 3095–3104 (2009).
19. Nakamura, F. *et al.* Molecular basis of filamin A-FilGAP interaction and its impairment in congenital disorders associated with filamin A mutations. *PLoS ONE* **4**, e4928 (2009).
20. Koenderink, G. H. *et al.* An active biopolymer network controlled by molecular motors. *Proc. Natl Acad. Sci. USA* **106**, 15192–15197 (2009).
21. Humphrey, D., Duggan, C., Saha, D., Smith, D. & Kas, J. Active fluidization of polymer networks through molecular motors. *Nature* **416**, 413–416 (2002).
22. Smith, D. M. *et al.* Molecular motor-induced instabilities and crosslinkers determine biopolymer organization. *Biophys. J.* **93**, 4445–4452 (2007).
23. Kanchanawong, P. *et al.* Nanoscale architecture of integrin-based cell adhesions. *Nature* **468**, 580–584 (2010).
24. Grashoff, C. *et al.* Measuring mechanical tension across vinculin reveals regulation of focal adhesion dynamics. *Nature* **466**, 263–266 (2010).
25. Na, S. *et al.* Rapid signal transduction in living cells is a unique feature of mechanotransduction. *Proc. Natl Acad. Sci. USA* **105**, 6626–6631 (2008).
26. Kiema, T. *et al.* The molecular basis of filamin binding to integrins and competition with talin. *Mol. Cell* **21**, 337–347 (2006).
27. Sanz-Moreno, V. *et al.* Rac activation and inactivation control plasticity of tumor cell movement. *Cell* **135**, 510–523 (2008).
28. Shifrin, Y., Arora, P. D., Ohta, Y., Calderwood, D. A. & McCulloch, C. A. The role of FilGAP-filamin A interactions in mechanoprotection. *Mol. Biol. Cell* **20**, 1269–1279 (2009).
29. Johnson, C. P., Tang, H. Y., Carag, C., Speicher, D. W. & Discher, D. E. Forced unfolding of proteins within cells. *Science* **317**, 663–666 (2007).
30. Krieger, C. C. *et al.* Cysteine shotgun-mass spectrometry (CS-MS) reveals dynamic sequence of protein structure changes within mutant and stressed cells. *Proc. Natl Acad. Sci. USA* **108**, 8269–8274 (2011).

**Supplementary Information** is linked to the online version of the paper at [www.nature.com/nature](http://www.nature.com/nature).

**Acknowledgements** The authors acknowledge the Harvard Materials Research and Engineering Center (DMR-0820484) for confocal imaging, and M. Ginsberg, J. Lippincott-Schwartz and V. Verkhusha for providing complementary DNA for PA-GFP and PA-mCherry constructs. We thank T. Collins for technical assistance, L. Jawerth and V. Zaburdaev for discussions, and J. Wilking and K. Guenther for help with the manuscript. This work was supported by grants NIH R01 HL19429 (T.P.S.) and NIH T32 HL07680 (A.J.E.) and by the Harvard University Science and Engineering Committee Seed Fund for Interdisciplinary Science (D.A.W., T.P.S., F.N.).

**Author Contributions** The project was initiated by T.P.S., F.N. and D.A.W. Experiments were designed by A.J.E., T.P.S., J.H.H. and F.N. Proteins and materials were synthesized and purified by F.N. and A.J.E. FLAC experiments were performed by A.J.E. and binding assays were performed by F.N. Data was analysed by A.J.E. All authors discussed data and aided in preparing the manuscript. A.J.E. and F.N. contributed equally to this project.

**Author Information** Reprints and permissions information is available at [www.nature.com/reprints](http://www.nature.com/reprints). The authors declare no competing financial interests. Readers are welcome to comment on the online version of this article at [www.nature.com/nature](http://www.nature.com/nature). Correspondence and requests for materials should be addressed to F.N. (fnakamura@rics.bwh.harvard.edu) or A.J.E. (aje@seas.harvard.edu).



## METHODS

**Protein design and synthesis.** Actin was purified from rabbit skeletal muscle and gel-filtered (HiLoad 16/60 Superdex 200pg; GE Healthcare) in G buffer<sup>12</sup> (2 mM Tris-HCl, 0.2 mM ATP, 0.2 mM CaCl<sub>2</sub>, 0.2 mM DTT and 0.005% NaN<sub>3</sub>, pH 8.0). Aliquots of purified G-actin were frozen in liquid nitrogen and stored at  $-80^{\circ}\text{C}$ . Before use, G-actin was thawed 12 h in advance and dialyzed against fresh G buffer. Myosin II from rabbit skeletal muscle was obtained from Cytoskeleton (Denver). Human full-length FLNA and FilGAP were expressed using a baculovirus expression system (Invitrogen) in sf9 insect cells and purified as previously described<sup>19</sup>. All the point or deletion mutants were generated using the QuickChange site-directed mutagenesis kit (Agilent Technologies). FilGAP and integrin constructs were expressed in sf9 cells as follows. The complementary DNA (cDNA) encoding PAFPs (PA-GFP and PA-mCherry, which were kind gifts from Jennifer Lippincott-Schwartz, NIH) were amplified by PCR using the forward primer GAAGATCTATGGTGAAGCAAGGGCGAGG and the reverse primer CGGGATCCCTGTACAGCTCGTCCATG, and introduced into BamHI sites of pFASTBAC-HTb vector<sup>12</sup> to construct pFASTBAC-HTb-PAFPs. The cDNA encoding the cytoplasmic domain (amino acids 769–789) of human  $\beta_7$ -integrin was amplified by PCR using pET15-G4-integrin  $\beta_7$  (a kind gift from Mark Ginsberg, UC San Diego) as a template with the forward primer GCGGATCCAACTGGAAGCAGGACAGTAATC and the reverse primer CGGAATTCAGCGAGGATTGATGGTGG, and inserted into BamHI/EcoRI sites of pFASTBAC-HTb-PAFPs. For FilGAP, the cDNA encoding PAFPs was introduced into pFASTBAC-HTa-FilGAP at the XbaI cleavage site<sup>19</sup>. The expressed proteins were purified by Ni-NTA affinity and gel filtration chromatography (Superose 12 and Superdex 200, GE Healthcare) as previously described<sup>19</sup>. Protein concentration was measured by absorption at 280 nm using parameters calculated with ProtParam (<http://au.expasy.org/tools/protparam.html>). Genetic fusion of PAFPs to the binding partners<sup>31</sup> did not affect the binding-partner activity. Purified PAFP FilGAP proteins interact with full-length FLNA in the same dose-dependent manner as unlabelled FilGAP, and do not bind to the FLNA M2474E mutant, which lacks the FilGAP-binding site (Supplementary Fig. 2a). The PAFP-tagged cytoplasmic tail of  $\beta_7$ -integrin was also found to retain its binding behaviour with FLNA, and predominantly interacts with the FLNA del41 variant, where the autoinhibitory ligand-binding site is constitutively exposed<sup>15,32</sup> (Supplementary Fig. 2b, c).

**Protein pull-down assay.** The purified His-FilGAP and His-PAFP FilGAP constructs were incubated with increasing amounts of FLAG-FLNA and 20  $\mu\text{l}$  of FLAG-specific mAb M2 agarose (50% (v/v) slurry, Sigma) in binding buffer (50 mM Tris-HCl, 150 mM NaCl, 0.1% (w/v) Triton X-100, 0.1 mM  $\beta$ -mercaptoethanol, 0.1 mM EGTA, pH 7.4; 400  $\mu\text{l}$ ) for 1 h at  $25^{\circ}\text{C}$ . The beads were sedimented and washed three times with binding buffer. Proteins bound to the beads were solubilized in SDS sample buffer and separated by 9.0% (w/v) SDS-PAGE followed by immunoblotting using rabbit polyclonal antibodies (pAbs) against FilGAP<sup>10</sup>. For integrin, the purified His-PAFP  $\beta_7$ -integrin (amino acids 769–789) was incubated with increasing amounts of wild-type and mutant (del41; amino-acid residues 2126–2167 are deleted) FLAG-FLNA and 40  $\mu\text{l}$  of FLAG-specific mAb M2 agarose (50% (v/v) slurry, Sigma) in binding buffer (25 mM Tris-HCl, 50 mM NaCl, 0.1% (w/v) Tween 20, 1 mM DTT, 10% sucrose, 5 mM MgCl<sub>2</sub>, 1 mM EGTA, pH 7.4; 400  $\mu\text{l}$ ) for 2 h at  $25^{\circ}\text{C}$ . The beads were sedimented and washed three times with the binding buffer. Proteins bound to the beads were solubilized in SDS sample buffer and separated by 10.0% (w/v) SDS-PAGE followed by immunoblotting using mouse mAb against His conjugated with horseradish peroxidase (Sigma). For the peptide pull-down assay, a synthetic peptide of the  $\beta_7$ -integrin cytoplasmic domain (Cys-<sup>771</sup>KQDSNPLYKSAITTTINPR<sup>789</sup>) was immobilized on Sulfo-Link agarose beads (1 mg ml<sup>-1</sup>) and mixed with increasing amounts of wild-type and mutant (del41, AA/DK, A2272D/A2274K) FLNA. Bound FLNA was detected by immunoblotting using mouse mAb to FLNA.

**Reconstitution of actin-FLNA networks.** Activity buffer<sup>10</sup> (AB; 25 mM imidazole, 150 mM KCl, 5 mM MgATP, 0.2 mM CaCl<sub>2</sub>, and 1 mM DTT, pH 7.4) and F-actin polymerization buffer<sup>33</sup> (FB; 20 mM Tris-HCl, 2 mM MgCl<sub>2</sub>, 100 mM KCl, 0.2 mM DTT, 0.2 mM CaCl<sub>2</sub>, 0.5 mM ATP, pH 7.5) were formulated as established previously. Shear cell samples consisted of 24  $\mu\text{M}$  actin, 0.12  $\mu\text{M}$  FLNA,  $\times 1$  FB, 2  $\mu\text{M}$  Alexa 546 phalloidin and either PA-GFP FilGAP or PA-GFP  $\beta_7$ -integrin. **Shear-cell design and measurements.** A P-780 (Physik Instrumente) piezo-motor, incorporated into a home-built microscope stage, was controlled using LABVIEW software (National Instruments). The sample component of the microscope stage had as its lower plate a stationary glass coverslip within a stainless steel frame and had a glass upper plate connected by a steel post to the piezo-motor. The gap between the lower and upper plates was 300  $\mu\text{m}$ . A lateral shear was applied as illustrated in Supplementary Fig. 8. Strain is defined as the change of length divided by the original length. Thus, a 300- $\mu\text{m}$  vertical distance that is deformed to 312  $\mu\text{m}$  when sheared laterally by 85  $\mu\text{m}$  is under an engineering strain of 1.04,

or 4%. The parameter  $\gamma$  is defined by the lateral shear divided by the sample thickness, yielding 85/300, or 0.28. Using a MATLAB-based Monte Carlo simulation of affine deformation, we calculated that a uniaxial shear strain of 0.28 causes the angle of an isotropic distribution of FLNA crosslinks initially at  $90^{\circ}$  to increase and decrease their opening angles symmetrically about  $90^{\circ}$  (on respective sides of the initially perpendicular intersection; Supplementary Fig. 8). Looking at the positive half of the distribution suggests that the weighted mean increase in opening angle is  $\sim 6.1^{\circ}$ , with a peak of  $\sim 7.6^{\circ}$ .

**Myosin II system.** To examine the effects of cytoskeleton-induced stress, and as a physiological technique complementary to external shear, we included 1  $\mu\text{M}$  myosin II in the networks to generate contractile stress as illustrated in Supplementary Fig. 9 and Supplementary Movie 3. Individual myosin II molecules bind their tail regions together to form minifilaments, bipolar assemblies of 8–13 myosin molecules<sup>21</sup>. These minifilaments allow the otherwise non-processive myosin II to operate collectively with an increased duty cycle, binding the minifilaments to actin filaments long enough for filament sliding and network contraction to occur. At 150 mM KCl, approximately 8–13 myosin molecules associate into each minifilament<sup>21</sup>. The number of myosin minifilaments per actin filament,  $N_{\text{mf/fil}}$ , may be calculated from  $N_{\text{mf/fil}} = [m]n_{\text{fil}}/[a]n_{\text{mf}}$  where  $[m]$  is the molar concentration of myosin,  $n_{\text{fil}}$  is the number of actin monomers per actin filament,  $[a]$  is the molar concentration of actin and  $n_{\text{mf}}$  is the number of myosin molecules per minifilament<sup>22</sup>. On the basis of an average actin filament length of  $\sim 5 \mu\text{m}$  and there being 13 myosin molecules per minifilament, we estimate that approximately six minifilaments bind per actin filament. Repeating this estimation with FLNA instead of myosin, we estimate that there are five FLNA crosslinks per actin filament, on the basis of each crosslink being composed of two FLNA molecules. Thus, the density of myosin minifilaments per actin filament is approximately equal to that of FLNA crosslinks.

Samples were composed of 24  $\mu\text{M}$  actin, 0.12  $\mu\text{M}$  FLNA, 1  $\mu\text{M}$  myosin II,  $\times 1$  AB and 2 mM caged ATP, along with 2  $\mu\text{M}$  Alexa 546 phalloidin and 50 nM PA-GFP FilGAP or 2  $\mu\text{M}$  Alexa 488 phalloidin and 50 nM PA-mCherry  $\beta_7$ -integrin.

Each sample was allowed to polymerize and consume available ATP over  $\sim 6$  h, at which point myosin minifilaments had ceased contracting and were in a rigor state. FLAC measurements were then performed on the ATP-free unstressed network. Subsequently, the caged ATP (Sigma) was released by a 4-s exposure to a diffuse, 50-mW, 365-nm light-emitting diode (Prizmatix). Within 3 s, the network could be seen to become active, and it substantially homogenized in approximately 5 min. FLAC measurements were repeated in the active myosin-stressed network 10–20 min after ATP release, to quantify the strain-dependent binding activity.

**Imaging and analysis.** Fluorescence recovery after photobleaching (FRAP) provides an effective method to measure the diffusion and binding interactions of fluorescent proteins<sup>11</sup>; however, the time resolution of FRAP is not adequate for fast transient events. To overcome this time limitation, we have developed FLAC, which takes advantage of the rapid photoactivation or conversion of novel PAFPs<sup>31</sup> (Supplementary Figs 4 and 5). In FLAC, an initially non-fluorescent sample is locally pulsed with 405-nm light, activating PAFP fluorescence, and the time-dependent decay of the PAFP intensity reveals its diffusion and binding kinetics. An additional advantage is that FLAC may present more accurate binding/diffusion information than FRAP, as adequate photobleaching requires harsh conditions<sup>34</sup>.

Time-dependent fluorescence images were acquired with a confocal microscope (TCS SP5, Leica) using a  $\times 10$ , 0.3 NA objective with images captured every 30–100 ms. PAFPs were activated using a 50-ms,  $\sim 5$ -mW shuttered pulse from an external, 405-nm laser (Bestofferbuy) coupled into the confocal microscope using its non-descanned X1 port. A custom-built filter cube was installed with the filter holder rotated azimuthally by  $90^{\circ}$  to allow the 405-nm laser light entering the X1 port to be reflected upwards to the objective through a long-pass dichroic filter (Di01-R405-25x36, Semrock) and illuminate a 2- $\mu\text{m}$  spot in the centre of the sample  $x$ - $y$  plane.

Fluorescence in the photoactivation region was monitored in time and constitutes the principal data for the experiments. Data was collected before, during and after photoactivation and analysed in MATLAB. Fluorescence before activation represents the background signal, and was mainly a mixture of detection noise and background fluorescence. The background was defined as zero and subtracted from the data for each measurement. Data collected after activation was normalized to its maximum value, which was reached  $\sim 10$  ms after photoactivation. Thus, fluorescence intensity data sets range from 1 at time zero after normalization and approach zero (background) at long times. Although a wide variety of fitting algorithms and procedures exist for FRAP, which in its analysis is mathematically similar to FLAC, we use a single exponential decay,  $I(t) = ae^{-t/k} + c$ , to fit our data. These fits are accurate, allow us to differentiate data quantitatively as simply as possible with a single time constant,  $k$  (the characteristic fluorescence decay time),

and do not invoke a variety of free parameters or models with a-priori assumptions<sup>11</sup>. In each case, the fluorescence intensity decay is quantified and numerically compared using the same individual sample with and without strain to ensure consistency, eliminate artefacts or variability, and isolate mechanical strain as the single variable. In the case of single-step uniaxial strain presented in Fig. 2, data were fitted to  $I(t) = ae^{-t/k} + 0.5e^{-t/(0.15s)} + c$  to provide a more accurate fit and compensate for the rapid diffusion of free fluorophore.

Photobleaching decays times were measured by photoactivating PAFP nonspecifically adsorbed to the glass surface, and were found to be in excess of 800 s, making them negligible on the timescale of FLAC experiments (<10 s), as shown in Supplementary Fig. 7. Photoconversion times were determined by acquiring

fluorescence intensity images of PAFP adsorbed to glass every 3 ms during a 50-ms, 405-nm activation flash, as shown in Supplementary Fig. 4.

31. Fernández-Suárez, M. & Ting, A. Y. Fluorescent probes for super-resolution imaging in living cells. *Nature Rev. Mol. Cell Biol.* **9**, 929–943 (2008).
32. van der Flier, A. *et al.* Different splice variants of filamin-B affect myogenesis, subcellular distribution, and determine binding to integrin  $\beta$  subunits. *J. Cell Biol.* **156**, 361–376 (2002).
33. Nakamura, F., Osborn, E., Janmey, P. A. & Stossel, T. P. Comparison of filamin A-induced cross-linking and Arp2/3 complex-mediated branching on the mechanics of actin filaments. *J. Biol. Chem.* **277**, 9148–9154 (2002).
34. Weissmann, C. *et al.* Microtubule binding and trapping at the tip of neurites regulate tau motion in living neurons. *Traffic* **10**, 1655–1668 (2009).

# Peripheral education of the immune system by colonic commensal microbiota

Stephanie K. Lathrop<sup>1†</sup>, Seth M. Bloom<sup>2</sup>, Sindhuja M. Rao<sup>1</sup>, Katherine Nutsch<sup>1</sup>, Chan-Wang Lio<sup>1</sup>, Nicole Santacruz<sup>1</sup>, Daniel A. Peterson<sup>3†</sup>, Thaddeus S. Stappenbeck<sup>2</sup> & Chyi-Song Hsieh<sup>1</sup>

**The instruction of the immune system to be tolerant of self, thereby preventing autoimmunity, is facilitated by the education of T cells in a specialized organ, the thymus, in which self-reactive cells are either eliminated or differentiated into tolerogenic Foxp3<sup>+</sup> regulatory T (T<sub>reg</sub>) cells<sup>1</sup>. However, it is unknown whether T cells are also educated to be tolerant of foreign antigens, such as those from commensal bacteria, to prevent immunopathology such as inflammatory bowel disease<sup>2–4</sup>. Here we show that encounter with commensal microbiota results in the peripheral generation of T<sub>reg</sub> cells rather than pathogenic effectors. We observed that colonic T<sub>reg</sub> cells used T-cell antigen receptors (TCRs) different from those used by T<sub>reg</sub> cells in other locations, implying an important role for local antigens in shaping the colonic T<sub>reg</sub>-cell population. Many of the local antigens seemed to be derived from commensal bacteria, on the basis of the *in vitro* reactivity of common colon T<sub>reg</sub> TCRs. These TCRs did not facilitate thymic T<sub>reg</sub>-cell development, implying that many colonic T<sub>reg</sub> cells arise instead by means of antigen-driven peripheral T<sub>reg</sub>-cell development. Further analysis of two of these TCRs by the creation of retroviral bone marrow chimaeras and a TCR transgenic line revealed that microbiota indigenous to our mouse colony was required for the generation of colonic T<sub>reg</sub> cells from otherwise naive T cells. If T cells expressing these TCRs fail to undergo T<sub>reg</sub>-cell development and instead become effector cells, they have the potential to induce colitis, as evidenced by adoptive transfer studies. These results suggest that the efficient peripheral generation of antigen-specific populations of T<sub>reg</sub> cells in response to an individual's microbiota provides important post-thymic education of the immune system to foreign antigens, thereby providing tolerance to commensal microbiota.**

Although T<sub>reg</sub> cells are required for the maintenance of gut tolerance<sup>3</sup>, commensal bacteria are not necessary for colonic T<sub>reg</sub>-cell generation<sup>5,6</sup> (Supplementary Fig. 1). Moreover, T<sub>reg</sub> cells from germ-free mice can protect against colitis<sup>7</sup>. In contrast, extrathymic generation of T<sub>reg</sub> cells that respond to foreign antigens has been demonstrated with TCR transgenic models of oral tolerance<sup>8,9</sup>. Peripheral T<sub>reg</sub>-cell development is also increased in the gut<sup>9,10</sup>, a response that is potentially related to the presence of specialized antigen-presenting cells<sup>9,11–13</sup>. Finally, species in the *Clostridium* genus<sup>14</sup>, and *Bacteroides fragilis*<sup>6</sup> by means of a protease-resistant capsular polysaccharide, can increase the frequency or function of colonic T<sub>reg</sub> cells, but may do so through innate immune receptors<sup>15</sup>. Thus, it remains unclear whether the protective colonic T<sub>reg</sub>-cell population is generated against self antigens or foreign antigens derived from the commensal bacteria found in each individual.

Although TCR transgenic lines that respond to antigens derived from commensal bacteria have been described<sup>16</sup>, the normal *in vivo* frequency of those TCRs in the T<sub>reg</sub>-cell subset as compared with the effector T-cell subsets is unknown. To study the TCRs normally found in

the colonic T<sub>reg</sub>-cell population, we analysed the colonic TCR repertoire. As a result of the great diversity of the fully polyclonal TCR repertoire, we and others have used genetically engineered mice with limited polyclonal repertoires<sup>17–19</sup>. The analysis of TCR  $\alpha$ -chain repertoires of CD4<sup>+</sup> T cells from the colonic lamina propria of mice expressing a fixed transgenic TCR  $\beta$  chain revealed that Foxp3<sup>+</sup> T<sub>reg</sub> cells use TCRs that are quite distinct from those of effector/memory (CD44<sup>hi</sup>) and naive (CD44<sup>lo</sup>) Foxp3<sup>–</sup> cells (Fig. 1a, b and Supplementary Figs 2 and 3). This is illustrated by using the Morisita–Horn similarity index (Fig. 1a), in which values from 0 to 1 represent low to high similarity between two data sets, and also by the analysis of the relative frequencies of individual common TCRs in each T-cell subset (Fig. 1b). Moreover, the analysis of TCR  $\alpha$  chains of cells pooled from the secondary lymphoid organs and colons of additional mice showed that T<sub>reg</sub> TCR usage in the colon differed greatly from that in the other organs (Fig. 1c, d and Supplementary Fig. 3). Like the T<sub>reg</sub>-cell population, the effector/memory T-cell population expressed TCRs largely unique to the colon; however, these two subsets showed very little overlap. Thus, consistent with our previous observations in other peripheral locations<sup>20</sup>, these TCR repertoire data suggest that the colonic T<sub>reg</sub>-cell population is strongly shaped by the local antigenic milieu.

To assess whether the local antigens were bacterial in origin, we expressed colon T<sub>reg</sub> TCRs (Supplementary Fig. 3) in a hybridoma cell line that contains a green fluorescent protein (GFP) reporter for nuclear factor of activated T cells (NFAT) activation as a readout for TCR engagement<sup>21</sup>. We initially screened these hybridomas against autoclaved colonic contents and were surprised to find that many (five of eight) showed some degree of reactivity to preparations from conventionally housed, but not germ-free, mice (Fig. 2a, Table 1 and Supplementary Fig. 4a, b). Colonic contents from Jackson Laboratories-sourced (Jax) *Rag1*<sup>–/–</sup> mice were not recognized by four of these colonic T<sub>reg</sub> TCRs unless they were first housed together with mice from our colony. In contrast to the colonic T<sub>reg</sub> TCRs, none of the eight abundant colonic activated/memory (CD44<sup>hi</sup>) TCRs (Supplementary Fig. 5), or of four other TCRs tested (including B8 and TR5 (ref. 20)) showed any reactivity (not shown). In addition, TCR recognition did not occur in the absence of dendritic cells and was blocked by antibodies against MHC class II (not shown). Thus, these data suggest that the antigens responsible for TCR activation are derived from microbes that can be passed between mice that are housed together.

We therefore attempted to identify bacteria recognized by these colonic T<sub>reg</sub> TCRs by screening small pools of two or three heat-killed bacteria isolated in pure culture from the colonic contents of mice in our colony (Fig. 2b and Supplementary Figs 4c and 6). Two colonic T<sub>reg</sub> TCRs (CT6 and CT7) reacted to one or more pools. Testing of individual isolates from these pools revealed that CT6 reacted with isolate ACNA18.1, identified by 16S ribosomal RNA gene sequencing as a previously uncharacterized *Clostridiales* species. All three isolates

<sup>1</sup>Department of Medicine, Division of Rheumatology, Washington University School of Medicine, St Louis, Missouri 63110, USA. <sup>2</sup>Department of Pathology and Immunology, Washington University School of Medicine, St Louis, Missouri 63110, USA. <sup>3</sup>Department of Food Science and Technology, University of Nebraska-Lincoln, Lincoln, Nebraska 68583, USA. <sup>†</sup>Present addresses: Laboratory of Intracellular Parasites, Rocky Mountain Laboratories, NIAID, NIH, Hamilton, Montana 59840, USA (S.K.L.); Department of Pathology, Johns Hopkins University School of Medicine, Baltimore, Maryland 21205, USA (D.A.P.).



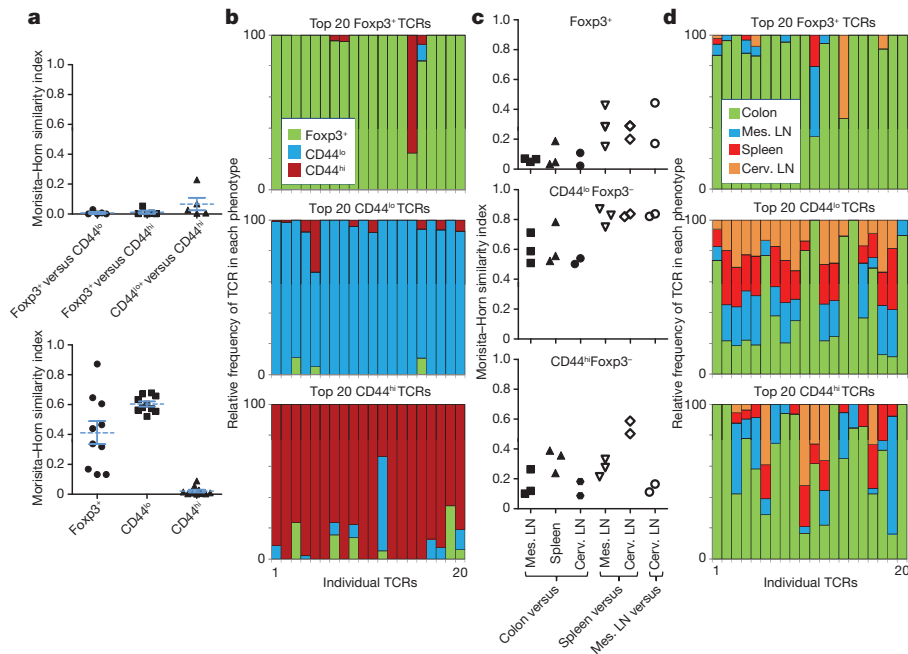


**Figure 1 | The colonic T<sub>reg</sub> TCR repertoire is unique.** **a**, TCR usage between colonic T-cell subsets. A total of 2,892 TRAV14 TCR $\alpha$  sequences from colonic naive, memory and T<sub>reg</sub> cells of five individual mice were compared (Supplementary Fig. 2). Each symbol represents a Morisita–Horn similarity comparison between two different T-cell subsets within each mouse (top), or a comparison of the same T-cell subset between different mice (bottom). Bars represent means  $\pm$  s.e.m. **b**, Analysis of individual TCRs. The relative distribution within all T-cell subsets is shown for the 20 most common individual TCRs in each colonic T-cell subset. For example, a TCR with equal percentage in the Foxp3<sup>+</sup> and CD44<sup>hi</sup> subset would be shown as a half-green/half-orange bar. This analysis uses the pooled data set, which includes

recognized by CT7, but none of 34 other sequenced isolates, were identified as *Parabacteroides distasonis* (Fig. 2c and Supplementary Fig. 6). To assess whether CT7 broadly recognizes commensal species within the *Parabacteroides/Bacteroides* genera, we screened it against an additional panel of closely related mouse-derived commensal *Parabacteroides* and *Bacteroides* species<sup>22</sup>. CT7, but not CT2 or CT6, recognized only a subset of these bacterial species, including a second isolate of *P. distasonis* (Fig. 2d). Importantly, isolates that did not stimulate CT7 were recognized by another TCR hybridoma, DP1 (Supplementary Fig. 7a), indicating that these preparations contained antigens capable of stimulating TCRs. The almost mutually exclusive specificity of CT7 and DP1 within the Bacteroidaceae family makes it unlikely that these TCRs recognize self antigens in the host that are differentially induced by these closely related bacteria<sup>22</sup> (Supplementary Fig. 7b). The TCR-specific reactivity patterns further suggest that TCR activation is not due to non-specific stimulation by generic immunostimulatory bacterial components or superantigens. Rather, these TCRs probably recognize distinct bacterial protein antigens, because predigestion of heat-killed *P. distasonis* with proteinase K abrogated recognition by the CT7 hybridoma (Supplementary Fig. 7c), in contrast with a report of T<sub>reg</sub>-cell induction by protease-insensitive capsular polysaccharide from *B. fragilis*<sup>6</sup>. Although proof of direct bacterial recognition will require the identification of specific epitopes, these data strongly argue for the recognition of a bacteria-derived peptide by colonic T<sub>reg</sub> TCR CT7.

More than half of the tested colonic T<sub>reg</sub> TCRs recognized colonic contents and/or bacterial isolates (Table 1). However, this may underestimate the true frequency of colonic T<sub>reg</sub> TCRs that respond to bacterial antigens. A lack of reactivity in our screen cannot be interpreted to mean that the TCR does not recognize bacteria, because the antigens may be rare in unfractionated colonic contents, lost on

sequencing from individual mice as well as 9,680 sequences from experiments 1–3, each consisting of cells from three to five mice (Supplementary Fig. 2). Note that one TCR is found in both Foxp3<sup>+</sup> (no. 15) and CD44<sup>hi</sup> (no. 3) plots, and one in both CD44<sup>lo</sup> (no. 5) and CD44<sup>hi</sup> (no. 12) plots; all others appear in only one plot. **c**, Anatomical distribution of colonic TCRs. Morisita–Horn indices comparing the colon data with those for other locations (filled symbols) or between each of the other locations (open symbols) are shown. Mes., mesenteric; cerv., cervical. **d**, Analysis of individual TCRs. The 20 most prevalent colonic TCRs for each subset in the pooled data set are shown, and their presence at other locations is represented in a manner analogous to **b**. LN, lymph node.

autoclaving, or derived from an organism that was not isolated in our screen. Thus, the specificity of common colonic T<sub>reg</sub> TCRs seems to be skewed towards the recognition of bacterial antigens.

Although T<sub>reg</sub> cells may develop extrathymically as a result of an encounter with bacterial antigens, it is also possible that these T<sub>reg</sub> cells are selected by self-antigen recognition in the thymus, followed by expansion in the periphery due to cross-reactivity. To assess the ability of these colonic T<sub>reg</sub> TCRs to facilitate thymic T<sub>reg</sub>-cell selection, we tracked the development of immature Foxp3<sup>gfp</sup> Rag1<sup>-/-</sup> thymocytes that were retrovirally transduced with a colonic T<sub>reg</sub> TCR. None of the colonic T<sub>reg</sub> TCRs generated an appreciable frequency of Foxp3<sup>+</sup> thymocytes (Fig. 3a and Supplementary Figs 8 and 9a), in contrast with T<sub>reg</sub> TCRs normally found at other peripheral locations (R19, G25 and R111; Supplementary Fig. 3). Note that G25 and R111 can be found at low frequency in the colonic T<sub>reg</sub>-cell subset, suggesting that the colon does contain some thymically derived T<sub>reg</sub> cells. The lack of T<sub>reg</sub> development in cells expressing colonic T<sub>reg</sub> TCRs cannot be attributed to an overwhelmed thymic niche<sup>23,24</sup> (Supplementary Fig. 9b). These data therefore demonstrate that many common colonic T<sub>reg</sub> TCRs facilitate thymic T<sub>reg</sub>-cell selection poorly, if at all, implying that these TCRs instead mediate peripheral T<sub>reg</sub>-cell development.

The retroviral transduction of thymocytes does not result in the emergence of sufficient numbers of transduced T cells from the thymus to permit their reliable detection in the periphery. We therefore retrovirally transduced self-renewing bone marrow progenitors and used them to create stable chimaeras, selecting colonic T<sub>reg</sub> TCRs CT2 and CT6 on the basis of their *in vitro* reactivity to colonic contents (Fig. 2a). In these chimaeras we observed virtually no development of Foxp3 expression in cells expressing CT2 or CT6 (Fig. 3b, left; Supplementary Fig. 10). We reasoned that CT2 and CT6 may not recognize the microbiota in these commercially sourced host mice (Fig. 2a), and

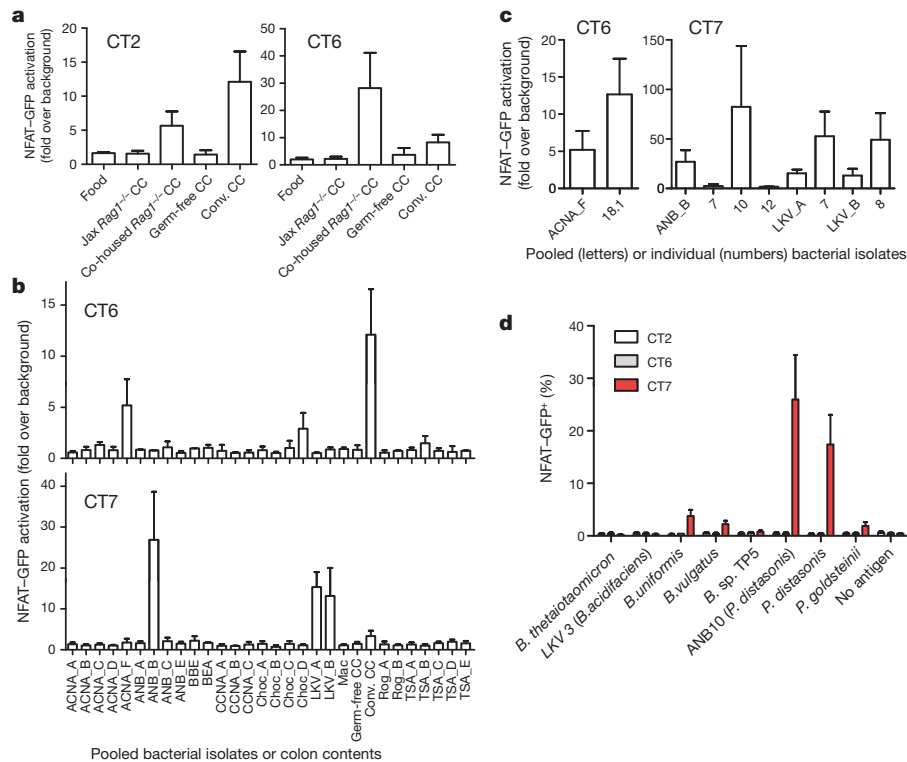


**Figure 2** | *In vitro* reactivity of colonic T<sub>reg</sub> TCRs to colonic contents and bacterial isolates. **a**, Reactivity to colonic contents. Colonic T<sub>reg</sub> TCR-expressing NFAT-GFP hybridoma cells were cultured with Flt3L-induced dendritic cells in the presence of autoclaved food homogenate, or autoclaved colonic contents (CC) isolated from Rag1<sup>-/-</sup> mice from Jackson Laboratories (Jax Rag1<sup>-/-</sup>), Jax Rag1<sup>-/-</sup> mice housed together with mice from our colony (co-housed Rag1<sup>-/-</sup>), germ-free mice and conventionally housed (conv.) mice in our colony. **b**, Reactivity to bacterial pools. Cultures of heat-killed commensal bacteria isolated from our colony (Supplementary Fig. 6) were pooled (denoted by culture conditions and a letter) and screened for their

ability to stimulate colonic T<sub>reg</sub> TCR-expressing hybridomas. For **a**, **b**, see Supplementary Fig. 4 for additional TCRs. **c**, Reactivity to individual isolates. Hybridomas showing reactivity against a pool of bacterial isolates were re-screened against the individual constituents (numbered). Data shown in **a–c** are the fold change in percentage GFP<sup>+</sup> over the no-antigen control from 2–4 experiments (means  $\pm$  s.e.m.). **d**, Specificity of colonic T<sub>reg</sub> TCRs. A panel of heat-killed *Parabacteroides* and *Bacteroides* species (Supplementary Fig. 7) was tested against hybridomas expressing CT2, CT6 and CT7. Data shown are means  $\pm$  s.e.m. for three experiments.

therefore performed experiments in which the chimaeras were housed together with mice from our colony. This resulted in the induction of CT2-expressing or CT6-expressing T<sub>reg</sub> cells preferentially localized in the colon (Fig. 3b, right, and Supplementary Fig. 11). In an observation paralleling that previously made in the thymus<sup>23,24</sup>, there also seems to be a saturable, antigen-specific T<sub>reg</sub>-cell niche in the periphery<sup>25</sup> (Supplementary Fig. 11c).

Although these data strongly suggest that many colonic T<sub>reg</sub> cells are generated extrathymically on encountering bacterial antigen, it remained possible that a rare population of thymically generated T<sub>reg</sub> cells below the limit of our detection expanded on encountering peripheral antigen<sup>25</sup>. We therefore generated CT6 TCR transgenic mice (Supplementary Fig. 12) and adoptively transferred CD44<sup>lo</sup> Foxp3<sup>-</sup> CT6 T cells mixed with congenic polyclonal CD4<sup>+</sup> 'filler' T cells into T-cell-deficient *Tcrb*<sup>-/-</sup> hosts. Consistent with the bone marrow chimaera data, the transferred CT6 T cells expanded and induced the

expression of Foxp3 only if the recipients were housed together with mice from our colony (Fig. 3c and Supplementary Fig. 13). Taken together with the observed lack of T<sub>reg</sub>-cell development by thymocytes expressing colonic T<sub>reg</sub> TCRs (Fig. 3a), these data suggest that a substantial proportion of the colonic T<sub>reg</sub> population arises extrathymically from antigen-specific interactions with the colonic microbiota.

The notion that most colonic T<sub>reg</sub> cells are generated as a result of microbial interactions is at odds with the observation that germ-free mice have normal T<sub>reg</sub>-cell frequencies<sup>6</sup> (Supplementary Fig. 1). However, we and others<sup>14</sup> have observed that most colonic T<sub>reg</sub> cells in conventionally housed, but not germ-free, mice are probably of peripheral origin, because these cells express low levels of the transcription factor Helios (Fig. 3d and Supplementary Fig. 14), a putative marker for thymically derived T<sub>reg</sub> cells<sup>26</sup>. We therefore speculate that germ-free conditions skew the colonic T<sub>reg</sub> TCR repertoire towards thymically derived T<sub>reg</sub> TCRs.

**Table 1** | Summary of *in vitro* screening of colonic T<sub>reg</sub>-cell TCRs

Name	CDR3 amino-acid residue sequence	Reactivity		
		Conv. CC	Transferred by co-housing	Bacterial isolate
CT1	AASWASGYNKLT	Yes	Yes	
CT2	AASAIWNTGYQNFY	Yes	Yes	
CT4	AASEYALGRLH			
CT6	AASGYALGRLH	Yes	Yes	<i>Clostridiales</i> sp. ACNA18.1
CT7	AASATGDNRF			<i>Parabacteroides distasonis</i>
CT8	AASLTGGYKVV			
CT9	AASADNRAGNKLT	Yes	Yes	
G57	AASELYQGGRALI	Yes		

Conv. CC, colonic contents from conventionally housed mice.

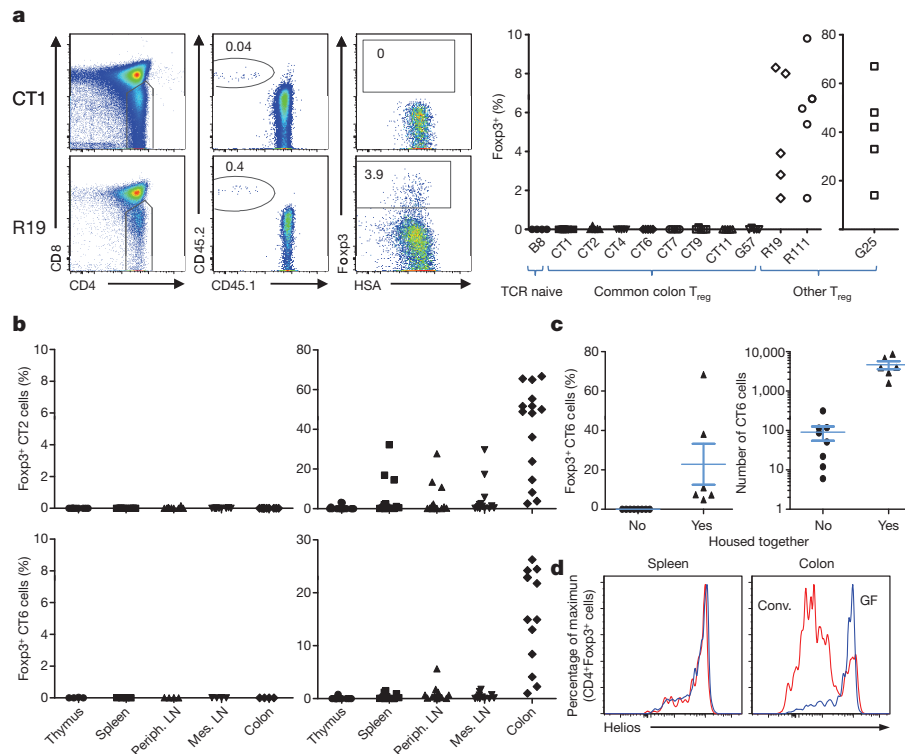


**Figure 3 | Colonic  $T_{reg}$  TCRs facilitate thymic  $T_{reg}$ -cell development poorly, if at all.** **a**, Assessment of thymic  $T_{reg}$ -cell development from TCR- $\alpha\beta$ -transduced  $Rag1^{-/-}$  thymocytes. The gating strategy (left), and summary of two to four experiments per TCR (right) are shown. See Supplementary Fig. 3 for additional TCR information, and Supplementary Figs 8 and 9 for plots and analysis of clonal frequencies. Comparison of colon versus other  $T_{reg}$  TCRs revealed  $P$ -values  $< 0.01$ . **b**, Mixed retroviral bone-marrow chimaeras. The percentage of Foxp3 $^{+}$  cells in the CT2-expressing or CT6-expressing CD45.2 $^{+}$  CD4 $^{+}$  population is shown in hosts housed together (right) or not (left) with mice from our colony. See Supplementary Figs 10 and 11 for additional analyses. Periph., peripheral. **c**, Peripheral conversion of CT6 TCR

transgenic cells. Naive CD45.2 CT6 cells and CD45.1 CD4 $^{+}$  filler cells were adoptively transferred into  $Tcrb^{-/-}$  hosts for 5 weeks. The percentage (left) of Foxp3 $^{+}$  CT6 cells (V $\alpha$ 2 $^{+}$  V $\beta$ 6 $^{+}$  CD45.2 $^{+}$  CD45.1 $^{-}$  CD4 $^{+}$ ) are shown. The number of CT6 cells (right) was determined by flow cytometry of the entire colonic lamina propria. Data are from three experiments; bars represent means  $\pm$  s.e.m. See Supplementary Fig. 13 for flow cytometric plots. **d**, Helios expression in  $T_{reg}$  cells. Representative intracellular Helios staining in CD4 $^{+}$  Foxp3 $^{+}$  cells from conventionally housed (conv.) and germ-free (GF)  $Foxp3^{GFP}$  mice is shown, and is summarized in Supplementary Fig. 14. For all plots in this figure, each symbol represents data from an individual host.

The efficient differentiation of naive T cells into  $T_{reg}$  rather than effector, cells may be important for generating colonic tolerance, because it has been observed that TCRs that facilitate thymic  $T_{reg}$ -cell development can be pathogenic when expressed on effector T cells<sup>17,27</sup>. To address this possibility, we performed an initial analysis of colonic TCR repertoires in mice expressing the fixed TCR  $\beta$  chain and undergoing spontaneous colitis due to genetic deficiencies in interleukin (IL)-2, IL-10 or transforming growth factor- $\beta$  receptor signalling (Supplementary Fig. 2a). We observed that several colonic TCRs almost exclusively found in the Foxp3 $^{+}$  data sets in normal mice were found in the effector/memory data sets in the diseased animals (Supplementary Fig. 15a). Although these genetic manipulations may affect  $T_{reg}$ -cell development or survival, the relatively high abundance of some of these TCRs in the CD44 $^{hi}$  subset suggests that effector cells expressing these TCRs are expanding in the colitic environment. To test for the pathogenic potential of colonic  $T_{reg}$  TCRs, we retrovirally expressed CT2 and CT6 TCRs on peripheral, monospecific TCR $\alpha\beta$  transgenic cells with known specificity for a foreign antigen (human CLIP peptide). Adoptive transfer of these cells, which were virtually all Foxp3 $^{-}$ , into  $Rag1^{-/-}$  hosts housed with mice from our colony induced weight loss and colitis (Fig. 4 and Supplementary Fig. 15b, c). In contrast, cells expressing only the transgenic TCR or a TCR from the naive T-cell subset (B8) did not. The failure of these retrovirally transduced T cells to upregulate Foxp3 and become regulatory in this situation is probably due to expansion in a lymphopenic environment, as well as *in vitro* T-cell activation—a requirement for retroviral

transduction. Thus, these data illustrate the potential pathological consequences of T-cell recognition of commensal bacterial antigens under conditions that disfavour  $T_{reg}$  development.

This analysis of common colonic  $T_{reg}$  TCRs in a fixed TCR $\beta$  repertoire suggests a model (Supplementary Fig. 16) in which T cells expressing these TCRs exist as naive T cells in the absence of antigen

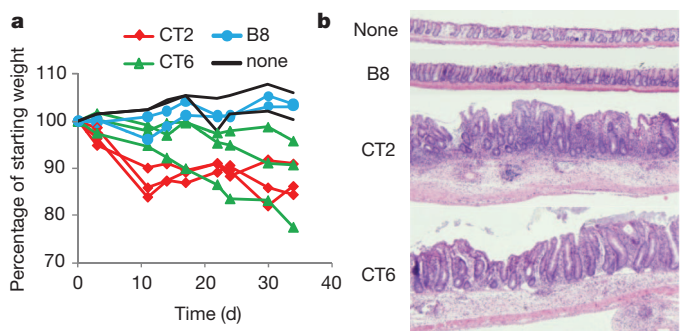


**Figure 4 | Pathogenic potential of colonic  $T_{reg}$  TCRs.** **a**, Adoptive transfer of peripheral T cells transduced with CT2 or CT6 into  $Rag1^{-/-}$  hosts housed with mice from our colony. Non-transduced T cells (none) or naive TCR transduced T cells (B8) were used as controls. Each line represents an individual recipient. One representative experiment is shown (summary in Supplementary Fig. 15b). **b**, A representative haematoxylin/eosin-stained section of the descending colon 7–10 weeks after T-cell transfer. Original magnification  $\times 4$ .



(Fig. 3b, left, and Supplementary Figs 10 and 11). Encounter with bacteria-derived foreign antigens in the colon seems to drive the generation of Foxp3<sup>+</sup> T<sub>reg</sub> cells efficiently (Fig. 3b), because it typically does not result in the substantial simultaneous development of CD44<sup>hi</sup> cells of the same specificity (Fig. 1a, b). This diversion of naive T cells with bacterial TCR specificity into the T<sub>reg</sub>-cell lineage may be crucial for preventing the generation of colitogenic effector cells (Fig. 4). Thus, these data support a model in which an individual's T-cell population is not only instructed by classic self/non-self discrimination mechanisms during thymic development but is also educated in the periphery to accommodate the variety of non-self antigens derived from the commensal microbiota at mucosal sites.

## METHODS SUMMARY

**Mice.** TCRβ Foxp3<sup>gfp</sup> Tcrα<sup>+/-</sup>; Foxp3<sup>IRES-GFP</sup>; Il-2<sup>-/-</sup>; Il-10<sup>-/-</sup>; and dnTGFβRII strains have been described (see Methods). C57BL/6 Rag1<sup>-/-</sup> and CD45.1 mice were obtained from Jackson Laboratories and the National Cancer Institute, respectively. Germ-free mice were generated in collaboration with J. Gordon. CT6 transgenic mice were generated as described<sup>23</sup>.

**TCR repertoire analysis.** Analyses of TRAV14 (Vα2) TCR sequences from TCRβ transgenic mice were performed as described<sup>20</sup>. Lamina propria cell suspensions from the entire colon were prepared as described<sup>9</sup>, and CD4<sup>+</sup> subsets were sorted with a FACSAria (Becton Dickinson).

**Hybridoma assays.** Hybridoma cells expressing GFP under an NFAT promoter<sup>21</sup> were retrovirally transduced with TCRβ-IRES-mCD4 and an individual TCR α chain. Hybridomas were cultured with flt3-ligand-elicited dendritic cells with the indicated antigen preparations and analysed by flow cytometry after 1.5 days. **Antigen preparations.** Whole colonic contents and food pellets were diluted with phosphate-buffered saline, vortex-mixed, homogenized, filtered, and autoclaved for 15 min. Colonic bacterial isolation was performed as described<sup>22</sup> (see Supplementary Fig. 6).

**In vivo developmental assays.** Retroviral transduction and intrathymic transfer of Rag1<sup>-/-</sup> thymocytes were performed as described in Methods. Analysis of CD4 SP thymocytes was performed about 2.5 weeks later. Retroviral bone marrow chimaeras were created as described<sup>23</sup>. Some recipients were housed together with mice from our colony 2 weeks after bone marrow reconstitution, for a period of 1 week.

**In vivo peripheral T-cell assays.** Retroviral transduction of peripheral TCRβ-Foxp3<sup>gfp</sup> Rag1<sup>-/-</sup> T cells was performed as described<sup>27</sup>, and cells were transferred intravenously into Rag1<sup>-/-</sup> hosts housed with them. Sorted CD4<sup>+</sup>CD44<sup>lo</sup>Foxp3<sup>-</sup> cells (5 × 10<sup>4</sup>) from CT6 transgenic mice were co-transferred with 5 × 10<sup>5</sup> CD45.1<sup>+</sup>CD4<sup>+</sup> 'filler' cells into Tcrb<sup>-/-</sup> mice. Recovered cells were analysed by flow cytometry 5 weeks later.

**Statistics.** The Wilcoxon rank sum test was used unless otherwise indicated.

**Full Methods** and any associated references are available in the online version of the paper at [www.nature.com/nature](http://www.nature.com/nature).

Received 29 November 2010; accepted 5 August 2011.

Published online 21 September 2011.

1. Josefowicz, S. Z. & Rudensky, A. Control of regulatory T cell lineage commitment and maintenance. *Immunity* **30**, 616–625 (2009).
2. Belkaid, Y. & Tarbell, K. Regulatory T cells in the control of host–microorganism interactions. *Annu. Rev. Immunol.* **27**, 551–589 (2009).
3. Barnes, M. J. & Powrie, F. Regulatory T cells reinforce intestinal homeostasis. *Immunity* **31**, 401–411 (2009).
4. Backhed, F., Ley, R. E., Sonnenburg, J. L., Peterson, D. A. & Gordon, J. I. Host–bacterial mutualism in the human intestine. *Science* **307**, 1915–1920 (2005).
5. Min, B. *et al.* Gut flora antigens are not important in the maintenance of regulatory T cell heterogeneity and homeostasis. *Eur. J. Immunol.* **37**, 1916–1923 (2007).
6. Round, J. L. & Mazmanian, S. K. Inducible Foxp3<sup>+</sup> regulatory T-cell development by a commensal bacterium of the intestinal microbiota. *Proc. Natl Acad. Sci. USA* **107**, 12204–12209 (2010).

7. Singh, B. *et al.* Control of intestinal inflammation by regulatory T cells. *Immunol. Rev.* **182**, 190–200 (2001).
8. Curotto de Lafaille, M. A. *et al.* Adaptive Foxp3<sup>+</sup> regulatory T cell-dependent and -independent control of allergic inflammation. *Immunity* **29**, 114–126 (2008).
9. Sun, C. M. *et al.* Small intestine lamina propria dendritic cells promote *de novo* generation of Foxp3 Treg cells via retinoic acid. *J. Exp. Med.* **204**, 1775–1785 (2007).
10. Zheng, Y. *et al.* Role of conserved non-coding DNA elements in the Foxp3 gene in regulatory T-cell fate. *Nature* **463**, 808–812 (2010).
11. Coombes, J. L. *et al.* A functionally specialized population of mucosal CD103<sup>+</sup> DCs induces Foxp3<sup>+</sup> regulatory T cells via a TGF-β and retinoic acid-dependent mechanism. *J. Exp. Med.* **204**, 1757–1764 (2007).
12. Mucida, D. *et al.* Reciprocal T<sub>H</sub>17 and regulatory T cell differentiation mediated by retinoic acid. *Science* **317**, 256–260 (2007).
13. Benson, M. J., Pino-Lagos, K., Roseblatt, M. & Noelle, R. J. All-trans retinoic acid mediates enhanced Treg cell growth, differentiation, and gut homing in the face of high levels of co-stimulation. *J. Exp. Med.* **204**, 1765–1774 (2007).
14. Atarashi, K. *et al.* Induction of colonic regulatory T cells by indigenous *Clostridium* species. *Science* **331**, 337–341 (2011).
15. Round, J. L. *et al.* The Toll-like receptor 2 pathway establishes colonization by a commensal of the human microbiota. *Science* **332**, 974–977 (2011).
16. Cong, Y., Feng, T., Fujihashi, K., Schoeb, T. R. & Elson, C. O. A dominant, coordinated T regulatory cell–IgA response to the intestinal microbiota. *Proc. Natl Acad. Sci. USA* **106**, 19256–19261 (2009).
17. Hsieh, C.-S. *et al.* Recognition of the peripheral self by naturally arising CD25<sup>+</sup>CD4<sup>+</sup> T cell receptors. *Immunity* **21**, 267–277 (2004).
18. Pacholczyk, R., Ignatowicz, H., Kraj, P. & Ignatowicz, L. Origin and T cell receptor diversity of Foxp3<sup>+</sup>CD4<sup>+</sup>CD25<sup>+</sup> T cells. *Immunity* **25**, 249–259 (2006).
19. Wong, J. *et al.* Adaptation of TCR repertoires to self-peptides in regulatory and nonregulatory CD4<sup>+</sup> T cells. *J. Immunol.* **178**, 7032–7041 (2007).
20. Lathrop, S. K., Santacruz, N. A., Pham, D., Luo, J. & Hsieh, C. S. Antigen-specific peripheral shaping of the natural regulatory T cell population. *J. Exp. Med.* **205**, 3105–3117 (2008).
21. Ise, W. *et al.* CTLA-4 suppresses the pathogenicity of self antigen-specific T cells by cell-intrinsic and cell-extrinsic mechanisms. *Nature Immunol.* **11**, 129–135 (2010).
22. Bloom, S. M. *et al.* Commensal *Bacteroides* species induce colitis in host-genotype-specific fashion in a mouse model of inflammatory bowel disease. *Cell Host Microbe* **9**, 390–403 (2011).
23. Bautista, J. L. *et al.* Intracellular competition limits the fate determination of regulatory T cells in the thymus. *Nature Immunol.* **10**, 610–617 (2009).
24. Leung, M. W., Shen, S. & Lafaille, J. J. TCR-dependent differentiation of thymic Foxp3<sup>+</sup> cells is limited to small clonal sizes. *J. Exp. Med.* **206**, 2121–2130 (2009).
25. Nishio, J., Feuerer, M., Wong, J., Mathis, D. & Benoist, C. Anti-CD3 therapy permits regulatory T cells to surmount T cell receptor-specified peripheral niche constraints. *J. Exp. Med.* **207**, 1879–1889 (2010).
26. Thornton, A. M. *et al.* Expression of Helios, an Ikaros transcription factor family member, differentiates thymic-derived from peripherally induced Foxp3<sup>+</sup> T regulatory cells. *J. Immunol.* **184**, 3433–3441 (2010).
27. Hsieh, C. S., Zheng, Y., Liang, Y., Fontenot, J. D. & Rudensky, A. Y. An intersection between the self-reactive regulatory and nonregulatory T cell receptor repertoires. *Nature Immunol.* **7**, 401–410 (2006).

**Supplementary Information** is linked to the online version of the paper at [www.nature.com/nature](http://www.nature.com/nature).

**Acknowledgements** We thank K. Murphy, T. Egawa, Y. Zheng, J. Scott-Browne, J. Fontenot and S. Wetzel for discussion and reading of the manuscript; A. Kau and J. Gordon for discussions and generation of germ-free animals; N. P. Malvin for assistance with bacteriology; and J. Hunn for technical assistance. C.S.H. and co-workers are funded by the National Institute of Allergy and Infectious Diseases and the Burroughs-Wellcome Fund. S.M.B. was supported by National Institutes of Health training grant 5T32AI0071632.

**Author Contributions** S.K.L., S.R., K.N. and N.S. performed most of the experiments. S.M.B. designed and performed the bacteriology. C.W.L. developed and assisted with the intrathymic transfer experiments. D.P. and T.S. were involved in study design. S.K.L. and C.S.H. designed the experiments and wrote the manuscript. All authors discussed the results and commented on the manuscript.

**Author Information** Reprints and permissions information is available at [www.nature.com/reprints](http://www.nature.com/reprints). The authors declare no competing financial interests. Readers are welcome to comment on the online version of this article at [www.nature.com/nature](http://www.nature.com/nature). Correspondence and requests for materials should be addressed to C.S.H. (chsieh@wustl.edu).

## METHODS

**Mice.** TCRβ *Foxp3<sup>gfp</sup> Tcrα<sup>+/-</sup>* (ref. 27), *Foxp3<sup>IRES-GFP</sup>* (ref. 28), *Il-2<sup>-/-</sup>* (ref. 29), *Il-10<sup>-/-</sup>* (ref. 30) and dnTGFβRII (ref. 31) strains on C57BL/6 background have been described. C57BL/6 *Rag1<sup>-/-</sup>* and C57BL/6 CD45.1 congenic mice were obtained from Jackson Laboratories and National Cancer Institute, respectively. Germ-free mice were generated in collaboration with J. Gordon. CT6 transgenic mice were generated as described<sup>23</sup>, with microinjection into B6 × 129 fertilized eggs. In experiments in which animals obtained from commercial vendors were housed together, a female bred in our facility was added to each cage of mice for 7 days, and then removed before the experiment. In retroviral bone marrow chimaeras, the animal was added 2 weeks after bone marrow transfer, for 1 week, then removed for the duration of the experiment. Animal experiments were performed in a specific pathogen-free facility in accordance with the guidelines of the Institutional Animal Care and Use Committee at Washington University.

**TCR repertoire analysis.** Analyses of TRAV14 (Vα2) TCR sequences from TCRβ transgenic mice were performed as described<sup>20</sup>. In brief, lamina propria cell suspensions were prepared from the entire colon (including the caecum) as described<sup>9</sup>, without the final Percoll enrichment, and sorted into CD4<sup>+</sup> T-cell subsets (CD44<sup>hi</sup>Foxp3<sup>-</sup>, CD44<sup>lo</sup>Foxp3<sup>-</sup> and Foxp3<sup>+</sup>) with a FACSARIA (Becton Dickinson). RNA was isolated, TCRα cDNA was isolated, and a TRAV14 (Vα2) cDNA library was generated by PCR and sequenced by the Genome Sequencing Center at Washington University. Comparison of TCR repertoires was performed with the Morisita–Horn statistical test<sup>32</sup>, which compares two populations, taking into account the overlap and relative abundance of the species in the two populations, and expresses their similarity on a scale from 0 (no similarity) to 1.0 (exactly the same).

**Hybridoma assays.** T-cell hybridoma cells, which do not express a T-cell receptor and express GFP under an NFAT promoter<sup>21</sup>, were retrovirally transduced with TCRβ-IRES-mCD4 and sorted for CD4 expression. TCR α chains of interest, selected on the basis of average frequency and presence in at least two independent data sets, were then retrovirally introduced, and Vα2-expressing cells were sorted. The hybridomas differ only in their retrovirally encoded TCR α chain, which does not confer any functional properties of the cell from which the TCR originated, thereby allowing a direct comparison of antigen recognition between TCRs from different T-cell subsets. These hybridoma cells ((2.5–5.0) × 10<sup>4</sup>) were cultured with flt3-ligand-elicited dendritic cells (5 × 10<sup>4</sup>) and the indicated antigen preparations, diluted 1:200, in flat-bottomed 96-well plates. The Vα2<sup>+</sup>CD4<sup>+</sup> cells were analysed for GFP expression after 1.5 days by flow cytometry on a FACSCanto or FACSARIA (Becton Dickinson). Controls without antigen were performed in parallel and used to normalize data against variations in background fluorescence between experiments.

**Antigen preparations.** Whole colonic contents were scraped from longitudinally opened colon and caecum; they were diluted with phosphate-buffered saline, then vortex-mixed, homogenized, filtered through a 70-μm mesh, and autoclaved for 15 min. Food antigen was also diluted with phosphate-buffered saline, homogenized, filtered and autoclaved. Preparations were stored short-term at -20 °C and long-term at -80 °C. For a description of the colonic bacterial isolation see Supplementary Fig. 6 and ref. 22. Isolates were named according to their culture conditions followed by a number; pools of two or three isolates were designated by a letter.

**Thymic T<sub>reg</sub>-cell developmental assay.** Retroviral transduction of *Foxp3<sup>gfp</sup>Rag1<sup>-/-</sup>* thymocytes was performed as described<sup>33</sup> by using a TCRα-P2A-TCRβ vector<sup>34</sup>. Thymocytes were injected into the thymus of sublethally irradiated (600 rad) CD45.1 congenic recipients; 14–16 days later, CD45.2<sup>+</sup>CD4<sup>+</sup>CD8<sup>-</sup> thymocytes were analysed by flow cytometry for expression of *Foxp3<sup>gfp</sup>* with the use of a FACSARIA. About half of each thymus (8 × 10<sup>7</sup>) was analysed by flow cytometry.

A total of 10<sup>6</sup> events were initially collected to determine the frequency of CD45.1 and CD45.2 cells. Subsequently, the storage gate was changed to include only CD45.2 cells for the rest of the sample at high speed (about 25,000–30,000 events s<sup>-1</sup>). Of the 45 recipients of cells expressing colonic T<sub>reg</sub> TCRs, 4 of 45 showed a handful of Foxp3<sup>+</sup> events (1/5 G57, 1/5 CT9, 2/5 CT2). We believe that many or all of these may be artefacts, because the Foxp3<sup>+</sup> events shown in Supplementary Fig. 8b have a larger than usual Forward Scatter (FSC) and Side Scatter (SSC), nor can they be found in ten CT2 retroviral bone marrow chimaeras (Supplementary Fig. 10, top). However, we cannot be certain that these events are artefacts, because they are few and not reproducibly observed in all recipients. The sensitivity for picking up Foxp3<sup>+</sup> cells may be estimated from the binomial distribution, in which a population frequency of 0.3% would result in at least 1 event per 1,000 with 95% confidence, and can be calculated from the number of CD4SP events processed (Supplementary Fig. 9b, bottom). However, increasing the number of CD4SP cells expressing a particular TCR may not increase the sensitivity of the assay, because it seems that T<sub>reg</sub> TCRs often show an inverse correlation between clonal frequency and T<sub>reg</sub>-cell development<sup>23,24</sup>.

**Retroviral bone marrow chimaeras.** *Foxp3<sup>IRES-GFP</sup> Rag1<sup>-/-</sup>* (CD45.2) bone marrow was retrovirally transduced with the CT2 or CT6 TCR using a TCRα-P2A-TCRβ vector<sup>34</sup> and injected intravenously with wild-type CD45.1 bone marrow into lethally irradiated (1,050 rad) CD45.1 hosts from NCI to create chimaeras as described<sup>23</sup>. Some recipients were housed together (co-housed) with mice from our colony for a period of 1 week, beginning 2 weeks after bone marrow reconstitution. Cells isolated from the thymus, spleen, mesenteric lymph node and colon were analysed by flow cytometry after 6–8 weeks.

**In vivo TCR-induced pathology.** Retroviral transduction of *in vitro* activated peripheral TCRβ *Foxp3<sup>gfp</sup> Rag1<sup>-/-</sup>* T cells was performed as described<sup>27</sup>. The entire T-cell population was transferred, and adjusted such that 6 × 10<sup>5</sup> transduced cells (14% mean transduction efficiency, range 5.8–22%) were intravenously transferred into each co-housed *Rag1<sup>-/-</sup>* mouse. After 7–10 weeks, tissue from the caecum and colon underwent fixation and staining with haematoxylin and eosin.

**CT6 TCR transgenic cell transfer experiment.** Naive (CD4<sup>+</sup>CD44<sup>lo</sup>Foxp3<sup>-</sup>) T cells were sorted from lymph node and spleen from CT6 *Foxp3<sup>IRES-GFP</sup> Rag1<sup>-/-</sup>* mice. Cells (5 × 10<sup>4</sup>) were transferred simultaneously with 5 × 10<sup>5</sup> CD45.1<sup>+</sup>CD4<sup>+</sup> congenic ‘filler’ cells into *Tcrb<sup>-/-</sup>* mice, with the notion that providing filler cells, which include T<sub>reg</sub> cells, may limit lymphopenic expansion and facilitate conversion. Vβ6<sup>+</sup>Vα2<sup>+</sup>CD45.2<sup>+</sup>CD45.1<sup>-</sup>CD4<sup>+</sup> CT6 Tg T cells in the colonic lamina propria were assessed for Foxp3 expression 5 weeks later.

**Statistics.** The Wilcoxon rank sum test was used unless otherwise indicated.

28. Lin, W. *et al.* Regulatory T cell development in the absence of functional Foxp3. *Nature Immunol.* **8**, 359–368 (2007).
29. Schorle, H., Holtschke, T., Hunig, T., Schimpl, A. & Horak, I. Development and function of T cells in mice rendered interleukin-2 deficient by gene targeting. *Nature* **352**, 621–624 (1991).
30. Kuhn, R., Lohler, J., Rennick, D., Rajewsky, K. & Muller, W. Interleukin-10-deficient mice develop chronic enterocolitis. *Cell* **75**, 263–274 (1993).
31. Gorelik, L. & Flavell, R. A. Abrogation of TGFβ signaling in T cells leads to spontaneous T cell differentiation and autoimmune disease. *Immunity* **12**, 171–181 (2000).
32. Magurran, A. E. *Ecological Diversity and its Measurement* (Princeton Univ. Press, 1988).
33. Haxhinasto, S., Mathis, D. & Benoist, C. The AKT-mTOR axis regulates de novo differentiation of CD4<sup>+</sup> Foxp3<sup>+</sup> cells. *J. Exp. Med.* **205**, 565–574 (2008).
34. Holst, J., Vignali, K. M., Burton, A. R. & Vignali, D. A. Rapid analysis of T-cell selection *in vivo* using T cell-receptor retrogenic mice. *Nature Methods* **3**, 191–197 (2006).

# Molecular organization of vomeronasal chemoreception

Yoh Isogai<sup>1,2</sup>, Sheng Si<sup>1</sup>, Lorena Pont-Lezica<sup>1†</sup>, Taralyn Tan<sup>1</sup>, Vikrant Kapoor<sup>1</sup>, Venkatesh N. Murthy<sup>1</sup> & Catherine Dulac<sup>1,2</sup>

The vomeronasal organ (VNO) has a key role in mediating the social and defensive responses of many terrestrial vertebrates to species- and sex-specific chemosignals<sup>1</sup>. More than 250 putative pheromone receptors have been identified in the mouse VNO<sup>2,3</sup>, but the nature of the signals detected by individual VNO receptors has not yet been elucidated. To gain insight into the molecular logic of VNO detection leading to mating, aggression or defensive responses, we sought to uncover the response profiles of individual vomeronasal receptors to a wide range of animal cues. Here we describe the repertoire of behaviourally and physiologically relevant stimuli detected by a large number of individual vomeronasal receptors in mice, and define a global map of vomeronasal signal detection. We demonstrate that the two classes (V1R and V2R) of vomeronasal receptors use fundamentally different strategies to encode chemosensory information, and that distinct receptor subfamilies have evolved towards the specific recognition of certain animal groups or chemical structures. The association of large subsets of vomeronasal receptors with cognate, ethologically and physiologically relevant stimuli establishes the molecular foundation of vomeronasal information coding, and opens new avenues for further investigating the neural mechanisms underlying behaviour specificity.

The discovery of large receptor families mediating olfactory and vomeronasal chemosensation has offered a unique opportunity to decode the molecular logic by which environmental information influences animal behaviour<sup>3,4</sup>. The VNO of rodents has a critical role in identifying sex- and species-specific chemical cues and in mediating mating, territorial aggression, defensive responses to predators and associated endocrine changes<sup>1,5</sup>. With rare exceptions<sup>6–8</sup>, the molecular identity of VNO receptors (VRs) recognizing distinct animal cues is unknown, thus limiting the ability to explore the sensory mechanisms underlying behavioural specificity. Prior studies suggested that vomeronasal detection is extremely sensitive and narrowly tuned to male, female or heterospecific cues<sup>5,9–11</sup>, but they have not allowed the identification of the activated receptors. We describe here a robust and high-throughput molecular readout of vomeronasal activation that enabled us to uncover the receptor specificity of 88 individual VRs to a vast range of ethologically relevant cues. These results establish the molecular and functional framework underlying vomeronasal signalling.

In initial experiments, we exposed female mice to clean bedding and to bedding used by male mice, and assessed the upregulation of the immediate early genes (IEGs) *Arc*, *c-Fos*, *c-Jun*, *Egr1*, *FosB* and *Nr4a1* by *in situ* hybridization on VNO tissue. Our data show that the sensitivity of *Egr1* induction following exposure to chemosignals far exceeds that of other IEGs (Fig. 1a, b) ( $60.1 \pm 7.1$  cells per  $0.2 \text{ mm}^2$  for *Egr1*,  $7.9 \pm 1.9$  cells per  $0.2 \text{ mm}^2$  for *c-Fos*). Indeed *c-Fos*, an IEG used in previous VNO stimulation studies, labels only a subset of *Egr1*-positive cells (Supplementary Fig. 1). In *TrpC2*<sup>−/−</sup> mutants, in which VNO activation is genetically impaired<sup>12</sup>, *Egr1* induction after semiochemical exposure is completely abolished ( $n = 3$ ), demonstrating the specificity of *Egr1* activation following sensory stimulation (Fig. 1c).

We then exposed animals to 29 distinct ethologically relevant cues<sup>5,13</sup>. Male and female bedding from different mouse subspecies and wild-derived strains, as well as a variety of heterospecific cues from sympatric competitors and predators, robustly induced *Egr1* expression in the VNO (Fig. 2a). Remarkably, food-related insect stimuli and cues from presumably neutral species such as woodchuck failed to generate VNO activation.

V1R and V2R neurons were equally activated by a large variety of stimuli, as judged by co-labelling of *Egr1* with *Gα<sub>i2</sub>*, a marker of V1R-expressing neurons<sup>14,15</sup> (Fig. 2b, Supplementary Fig. 2a). Interestingly, simultaneous exposure to multiple cues from the same class of animals (for example, *Peromyscus* species, reptiles, or predatory birds) did not significantly increase the number of *Egr1*-positive cells when compared to activation by a single stimulus ( $P > 0.4$ , two-tailed *t*-test when the strongest of each stimulus class was compared to the corresponding mix), indicating that neuronal populations activated by related animals are largely overlapping (Fig. 2a). In contrast, simultaneous exposure to all heterospecific stimuli significantly increased *Egr1*-positive cells from 5% to 10% per cue to up to ~30% ( $P < 0.01$ , two-tailed *t*-test), indicating that distinct heterospecific cues have different response profiles. Moreover, whereas mouse bedding activated 5% to 7% of VNO neurons in animals of the opposite sex, mixes of conspecific and heterospecific scents activated ~35% of neurons (Fig. 2a), suggesting that receptors activated by both types of cues are also largely distinct.

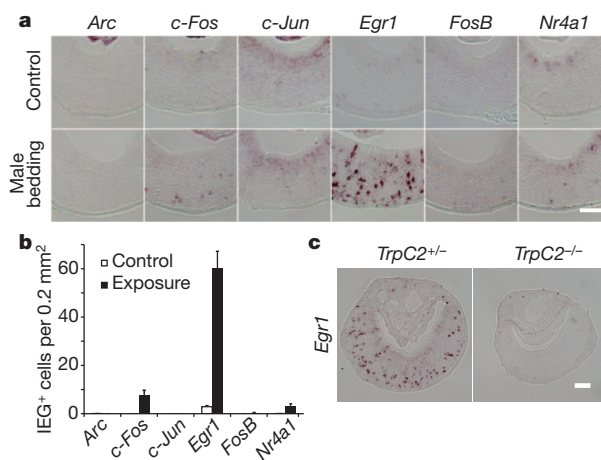
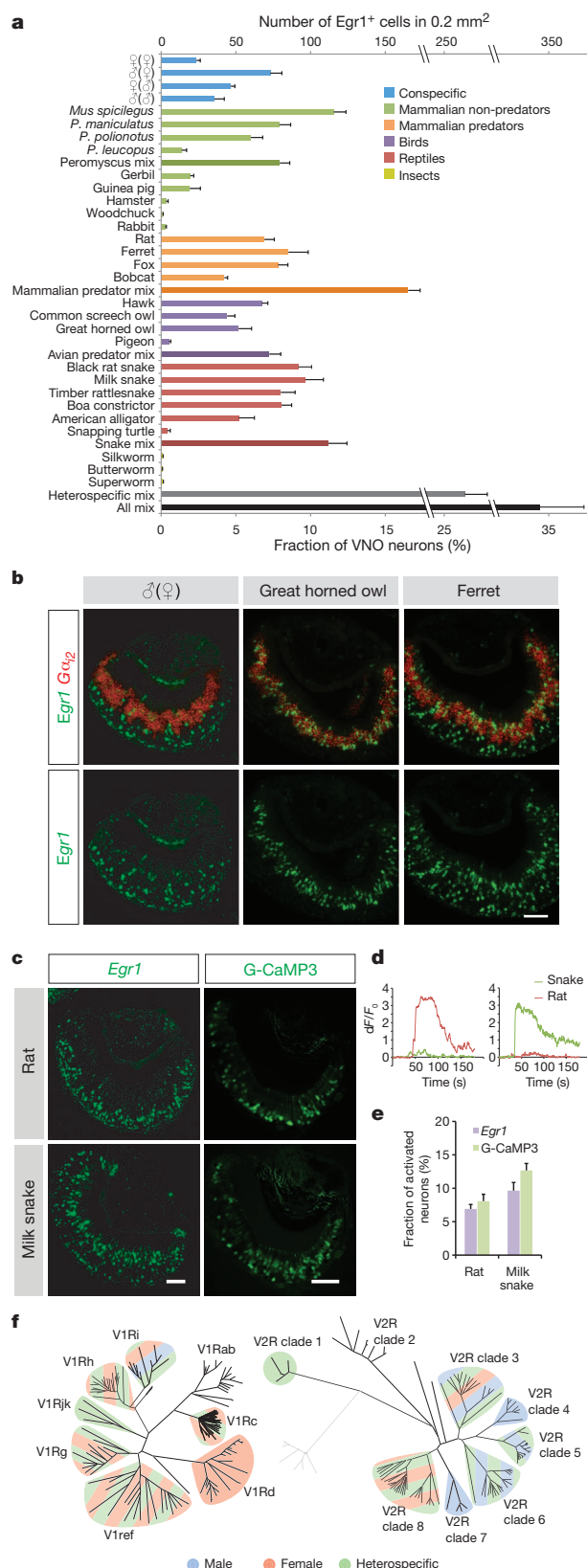


**Figure 1 | *Egr1* expression is robustly induced by pheromone-evoked VNO neuronal activation.** Female CD-1 mice were exposed to clean or male mouse bedding and their VNOs analysed for expression of various immediate early genes (IEGs). **a**, *In situ* hybridization with RNA probes to *Arc*, *c-Fos*, *c-Jun*, *Egr1*, *FosB* and *Nr4a1*. **b**, Numbers of IEG-positive cells after bedding exposure (10 sections per VNO,  $n = 3$  animals). Error bars, s.e.m. **c**, *TrpC2*, a cation channel involved in VNO signal transduction is required for *Egr1* induction. Female *TrpC2*<sup>+/+</sup> or *TrpC2*<sup>−/−</sup> mice were exposed to male conspecific bedding and *Egr1* expression was visualized in the VNO. Scale bar, 100  $\mu\text{m}$ .

<sup>1</sup>Department of Molecular and Cellular Biology, Center for Brain Science, Harvard University, Cambridge, Massachusetts 02138, USA. <sup>2</sup>Howard Hughes Medical Institute, Department of Molecular and Cellular Biology, Center for Brain Science, Harvard University, Cambridge, Massachusetts 02138, USA. <sup>†</sup>Present address: Ecole Normale Supérieure, Paris 75005, France.





To assess *Egr1* as a readout of VNO activation, we compared it to cue-evoked neuronal responses visualized by the genetically encoded calcium indicator, G-CaMP3 (ref. 16). Strikingly, *Egr1* and G-CaMP3 reported remarkably similar patterns of activities in the basal, or basal-plus-apical VNO neuroepithelium following exposure to rat and snake stimuli, respectively (Fig. 2c–e), confirming *Egr1* induction as an exquisitely sensitive and accurate marker of VNO neuronal activation.

**Figure 2 | Widespread activation of VNO receptors by conspecific and heterospecific cues.** **a**, Survey of ethologically relevant vomeronasal stimuli. Vomeronasal neural activation on exposure to conspecific and heterospecific cues was visualized by *Egr1* induction and quantified. Detection of female cues by males is designated as  $\varphi(\sigma^*)$ . Unless specified, female mice were used. Mixed heterospecific cues activated *Egr1* in significantly more cells than individual stimuli ( $P < 0.01$ , two-tailed *t*-test). Co-exposure to heterospecific and conspecific stimuli (all mix,  $n = 6$ ) resulted in significantly more *Egr1*-positive cells ( $P < 0.05$ , two-tailed *t*-test). **b**, Widespread activation of VNO neurons by conspecific and heterospecific cues. Shown are *in situ* hybridization results with probes against *Gx12* (red) and *Egr1* (green). **c**, Comparison between *Egr1* and G-CaMP3-evoked signal in response to rat or milk snake chemosignals. G-CaMP3 images are 10-s averages of  $\Delta F$  frames within stimulus period. **d**, Differential response profiles of neurons to rat or snake signals. Stimuli were perfused from 20 s to 60 s. **e**, Quantitative comparison between *Egr1* and G-CaMP3-evoked signals. The percentage of activated cells identified by G-CaMP3 ( $n = 356$  cells for rat stimuli,  $n = 566$  cells for snake stimuli, 9 VNO slices from 3 animals) among those responsive to 40 mM KCl was plotted in the graph. Data for *Egr1* were taken from **a**. The difference between *Egr1* and G-CaMP3 was not statistically significant ( $P > 0.1$ , two-tailed *t*-test). **f**, Clade-level maps of V1R (left) and V2R (right) activation show distinct clade specificity for male, female or heterospecific cues. Hatched patterns indicate response to multiple types of cues. Error bars, s.e.m. Scale bars, 100  $\mu\text{m}$ .

Next, we developed a high-throughput platform to uncover the receptors activated by specific cues. With the exception of widely expressed V2R2 receptors<sup>17</sup>, vomeronasal neurons are thought to express a unique receptor gene from the V1Rs or V2Rs. We generated 209 RNA probes that specifically identify individual or subgroups of VRs by *in situ* hybridization. A collection of clade-specific probes was designed to target all receptor sequences within each of the eight distinct V1R or V2R clades (Fig. 2f). Probes with higher specificity that readily distinguish a single or few closely related VR sequences were designed on the basis of divergent 5'-UTR/intron<sup>18</sup> and 3'-UTR regions in VR genes. The specificity of these probes for closely related VRs was validated by dual colour *in situ* hybridization (Supplementary Fig. 3). Although detecting all VRs at single gene resolution was technically impossible, our probes targeted 139 distinct VRs with a specificity of a single (or at most a few) gene.

We then used a hierarchical approach to systematically uncover VRs activated by distinct cues (Supplementary Figs 2b, 4). First, the co-expression of *Egr1* with either  $G\alpha_{i2}$ ,  $G\alpha_o$  or formyl peptide receptors (FPRs)<sup>19,20</sup> identified the nature of the activated neurons as expressing a V1R, V2R or FPR, respectively. Most stimuli activated both V1R- and V2R-expressing neurons, while a few activated only V1R- (hawk and owls) or V2R-expressing cells (rat, fox and male mouse cues in females) (Supplementary Table 1). We found no activation of FPR-expressing cells. We then assessed the specific V1R or V2R clades associated with the activated neurons (Fig. 2f, Supplementary Fig. 2c). Interestingly, some clades appeared specifically stimulated by a distinct class of cues, for example, V1Rd and V2R clades 4 and 7 by sex-specific cues. Subsequently, receptor specific probes were used to unmask the exact molecular identity of the *Egr1*-positive cells. By collecting data from 9,948 VNO slices, each containing approximately 1,000 neurons, we succeeded in the identification of 88 receptors (56 V1Rs and 32 V2Rs, 78 single and 10 unresolved receptors) associated with distinct cues (Supplementary Fig. 5, Supplementary Table 1, 2). Importantly, these receptors span most V1R and V2R clades, thus generating the most comprehensive functional map of vomeronasal receptors to date.

The vomeronasal system plays an essential part in regulating sex-specific behaviours. Previous reports suggest that vomeronasal neurons detect sex-specific cues in mouse urine, tear and saliva<sup>9,10,13,21,22</sup>, and Vmn2r116 (or V2Rp5) was identified as detecting the male pheromone ESP1 (ref. 6; Supplementary Fig. 6). Our strategy uncovered 28 receptors (25 single, 3 unresolved) detecting mouse cues, among which 26 detecting sex-specific cues (Fig. 3a–c, Supplementary Table 1). Only two receptors (Vlri9, Vlri10) responded to both male and female mouse cues, consistent with the desensitization of IEG induction *in*

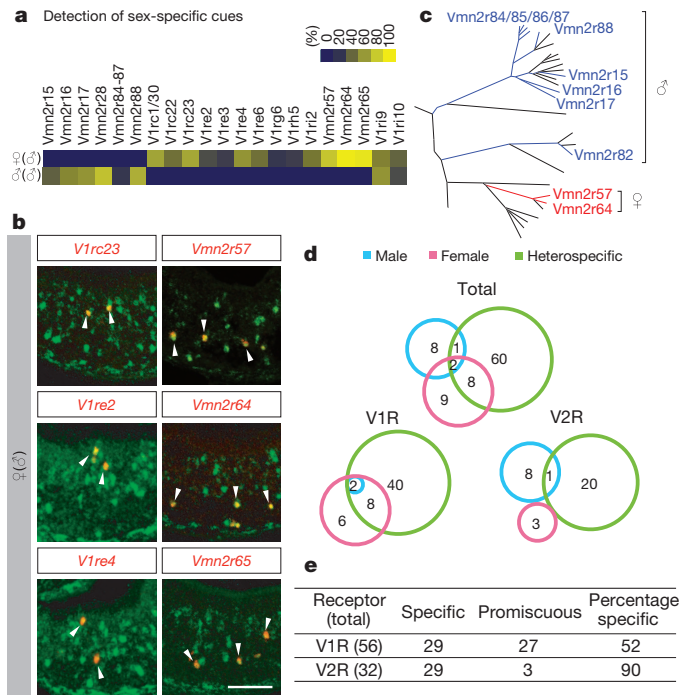


**Figure 3 | Receptor responses to sex-specific cues.** **a**, **b**, Male and female mouse cues are each detected by a specific subset of V1Rs and V2Rs. **a**, Heat maps representing the co-localization between *Egr1* and representative vomeronasal receptor genes (yellow, 100% overlap; dark blue, 0% overlap). **b**, *In situ* hybridization of *Egr1* (green) and individual receptors (red), with arrows marking co-localization of *Egr1* and receptor signals. Scale bars, 100  $\mu$ m. **c**, Clade organization of V2Rs detecting male (blue) or female (red) cues. **d**, Receptors detecting male (blue), female (red) and heterospecific (green) cues are largely distinct. **e**, V1Rs and V2Rs display distinct specificity. Shown are the numbers of receptors that detect unique types of cues (specific) versus multiple types (promiscuous) among the following categories: male, female, mammalian non-predator, mammalian predator, reptile, and avian predator.

*vivo* by self-secreted stimuli<sup>6</sup>. Four receptors (V1re2, V1re3, V1re6, V1rg6) were selectively activated by female cues in males and females, while a larger set of V1Rs and V2Rs responded to female cues only in males (Fig. 3a–c, Supplementary Table 1). In addition, responses to male-specific signals involved Vmn2r116, Vmn2r28, Vmn2r15, Vmn2r16 and Vmn2r17 in males and females, Vmn2r66 and Vmn2r82 in females, and Vmn2r84/85/86/87 and Vmn2r88 in males (Fig. 3a–c, Supplementary Table 1). Interestingly, no V1R was found to specifically respond to male cues. Thus, consistent with a previous report<sup>9</sup>, the detection of sex-specific cues appears to rely on a small and specific subset of VNO neurons, the identity of which is now clearly established. This molecular logic is likely to underlie the initiation of sex-dependent behavioural interactions, such as male–male aggression and mating behaviours.

Vomeronasal detection of heterospecific cues, or kairomones, is involved in adaptive defensive behaviours<sup>5,13,23</sup>. Indeed, rat bedding induces robust avoidance to the predator cues in *TrpC2*<sup>+/−</sup> but not in *TrpC2*<sup>−/−</sup> animals (Fig. 4g, h). Moreover, *TrpC2*<sup>−/−</sup> animals exhibited abnormal ingestive behaviour of the predator bedding, suggesting that VNO inputs also inhibit foraging<sup>24,25</sup> (Supplementary Fig. 7).

We report here the identity of 71 (63 single, 8 unresolved) receptors activated by heterospecific scents. Consistent with the distinct behavioural outputs generated by pheromones and kairomones, we found that only 11 receptors were common to both types of cues, whereas 60 were uniquely activated by heterospecific stimuli, and 17 by mouse cues only (Fig. 3d). The detection of kairomones thus emerges as a major function of the VNO<sup>5,13</sup>. The identity of one of the identified receptor population for the detection of predator cues was confirmed independently by *Egr1* activation in cells expressing YFP under the V1Rh7

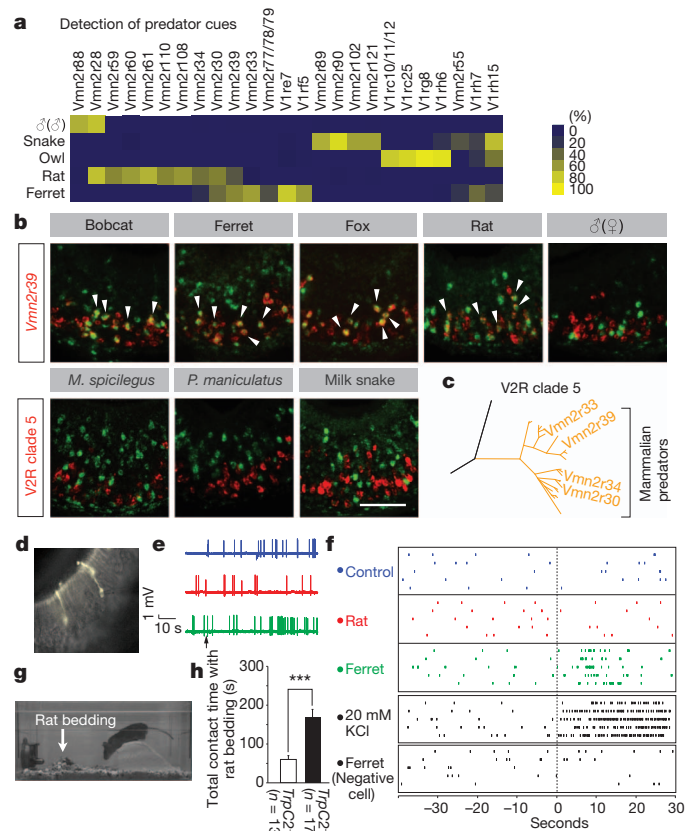


**Figure 4 | Receptor responses to heterospecific cues.** **a**, **b**, Predator cues are detected by a specific subset of V1Rs and V2Rs. **a**, Heat map representing the co-localization between *Egr1* and representative vomeronasal receptor genes (colour coding as Fig. 3a). **b**, *In situ* hybridization of *Egr1* (green) and vomeronasal receptors (red), with arrows marking co-localization of *Egr1* and receptor signals. Scale bar, 100  $\mu$ m. **c**, Mammalian predator cues commonly activate V2R clade 5 receptors. Owing to high homology among V2R clade 5 genes, the Vmn2r30, 33, 34, 39 probes detect multiple receptors. **d**, Fluorescence image showing a patched V1rh7-YFP neuron. The arrow indicates perfusion start. **e**, Loose-patch recordings of a V1rh7-YFP neuron. The stimulus perfusion started at −30 s and lasted 20 s. **f**, Spike raster for three different VNO neurons, showing responses of a V1rh7-YFP neuron to ferret, but not to rat stimuli, and no response of a V1rh7-YFP-negative neuron to ferret stimuli. The stimulus perfusion started at −30 s and lasted 20 s. **g**, Rat bedding (arrow) elicits robust avoidance behaviours in control *TrpC2*<sup>+/−</sup> mice, but significantly less in *TrpC2*<sup>−/−</sup> mice lacking VNO activity. **h**, Total contact time with rat bedding (s). \*\*\**P* < 0.0001 (two-tailed Student's *t*-test). Error bars, s.e.m. (*TrpC2*<sup>+/−</sup>, *n* = 13; *TrpC2*<sup>−/−</sup>, *n* = 17).

promoter<sup>26</sup> (Supplementary Fig. 8). Further, loose patch recording of V1Rh7-YFP expressing neurons demonstrated significant increase in firing rates following exposure to ferret, but not to rat stimuli ( $1.732 \pm 0.170$  Hz for ferret,  $0.420 \pm 0.061$  Hz for rat, *n* = 4) (Fig. 4d–f, Supplementary Fig. 9).

Remarkably, some receptors show unique association with distinct classes of predators. Vmn2r89 and Vmn2r121 were exclusively activated by scents from snakes, V1rc10/11/12 by owls. Also, up to 70% of V2R clade 5 neurons were activated by every mammalian predator tested, but not by sympatric non-predators (Fig. 4a–c, Supplementary Fig. 5, 10). Moreover, each predator cue generated a distinct receptor signature: for example, rat stimuli activate Vmn2r59, Vmn2r60, Vmn2r61, Vmn2r108 and Vmn2r110, all within clade 8, whereas ferret cues activate V1rf5 and Vmn2r77/78/79, suggesting that the mouse VNO has the sensory machinery to discriminate predator species.

We then searched for receptors detecting the sympatric species *Mus spicilegus* and *Mus musculus*, which diverged evolutionarily ~1.5 million years ago and do not breed in the wild<sup>27,28</sup>. Receptors activated by *M. spicilegus* and *M. musculus* male cues appear mostly distinct, though often closely related (Supplementary Figs 5, 11). For



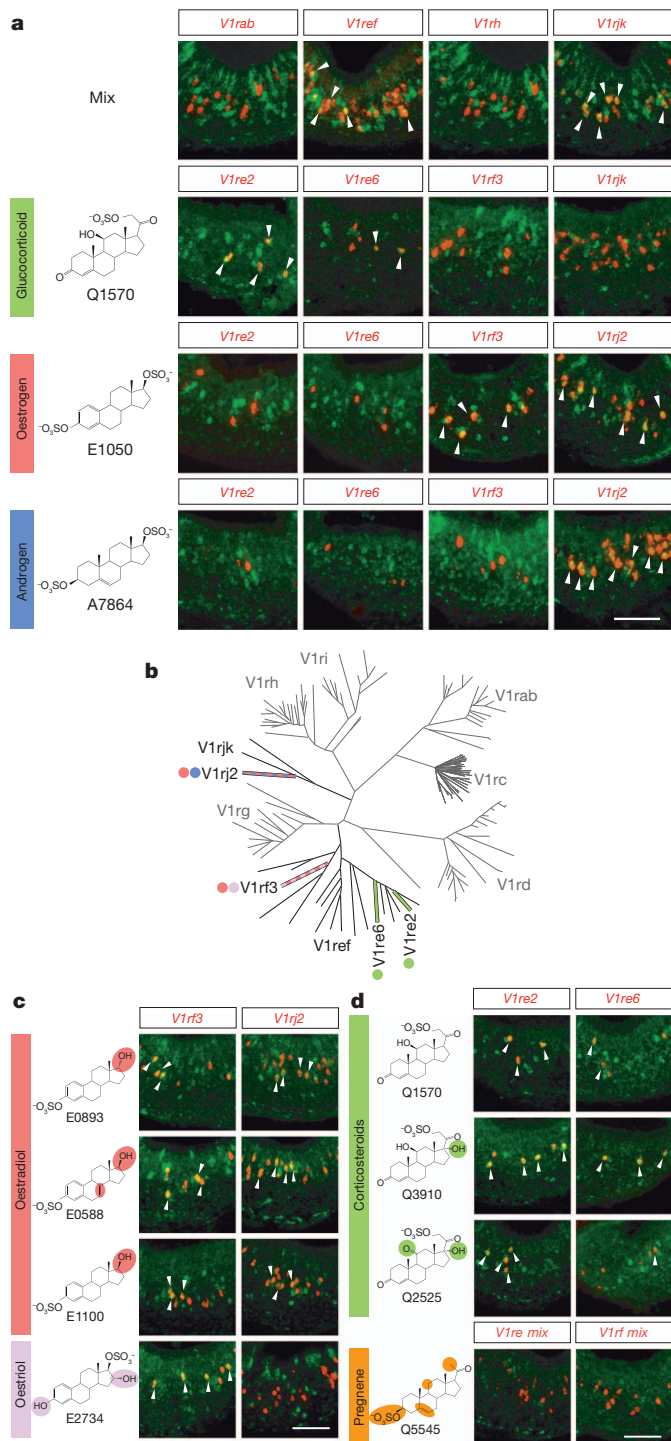


**Figure 5 | Sulphated steroids detection by V1Rs.** **a**, V1Ref and V1Rjk clade-specific probes (red) co-localize with *Egr1* (green) after VNO stimulation by a mix of steroids containing glucocorticoids such as Q1570 (green), oestrogens such as E1050 (red) and androgens such as A7864 (blue). Each of these compounds on its own elicits activity in distinct populations of vomeronasal neurons (V1re2, V1re6, V1rf3 and V1rj2), also represented in the molecular tree of V1R receptors (**b**). Specific receptors detecting each steroid are indicated by dots, using the same colour scheme as **a** and **c**. **c**, The three distinct oestradiols (red) activate both V1rf3 and V1rj2 whereas the oestril (purple) only activates V1rf3. **d**, The sulphate group position in pregnenes (corticosteroids in green, pregnenolone in orange) determines the specificity of ligand detection by V1re2 and V1re6. Differences in chemical structures among tested compounds are highlighted by coloured circles. Arrowheads mark co-localization between *Egr1* and receptor signals. Scale bar, 100  $\mu$ m.

example, Vmn2r8/9 and Vmn2r11, activated by *M. spicilegus*, and Vmn2r15, Vmn2r16 and Vmn2r17, activated by *M. musculus*, belong to clade 6 (Supplementary Fig. 11b). Likewise, Vmn2r69 (activated by *M. spicilegus*) and Vmn2r66 (activated by *M. musculus*) belong to clade 3. Thus, through the activation of specialized receptors, *M. musculus* may readily discriminate scents emitted by closely related but reproductively incompatible species, a property that could be linked to the reproductive isolation of these species.

V1Rs and V2Rs are associated with segregated neural pathways<sup>29</sup>, raising the possibility that fundamental functional differences may exist between the two families. Remarkably, our data suggest that V1Rs and V2Rs display different receptor properties. Nearly half of the V1Rs (27 out of 56) exhibit generalized activation by multiple cues (Fig. 3e), including signals with apparent conflicting behavioural significance. For example, receptors within the V1Rh, V1Rc and V1Re clades were activated by mouse, predator and non-predator cues (Supplementary Tables 1 and 2, Supplementary Fig. 12). In contrast, most V2Rs (29 out of 32) are activated by cues reflecting a unique ethological context such as a male, a female, or a given type of predator or non-predator. In addition, hierarchical clustering across all identified receptors revealed clear segregation between V1Rs and V2Rs (Supplementary Fig. 5). These results suggest that V1R and V2R pathways may encode different types of information: individual V2Rs appear uniquely poised to encode information about the identity of emitters with clear behavioural significance—for example, the sex of a conspecific or the nature (predator or competitor) of a heterospecific. In contrast, individual V1Rs may encode other forms of biologically relevant information.

To gain further insight into the molecular logic of V1R-mediated signalling, we investigated the detection of sulphated steroids, which are thought to account for 80% of VNO neuronal activation by female urine<sup>30</sup> (probably through V1Rs<sup>11</sup>). Our data show that, when male mice were exposed to a mix of synthetic steroid sulphates, receptors from V1Ref and V1Rjk clades were specifically activated (Fig. 5a, b). We then tested individual compounds to attempt the pairing of specific steroid ligands with their cognate receptors. Corticosterone-21 sulphate (Q1570), a compound in female urine<sup>30</sup>, strongly activated V1re2 and more weakly V1re6 cells (Fig. 5a, b). Both receptors were shown in earlier experiments to be specifically activated by female cues (Fig. 3a). In addition, we uncovered strong activation of V1rf3 by 17 $\beta$ -oestradiol sulphate (E1050) and V1rj2 by 17 $\beta$ -oestradiol disulphate (A7864) (Fig. 5a), although these two receptors were not activated by female bedding, indicating that these steroids are not secreted under normal conditions.

Thus, our approach efficiently achieved single compound resolution, offering the unique opportunity to test the receptor specificity to a variety of individual chemicals. We further tested four sulphated oestrogen compounds structurally related to E1050, and three additional sulphated pregnenes structurally related to Q1570. V1rf3 appeared broadly selective to oestradiols, oestriols and related stereoisomers, regardless of sulphate positions, but did not respond to androgens or glucocorticoids (Fig. 5c). Interestingly, no other V1rf receptor was activated by these ligands. In contrast, V1rj2 was activated by androgens and oestradiols but not oestriols. Similarly, V1re2 and V1re6 selectively detected corticosteroids (Fig. 5d). Therefore, V1R receptors can distinguish distinct structural classes of steroids. Androgens, oestrogens and glucocorticoids are ubiquitous though sensitive reporters of the animal endocrine state. Our results thus suggest that V1Rs may serve as detectors of the physiological status of an animal.

In conclusion, our data have begun to uncover the molecular logic by which vomeronasal receptors of different families, clades and receptor sequences extract biological information and trigger appropriate behavioural responses to animals of a given sex, species and physiological status. The collection of receptors uncovered in this study provides a molecular foundation to further dissect the neural circuits governing social and sexual communication in rodents.



## METHODS SUMMARY

Stimulus exposure was conducted by introducing a subject animal (male or female CD-1 mice, 8 to 14 weeks old) in a fresh cage containing distinct animal cues for 30 min (for Fig. 1) or 40 min (for Figs 2–5). The dissected VNOs were embedded in OCT (Tissue-Tek) and frozen in dry ice. Cryosections (16 µm) of VNO were subjected to RNA *in situ* hybridization using IEG and VR probes.

**Full Methods** and any associated references are available in the online version of the paper at [www.nature.com/nature](http://www.nature.com/nature).

**Received 13 January; accepted 8 August 2011.**

**Published online 21 September 2011.**

- Dulac, C. & Torello, A. T. Molecular detection of pheromone signals in mammals: from genes to behaviour. *Nature Rev. Neurosci.* **4**, 551–562 (2003).
- Zhang, X., Marcucci, F. & Firestein, S. High-throughput microarray detection of vomeronasal receptor gene expression in rodents. *Front. Neuroscience* **4**, 164 (2010).
- Dulac, C. & Axel, R. A novel family of genes encoding putative pheromone receptors in mammals. *Cell* **83**, 195–206 (1995).
- Buck, L. & Axel, R. A novel multigene family may encode odorant receptors: a molecular basis for odor recognition. *Cell* **65**, 175–187 (1991).
- Papes, F., Logan, D. W. & Stowers, L. The vomeronasal organ mediates interspecies defensive behaviors through detection of protein pheromone homologs. *Cell* **141**, 692–703 (2010).
- Haga, S. *et al.* The male mouse pheromone ESP1 enhances female sexual receptive behaviour through a specific vomeronasal receptor. *Nature* **466**, 118–122 (2010).
- Leinders-Zufall, T., Ishii, T., Mombaerts, P., Zufall, F. & Boehm, T. Structural requirements for the activation of vomeronasal sensory neurons by MHC peptides. *Nature Neurosci.* **12**, 1551–1558 (2009).
- Boschat, C. *et al.* Pheromone detection mediated by a V1r vomeronasal receptor. *Nature Neurosci.* **5**, 1261–1262 (2002).
- He, J., Ma, L., Kim, S., Nakai, J. & Yu, C. R. Encoding gender and individual information in the mouse vomeronasal organ. *Science* **320**, 535–538 (2008).
- Leinders-Zufall, T. *et al.* Ultrasensitive pheromone detection by mammalian vomeronasal neurons. *Nature* **405**, 792–796 (2000).
- Holekamp, T. F., Turaga, D. & Holy, T. E. Fast three-dimensional fluorescence imaging of activity in neural populations by objective-coupled planar illumination microscopy. *Neuron* **57**, 661–672 (2008).
- Stowers, L., Holy, T. E., Meister, M., Dulac, C. & Koentges, G. Loss of sex discrimination and male-male aggression in mice deficient for TRP2. *Science* **295**, 1493–1500 (2002).
- Ben-Shaul, Y., Katz, L. C., Mooney, R. & Dulac, C. *In vivo* vomeronasal stimulation reveals sensory encoding of conspecific and allospecific cues by the mouse accessory olfactory bulb. *Proc. Natl Acad. Sci. USA* **107**, 5172–5177 (2010).
- Berghard, A. & Buck, L. B. Sensory transduction in vomeronasal neurons: evidence for  $G\alpha_o$ ,  $G\alpha_{i2}$ , and adenylyl cyclase II as major components of a pheromone signaling cascade. *J. Neurosci.* **16**, 909–918 (1996).
- Jia, C. & Halpern, M. Subclasses of vomeronasal receptor neurons: differential expression of G proteins ( $G\alpha_{i2}$  and  $G\alpha_o$ ) and segregated projections to the accessory olfactory bulb. *Brain Res.* **719**, 117–128 (1996).
- Tian, L. *et al.* Imaging neural activity in worms, flies and mice with improved GCaMP calcium indicators. *Nature Methods* **6**, 875–881 (2009).
- Martini, S., Silvotti, L., Shirazi, A., Ryba, N. J. & Tirindelli, R. Co-expression of putative pheromone receptors in the sensory neurons of the vomeronasal organ. *J. Neurosci.* **21**, 843–848 (2001).
- Stewart, R. & Lane, R. P. V1R promoters are well conserved and exhibit common putative regulatory motifs. *BMC Genomics* **8**, 253 (2007).
- Liberles, S. D. *et al.* Formyl peptide receptors are candidate chemosensory receptors in the vomeronasal organ. *Proc. Natl Acad. Sci. USA* **106**, 9842–9847 (2009).
- Rivière, S., Challet, L., Flügge, D., Spehr, M. & Rodriguez, I. Formyl peptide receptor-like proteins are a novel family of vomeronasal chemosensors. *Nature* **459**, 574–577 (2009).
- Holy, T. E., Dulac, C. & Meister, M. Responses of vomeronasal neurons to natural stimuli. *Science* **289**, 1569–1572 (2000).
- Taha, M., McMillon, R., Napier, A. & Wekesa, K. S. Extracts from salivary glands stimulate aggression and inositol-1, 4, 5-triphosphate (IP3) production in the vomeronasal organ of mice. *Physiol. Behav.* **98**, 147–155 (2009).
- Samuelson, C. L. & Meredith, M. The vomeronasal organ is required for the male mouse medial amygdala response to chemical-communication signals, as assessed by immediate early gene expression. *Neuroscience* **164**, 1468–1476 (2009).
- Brown, J., Kotler, B., Smith, R. & Wirtz, W. The effects of owl predation on the foraging behavior of heteromyid rodents. *Oecologia* **76**, 408–415 (1988).
- Sundell, J. *et al.* Variation in predation risk and vole feeding behaviour: a field test of the risk allocation hypothesis. *Oecologia* **139**, 157–162 (2004).
- Wagner, S., Gresser, A. L., Torello, A. T. & Dulac, C. A multireceptor genetic approach uncovers an ordered integration of VNO sensory inputs in the accessory olfactory bulb. *Neuron* **50**, 697–709 (2006).
- Chevret, P., Veyrunes, F. & Britton-Davidian, J. Molecular phylogeny of the genus *Mus* (Rodentia: Murinae) based on mitochondrial and nuclear data. *Biol. J. Linn. Soc.* **84**, 417–427 (2005).
- Guénet, J. L. & Bonhomme, F. Wild mice: an ever-increasing contribution to a popular mammalian model. *Trends Genet.* **19**, 24–31 (2003).
- Dulac, C. & Wagner, S. Genetic analysis of brain circuits underlying pheromone signaling. *Annu. Rev. Genet.* **40**, 449–467 (2006).
- Nodari, F. *et al.* Sulfated steroids as natural ligands of mouse pheromone-sensing neurons. *J. Neurosci.* **28**, 6407–6418 (2008).

**Supplementary Information** is linked to the online version of the paper at [www.nature.com/nature](http://www.nature.com/nature).

**Acknowledgements** We acknowledge H. Fisher, H. Hoekstra, E. Kay, M. Kirchgeßner, N. Uchida, A. Wang, X.-D. Wang, B. Watson, W. Tong, Harvard Museum of Natural History, Harvard Concord Field Station, Museum of Science, Boston, and New England Wildlife Center, for providing stimulus materials used in this study, L. Looger for the G-CaMP3 construct, M. Wienisch, F. Markopoulos and D. Mak for help with electrophysiology and imaging experiments, and B. Goetze and the Harvard Center for Biological Imaging for help with microscopy. We also thank members of the Dulac laboratory for critical reading of the manuscript, S. Andreeva for technical support and R. Hellmiss for help with figure artwork. This work was supported by the NIDCD at the National Institute of Health, the Howard Hughes Medical Institute and the Damon Runyon Cancer Research Foundation (Y.I., DRG-1981-08).

**Author Contributions** Y.I. and C.D. designed the study. Y.I., S.S. and T.T. designed and generated RNA probes, performed RNA *in situ* hybridization, and analysed data. L.P.-L. performed pilot experiments for data shown in Fig. 1 and produced recombinant ESP1. Y.I. and V.K. performed calcium imaging and electrophysiology. V.N.M. supervised physiology experiments. Y.I. and C.D. wrote the paper.

**Author Information** Reprints and permissions information is available at [www.nature.com/reprints](http://www.nature.com/reprints). The authors declare no competing financial interests. Readers are welcome to comment on the online version of this article at [www.nature.com/nature](http://www.nature.com/nature). Correspondence and requests for materials should be addressed to C.D. ([dulac@fas.harvard.edu](mailto:dulac@fas.harvard.edu)).

## METHODS

**Sampling of animal stimuli.** Bedding materials used in this study were all freshly sampled from cages that house live animals (Harvard University, Harvard Museum of Natural History, Harvard Concord Field Station, Tufts University, Museum of Science, Boston, and New England Wildlife Center). Soiled bedding represents the most complete stimulus source for animals, and is also of ecological relevance. Bedding materials typically absorb a wide range of chemical stimuli excreted by animals, such as urine, faeces, saliva, fur, and other gland secretions. Since different animals are housed in different environments, we flexibly adjusted the sampling procedures. For instance, chemosignals emitted by heterospecific mammals and birds (male rat, female fox, male ferret, female bobcat, male *Peromyscus*, male *M. spicilegus*, male and female gerbils, male and female hamsters, male and female rabbits, woodchuck, pigeon, red tailed hawk, screech owl, and great horned owl) were sampled as soiled bedding (paper, woodchips or corn cob). For reptiles, we sampled faeces, urate and other gland secretions absorbed in woodchips or paper. These bedding materials were directly used for exposure experiments (as described separately below). For aquatic animals such as alligators, only faecal pellets were sampled. For insect larvae, live animals were directly used for exposure experiments. Some predators such as snake and predatory birds were fed mice as part of their diet, and we took great care to avoid potential odour contamination. For example, on bedding sampling we avoided areas where mouse carcass was present in animal cages. Second, to sample milk snake odour, which we extensively used for our study, we changed bedding after the feeding to avoid potential odour contamination from mice. We also tested materials from multiple individuals whenever possible. Judging from the number of *Egr1*-positive cells, we did not find extensive individual variability in these samples. If multiple individuals were not available, especially for bobcat, hawk and great horned owl, we tested stimulus samples from different collection dates. We stored these bedding materials at 4 °C for the short term (one week) and at -20 °C for the long term. These materials, even after long term storage at -20 °C when the amount of volatiles was significantly reduced, did not appreciably lose their ability to robustly stimulate vomeronasal neurons.

For conspecific stimuli, to represent a potential diversity of chemical cues emitted by different subspecies of mice, we collected bedding samples from 5 different strains of mice: BALB/c (Jackson Labs), PWD/PhJ (Jackson Labs), CAST/Eij (Jackson Labs), Idaho<sup>31</sup> and Chuuk<sup>31</sup>, and exposed these samples as a mixture. It is known that mice secrete different vomeronasal cues reflecting their physiological states, for example, different phases of oestrous<sup>9</sup>, prompting us to sample materials freshly from cages that house multiple animals over 1 week. Thus, conspecific stimuli used in our study probably contain chemosignals secreted over different phases of the oestrous cycles. We stored these materials at 4 °C for the short term and -20 °C for the long term.

**Stimulus exposure.** For most exposure experiments involving bedding stimuli, approximately 50 ml (in volume) of bedding containing animal cues were placed in a clean cage. We introduced a subject mouse (male or female CD-1, from 8 weeks to 14 weeks old, Charles River), which voluntarily made extensive direct contacts with introduced stimuli in freely behaving conditions. The animals were exposed to stimuli for 30 min (for Fig. 1) or 40 min (for Figs 2–5). Subsequently, the dissected VNOs were embedded in OCT (Tissue-Tek) and frozen in dry ice. VNO cryosections (16 µm) were used for RNA *in situ* hybridization using IEG and vomeronasal receptor probes. Control experiments were conducted using fresh bedding in an identical manner. For insect larvae exposure, 3–4 insect larvae were directly introduced to the cages. For alligator stimuli, a few faecal pellets were used. For heterospecific mix exposure experiments, ~100 ml mixture of the following bedding sample was used: *Peromyscus* (*P. maniculatus*, *P. leucopus*, *P. polionotus*), mammalian predators (bobcat, fox, ferret, rat), avian predators (screech owl, great horned owl, red tail hawk), reptiles (rat snake, milk snake, rattlesnake, boa, alligator), and *M. spicilegus*. For pure chemicals such as ESP1 and sulphated steroids, ~5 µl of Ringer's (in mM; 115 NaCl, 5 KCl, 2 CaCl<sub>2</sub>, 2 MgCl<sub>2</sub>, 25 NaHCO<sub>3</sub> and 5 HEPES) containing the stimuli were directly spotted on each nostril. Recombinant ESP1 was purified as a GST fusion protein overexpressed in *Escherichia coli* using pET41 vector (Novagen), followed by thrombin cleavage to release the ESP1 peptide. 2 µg of the peptide was exposed to each animal.

**Sulphated steroid exposure.** Steroids were purchased from Steraloids. A mix of steroids (A6940, epitestosterone sodium sulphate; A7864, 5-androsten-3β, 17β-diol disulphate; E1050, 17β-oestradiol sulphate; E0893, 17α-oestradiol sulphate; P3817, allopregnanolone sulphate; P8200, epipregnanolone sulphate, Q1570, corticosterone 21-sulphate; Q3470, deoxycorticosterone 21-glucoside; each at 250 µM in Ringer's) were used for initial screens. Subsequently, individual steroids (Q1570; E1050; A7864; E0893; E0588, 17β-dihydroequilin 3-sodium sulphate; E1100, 17β-oestradiol 3-sulphate; E2734, oestriol 17-sulphate; Q3910, hydrocortisone 21-sodium sulphate; Q2525, cortisone 21-sulphate; Q5545, 3β-hydroxy-5-pregnen-20-one 3-sulphate) were used at 500 µM in Ringer's. 5 µl of steroid

solution were spotted on each nostril of male CD-1 animals (8–14 weeks), and the animals were exposed to steroids for 40 min. Experiments were conducted for at least three animals.

**Preparation of RNA probes.** For immediate early gene probes, we have cloned complementary DNA of *Arc*, *c-Fos*, *c-Jun*, *Egr1*, *FosB* and *Nr4a1* in approximately 900-base-pair (bp) segments to pCRII-TOPO or pCR4-TOPO vector (Invitrogen). Antisense cRNA probes were synthesized using T3, T7 or Sp6 polymerases (Promega) and digoxigenin (DIG) or fluorescein (FITC) labelling mix (Roche) from PCR templates. All IEG probes consisted of a cocktail of 2–3 probes to cover nearly the full length of these messenger RNAs.

For V1R clade-specific probes, we cloned full length coding sequence of V1R receptors (V1rab: *V1ra1*, *a2*, *a3*, *a4*, *a5*, *a6*, *a7*, *a8*, *b1*, *b2*, *b7*, *b8*, *b9*; V1rc: *V1rc3*, *c8*, *c10*, *c16*, *c28*; V1rd: *V1rd6*, *d9*, *d11*, *d12*, *d14*, *d22*, *Vmn1r167*; V1ref: *V1re1*, *e2*, *e3*, *e4*, *e6*, *e7*, *e8*, *e9*, *e10*, *e11*, *e12*, *e13*, *Vmn1r224*, *f1*, *f2*, *f3*, *f4*, *f5*; V1rh: *V1rh1*, *h20*; V1ri: *V1ri1*, *i3*, *i4*, *i5*, *i6*, *i8*; V1rjk: *V1rj2*, *j3*, *k1*) and combined these probes to generate a clade-specific probe set. For V1rg receptors, ~1 kilobase (kb) 5'-UTR/intron sequences of the following genes were used: *V1rg1*, *g2*, *g3*, *g4*, *g5*, *g6*, *g7*, *g8*, *g9*, *g10*, *g11*, *g12*, *Vmn1r77*, which were combined with *V1rl* cDNA probe to generate the V1Rgl clade probe set.

To generate clade-specific V2R probes, we cloned the first ~900 bp of annotated V2R receptor coding sequence (V2R clade 1: *Vmn2r55*; V2R clade 2: *Vmn2r19*, *Vmn2r20*, *Vmn2r24*; V2R clade 3: *Vmn2r65*, *Vmn2r69*, *Vmn2r76*, *Vmn2r77*; V2R clade 4: *Vmn2r115*; V2R clade 5: *Vmn2r28*, *Vmn2r48*; V2R clade 6: *Vmn2r8*, *Vmn2r15*, *Vmn2r17*, *Vmn2r84*, *Vmn2r89*, *Vmn2r118*; V2R clade 7: *Vmn2r18*, *Vmn2r81*, *Vmn2r83*, *Vmn2r120*; V2R clade 8: *Vmn2r57* 3'-UTR probe, *Vmn2r58*, *Vmn2r63*, *Vmn2r58*, *Vmn2r90*, *Vmn2r93*, *Vmn2r96*, *Vmn2r97*, *Vmn2r99*, *Vmn2r102*, *Vmn2r104*, *Vmn2r105*, *Vmn2r106*, *Vmn2r108*, *Vmn2r110*, and *Vmn2r64* 3'-UTR probe) and combined these probes to generate clade-specific probe sets. To generate cRNA probes specific to individual V1R genes, we cloned ~1 kb 5'-UTR intron sequence of V1R genes to pCRII vector (Invitrogen). To produce cRNA probes specific to individual V2R receptors, we cloned ~600 bp of V2R 3'-UTR segments. These RNA probes were first used to test mRNA expression. We found that some annotated vomeronasal receptor genes did not appear to be expressed, since these RNA probes gave no discernible signals. For all vomeronasal receptor genes, for which we could confirm the expression, we tested the specificity of these probes by dual colour *in situ* hybridization using DIG and FITC probes and used for receptor mapping experiments. Probes generated in our study to detect specific receptors are listed in Supplementary Table 1. The VR nomenclature was based on that of GenBank and Mouse Genome Informatics.

**RNA *in situ* hybridization.** Single colour RNA *in situ* hybridization was conducted essentially as described<sup>32</sup>. We used DIG labelled cRNA probes at 2 ng µl<sup>-1</sup> and used a hybridization temperature of 65 °C for experiments shown in Fig. 1. For *Egr1* *in situ* hybridization experiments shown in Fig. 2, we used 68 °C as the hybridization temperature. Dual colour fluorescence *in situ* hybridization was conducted in the following steps. First, the tissue was fixed in 4% formaldehyde/1× PBS for 10 min, and washed 3 times with 1× PBS for 3 min each. The tissues were treated with acetylation solution (0.1 M triethanolamine with 2.5 µl ml<sup>-1</sup> acetic anhydride) for 10 min. After 3 washes with 1× PBS, each for 5 min, the slide was incubated with the pre-hybridization solution (50% formamide, 5× SSC, 5× Denhardt's, 2.5 mg ml<sup>-1</sup> yeast RNA, 0.5 mg ml<sup>-1</sup> herring sperm DNA) for 2 h. The hybridization buffer (4% dextran sulphate, Millipore, added to pre-hybridization buffer) containing FITC labelled *Egr1* probes (a cocktail of three probes, each at 50 pg µl<sup>-1</sup>) and DIG labelled VR probes (at 0.5 ng µl<sup>-1</sup> for cDNA probes, and 1 ng µl<sup>-1</sup> for 5'-UTR-intron and 3'-UTR probes) was heated at 95 °C for 3 min and immediately chilled on ice for 5 min. The hybridization solution was applied to the slides, which were covered with parafilm and incubated in a sealed chamber for 16 h at 68 °C. Following hybridization, the slides were washed with 5× SSC once for 5 min, and with 0.2× SSC three times, each for 20 min at 68 °C. Slides were washed at room temperature with 0.2× SSC for 5 min and subsequently with TNT buffer (100 mM Tris, pH 7.5, 150 mM NaCl, 0.05% Tween 20) for 5 min.

After the post-hybridization washes, 200 µl of anti-FITC-POD (Roche, at 1/250 dilution in TNB blocking buffer, Perkin-Elmer) was applied and incubated for 3 h at room temperature. Slides were washed with TNT buffer for a total of 1 h, with buffer exchanges every 10 min. The signal was developed using the TSA biotin plus kit (Perkin Elmer), as per manufacturer's protocol. The slides were washed with TNT buffer 3 times, each for 5 min, and subsequently treated with 3% H<sub>2</sub>O<sub>2</sub>/1× PBS to kill residual peroxidase activity. Slides were washed again 3 times with 1× PBS and TNT, each for 5 min. DIG antibody solution (anti-DIG-POD, Roche, at 1/500 dilution, and Streptavidin-Alexa488, Invitrogen, at 1/250 dilution in TNB buffer) were applied to the slides and incubated overnight at 4 °C. After washing slides with TNT (6 times, 10 min each), the signal was developed using the TSA

Cy3 plus kit (Perkin Elmer) as per manufacturer's protocol. Slides were washed with TNT (3 times, 5 min each and once for 1 h), and tissues were mounted with Vectashield (Vector labs) containing  $8 \mu\text{g ml}^{-1}$  DAPI. All the microscopy images were acquired using LSM510 or AxioImager Z2 (Zeiss).

**Analysis of *in situ* hybridization images.** For single colour *in situ* hybridization images, quantitation was conducted using a minimum of 10 VNO sections per animal and 3 animals (data in Fig. 1) or 3–4 animals (data in Fig. 2). Since we found that  $0.2 \text{ mm}^2$  represents areas occupied by medial cryostat sections of the VNO and contain approximately 1,000 VNO cells, we used the average number of *Egr1*-positive cells per  $0.2 \text{ mm}^2$  in Fig. 1, and we converted these numbers to percentage of activated neurons among total VNO neurons in Fig. 2. For dual colour *in situ* hybridization, we quantitated the co-localization of *Egr1* and receptor signals over four sections per VNO, for a minimum of three animals. We then calculated the percentage of activated neurons in specific receptor neurons, for each odour class, and generated a co-localization matrix. In many cases, we found that individual receptor mapping is unnecessary when the hierarchical screen can unequivocally demonstrate that there are no activated neurons in specific receptor clades. In these cases, we input zero values to the co-localization matrix. For hierarchical clustering of the co-localization matrix, we used the Cluster program (<http://bonsai.hgc.jp/~mdehoon/software/cluster/software.htm>), with average linkage in Euclidian distance. To generate the clustering diagram in Supplementary Fig. 4, we calculated the average number of receptor neurons per receptor in 12 sections and used this as a weight. The heat map and clustering dendrogram were generated using the Java Treeview program (<http://jtreeview.sourceforge.net/>).

**Behavioural assay.** Male *TrpC2* mice (+/+ or -/-, 8–14 weeks old, ref. 12) were single-housed three days before the experiment in a manner blind to the experimenter. The behaviour experiment was conducted by introducing 50 ml volume of fresh or rat bedding to one side of the cage, away from the nest area. The behaviours of the subject mice were video recorded and total contact time as well as ingestive behaviour were scored by an individual blind to the genotype. We defined ingestive behaviour as animals engaged in ingestion while holding a food pellet with two forepaws.

**Generation of OMP-GCaMP3 transgenic line.** pJOMP plasmid containing the rat olfactory marker protein (OMP) genomic sequence<sup>33</sup> was modified so that the GCaMP3 ORF sequence completely replaces the OMP ORF. Linearized vector was used for pronuclear injection (performed by Harvard Genome Modification Facility), and transgenic founders were further backcrossed to C57Bl/6 mice to establish an OMP-GCaMP3 line. This line expresses the transgene uniformly throughout the vomeronasal epithelium and showed no sign of reported cell toxicity<sup>15</sup>.

**Calcium imaging on VNO slices.** Calcium imaging was carried out essentially as described<sup>9</sup>, using 5–8-week-old female OMP-GCaMP3 mice. The VNOs were acutely dissected, separated from bones, and embedded in 4% low melting point agar in mACSF (in mM; 130 NaCl, 5 KCl, 1 MgCl<sub>2</sub>, 2.5 CaCl<sub>2</sub>, 1.25 NaH<sub>2</sub>PO<sub>4</sub>, 25

NaHCO<sub>3</sub>, 10 glucose). The coronal vibratome sections (200  $\mu\text{m}$ ) were cut, and slices were kept in continuously oxygenated mACSF for up to 8 h at 25 °C. The flow rate of the stimulus was approximately  $0.3 \text{ ml min}^{-1}$ , and we delivered stimulus for 40 s. All imaging was conducted at 25 °C. The fluorescence changes due to calcium transients were monitored using a LSM710 microscope with a GaAsP detector (Zeiss). We used a 1:100 dilution of freshly sampled rat urine from 2–6-month-old CD male rats (Charles River) in mACSF. For snake stimuli, shredded snake bedding (that is, paper) was extracted with mACSF, filtered and used for stimulation. To quantify the number of activated cells, we first generated  $\Delta F$  images by subtracting an average of 20 s frames corresponding to initial resting period from the raw images. We then created an average  $\Delta F$  image consisting of 10 s frames corresponding to the maximum fluorescence interval (shown in Fig. 2c). This operation significantly reduced the fluorescence signals from spontaneous activity, which is typically short (lasting 1–2 s) and consists of small bursts, and enriched evoked activity, which is a more sustained (more than 10 s), larger rise in fluorescent intensity. The fluorescence traces of individual positive cells were further examined to confirm the sustained nature of the response. The number of activated cells was quantified using ImageJ. To quantify the number of viable cells during the imaging experiments, we counted the number of G-CaMP3-positive cells responsive to 40 mM KCl in mACSF.

**Electrophysiology.** Loose patch recordings were performed at room temperature with a Multiclamp 700B (Axon Instruments). Data were recorded at 10 kHz, low pass filtered at 2 kHz and digitized with a Digidata 1440A digitizer (Axon Instruments). Borosilicate glass (Sutter Instruments Co., o.d. 1.5 mm, i.d. 0.86 mm) patch pipettes (3–8 M $\Omega$ ) were pulled on a Flaming/Brown micropipette puller (Sutter Instrument Co.). The same mACSF was used as for the pipette solution. Data were acquired with pClamp and analysed in Matlab. Pneumatic electronic valves (Clippard Instruments) were used to control the flow of stimuli. Electronic valves were controlled via digital output from the Digidata 1440 A digitizer. The valves were opened for 20 s in every stimulated trial. For rat stimulus, we used 1:200 dilution of rat urine (male CD rats, Charles River, 2–6 months old) in mACSF. For ferret stimuli, ~50 ml volume of ferret bedding containing urine, faeces, fur and gland excretions was extracted with 50 ml of mACSF overnight at 4 °C, then filtered and used for experiments.

11. Miller, R. A. *et al.* Mouse (*Mus musculus*) stocks derived from tropical islands: new models for genetic analysis of life-history traits. *J. Zool.* **250**, 95–104 (2000).
12. Schaeren-Wiemers, N. & Gerfin-Moser, A. A single protocol to detect transcripts of various types and expression levels in neural tissue and cultured cells: *in situ* hybridization using digoxigenin-labelled cRNA probes. *Histochemistry* **100**, 431–440 (1993).
13. Danciger, E., Mettling, C., Vidal, M., Morris, R. & Margolis, F. Olfactory marker protein gene: its structure and olfactory neuron-specific expression in transgenic mice. *Proc. Natl Acad. Sci. USA* **86**, 8565–8569 (1989).



# A natural polymorphism alters odour and DEET sensitivity in an insect odourant receptor

Maurizio Pellegrino<sup>1†</sup>, Nicole Steinbach<sup>1†</sup>, Marcus C. Stensmyr<sup>3</sup>, Bill S. Hansson<sup>3</sup> & Leslie B. Vosshall<sup>1,2</sup>

Blood-feeding insects such as mosquitoes are efficient vectors of human infectious diseases because they are strongly attracted by body heat, carbon dioxide and odours produced by their vertebrate hosts. Insect repellents containing DEET (*N,N*-diethyl-*meta*-toluamide) are highly effective, but the mechanism by which this chemical wards off biting insects remains controversial despite decades of investigation<sup>1–11</sup>. DEET seems to act both at close range as a contact chemorepellent, by affecting insect gustatory receptors<sup>12</sup>, and at long range, by affecting the olfactory system<sup>1–11</sup>. Two opposing mechanisms for the observed behavioural effects of DEET in the gas phase have been proposed: that DEET interferes with the olfactory system to block host odour recognition<sup>1–7</sup> and that DEET actively repels insects by activating olfactory neurons that elicit avoidance behaviour<sup>8–11</sup>. Here we show that DEET functions as a modulator of the odour-gated ion channel formed by the insect odourant receptor complex<sup>13,14</sup>. The functional insect odourant receptor complex consists of a common co-receptor, ORCO (ref. 15) (formerly called OR83B; ref. 16), and one or more variable odourant receptor subunits that confer odour selectivity<sup>17</sup>. DEET acts on this complex to potentiate or inhibit odour-evoked activity or to inhibit odour-evoked suppression of spontaneous activity. This modulation depends on the specific odourant receptor and the concentration and identity of the odour ligand. We identify a single amino-acid polymorphism in the second transmembrane domain of receptor OR59B in a *Drosophila melanogaster* strain from Brazil that renders OR59B insensitive to inhibition by the odour ligand and modulation by DEET. Our data indicate that natural variation can modify the sensitivity of an odour-specific insect odourant receptor to odour ligands and DEET. Furthermore, they support the hypothesis that DEET acts as a molecular ‘confusant’ that scrambles the insect odour code, and provide a compelling explanation for the broad-spectrum efficacy of DEET against multiple insect species.

Previous work has shown that the odour of *Drosophila* food potently attracts adult *D. melanogaster* vinegar flies and that DEET blocks this attraction<sup>5,7</sup>. The behavioural effects of DEET require an intact olfactory system and the olfactory co-receptor ORCO<sup>7</sup>. These results implicated the olfactory system in the observed behavioural effects but failed both to distinguish between the two competing models of action for DEET and to determine whether DEET acts on the odour-specific odourant receptors, ORCO or both. We carried out electrophysiological recordings of *Drosophila* olfactory sensory neurons (OSNs) to test these competing possibilities.

In response to the suggestion that DEET and odours may interact in the vapour phase<sup>9,10</sup>, we first quantified the respective amounts of vapour-phase 1-octen-3-ol emitted from the stimulus pipette in the presence and absence of DEET, using solid-phase microextraction (SPME) followed by gas chromatography mass spectroscopy analysis (GC–MS). The SPME measurements coupled to GC–MS (Fig. 1a) showed that the addition of a second filter paper containing pure

DEET in the stimulus pipette had no significant effect on the release of 1-octen-3-ol ( $10^{-2}$  dilution). Thus, we can rule out any fixative role of DEET under the conditions used here.

We next performed extracellular recordings to measure the effect of DEET on responses elicited by odours in *Drosophila* OSNs housed within the ab2 (Fig. 1a and Supplementary Fig. 1) or ab3 (Supplementary Fig. 2) olfactory hairs, or sensilla, on the fly antenna. Each of these sensilla houses two OSNs expressing different odourant receptors with unique odour response profiles<sup>17</sup>. We measured the activity of these OSNs simultaneously and compared their responses to odour with and without co-presentation of DEET (Fig. 1b, c).

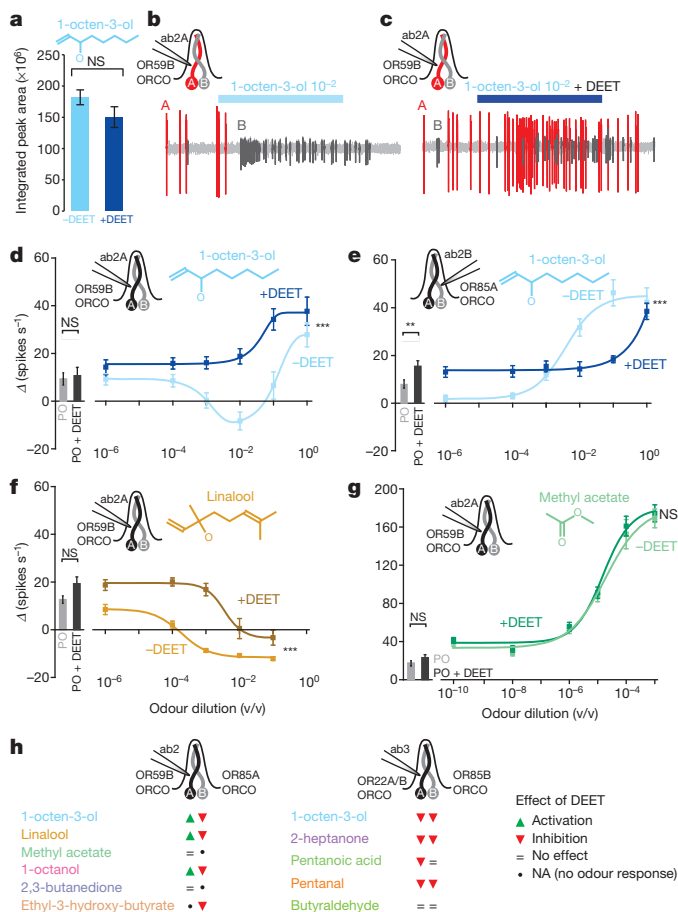
The effect of DEET on four OSNs stimulated with ten structurally diverse odours was complex and dependent on odourant receptor, odour and concentration. In some OSNs, DEET suppressed odour-mediated inhibition (Fig. 1d, f and Supplementary Fig. 1a), in others it decreased odour-induced activation (Fig. 1e, Supplementary Fig. 1b, d, e and Supplementary Fig. 2a–g) and in others it had no effect (Fig. 1g and Supplementary Figs 1c and 2h–j). Moreover, the effects of DEET were strongly concentration dependent, such that high odour concentrations often overcame the effects of DEET (Fig. 1 and Supplementary Figs 1 and 2). DEET presented alone, without odour stimuli, elicited no response above that evoked by solvent in ab2A and ab3A neurons, slightly activated ab2B neurons and slightly inhibited ab3B neurons; but responses were considerably smaller than those elicited by cognate odour ligands (Supplementary Fig. 3). Therefore, DEET alone has a negligible effect on olfactory responses in ab2 and ab3 neurons.

Notably, 1-octen-3-ol presented in a dilution of  $10^{-2}$  had opposite effects on the two neurons housed in ab2 sensilla, inhibiting the ab2A neuron expressing OR59B–ORCO (Fig. 1d) and activating the ab2B neuron expressing OR85A–ORCO (Fig. 1e). Co-application of DEET inverted OSN responses to odour, leading to activation of the ab2A neuron (Fig. 1d) and suppressing the odour-induced activation of the ab2B neuron (Fig. 1e). Similar opposite effects of DEET were observed when the ab2 sensillum was stimulated with a different odour, 1-octanol (Supplementary Fig. 1a, b).

Taken together, our results support the hypothesis that DEET acts as a molecular confusant, scrambling the *Drosophila* odour code by direct modulation of odourant receptor activity dependent on the type of odour and its concentration (Fig. 1h). Recent work examining the effect of DEET on mosquito odourant receptors in heterologous cells supports this hypothesis<sup>18</sup>.

Because the effects of DEET varied with the specific OSN and odour tested, it seems unlikely that DEET acts directly and solely on the conserved co-receptor ORCO, which is co-expressed in all the OSNs examined here. To determine whether DEET acts on the odour-specific odourant receptor subunit, we focused on the pharmacology of the OR59B–ORCO complex in ab2A OSNs. 1-octen-3-ol inhibits basal activity of OR59B–ORCO at low concentrations but acts as an agonist at high concentrations (Fig. 1d). DEET interfered with inhibition of

<sup>1</sup>Laboratory of Neurogenetics and Behaviour, The Rockefeller University, 1230 York Avenue, Box 63, New York, New York 10065, USA. <sup>2</sup>Howard Hughes Medical Institute, The Rockefeller University, 1230 York Avenue, Box 63, New York, New York 10065, USA. <sup>3</sup>Max Planck Institute for Chemical Ecology, Department of Evolutionary Neuroethology, Hans Knöll Strasse 8, 07745 Jena, Germany. †Present addresses: Department of Molecular & Cell Biology, University of California, Berkeley, California 94720 USA (M.P.); Integrated PhD Program in Cellular, Molecular and Biomedical Studies, Columbia University, New York, New York 10032, USA (N.S.).



OR59B-ORCO by 1-octen-3-ol, 1-octanol and linalool, but had no effect on odour-dependent activation by methyl acetate and 2,3-butanedione (Fig. 1g and Supplementary Fig. 1c). Notably, DEET had no effect on the OR59B-ORCO activation seen at higher concentrations of 1-octen-3-ol. This selective effect on inhibition might be explained by the presence on the OR59B receptor of distinct 1-octen-3-ol-interaction sites, a high-affinity site that inhibits the odorant receptor complex and is modulated by DEET and a low-affinity DEET-independent site that activates the odorant receptor complex.

To investigate the mechanistic basis of OR59B modulation by DEET, we turned to analysis of this receptor in *D. melanogaster* strains collected around the world. Polymorphisms in natural populations have been previously connected to different sensitivity to odours in

humans<sup>19,20</sup>, and oxygen and carbon dioxide sensing in the nematode *Caenorhabditis elegans*<sup>21</sup>. We reasoned that naturally occurring polymorphisms in insect odorant receptors might modify odorant receptor/odorant interaction sites and affect their sensitivity to DEET. To search for putative polymorphisms that affect DEET responses, we assessed responses of ab2A neurons to 1-octen-3-ol in  $10^{-2}$  dilution in the absence or presence of DEET in 18 wild-type *D. melanogaster* strains from locations around the world, and compared these responses with those obtained in the  $w^{1118}$  laboratory control strain (Fig. 2a, b and Supplementary Fig. 4a). In each strain, ab2 sensilla were identified by the characteristic size and location of the sensilla and responses of the ab2A cell to its cognate ligand, methyl acetate (data not shown). In 17 of the 18 strains, DEET increased responses of ab2A neurons to  $10^{-2}$  1-octen-3-ol (Fig. 2b). However, ab2A neurons in the Brazilian strain Boa Esperança were not inhibited by 1-octen-3-ol at any concentration tested and were therefore insensitive to modulation by DEET (Figs 2c and 3a, b and Supplementary Fig. 4b). In addition to the loss of inhibition by 1-octen-3-ol, the ab2A cell in the Brazilian strain showed robust activation by 1-octanol and ethyl hexanoate, odours that normally inhibit the ab2A cell in wild-type strains. Inhibition by linalool was equivalent in wild-type and Boa Esperança strains (Fig. 3e). Excitatory responses to methyl acetate, ethyl acetate and 2,3-butanedione, both in the absence and presence of DEET, did not differ when compared with the corresponding  $w^{1118}$  neuron (Fig. 3c, d and Supplementary Fig. 5; data not shown). In control experiments, we confirmed that the odour response profiles of ab2A and ab2B OSNs in the Brazilian strain are otherwise similar to that of our  $w^{1118}$  control strain (Fig. 3f and Supplementary Fig. 5).

We proposed that a genetic polymorphism in *Or59b* in the Boa Esperança strain may account for the changed responses to odour and DEET. We therefore sequenced and compared the coding region of *Or59b* in the 19 strains with the published *Or59b* sequence (NCBI reference sequence, NP\_523822.1), and found seven missense polymorphisms and 36 silent polymorphisms among all strains (Supplementary Table 1 and Supplementary Fig. 6). The protein sequence of OR59B in Boa Esperança is referred to as OR59B<sup>Boa</sup> and varies from the NCBI reference at four amino-acid residues (Val41Phe, Val91Ala, Tyr376Ser and Val388Ala). Among these, two are unique to this strain: Val41Phe, located in the amino terminus near transmembrane domain 1 (TM1), and Val91Ala, located within TM2 (Fig. 4a, b and Supplementary Fig. 6). On the basis of our within-strain sampling, we detected only one protein variant per strain except for the  $w^{1118}$  control strain, for which we identified two sequences: one identical to the published OR59B sequence (OR59B<sup>NCBI REF</sup>), and one containing two missense changes (OR59B<sup>M352I T376S</sup>; Fig. 4a and Supplementary Table 1). We analysed electrophysiological recordings obtained from the  $w^{1118}$  control strain for each odour tested and found no evidence that the responses sort into two phenotypically separable clusters. Therefore, we assume that the OR59B<sup>NCBI REF</sup> and OR59B<sup>I352 S376</sup> haplotypes are functionally equivalent, at least for the odours tested in this study. The coding sequences of *Orco* in the  $w^{1118}$  and Boa Esperança strains did not differ from the NCBI reference (data not shown), which suggests that the protein sequence variations in the odour-specific subunit OR59B, rather than the co-receptor ORCO, eliminate inactivation by low concentrations of 1-octen-3-ol and thereby render the odorant receptor complex insensitive to modulation by DEET.

To test the functional consequences of the four OR59B missense changes in the Boa Esperança strain, we generated transgenic flies carrying receptor variants each containing one of the four changes (Val41Phe, Val91Ala, Tyr376Ser or Val388Ala), a combination of the two unique to Boa Esperança (Val41Phe and Val91Ala) or those shared with other strains (Tyr376Ser and Val388Ala), based on the OR59B<sup>NCBI REF</sup> backbone. OR59B variants were selectively expressed in the *Drosophila* *Ahelo* 'empty neuron' system<sup>17,22</sup>, in which the endogenous odour-specific odorant receptors in ab3A OSNs were replaced

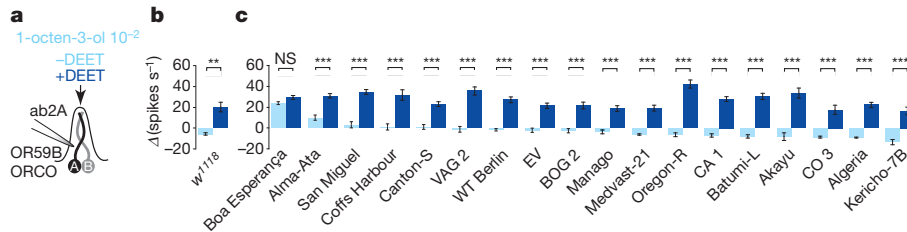


**Figure 2 | OR59B-ORCO sensitivity to DEET varies across wild-type *D. melanogaster* strains.** **a**, Schematic of the screening protocol:  $10^{-2}$  1-octen-3-ol was delivered in the absence and presence of DEET. **b–c**, Bar plots of odour-

evoked responses of the  $w^{1118}$  strain (**b**) and 18 wild-type strains (**c**) to  $10^{-2}$  1-octen-3-ol in the absence (light blue) or presence (dark blue) of DEET (*t*-test with Bonferroni correction; mean  $\pm$  s.e.m.,  $n = 10$ –17).

with our OR59B mutants (Fig. 4c and Supplementary Fig. 7). As expected,  $10^{-2}$  1-octen-3-ol caused inhibition of ab3A neurons expressing OR59B<sup>NCBI REF</sup> and activation of ab3A neurons expressing OR59B<sup>Boa</sup> (Fig. 4c). Whereas OR59B<sup>T376A</sup>, OR59B<sup>V388A</sup> and OR59B<sup>T376A V388A</sup> showed normal inhibition to this odour, any variant of OR59B containing the Val91Ala change showed a loss of odour inhibition by 1-octen-3-ol and insensitivity to DEET (Fig. 4c). This demonstrates that the Val91Ala change is sufficient to phenocopy the electrophysiological properties of the endogenous Boa Esperança OR59B (Fig. 4c). It has previously been shown that responses of

OR59B expressed in the empty neuron faithfully recapitulate receptor function measured in the endogenous ab2A neuron<sup>23</sup>. We therefore assume that a strain carrying only the OR59B<sup>V91A</sup> polymorphism would have the same phenotype as Boa Esperança.

DEET shows behavioural efficacy in insects as diverse as *Drosophila*<sup>5,7</sup> and mosquitoes<sup>1–4,6,8–11</sup>. We have shown that a single, naturally occurring polymorphism in an odour-specific odorant receptor can modify receptor interactions with an inhibitory odour and render the receptor insensitive to modulation by DEET. These results provide compelling evidence that DEET interacts directly with an odour-specific odorant receptor. Consistent with this, recent work showed that an odour-specific OR subunit is required for the behavioural effects of DEET on mosquito larvae<sup>11</sup>. Our data imply a complexity in ligand-binding interactions within a single insect odorant receptor complex that bears further investigation. The Val91Ala polymorphism is located in the second predicted transmembrane domain but little is known about which domains of this novel class of odour-gated ion channels contribute to ligand binding or ion channel function<sup>13,14</sup>. A recent study implicated the third predicted transmembrane

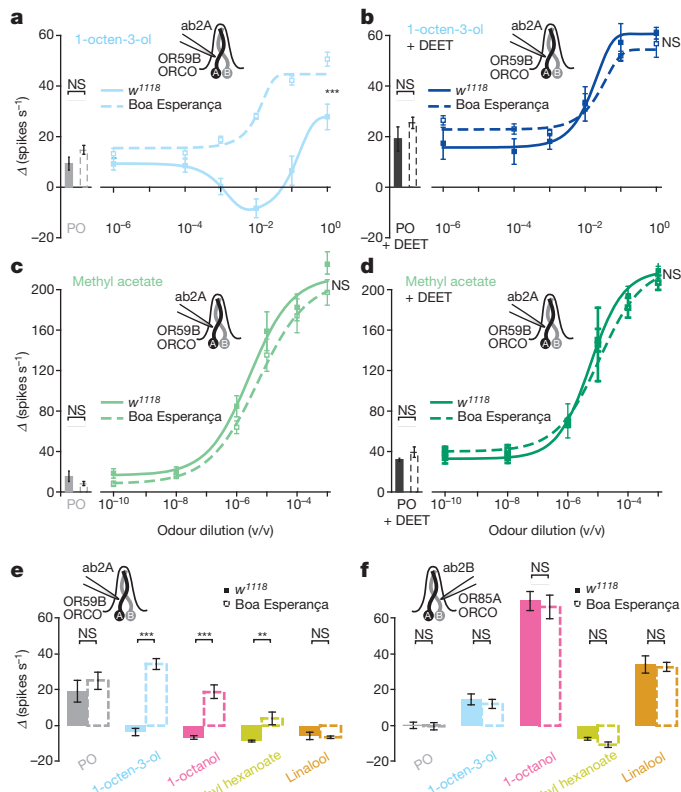


**Figure 3 | OR59B-ORCO neurons in the Boa Esperança strain are insensitive to modulation by DEET.** **a–d**, Dose–response curves of the OR59B-ORCO ab2A OSN in wild-type  $w^{1118}$  (solid line) and Boa Esperança (dashed line) strains stimulated with increasing concentrations of 1-octen-3-ol (**a**, **b**) or methyl acetate (**c**, **d**), with (**b**, **d**) or without (**a**, **c**) DEET (*F*-test with Bonferroni correction; mean  $\pm$  s.e.m.,  $n = 5$ –14). The dose–response curve of  $w^{1118}$  to 1-octen-3-ol in **a** and **b** is reproduced from Fig. 1d for comparison. Bar plots next to the dose–response curves represent responses of the solvent paraffin oil in the absence (grey bar) or presence (black bar) of DEET (*F*-test with Bonferroni correction; mean  $\pm$  s.e.m.,  $n = 5$ –11). **e**, **f**, Bar plots comparing responses of OR59B-ORCO in ab2A (**e**) and OR85A-ORCO in ab2B (**f**) in  $w^{1118}$  (solid bar) and Boa Esperança (dashed bar) strains to  $10^{-2}$  1-octen-3-ol,  $10^{-1}$  1-octanol,  $10^{-1}$  ethyl hexanoate and  $10^{-1}$  linalool (*t*-test with Bonferroni correction; mean  $\pm$  s.e.m.,  $n = 9$ –11).

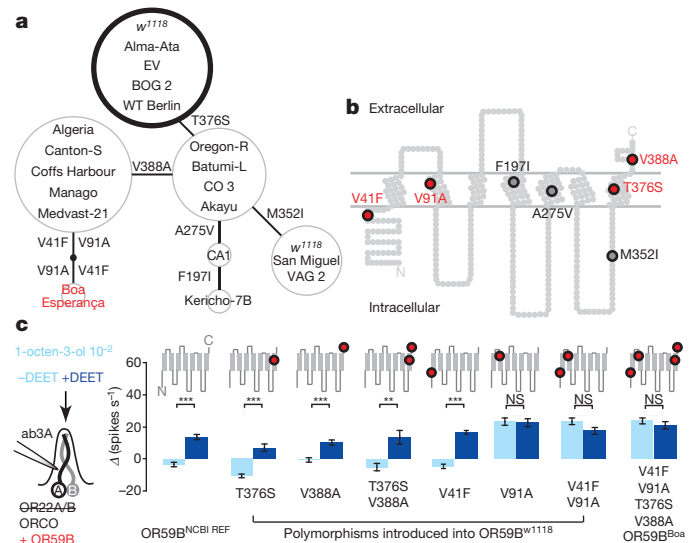


**Figure 4 | A single natural polymorphism in OR59B confers insensitivity to DEET.** **a**, Haplotype network of OR59B protein variants. Each circle represents a unique OR59B protein variant, its size proportional to the number of strains containing each variant. Connecting lines show the amino-acid substitutions that separate each variant. The bold circle represents the OR59B<sup>NCBI REF</sup> variant with NCBI accession code NP\_523882.1. The Boa Esperança strain is shown in red. **b**, Snake plot of OR59B showing the location of missense polymorphisms. Changes that differentiate Boa Esperança from the NCBI reference are shown in red. **c**, Bar plots show the responses of *Or59b* variants ectopically expressed in ab3A neurons lacking endogenous OR22A and OR22B to  $10^{-2}$  1-octen-3-ol in the absence (light blue) or presence (dark blue) of DEET. The locations of variant amino acids in OR59B are depicted in the cartoon snake plot on top of each set of bar graphs (*t*-test with Bonferroni correction; mean  $\pm$  s.e.m.,  $n = 7$ –11).



domain of an insect odorant receptor in ligand interactions<sup>24</sup>, and additional structure–function work of this nature will ultimately reveal how these membrane proteins interact with odorants and modulators including DEET. Although Val and Ala are both amino acids with small aliphatic side chains, Val–Ala substitutions have been shown to affect other cation channels<sup>25</sup>. It therefore is plausible that this change would affect the function of the odour-gated ion channel subunit encoded by OR59B. We speculate that the Val91Ala polymorphism inactivates a high-affinity binding site for 1-octen-3-ol that locks the receptor into a closed configuration at low odour concentration. A separate site on the receptor would have a low-affinity binding site that would lead to activation. In this model, DEET would selectively interfere with the high-affinity binding site. Future investigation of the structure–function relation of this receptor is needed to test these ideas. Genetic insensitivity to DEET has previously been shown to exist in both *Drosophila* flies<sup>5</sup> and *Aedes aegypti* mosquitoes<sup>10</sup> but the genes responsible remain unknown. It will be interesting to investigate whether accumulated odorant receptor polymorphisms contribute to these phenotypes.

It has recently been proposed that DEET directly activates behavioural repulsion through the activation of odorant receptors that mediate avoidance behaviours<sup>8–10</sup>. The insect odorant receptor repertoire is highly diverse with very low protein similarity across insect species<sup>26–28</sup>. Furthermore, different species respond very selectively to host odour cues that meet disparate ecological needs<sup>29,30</sup>. It seems unlikely that a single molecule like DEET would activate a different yet similarly potent repulsive behaviour in all insects tested. Instead, our data support the hypothesis that DEET is a broad-selectivity insect odorant receptor modulator that alters the fine-tuning of the insect olfactory system. DEET-mediated scrambling of the odour code would interfere with behavioural responses as diverse as mosquitoes orienting to host odours produced by humans<sup>29</sup> and the attraction of *Drosophila* to yeast on rotting fruit<sup>30</sup>.

## METHODS SUMMARY

**Fly strains and molecular biology.** *D. melanogaster* stocks were maintained on conventional cornmeal–agar–molasses medium in a 12-h-light, 12-h-dark cycle at 25 °C. Details of molecular biology manipulations, all primers and fly strains are in Methods.

**Single-sensillum extracellular recordings.** Recordings of female fly antennae were performed as described previously<sup>7</sup> and are detailed in Methods. The respective amounts of 1-octen-3-ol emitted from the stimulus pipettes with and without DEET was investigated through SPME and linked GC–MS analysis as detailed in Methods.

**Full Methods** and any associated references are available in the online version of the paper at [www.nature.com/nature](http://www.nature.com/nature).

Received 17 September 2010; accepted 8 August 2011.

Published online 21 September 2011.

1. Davis, E. E. & Sokolove, P. G. Lactic acid-sensitive receptors on the antennae of the mosquito, *Aedes aegypti*. *J. Comp. Physiol. A* **105**, 43–54 (1976).
2. McIver, S. B. A model for the mechanism of action of the repellent DEET on *Aedes Aegypti* (Diptera: Culicidae). *J. Med. Entomol.* **18**, 357–361 (1981).
3. Dogan, E. B., Ayres, J. W. & Rossignol, P. A. Behavioural mode of action of DEET: inhibition of lactic acid attraction. *Med. Vet. Entomol.* **13**, 97–100 (1999).
4. Dogan, E. B. & Rossignol, P. A. An olfactometer for discriminating between attraction, inhibition, and repellency in mosquitoes (Diptera: Culicidae). *J. Med. Entomol.* **36**, 788–793 (1999).
5. Reeder, N. L., Ganz, P. J., Carlson, J. R. & Saunders, C. W. Isolation of a deet-insensitive mutant of *Drosophila melanogaster* (Diptera: Drosophilidae). *J. Econ. Entomol.* **94**, 1584–1588 (2001).
6. Kline, D. L., Bernier, U. R., Posey, K. H. & Barnard, D. R. Olfactometric evaluation of spatial repellents for *Aedes aegypti*. *J. Med. Entomol.* **40**, 463–467 (2003).

7. Ditzgen, M., Pellegrino, M. & Vosshall, L. B. Insect odorant receptors are molecular targets of the insect repellent DEET. *Science* **319**, 1838–1842 (2008).
8. Xia, Y. *et al.* The molecular and cellular basis of olfactory-driven behavior in *Anopheles gambiae* larvae. *Proc. Natl Acad. Sci. USA* **105**, 6433–6438 (2008).
9. Syed, Z. & Leal, W. S. Mosquitoes smell and avoid the insect repellent DEET. *Proc. Natl Acad. Sci. USA* **105**, 13598–13603 (2008).
10. Stanczyk, N. M., Brookfield, J. F., Ignell, R., Logan, J. G. & Field, L. M. Behavioral insensitivity to DEET in *Aedes aegypti* is a genetically determined trait residing in changes in sensillum function. *Proc. Natl Acad. Sci. USA* **107**, 8575–8580 (2010).
11. Liu, C. *et al.* Distinct olfactory signaling mechanisms in the malaria vector mosquito *Anopheles gambiae*. *PLoS Biol.* **8**, e1000467 (2010).
12. Lee, Y. S., Kim, S. H. & Montell, C. Avoiding DEET through insect gustatory receptors. *Neuron* **67**, 555–561 (2010).
13. Sato, K. *et al.* Insect olfactory receptors are heteromeric ligand-gated ion channels. *Nature* **452**, 1002–1006 (2008).
14. Wicher, D. *et al.* *Drosophila* odorant receptors are both ligand-gated and cyclic-nucleotide-activated cation channels. *Nature* **452**, 1007–1011 (2008).
15. Larsson, M. C. *et al.* Or83b encodes a broadly expressed odorant receptor essential for *Drosophila* olfaction. *Neuron* **43**, 703–714 (2004).
16. Vosshall, L. B. & Hansson, B. S. A unified nomenclature system for the insect olfactory co-receptor. *Chem. Senses* **36**, 497–498 (2011).
17. Hallem, E. A. & Carlson, J. R. Coding of odors by a receptor repertoire. *Cell* **125**, 143–160 (2006).
18. Bohbot, J. D. & Dickens, J. C. Insect repellents: modulators of mosquito odorant receptor activity. *PLoS ONE* **5**, e12138 (2010).
19. Keller, A., Zhuang, H., Chi, Q., Vosshall, L. B. & Matsunami, H. Genetic variation in a human odorant receptor alters odour perception. *Nature* **449**, 468–472 (2007).
20. Menashe, I. *et al.* Genetic elucidation of human hyperosmia to isovaleric acid. *PLoS Biol.* **5**, e284 (2007).
21. McGrath, P. T. *et al.* Quantitative mapping of a digenic behavioral trait implicates globin variation in *C. elegans* sensory behaviors. *Neuron* **61**, 692–699 (2009).
22. Gross, S. P., Guo, Y., Martinez, J. E. & Welte, M. A. A determinant for directionality of organelle transport in *Drosophila* embryos. *Curr. Biol.* **13**, 1660–1668 (2003).
23. Hallem, E. A., Ho, M. G. & Carlson, J. R. The molecular basis of odor coding in the *Drosophila* antenna. *Cell* **117**, 965–979 (2004).
24. Nichols, A. S. & Luetje, C. W. Transmembrane segment 3 of *Drosophila melanogaster* odorant receptor subunit 85b contributes to ligand-receptor interactions. *J. Biol. Chem.* **285**, 11854–11862 (2010).
25. Laish-Farkash, A. *et al.* A novel mutation in the HCN4 gene causes symptomatic sinus bradycardia in Moroccan Jews. *J. Cardiovasc. Electrophysiol.* **21**, 1365–1372 (2010).
26. Robertson, H. M., Warr, C. G. & Carlson, J. R. Molecular evolution of the insect chemoreceptor gene superfamily in *Drosophila melanogaster*. *Proc. Natl Acad. Sci. USA* **100** (suppl. 2), 14537–14542 (2003).
27. Robertson, H. M. & Wanner, K. W. The chemoreceptor superfamily in the honey bee, *Apis mellifera*: expansion of the odorant, but not gustatory, receptor family. *Genome Res.* **16**, 1395–1403 (2006).
28. Bohbot, J. *et al.* Molecular characterization of the *Aedes aegypti* odorant receptor gene family. *Insect Mol. Biol.* **16**, 525–537 (2007).
29. Takken, W. & Knols, B. G. Odor-mediated behavior of Afrotropical malaria mosquitoes. *Annu. Rev. Entomol.* **44**, 131–157 (1999).
30. Stensmyr, M. C., Giordano, E., Balloi, A., Angioy, A. M. & Hansson, B. S. Novel natural ligands for *Drosophila* olfactory receptor neurons. *J. Exp. Biol.* **206**, 715–724 (2003).

**Supplementary Information** is linked to the online version of the paper at [www.nature.com/nature](http://www.nature.com/nature).

**Acknowledgements** We thank C. Bargmann, K. Lee, K. Scott, L. Stowers and members of the Vosshall lab for discussion and comments on the manuscript; and K. Weniger for technical assistance with the SPME and GC–MS experiments. This work was funded in part by a grant to R. Axel and L.B.V. from the Foundation for the National Institutes of Health through the Grand Challenges in Global Health Initiative and by a grant to L.B.V. from the NIH (R01 DC008600). L.B.V. is an investigator at the Howard Hughes Medical Institute. M.C.S. and B.S.H. are supported by the Max Planck Society.

**Author Contributions** M.P. carried out all the experiments and analysed the data. N.S. contributed to sequencing *Or59b* in the 19 strains and generated the *Or59b* mutants. M.C.S. and B.S.H. designed and supervised the SPME collections and GC–MS analysis in Fig. 1a. M.P. and L.B.V. together designed the experiments, interpreted the results, produced the figures and wrote the paper.

**Author Information** Reprints and permissions information is available at [www.nature.com/reprints](http://www.nature.com/reprints). The authors declare no competing financial interests. Readers are welcome to comment on the online version of this article at [www.nature.com/nature](http://www.nature.com/nature). Correspondence and requests for materials should be addressed to L.B.V. ([leslie.vosshall@rockefeller.edu](mailto:leslie.vosshall@rockefeller.edu)).

## METHODS

**Genomic DNA.** DNA was prepared according to the Quick Fly Genomic DNA Prep protocol from the Berkeley Drosophila Genome Project (<http://www.fruitfly.org/about/methods/inverse.pcr.html>). DNA (1.5 µl) was used for amplification using the KOD PCR Kit (Novagen). For *Or59b*, primers were designed to anneal to the 5' and 3' untranslated regions of the *w<sup>1118</sup> Or59b* locus: 5'-gaattcTCCGGG TATAAAGTGCAGGTGCTGGCACCG-3' (forward); 5'-ctcgagGCTCTTTTTT GCGGGGGCTCATGGGTGCAG-3' (reverse).

*Orco* was amplified using primers that amplify the complete coding region: 5'-gaattcATGACAACCTCGATGCAG-3' (forward); 5'-caattgCTTGAGCTGCA CCAGCACCA-3' (reverse).

PCR products were cloned into pGEM-T Easy (Promega Corporation), sequenced (GENEWIZ, Inc.) and analysed using SeqMan software (DNASTAR, Inc.). For each strain, at least four independent samples were analysed, derived from at least two different genomic preparations and two different PCR reactions. These were sequenced and compared to NCBI reference sequences for each gene (*Or59b*: NM\_079098.1; *Orco*: NM\_079511.4).

**Complementary DNA preparation and transgenic flies.** Total RNA was extracted from *w<sup>1118</sup>* and Boa Esperança antennae using the RNeasy Mini Kit (QIAGEN).

Complementary DNA (cDNA) synthesis was performed according to the SuperScript III First-Strand Synthesis System for RT-PCR (Invitrogen) using oligo(dT) primers. *Or59b* cDNA from both *w<sup>1118</sup>* and Boa Esperança was amplified using these gene-specific primers: 5'-gaattcATGGCGGTGTCAAGCT AATCAAACCG-3' (forward); 5'-ctcgagTTACTGGAAGTCTCGGCCAGATT CA-3' (reverse).

PCR products representing full-length *w<sup>1118</sup> Or59b<sup>NCBI REF</sup>* and *Or59b<sup>Boa</sup>* cDNAs were cloned into pGEM-T Easy, completely sequenced and subcloned into the pUAST attB vector<sup>31</sup> using EcoRI and XhoI restriction sites.

Single point mutations were introduced into the *w<sup>1118</sup> Or59b<sup>NCBI REF</sup>* cDNA by directed PCR mutagenesis. Two independent reactions were prepared: one contained the forward primer with the desired mutation and the reverse SP6 vector primer (5'-ATTTAGGTGACACTATAG-3'). The second contained the reverse mutating primer and the forward T7 vector primer (5'-TAATACGACTCAC TATAGGG-3'). PCR products from the reactions were purified and 1 µl of each was used as a template and mixed in a second round of amplification with T7 and SP6 primers to obtain the full gene. For each mutagenesis, the final PCR product was purified and subcloned in pGEM-T Easy, and the complete *Or59b* cDNA carrying the induced mutations was sequenced for verification and compared with the *Or59b<sup>NCBI REF</sup>* sequence.

The double mutants *Or59b<sup>V41F V91A</sup>* and *Or59b<sup>T376S V388A</sup>* were generated using *Or59b<sup>V41F</sup>* or *Or59b<sup>T376S</sup>* as a template and a second round of mutagenesis was implemented with the corresponding primers.

The following primers were used. *Or59b<sup>V41F</sup>*: 5'-CCGCCGAAGGAGGGATT CCTGCGCTACGTGT-3' (forward); 5'-ACACGTAGCGCAGGAATCCCTCC TTCGGCGG-3' (reverse). *Or59b<sup>V91A</sup>*: 5'-AGGTGTGCATCAATCGGTATGGC GCCTCGG-3' (forward); 5'-CCGAGGCGCCATACGCATTGATGCACACCTC-3' (reverse). *Or59b<sup>T376S</sup>*: 5'-TGAACAGCAACATAAGCGTGCCCAAGTTC GC-3' (forward); 5'-GCGAAGCTTGGCAGCCTTATGTGCTGTTCAT-3' (reverse). *Or59b<sup>V388A</sup>*: 5'-GCATCATTACAATAGCGCGACAAATGAATCT-3' (forward); 5'-AGATTCAATTGTGCGCTATTGTAATGATGC-3' (reverse).

Transgenic animals were generated in the *w<sup>1118</sup>* genetic background (Genetic Services, Inc.) using the phiC31-based integration system<sup>31</sup> targeted at the attP2-docking site on chromosome II (ref. 32).

**Fly stocks.** *Drosophila melanogaster* stocks were maintained on conventional cornmeal–agar–molasses medium in a 12-h-light, 12-h-dark cycle at 25 °C. The *w<sup>1118</sup>* strain was used as wild-type control.

The following wild-type strains were used: Akayu [*Drosophila* Genetic Resource Center (DGRC) #103389; origin, Japan]; Algeria (isogenic for II and III chromosomes, DGRC #103390; origin, Algeria); Alma-Ata (DGRC #103391; origin, Kazakhstan); Canton-S (isogenic for II and III, lab stock; origin, Ohio, USA); CA1 (Bloomington *Drosophila* Stock Center #3846; origin, Cape Town, South Africa); Coffs Harbour (DGRC #103411; origin, New South Wales, Australia); Kericho-7B (DGRC #103428; origin, Kericho, Kenya); Manago (isogenic for II and III, DGRC #103433; origin, Hawaii, USA); Oregon-R (isogenic for II and III, lab stock; origin, Oregon, USA); San Miguel (isogenic for II and III, DGRC #103450; origin, Buenos Aires, Argentina); WT Berlin (isogenic for II and III, Heisenberg laboratory, Würzburg, Germany; origin, Berlin, Germany); Batumi-L (DGRC #103396; origin, Batumi, Georgia); Boa Esperança (DGRC #103400; origin, Minas Gerais, Brazil); BOG2 (Bloomington #3842; origin, Bogota, Colombia); CO3 (Bloomington #3848; origin, Commack, New York, USA); EV (Bloomington #3851; origin, Ellenville, New York, USA); Medvast-21 (DGRC #103435; origin, Finland); VAG 2 (Bloomington #3876; origin, Athens, Greece).

The following mutant alleles and transgenic flies were used: *Or22a/b<sup>Ahalo</sup>* (ref. 33) and *Or22a-Gal4* (ref. 34). The genotypes of the flies used for Fig. 4c and Supplementary Fig. 8 are as follows: *Or22a/b<sup>Ahalo</sup>, Or22a-Gal4/UAS-Or59b* (labelled *Or59b<sup>NCBI REF</sup>* in the figure), *Or22a/b<sup>Ahalo</sup>, Or22a-Gal4/UAS-Or59b<sup>V41F</sup>* (*V41F*), *Or22a/b<sup>Ahalo</sup>, Or22a-Gal4/UAS-Or59b<sup>V91A</sup>* (*V91A*), *Or22a/b<sup>Ahalo</sup>, Or22a-Gal4/UAS-Or59b<sup>V41F V91A</sup>* (*V41F V91A*), *Or22a/b<sup>Ahalo</sup>, Or22a-Gal4/UAS-Or59b<sup>T376S</sup>* (*T376S*), *Or22a/b<sup>Ahalo</sup>, Or22a-Gal4/UAS-Or59b<sup>V388A</sup>* (*V388A*), *Or22a/b<sup>Ahalo</sup>, Or22a-Gal4/UAS-Or59b<sup>T376S V388A</sup>* (*T376S V388A*) and *Or22a/b<sup>Ahalo</sup>, Or22a-Gal4/UAS-Or59b<sup>V41F V91A T376S V388A</sup>* (*V41F V91A T376S V388A*).

**SPME quantification of emitted volatiles.** The effect of DEET on the amount of 1-octen-3-ol emitted from the stimulus pipettes was investigated through SPME and linked GC-MS analysis. Stimulus pipettes, prepared as per the electrophysiology experiments, were loaded either with one filter strip impregnated with 5 µl of 1-octen-3-ol ( $10^{-2}$ ) and with a second strip containing 5 µl of paraffin oil, or with the second strip impregnated with 5 µl of pure DEET. The pipettes were connected to a stimulus controller (Syntech CS 55; [www.syntech.nl](http://www.syntech.nl)) and volatiles emitted from the pipettes during ten puffs, of 2-s duration each, delivered with 1-s intervals, were trapped on a SPME fibre (Supelco blue fibre; 57310-U; polydimethylsiloxane/divinylbenzene, 65-µm coating; <http://www.sigmaaldrich.com>), inserted 2 cm into the pipette tip. After completion of the stimulus cycle, the SPME fibres were immediately retracted and injected into a GC-MS device for quantification. This device (Agilent GC6890N fitted with MS5975B unit; <http://www.agilent.com>) was equipped with a HP5-MS column (Agilent Technologies) and operated as follows. The inlet temperature was set to 250 °C. Desorption time was 1 min. The temperature of the gas chromatography oven was held at 70 °C for 2 min and then increased by 20 °C min<sup>-1</sup> to 280 °C, with the final temperature held for 2 min. For mass spectroscopy, the transfer line was held at 280 °C, the source at 230 °C and the quad at 150 °C. Mass spectra were taken in EI mode (at 70 eV) in the range from 33 m/z to 350 m/z, with a scanning rate of 4.42 scans per second. GC-MS data were processed with the MDS-CHEMSTATION software (Agilent Technologies), and peak areas were autointegrated. Five replicates were collected for each condition and data were plotted as mean ± s.e.m. Statistical significance was assessed using a *t*-test.

**Electrophysiology and odors.** Female transgenic flies were recorded at 5 d after adult eclosion. All other flies were recorded at 5–10 d after adult eclosion. Single-sensillum recordings were performed as described previously<sup>35,36</sup>. For each experiment in which we recorded OR59B variants expressed in the ab3A neuron, we verified that responses of endogenous OR59B in the native ab2A neuron showed normal inhibition by  $10^{-2}$  1-octen-3-ol (data not shown). Odorants were obtained from Sigma-Aldrich at high purity and diluted (v/v) in paraffin oil as indicated. DEET was obtained from Alfa Aesar and was applied undiluted. Chemical Abstracts Service (CAS) numbers are as follows: paraffin oil (8012-95-1); 1-octen-3-ol (3391-86-4); pentanal (110-62-3); pentanoic acid (109-52-4); 2-heptanone (110-43-0); 1-octanol (111-87-5); (–)-linalool (126-91-0); methyl acetate (79-20-9); 2,3-butanedione (431-03-8); ethyl hexanoate (123-66-0); butyraldehyde (123-72-8); ethyl-3-hydroxybutyrate (5405-41-4); ethyl acetate (141-78-6); hexanol (111-27-3); DEET (134-62-3).

The desired odour dilution (30 µl) was pipetted onto a filter paper strip (3 mm × 50 mm) and 30 µl of undiluted DEET or paraffin oil solvent was pipetted onto a second filter paper strip. Both filter paper strips were then carefully inserted into a glass Pasteur pipette. Before any recordings, charcoal-filtered air was forced through the pipette for 1–3 s to remove dead space in the odour delivery system. For actual recordings, charcoal-filtered air was continuously applied to the insect antenna, with odour delivered through the pipette to the fly antennae for 1 s. Each pipette was used at most three times and no more than three sensilla were tested per animal. Sensilla types were identified by size, location on the antenna and responsiveness to known preferred odorants<sup>37</sup>.

Data were collected using AUTOSPIKE (Syntech) and analysed by custom spike-sorting algorithms<sup>35</sup>. Responses were initially classified as excitatory or inhibitory by visual inspection of the responses after odour application. An odour was classified as excitatory if it increased the spontaneous firing rate and inhibitory if it decreased the spontaneous firing rate. The data were then analysed by subtracting average spontaneous activity (expressed as spikes per second) in the 15 s before odour application from activity either in the first 600 ms after odour delivery, for excitatory odorants, or in the first 1 s, for inhibitory odorants. This value is referred to as *A*, and will typically have a negative value for inhibitory odorants and a positive value for excitatory odorants. The onset of odour-evoked responses varied owing to slight variations in the position of the odour delivery system relative to the sensillum being recorded. To correct for this, we calibrated the inferred odour onset on the basis of excitatory responses elicited by control stimuli applied at the beginning of each trial (ab2,  $10^{-5}$  methyl acetate; ab3,  $10^{-5}$  2-heptanone).

**Statistical analysis.** Dose–response curves were fitted with ORIGINPRO 8 (OriginLab) using a logistic function, except for responses to 1-octen-3-ol in Fig. 1d, which used a biphasic function.

Comparisons of paired dose–response curves in Figs 1 and 3 and Supplementary Figs 1, 2 and 4 used an *F*-test to assess the statistical significance of differences between the two curve fits. A two-tailed *t*-test was performed for all comparisons in Fig. 1i (non-paired), Figs 2–4 and Supplementary Figs 3, 4 and 7 (paired). Type I errors were addressed by using a Bonferroni correction for multiple comparisons applied to each set of experiments. Data in Supplementary Fig. 6 were fitted using a linear regression analysis.

The OR59B snake plots in Fig. 4 and Supplementary Fig. 7 were hand-composed on the basis of transmembrane domain predictions generated with the PredictProtein algorithm<sup>38</sup>.

31. Bischof, J., Maeda, R. K., Hediger, M., Karch, F. & Basler, K. An optimized transgenesis system for *Drosophila* using germ-line-specific phiC31 integrases. *Proc. Natl Acad. Sci. USA* **104**, 3312–3317 (2007).
32. Markstein, M., Pitsouli, C., Villalta, C., Celniker, S. E. & Perrimon, N. Exploiting position effects and the gypsy retrovirus insulator to engineer precisely expressed transgenes. *Nature Genet.* **40**, 476–483 (2008).
33. Dobritsa, A. A., van der Goes van Naters, W., Warr, C. G., Steinbrecht, R. A. & Carlson, J. R. Integrating the molecular and cellular basis of odor coding in the *Drosophila* antenna. *Neuron* **37**, 827–841 (2003).
34. Fishilevich, E. & Vosshall, L. B. Genetic and functional subdivision of the *Drosophila* antennal lobe. *Curr. Biol.* **15**, 1548–1553 (2005).
35. Ditzen, M., Pellegrino, M. & Vosshall, L. B. Insect odorant receptors are molecular targets of the insect repellent DEET. *Science* **319**, 1838–1842 (2008).
36. Pellegrino, M., Nakagawa, T. & Vosshall, L. B. Single sensillum recordings in the insects *Drosophila melanogaster* and *Anopheles gambiae*. *J. Vis. Exp.* **36**, 1–5 (2010).
37. Hallem, E. A. & Carlson, J. R. Coding of odors by a receptor repertoire. *Cell* **125**, 143–160 (2006).
38. Rost, B., Yachdav, G. & Liu, J. The PredictProtein server. *Nucleic Acids Res.* **32**, W321–W326 (2004).



# The crystal structure of dynamin

Marijn G. J. Ford<sup>1</sup>, Simon Jenni<sup>2</sup> & Jodi Nunnari<sup>1</sup>

**Dynamin-related proteins (DRPs) are multi-domain GTPases that function via oligomerization and GTP-dependent conformational changes to play central roles in regulating membrane structure across phylogenetic kingdoms. How DRPs harness self-assembly and GTP-dependent conformational changes to remodel membranes is not understood. Here we present the crystal structure of an assembly-deficient mammalian endocytic DRP, dynamin 1, lacking the proline-rich domain, in its nucleotide-free state. The dynamin 1 monomer is an extended structure with the GTPase domain and bundle signalling element positioned on top of a long helical stalk with the pleckstrin homology domain flexibly attached on its opposing end. Dynamin 1 dimer and higher order dimer multimers form via interfaces located in the stalk. Analysis of these interfaces provides insight into DRP family member specificity and regulation and provides a framework for understanding the biogenesis of higher order DRP structures and the mechanism of DRP-mediated membrane scission events.**

Dynamin-related proteins (DRPs) belong to a highly conserved (Supplementary Fig. 1) GTPase superfamily that catalyses diverse membrane remodelling events<sup>1,2</sup>. Membrane scission DRPs include dynamin 1, which catalyses clathrin-coated vesicle scission at the plasma membrane and Drp1/Dnm1, which divide mitochondria. Despite their functional diversity, all DRPs undergo GTP cycle-dependent conformational changes to regulate self-assembly and disassembly<sup>3–8</sup>. DRP architecture includes an amino-terminal GTPase domain, a bundle signalling element (BSE), a middle domain (MD) and a GTPase effector domain (GED)<sup>9,10</sup>. Many DRPs also have a variable region between the MD and GED; in dynamin 1, this is a pleckstrin homology domain (PH) that binds to phosphatidylinositol-4,5-bisphosphate (PtdIns-4,5-P<sub>2</sub>)-containing membranes to facilitate targeting and possibly membrane remodelling via membrane insertion<sup>11–14</sup>.

Assembled DRPs can form helical structures *in vitro*<sup>15,16</sup>. Within these structures, GTP cycle-driven conformational changes result in membrane remodelling<sup>4,5,7,17</sup>. The structural basis for DRP self-assembly and GTP cycle-dependent conformational changes are not fully understood. The mechanism of assembly has been informed by the structure of the 'stalk' of MxA, a distantly related DRP, in which the MD and part of the GED form an extended helical bundle that mediates self-assembly via conserved interfaces<sup>18</sup>. Several structures have also provided insight into DRP GTP cycle conformational changes (Supplementary Fig. 2)<sup>19–24</sup>. Cryo-electron microscopic structures of assembled dynamin in guanosine-5'-[( $\beta,\gamma$ )-methylene]triphosphate (GMPPCP)-bound and nucleotide-free states have provided models for the assembled oligomers and the location of the GTPase and PH domains within the helical structures<sup>17,25</sup>. However, to understand the basis of DRP self-assembly and mechanism, the architecture of DRP domains within a single molecule must be elucidated. Here, we report the crystal structure of an assembly-deficient dynamin 1 in the nucleotide-free state that lacks only the unstructured carboxy-terminal proline-rich domain (PRD).

## G397D, an assembly-deficient dynamin 1 mutant

The propensity of DRPs to assemble has been an obstacle to obtaining crystals suitable for diffraction experiments. We identified the mutation G436D, an invariant MD residue, in the *Saccharomyces cerevisiae* mitochondrial division DRP Dnm1, by screening for mutations that possessed the same phenotype as assembly-deficient Dnm1 G385D,

specifically mutations that shifted Dnm1–green fluorescent protein (GFP) fusion from a punctate to a more diffuse localization pattern in yeast cells<sup>16</sup>. We expressed and purified (Supplementary Fig. 3a) the orthologous rat dynamin 1 mutant protein lacking the PRD (Dyn1 G397D  $\Delta$ PRD) and examined its ability to self assemble using light scattering (Fig. 1a). Addition of GMPPCP caused an increase in scattering in Dyn1  $\Delta$ PRD samples, but caused no change in scattering in Dyn1 G397D  $\Delta$ PRD samples. Using a combination of size-exclusion chromatography and sucrose gradient centrifugation<sup>26</sup>, Dyn1  $\Delta$ PRD and Dyn1 G397D  $\Delta$ PRD were estimated to be dimeric (Supplementary Fig. 3b and Supplementary Table 1) under non-assembly conditions, similar to other assembly-deficient DRP mutants<sup>16,27</sup>. Under assembly conditions, we observed an increase in the sedimentation coefficient of Dyn1  $\Delta$ PRD, but not for Dyn1 G397D  $\Delta$ PRD (Supplementary Table 1). Dyn1 G397D  $\Delta$ PRD was defective for assembly-stimulated GTP hydrolysis (Fig. 1b and Supplementary Table 2) and failed to assemble into helical structures on phosphatidylinositol 4-phosphate (PtdIns-4P)-containing lipid nanotubes, in contrast to Dyn1  $\Delta$ PRD (Fig. 1c). Dyn1 G397D  $\Delta$ PRD was also soluble at higher concentrations than Dyn1  $\Delta$ PRD. Together, these data indicate that the G397D mutation severely hampers dynamin self assembly and substantiates the critical role of the MD in intermolecular interactions<sup>16,18,27–29</sup>. Given these characteristics, it presented an attractive target for crystallization.

## Crystallization and structure of Dyn1 G397D $\Delta$ PRD

We obtained orthorhombic crystals of Dyn1 G397D  $\Delta$ PRD that diffracted to a minimum Bragg spacing of 3.1 Å (Methods and Supplementary Table 3). The structure was solved by molecular replacement, using the nucleotide-free rat dynamin 1 GTPase domain, the human dynamin 1 PH and a portion of the human MxA stalk, as sequential search models (Methods)<sup>11,13,18,30</sup>. We traced the complete model, except for some disordered loops, and assigned amino acids after refinement of the molecular replacement solution. The model was refined to  $R/R_{\text{free}}$  values of 0.21/0.27. A representative example of the B-sharpened likelihood-weighted  $2mF_{\text{obs}} - DF_{\text{calc}}$  electron density map is shown in Fig. 2c.

Dyn1 G397D  $\Delta$ PRD forms an extended structure with the GTPase and PH domains separated by a stalk consisting of an anti-parallel helical bundle of the MD and a helix from the GED (Fig. 2a, b). By

<sup>1</sup>Department of Molecular and Cellular Biology, University of California, Davis, Davis, California 95616, USA. <sup>2</sup>Department of Biological Chemistry and Molecular Pharmacology, Harvard Medical School, Boston, Massachusetts 02115, USA.

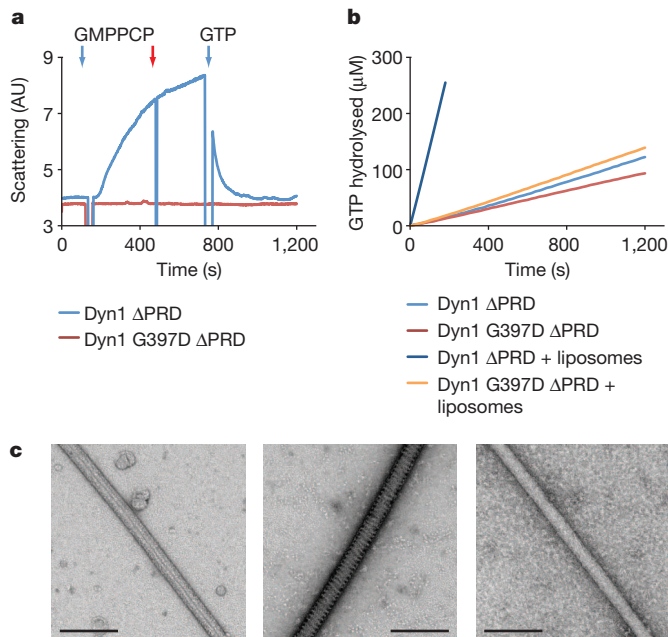


**Figure 1 | The G397D mutation in Dyn1  $\Delta$ PRD blocks self-assembly.** **a**, 90° light scattering. Dyn1  $\Delta$ PRD (blue, 1  $\mu$ M) and Dyn1 G397D  $\Delta$ PRD (red, 1  $\mu$ M) were monitored after addition of 0.5 mM GMPPCP and, in the case of Dyn1  $\Delta$ PRD, 1 mM GTP (blue arrows). Red arrow indicates opening of sample port. AU, arbitrary units. **b**, Steady-state GTP hydrolysis kinetics of Dyn1  $\Delta$ PRD and Dyn1 G397D  $\Delta$ PRD in the absence (light blue and red) and presence (dark blue and orange) of 0.1 mg ml<sup>-1</sup> liposomes containing 10% PtdIns-4P, monitored by a NADH-dependent coupled assay as described<sup>43</sup>. A representative trace is shown with 1 mM GTP. **c**, Transmission electron microscopy of negative-stained 0.25 mg ml<sup>-1</sup> 10% PtdIns-4P lipid nanotubes with Dyn1  $\Delta$ PRD (middle) and Dyn1 G397D  $\Delta$ PRD (right) and no added protein (left) and 0.5 mM GMPPCP. Scale bars, 200 nm.

contrast, the distantly related bacterial dynamin-like protein (BDLP) is compactly folded in its nucleotide-free and GDP-bound states (Supplementary Fig. 2a), with its ‘paddle’, in an analogous region to the PH domain of dynamin, in close proximity to the GTPase domain<sup>19,20</sup>. Thus, unlike BDLP, GTP binding in dynamin is not harnessed to form an extended structure, consistent with nucleotide-independent assembly of dynamin on liposomes<sup>4,8,31,32</sup>. Linkers connecting the MD to the PH and the PH to the GED are disordered, indicating a flexibly tethered PH. Thus, any of three crystallographic symmetry-related PH domains could connect to the remainder of the structure (Fig. 2d). The probable PH partner, based on the fit with the envelope of an assembly-deficient dynamin dimer determined by small-angle X-ray scattering<sup>33</sup> (SAXS), is shown in Fig. 2b. The structure of the PH is similar to those previously determined<sup>11,13</sup>, with expected differences concentrated in the variable loops.

The structure of the GTPase domain is similar to that of the previously determined nucleotide-free dynamin GTPase domain structure<sup>30</sup>. There are minor expected changes in the poorly resolved switch 2 region, the dynamin-specific loop and in the loop connecting the N<sub>GTPase</sub> to the GTPase domain. The C<sub>GTPase</sub> helix is kinked at the conserved proline 294 and, together with the N<sub>GTPase</sub> helix and a helix at the C terminus of the GED (C<sub>GED</sub>), forms the three-helix BSE<sup>9</sup>. C<sub>GED</sub> covers a groove of 937 Å<sup>2</sup> between the N<sub>GTPase</sub> and C<sub>GTPase</sub> helices. In the nucleotide-free dynamin 1 GTPase and the GDP-bound *Dictyostelium discoideum* dynamin A GTPase structures, a myosin peptide substitutes for C<sub>GED</sub>, indicating the importance of this interface for GTPase domain stability<sup>30,34</sup>.

A linker with elevated crystallographic temperature factors connects the C<sub>GTPase</sub> to the dynamin stalk (Fig. 2a, b) and contains two prolines (319 and 322), whose equivalents in the distantly related DRP atlastin 1 connect the GTPase and MD (Supplementary Fig. 2b).

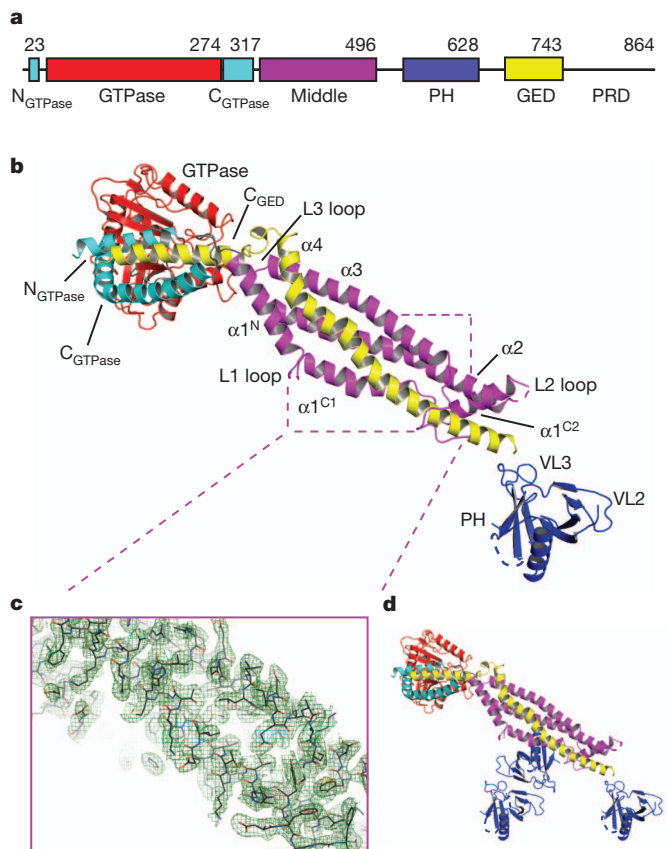


**Figure 2 | The crystal structure of Dyn1 G397D  $\Delta$ PRD.** **a**, Schematic of the Dyn1 domain structure. Numbers indicate domain-ending amino acid. Colour scheme used here is retained. **b**, Crystal structure of Dyn1 G397D  $\Delta$ PRD. Linkers between the N<sub>GTPase</sub> and GTPase domain and the C<sub>GTPase</sub> and MD are shown in grey. Loops with no density are represented with dashed lines. Stalk nomenclature is based on that of the MxA stalk structure<sup>18</sup>. VL, variable loop. **c**, An example of the refined to B-sharpened  $2mF_{\text{obs}} - DF_{\text{calc}}$  map, contoured at 1 $\sigma$ . The region shown is part of the stalk boxed by purple dotted lines in **(b)**. **d**, Three symmetry-related PH domains in the lattice.

Although the dynamin stalk sequence shares limited identity to MxA, its overall structure is similar and the MxA nomenclature is retained<sup>18</sup> (Supplementary Fig. 4a). As for MxA, helix  $\alpha$ 1 is split by a disordered loop, L1. The remainder of  $\alpha$ 1 diverges from MxA and is split into two helices, termed  $\alpha$ 1<sup>C1</sup> and  $\alpha$ 1<sup>C2</sup>. Helix  $\alpha$ 1<sup>C2</sup> connects to helix  $\alpha$ 2 via a short disordered loop, L2. Helices  $\alpha$ 2 and  $\alpha$ 3 run the length of the stalk and are joined by a short loop, L3. The stalk is completed by GED-derived helix  $\alpha$ 4 that spans the stalk and connects to C<sub>GED</sub> via a linker. Following helix  $\alpha$ 3 is a coil that folds across  $\alpha$ 4 that is strongly conserved in dynamins, Drp1s and Dnm1, but absent in MxA.

## The dynamin–dimer interface

The crystal lattice contains linear filaments of dynamin assembled via three stalk interfaces, similar to MxA<sup>18</sup>, resulting in layers of interacting stalks separated by GTPase and PH domains (Fig. 3a, b). Interface 2, the largest with a buried surface of 1,339 Å<sup>2</sup>, has two-fold symmetry and is formed by residues from stalk helices  $\alpha$ 4 and  $\alpha$ 3 (Fig. 3c), with an additional residue from  $\alpha$ 1<sup>C1</sup> (H367). Each protomer in the interface contributes seven direct hydrogen bonds and eight hydrophobic residues line the site of contact between  $\alpha$ 3 and  $\alpha$ 4 (Fig. 3c).

Interface 2 sequence conservation indicates a mechanism for dimer specificity within the DRP superfamily. Phylogenetic analysis of the hydrogen bonding partners within this region in dynamins, Drp1s and Dnm1, and Mx proteins allowed us to categorize three classes of residues: conserved in dynamins, Drp1/Dnm1, and Mx proteins (in

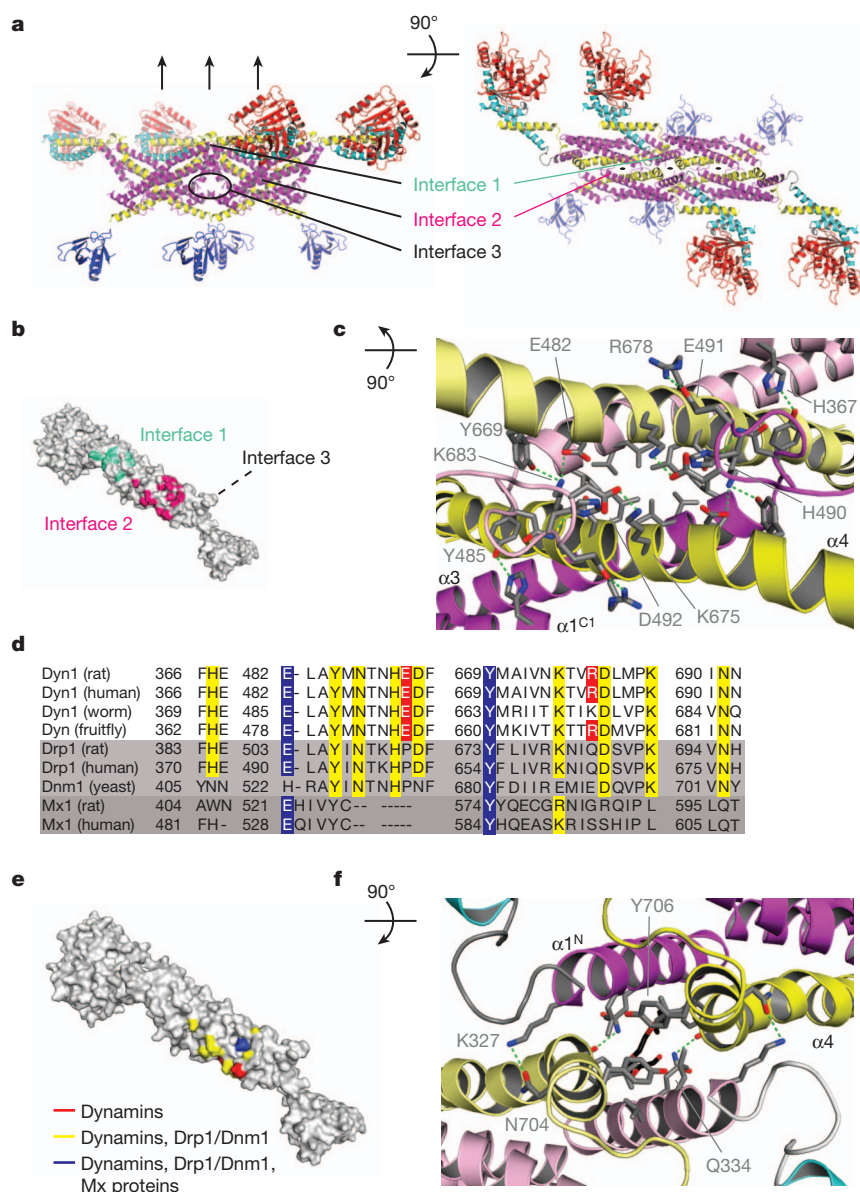


**Figure 3 | Dyn1 G397D ΔPRD stalk interfaces mediate self-assembly.**

**a**, Schematic diagram of four monomers showing interfaces in the crystal lattice. **b**, Surface representation showing the locations of interfaces 1 and 2. **c**, Detail of interface 2. Protomers are shown in lighter and darker hues. Green dotted lines are hydrogen bonds. **d**, Conservation of interface 2 residues involved in hydrogen bonding in dynamin, Drp1/Dnm1 and Mx proteins. Blue, conserved in dynamin, Drp1/Dnm1 and Mx proteins; yellow, conserved in dynamin and

Drps; red, conserved only within dynamin and Drp1/Dnm1 (in yellow), and conserved only in the dynamin (in red) (Fig. 3d). Plotting these classes onto a surface representation of the dynamin monomer (Fig. 3e) indicates that dimerization specificity is controlled by a spatial combinatorial code. As predicted from this code, hetero-oligomers consisting of dynamin 1 and dynamin 2 are observed<sup>35</sup>. Several residues contributing to the apparent specificity are localized in the strongly conserved coil of dynamin, Drp1 and Dnm1 that follows  $\alpha 3$ .

### Dynamin stalk interfaces drive self assembly

Interfaces 1 and 3 are also stalk-localized and mediate higher order assembly of dynamin dimers (Fig. 3a). Interface 1 is at the tips of interacting stalks, proximal to the GTPase domain and BSE (Fig. 3f) and is formed through interactions between protomer helices  $\alpha 4$  and  $\alpha 1^N$ . The interface is capped by a stacking interaction between

Drps; red, conserved in dynamin. Alignment shows a subset of sequences used to determine the conservation. Sequences are identical to Supplementary Fig. 1, with the addition of *Rattus norvegicus* Mx1 (P18588.1) and *Homo sapiens* Mx1 (P20591.4). Fruitfly, *Drosophila melanogaster*; human, *Homo sapiens*; rat, *Rattus norvegicus*; worm, *Caenorhabditis elegans*; yeast, *Saccharomyces cerevisiae*. **e**, Surface representation of conservation data shown in (d). **f**, Interface 1. Density interpreted as a PEG400 molecule is shown in black.

opposing and flexible Y706 residues, conserved in dynamin and Drp1s. Interface 1 includes four hydrogen bonds (Fig. 3f, dashed green lines), with the remainder consisting of hydrophobic residues. The buried surface area of interface 1 is relatively small (624 Å<sup>2</sup>) and is likely to be dynamic to tolerate protomer interactions in a range of orientations.

Interface 3 is at the distal end of the stalk, where L2 loops from symmetry-related molecules are in close proximity (Supplementary Fig. 4b). The G397D mutation is within L2, which could not be traced due to poor density. The N-terminal region of L2 is also in close proximity to a symmetry-related L1, which features a highly conserved glycine, G346, that when mutated in Dnm1 (G385D) blocks assembly beyond the dimer<sup>16</sup>. We therefore predict that G397 and G346 are near one another in assembled dynamin. In addition, mutations at two dynamin arginine residues, R399 (in L2) and R361 (in  $\alpha 1^C$ , following L1), and the corresponding interface 3 mutations in



MxA also inhibit assembly and stabilize dimeric forms<sup>18,27</sup>. In contrast, disruption of MxA interface 1 yields a mixture of dimers and tetramers<sup>18</sup>. Thus, our data indicate that interface 3 is critical at an early step in the dynamin assembly pathway as its disruption stabilizes dimeric dynamin and allows linear filament formation. In contrast, interface 1 interactions probably function only to stabilize oligomerization.

From our structure, we propose that the dynamin dimer interface 2 is constitutive and relatively rigid. As compared to linear arrangement in the crystal, in helical assemblies we propose that the necessary rotational and translational shifts occur between adjacent dimers at interfaces 1 and 3 (Fig. 4a). Indeed, stalk dimers fit into the GMPPCP-bound helical electron microscopic reconstruction of dynamin<sup>25</sup> (Fig. 4b) possess a more tightly packed interface 3 and interface 1. These differences can be attributed to the disordered interface 3 in the crystal that is probably due to steric hindrance from the G397D mutation, and the dynamic nature of the hydrophobic interface 1.

## Regulation of DRPs

The dynamin PH is essential for endocytosis and interacts with inositol phospholipids with low affinity<sup>12,36</sup>. Centronuclear myopathy (CNM) disease mutations cluster at the C terminus of the PH  $\alpha$ -helix (Supplementary Fig. 5a), underscoring its importance. They cause an increase in basal GTPase activity, without altering interactions with inositol phospholipids<sup>33</sup>. In addition, SAXS analysis of an assembly-deficient dynamin indicates that the CNM mutants have a different conformation compared to wild type<sup>33,37</sup>. In our lattice, three PH domains related by crystallographic symmetry lie close to interface 3 and the L1 loop (Fig. 2d), suggesting an interaction. Thus, the PH may serve to regulate access to this key multimerization interface to couple dynamin membrane interactions to dynamin assembly. Phosphoinositide binding by the PH variable loops and penetration of the membrane by variable loop 1<sup>14</sup> could help to expose dynamin interface 3 and/or L1 and thus promote multimerization.

Alignment of the dynamin PH and corresponding sequences from Drp1s shows conservation of key residues (Supplementary Figs 1 and 5b), indicating that lipids may similarly regulate mammalian mitochondrial division. However, mammalian Drp1s lack most of the C-terminal PH  $\alpha$ -helix, including residues mutated in CNM. The

details of Drp1 interface 3 regulation may therefore be different. Consistently, Drp1 splice variants have deletions in this region, pointing to a potential regulatory role. By contrast, *Danio rerio* Drp1 and fungal Dnm1 have an insert B of unknown structure in this region. Mitochondrial division DRPs can therefore be subdivided on this basis, which correlates with the divergence of their corresponding effectors, yeast Mdv1 and mammalian Mff<sup>38,39</sup>.

## Discussion

Our structure provides insight into the mechanism and regulation of dynamin assembly and into how the dynamin GTPase cycle is harnessed for function. Several observations point to a key role of the dynamin BSE in the formation of the GTPase–GTPase dimer interface observed in the GTPase–C<sub>GED</sub> GDP•AlF<sub>4</sub><sup>−</sup> crystal structure<sup>10</sup>. This interface is likely to form from adjacent rungs of a dynamin helix and is critical to dynamin function as it mediates assembly-stimulated GTP hydrolysis. Comparison of the GTPase–GTPase dimer with our nucleotide-free structure indicates that in addition to expected differences, the BSE is flexible. Dynamin genetic data also support a role for the BSE in the regulation of GTPase–GTPase interface formation. Specifically, the dynamin switch 2 *shibire* ts2 mutation, G146S, which causes endocytic intermediates with ‘collared’ dynamin necks to accumulate<sup>40</sup>, is suppressed by the *sushi* mutation A738T<sup>41,42</sup>, located in the C<sub>GED</sub> peptide, facing the hydrophobic groove (Fig. 5a). Insight into how dynamin undergoes conformational changes also comes from distantly related DRP structures (Supplementary Fig. 2). GTP-dependent GTPase domain dimerization is also observed for guanylate binding protein, indicating that this may be a common feature of the DRP superfamily<sup>22</sup> (Supplementary Fig. 2c). In addition, two recent structures of the atlastin 1 cytosolic domain, thought to represent pre- and post-endoplasmic reticulum membrane fusion conformations<sup>23,24</sup>, indicate that large changes occur in the position of the 3-helix bundle ‘middle domain’ relative to the GTPase domain (Supplementary Fig. 2b).

We propose that GTP binding and self-assembly promote dynamin GTPase–GTPase dimer formation via an opening of the BSE relative to the GTPase domain. In support, a modified version of our structure can be fit into the cryo-electron microscopic reconstruction of GMPPCP-bound dynamin with the BSE in a substantially more open

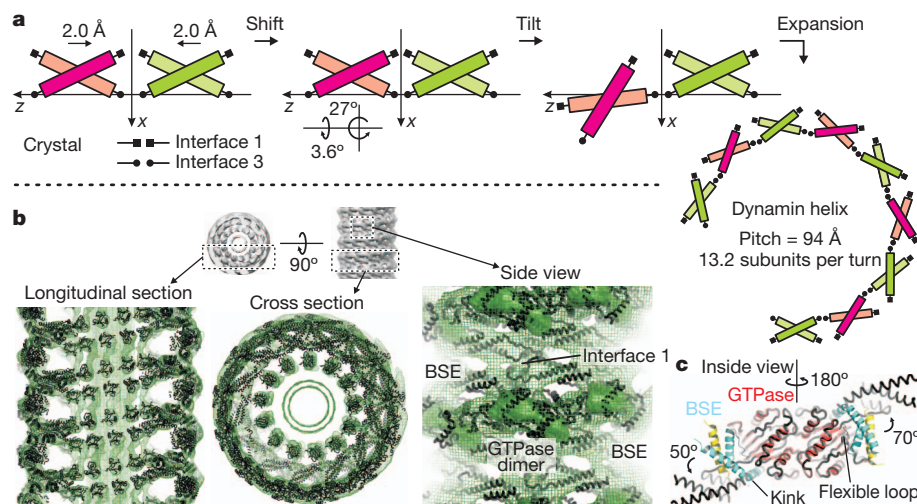


**Figure 4 | Oligomerization of dynamin into helical structures.** **a**, Dynamin helices derived from the linear arrangement in our crystal structure. Two stalk dimers (green and magenta) that engage in interface 1 and 3 are related by crystallographic translation. Experimentally determined helical parameters for dynamin assembled into helices in the GMPPCP-bound state<sup>25</sup> were matched by applying a small shift and tilt of one stalk dimer with respect to the other. **b**, Placement of oligomerized dynamin model into the electron microscopy

density map contoured at 1.2 $\sigma$ . In side view: the fit of the GTPase domain as a GTPase–GTPase dimer with the BSE in open conformation to connect to interface 1 of the stalk helix (solid density is contoured at 3.6 $\sigma$ ). **c**, Observed conformational flexibility of the BSE. Model fitted into the helical reconstruction is shown as black superimposed ribbon on the crystal structure of the GTPase–C<sub>GED</sub> fusion dimer (PDB accession no. 2X2E)<sup>10</sup>.

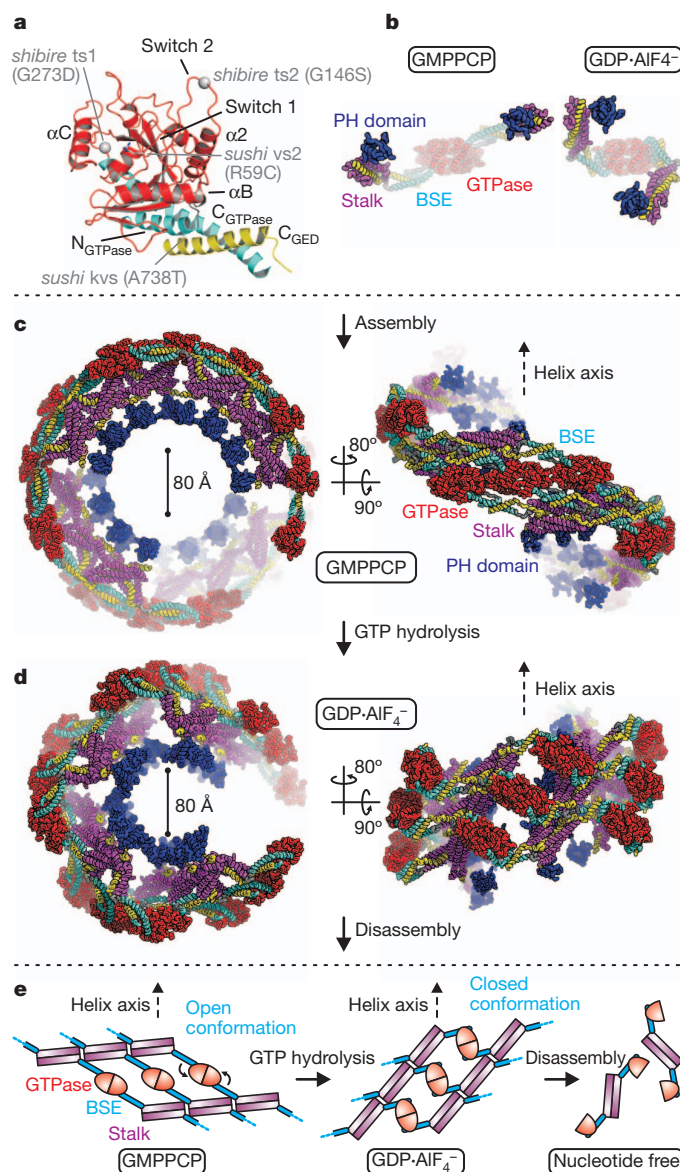


**Figure 5 | Model for dynamin GTP cycle conformational changes.**

**a**, Mapping of dynamin *shibire* and *sushi* mutations. **b**, Nucleotide-dependent dynamin conformations. The GTPase core domains (red) are in the same orientation. Left, GTP-bound state with open BSE conformation of dynamin as fitted into the GMPPCP-bound electron microscopic reconstruction shown in Fig. 4. Right, transition state of dynamin obtained by superposition of the BSE residues 291–312 and 727–743 of our structure on the corresponding residues of the GDP·AlF<sub>4</sub><sup>−</sup>-bound GTPase–C<sub>GED</sub> fusion dimer (PDB accession no. 2X2E)<sup>10</sup>. Transition from open to closed BSE conformation results in movement of stalk domains. **c**, Model for Dyn1 ΔPRD GTP-bound helix. The BSE is opened to allow GTPase–GTPase dimer formation. **d**, GTP hydrolysis closes the BSE and adopts the conformation of the GDP·AlF<sub>4</sub><sup>−</sup>-bound transition state. This results in a substantial global constriction of the helical oligomeric assembly causing membrane deformation and scission. **e**, Schematic of how the proposed GTP hydrolysis triggered BSE conformational change is transmitted to oligomerized stalk domains.

conformation (Fig. 4b). We obtained a good fit of the GTPase–GTPase dimer domains and stalk interface 1 using constraints dictated by the helical fit of the oligomeric stalk and the strong GTPase domain-derived density (Fig. 4b). The BSE  $\alpha$ -helices fit into the density stretching from the GTPase domain to the oligomeric stalk, indicating that a BSE flipping-out motion occurs at two hinge regions: the  $\alpha$ -helical kink at P294 and in the loop connecting the N<sub>GTPase</sub> and the GTPase domain, at P32 (Fig. 4c). Consistently, superposition of GDP·AlF<sub>4</sub><sup>−</sup>

GTPase–C<sub>GED</sub> fusion GTPase–GTPase dimer partners indicates a smaller yet directionally equivalent opening of the BSE in one proto-monomer<sup>10</sup>. This proposed conformational change is feasible as there are relatively few contacts that hold the N<sub>GTPase</sub> helix to the body of the GTPase domain in our structure. In addition, the BSE links the GTPase domain to the stalk and interface 1 via a short turn, making it well placed to transmit conformational alterations. As previously noted, comparison of the nucleotide-free and GMPPCP-bound electron microscopic reconstructions indicates that the GMPPCP-bound helix has a relatively smaller diameter<sup>17</sup>. In addition, the stalk density is more ‘kinked’ in the GMPPCP-bound form<sup>17</sup>. When we dock our structure, we observed that the bases of the stalks do not fit the density of the GMPPCP-bound helix. However, where the fit becomes poor there are strongly conserved prolines in  $\alpha$ 2 and  $\alpha$ 4 and a partially conserved proline in  $\alpha$ 1<sup>C1</sup> clustered in the stalk. We propose that these proline residues facilitate the formation of a kink at the stalk base in the GMPPCP-bound helix, which might allow interface 1 to form more fully in the assembled helix.

As predicted by our model, GTP hydrolysis would induce closure of the BSE via a transition state represented by the structure of the GTPase domain–BSE fusion in the presence of GDP·AlF<sub>4</sub><sup>−</sup>, towards the conformation observed in our nucleotide-free structure (Fig. 5b). As GTP binding to dynamin is not rate limiting and GTP hydrolysis is stimulated by the formation of the GTPase–GTPase interface between adjacent rungs, it is likely that the BSE-dependent conformational change occurs in the context of short dynamin helical assemblies rather than within a helix consisting of many rungs<sup>8,32</sup>. Short assemblies could also result in an approximate temporally coordinated conformational change (Fig. 5c–e). The conformational changes we propose would cause disruption to the assembled helix and the underlying membrane via local rung shifts. Interface 1 in our structure, which buries a relatively small surface area in the assembled stalk lattice, will be especially susceptible to change by inter-rung GTPase–GTPase dimer formation and its subsequent disruption by GTP hydrolysis, and these changes will be transmitted to interface 3 and the PH. The combined effects of curvature stress imposed by a short dynamin helical assembly coupled with PH insertion into the membrane is likely to destabilize the membrane and result in membrane fission<sup>14</sup>. Given the strong similarities between dynamins and other DRP family members, the structure of dynamin and our proposed model will serve to guide studies on the mechanisms of action of DRPs in diverse cellular functions.

## METHODS SUMMARY

The conserved Dyn1 ΔPRD assembly-defective mutant G397D was identified by a cytological assay using the yeast mitochondrial fission DRP Dnm1–GFP. Dyn1 ΔPRD and Dyn1 G397D ΔPRD were expressed in *E. coli* and were purified as described in Methods. Light scattering, sucrose density gradient centrifugation, mass determination, continuous GTPase assays and electron microscopy were performed as described in Methods. Crystals were grown by microbatch from 3.2  $\mu$ l droplets containing 52.5 mM Tris/Cl pH 7.7, 175 mM NaCl, 32.5 mM NaNO<sub>3</sub>, 20% v/v PEG 400, 0.97 mM  $\beta$ -mercaptoethanol and 31.9  $\mu$ M Dyn1 G397D ΔPRD and cryo-protected with ParetoN. Reflection data were collected at 100 K at Beamline 8.3.1 at the Advanced Light Source (Berkeley, California, USA) at a wavelength of 0.9488 Å. Data collection and processing are described in Methods. The structure was determined by molecular replacement, using known structures of the nucleotide-free rat dynamin 1 GTPase domain (PDB accession no. 2AKA chain B), the human dynamin 1 PH domain (PDB accession no. 2DYN chain B) and a truncated form of the human MxA stalk (PDB accession no. 3LJB chain B) as sequential search models. Structure refinement is described in Methods. The stalk interface 2 dimer was fit into the previously described cryo-electron microscopic reconstruction of GMPPCP-bound dynamin by applying tilt and twist to the sequential dimers from the linear filaments observed in the crystal to match the helical parameters described for the reconstruction. The previously described GTPase domain dimer formed in the presence of GDP·AlF<sub>4</sub><sup>−</sup> was subsequently fit into the density. Connection of the GTPase domain to the stalk required a conformational rearrangement of the BSE, which was independently fit into the visible density. The fit was subjected to rigid body refinement as described in Methods.



Received 10 May; accepted 12 August 2011.

Published online 18 September 2011.

1. Praefcke, G. J. & McMahon, H. T. The dynamin superfamily: universal membrane tubulation and fission molecules? *Nature Rev. Mol. Cell Biol.* **5**, 133–147 (2004).
2. Hoppins, S., Lackner, L. & Nunnari, J. The machines that divide and fuse mitochondria. *Annu. Rev. Biochem.* **76**, 751–780 (2007).
3. Marks, B. *et al.* GTPase activity of dynamin and resulting conformational change are essential for endocytosis. *Nature* **410**, 231–235 (2001).
4. Stowell, M. H. B., Marks, B., Wigge, P. & McMahon, H. T. Nucleotide-dependent conformational changes in dynamin: evidence for a mechanochemical molecular spring. *Nature Cell Biol.* **1**, 27–32 (1999).
5. Mears, J. A. *et al.* Conformational changes in Dnm1 support a contractile mechanism for mitochondrial fission. *Nature Struct. Mol. Biol.* **18**, 20–26 (2011).
6. Warnock, D. E., Hinshaw, J. E. & Schmid, S. L. Dynamin self-assembly stimulates its GTPase activity. *J. Biol. Chem.* **271**, 22310–22314 (1996).
7. Danino, D., Moon, K. H. & Hinshaw, J. E. Rapid constriction of lipid bilayers by the mechanochemical enzyme dynamin. *J. Struct. Biol.* **147**, 259–267 (2004).
8. Pucadyil, T. J. & Schmid, S. L. Real-time visualization of dynamin-catalyzed membrane fission and vesicle release. *Cell* **135**, 1263–1275 (2008).
9. Chappie, J. S. *et al.* An intramolecular signaling element that modulates dynamin function *in vitro* and *in vivo*. *Mol. Biol. Cell* **20**, 3561–3571 (2009).
10. Chappie, J. S., Acharya, S., Leonard, M., Schmid, S. L. & Dyda, F. G domain dimerization controls dynamin's assembly-stimulated GTPase activity. *Nature* **465**, 435–440 (2010).
11. Timm, D. *et al.* Crystal structure of the pleckstrin homology domain from dynamin. *Nature Struct. Biol.* **1**, 782–788 (1994).
12. Achiriloaie, M., Barylko, B. & Albanesi, J. P. Essential role of the dynamin pleckstrin homology domain in receptor-mediated endocytosis. *Mol. Cell Biol.* **19**, 1410–1415 (1999).
13. Ferguson, K. M., Lemmon, M. A., Schlessinger, J. & Sigler, P. B. Crystal structure at 2.2 Å resolution of the pleckstrin homology domain from human dynamin. *Cell* **79**, 199–209 (1994).
14. Ramachandran, R. *et al.* Membrane insertion of the pleckstrin homology domain variable loop 1 is critical for dynamin-catalyzed vesicle scission. *Mol. Biol. Cell* **20**, 4630–4639 (2009).
15. Hinshaw, J. E. & Schmid, S. L. Dynamin self-assembles into rings suggesting a mechanism for coated vesicle budding. *Nature* **374**, 190–192 (1995).
16. Ingberman, E. *et al.* Dnm1 forms spirals that are structurally tailored to fit mitochondria. *J. Cell Biol.* **170**, 1021–1027 (2005).
17. Mears, J. A., Ray, P. & Hinshaw, J. E. A corkscrew model for dynamin constriction. *Structure* **15**, 1190–1202 (2007).
18. Gao, S. *et al.* Structural basis of oligomerization in the stalk region of dynamin-like MxA. *Nature* **465**, 502–506 (2010).
19. Low, H. H., Sachse, C., Amos, L. A. & Lowe, J. Structure of a bacterial dynamin-like protein lipid tube provides a mechanism for assembly and membrane curving. *Cell* **139**, 1342–1352 (2009).
20. Low, H. H. & Lowe, J. A bacterial dynamin-like protein. *Nature* **444**, 766–769 (2006).
21. Prakash, B., Praefcke, G. J., Renault, L., Wittinghofer, A. & Herrmann, C. Structure of human guanylate-binding protein 1 representing a unique class of GTP-binding proteins. *Nature* **403**, 567–571 (2000).
22. Ghosh, A., Praefcke, G. J., Renault, L., Wittinghofer, A. & Herrmann, C. How guanylate-binding proteins achieve assembly-stimulated processive cleavage of GTP to GMP. *Nature* **440**, 101–104 (2006).
23. Bian, X. *et al.* Structures of the atlastin GTPase provide insight into homotypic fusion of endoplasmic reticulum membranes. *Proc. Natl Acad. Sci. USA* **108**, 3976–3981 (2011).
24. Byrnes, L. J. & Sondermann, H. Structural basis for the nucleotide-dependent dimerization of the large G protein atlastin-1/SPG3A. *Proc. Natl Acad. Sci. USA* **108**, 2216–2221 (2011).
25. Zhang, P. & Hinshaw, J. E. Three-dimensional reconstruction of dynamin in the constricted state. *Nature Cell Biol.* **3**, 922–926 (2001).
26. Siegel, L. M. & Monty, K. J. Determination of molecular weights and frictional ratios of proteins in impure systems by use of gel filtration and density gradient centrifugation. Application to crude preparations of sulfite and hydroxylamine reductases. *Biochim. Biophys. Acta* **112**, 346–362 (1966).
27. Ramachandran, R. *et al.* The dynamin middle domain is critical for tetramerization and higher-order self-assembly. *EMBO J.* **26**, 559–566 (2007).
28. Gao, S. *et al.* Structural basis of oligomerization in the stalk region of dynamin-like MxA. *Nature* **465**, 502–506 (2010).
29. Song, B. D., Yarar, D. & Schmid, S. L. An assembly-incompetent mutant establishes a requirement for dynamin self-assembly in clathrin-mediated endocytosis *in vivo*. *Mol. Biol. Cell* **15**, 2243–2252 (2004).
30. Reubold, T. F. *et al.* Crystal structure of the GTPase domain of rat dynamin 1. *Proc. Natl Acad. Sci. USA* **102**, 13093–13098 (2005).
31. Sweitzer, S. M. & Hinshaw, J. E. Dynamin undergoes a GTP-dependent conformational change causing vesiculation. *Cell* **93**, 1021–1029 (1998).
32. Bashkurov, P. V. *et al.* GTPase cycle of dynamin is coupled to membrane squeeze and release, leading to spontaneous fission. *Cell* **135**, 1276–1286 (2008).
33. Kenniston, J. A. & Lemmon, M. A. Dynamin GTPase regulation is altered by PH domain mutations found in centronuclear myopathy patients. *EMBO J.* **29**, 3054–3067 (2010).
34. Niemann, H. H., Knetsch, M. L., Scherer, A., Manstein, D. J. & Kull, F. J. Crystal structure of a dynamin GTPase domain in both nucleotide-free and GDP-bound forms. *EMBO J.* **20**, 5813–5821 (2001).
35. Barylko, B. *et al.* The proline/arginine-rich domain is a major determinant of dynamin self-activation. *Biochemistry* **49**, 10592–10594 (2010).
36. Vallis, Y., Wigge, P., Marks, B., Evans, P. R. & McMahon, H. T. Importance of the pleckstrin homology domain of dynamin in clathrin-mediated endocytosis. *Curr. Biol.* **9**, 257–263 (1999).
37. Durieux, A. C., Prudhon, B., Guicheney, P. & Bitoun, M. Dynamin 2 and human diseases. *J. Mol. Med.* **88**, 339–350 (2010).
38. Lackner, L. L., Horner, J. S. & Nunnari, J. Mechanistic analysis of a dynamin effector. *Science* **325**, 874–877 (2009).
39. Gandre-Babbe, S. & van der Bliek, A. M. The novel tail-anchored membrane protein Mff controls mitochondrial and peroxisomal fission in mammalian cells. *Mol. Biol. Cell* **19**, 2402–2412 (2008).
40. Kosaka, T. & Ikeda, K. Possible temperature-dependent blockage of synaptic vesicle recycling induced by a single gene mutation in *Drosophila*. *J. Neurobiol.* **14**, 207–225 (1983).
41. Ramaswami, M., Rao, S., van der Bliek, A., Kelly, R. B. & Krishnan, K. S. Genetic studies on dynamin function in *Drosophila*. *J. Neurogenet.* **9**, 73–87 (1993).
42. Narayanan, R., Leonard, M., Song, B. D., Schmid, S. L. & Ramaswami, M. An internal GAP domain negatively regulates presynaptic dynamin *in vivo*: a two-step model for dynamin function. *J. Cell Biol.* **169**, 117–126 (2005).
43. Ingberman, E. & Nunnari, J. A continuous, regenerative coupled GTPase assay for dynamin-related proteins. *Methods Enzymol.* **404**, 611–619 (2005).

**Supplementary Information** is linked to the online version of the paper at [www.nature.com/nature](http://www.nature.com/nature).

**Acknowledgements** The authors would like to express thanks to I. Stokes-Rees for assistance with the Wide Space Molecular Replacement, J. Holton for advice and assistance with data collection and H. McMahon for the kind gift of the dynamin clone. We would also like to thank J. Al-Bassam, J. Chappie, A. McCoy, S. Harrison, D. Owen, A. Fisher, E. Baldwin, L. Lackner, G. Adamson, N. Varlakhanova and members of the Nunnari lab for extensive discussions. S.J. is a Damon Runyon Cancer Research Foundation Fellow supported by the Howard Hughes Medical Institute (DRG-2004-09). This work was supported by an American Heart Innovator Award and NIH grants (R01GM062942S1 and R01GM097432) to J.N. The Advanced Light Source is supported by the Director, Office of Science, Office of Basic Energy Sciences, of the US Department of Energy under Contract No. DE-AC02-05CH11231.

**Author Contributions** M.G.J.F. purified, biochemically characterized and crystallized the Dyn1 G397D ΔPRD. M.G.J.F. collected X-ray diffraction data and M.G.J.F. and S.J. solved the structure. M.G.J.F. and J.N. designed experiments and M.G.J.F., S.J. and J.N. interpreted data and prepared the manuscript.

**Author Information** Atomic coordinates and structure factors for Dyn1 G397D ΔPRD have been deposited with the Protein Data Bank under accession code 3ZVR. Reprints and permissions information is available at [www.nature.com/reprints](http://www.nature.com/reprints). The authors declare no competing financial interests. Readers are welcome to comment on the online version of this article at [www.nature.com/nature](http://www.nature.com/nature). Correspondence and requests for materials should be addressed to J.N. ([jmnunnari@ucdavis.edu](mailto:jmnunnari@ucdavis.edu)).



## CORRIGENDUM

doi:10.1038/nature10459

### **Detection of prokaryotic mRNA signifies microbial viability and promotes immunity**

Leif E. Sander, Michael J. Davis, Mark V. Boekschoten,  
Derk Amsen, Christopher C. Dascher, Bernard Ryffel,  
Joel A. Swanson, Michael Müller & J. Magarian Blander

*Nature* **474**, 385–389 (2011).

In Fig. 1d of this Letter, the labels HKEC and EC were swapped in the print version. The lane labelled HKEC should be labelled EC and the lane labelled EC should be labelled HKEC. The error has been corrected online in the HTML and PDF versions.

# Spontaneous epigenetic variation in the *Arabidopsis thaliana* methylome

Claude Becker<sup>1\*</sup>, Jörg Hagmann<sup>1\*</sup>, Jonas Müller<sup>1</sup>, Daniel Koenig<sup>1</sup>, Oliver Stegle<sup>2</sup>, Karsten Borgwardt<sup>2</sup> & Detlef Weigel<sup>1</sup>

**Heritable epigenetic polymorphisms, such as differential cytosine methylation, can underlie phenotypic variation<sup>1,2</sup>. Moreover, wild strains of the plant *Arabidopsis thaliana* differ in many epialleles<sup>3,4</sup>, and these can influence the expression of nearby genes<sup>1,2</sup>. However, to understand their role in evolution<sup>5</sup>, it is imperative to ascertain the emergence rate and stability of epialleles, including those that are not due to structural variation. We have compared genome-wide DNA methylation among 10 *A. thaliana* lines, derived 30 generations ago from a common ancestor<sup>6</sup>. Epimutations at individual positions were easily detected, and close to 30,000 cytosines in each strain were differentially methylated. In contrast, larger regions of contiguous methylation were much more stable, and the frequency of changes was in the same low range as that of DNA mutations<sup>7</sup>. Like individual positions, the same regions were often affected by differential methylation in independent lines, with evidence for recurrent cycles of forward and reverse mutations. Transposable elements and short interfering RNAs have been causally linked to DNA methylation<sup>8</sup>. In agreement, differentially methylated sites were farther from transposable elements and showed less association with short interfering RNA expression than invariant positions. The biased distribution and frequent reversion of epimutations have important implications for the potential contribution of sequence-independent epialleles to plant evolution.**

Although there is no doubt that DNA sequence mutations are the primary raw material for evolutionary change, local DNA methylation variants with major effects on the expression of nearby genes can be inherited over many generations<sup>1,2</sup>. However, such epialleles are not always as stable as the primary DNA sequence<sup>3,9–11</sup>. New sequencing technologies have recently enabled the direct determination of spontaneous DNA mutation rates<sup>12</sup>, and we have previously reported that *A. thaliana* experiences about one single-base-pair mutation per haploid genome and generation<sup>7</sup>. This analysis was based on a set of five mutation accumulation lines that had been derived from a single individual of the inbred strain used to produce the high-quality reference genome sequence for *A. thaliana*. These lines had been separately propagated in a common environment by single-seed descent for 30 generations<sup>6</sup>. We examined whole-genome cytosine methylation<sup>13,14</sup> in these five lines plus five additional lines of the same population by Illumina sequencing. We interrogated two siblings each of the 31st generation with an average strand-specific coverage depth of 20× per individual; changes shared within a line should predominantly reflect differences that had accumulated by the 30th generation. Because seeds from the founders were no longer available, we compared the 31st generation individuals to two independent lines that had been propagated for only three generations (Supplementary Fig. 1).

Out of all cytosine residues with high-quality sequencing support (see Supplementary Methods), on average 2.8 million were found to be methylated in each line (Supplementary Table 1). The higher genome-wide methylation rate in our analysis compared to previous studies<sup>13,14</sup>

reflects the greater statistical power afforded by increased sequencing depth. We subsequently evaluated 13.9 million cytosines that had at least threefold coverage in all individuals, of which 3 million were methylated in at least one strain. Using Fisher's exact test, we identified about 186,000 (6.2%) positions with a significant change in methylation (false discovery rate <0.05) between at least one 31st generation and both 3rd generation lines. Almost all, 99.6%, of these differentially methylated positions (DMPs) were also detected with an entropy-based method<sup>15</sup>. Given the limited statistical power for weakly methylated or poorly covered sites (Supplementary Fig. 2–4), our DMP estimate would almost certainly increase with higher sequencing depth. For further analyses, we considered sites that agreed between 31st generation siblings (on average, 99.8%) and between the two strains closest to the founder generation (99.7%).

CG sites were highly over-represented among DMPs (Fig. 1a). This is unlikely to reflect greater instability of CG compared to CHG and CHH positions (where H is A, T or C), but rather higher statistical power in detecting a change at CG sites, which are on average much more highly methylated<sup>13,14</sup> (Supplementary Fig. 4). Among CG sites in genic regions, including those producing non-coding RNAs, relative abundance of DMPs was two- to fourfold higher compared with non-differentially methylated positions (N-DMPs). The opposite was the case for CG positions in transposable elements and intergenic regions, with a similar, but less pronounced, bias for CHG and CHH sites (Fig. 1b). These observations were in agreement with CG-DMPs being found most often on chromosome arms, which have the highest gene density (Fig. 1c), even though cytosine methylation near the centromeres is the highest<sup>13,14</sup>. Gene body methylation gradually increases towards the 3' end, before sharply decreasing at the end of the last exon<sup>13,14,16,17</sup>, although genes 1 kb or less in length were generally only weakly methylated (Supplementary Fig. 5a). The profiles of DMPs and N-DMPs were similar across individual genes, exons, introns and transposable elements (Fig. 1d and Supplementary Fig. 5b, c), but DMPs were less frequent in promoter and downstream regions. Notably, CG-DMPs accounted for 42% of methylated sites in gene bodies, despite all CG-N-DMPs outnumbering CG-DMPs four to one.

Twenty-four-nucleotide-long small interfering RNAs (siRNAs) are important in maintaining DNA methylation<sup>8</sup>, and N-DMPs coincided seven times more often than DMPs with sites to which 24-nt siRNAs mapped<sup>18</sup>. N-DMPs were also on average only half as far from such sites as DMPs ( $P < 2.2 \times 10^{-16}$ ) (Fig. 1e and Supplementary Fig. 6a). siRNAs are enriched in and around transposable elements<sup>19</sup>. In agreement, the average distance to the closest transposable element was much shorter for N-DMPs outside of transposable elements, compared to DMPs ( $P < 2.2 \times 10^{-16}$ ), even when only considering those in the centromere-distant regions of each chromosome, which contain relatively few transposable elements (Fig. 1e and Supplementary Fig. 6b, c).

A first major insight from our analyses is that transgenerational maintenance of CG methylation in transposable elements is apparently

<sup>1</sup>Department of Molecular Biology, Max Planck Institute for Developmental Biology, 72076 Tübingen, Germany. <sup>2</sup>Machine Learning and Computational Biology Research Group, Max Planck Institute for Developmental Biology and Max Planck Institute for Intelligent Systems, 72076 Tübingen, Germany.

\*These authors contributed equally to this work.

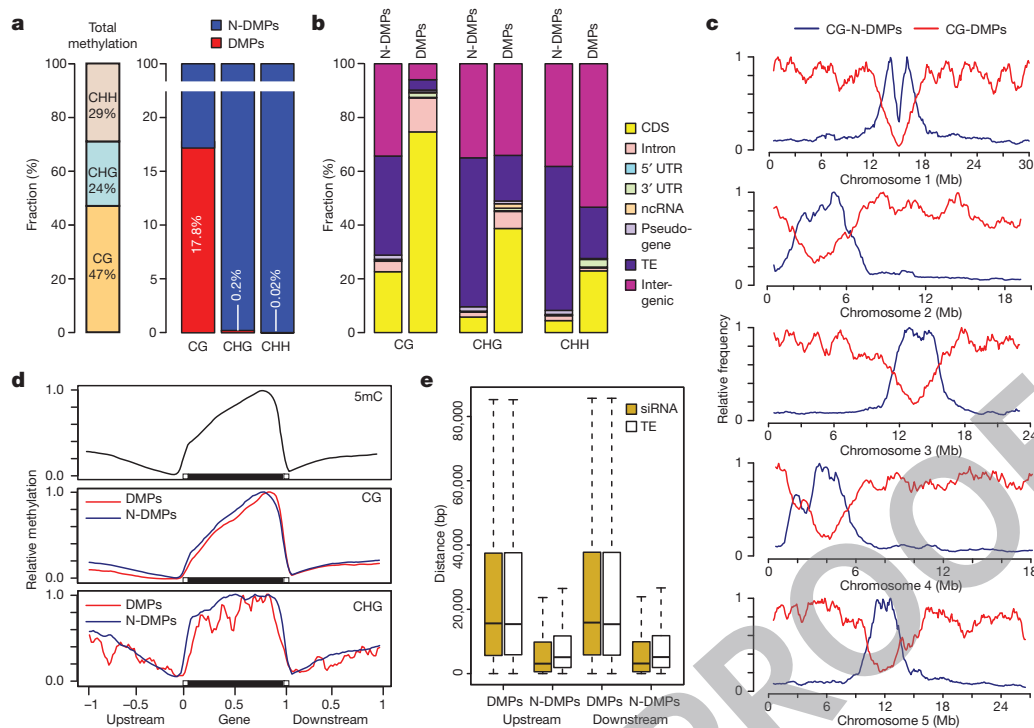


**Figure 1 | Genome-wide distribution of methylation polymorphisms.**

**a**, Contribution of CG, CHH and CHG sites to total and differential cytosine methylation. 32.8% of all CG, 15.7% of CHG and 4.6% of CHH sites, adding up to 10.8% of all cytosines, showed evidence of methylation. **b**, Distribution of DMPs and N-DMPs according to local annotation. CDS, coding sequence; ncRNA, non-coding RNA; TE, transposable element. **c**, Distribution of CG-N-DMPs and CG-DMPs along each chromosome. Data were normalized to the

much more stable than CG methylation of protein-coding genes, consistent with DNA methylation being more important for controlling the activity of transposable element compared to the latter<sup>14,17,20,21</sup>. This also agrees with a report that genic methylation is much more variable between wild strains of *A. thaliana* than methylation of transposable elements<sup>3</sup>.

Hierarchical clustering based on DMPs grouped siblings as well as 3rd and 31st generation lines together. An arbitrary selection of methylated positions, which included about 6% DMPs, produced a similar pattern; however, with N-DMPs only, clusters became much more random (Fig. 2a). These observations indicate that our DMPs capture most of the methylation differences between lines. We next calculated the pairwise distance between strains based on DMPs (Fig. 2b). Correlation was highest between the two 3rd generation strains, and each individual of the 31st generation was more similar to these two lines, from which they were separated by 34 generations, than to the other lines from the 31st generation, from which they had diverged for 62 generations. Taken together, we conclude that whole-genome methylation patterns are largely stable and therefore heritable in *A. thaliana*, but that differences in methylation status accumulate gradually, similar to genetic mutations.

One strain, 69, was exceptional and had 40% more DMPs in comparison with the 3rd generation than the other 31st generation lines (Fig. 2b). To determine whether this strain might have a defect in the methylation machinery, we sequenced its genome with more and longer reads compared to our previous analysis<sup>7</sup>. We found a non-synonymous change in *MATERNAL EFFECT EMBRYO ARREST 57* (*MEE57*), which encodes a protein related to METHYLTRANSFERASE 1 (MET1) (Supplementary Fig. 7). *MEE57* has been reported as essential for endosperm development<sup>22</sup>, although several *A. thaliana* strains lack functional *MEE57* copies<sup>23</sup>. Thus, whether the *MEE57* mutation contributes to the increased DMP number in line 69 remains unclear. The fact that

the siblings of this line were as similar to each other as other sibling pairs (Fig. 2a) argues against a generally increased epimutation rate. Compared to genetic mutations, the frequency of epimutations at single cytosine residues was many orders of magnitude higher, with an average of close to 30,000 DMPs in the analysed sequence space, compared with less than 30 DNA sequence mutations per strain<sup>7</sup>. Thirty-two per cent of DMPs between generations 3 and 31 occurred more than once, and 13% more than twice (Fig. 2c). If DMPs arose randomly, we would expect less than 1% of recurrent events. That we observe many more indicates that certain positions are particularly prone to increases or decreases in methylation rate. To investigate directly how many DMPs emerge from one generation to the next, we analysed the 32nd generation of lines 39 and 49. These individuals were progeny of siblings of the individuals interrogated in the 31st generation, and shared changes in the 32nd generation should reflect differences that arose between the 30th and 31st generation. We found on average over 3,300 between-generation DMPs. This is in the same range as DMPs between siblings (on average, about 5,000), but more than we would have expected from the 30,000 that had accumulated between the 3rd and each of the 31st generation lines. One explanation is that frequent transgenerational changes in methylation status occur at a limited number of sites, and that only a fraction of new DMPs is maintained over the longer term. This is corroborated by the observation that more than two-thirds of DMPs distinguishing the 32nd from the 31st generation in lines 39 and 49 had already been found in other 31st generation individuals.

the siblings of this line were as similar to each other as other sibling pairs (Fig. 2a) argues against a generally increased epimutation rate.

Compared to genetic mutations, the frequency of epimutations at single cytosine residues was many orders of magnitude higher, with an average of close to 30,000 DMPs in the analysed sequence space, compared with less than 30 DNA sequence mutations per strain<sup>7</sup>. Thirty-two per cent of DMPs between generations 3 and 31 occurred more than once, and 13% more than twice (Fig. 2c). If DMPs arose randomly, we would expect less than 1% of recurrent events. That we observe many more indicates that certain positions are particularly prone to increases or decreases in methylation rate. To investigate directly how many DMPs emerge from one generation to the next, we analysed the 32nd generation of lines 39 and 49. These individuals were progeny of siblings of the individuals interrogated in the 31st generation, and shared changes in the 32nd generation should reflect differences that arose between the 30th and 31st generation. We found on average over 3,300 between-generation DMPs. This is in the same range as DMPs between siblings (on average, about 5,000), but more than we would have expected from the 30,000 that had accumulated between the 3rd and each of the 31st generation lines. One explanation is that frequent transgenerational changes in methylation status occur at a limited number of sites, and that only a fraction of new DMPs is maintained over the longer term. This is corroborated by the observation that more than two-thirds of DMPs distinguishing the 32nd from the 31st generation in lines 39 and 49 had already been found in other 31st generation individuals.

DNA methylation is known to occur nonrandomly, and to cluster in specific segments of the genome<sup>3,17,24</sup>. We identified 249 differentially methylated regions (DMRs) that were at least 50 bp long (median 100 bp, maximum 650 bp) (Supplementary Table 2 and Supplementary Methods). Although probably a conservative estimate, the number of DMRs per line is in the same range as the DNA sequence mutations,



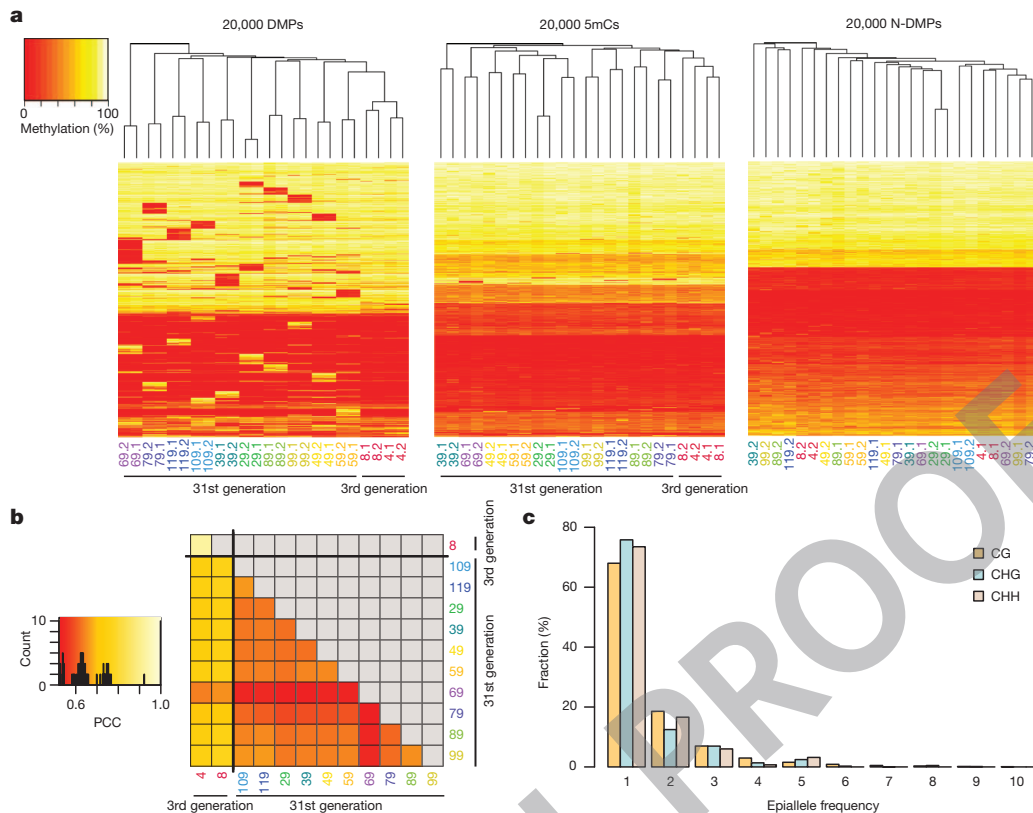


**Figure 2 | Epigenetic diversity in the analysed population.** **a**, Hierarchical clustering based on 20,000 sites each, drawn randomly from DMPs identified in pairwise comparison between all strains, cytosines methylated in at least one of the analysed strains (including about 6% DMPs), or N-DMPs. **b**, Heat map representing pairwise Pearson's correlation coefficient (PCC) between

individuals, considering all 250,000 DMPs identified between all strains. PCCs between 3rd generation strains, 0.92; between 3rd and 31st generation, 0.63–0.77; between 31st generation lines, 0.52–0.66. The histogram on top of the colour key indicates counts of PCC bins. **c**, Epiallele frequency of DMPs in the 31st generation.

less than 30 per line<sup>7</sup>. As with CG-DMPs, DMRs preferentially localized to genes (Fig. 3a). DMRs did not overlap with known DNA mutations in these strains<sup>7</sup>. Similarly, structural variant discovery with established methods<sup>23,25</sup> did not reveal evidence for DMRs being due to gross DNA lesions. The frequency of DMRs along genes was similar to the overall distribution of methylated cytosines, and was reminiscent of the pattern of variation seen in wild strains of *A. thaliana*<sup>3</sup> (Supplementary Fig. 8). There were almost ten times as many DMRs in exons as in introns (Fig. 3a). Because exon-specific methylation may influence RNA splicing patterns<sup>26,27</sup>, this could also be a source of variation in gene activity. Hierarchical clustering according to DMRs separated early- and late-generation strains into distinct groups (Fig. 3b). Notably, if we consider the methylation status in the 3rd generation individuals as largely reflecting the ancestral pattern, similar fractions of DMRs had lost or gained methylation by the 31st generation (Fig. 3c).

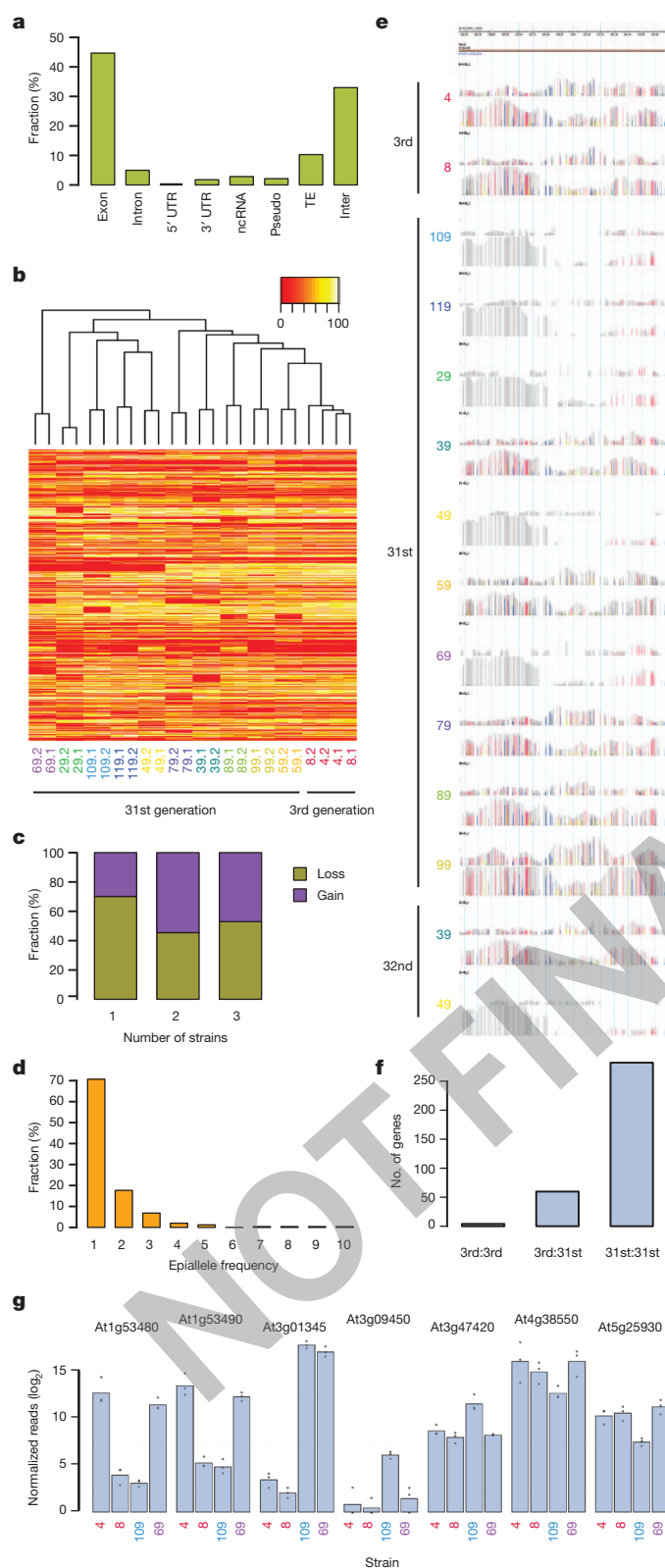
Similarly to DMPs, recurrent events constituted more than one-third of all DMRs, indicating that the affected genomic regions were privileged sites of change (Fig. 3d, e). In addition, comparison of generations 32 and 31 identified four short DMRs per line, with re-methylation of one segment that had become unmethylated in generation 31 (Supplementary Fig. 9). Together, these observations demonstrate that large changes in methylation, although rare, can occur even within a single generation.

Differences in promoter and genic DNA methylation can affect RNA levels<sup>16</sup>. We compared the transcriptomes of two randomly selected strains of the 31st generation with the 3rd generation strains by RNA-seq (Supplementary Fig. 10) and identified 320 differentially expressed genes in pairwise comparisons between strains (Fig. 3f and Supplementary Table 3). The two 31st generation lines were separated from each other by the most changes, and the two 3rd generation lines by the fewest. Seven differentially expressed genes overlapped with a

DMR in these strains (Fig. 3g). For the three genes with the highest difference in expression level and overlapping with the most conspicuous DMRs, we observed a negative correlation between DNA methylation and gene expression. The remaining four genes overlapped with much shorter DMRs and no correlation was apparent (Fig. 3e, g and Supplementary Fig. 11).

We have presented a high-resolution analysis of transgenerational variation in DNA methylation of *A. thaliana*. The molecular mechanisms underlying these changes remain elusive, but siRNAs, which map very often in or near transposable elements<sup>19</sup>, probably have a role in stabilizing DNA methylation, which is corroborated by our finding that DMPs tend to be farther from transposable elements and to be associated with lower local siRNA activity than N-DMPs. These observations indicate that the density and distribution of transposable elements, which can differ greatly even between closely related species<sup>28</sup>, affect epigenetic variation throughout the genome. In the material analysed here, there was no evidence for DNA mutations acting *in cis* as an important cause of DMRs, although we cannot rule out that a non-synonymous mutation in a *MET1* homologue might contribute to increased variation in DNA methylation *in trans* in one of the lines.

In contrast to the high frequency of single-nucleotide methylation polymorphisms, larger regions appear to change methylation status at a rate that is comparable to genetic mutations. On the basis of previous work<sup>7</sup>, it is conceivable that the emergence of DMRs requires specific structural features such as nearby repeats. Although DMRs are rare, we found evidence for DMRs affecting gene expression, indicating that natural, sequence-independent epialleles could potentially contribute to phenotypic diversity. There are subtle morphological differences between the mutation accumulation lines<sup>6</sup>, and quantitative genetic approaches could be used to link specific DNA mutations or DMRs with such traits. How many of the methylation differences found



between wild strains<sup>3</sup> are due to sequence-independent changes versus ones driven by transposable elements and other structural variants is an important area for further investigation. In addition, it will be necessary to follow DNA methylation not only under benign greenhouse conditions, but also in the much more variable and stressful natural environment.

Perhaps our most important finding is that the number of epimutations does not increase linearly with time, indicating that many are not

**Figure 3 | Differentially methylated regions (DMRs).** **a**, Distribution of DMRs according to local annotation. Inter, intergenic; pseudo, pseudogene. **b**, Hierarchical clustering of individuals from the 3rd and 31st generation based on methylated sites in DMRs, ranked according to their position in the genome. Note the shared methylation differences across lines, but strict pairing of siblings. **c**, Regions with losses and gains of methylation in 1, 2 or 3 strains in generation 31 compared to the 3rd generation strains. **d**, Epiallele frequency of DMRs. **e**, DMR at At3g01345 (Chr3:129,159–130,670) across all strains. Methylation on both strands is indicated for each strain. Colours indicate methylated reads (red, CG; blue, CHG; yellow, CHH). Grey indicates reads supporting non-methylation. For simplicity, only one sibling is shown per strain. **f**, Differentially expressed genes in comparisons between 3rd and 31st generation strains. **g**, Average RNA expression levels of the genes overlapping with the regions in **e** and in Supplementary Fig. 11. Dots indicate values of individual samples.

stably inherited over the long term. In addition to DMPs and DMRs that arose apparently independently in several strains, we even discovered a DMR that had become demethylated after 31 generations, but was re-methylated in the following generation. This suggests that DNA methylation in specific regions of the genome can fluctuate over relatively short timescales. Such sites can be considered as going through recurrent cycles of forward and reverse epimutation, which is very different from what is found at the level of the genome sequence, where reverse mutations are exceedingly rare. Importantly, reversion rates directly determine the ability of any type of allele to be subject to Darwinian selection. This needs to be taken into account when considering the potential of epialleles as a factor in evolution<sup>5</sup>.

## METHODS SUMMARY

**Methylome sequencing.** DNA was prepared from nuclei isolated from leaf tissue, bisulphite treated using a modification of a published protocol<sup>14</sup>, and paired-end sequenced on the Illumina GAIIx platform. After image analysis and base calling with the Illumina pipeline, reads were processed using SHORE<sup>7,29</sup>, and aligned to the Col-0 reference genome with GenomeMapper<sup>30</sup>, adapted to the analysis of bisulphite sequencing data. Bisulphite conversion rates, as determined from unmethylated chloroplast and spiked-in lambda phage DNA, were 99.72% to 99.84%.

**Analysis of methylated positions.** Single sites were classified as methylated or unmethylated by fitting a binomial model based on reads falsely reporting methylation on the unmethylated plastid genome. We only considered cytosine residues covered by at least three independent high-quality base calls in all strains. For the determination of significant differences in methylation across strains on single sites or regions, we used Fisher's exact test.

**Data visualization.** A Gbrowse instance of the methylation profiles is available at [http://gbrowse.weigelworld.org/fgb2/gbrowse/ath\\_methyl\\_ma](http://gbrowse.weigelworld.org/fgb2/gbrowse/ath_methyl_ma).

**Full Methods** and any associated references are available in the online version of the paper at [www.nature.com/nature](http://www.nature.com/nature).

Received 19 July; accepted 13 September 2011.

Published online 20 September 2011.

- Richards, E. J. Population epigenetics. *Curr. Opin. Genet. Dev.* **18**, 221–226 (2008).
- Paszkowski, J. & Grossniklaus, U. Selected aspects of transgenerational epigenetic inheritance and resetting in plants. *Curr. Opin. Plant Biol.* **14**, 195–203 (2011).
- Vaughn, M. W. *et al.* Epigenetic natural variation in *Arabidopsis thaliana*. *PLoS Biol.* **5**, e174 (2007).
- Rangwala, S. H. *et al.* Meiotically stable natural epialleles of Sadhu, a novel *Arabidopsis* retroposon. *PLoS Genet.* **2**, e36 (2006).
- Slatkin, M. Epigenetic inheritance and the missing heritability problem. *Genetics* **182**, 845–850 (2009).
- Shaw, R. G., Byers, D. L. & Darms, E. Spontaneous mutational effects on reproductive traits of *Arabidopsis thaliana*. *Genetics* **155**, 369–378 (2000).
- Ossowski, S. *et al.* The rate and molecular spectrum of spontaneous mutations in *Arabidopsis thaliana*. *Science* **327**, 92–94 (2010).
- Law, J. A. & Jacobsen, S. E. Establishing, maintaining and modifying DNA methylation patterns in plants and animals. *Nature Rev. Genet.* **11**, 204–220 (2010).
- Teixeira, F. K. *et al.* A role for RNAi in the selective correction of DNA methylation defects. *Science* **323**, 1600–1604 (2009).
- Reinders, J. *et al.* Compromised stability of DNA methylation and transposon immobilization in mosaic *Arabidopsis* epigenomes. *Genes Dev.* **23**, 939–950 (2009).
- Widman, N., Jacobsen, S. E. & Pellegrini, M. Determining the conservation of DNA methylation in *Arabidopsis*. *Epigenetics* **4**, 119–124 (2009).
- Lynch, M. Evolution of the mutation rate. *Trends Genet.* **26**, 345–352 (2010).

13. Cokus, S. J. *et al.* Shotgun bisulphite sequencing of the *Arabidopsis* genome reveals DNA methylation patterning. *Nature* **452**, 215–219 (2008).
14. Lister, R. *et al.* Highly integrated single-base resolution maps of the epigenome in *Arabidopsis*. *Cell* **133**, 523–536 (2008).
15. Zhang, Y. *et al.* QDMR: a quantitative method for identification of differentially methylated regions by entropy. *Nucleic Acids Res.* **39**, e58 (2011).
16. Zilberman, D., Gehring, M., Tran, R. K., Ballinger, T. & Henikoff, S. Genome-wide analysis of *Arabidopsis thaliana* DNA methylation uncovers an interdependence between methylation and transcription. *Nature Genet.* **39**, 61–69 (2007).
17. Zhang, X. *et al.* Genome-wide high-resolution mapping and functional analysis of DNA methylation in *Arabidopsis*. *Cell* **126**, 1189–1201 (2006).
18. Fahlgren, N. *et al.* MicroRNA gene evolution in *Arabidopsis lyrata* and *Arabidopsis thaliana*. *Plant Cell* **22**, 1074–1089 (2010).
19. Kasschau, K. D. *et al.* Genome-wide profiling and analysis of *Arabidopsis* siRNAs. *PLoS Biol.* **5**, e57 (2007).
20. Slotkin, R. K. *et al.* Epigenetic reprogramming and small RNA silencing of transposable elements in pollen. *Cell* **136**, 461–472 (2009).
21. Lisch, D. Epigenetic regulation of transposable elements in plants. *Annu. Rev. Plant Biol.* **60**, 43–66 (2009).
22. Pagnussat, G. C. *et al.* Genetic and molecular identification of genes required for female gametophyte development and function in *Arabidopsis*. *Development* **132**, 603–614 (2005).
23. Cao, J. *et al.* Whole-genome sequencing of multiple *Arabidopsis thaliana* populations. *Nature Genet.* doi:10.1038/ng.911 (28 August 2011).
24. Tran, R. K. *et al.* DNA methylation profiling identifies CG methylation clusters in *Arabidopsis* genes. *Curr. Biol.* **15**, 154–159 (2005).
25. Mirouze, M. *et al.* Selective epigenetic control of retrotransposition in *Arabidopsis*. *Nature* **461**, 427–430 (2009).
26. Chodavarapu, R. K. *et al.* Relationship between nucleosome positioning and DNA methylation. *Nature* **466**, 388–392 (2010).
27. Laurent, L. *et al.* Dynamic changes in the human methylome during differentiation. *Genome Res.* **20**, 320–331 (2010).
28. Hollister, J. D. *et al.* Transposable elements and small RNAs contribute to gene expression divergence between *Arabidopsis thaliana* and *Arabidopsis lyrata*. *Proc. Natl Acad. Sci. USA* **108**, 2322–2327 (2011).
29. Ossowski, S. *et al.* Sequencing of natural strains of *Arabidopsis thaliana* with short reads. *Genome Res.* **18**, 2024–2033 (2008).
30. Schneeberger, K. *et al.* Simultaneous alignment of short reads against multiple genomes. *Genome Biol.* **10**, R98 (2009).

**Supplementary Information** is linked to the online version of the paper at [www.nature.com/nature](http://www.nature.com/nature).

**Acknowledgements** We are grateful to R. Shaw for providing seeds of the mutation accumulation lines. We thank C. Lanz for help with Illumina sequencing, J. Fitz for help with the Gbrowse implementation, K. Schneeberger for help with DNA mutation analysis, D. Zilberman for providing bisulphite sequencing protocols, and R. Clark, M. Pellegrini, R. Neher and J. Paszkowski for discussion. This work was supported by an HFSP Long-Term Fellowship (D.K.), the Volkswagen Foundation (O.S.), FP7 Collaborative Project AENEAS (contract KBBE-2009-226477), a Gottfried Wilhelm Leibniz Award of the DFG, and the Max Planck Society (D.W.).

**Author Contributions** C.B., J.H. and D.W. conceived the study; C.B. performed the experiments; C.B., J.H., J.M., D.K. and O.S. analysed the data; K.B. provided advice on statistical analysis; and C.B. and D.W. wrote the paper with contributions from all authors.

**Author Information** DNA sequencing data are deposited in the European Nucleotide Archive (<http://www.ebi.ac.uk/ena/data/view/ERP000902>) under accession number ERP000902. Reprints and permissions information is available at [www.nature.com/reprints](http://www.nature.com/reprints). The authors declare no competing financial interests. Readers are welcome to comment on the online version of this article at [www.nature.com/nature](http://www.nature.com/nature). Correspondence and requests for materials should be addressed to D.W. ([weigel@weigelworld.org](mailto:weigel@weigelworld.org)).



## METHODS

**Plant growth and material.** Seeds were derived from *Arabidopsis thaliana* Columbia-0 lines in generation 3 (lines 4 and 8), generation 31 (lines 29, 39, 49, 59, 69, 79, 89, 99, 109 and 119) and generation 32 (lines 39 and 49), counting from the founders, as described by Shaw and colleagues<sup>6</sup> (Supplementary Fig. 1). Plants were grown on soil under long-day conditions (23 °C, 16 h light, 8 h dark) after seeds had been stratified in 150 nM GA-supplemented water at 4 °C for 6 days. Siblings were grown independently at different time points. Positions of the pots were randomized.

**Nucleic acid extraction.** DNA was extracted from rosettes of individual 21-day-old plants. Plant material was flash-frozen in liquid nitrogen and ground in a mortar. The ground tissue was re-suspended in nuclei extraction buffer (10 mM Tris-HCl pH 9.5, 10 mM EDTA, 100 mM KCl, 0.5 M sucrose, 0.1 mM spermine, 0.4 mM spermidine, 0.1%  $\beta$ -mercaptoethanol). After cell lysis in nuclei extraction buffer with 10% Triton X-100, nuclei were pelleted by centrifugation at 2,000g for 120 s. Genomic DNA was extracted using the Qiagen Plant DNeasy kit (Qiagen). Total RNA was extracted from rosette leaves of individual plants using the Trizol (Invitrogen) method according to the manufacturer's instructions. Residual DNA was eliminated by DNase I (Thermo Fisher Scientific) treatment.

**Library preparation.** Preparation of DNA libraries for genomic sequencing was done using the NEBNext DNA Sample Prep Reagent Set 1 (New England Biolabs), following the Illumina Genomic Sample Prep Guide (Illumina). 500–1,000 ng genomic DNA was fragmented to 300 bp average size with a Covaris S2 instrument using the following settings for 120 s in frequency sweeping mode: intensity 5, duty cycle 10%, 200 cycles per burst. DNA was purified on Qiaquick PCR purification columns. Preparation of DNA libraries for bisulphite sequencing was adapted from ref. 14. Input DNA was fragmented as described above. Libraries were constructed using the NEBNext DNA Sample Prep Reagent Set 1 (New England Biolabs) according to the Illumina Genomic Sample Prep Guide with the following modifications. We used the Illumina Early Access Methylation Adapter Oligo Mix (catalogue number ME-100-0010). After size selection, the non-methylated cytosine residues were converted to uracil using the EpiTect Plus DNA Bisulfite kit (Qiagen) according to the manufacturer's guidelines. For higher conversion efficiency the bisulphite incubation was repeated. Library enrichment was performed with Pfu Cx HotStart Polymerase (Agilent) and 18 PCR cycles. Libraries for RNA sequencing were prepared from 4  $\mu$ g of total RNA using the Illumina Truseq RNA sample prep kit B according to the manufacturer's protocol.

**Sequencing.** All sequencing was performed on an Illumina GAIIx instrument. Genomic and bisulphite-converted libraries were sequenced with 2  $\times$  101-bp paired-end reads. For bisulphite sequencing, conventional *A. thaliana* DNA genomic libraries were analysed in control lanes. Transcriptome libraries were sequenced with 101-bp single end reads, with three libraries with different indexing adapters pooled in one lane; no control lane was used. For image analysis and base calling, we used the Illumina OLB software version 1.8.

**Processing and alignment of bisulphite-treated reads.** The SHORE pipeline<sup>29</sup> was used to trim and quality-filter the reads. Its default parameters were applied for the filtering step: reads with more than 2 (or 5) bases in the first 12 (or 25) positions with a quality score less than 3 were discarded. Reads were trimmed to the right-most occurrence of two adjacent bases with quality values equal to or greater than 5. Trimmed reads shorter than 50 bases were discarded. The remaining high quality sequences (on average 82% of raw reads across the sequenced strains) were aligned against the *Arabidopsis thaliana* genome sequence version TAIR9 ([http://www.arabidopsis.org/portals/genAnnotation/gene\\_structural\\_annotation/annotation\\_data.jsp](http://www.arabidopsis.org/portals/genAnnotation/gene_structural_annotation/annotation_data.jsp)) using a modified version of the mapping tool GenomeMapper<sup>30</sup> that supports the alignment of bisulphite converted reads. Bisulphite converts non-methylated cytosines into uracils, which are propagated as adenine-thymine base pairs after PCR amplification. GenomeMapper tolerates asymmetrical T-to-C or A-to-G mismatches (read base against reference base) and can distinguish between reads from the bisulphite-converted strand of a DNA fragment and sequences from its complementary amplified strand, if the reads have been obtained by paired-end sequencing. Only the read from the strand with converted Cs is informative about the methylation status of the underlying cytosine site. We allowed for up to 10% single-base-pair substitutions along the read length in the alignment process for each read to retain most coverage. GenomeMapper reports all alignments with the least amount of mismatches for each read. However, only reads mapping uniquely to a single position were used for this study. Furthermore, all but one read were removed from further analysis if their 5' ends aligned to the same genomic position, to account for amplification biases. A paired-end correction method<sup>23</sup> was used to discard repetitive reads by comparing the distance between reads and their partner to the average distance between all read pairs. Reads with abnormal distances were removed if there was at least one other alignment of this read in a concordant distance to its partner. Finally, read counts on all cytosine sites were obtained with SHORE. The 'scoring matrix approach' of SHORE<sup>23</sup> assigns a score to each site by

testing against different sequence and alignment related features. The criteria and complete scoring matrix can be found in Supplementary Table 4. For comparisons across lines, cytosines were accepted if at most one intermediate penalty on its score was applicable to at least one strain (score  $\geq 32$ ). In this case, the threshold for the other strains was lowered, accepting at most one high penalty (score  $\geq 15$ ). In this way, information from other strains is used to assess sites from the focal strain under the assumption of mostly conserved methylation patterns, allowing the analysis of additional sites. The methylation statistics on each single strain assumed a quality score of 25 or higher, which means no more than two intermediate penalties.

**Determination of methylated sites.** Sequencing errors, noise and imperfections of the bisulphite conversion contribute to the occurrence of sites that appear to be weakly methylated. Reads mapping against the non-methylated chloroplast sequence allow for objective estimation of the effective background rate of false-positive methylation detection. For this purpose, we fitted an independent binomial model to the relative proportions of converted and unconverted reads that cover cytosines in the chloroplasts. We estimated the binomial rate of false-positive methylation from the maximum likelihood estimate, separately for each library and for different bins of total read coverage:

$$= \arg \max_s \Pi \text{Binomial}(\bar{n}_s, (n_s + \bar{n}_s) | r).$$

Here,  $n_s$  and  $\bar{n}_s$  denote the number of converted and unconverted reads from the considered cytosine sites. Supplementary Fig. 12a shows the obtained background methylation rate for a single strain, line 30-39, as a function of the total read coverage per site. The overall false methylation rate when combining read data across the range of read coverage was 0.22%, which deviates significantly from higher error estimates when considering low-coverage regions in isolation. To account for the variability in error rates in the downstream analyses, we used specific error models for each strain and for read-coverage bins of multiples of fivefold, yielding error rates between 0.2% and 5.0% (Supplementary Fig. 12b). For coverage bins with too few sites for robust statistical estimation ( $< 50$ ), we imputed the false methylation rate from the closest sufficiently populated coverage bin. Given the estimated rates for false methylation, we carried out a genome-wide test for significant methylation of cytosines. For each site, we calculated the  $P$  value under the background model. We then used Storey's method<sup>31</sup>, an extension of the Benjamini-Hochberg stepdown procedure, to assess genome-wide significance using  $q$  values. At a joint false discovery rate (FDR) of 5% we found between 2,316,966 and 3,458,949 methylated sites in each strain (Supplementary Table 1). When reducing FDR to 0.1%, we still retained almost 85% of the methylated sites, showing that the number of sites with weak methylation evidence was low. For analysis of methylated sites reported in this study, an FDR of 5% was deemed to be acceptable.

**Identification of differentially methylated positions.** From the 13.9 million cytosines for which we had at least three independent high-quality reads in each strain, we selected sites that showed significant methylation in at least one strain, resulting in 3,067,017 positions. Sites with statistically significant methylation differences were identified with Fisher's exact test.  $P$  values from individual tests per site were combined into single  $P$  values via conservative Bonferroni correction. Genome-wide FDRs were then estimated using Storey's method<sup>31</sup>. To limit false-positive DMPs, we first identified 69,583 DMPs between siblings at a relaxed FDR of 10%. These sites were excluded as were 8,893 DMPs distinguishing the two 3rd generation strains. This left 2,988,541 positions as the final set to test for differential methylation between generations. Twenty pairwise tests of each of the ten 31st generation strains against both 3rd generation strains were conducted on sites consistently methylated between 31st generation siblings and in the 3rd generation. At an FDR of 5%, this yielded 186,248 DMPs. DMP allele frequency was obtained by progressively removing the strain with the lowest  $q$  value and correcting the remaining  $P$  values for multiple testing by the methods described above.

We applied the same strategy to identify DMPs that differed either between the 31st and 3rd generation, or between 31st generation strains. Count data from replicates were combined for each site, followed by pairwise Fisher's exact tests between all combinations of strains (66 tests). We estimated  $P$  values for at least one differential pair using a Bonferroni correction, followed by Storey's method<sup>31</sup> to assess genome-wide significance. At a joint FDR of 5%, this identified 253,546 DMPs across all 12 strains.

**Assessing statistical power.** Two main factors influence the power to detect methylation differences: the number of statistical tests and local read coverage. To assess the impact of multiple testing, we applied the approach described above to all sites with at least threefold coverage in at least 12 of 24 individuals examined. Of 25.3 million such positions, 4,547,568 were found to be methylated in at least one of the lines, compared to 3,067,017 out of 13.9 million positions when considering only sites with complete information. The number of sites assessed as methylated thus increased roughly linearly with the number of tested sites, as did

the number of differentially methylated positions. Similarly, the fraction of DMPs shared in more than one 31st generation strain, ~31%, was very similar to the ~32% found among sites with complete information. We conclude that our method is largely insensitive to the number of tests performed.

To assess the effect of read coverage, we determined how many DMPs could be identified after subsampling at 25%, 50% and 75% of total coverage. We identified almost twice as many DMPs with 50% compared to 25% coverage, but only 13% additional DMPs were identified when increasing coverage from 75% to 100% (Supplementary Fig. 13). Although not yet asymptotic, we estimate that the false-negative rate is well below 50%, and most likely closer to 10%.

**Identification of differentially methylated regions.** The ~186,000 DMPs distinguishing 31st from both 3rd generation lines were consolidated into regions of adjacent DMPs for each strain, with a maximum distance of 50 bp between DMPs. We then used Fisher's exact test on the sum of methylated and unmethylated reads in both siblings, averaged across positions within the region. Resulting *P* values were corrected with Storey's method<sup>31</sup> and an FDR of 5% was accepted. Statistically significant regions from different strains were merged if they overlapped by at least 20% of their combined length and if the methylation change was in the same direction compared to the 3rd generation lines. Short regions containing only a small number of strongly differential sites were excluded by requiring DMRs to have a minimum length of 50 bp and to contain at least ten methylated positions and at least five DMPs.

**Mapping of DMPs, N-DMPs and DMRs to genomic elements.** We used the TAIR10 annotation ([http://www.arabidopsis.org/portals/genAnnotation/gene\\_structural\\_annotation/annotation\\_data.jsp](http://www.arabidopsis.org/portals/genAnnotation/gene_structural_annotation/annotation_data.jsp)) to determine overlap of genes, pseudogenes and transposable elements with methylated positions. We defined intergenic regions as regions that did not correspond to any annotated feature. A DMR was considered mapping to a particular genomic element if it overlapped with such an element for more than 20% of its length.

**Assessing the distance to the closest siRNA or transposable element.** We determined the distance between a methylated position and the closest upstream and downstream siRNA using a published data set for *A. thaliana* aerial tissue<sup>18</sup> (NCBI GEO accession number GSM518432). For transposable elements, we used

the TAIR10 annotation. Statistical significance was tested with a two-sided, unpaired Student's *t*-test on the measured distances. Pericentromeric regions were defined as described<sup>23</sup>.

**Analysis of gene expression.** DNA sequences resulting from RNA library preparation were barcode-sorted and quality filtered in SHORE<sup>29</sup>, and aligned using BWA<sup>32</sup> to the TAIR10 gene annotation. Reads were filtered for duplicates and required to have a mapping quality of at least 37. The remaining mappings were used to generate gene-level counts for expression analysis. We only considered genes for which the total counts in all samples combined exceeded 30. Between-sample expression correlations and strain-distribution plots were used for quality control to identify poor samples, and pairwise comparisons of expression were performed using the DESeq package<sup>33</sup> implemented in R. Differentially expressed genes were identified by a combination of per-gene variance ( $P \leq 0.01$ , with Benjamini and Yekutieli correction<sup>34</sup>) and common variance ( $\geq 2\times$  change). Density of genes without expression support were plotted along chromosomes in sliding windows considering only genes with at least 50 methylated or unmethylated calls. Windows of gene methylation were calculated for entire gene bodies as the fraction of methylated positions (methylated in any sample) divided by the total number of called positions. Very similar results were obtained considering sites methylated in all samples. Data were visualized with the ggplots package in R<sup>35</sup>.

**Data visualization.** A Gbrowse instance of the methylation profiles is available at [http://gbrowse.weigelworld.org/fgb2/gbrowse/ath\\_methyl\\_ma](http://gbrowse.weigelworld.org/fgb2/gbrowse/ath_methyl_ma).

31. Storey, J. D. & Tibshirani, R. Statistical significance for genomewide studies. *Proc. Natl Acad. Sci. USA* **100**, 9440–9445 (2003).
32. Li, H. & Durbin, R. Fast and accurate short read alignment with Burrows-Wheeler transform. *Bioinformatics* **25**, 1754–1760 (2009).
33. Robinson, M. D., McCarthy, D. J. & Smyth, G. K. edgeR: a Bioconductor package for differential expression analysis of digital gene expression data. *Bioinformatics* **26**, 139–140 (2010).
34. Benjamini, Y. & Yekutieli, D. The control of the false discovery rate in multiple testing under dependency. *Ann. Stat.* **29**, 1165–1188 (2001).
35. Wickham, H. *ggplot2: Elegant Graphics for Data Analysis* (Springer, 2009).